



UNIVERSITÀ
DEGLI STUDI
DI PADOVA

UNIVERSITÀ DEGLI STUDI DI PADOVA

**DIPARTIMENTO DI TECNICA E GESTIONE
DEI SISTEMI INDUSTRIALI**

**SCUOLA DI DOTTORATO DI RICERCA IN
INGEGNERIA MECCATRONICA E DELL'INNOVAZIONE
MECCANICA DEL PRODOTTO**

CICLO XXVIII

**LOCAL APPROACHES APPLIED TO
FRACTURE AND FATIGUE PROBLEMS**

Direttore della Scuola: Ch.mo Prof. Alessandro Persona

Supervisore: Ch.mo Prof. Filippo Berto

Dottorando: Alberto Campagnolo

*Quella del mistero
è la migliore esperienza
che possiamo avere.
È l'emozione fondamentale
che veglia la culla della vera arte
e della vera scienza.*

Albert Einstein

*Ai miei genitori e mio fratello Luca,
sempre vicini in ogni traguardo della mia vita*

*A Giulia, che con gioia e amore
ha illuminato la mia vita*

Contents

<i>Abstract</i>	I
<i>Sommario</i>	V
I Introduction to local approaches	1
1.1 Introduction	3
1.2 Sharp V-notches	3
1.2.1 Local stress fields and Notch Stress Intensity Factors	3
1.2.2 Averaged Strain Energy Density approach	9
1.2.3 Peak Stress Method	22
1.3 Blunt V-notches	27
1.3.1 Local stress fields and Generalised Notch Stress Intensity Factors	27
1.3.2 Averaged Strain Energy Density approach	30
References	33

II	Brittle fracture under mixed mode static loading	37
2.1	Brittle fracture of blunt notched components made of PMMA under mixed mode I+II loading	39
2.1.1	Introduction	40
2.1.2	Experiments	43
2.1.3	Fracture criterion based on the Strain Energy Density averaged over a control volume	54
2.1.4	SED approach in fracture analysis of the tested PMMA specimens	60
2.1.5	Discussion	73
2.2	Brittle Fracture of blunt notched components made of isostatic graphite under mixed mode I+III loading	75
2.2.1	Introduction	76
2.2.2	Fracture Experiments	78
2.2.3	Strain Energy Density averaged over a control volume: the fracture criterion	88
2.2.4	SED approach in fracture analysis of the tested graphite specimens	90
2.2.5	Discussion	102
2.3	Brittle fracture of PMMA cracked components under mixed mode I+III loading	103
2.3.1	Introduction	104
2.3.2	Mixed mode fracture experiments	105
2.3.3	Strain Energy Density averaged over a control volume: the fracture criterion	112
2.3.5	Discussion	117
	References	119

III	Multiaxial fatigue loadings	129
3.1	Notched components made of Ti-6Al-4V under multiaxial loading	131
3.1.1	Introduction	132
3.1.2	Material properties and geometry of the specimens	135
3.1.3	Results from the fatigue tests	139
3.1.4	Fracture surface analysis	146
3.1.5	A synthesis in terms of linear elastic SED averaged over a control volume	149
3.1.6	Discussion	159
3.2	Fatigue strength of welded joints – Industrial case study: steel rollers	161
3.2.1	Introduction	162
3.2.2	Approach based on the local SED: analytical preliminaries	167
3.2.3	Modelling of the rollers and evaluation of the local SED	172
3.2.4	Fatigue strength in terms of strain energy density averaged in a finite size volume	188
3.2.5	Discussion	191
3.3	Sharp V-notches under multiaxial fatigue: analytical investigation of the phase angle effect	193
3.3.1	Introduction	194
3.3.2	Analytical frame	198
3.3.3	Results and discussions	207
3.3.4	Some experimental evidences	215
3.3.5	Discussion	218
	References	221

IV	Three-dimensional effects	231
4.1	Three-dimensional effects on cracked components	233
4.1.1	Introduction	234
4.1.2	Finite element modelling	242
4.1.3	Results	246
4.1.4	Discussion	266
4.1.5	Strain energy density through the thickness	268
4.1.6	Final discussion	271
4.2	Three-dimensional effects on cracked components: influence of boundary conditions	273
4.2.1	Introduction	274
4.2.2	Analytical framework: stress and displacement fields under Mode III	276
4.2.3	Strain energy density (SED) under Mode III	279
4.2.4	Finite element analysis of three-dimensional cracked discs	282
4.2.5	Results	286
4.2.6	Discussion	303
4.3	Three-dimensional effects on notched components under cyclic plasticity	305
4.3.1	Introduction	306
4.3.2	Analytical frame	311
4.3.3	Case studies	316
4.3.4	Incremental cyclic plasticity procedure	326
4.3.5	Finite Element modelling	327
4.3.6	Material parameters	328
4.3.7	Results and discussions	332
4.3.8	A link between cyclic plasticity and the	350

	averaged strain energy density criterion	
	4.3.9 Discussion	357
	References	359
V	Comparison among fracture criteria for sharp V-notches	369
5.1	Comparison among energy-based criteria for fracture assessment of sharp V-notched components under Mode I loading	371
5.1.1	Introduction	372
5.1.2	Analytical frame	376
5.1.3	Failure criteria for sharp V-notches	381
5.1.4	Analytical comparison	390
5.1.5	Experimental validation	393
5.1.6	Discussion	398
5.2	Comparison among energy-based criteria for fracture assessment of sharp V-notched components under Mode II loading	401
5.2.1	Introduction	402
5.2.2	Analytical frame	406
5.2.3	Failure criteria for sharp V-notches under pure Mode II loading	411
5.2.4	Analytical comparison	423
5.2.5	Experimental validation	426
5.2.6	Discussion	430
	References	431

VI	Link between Peak Stress Method (PSM) and Strain Energy Density (SED)	437
6.1	Link between the Peak Stress Method (PSM) and the averaged Strain Energy Density (SED): long cracks under mixed mode (I+II) loading	439
6.1.1	Introduction	441
6.1.2	The Peak Stress Method for pure modes of loading	448
6.1.3	The Peak Stress Method for mixed mode (I+II) loading	450
6.1.4	The peak stress approach to estimate the SED parameter for mixed mode (I+II) loading	453
6.1.5	An example of a practical application	468
6.1.6	Discussion	472
6.2	Link between the Peak Stress Method (PSM) and the averaged Strain Energy Density (SED): short cracks under mixed mode (I+II) loading with inclusion of T-stress contribution	475
6.2.1	Introduction	477
6.2.2	The Peak Stress Method to rapidly evaluate K_I and K_{II}	486
6.2.3	A FE-based technique to evaluate rapidly the T-stress	495
6.2.4	The nodal stress approach to rapidly estimate the averaged SED with inclusion of the T-stress	501
6.2.5	Discussion	513
6.3	Link between the PSM and the averaged SED - example of practical application: fatigue strength	515

	assessment of butt welded joints under mode I loading	
6.3.1	Introduction	517
6.3.2	Joint geometries and FE stress analyses according to the Peak Stress Method	525
6.3.3	Assessment of weld toe and weld root fatigue failures	534
6.3.4	Discussion	536
6.4	Link between the Peak Stress Method (PSM) and the averaged Strain Energy Density (SED): cracked bars under mixed mode (I+III) loading	539
6.4.1	Introduction	541
6.4.2	The peak stress approach to estimate the averaged SED under mixed mode I+III loading	551
6.4.3	Range of applicability of the SED expression (6.4.4)	554
6.4.4	Validation of the peak stress method to estimate the averaged SED under mixed mode (I+III) loading	558
6.4.5	The peak stress approach coarsening the mesh further	561
6.4.6	Discussion	561
6.5	Link between the PSM and the averaged SED - example of practical application: fatigue strength assessment of tube-to-flange steel welded joints under mode III loading	563
6.5.1	Introduction	565
6.5.2	Peak Stress Method for mode III loading	570
6.5.3	Defining a SED-based design stress using the PSM	573
6.5.4	Torsional fatigue tests on tube-to-flange steel	575

Contents

welded joints	
6.5.5 Fatigue test results in terms of nominal stress	581
6.5.6 Analysis of experimental data using the equivalent peak stress	582
6.5.7 Discussion	586
References	589
Conclusions	597
Bibliography	599

Abstract

Intentionally designed or accidentally caused, notches, cracks or defects are inevitably present in engineering components and can induce high stress gradients when a far field loading is applied. Then, structural strength assessments are often based on the local stress and strain state in the close neighbourhood of the stress raisers.

The present PhD thesis, focused on the application of local approaches to fracture and fatigue problems, is divided into six Chapters corresponding to different research topics, all related to new applications of the averaged strain energy density criterion and other widely employed local approaches to notched or cracked structural components.

In the *first Chapter*, the adopted local approaches, namely the Notch Stress Intensity Factor-based approach (NSIF), the averaged Strain Energy Density (SED) criterion and the Peak Stress Method (PSM), are briefly introduced and described along with their theoretical frameworks.

The *second Chapter* deals with brittle fracture under mixed mode static loading. A wide experimental campaign has been carried out on PMMA specimens weakened by blunt notches and subjected to in-plane mixed mode I+II loading, as well as on graphite specimens weakened by blunt notches and on PMMA cracked specimens subjected to out-of-plane mixed mode I+III loading. Then, all experimental results have been reanalysed by means of the SED approach obtaining a very good accuracy in the assessment of the static critical loads. In particular two different criterion formulations have been proposed to address the problem of out-of-plane mixed mode loading.

The *third Chapter* deals with multiaxial fatigue loadings. First, the fatigue strength of severely notched titanium grade 5 alloy, Ti-6Al-4V, has been investigated. The results of experimental tests under combined tension and torsion loading, both in-phase and out-of-phase, have been summarised in terms of the linear elastic SED. Then, the SED criterion has been applied for the first time to an industrial case study, that is the multiaxial fatigue strength assessment of steel

welded rollers produced by Rulmeca S.p.a with failures at the weld root. The investigation has been performed by means of 3D FE analyses and experimental tests. Finally, some remarks about the phase angle effect on sharp V-notched components under multiaxial fatigue have been drawn on the basis of a proposed analytical frame, based on the maximum value of the shear stress averaged over a fatigue cycle.

The *fourth Chapter* addresses the numerical study of 3D effects in notched and cracked components. Initially, the attention has been focused on coupled modes and on the effect of different boundary conditions in 3D cracked discs and plates subjected to nominal mode III or mode II loading. The intensity of the local through-the-thickness stress and strain state has been evaluated by means of the averaged SED, which allows to combine the influence of the applied mode with the induced fracture modes. Then, the presence of three-dimensional effects has been investigated both theoretically and numerically in blunt notched components under cyclic plasticity conditions. Two different approaches have been considered: the first one is an incremental procedure, which combines a material elastic-plastic model with an approximate method to estimate the elastic-plastic stress and strain components from the linear-elastic ones; the second approach, instead, is based on cyclic elastic-plastic FE analyses. The theoretical estimations have been compared with the numerical results considering several case studies under uniaxial and multiaxial cyclic loading. Finally a link between the elastic-plastic SED averaged over a control volume and the area inside the hysteresis loops at the notch tip has been derived.

The *fifth Chapter*, instead, is related to the comparison between different fracture criteria. The SED approach and that based on the Finite Fracture Mechanics (FFM) have been compared considering sharp V-notches under pure mode I or mode II loading. Dealing with mode II loading, a new expression of the control radius for SED evaluation has been successfully proposed. The criteria have been compared first analytically and then considering several experimental data taken from the literature and related to different brittle materials.

Finally the *sixth Chapter* address the link between the SED approach and the Peak Stress Method (PSM). First, cracks under in-plane mixed mode I+II loading

have been investigated. A method to rapidly calculate the averaged SED based on the peak stresses evaluated at the crack tip has been proposed for both long and short cracks. On the basis of the derived link, a practical application related to the fatigue strength assessment of aluminium and steel butt welded joints has been carried out. Then, also the case of cracks subjected to out-of-plane mixed mode I+III loading has been addressed. Also in this case, a method to rapidly evaluate the averaged SED based on the peak stresses at the crack tip has been proposed. The obtained link has been adopted in a structural problem related to the fatigue strength assessment of tube-to-flange steel welded joints under torsion loading.

Sommario

Variazioni geometriche, come intagli, cricche o difetti in generale, sono comunemente presenti nella maggior parte dei componenti meccanici e possono indurre elevati gradienti di tensione per effetto dei carichi esterni. La valutazione della resistenza strutturale dei componenti meccanici è perciò generalmente basata sullo stato di tensione e deformazione locale nelle adiacenze di tali variazioni geometriche.

La presente tesi di dottorato, focalizzata sull'applicazione di approcci locali per la previsione della resistenza statica ed a fatica, è divisa in sei Capitoli corrispondenti a diversi argomenti di ricerca, tutti relativi a nuove applicazioni del criterio basato sulla densità di energia di deformazione mediata (SED) e di altri importanti approcci locali a componenti strutturali intagliati o criccati.

Nel *primo Capitolo*, sono brevemente introdotti e descritti gli approcci locali adottati, cioè l'approccio basato sul Notch Stress Intensity Factor (NSIF), il criterio basato sulla densità di energia di deformazione mediata (SED) e il Peak Stress Method (PSM), assieme alle loro basi teorico-analitiche.

Il *secondo Capitolo* si occupa della frattura fragile sotto carichi statici di modo misto. Una campagna sperimentale è stata eseguita su provini in PMMA indeboliti da intagli blandi e soggetti a carichi di modo misto nel piano I+II, così come su provini in grafite indeboliti da intagli blandi e su provini in PMMA criccati soggetti a carichi di modo misto fuori piano I+III. In seguito, tutti i dati sperimentali sono stati rianalizzati per mezzo dell'approccio SED, ottenendo un'ottima accuratezza nella stima dei carichi critici statici. In particolare, per trattare in maniera più efficace il caso di carichi di modo misto fuori piano I+III sono state proposte due diverse formulazioni del criterio.

Il *terzo Capitolo* tratta il tema della fatica multiassiale. Inizialmente, è stata investigata la resistenza a fatica di una lega di titanio grado 5, Ti-6Al-4V, severamente intagliata. I risultati dei test sperimentali sotto carichi di trazione e torsione combinati, sia in fase che fuori fase, sono stati riassunti in termini di SED lineare elastico. In seguito, il criterio SED è stato applicato per la prima volta ad

un caso studio di interesse industriale: la valutazione della resistenza a fatica multiassiale di rulli saldati in acciaio, prodotti da Rulmeca S.p.a. e caratterizzati da cedimenti alla radice del cordone di saldatura. Lo studio è stato eseguito per mezzo di analisi FEM 3D e test sperimentali a fatica. Infine, prendendo in esame componenti indeboliti da intagli a V acuti soggetti a carichi di fatica multiassiale, sono state tratte alcune osservazioni sull'effetto dell'angolo di fase, sulla base di un nuovo approccio analitico basato sul valore massimo della tensione tangenziale mediata su un ciclo di fatica.

Il *quarto Capitolo* tratta lo studio numerico e teorico degli effetti 3D in componenti intagliati e criccati. Inizialmente, l'attenzione è stata focalizzata sui modi accoppiati e sull'effetto di diverse condizioni al contorno in dischi e piastre criccate, tridimensionali e soggette ad un carico nominale di modo III o modo II. L'intensità dello stato di tensione e deformazione locale è stata valutata attraverso lo spessore per mezzo del SED mediato, che consente di combinare l'effetto del modo di carico applicato e dei modi di frattura indotti. Infine la presenza di effetti 3D è stata investigata sia dal punto di vista teorico che numerico in componenti indeboliti da intagli blandi e in condizioni di plasticità ciclica. Sono stati considerati due diversi approcci: il primo è una procedura incrementale, che combina un modello elasto-plastico del materiale con un metodo approssimato per stimare le componenti di tensione e deformazione elasto-plastiche a partire da quelle lineari elastiche; il secondo approccio, invece, è basato su analisi FEM elasto-plastiche cicliche. Le stime teoriche sono state confrontate con i risultati numerici considerando diversi casi studio soggetti a carichi ciclici sia monoassiali che multiassiali. Infine è stato ricavato un legame tra il SED mediato elasto-plastico e l'area all'interno del ciclo di isteresi all'apice dell'intaglio.

Il *quinto Capitolo*, invece, è relativo al confronto tra diversi criteri di cedimento. Sono stati confrontati l'approccio SED e quello basato sulla teoria della Finite Fracture Mechanics (FFM), considerando intagli a V acuti soggetti a puro modo I o puro modo II. Con riferimento a carichi di puro modo II, è stata proposta con successo una nuova espressione del raggio di controllo per il calcolo del SED. I criteri sono stati confrontati prima analiticamente e in seguito

considerando dati sperimentali tratti dalla letteratura e relativi a diversi materiali fragili.

Infine, nel *sesto Capitolo* è stato investigato un legame tra il criterio SED ed il Peak Stress Method (PSM). Prima di tutto sono stati considerati componenti strutturali criccati soggetti a carichi di modo misto nel piano I+II. È stato proposto un metodo, valido sia per cricche lunghe che corte, per calcolare rapidamente il SED a partire dalle tensioni di picco valutate all'apice di cricca. Il legame ottenuto tra PSM e SED è stato poi impiegato nella stima della resistenza a fatica di giunti saldati testa a testa in acciaio ed alluminio. In seguito, è stato trattato anche il caso di componenti criccati soggetti a carichi di modo misto fuori piano I+III. Anche in questo caso, è stato proposto un metodo per valutare rapidamente il SED a partire dalle tensioni di picco all'apice di cricca. Sulla base del legame tra PSM e SED, è stata stimata la resistenza a fatica di giunti saldati tubo-su-flangia in acciaio sottoposti a carichi torsionali.

CHAPTER 1

INTRODUCTION TO LOCAL APPROACHES

1.1 Introduction

In the next chapters, some of the most important and widely employed local approaches will be adopted in fracture and fatigue problems of notched and cracked structural components, with particular attention to eventual three-dimensional effects. The considered local approaches will also be compared with other fundamental criteria proposed in the literature and the link between different methods will be investigated.

In this chapter, the above local approaches, namely the notch stress intensity factor-based approach (NSIF), the averaged strain energy density (SED) criterion and the peak stress method (PSM), will be briefly described along with their theoretical frameworks. For a most comprehensive description of the above local approaches the reader can refer to the recent reviews by Radaj focused on the NSIF approach [1] and on the local SED concept and its relation to the PSM [2]. The SED criterion and its applications to fracture and fatigue problems have been recently reviewed also by Berto and Lazzarin [3,4].

In the following the description of the above approaches will be subdivided into two sections focused on structural components weakened by sharp V-notches (which include the crack case) and blunt V-notches.

1.2 Sharp V-notches

1.2.1 Local stress fields and Notch Stress Intensity Factors

The stress intensity factor (SIF) concept has originally been developed in the context of fracture mechanics. For fracture phenomena, both brittle fracture and fatigue failure, the asymptotic singular stress field at the pointed crack or slit tip is most important. The stress level around the singularity is described by the SIF, possibly superimposed by the crack-parallel non-singular T-stress. The local three-dimensional stress singularity at a definite point of the crack or slit front can generally be described by superimposition of three two-dimensional stress singularities corresponding to three independent loading or opening modes of the crack tip: transverse tensile loading (mode I), in-plane shear loading (mode II) and out-of-plane shear loading (mode III). The appertaining SIFs are K_I , K_{II} and K_{III} .

Non-singular stresses may be superimposed: crack-parallel stresses (the T-stress) as well as normal stresses and symmetric shear stresses in the crack front direction.

The well-known concept of SIFs describing the stress singularity at crack tips or slit tips under linear–elastic material conditions can be transferred to pointed re-entrant corner notches (e.g. V-notches, stepped bars and weld toe notches). The SIF concept has been substantially extended since Williams' basic contribution (1952) on stress fields at angular corners [5].

Whereas the asymptotic stress drop from the singularity at the crack tip is described by the inverse square root of the radial distance r from the crack tip (the exponent is minus 0.5), a smaller, notch-angle-dependent exponent occurs in the case of corner notches, which means that the degree of the singularity is reduced [5]. The stress field close to corner notches (just as the stress field close to crack tips) can be described by stress intensity factors [6]. These are named 'notch stress intensity factors' as distinguished from the conventional SIFs of crack tips. The singular in-plane and out-of-plane stress fields at pointed corner notches can be specified by three notch loading modes (in analogy to the crack opening modes) related to the bisector plane of the notch: symmetric in-plane stresses (mode 1), anti-metric in-plane stresses (mode 2) and out-of-plane shear stresses (mode 3). The corresponding notch loading modes are in-plane tensile loading, in-plane shear loading and out-of-plane shear loading. The three basic loading modes with singular stresses at the notch tip produce the following asymptotic stress distribution (stress tensor σ_{ij} and σ_{kz}) around the notch tip, restricted to the first-order terms (Figs. 1.2.1 and 1.2.2) [5,7]:

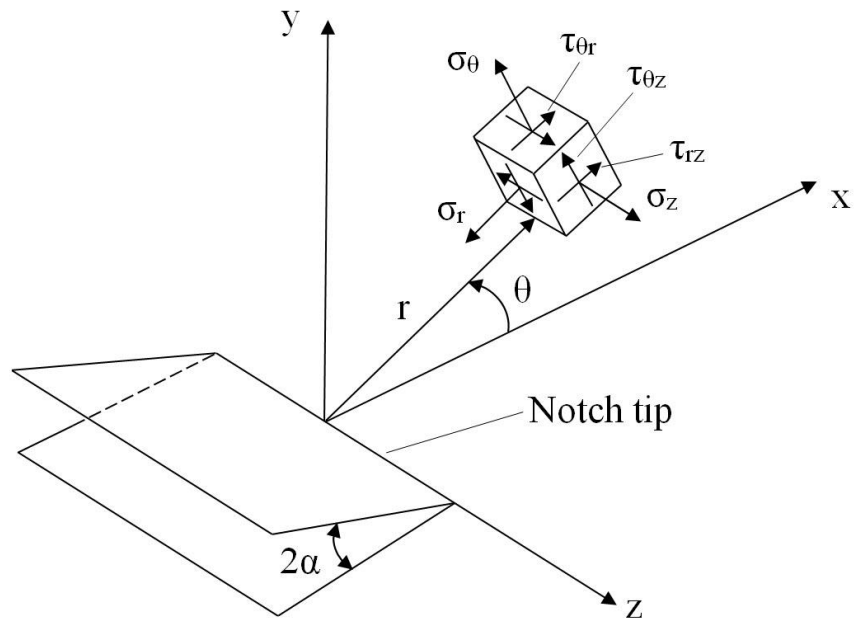


Figure 1.2.1. Sharp V-notch: generic three-dimensional stress field in a polar reference system.

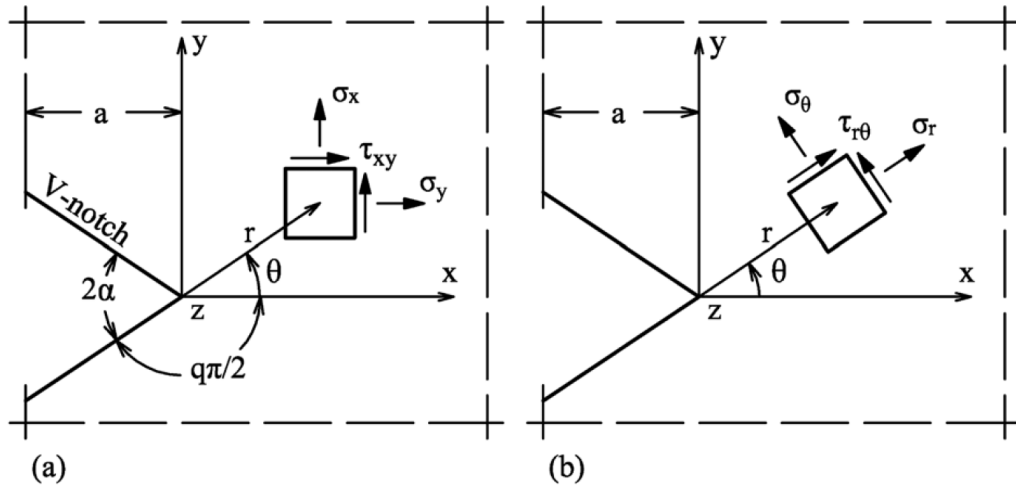


Figure 1.2.2. Sharp V-notch: in-plane stress field in (a) Cartesian and (b) polar reference systems.

$$\sigma_{ij} = \frac{1}{\sqrt{2\pi}} [K_1 \cdot r^{\lambda_1-1} \cdot f_{1,ij}(\theta) + K_2 \cdot r^{\lambda_2-1} \cdot f_{2,ij}(\theta)]$$

with $i, j = x, y$ or $i, j = r, \theta$

(1.2.1)

$$\sigma_{kz} = \frac{1}{\sqrt{2\pi}} K_3 \cdot r^{\lambda_3-1} \cdot f_{3,kz}(\theta) \quad \text{with } k = x, y \text{ or } k = r, \theta \quad (1.2.2)$$

The NSIFs K_1 , K_2 and K_3 depend on the magnitude of the load, the notch depth a , the notch opening angle 2α and further geometric parameters of the considered configuration. The angular functions $f_{1,ij}$, $f_{2,ij}$ and $f_{3,kz}$ describe the angular distribution of the stress close to the notch tip. The aforementioned relationship is strictly valid for $r \rightarrow 0$ and approximately valid for values of r , which are small in relation to the notch depth and other geometrical parameters of the configuration. Just as with the crack problem ($2\alpha = 0$), the complete solution comprises additional non-singular higher-order terms. Williams' solution for the in-plane stress field is based on the Airy stress function in polar coordinates in the following form, which comprises a symmetrical component and an anti-metrical component [5]:

$$F(r, \theta) = r^{\lambda+1} \cdot f(\theta) \quad (1.2.3)$$

where the values of λ have to be determined as part of the solution. The angular functions have to comply with the boundary conditions on the load-free faces of the V-notch. The stress can now be expressed in terms of r , λ and $f(\theta)$. Application of the boundary conditions produces a system of four simultaneous equations for four unknown constants. This system can be separated into two independent sets of equations related to the symmetrical and anti-metrical stress fields. A non-trivial solution can be obtained only if the determinants of the coefficient matrices are equal to zero each. From this requirement, the condition follows:

$$\sin \lambda(2\pi - 2\alpha) = \pm \lambda \cdot \sin(2\pi - 2\alpha) \quad (1.2.4)$$

Because the notch opening angle 2α is a fixed parameter for a specific wedge or notch, Eq. (1.2.4) provides the values λ_1 and λ_2 , called 'eigenvalues', necessary to ensure a nontrivial solution. Williams' solution has been widely used under the name 'eigenfunction expansion method'. Another, more versatile function-analytical approach for solving the problem of the in-plane loaded blunt V-notch comprising the sharp V-notch as a special case has been applied by Lazzarin and Tovo [8,9], Lazzarin et al. [10] and Atzori et al. [11]: the Kolosov–Muskhelishvili

complex stress function method. The principal mathematical steps remain the same as in the Airy stress function method. The stress field analysis for the V-notch subjected to out-of-plane shear loading (mode 3) is easier to perform, because the governing equation in terms of the out-of-plane displacements is a potential function substituting the bi-potential stress function in the case of the in-plane stresses. Performing similar mathematical steps as before, the following eigenvalue equation is found [7]:

$$\sin \lambda_3(2\pi - 2\alpha) = 0 \quad (1.2.5)$$

The smallest positive eigenvalues λ_1 , λ_2 and λ_3 defining the degree of the stress singularity at the notch tip depend solely on the notch opening angle 2α (Fig. 1.2.3). The eigenvalue 0.5 is related to crack tips, $2\alpha = 0$, and the eigenvalue 1.0 (no singularity) to straight edges, $2\alpha = \pi$ (but only for modes 1 and 3). The eigenvalues for mode 1 loading are slightly smaller than those for mode 3 loading. They are substantially smaller in relation to mode 2 loading, thus designating severer singularities. The stress singularity in mode 2 loading is weaker and vanishes completely for $2\alpha \geq 102.6^\circ$ [12]. The characteristic stress components in the bisector plane ($\theta = 0$) have the following simple form:

$$\sigma_{\theta\theta}(r, 0) = \frac{1}{\sqrt{2\pi}} K_1 \cdot r^{\lambda_1-1} \quad (1.2.6)$$

$$\tau_{r\theta}(r, 0) = \frac{1}{\sqrt{2\pi}} K_2 \cdot r^{\lambda_2-1} \quad (1.2.7)$$

$$\tau_{\theta z}(r, 0) = \frac{1}{\sqrt{2\pi}} K_3 \cdot r^{\lambda_3-1} \quad (1.2.8)$$

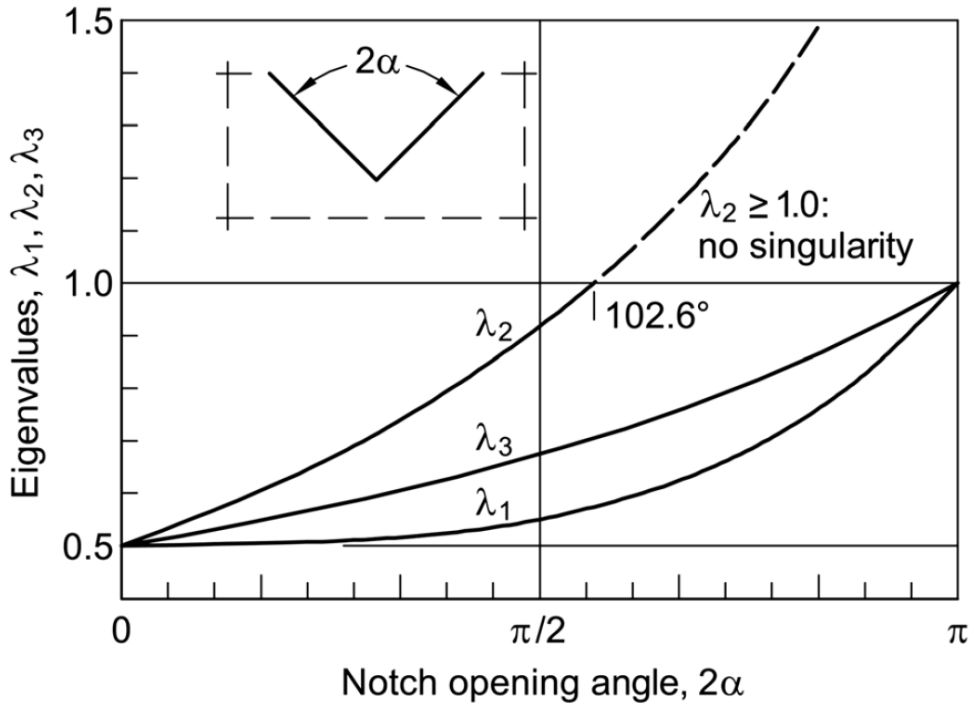


Figure 1.2.3. Eigenvalues λ_1 , λ_2 and λ_3 defining the degree of stress singularity at sharp V-notches subjected to modes 1, 2 and 3 loading conditions, dependent on notch opening angle 2α (Lazzarin et al. [12]).

The NSIFs K_1 , K_2 and K_3 may be evaluated on the basis of the aforementioned characteristic stress components considering the limit values for $r \rightarrow 0$ [6]:

$$K_1 = \lim_{r \rightarrow 0} \sqrt{2\pi} \cdot r^{1-\lambda_1} \cdot \sigma_{\theta\theta}(r, 0) \quad (1.2.9)$$

$$K_2 = \lim_{r \rightarrow 0} \sqrt{2\pi} \cdot r^{1-\lambda_2} \cdot \tau_{r\theta}(r, 0) \quad (1.2.10)$$

$$K_3 = \lim_{r \rightarrow 0} \sqrt{2\pi} \cdot r^{1-\lambda_3} \cdot \tau_{\theta z}(r, 0) \quad (1.2.11)$$

The dimensions of K_1 , K_2 and K_3 are $\text{MPa} \cdot \text{mm}^{1-\lambda_1}$; $\text{MPa} \cdot \text{mm}^{1-\lambda_2}$ and $\text{MPa} \cdot \text{mm}^{1-\lambda_3}$.

It should be noted that the elastic notch stress intensity factors are used to describe the fatigue strength of fillet-welded attachment joints, moreover the fracture toughness of brittle materials may also be evaluated on this basis. The numerical values of K_1 , K_2 and K_3 can be set into comparison, e.g. as failure criteria,

provided their dimension is identical, i.e. only under the condition of an identical notch angle besides an identical loading mode.

The NSIFs K_1 , K_2 and K_3 of V-notches or re-entrant corners can easily be analysed on the basis of the FEM using a very fine mesh near the sharp notch tip.

1.2.2 Averaged Strain Energy Density approach

It is not the elastic maximum notch stress that controls static, dynamic or cyclic crack initiation at notches of structural members, but rather the notch stresses averaged over a definite finite volume of the material at the notch root, which is assumed as homogeneous. This idea goes back to Neuber [13,14] who formulated the hypothesis of an ‘elementary material volume’ or ‘microstructural support length’ for this purpose. Determining the average value of the partly multiaxial and singular notch stresses in a finite volume around the notch tip needs further sophistication. On this track, the local SED approach has been proposed and analytically developed by Lazzarin and Zambardi [15]. In the case of sharp notch tips, not only the stresses at the notch tip tend towards infinity but also the SED. Contrary to this, the averaged SED in a local finite volume around the notch (or crack) tip has a finite value. This value is considered to be the material parameter that describes the initiation of brittle fracture or fatigue failure. The proposal to use the SED as a strength parameter goes back to Beltrami (1885) [16]. In the following, the local SED concept for sharp V-notches is presented: the basic relationships for the total local SED are derived and the applications to the brittle fracture strength and to the high-cycle fatigue strength are demonstrated.

The question is, what shape and size the finite volume around the notch tip should have. It is conceived as a sector-shaped cylinder of radius R along the notch tip line, termed ‘control volume’.

For simplicity, in the following a structural component weakened by a sharp V-notch and subjected to in-plane mixed mode I+II will be referred to. The analytical frame of the local SED approach refers to the stress conditions in the cross-sectional plane, Fig. 1.2.4b. The polar coordinate system is brought into line with the notch bisector ($\theta = 0$), Fig. 1.2.4a. The material is assumed to be isotropic and linear-elastic. The first analysis step consists of defining the stresses $\sigma_{ij}(r,\theta)$

and strains $\varepsilon_{ij}(r,\theta)$ in terms of the mode-related notch stress intensity factors K_1 and K_2 [6] and Williams' eigenvalues λ_1 and λ_2 [5]. Therefore, the SED $W(r,\theta)$ is derived consisting of the components W_1 , W_2 and W_{12} related to the mode 1, mode 2 and mixed mode stress and strain fields. The component W_{12} is not further needed, because its contribution to the averaged SED vanishes for symmetric sector areas. The component W_2 may be neglected for $2\alpha \geq 102.6^\circ$, which produces a non-singular stress field. The second analysis step is to determine the averaged SED within a sector area of radius R around the notch tip. The radius R should be small enough, so that the sector area remains within the range of validity of the one-term stress expansion resulting in the NSIF.

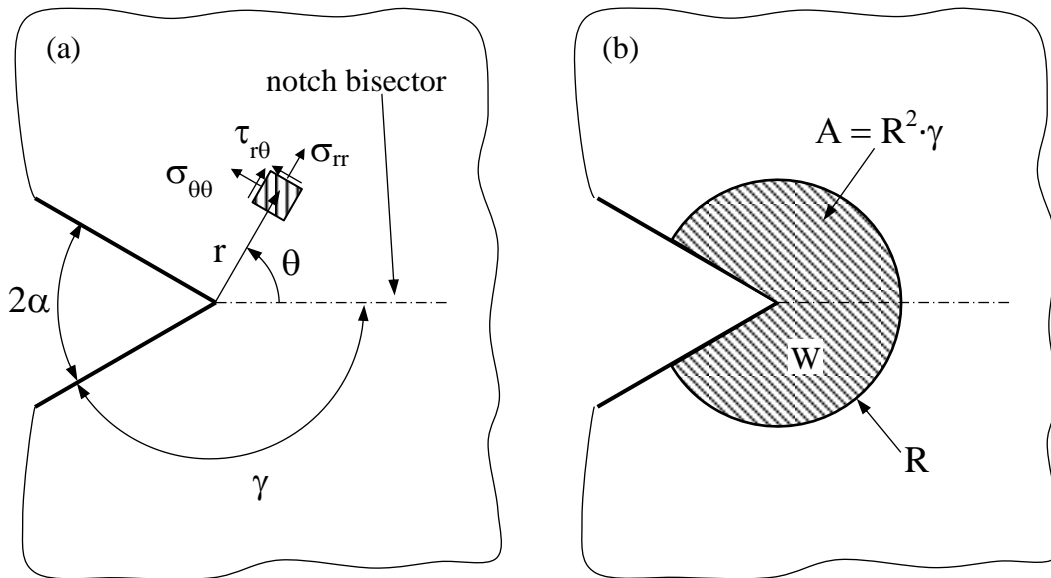


Figure 1.2.4. Polar coordinate system centred at the V-notch tip (a) and control volume (area) of radius R surrounding the V-notch tip (b) (Lazzarin and Zambardi [15]).

In more detail, according to Beltrami [16], the total strain energy density (SED) is equal to the total work done by the system and it is given by Eq. (1.2.12), expressed in terms of the principal stresses in a given reference system.

$$W(r, \theta) = \frac{1}{2E} [\sigma_1^2 + \sigma_2^2 + \sigma_3^2 - 2\nu(\sigma_1\sigma_2 + \sigma_1\sigma_3 + \sigma_2\sigma_3)] \quad (1.2.12)$$

In the case of a V-notch under mixed mode I+II loading, when only the contribution of the first singular terms is significant, the SED can be directly

linked to the NSIFs, K_1 and K_2 , by substituting into Eq. (1.2.12) the singular stress field given by Eq. (1.2.1). The strain energy density, averaged in a circular sector of radius R surrounding the notch tip (Fig. 1.2.4b), is given by the ratio between the elastic strain energy $E(R)$ and the area of the circular sector $A(R)$. The sector area of radius R , over which the averaged SED is determined, is given by:

$$A(R) = \int_0^R \int_{-\gamma}^{+\gamma} r \, dr d\theta = R^2 \cdot \gamma \quad (1.2.13)$$

By integration of $W(r,\theta)$ over the symmetric sector area and division by $A(R)$, the averaged local SED turns out to be:

$$\begin{aligned} \bar{W}(R) &= \frac{E(R)}{A(R)} = \frac{\int_A W \, dA}{\int_A dA} = \frac{\int_0^R \int_{-\gamma}^{+\gamma} W(r, \theta) r \, dr d\theta}{\int_0^R \int_{-\gamma}^{+\gamma} r \, dr d\theta} \\ &= \frac{1}{E} e_1 \cdot K_1^2 \cdot R^{2(\lambda_1-1)} + \frac{1}{E} e_2 \cdot K_2^2 \cdot R^{2(\lambda_2-1)} \end{aligned} \quad (1.2.14)$$

$$e_1(\gamma) = \frac{I_1(\gamma)}{4\lambda_1\gamma}, \quad e_2(\gamma) = \frac{I_2(\gamma)}{4\lambda_2\gamma} \quad (1.2.15)$$

$$I_1(\gamma) = \int_{-\gamma}^{+\gamma} f_1(\theta) d\theta, \quad I_2(\gamma) = \int_{-\gamma}^{+\gamma} f_2(\theta) d\theta \quad (1.2.16)$$

The internal notch angle 2γ being linked to the notch opening angle $2\alpha = 2\pi - 2\gamma$, the total SED coefficients e_1 and e_2 can be plotted dependent on the notch opening angle 2α , Fig. 1.2.5 (for plane strain conditions). For sufficiently small values of 2α , the value of e_2 is substantially larger than that of e_1 . Even for $2\alpha \geq 102.6^\circ$, where the SED field is non-singular, e_1 and e_2 have approximately the same value. This is not an indication that the SED values are approximately the same. Actually, $\bar{W}_2 \ll \bar{W}_1$ because of the missing singularity in the stress and strain field of mode 2 loading.

For the sake of completeness, out-of-plane shear loading (mode 3) has also been considered [12]. The local averaged SED turns out to be:

$$\bar{W}_3(R) = \frac{1}{E} e_3 \cdot K_3^2 \cdot R^{2(\lambda_3-1)} \quad (1.2.17)$$

$$e_3(\gamma) = \frac{(1 + \nu) \cdot I_3(\gamma)}{6\lambda_3\gamma} \quad (1.2.18)$$

$$I_3(\gamma) = \int_{-\gamma}^{+\gamma} f_3(\theta) d\theta \quad (1.2.19)$$

The energy coefficient e_3 is dependent on the notch opening angle 2α as supplemented in Fig. 1.2.5. It should be noted that the values of e_3 are larger than those of e_2 and e_1 .

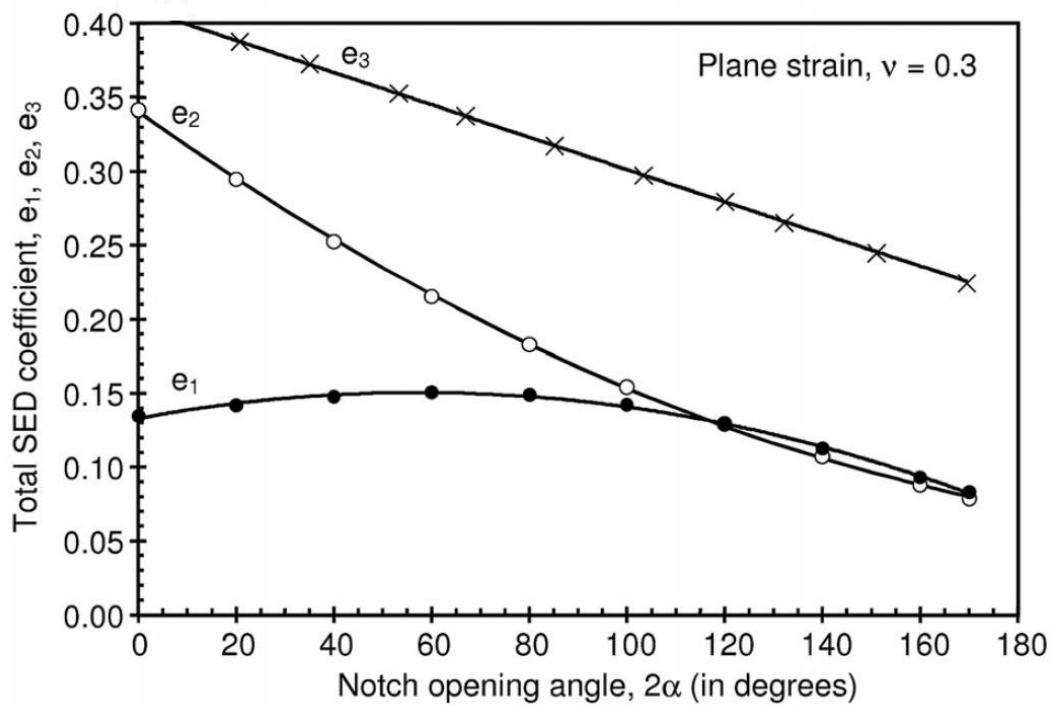


Figure 1.2.5. Total SED coefficients e_1 , e_2 and e_3 dependent on notch opening angle 2α under plane strain conditions (Lazzarin and Zambardi [15]).

1.2.2.1 Static loading

The characteristic feature of brittle fracture is that it occurs under elastic stress field conditions, either without any plastic deformation (glass and ceramics) or without deformation on a macroscale (brittle technical metals). The SED concept is applicable to sharp V-notches made of brittle materials in the following form proposed by Lazzarin and Zambardi [15]. Brittle fracture at sharp V-notches may be assumed to occur when the averaged local SED \bar{W} within the control volume reaches a critical value W_c independent of the notch opening angle and independent of the loading type (tensile or in-plane shear loading). This corresponds to the Beltrami failure criterion [16]. The material parameter W_c may be determined from the ultimate tensile strength σ_c of unnotched specimens:

$$\bar{W} \leq W_c, \quad W_c = \frac{\sigma_c^2}{2E} \quad (1.2.20)$$

The radius R_0 of the control volume (termed ‘critical distance R_c ’ by the first authors [15]), where the critical local SED value W_c occurs, may be determined from the plane strain fracture toughness K_{Ic} . It is considered to be a material parameter. When the mode 2 SED \bar{W}_2 is zero (symmetric geometry and loading) or negligibly small (large notch opening angle with vanishing mode 2 singularity), the NSIF K_1 can be correlated with the averaged local SED \bar{W}_1 according to Eq. (1.2.14):

$$K_1 = \sqrt{\frac{4E\lambda_1\gamma}{I_1(\gamma)}} \bar{W}_1 R_0^{(1-\lambda_1)} \quad (1.2.21)$$

The critical condition is expressed by introducing $\bar{W}_1 = W_c = \sigma_c^2/2E$ from Eq. (1.2.20):

$$K_{1c} = \sqrt{\frac{2\lambda_1\gamma}{I_1(\gamma)}} \sigma_c R_0^{(1-\lambda_1)} = f_1(2\alpha) \sigma_c R_0^{(1-\lambda_1)} \quad (1.2.22)$$

where the intensity coefficient $f_1(2\alpha)$ should not be confused with $f_1(\theta)$ in Eq. (1.2.16). When the V-notch becomes a crack ($2\alpha = 0$), K_{Ic} coincides with the fracture toughness K_{Ic} :

$$K_{Ic} = f_1(0)\sigma_c\sqrt{R_0} \quad (1.2.23)$$

Thus, the control volume radius R_0 turns out to be:

$$R_0 = \left(\frac{K_{Ic}}{f_1(0)\sigma_c}\right)^2 = \frac{I_1(\pi)}{\pi} \left(\frac{K_{Ic}}{\sigma_c}\right)^2 \quad (1.2.24)$$

or in an explicit form related to plane strain conditions [17]:

$$R_0 = \frac{(1 + \nu)(5 - 8\nu)}{4\pi} \left(\frac{K_{Ic}}{\sigma_c}\right)^2 \quad (1.2.24)$$

The corresponding expression for plane stress conditions reads with K_c (depending on plate thickness t) substituting K_{Ic} [18]:

$$R_0 = \frac{5 - 3\nu}{4\pi} \left(\frac{K_c}{\sigma_c}\right)^2 \quad (1.2.24)$$

The control volume radius R_0 depends on the material. Its value decreases with rising brittleness. It does not depend on the notch opening angle per definition. The described analytical approach referring to the total SED has been validated on the basis of experimental data reported in the literature [4,15].

1.2.2.2 Fatigue loading

The total fatigue life of notched components or welded joints quantified by number of cycles up to total failure consists of the crack initiation and crack propagation portions. The crack initiation life is terminated by a technical surface crack of about 0.25 mm depth. The relation of the crack initiation to the crack propagation portion varies considerably. The crack initiation life portion is larger in the high-cycle than in the low-cycle fatigue range, it is larger for high-strength steels and it is prevailing in unnotched or mildly notched members. It has been

shown that the NSIF is a parameter that controls the crack initiation phase in members with sharp notches, especially too in welded joints. It can also be used for expressing the total fatigue life of welded joints. A necessary condition is that the dimension of the relevant NSIF does not vary, which means that the notch opening angle must be the same for the evaluated specimens. The restriction to only one notch opening angle is removed by evaluating the averaged local SED instead of the NSIF.

In the following, the specific application of the SED approach to welded joints under fatigue loading is described, however the general considerations remain valid for a generic component weakened by a sharp V-notch and subjected to fatigue loading conditions.

The averaged local SED at the notch tip of the weld toe is evaluated for linear-elastic material behaviour which is an appropriate approximation in the high-cycle fatigue range ($N \geq 5 \cdot 10^5$ cycles). It is also used in the medium-cycle fatigue range ($10^4 \leq N \leq 5 \cdot 10^5$ cycles) where plastic deformations occur. The plastic zone may even be larger than the control volume with radius $R_0 \approx 0.3$ mm for steels or 0.1 mm for aluminium alloys. The justification to use the linear-elastic strain energy under small-scale yielding conditions is provided by the ‘equivalent strain energy density approach’ according to Glinka [19]. Following this approach, which works well under plane strain conditions, the elastic-plastic SED at the root of a rounded notch is set equal to the SED determined under purely elastic conditions. This concept is not directly applicable to sharp V-notches because the SED at the notch tip tends towards infinity both for linear-elastic and power law elastic-plastic material behaviour. If applied to the averaged SED in the control volume at the notch tip, this problem is removed [20]. The elastic SED concept is thus applicable over the whole medium-cycle and high-cycle fatigue range. The first step in the local SED approach is the determination of the control volume radius R_0 for the specimens under investigation. It depends on the material and on the multiaxial failure criterion. This task is more complicated for welded joints under cyclic loading producing fatigue failure than for specimens under static loading producing brittle fracture. In the former case, the material is locally inhomogeneous in the as-welded condition and the cracking phenomena

change to some extent with the cyclic load level or the endured load cycles. The control volume radius R_0 is determined for fillet-welded joints ($2\alpha = 135^\circ$) with experimental data gained in the high-cycle fatigue range. Only the mode 1 averaged local SED \bar{W}_1 is evaluated whereas the mode 2 component \bar{W}_2 remains negligibly small. Plane strain conditions are assumed together with the Beltrami total strain energy criterion [16]. The control volume radius R_0 is then given by the following expression proposed by Lazzarin and Zambardi [15] in analogy to Eq. (1.2.24):

$$R_0 = \left(\frac{\Delta K_{I,A}}{f_1 \Delta \sigma_A} \right)^{\frac{1}{1-\lambda_1}} = \left(\frac{\sqrt{2e_1} \Delta K_{I,A}}{\Delta \sigma_A} \right)^{\frac{1}{1-\lambda_1}} \quad (1.2.25)$$

where λ_1 and f_1 depend on the notch opening angle 2α , while $\Delta K_{I,A}$ is the reference value of the endurable NSIF range for the fillet-welded joints and $\Delta \sigma_A$ is the reference value of the endurable stress range at a flush ground butt weld, which simulates the material behaviour at the weld toe or root. The reference values $\Delta K_{I,A}$ and $\Delta \sigma_A$ are mean values ($P_S = 50\%$) at $N_A = 2 \cdot 10^6$ cycles (IIW design recommendations [21]) or $5 \cdot 10^6$ cycles (other authors) with load ratio $R = 0$. With the usual inverse slope exponent $k = 3$ for welded joints of steel, the factor 1.36 occurs between the fatigue strength at $2 \cdot 10^6$ compared with the fatigue strength at $5 \cdot 10^6$ cycles. With the common scatter range index, the factor 1.37 occurs between the data for $P_S = 50\%$ compared with those for $P_S = 2.3\%$. For $2\alpha = 135^\circ$, the parameters in Eq. (1.2.25) are $f_1 = 2.065$ and $\lambda_1 = 0.674$, whereas for $2\alpha = 0^\circ$, $f_1 = 1.936$ and $\lambda_1 = 0.5$. Recommended parameter values for welded joints of carbon steels with toe failure ($2\alpha = 135^\circ$) are [22]:

- $R_0 = 0.28$ mm, $\Delta K_{I,A} = 211$ MPa·mm^{0.326}, $\Delta \sigma_A = 155$ MPa ($P_S = 50\%$, $N = 5 \cdot 10^6$ cycles)

The relevant data for welded joints of aluminium alloys are [22]:

- $R_0 = 0.12$ mm, $\Delta K_{I,A} = 100$ MPa·mm^{0.326}, $\Delta \sigma_A = 96$ MPa ($P_S = 50\%$, $N = 5 \cdot 10^6$ cycles)
-

Different values of R_0 may be appropriate under mode 1 and mode 3 loading conditions. A uniform material-dependent value of R_0 is used for evaluating test data not only in the high-cycle fatigue range but also in the medium-cycle and low-cycle fatigue range [3,4,15,22]. This is a simplification appropriate for engineers, considering that under small-scale yielding conditions, the elastic-plastic SED matches the elastic SED under plane strain conditions. Thinking ‘more physically’, the control radius should be dependent on the endured number of cycles to some extent, $R_0 = R_0(N)$.

It should be noted that the local SED concept for sharp V-notches (which include also welded joints) can be applied also to generic multiaxial loading conditions (modes 1, 2, 3 superimposed). The relevant expression for the averaged total SED \bar{W} reads as follows, compare Eqs. (1.2.14) and (1.2.17) [12]:

$$c_W \Delta \bar{W} = c_W \left[\frac{e_1}{E} \cdot \left(\frac{\Delta K_1}{R_0^{(1-\lambda_1)}} \right)^2 + \frac{e_2}{E} \cdot \left(\frac{\Delta K_2}{R_0^{(1-\lambda_2)}} \right)^2 + \frac{e_3}{E} \cdot \left(\frac{\Delta K_3}{R_0^{(1-\lambda_3)}} \right)^2 \right] \quad (1.2.26)$$

The coefficient c_W in Eq. (1.2.26), which must be applied for the SED calculation dealing with fatigue loading conditions, takes the influence of the nominal load ratio R into account, $c_W = 1.0$ for $R = 0$ and $c_W = 0.5$ for $R = -1$, according to Eq. (1.2.27) which has been plotted also in Fig. 1.2.6.

$$c_W = \begin{cases} \frac{1 + R^2}{(1 - R)^2} & \text{for } -\infty \leq R < 0 \\ 1 & \text{for } R = 0 \\ \frac{1 - R^2}{(1 + R)^2} & \text{for } 0 < R \leq 1 \end{cases} \quad (1.2.27)$$

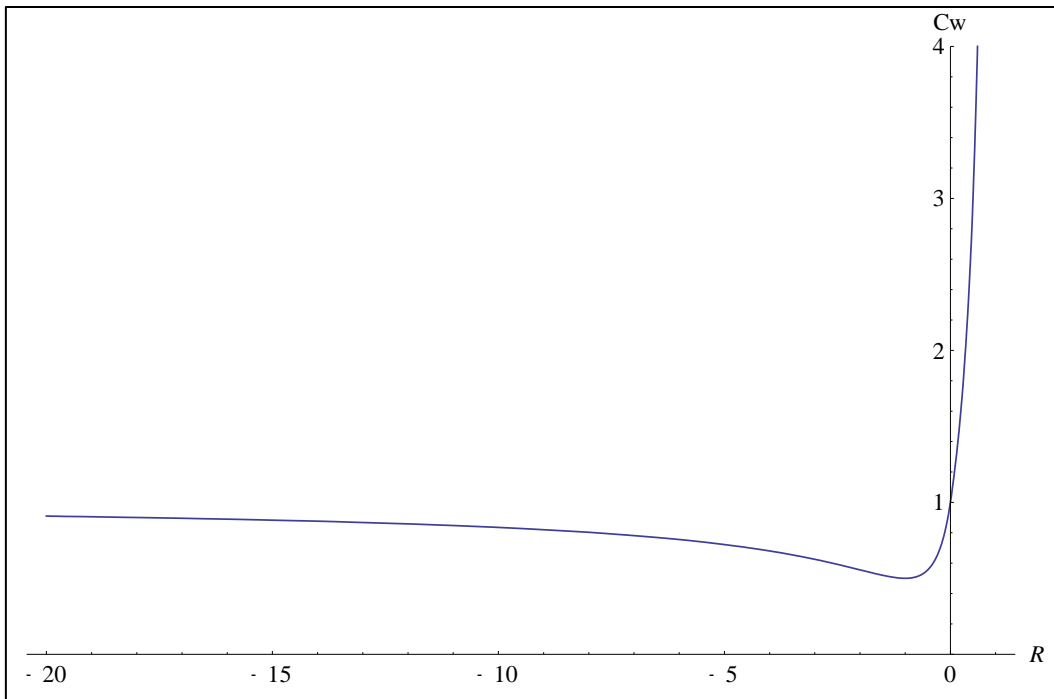
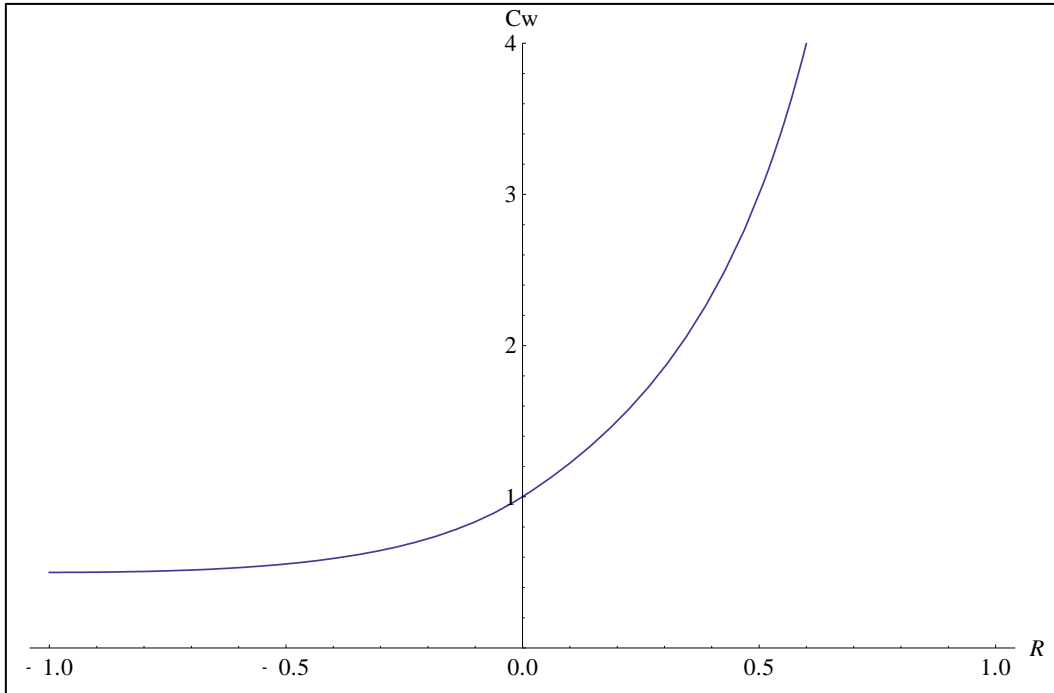


Figure 1.2.6. Coefficient c_w as a function of the nominal load ratio R : (a) $-1 \leq R < 1$ (most interesting cases), (b) $-\infty < R < 1$ (Lazzarin et al. [12][15][15][15]).

The above expression of the weighting factor c_W as a function of the nominal load ratio ($R = \sigma_{\min}/\sigma_{\max}$) is based on mere algebraic considerations, which will be described in detail below.

The case of a nominal load ratio $R = 0$, for which the stress range coincides with the maximum stress value, is considered as the reference one. In this case, the SED range $\Delta W_{R=0}$ can be properly evaluated with the area of a triangle as following (see Fig. 1.2.7a):

$$\Delta W_{R=0} = \frac{\Delta\sigma^2}{2E} = \frac{(\sigma_{\max} - \sigma_{\min})^2}{2E} = \frac{\sigma_{\max}^2 \cdot (1 - R)^2}{2E} \quad (1.2.28)$$

In the case of a positive nominal load ratio $0 < R < 1$, the SED range ΔW_R can be evaluated by means of the following expression based on Fig. 1.2.7b:

$$\Delta W_R = \frac{\sigma_{\max}^2}{2E} - \frac{\sigma_{\min}^2}{2E} = \frac{\sigma_{\max}^2 \cdot (1 - R^2)}{2E} \quad (1.2.29)$$

Now, it can be defined the ratio c_W between the actual SED range ΔW_R and the fictitious one $\Delta W_{R=0}$ calculated as if the nominal load ratio were zero, i.e. by means of the area of a triangle. The expression reported in Eq. (1.2.27) is obtained:

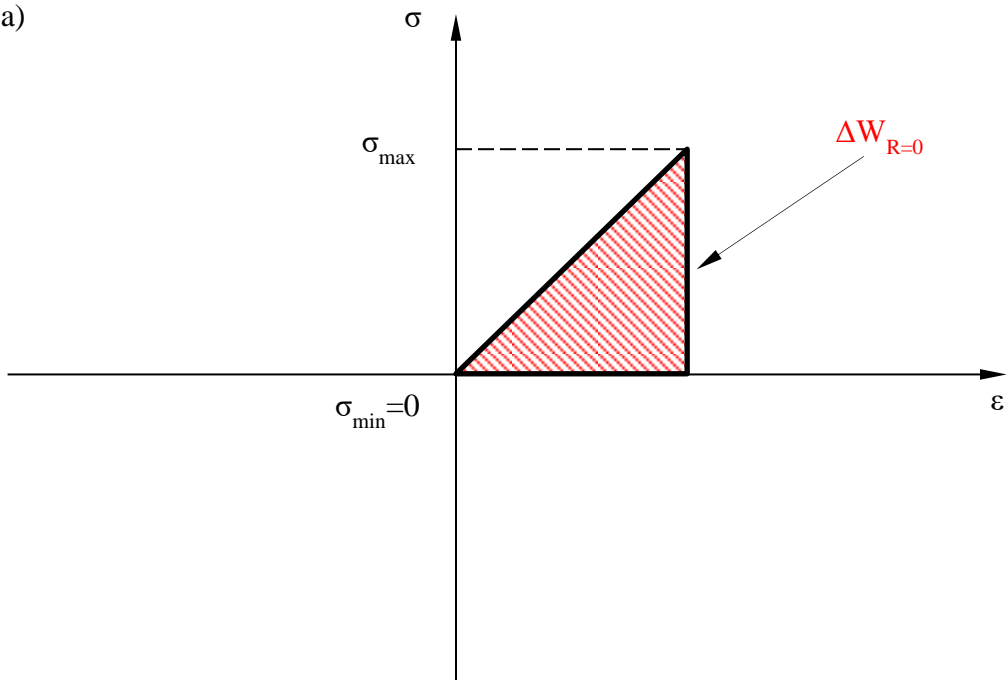
$$c_W = \frac{\Delta W_R}{\Delta W_{R=0}} = \frac{1 - R^2}{(1 - R)^2} \quad (1.2.30)$$

The same consideration can be applied also to the case of a negative nominal load ratio, $-\infty < R < 0$ see Fig. 1.2.7c. The following expressions can be obtained:

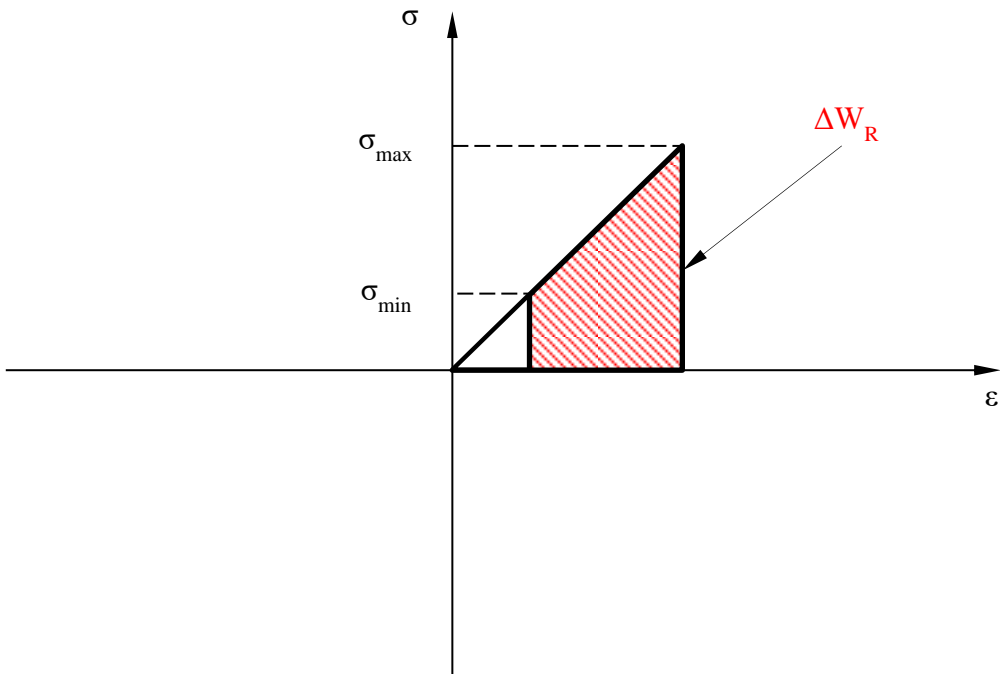
$$\Delta W_R = \frac{\sigma_{\max}^2}{2E} + \frac{\sigma_{\min}^2}{2E} = \frac{\sigma_{\max}^2 \cdot (1 + R^2)}{2E} \quad (1.2.31)$$

$$c_W = \frac{\Delta W_R}{\Delta W_{R=0}} = \frac{1 + R^2}{(1 - R)^2} \quad (1.2.32)$$

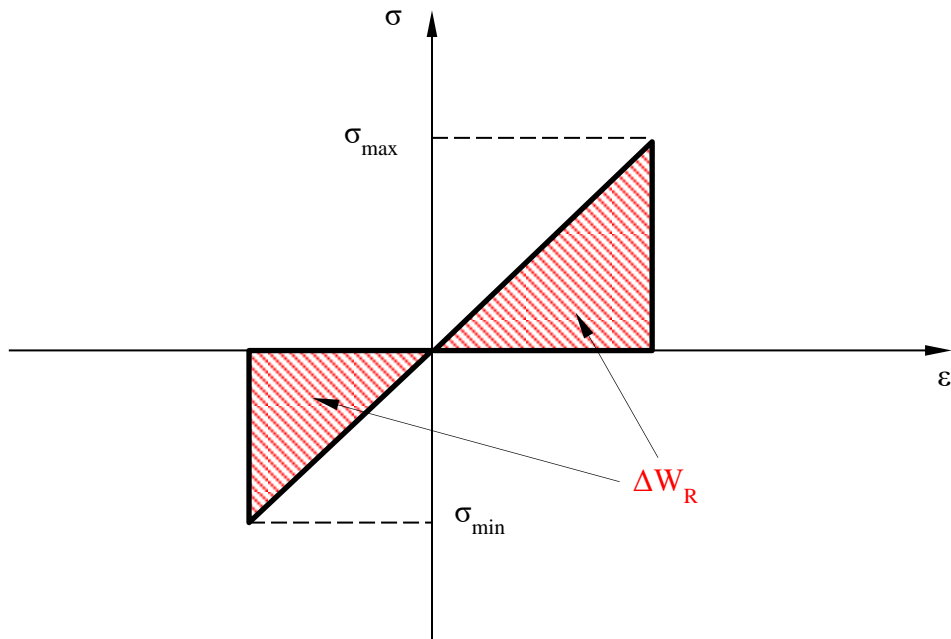
(a)



(b)



(c)



(d)

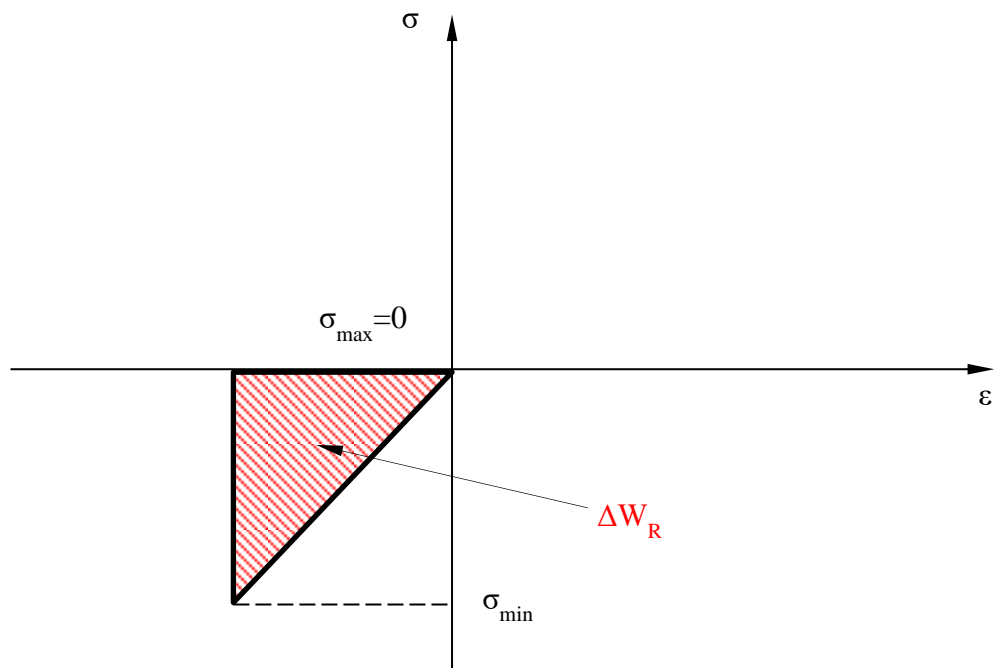


Figure 1.2.7. SED definition as a function of the nominal load ratio R : (a) $R = 0$ (reference case), (b) $0 < R < 1$, (c) $-\infty < R < 0$, (d) $R = -\infty$ (Lazzarin et al. [12][15][15][15]).

In particular, for welded joints under fatigue loading in the as-welded condition, $c_w = 1.0$ is appropriate, independently of R , because of the tensile residual stresses produced by welding. The value $c_w = 0.5$ should be used for welded joints with a stress relief treatment when tested for $R = -1$.

1.2.2.3 Coarse mesh option

The coarse mesh option for the FE analysis of sharp V-notches comprises two different procedures, the SED-based coarse mesh evaluation and the peak stress method. The SED-based coarse mesh evaluation benefits from the fact that the requirements on mesh refinement for an accurate determination of the local strain energy are much lower than the corresponding requirements in the case of stress field evaluations.

The averaged local SED at sharp or rounded notches can be evaluated with high accuracy based on coarse FE meshes. The NSIF or maximum notch stress values, respectively, derived therefrom are sufficiently accurate for engineering applications. The extremely fine meshes required for determining the NSIF values based on the usual limit value $r \rightarrow 0$ procedure are avoided, as well as the correspondingly fine meshes for an accurate maximum stress analysis.

The reason for the excellent performance of SED evaluations within the widely used displacement (or stiffness) method of finite element analysis is the fact that the nodal point displacements of the FE structural system are the primary unknown parameters that are determined based on a variational formulation of the potential Π leading to the principle of virtual work. Within this approach, the element strains are fully compatible whereas the stresses are not equilibrated at the element boundaries. Therefore, the evaluation of the strain energy from the nodal point displacements is superior to its evaluation from the element stresses. The procedural steps in terms of FE analysis are readily available [23,24].

1.2.3 Peak Stress Method

The peak stress method is a simplified, FE-based method to approximate the NSIFs at sharp V-notches inclusive of slits or cracks.

The PSM takes its origins by a numerical technique proposed by Nisitani and Teranishi [25,26] to rapidly estimate by FEM the SIF of a crack emanating from an ellipsoidal cavity. Such a procedure is based on the usefulness of the linear elastic peak stress σ_{peak} calculated at the crack tip by means of FE analyses characterized by a mesh pattern having a constant element size. In particular, Nisitani and Teranishi [25,26] were able to show that the ratio K_I/σ_{peak} depends only on the element size, such that σ_{peak} can be used to rapidly estimate K_I , provided that the adopted mesh pattern has previously been calibrated on geometries for which the exact K_I values are known. A theoretical justification to the PSM has been provided later on and the method has been extended also to sharp and open V-notches in order to rapidly evaluate the mode 1 Notch Stress Intensity Factor (NSIF) [27]. Subsequently, the PSM has been formalised to include also cracked components under mode 2 loading conditions [28] and open V-notches subjected to pure mode 3 (anti-plane) stresses [29].

In more detail, the PSM enables to rapidly estimate the NSIFs K_1 , K_2 and K_3 (Eqs. (1.2.9)-(1.2.11)) from the notch tip singular, linear elastic, opening, sliding and tearing FE peak stresses $\sigma_{yy,\text{peak}}$, $\tau_{xy,\text{peak}}$ and $\tau_{yz,\text{peak}}$, respectively, which are referred to the notch bisector line according to Fig. 1.2.8. The peak stresses are defined as the maximum linear elastic stresses in the considered crack tip or notch tip nodal point of the mesh. Each nodal point stress results as the arithmetic mean of the stress components in the two ($2\alpha > 90^\circ$, as described in detail below) or four elements ($2\alpha < 90^\circ$) meeting in the nodal point.

The element size required to evaluate K_1 , K_2 and K_3 from $\sigma_{yy,\text{peak}}$, $\tau_{xy,\text{peak}}$ and $\tau_{yz,\text{peak}}$, respectively, is several orders of magnitude greater than that required to evaluate the entire local stress field. The second advantage of using $\sigma_{yy,\text{peak}}$, $\tau_{xy,\text{peak}}$ and $\tau_{yz,\text{peak}}$ is that a single stress value is sufficient to estimate K_1 , K_2 and K_3 , respectively, instead of a number of stress FE data, as is usually made by applying definitions (1.2.9)-(1.2.11).

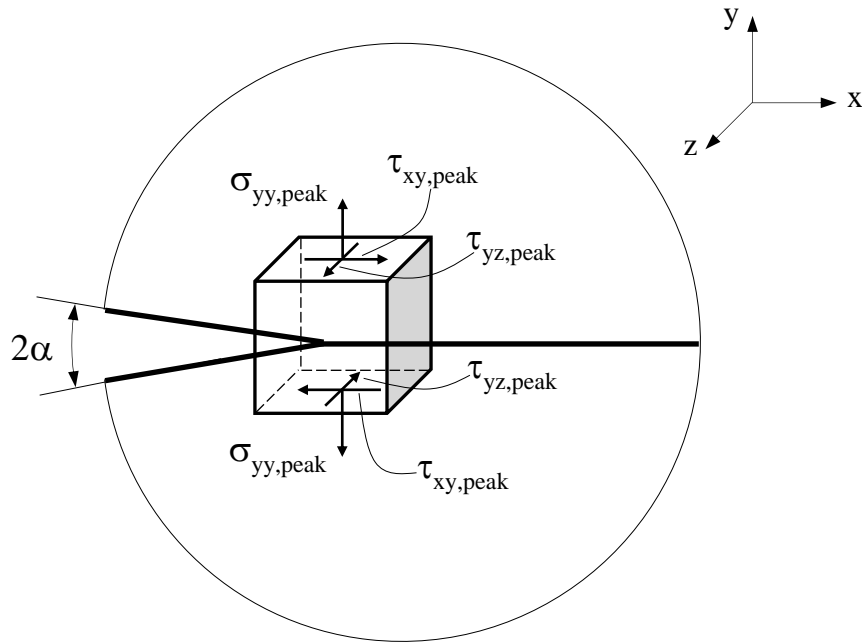


Figure 1.2.8. Definition of the notch tip singular, linear elastic, opening, sliding and tearing FE peak stresses $\sigma_{yy,peak}$, $\tau_{xy,peak}$ and $\tau_{yz,peak}$, respectively, which are referred to the bisector line according to PSM.

More precisely, the following expressions are valid [27–29]:

$$K_{FE}^* = \frac{K_1}{\sigma_{yy,peak} \cdot d^{1-\lambda_1}} \cong 1.38 \quad (1.2.33)$$

$$K_{FE}^{**} = \frac{K_2}{\tau_{xy,peak} \cdot d^{1-\lambda_2}} \cong 3.38 \quad (1.2.34)$$

$$K_{FE}^{***} = \frac{K_3}{\tau_{yz,peak} \cdot d^{1-\lambda_3}} \cong 1.93 \quad (1.2.35)$$

where d is the so-called ‘global element size’ parameter to input in Ansys[®] FE code, i.e. the average FE size adopted by the free mesh generation algorithm available in the FE code. It is proven that the above ratios depend mainly on the element size and type, modified solely by the stress singularity exponent λ_i ($i = 1, 2$ and 3) which depends on the notch opening angle 2α .

Eqs. (1.2.33)-(1.2.35) were derived using particular 2D or 3D finite element types and sizes, so that a range of applicability exists, which has been presented in detail in previous contributions [27–29].

More precisely, Eqs. (1.2.33)-(1.2.35) are valid under the following conditions:

- concerning Eqs. (1.2.33) and (1.2.34) related to mode 1 and mode 2 loadings, respectively, use of 4-node quadrilateral finite elements with linear shape functions, as implemented in ANSYS® numerical software (PLANE 42 of the Ansys® element library or alternatively PLANE 182 with K-option 1 set to 3, which corresponds to a simplified enhanced strain formulation of the finite elements). Concerning instead Eq. (1.2.35) related to mode 3 loading, use of two-dimensional, harmonic, 4-node linear quadrilateral elements, as implemented in ANSYS® numerical code (PLANE 25 of Ansys® element library). Finally, the use of three-dimensional, eight-node brick elements (SOLID 45 of Ansys® element library or equivalently SOLID 185 with K-option 2 set to 3) is allowed for all loading modes, i.e. for Eqs. (1.2.33)-(1.2.35);
- the pattern of finite elements around a notch or crack tip must be that shown in Fig. 1.2.9 (see also [27–29]); in particular, four elements share the node located at the notch tip if the notch opening angle 2α is lower than 90° , while two elements share the node at notch tip when the notch opening angle is $2\alpha > 90^\circ$, as shown in Fig. 1.2.9 taking advantage of the geometrical symmetry;
- concerning Eqs. (1.2.33) and (1.2.35) related to mode 1 and mode 3 loadings, respectively, V-notches are characterised by an opening angle 2α ranging from 0° to 135° ; while it should be remembered that calibration for mode 2 loading is restricted to $2\alpha = 0$ (crack case);
- for mode 1 loading (Eq. (1.2.33)) the mesh density ratio a/d that can be adopted in numerical analyses must be $a/d \geq 3$ to obtain $K_{FE}^* = 1.38 \pm 3\%$, a being the minimum between the notch depth (or crack length) and the ligament lengths; for mode 2 loading (Eq. (1.2.34)) more refined meshes are required, the mesh density ratio a/d having to satisfy $a/d \geq 14$

to obtain $K_{FE}^{**} = 3.38 \pm 3\%$; finally, in case of mode 3 loading (Eq. (1.2.35)) the condition $a/d \geq 3$ must again be satisfied to obtain $K_{FE}^{***} = 1.93 \pm 3\%$.

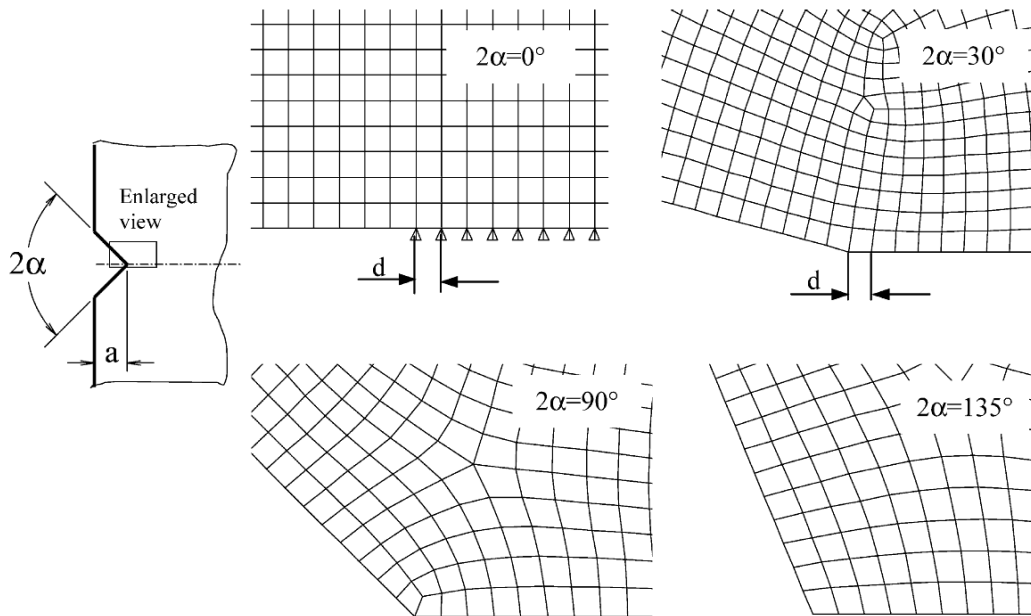


Figure 1.2.9. Mesh patterns according to PSM. The automatic free mesh generator available in ANSYS code was used and the global element size d was set equal to 1 mm (Meneghetti and Lazzarin [27]).

It should be noted that different stress extrapolation rules from the integration points to the nodal points lead to different values of the peak stresses, moreover finite element analyses performed using higher-order elements or significantly different FE patterns imply that coefficients of Eqs. (1.2.33)-(1.2.35) should be recalculated.

Based on the NSIFs and the appertaining locally averaged $\Delta\bar{W}$ values, the fatigue strength of welded joints can be given in terms of weighted peak stresses. The method was originally based on two-dimensional FE models. Recently, the PSM has also been combined with 3D numerical models and eight-node brick elements to assess the fatigue strength of steel-welded joints having complex geometry and characterised by toe as well as root cracking [30,31].

1.3 Blunt V-notches

1.3.1 Local stress fields and Generalised Notch Stress Intensity Factors

The NSIF concept referring to sharp V-notch tips with inclusion of the conventional SIF approach referring to pointed crack tips has been extended also to the generalised NSIF concept referring to rounded notches with crack shape or V-notch shape in two variants: parabolic, elliptic or hyperbolic notches ('blunt notches') on the one hand and root hole notches ('keyholes' when considering crack shapes) on the other hand.

Notch rounding changes the stresses at the V-notch or crack tip substantially insofar as the stress singularity is removed. This means that the notch stresses remain finite, but their angular and radial distribution is linked to that of the corresponding sharp notches. Indeed, the stress distribution connected with the singularity remains widely unchanged at distances from the notch root larger than one half of the notch radius ρ , provided the radius is sufficiently small in relation to the notch depth or crack length (sharp notches).

It is shown that the stress distribution at sharply rounded notches subjected to the loading modes 1, 2 and 3 can be described by the generalised NSIFs $K_{1\rho}$, $K_{2\rho}$ and $K_{3\rho}$ as the governing field parameters. These NSIFs are related to the maximum notch stresses σ_{\max} , τ_{\max} and τ^*_{\max} , which constitute the conventional stress concentration factors (SCFs). In contrast to the SCFs, the generalised NSIFs describe not only the maximum stress at one point but also the whole stress field in the vicinity of the notch root. In consequence, notched components scaled in geometrical proportion have the same value of the SCF K_t but different values of the NSIF. The field information provided by the NSIFs is needed for assessing failure processes such as crack initiation and propagation or microstructural damaging phenomena. In the following, the stress field equations for blunt V-notches subjected to the three basic loading modes are shortly discussed.

A general solution for the stress field at sharply rounded (blunt) V-notches, subjected to in-plane tensile and shear loading, is available in the literature [8,32,33]. The reference nomenclature is shown in Fig. 1.3.1. The theoretical frame, namely Kolosov–Muskhelishvili's complex stress function method

combined with Neuber's auxiliary system of curvilinear coordinates, has already been mentioned when considering sharp V-notches. Here, the improved solution by Filippi is evaluated with respect to blunt V-notches. The solution provides a second singular term perturbing the one-term sharp notch solution (exponents - 0.5 and -1.5 in the case of $2\alpha = 0$). The singularity is outside of the physical domain for blunt notches.

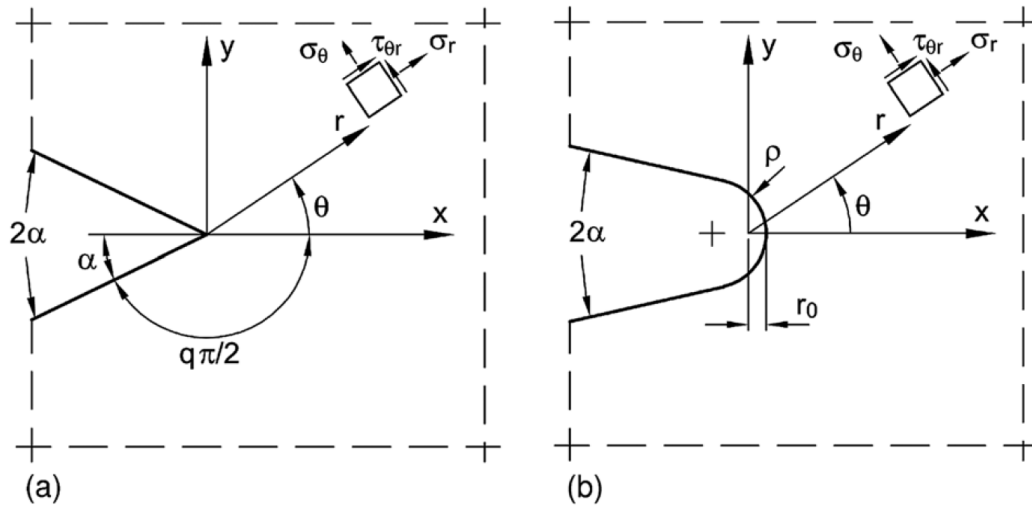


Figure 1.3.1. Coordinate systems, symbols and in-plane notch stress components at (a) sharp V-notch and at (b) the corresponding rounded V-notch; with $r_0 = \rho(q-1)/q$; (Lazzarin et al. [8,32,33]).

Referring to the auxiliary system of curvilinear coordinates (conformal mapping function $z = w^q$), the following relationships apply:

$$q = \frac{2\pi - 2\alpha}{\pi} \quad (1.3.1)$$

$$r_0 = \frac{q - 1}{q} \cdot \rho \quad (1.3.2)$$

with radius ρ of notch root curvature and distance r_0 between the origin of the x - y coordinate system and the notch root. Only for the parabolic notch ($2\alpha = 0$, $q = 2$), the simple relationship $r_0 = \rho/2$ is valid.

The characteristic stress components in the bisector plane ($\theta = 0$) of the blunt V-notches are found proportional to K_1 or K_2 , the first term being identical with that

in Eq. (1.2.1) for sharp V-notches, the additive non-singular term being related to r/r_0 . In the considered early solutions [8,32], the conventional NSIFs K_1 and K_2 of the corresponding sharp V-notch have been used. In accordance with the further development of the theory [33], the generalised NSIFs substitute the simple NSIFs in the stress field equations.

Within the more general theoretical frame, the generalised NSIFs $K_{1\rho}$, $K_{2\rho}$ and also $K_{3\rho}$ may be found by evaluating the corresponding maximum stresses in the bisector plane of the rounded notch or crack as limit values for $r \rightarrow r_0$ (or $r \rightarrow r_0^+$, the position of $\tau_{r\theta_{\max}}$ in mode 2 loading). The procedure may be combined with averaging these NSIFs over a small distance ahead of the notch root. The following formulae are applicable to V-notches inclusive of cracks [33,34]:

$$K_{1\rho} = \lim_{r \rightarrow r_0} \frac{\sqrt{2\pi} \cdot r^{1-\lambda_1} \cdot \sigma_{\theta\theta}(r, 0)}{1 + \tilde{\omega}_1 \left(\frac{r}{r_0}\right)^{\mu_1-\lambda_1}} = \frac{\sqrt{2\pi} \cdot r_0^{1-\lambda_1} \cdot \sigma_{\theta\theta}(r_0, 0)}{1 + \tilde{\omega}_1} \quad (1.3.3)$$

$$K_{2\rho} = \lim_{r \rightarrow r_0^+} \frac{\sqrt{2\pi} \cdot r^{1-\lambda_2} \cdot \tau_{r\theta}(r, 0)}{1 + \tilde{\omega}_2 \left(\frac{r}{r_0}\right)^{\mu_2-\lambda_2}} = \frac{\sqrt{2\pi} \cdot r_0^{1-\lambda_2} \cdot \tau_{r\theta}(r_0^+, 0)}{1 - \left(\frac{r_0^+}{r_0}\right)^{\mu_2-\lambda_2}} \quad (1.3.4)$$

$$K_{3\rho} = \lim_{r \rightarrow r_0} \sqrt{2\pi} \cdot r^{1-\lambda_3} \cdot \tau_{\theta z}(r, 0) = \sqrt{2\pi} \cdot r_0^{1-\lambda_3} \cdot \tau_{\theta z}(r_0, 0) \quad (1.3.5)$$

The value $\tilde{\omega}_2 = -1$ in Eq. (1.3.4) is part of the stress field solution. The limit value $r \rightarrow r_0^+$ instead of $r \rightarrow r_0$ in mode 2 loading is proposed by Radaj in [1] in order to avoid numerical problems when introducing $r = r_0$.

The generalised NSIFs $K_{1\rho}$, $K_{2\rho}$ and also $K_{3\rho}$ differ from the conventional NSIFs K_1 , K_2 and also K_3 for finite values of ρ . They are slightly larger than K_1 , K_2 and K_3 , in particular their values increase with enlarged notch radii ρ . The following relationship should be true, since $r_0 \propto \rho$:

$$K_i = \lim_{\rho \rightarrow 0} K_{i\rho} \quad \text{with } i = 1, 2, 3 \quad (1.3.6)$$

1.3.2 Averaged Strain Energy Density approach

The local averaged SED concept, first proposed by Lazzarin and Zambardi dealing with sharp V-notches [15], has been later extended by Lazzarin and Berto [35] to blunt V-notches inclusive of U-notches and circle-arc V-notches. Tensile loading (mode 1) has been considered first in the analytic derivations [35], which are then transferred to mixed mode 1+2 loading conditions based on a semi-empirical, but numerically confirmed procedure [36]. The determining geometrical parameters of the crescent-shaped control volume area at blunt V-notches in comparison to the sharp notch situation are shown in Fig. 1.3.2. The area A of the averaged local SED has the circular notch edge with radius ρ as the boundary on one side and a circle arc with radius $R_0 + r_0$ as the boundary on the other side. The two radii are differently centred. The centre of the radius ρ is geometrically given. The centre of the radius $R_0 + r_0$ is identical with the centre of the polar coordinate system in the analytical solution for the corresponding blunt V-notch problem (see previous Section 1.3.1). The parameter r_0 depends on the notch opening angle 2α according to Eq. (1.3.2). It is $r_0 = \rho/2$ for $2\alpha = 0$ and $r_0 \rightarrow 0$ for $2\alpha \rightarrow \pi$, that is, the considered centre of the polar coordinates moves closer to the notch root for larger notch opening angles. The control volume radius R_0 is introduced as a material parameter, which is independent of the notch geometry.

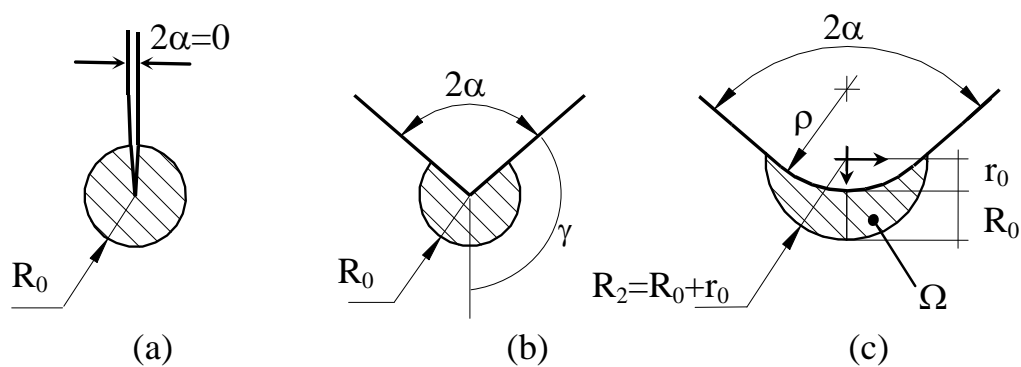


Figure 1.3.2. Geometrical parameters of the control volume area used for averaging the SED in the close vicinity of the notch root: (a) crack, (b) sharp V-notch and (b) blunt V-notch; (Lazzarin and Berto [35]).

The elastic local averaged SED under mode 1 loading is expressed in the following form [35]:

$$\bar{W}_1 = F(2\alpha) \cdot H\left(2\alpha, \frac{R_0}{\rho}\right) \cdot \frac{\sigma_{\max}^2}{E} \quad (1.3.7)$$

By introducing the generalised NSIF $K_{1\rho}$ together with the notch radius ρ instead of the maximum notch stress σ_{\max} , a more compact form of Eq. (1.3.7) is gained:

$$\bar{W}_1 = H\left(2\alpha, \frac{R_0}{\rho}\right) \cdot \frac{K_{1\rho}^2}{E} \cdot \rho^{2(\lambda_1-1)} \quad (1.3.8)$$

In cases of superimposed tensile and shear loading (mixed mode 1+2), the procedure above, developed for tensile loading can be transferred on a semi-empirical, but numerically confirmed basis.

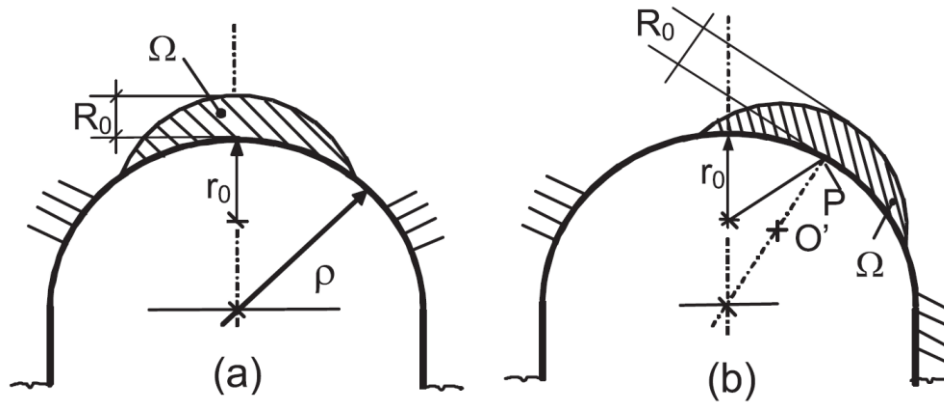


Figure 1.3.3. Geometrical parameters of the control volume area used for averaging the SED in the close vicinity of a U-notch root under (a) mode I and (b) mixed mode I+II loading conditions; (Berto et al. [36]).

Under in-plane mixed mode 1+2 conditions, the maximum principal stress does not occur at the notch root in the bisector plane but it is shifted to a notch edge point out of the bisector plane. It has been proven numerically (by means of FE analyses) that correct averaged SED values are gained, if the crescent-shaped control volume and the appertaining base point of r_0 are rotated by the polar angle θ^* around the base point of ρ into the direction of the point of maximum stress,

assuming a circle arc [36] as it is shown in Fig. 1.3.3b. The angle θ^* , which denotes simultaneously the crack initiation point and the crack propagation direction, depends on the ratio of tensile to shear loads.

It should be noted that for blunt V-notches under in-plane mixed mode 1+2, as well as under pure modes 2 or 3 loading conditions, there are no theoretical formulations in the literature similar to that reported in Eq. (1.3.8) for pure mode 1 loading, which allow to calculate analytically the SED averaged over the control volume. However, Lazzarin and co-workers [24] provided evidence that it is possible to evaluate numerically the SED parameter directly from the results of FE analyses, \bar{W}_{FEM} , by summing up the strain energies $W_{FEM,i}$ calculated for the i -th finite element located inside the control volume (SENE in ANSYS[®] numerical software) and subsequently by dividing by the total volume (A in Fig. 1.2.4, VOLU in ANSYS[®] numerical software):

$$\bar{W}_{FEM} = \frac{\sum_A W_{FEM,i}}{A} = \frac{\sum_A SENE}{\sum_A VOLU} \quad (\text{for application in ANSYS}^{\text{®}}) \quad (1.3.9)$$

Equation (1.3.9) defines the so-called direct approach to evaluate the SED parameter. Additionally, it has been shown that the adopted FE meshes can be very coarse inside the control volume having radius R_0 [24], as discussed also in previous Section 1.2.2.3.

Finally, it is important to underline that the averaged SED approach can be successfully applied also to fracture and fatigue problems of structural components weakened by blunt notches, according to the same procedures and considerations previously described with reference to sharp notches and which are not recalled here for the sake of brevity. Some of the most recent applications of the averaged SED concept to blunt notches can be found in the comprehensive review by Berto and Lazzarin [4].

References

- [1] Radaj D. State-of-the-art review on extended stress intensity factor concepts. *Fatigue Fract Eng Mater Struct* 2014;37:1–28.
- [2] Radaj D. State-of-the-art review on the local strain energy density concept and its relation to the J -integral and peak stress method. *Fatigue Fract Eng Mater Struct* 2015;38:2–28.
- [3] Berto F, Lazzarin P. A review of the volume-based strain energy density approach applied to V-notches and welded structures. *Theor Appl Fract Mech* 2009;52:183–94.
- [4] Berto F, Lazzarin P. Recent developments in brittle and quasi-brittle failure assessment of engineering materials by means of local approaches. *Mater Sci Eng R Reports* 2014;75:1–48.
- [5] Williams ML. Stress singularities resulting from various boundary conditions in angular corners of plates in tension. *J Appl Mech* 1952;19:526–8.
- [6] Gross B, Mendelson A. Plane elastostatic analysis of V-notched plates. *Int J Fract Mech* 1972;8:267–76.
- [7] Qian J, Hasebe N. Property of eigenvalues and eigenfunctions for an interface V-notch in antiplane elasticity. *Eng Fract Mech* 1997;56:729–34.
- [8] Lazzarin P, Tovo R. A unified approach to the evaluation of linear elastic stress fields in the neighborhood of cracks and notches. *Int J Fract* 1996;78:3–19.
- [9] Lazzarin P, Tovo R. A notch intensity factor approach to the stress analysis of welds. *Fatigue Fract Eng Mater Struct* 1998;21:1089–103.
- [10] Lazzarin P, Tovo R, Filippi S. Elastic stress distributions in finite size plates with edge notches. *Int J Fract* 1998;91:269–82.
- [11] Atzori B, Lazzarin P, Tovo R. Stress distributions for V-shaped notches under tensile and bending loads. *Fatigue Fract Eng Mater Struct* 1997;20:1083–92.
- [12] Lazzarin P, Sonsino CM, Zambardi R. A notch stress intensity approach to assess the multiaxial fatigue strength of welded tube-to-flange joints subjected to combined loadings. *Fatigue Fract Eng Mater Struct* 2004;27:127–40.
- [13] Neuber H. *Kerbspannungslehre*, 2nd Edition. Berlin: Springer-Verlag; 1958.
- [14] Neuber H. *Kerbspannungslehre*, 3rd Edition. Berlin: Springer-Verlag; 1985.
- [15] Lazzarin P, Zambardi R. A finite-volume-energy based approach to predict the static and fatigue behavior of components with sharp V-shaped notches. *Int J Fract* 2001;112:275–98.

- [16] Beltrami E. Sulle condizioni di resistenza dei corpi elastici. *Il Nuovo Cimento* 18 (in Italian); 1885.
- [17] Yosibash Z, Bussiba A, Gilad I. Failure criteria for brittle elastic materials. *Int J Fract* 2004;307–33.
- [18] Lazzarin P, Berto F. From Neuber's Elementary Volume to Kitagawa and Atzori's Diagrams: An Interpretation Based on Local Energy. *Int J Fract* 2005;135:L33–8.
- [19] Glinka G. Energy density approach to calculation of inelastic strain-stress near notches and cracks. *Eng Fract Mech* 1985;22:485–508.
- [20] Lazzarin P, Zambardi R. The Equivalent Strain Energy Density approach re-formulated and applied to sharp V-shaped notches under localized and generalized plasticity. *Fatigue Fract Eng Mater Struct* 2002;25:917–28.
- [21] Hobbacher A. Recommendations for Fatigue design of welded joints and components. 2008.
- [22] Livieri P, Lazzarin P. Fatigue strength of steel and aluminium welded joints based on generalised stress intensity factors and local strain energy values. *Int J Fract* 2005;133:247–76.
- [23] Lazzarin P, Berto F, Gomez F, Zappalorto M. Some advantages derived from the use of the strain energy density over a control volume in fatigue strength assessments of welded joints. *Int J Fatigue* 2008;30:1345–57.
- [24] Lazzarin P, Berto F, Zappalorto M. Rapid calculations of notch stress intensity factors based on averaged strain energy density from coarse meshes: Theoretical bases and applications. *Int J Fatigue* 2010;32:1559–67.
- [25] Nisitani H, Teranishi T. KI value of a circumferential crack emanating from an ellipsoidal cavity obtained by the crack tip stress method in FEM. In: Guagliano M, Aliabadi MH, editors. *Proc. 2nd Int. Conf. Fract. damage Mech.*, 2001, p. 141–6.
- [26] Nisitani H, Teranishi T. KI of a circumferential crack emanating from an ellipsoidal cavity obtained by the crack tip stress method in FEM. *Eng Fract Mech* 2004;71:579–85.
- [27] Meneghetti G, Lazzarin P. Significance of the elastic peak stress evaluated by FE analyses at the point of singularity of sharp V-notched components. *Fatigue Fract Eng Mater Struct* 2007;30:95–106.
- [28] Meneghetti G. The use of peak stresses for fatigue strength assessments of welded lap joints and cover plates with toe and root failures. *Eng Fract Mech* 2012;89:40–51.
- [29] Meneghetti G. The peak stress method for fatigue strength assessment of tube-to-flange welded joints under torsion loading. *Weld World* 2013;57:265–75.
- [30] Meneghetti G, Guzzella C. The peak stress method to estimate the mode I notch stress intensity factor in welded joints using three-dimensional finite element models. *Eng Fract Mech* 2014;115:154–71.

- [31] Meneghetti G, Guzzella C, Atzori B. The peak stress method combined with 3D finite element models for fatigue assessment of toe and root cracking in steel welded joints subjected to axial or bending loading. *Fatigue Fract Eng Mater Struct* 2014;37:722–39.
- [32] Filippi S, Lazzarin P, Tovo R. Developments of some explicit formulas useful to describe elastic stress fields ahead of notches in plates. *Int J Solids Struct* 2002;39:4543–65.
- [33] Lazzarin P, Filippi S. A generalized stress intensity factor to be applied to rounded V-shaped notches. *Int J Solids Struct* 2006;43:2461–78.
- [34] Zappalorto M, Lazzarin P, Yates JR. Elastic stress distributions for hyperbolic and parabolic notches in round shafts under torsion and uniform antiplane shear loadings. *Int J Solids Struct* 2008;45:4879–901.
- [35] Lazzarin P, Berto F. Some expressions for the strain energy in a finite volume surrounding the root of blunt V-notches. *Int J Fract* 2005;135:161–85.
- [36] Berto F, Lazzarin P, Gómez FJ, Elices M. Fracture assessment of U-notches under mixed mode loading: two procedures based on the “equivalent local mode I” concept. *Int J Fract* 2007;148:415–33.

CHAPTER 2

BRITTLE FRACTURE UNDER MIXED MODE STATIC LOADING

2.1. Brittle fracture of blunt notched components made of PMMA under mixed mode I+II loading ^(*)

Nomenclature

d	slit length
D	disk diameter
E	Young's modulus
K_{Ic}	fracture toughness
P	fracture load
P_{av}	average fracture load
r_0	distance between notch tip and origin of the reference system
R_c	control radius
\overline{W}	SED measured over the control volumes
W_c	critical SED value of the considered material

Symbols

2α	notch opening angle
β	loading angle
ν	Poisson's ratio
ρ	notch tip radius
σ_t	ultimate tensile strength

(*) See also:

- Torabi, A. R.; Campagnolo, A.; Berto, F. Investigation of mixed mode brittle fracture in key-hole notches using the local energy. *Acta Mechanica*; 226 (7): 2313-2322 (2015);
- Torabi, A. R.; Campagnolo, A.; Berto, F. Static strength of V-notches with end holes under combined tension-shear loading: Experimental measurement by the disk test and theoretical prediction by the local energy. *ASTM Journal of Testing and Evaluation* (In press).

2.1.1. Introduction

About two decades ago, a new branch was born inside the classic fracture mechanics (FM), called the notch fracture mechanics (NFM), which investigates failure of notched domains made of brittle and ductile materials. Most of the investigations in the NFM concentrate on the static and monotonic failure of notched members. The modes of loading for a notched member is completely the same with those for a cracked member, namely the opening mode (i.e. mode I), the in-plane shear mode (i.e. mode II), the out-of-plane shear mode (i.e. mode III), and any combinations of these modes, so called mixed mode loading. The fundamental failure concepts in the NFM are also the same with those in the classic fracture mechanics. For example, the cohesive zone model (CZM) [1–4], the maximum tangential stress (MTS) and the mean stress (MS) [5–20], the J-integral [21–27], the finite fracture mechanics (FFM) [28,29], the theory of critical distances (TCD) [30] and the strain energy density (SED) [31–42] are the names a few.

Brittle fracture has been certainly the most important topic in the context of NFM because of its catastrophic nature. This failure mode usually takes place suddenly in brittle and quasi-brittle materials like ceramics, brittle polymers, rocks, graphite, high-strength metals and alloys etc. Due to simplicity, most of brittle fracture investigations in NFM have been performed under mode I loading. Mixed mode I+II notch investigations are much more complicated than mode I ones from the viewpoints of both experiment and theory. During the past few years, mixed mode I+II brittle fracture assessment of notched components has been accelerated by the researchers, aiming to measure experimentally the notch fracture toughness (NFT) and to predict the experimentally obtained NFT values by means of appropriate brittle fracture criteria. This is because mixed mode I+II loading is widely present in real engineering applications and it is complicated to be investigated.

As mentioned earlier, various failure concepts have been previously proposed in the literature to predict brittle fracture in notched domains. One of the most well established criteria in the field of brittle fracture is certainly the strain energy density (SED) criterion. Sih [43] proposed the strain energy density factor (SEDF)

for cracked elements by taking into consideration simultaneously both the strain energy density (SED) and the critical distance measured from the crack tip. According to Sih's criterion, brittle fracture happens in a cracked brittle component when the SEDF reaches to its critical value [43]. By setting a minimum condition on the SEDF, the direction of crack propagation could also be determined [43]. Although Sih's point-wise criterion was proposed for cracked bodies, it became the start point for the other researchers who extended the SED concept to sharp and round-tip notches (sharp and blunt V-notches, U-notches etc.) by averaging SED over a specified control volume which embraces the notch edge, in order to predict brittle fracture in notched domains under various loading conditions [31,32,34–37,44]. The SED predictions have been frequently verified by means of the experimental results obtained from testing various materials, specimens, and notches under different loading conditions including mode I, mode II and mixed mode I+II etc. [31,32,34–37,41,44]. Some recent works on the fracture analysis of blunt notches by means of SED are those published in Refs. [40,45–48]. The SED criterion has been utilized to estimate the maximum load that U-notched Brazilian disk (UNBD) specimens made of coarse-grained polycrystalline graphite could sustain under pure mode I [45], pure mode II [46] and mixed mode I+II [47] loadings. Mode I fracture of blunt V-notches introduced in three different test specimens made of graphite has been also analyzed by means of SED [48]. In some recent researches, the SED criterion has also been extended successfully to torsion [38] and compression [39] loadings. Other than SED, a few failure concepts have also been suggested and utilized for predicting fracture in notched components. For instance, the point-stress (with different names e.g. the maximum tangential stress; MTS) and the mean-stress concepts have been frequently employed to predict fracture in V- and U-notches under mode I [5–11], mode II [12,13] and mixed mode I+II [14–20] loading conditions. Moreover, the cohesive zone model [1–4], the finite fracture mechanics [28,29], the theory of critical distances [49], and the J-integral [21–27] have been employed for theoretical fracture assessment of sharp and blunt notches.

Some notch features are not fundamentally original, but they are resulted from applying a repairing method to the original notch shapes weakened by crack(s) and damage(s) emanating from the notch border. For example, consider a U- or V-notch damaged by a crack in its border (see Fig. 2.1.1). The most common repairing method for this damaged notch is to remove the crack by drilling a hole with the radius of normally equal to the crack length. If the crack length is small and larger than the notch tip radius, a key-hole notch or a V-notch with end hole (VO-notch), respectively, will be obtained from the repairing process. Since the notch feature after repair (key-hole or VO-notch) is different from the original U- or V-shape, the stress distribution and the stress gradient at the neighborhood of the new notch are different from those of the original notch needing necessarily a new fracture assessment.

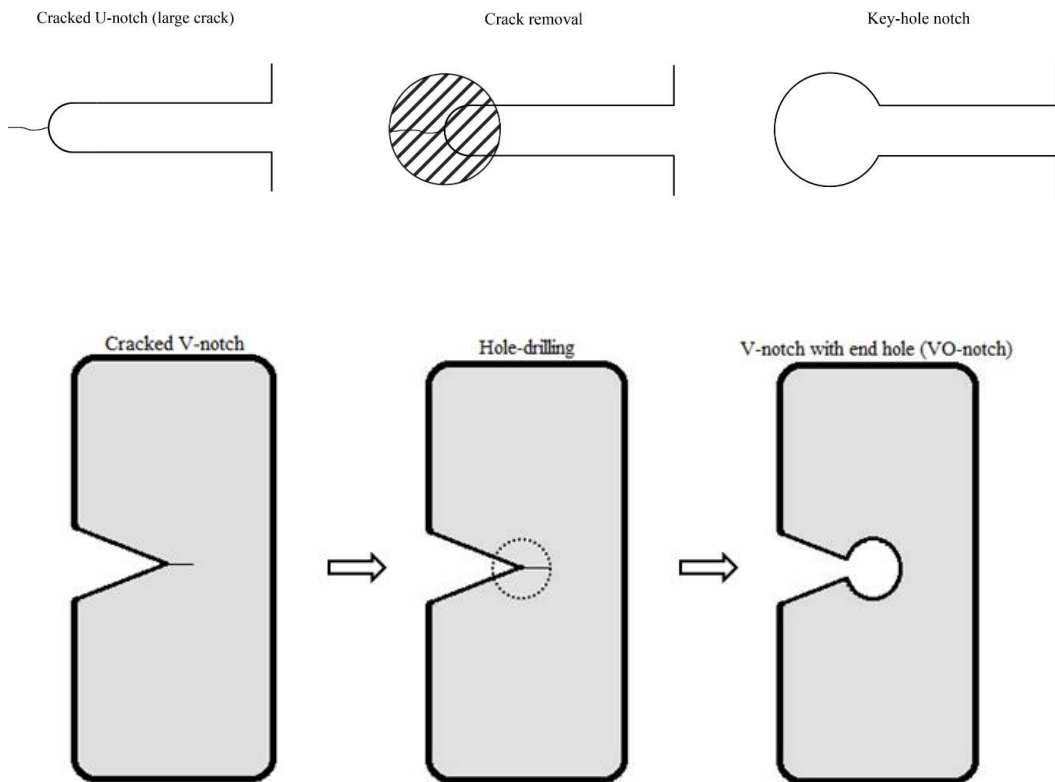


Figure 2.1.1. (a) Key-hole notch resulted from removing a small crack from a U-notch border. (b) V-notch with end hole (VO-notch) resulted from removing a small crack from a V-notch border.

In this research, the Brazilian disk specimen weakened by keyholes, called Key-BD specimen, and that weakened by V-notches with end holes, called VO-BD specimen, made of PMMA was utilized to perform brittle fracture tests at room temperature under mixed mode I+II loading. The experimentally recorded fracture loads were theoretically predicted by means of the SED criterion. A very good agreement was shown to exist between the experimental and theoretical results for various notch angles and different notch radii.

2.1.2. Experiments

A large bulk of new experimental results was provided in this study on key-hole notched and on recently proposed [50] VO-notched disk-type specimens under mixed mode I+II loading. The experimental program is elaborated in the next subsections.

2.1.2.1. Material

The material utilized in the experiments was Polymethyl-metacrylate (PMMA). PMMA is widely used in typical brittle fracture tests because it is cheap compared to the other brittle materials. Most of PMMAs exhibit quasi-brittle behavior at room temperature and brittle behavior at low temperatures (usually below $-60\text{ }^{\circ}\text{C}$). The type of PMMA in this study was completely the same with that reported in Refs. [15,18]. Some of the mechanical properties of the tested PMMA at room temperature are presented in Table 2.1.1 [15,18].

Table 2.1.1. Some of the mechanical properties of PMMA at room temperature [15,18].

Material property	Value
Elastic modulus, E (GPa)	2.96
Poisson's ratio, ν	0.38
Ultimate tensile strength (MPa)	70.5
Plane-strain fracture toughness ($\text{MPa m}^{0.5}$)	1.96

2.1.2.2. Tested Specimen

2.1.2.2.1 Keyhole notched specimens

The Brazilian disk specimen containing a central dumbbell-shaped slit with two key-ends (Key-BD specimen) was utilized in the present study for testing under mixed mode I+II loading (see Fig. 2.1.2). According to Fig. 2.1.2, as the loading angle β (i.e. the angle between the slit bisector line and the loading direction) increases from zero to larger values, various in-plane loading conditions between pure mode I and pure mode II can be achieved. In order to perform fracture experiments under mixed mode I+II loading, the loading angle corresponding to pure mode II loading (β_{II}) should first be determined. For this purpose, finite element (FE) stress analysis was performed. Details of determining β_{II} are briefly described herein.

For $\beta = 0^\circ$, the key-ends encounter opening and hence, they experience pure mode I loading. In this state, the notch bisector line at the vicinity of the notch experiences only the tensile stress. As β increase gradually from zero, the value of tensile stress decreases and conversely, that of the shear stress increases. For a specific β value, called β_{II} , the tensile stress on the notch bisector line becomes zero meaning that the notch does not experience opening. Trivially, this means pure mode II loading. In other words, to obtain β_{II} , one should increase β from zero till the tensile stresses at the notch bisector line becomes equal to zero.

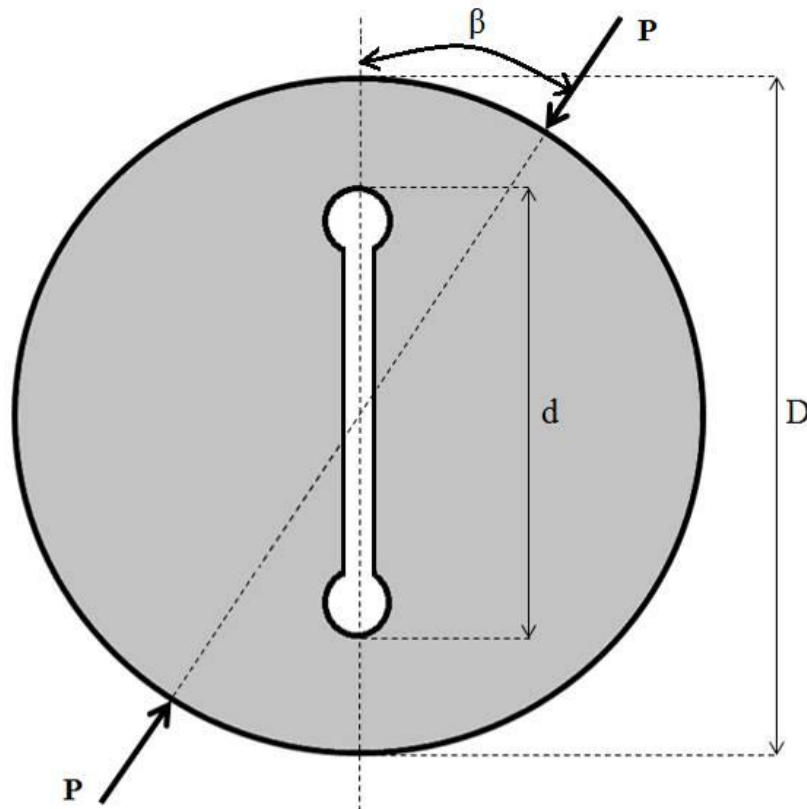


Figure 2.1.2. The Key-BD specimen subjected to mixed mode I+II loading.

The disk diameter (D) and the thickness were equal to 80 mm and 10 mm, respectively. The slit length (d) was considered to be equal to 24 mm and 40 mm (the relative notch length ratio (RNL) d/D was equal to 0.3 and 0.5, respectively). To produce the Key-BD specimens, a PMMA plate of 10 mm thick was first provided and then, the drawing of each specimen was submitted to a high-precision 2-D CNC water-jet cutting machine for fabrication. Finally, the cut surfaces were accurately polished by means of fine abrasive papers. For the specimens with $d/D = 0.3$, three notch radii of 1, 2 and 4 mm were considered while for $d/D=0.5$, four radii of 1, 2, 4 and 6 mm. The tests were conducted under mixed mode I+II loading conditions. Since β_{II} values were obtained from FE analysis to be equal to approximately 31 (deg.) and 26 (deg.) for $d/D = 0.3$ and $d/D = 0.5$, respectively, four loading angles of $\beta = 0, 10, 20$ and 31 (deg.) and $\beta = 0, 10, 15$ and 26 (deg.) were considered in the tests for the above mentioned d/D values, respectively. Each test was repeated three times in order to check the

repeatability of the tests. All in all, 84 tests were performed in the present investigation. In order to provide monotonic loading conditions, the test speed was set to be equal to 0.3 mm/min. Figs. 2.1.3 and 2.1.4 represent several Key-BD specimens during and after fracture tests, respectively.



Figure 2.1.3. A Key-BD specimen under mixed mode I+II fracture test.

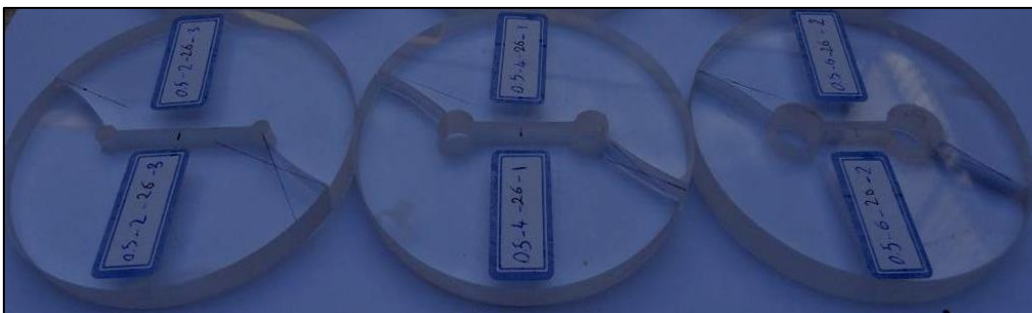


Figure 2.1.4. A few Key-BD specimens after fracture.

2.1.2.2.2 VO-notched specimens

A new version of the well-known Brazilian disk specimen weakened by central V-notches with end holes, called VO-BD specimen, which has been recently

proposed [50], was utilized in this study to conduct mixed mode I+II fracture experiments on VO-notches. Fig. 2.1.5 clearly shows that various in-plane loading conditions can be achieved for the VO-notch by changing the loading angle β (i.e. the angle between the loading direction and the slit bisector line) from zero (for pure mode I loading) to larger values (for mixed mode I+II loading). In other words, different β values mean different mode mixities; i.e. various contributions of tensile and shear stresses at the notch tip vicinity.

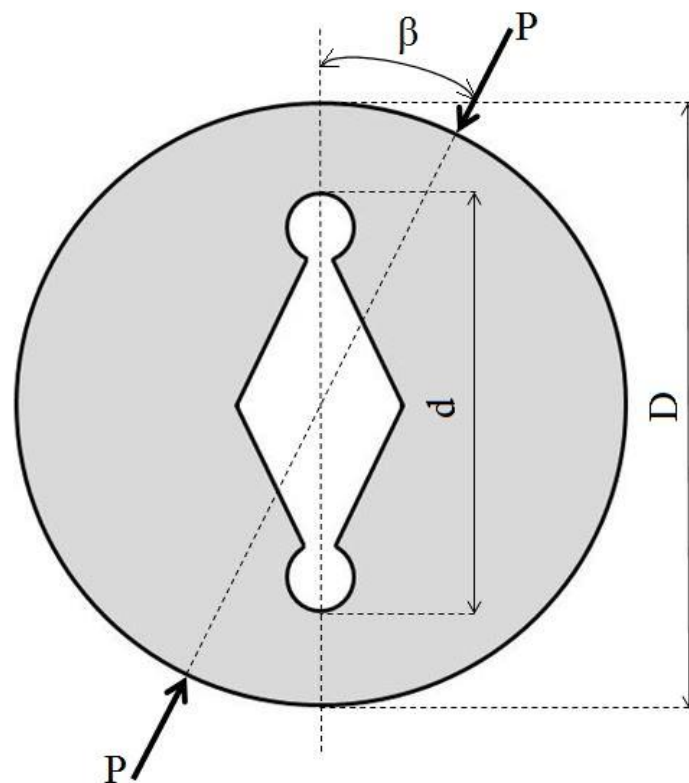


Figure 2.1.5. The VO-BD specimen subjected to mixed mode I+II loading.

The disk diameter (D), the overall slit length (d), and the disk thickness were equal to 80 mm, 40 mm and 10 mm, respectively. For producing the VO-BD specimens, a PMMA plate of 10 mm thick was first provided. Then, the drawing of each specimen was given to a high-precision 2-D CNC water-jet cutting machine for fabrication. Three notch angles of 30, 60 and 90 (deg.) and four notch radii of 0.5, 1, 2 and 4 mm were considered in the tests meaning twelve different VO-notch geometries.

Four various loading angles β have also been examined for each notch geometry providing different mode mixities. In order to select appropriate β angles, the β value for which pure mode II loading is resulted ($\beta = \beta_{II}$) is essentially needed. It was found by the finite element (FE) stress analysis that β_{II} depends considerably upon the notch angle and slightly on the notch radius (β_{II} values were obtained to be approximately equal to 25, 28, and 33 (deg.) for the notch angles 30, 60, and 90 (deg.), respectively). For notch angles 30, 60 and 90 (deg.), the loading angles β were considered to be (0, 10, 15, 25), (0, 10, 20, 28) and (0, 10, 20, 33), respectively. Each test was repeated three times in order to check the repeatability of the tests. All in all, 144 new fracture tests were performed in this study. The method of determining β_{II} is briefly described in the next paragraph.

For $\beta = 0^\circ$, the VO-ends of the central slit encounter opening and thus, they experience pure mode I loading. In this state, the notch bisector line at the neighborhood of the notch experiences only the tensile stresses. As β increases gradually from zero, the value of tensile stress decreases and conversely, that of the shear stress increases. For a specific β value, called β_{II} , the tensile stress on the notch bisector line becomes zero meaning that the notch does not experience opening. This means trivially pure mode II loading. In other words, to achieve β_{II} , one should increase β from zero till the tensile stresses at the notch bisector line becomes equal to zero.

Figure 2.1.6 represents a VO-BD specimen subjected to mixed mode I+II loading inside the test machine. Some VO-BD specimens after fracture are also shown in Fig. 2.1.7. The test speed was set to be 0.5 mm/min providing monotonic loading conditions.



Figure 2.1.6. A VO-BD specimen subjected to mixed mode I+II loading inside the test machine.

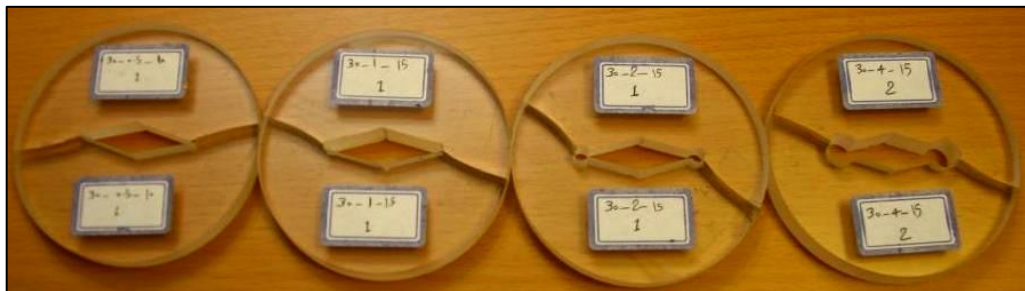


Figure 2.1.7. Some VO-BD specimens after fracture.

2.1.2.3. Test results

2.1.2.3.1 Keyhole notched specimens

Table 2.1.2 summarizes the experimentally recorded fracture loads for different notch radii and various values of the RNL ratio. Each specimen is denoted by a specific index $X-Y-Z$ where X , Y and Z denote the RNL, the notch radius and the loading angle β , respectively. For instance, the index 0.3-1-10 identifies the Key-BD specimen with $d/D = 0.3$ having the notch radius of 1 mm loaded under $\beta = 10$

(deg.). Meanwhile, P_i ($i = 1, 2, 3$) denotes the fracture loads for the three tests repeated.

Table 2.1.2. The experimental fracture loads of the Key-BD specimens.

Specimen index	P_1 (N)	P_2 (N)	P_3 (N)	$P_{av.}$ (N)
0.3-1-0	9391	9080	9302	9258
0.3-1-10	8573	7967	8935	8492
0.3-1-20	8510	8439	8369	8440
0.3-1-31	7288	7333	7220	7280
0.3-2-0	8664	9361	9691	9239
0.3-2-10	10669	9868	10268	10268
0.3-2-20	9423	9631	9480	9511
0.3-2-31	7900	8295	8690	8295
0.3-4-0	10891	10635	10768	10765
0.3-4-10	9212	9510	9808	9510
0.3-4-20	8599	7965	7332	7966
0.3-4-31	9987	8671	7356	8671
0.5-1-0	6928	6859	6748	6845
0.5-1-10	6010	5921	5685	5872
0.5-1-15	5171	5023	5538	5244
0.5-1-26	4873	5054	4486	4804
0.5-2-0	7015	6991	7040	7015
0.5-2-10	6991	6835	6679	6835
0.5-2-15	6719	6737	6755	6737
0.5-2-26	5388	5250	5113	5250
0.5-4-0	6889	5992	6441	6441
0.5-4-10	7177	7422	7299	7299
0.5-4-15	7109	7109	7109	7109
0.5-4-26	6427	6478	6499	6468
0.5-6-0	7173	6608	5957	6579
0.5-6-10	6928	6991	5219	6379
0.5-6-15	6093	5759	6427	6093
0.5-6-26	4665	4409	4369	4481

The experimental observations confirmed that the load-displacement plots for the Key-BD specimens were linear up to final breakage. No evidences of large deformations around the notch and abrupt fall of the load from a maximum to zero confirmed sudden fracture of the specimens. Thus, using brittle fracture criteria for predicting the experimental results is fundamentally permissible. In the forthcoming sections, the SED averaged over a specified control volume which embraces the notch edge is employed to predict the experimental fracture loads of the Key-BD specimens presented in Table 2.1.2.

2.1.2.3.2 VO-notched specimens

Table 2.1.3 summarizes the experimental fracture loads of the VO-BD PMMA specimens for various notch angles and different notch radii. Each specimen is identified by an index (see the first column of Table 2.1.3) consisting of three numbers like X-Y-Z in which X, Y and Z associate with the notch angle, the notch radius and, the loading angle, respectively. For example, the index 60-1-20 belongs to a VO-notch with 60 (deg.) angle and 1 mm radius subjected to a compressive load with $\beta = 20$ (deg.). Note that P_1 , P_2 and P_3 denote the fracture loads in the repeated tests. The average fracture loads are also presented in the last column.

Table 2.1.3. The experimental fracture loads of the VO-BD PMMA specimens subjected to mixed mode loading.

2α=30 (deg.)				
Specimen index	P₁ (N)	P₂ (N)	P₃ (N)	P_{av.} (N)
30-0.5-0	5635	5277	5724	5545.3
30-0.5-10	4754	4332	4707	4597.6
30-0.5-15	4395	4650	5203	4749.3
30-0.5-25	3982	3988	4267	4079
30-1-0	5203	5612	5128	5314.3
30-1-10	4395	5505	4651	4850.3
30-1-15	4127	4533	4949	4536.3
30-1-25	4479	4589	4369	4479
30-2-0	6497	6081	6389	6322.3
30-2-10	6699	6082	6427	6402.6
30-2-15	5203	4815	5308	5108.6
30-2-25	5276	4904	5579	5253
30-4-0	6997	6530	6730	6752.3
30-4-10	6261	6156	6208	6208.3
30-4-15	5742	5456	6156	5784.6
30-4-25	6369	6118	5203	5896.6

2α=60 (deg.)				
Specimen index	P₁ (N)	P₂ (N)	P₃ (N)	P_{av.} (N)
60-0.5-0	3857	3790	3566	3737.6
60-0.5-10	3857	3834	3620	3770.3
60-0.5-20	3734	3935	3834	3834.3
60-0.5-28	5008	4815	4755	4859.3
60-1-0	4073	4089	4533	4231.6
60-1-10	4395	3834	4280	4169.6
60-1-20	4357	4318	4280	4318.3
60-1-28	4395	4345	3857	4199
60-2-0	5325	5440	4754	5173
60-2-10	4874	4993	4844	4903.6

60-2-20	4228	4561	4693	4494
60-2-28	5038	4859	4829	4908.6
60-4-0	5793	5866	5939	5866
60-4-10	5758	5305	5686	5583
60-4-20	5399	5686	5488	5524.3
60-4-28	5776	5776	5054	5535.3

2α=90 (deg.)				
Specimen index	P₁ (N)	P₂ (N)	P₃ (N)	P_{av.} (N)
90-0.5-0	2290	2481	2360	2377
90-0.5-10	2371	2353	2609	2444.3
90-0.5-20	2738	3013	2886	2879
90-0.5-34	4622	5901	6226	5583
90-1-0	2570	2473	2385	2476
90-1-10	2722	2915	2907	2848
90-1-20	3279	3279	2969	3175.6
90-1-34	5159	5187	5173	5173
90-2-0	2827	3013	3013	2951
90-2-10	3359	2862	2916	3045.6
90-2-20	3319	3439	3445	3401
90-2-34	5039	5309	4919	5089
90-4-0	3779	3947	3971	3899
90-4-10	3700	3911	3947	3852.6
90-4-20	3745	4071	3900	3905.3
90-4-31	4485	5054	5171	4903.3

It was found from the experiments that the load-displacement curves of the VO-BD specimens were linear up to final breakage (see an instance in Fig. 2.1.8). The recorded curves were in a good consistency with the experimental observations from which no considerable plastic deformations were obtained at the notch tip vicinity. Sudden fall of the load from a maximum (i.e. the fracture load) to zero in Fig. 2.1.8 suggests sudden fracture of the VO-BD specimen. Experimental observations confirmed the curve since fracture took place suddenly without a

precaution, e.g. a crack initiation etc. From the statements above, it is concluded that brittle fracture has taken place in VO-BD PMMA specimens in the linear-elastic regime. Thus, different brittle fracture criteria in the area of the linear elastic notch fracture mechanics (LENFM), e.g. the SED criterion, could be used for predicting the experimental results.

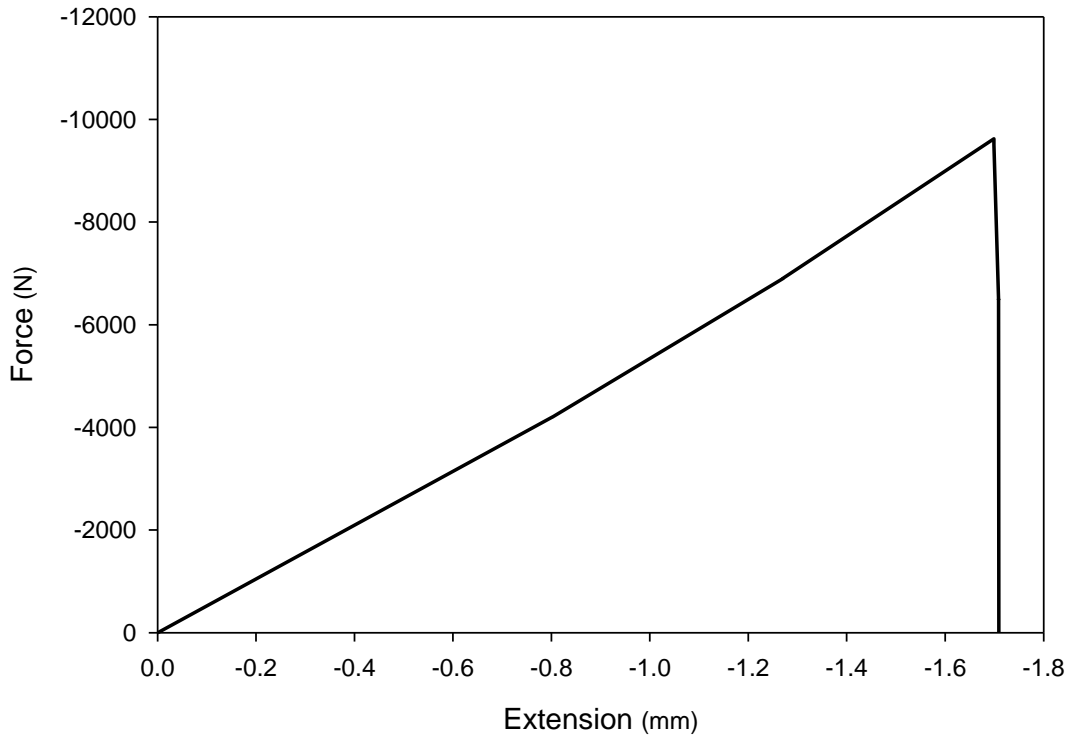


Figure 2.1.8. A sample load–displacement plot for a VO-BD PMMA specimen at room temperature.

In the next section, the experimental fracture loads of the VO-BD specimens presented in Table 2.1.3 are theoretically predicted by means of the average strain energy (SED) criterion.

2.1.3. Fracture criterion based on the Strain Energy Density averaged over a control volume

With the aim of estimating the critical loads of PMMA components weakened by cracks or notches, designers need appropriate fracture criteria which take into account the local behaviour of material around the stress concentrators. In the

present section a criterion based on the local strain energy and useful for the theoretical estimation of the fracture loads of notched components is described.

Different from Sih's criterion [43], which is a point-wise criterion, the averaged strain energy density criterion (SED), as presented in Ref. [31], states that brittle failure occurs when the mean value of the strain energy density over a given control volume is equal to a critical value, W_c . This critical value varies for different materials but it does not depend on the notch geometry and sharpness. The control volume is thought of as dependent on the ultimate tensile strength σ_t and the fracture toughness, K_{Ic} , in the case of brittle or quasi-brittle materials subjected to static loads.

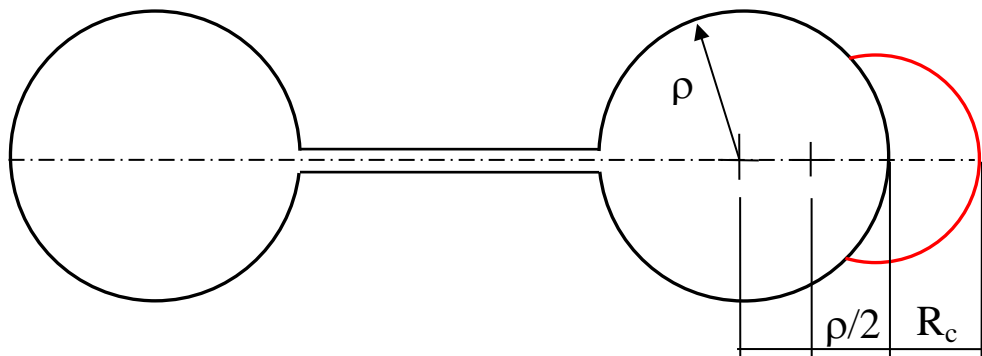
This approach was first proposed in the literature for sharp V-notched components subjected to mode I or mixed I+II loading conditions [31] and then formulated also for blunt notched components [44].

In the case of components weakened by cracks, the control volume becomes a circle centered at the tip and characterized by a radius R_c [31]. With reference to a state of plane strain, the size of the control volume, R_c , can be estimated by means of the expression [31,44]:

$$R_c = \frac{(1 + \nu)(5 - 8\nu)}{4\pi} \left(\frac{K_{Ic}}{\sigma_t} \right)^2 \quad (2.1.1)$$

where K_{Ic} is the fracture toughness, ν the Poisson's ratio and σ_t the ultimate tensile strength of a plain specimen that obeys a linear elastic behavior.

(a)



(b)

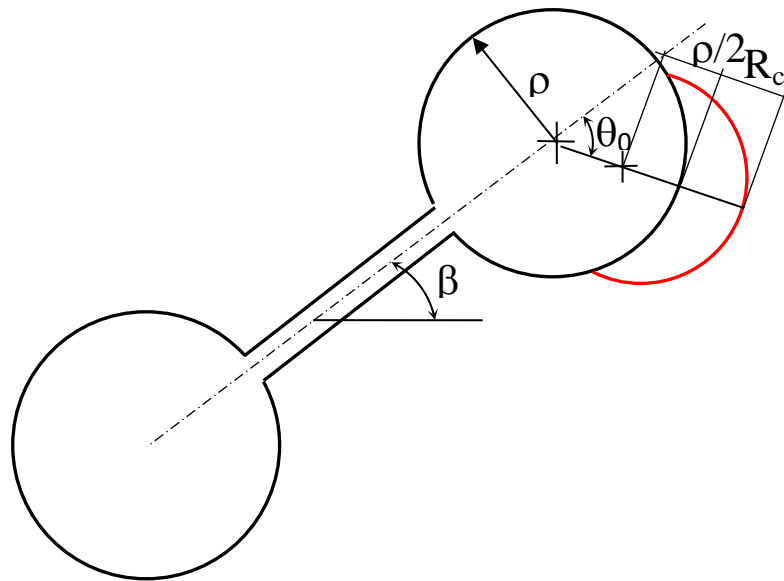
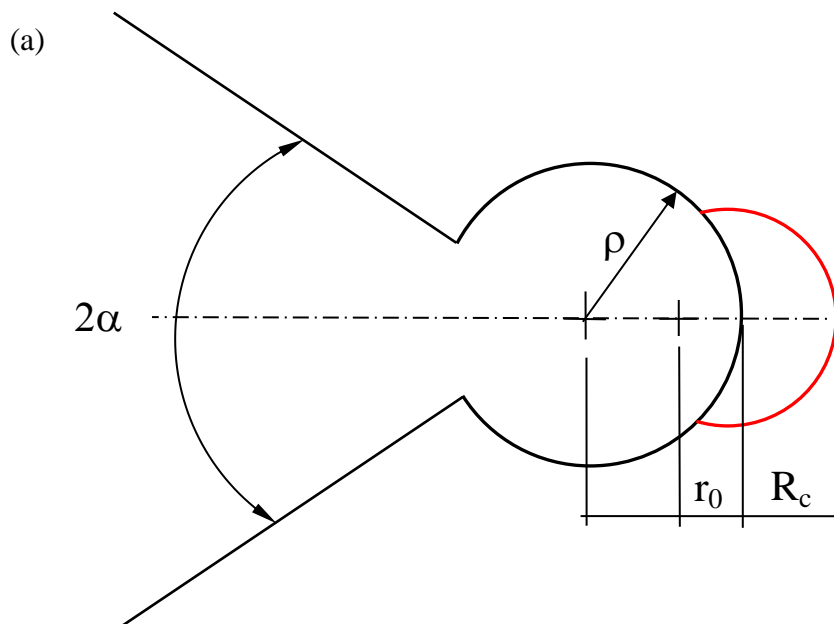


Figure 2.1.9. Control volume under (a) mode I and (b) mixed mode I+II loading for key-hole notched specimens. θ_0 represents the angular position of the point where the principal stress reaches its maximum value, with respect to the notch bisector line.



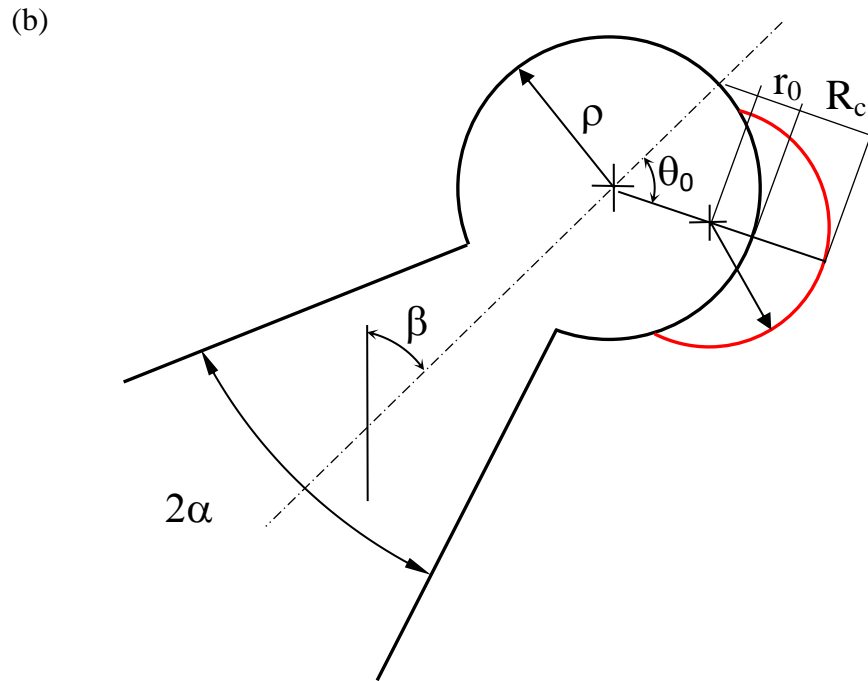


Figure 2.1.10. Control volume (a) mode I and (b) mixed mode I+II loading for VO-notched specimens. θ_0 represents the angular position of the point where the principal stress reaches its maximum value, with respect to the notch bisector line.

In the case of components weakened by blunt notches and subjected to Mode I loading condition, the control volume assumes a crescent shape [51], where R_c represents the size evaluated along the bisector line. The control volume (Fig. 2.1.9a-10a) is characterized by an outer radius that equals $R_c + r_0$. The parameter r_0 is a function of the opening angle (2α) and of the notch tip radius (ρ) as highlighted by the following relationship:

$$r_0 = \frac{q-1}{q} \rho \quad (2.1.2)$$

with q defined as:

$$q = \frac{2\pi - 2\alpha}{\pi} \quad (2.1.3)$$

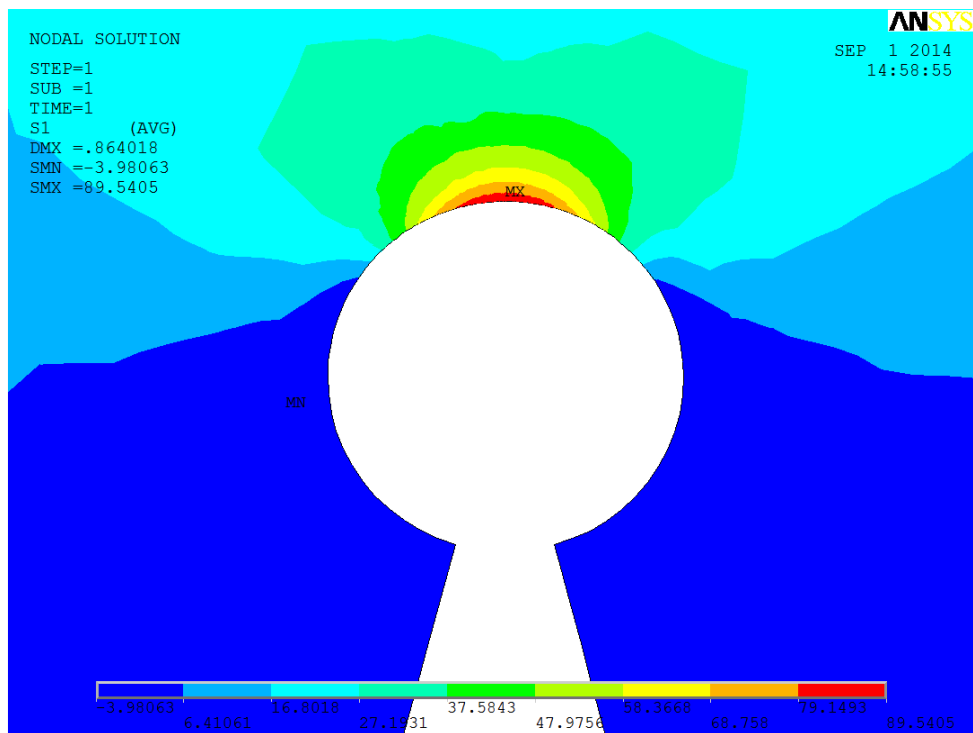
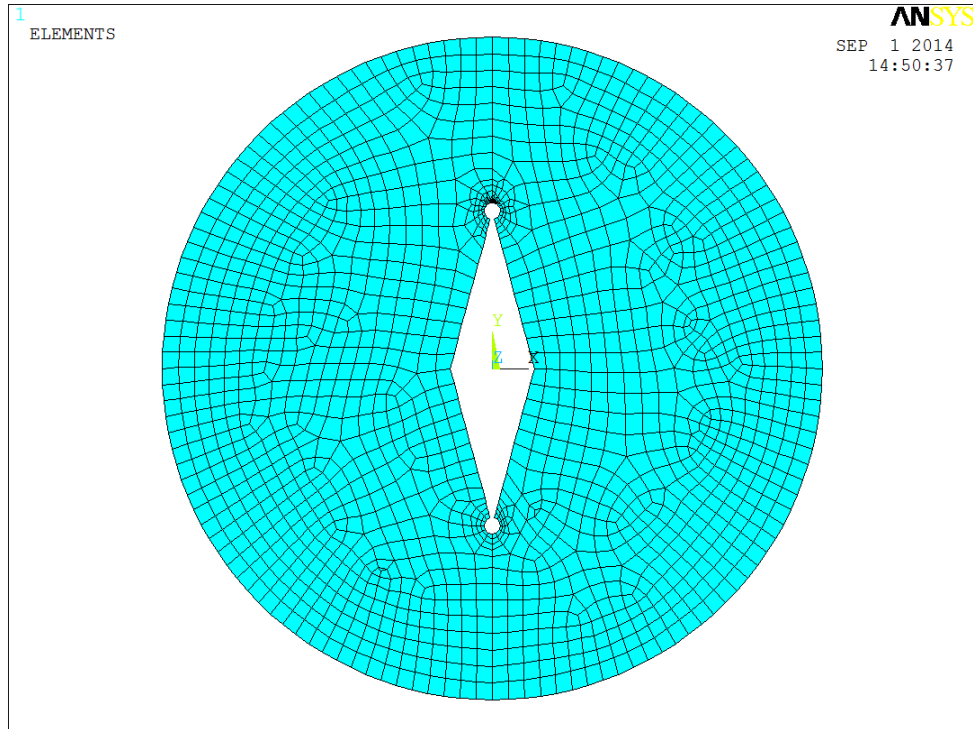
Under mixed mode loading, the critical volume is no longer centered on the notch tip (see Figure 2.1.9b-10b), but rather on the point where the principal stress reaches its maximum value along the edge of the notch [34]. It is assumed that the crescent shape volume rotates rigidly under mixed mode, with no change in shape and size. This is the governing idea of the ‘*equivalent local mode I*’ approach, as has been proposed and applied to U and V-notches by Lazzarin and Elices together with their co-authors [34].

As it is discussed above, the idea of the ‘*equivalent local mode I*’ approach, as proposed and applied to plates made of PMMA and weakened by U-notches and V-notches [34,44], is used here dealing with Brazilian disk specimens weakened by key-hole notches and V-notches with end-holes under mixed mode I+II loading. With this aim two models are created for each geometry. The first model is mainly oriented to the determination of the point where the maximum principal stress and the maximum SED are located; the second model is characterized by an accurate definition of the control volume where the strain energy density should be averaged.

The values of the strain energy density averaged over the control volume have been evaluated by means of finite element analyses performed in ANSYS, version 14.5. All the analyses are carried out by using eight-node elements under the hypothesis of plane strain conditions. The procedure for building the two models to determine the SED in the rotated volume can be easily automated by simply writing an APDL (ANSYS Parametric Design Language) subroutine which permits the direct evaluation of the SED in the control volume.

One of the most important advantages of the mean SED approach is the mesh independency [52]. As widely documented in [52], refined meshes are not necessary, because the mean value of the SED on the control volume can be directly determined *via* the nodal displacements, without involving their derivatives. As soon as the average SED is known, the notch stress intensity factors (NSIFs) can be calculated *a posteriori* on the basis of very simple expressions linking the local SED and the relevant NSIFs. This holds true also for the stress concentration factors (SCFs), at least when the local stress distributions ahead of the blunt notch are available for the plane problem. An example is shown

in Figure 2.1.11 depicting a typical mesh (Fig. 2.1.11a) together with the principal stress (Fig. 2.1.11b) and SED (Fig. 2.1.11c) contour lines.



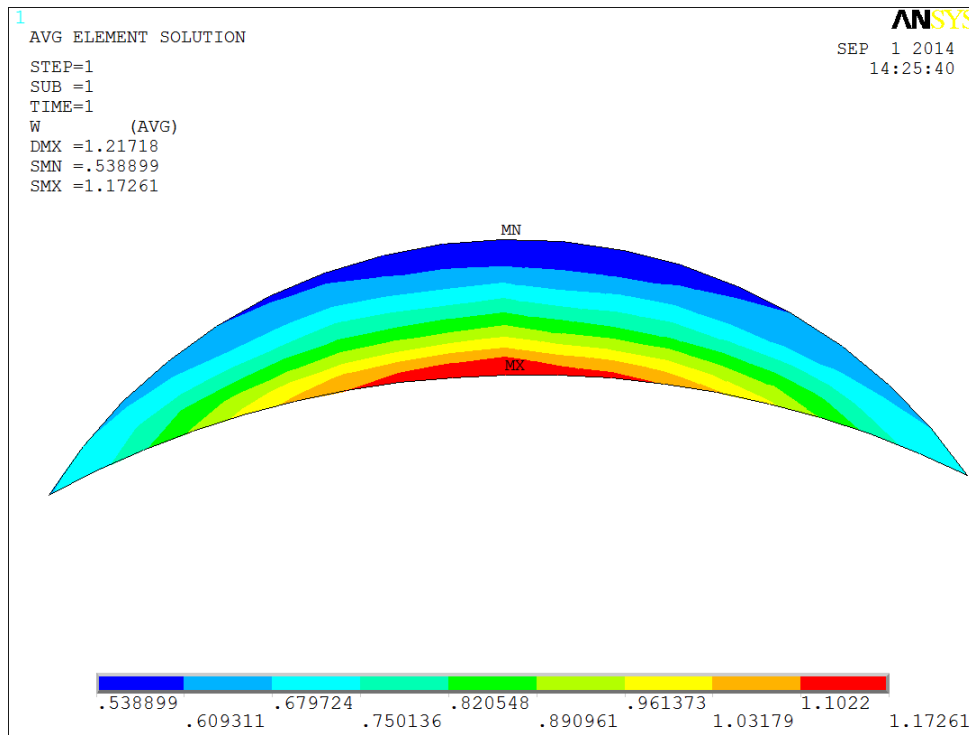


Figure 2.1.11. Typical mesh used to evaluate the SED under mode I loading. Mesh (a), principal stress contour lines (b) and SED contour lines (c).

2.1.4. SED approach in fracture analysis of the tested PMMA specimens

The fracture criterion described in the previous section is employed here to estimate the fracture loads obtained from the experiments conducted on the PMMA specimens weakened by key-holes and V-notches with end holes under mixed mode I+II loading. The SED values have been evaluated by means of a FE model of each specimen. The averaged strain energy density criterion (SED) states that failure occurs when the mean value of the strain energy density over a control volume, \bar{W} , is equal to a critical value, W_c , which depends on the material but not on notch geometry [31,32,34,44]. This critical value can be determined from the ultimate tensile strength σ_t according to Beltrami's expression:

$$W_c = \frac{\sigma_t^2}{2E} \quad (2.1.4)$$

In parallel, the control volume definition via the control radius R_c needs the knowledge of the fracture toughness, K_{Ic} , and the Poisson's ratio, ν , see Eq. (2.1.1). The critical load that is sustainable by a notched component can be estimated by imposing \bar{W} equal to the critical value W_c . This critical value is considered here constant under mode I, mode II and in-plane mixed-mode conditions. This assumption has extensively been verified for a number of different brittle and quasi-brittle materials [44].

As it is mentioned earlier, the properties of the PMMA considered in the present investigation are: $\sigma_t = 70.5$ MPa, $K_{Ic} = 1.96$ MPa $\sqrt{\text{m}}$, Poisson's ratio $\nu = 0.38$. As a result, the critical SED for the tested PMMA is $W_c = 0.839$ MJ/m³, whereas the radius of the control volume is $R_c = 0.166$ mm for plane strain conditions.

2.1.4.1 Keyhole notched specimens

Table 2.1.4 summarizes the outlines of the experimental, numerical and theoretical findings for the tested PMMA specimens, re-analyzed here by means of SED concepts. In particular, the table summarizes the experimental loads to failure (P) for each notch radius ρ compared with the theoretical values (P_{th}) based on the SED evaluation. The table also gives us the SED value as obtained directly from the FE models of the PMMA specimens by applying to the model the average experimental load P_{av} .

Table 2.1.4. Experimental fracture loads compared with theoretical loads evaluated by means of SED. The SED in the Table has been evaluated applying in the numerical model a load corresponding to the average experimental value, being $P=P_{av}$.

Specimen index	d/2	P ₁ (N)	P ₂ (N)	P ₃ (N)	P _{av.} (N)	SED (MJ/m ³)	P _{th} (N)	Δ%		
0.3-1-0	12	9391	9080	9302	9258	0.873	9076	-3.35	-0.04	-2.43
0.3-1-10	12	8573	7967	8935	8492	0.944	8010	-6.57	0.54	-10.35
0.3-1-20	12	8510	8439	8369	8439	0.969	7858	-7.66	-6.88	-6.11
0.3-1-31	12	7288	7333	7220	7280	0.895	7052	-3.24	-3.83	-2.33
0.3-2-0	12	8664	9361	9691	9239	0.718	9989	15.29	6.71	3.08
0.3-2-10	12	10669	9868	10268	10268	0.965	9582	-10.19	-2.90	-6.68
0.3-2-20	12	9423	9631	9480	9511	0.990	8762	-7.01	-9.02	-7.57
0.3-2-31	12	7900	8295	8690	8295	0.755	8746	10.71	5.44	0.64
0.3-4-0	12	10891	10635	10768	10765	0.842	10744	-1.35	1.02	-0.22
0.3-4-10	12	9212	9510	9808	9510	1.127	8209	-10.89	-13.68	-16.30
0.3-4-20	12	8599	7965	7332	7965	1.317	6361	-26.03	-20.14	-13.24
0.3-4-31	12	9987	8671	7356	8671	0.614	10136	1.49	16.90	37.79
0.5-1-0	20	6928	6859	6748	6845	1.055	6103	-11.91	-11.02	-9.56
0.5-1-10	20	6010	5921	5685	5872	0.987	5416	-9.88	-8.53	-4.73
0.5-1-15	20	5171	5023	5538	5244	0.990	4829	-6.61	-3.86	-12.80
0.5-1-26	20	4873	5054	4486	4804	0.993	4417	-9.36	-12.60	-1.54
0.5-2-0	20	7015	6991	7040	7015	0.895	6794	-3.15	-2.82	-3.49
0.5-2-10	20	6991	6835	6679	6835	0.952	6420	-8.17	-6.07	-3.88
0.5-2-15	20	6719	6737	6755	6737	0.917	6447	-4.05	-4.30	-4.56
0.5-2-26	20	5388	5250	5113	5250	0.772	5476	1.63	4.30	7.10
0.5-4-0	20	6889	5992	6441	6441	0.660	7262	5.41	21.19	12.75
0.5-4-10	20	7177	7422	7299	7299	0.972	6786	-5.45	-8.57	-7.03
0.5-4-15	20	7109	7109	7109	7109	0.966	6628	-6.77	-6.77	-6.77
0.5-4-26	20	6427	6478	6499	6468	0.865	6372	-0.86	-1.64	-1.95
0.5-6-0	20	7173	6608	5957	6579	0.709	7155	-0.25	8.28	20.11
0.5-6-10	20	6928	6991	5219	6379	1.115	5537	-20.08	-20.80	6.09
0.5-6-15	20	6093	5759	6427	6093	1.133	5245	-13.92	-8.93	-18.39
0.5-6-26	20	4665	4409	4369	4481	0.650	5093	9.17	15.51	16.57

The last columns of Table 2.1.4 reports the relative deviations between experimental and theoretical loads ($\Delta\% = (P_{th} - P) \cdot 100/P$). As it is widely

discussed in Ref. [44], acceptable engineering values range between -20% and +20%, being this scatter slightly higher under mixed mode loading or pure mode II loading [34]. As can be noticed from the table, this range is satisfied for the majority of the present data with only few exceptions falling outside the range from -20% and +20%.

The results are given also in graphical form in Figs. 2.1.12-2.1.15 where the *experimental* values of the critical loads (open dots) are compared with the *theoretical* predictions based on the constancy of the SED in the control volume (solid line). The plots are given for the notched PMMA specimens as a function of the notch tip radius ρ . The trend of the theoretically predicted loads is in good agreement with the experimental ones.

A synthesis in terms of the square root value of the local energy averaged over the control volume (of radius R_c), normalized with respect to the critical energy of the material as a function of the notch tip radius is shown in Fig. 2.1.16. The plotted parameter is proportional to the fracture load. The new data are plotted together independent of the notch geometries and specimens shape. The aim is to investigate the influence of the notch tip radius on the fracture assessment based on SED. From the figure, it is clear that the scatter of the data is very limited and almost independent of the notch radius. Most of the values fall inside a scatter ranging from 0.80 to 1.20, with the great majority of the data inside 0.85 to 1.15. The synthesis confirms also the choice of the control volume which seems to be suitable to characterize the material behaviour under mixed mode I+II loading. The scatter of the experimental data presented here is in good agreement with the recent database in terms of SED reported in Refs. [34,44].

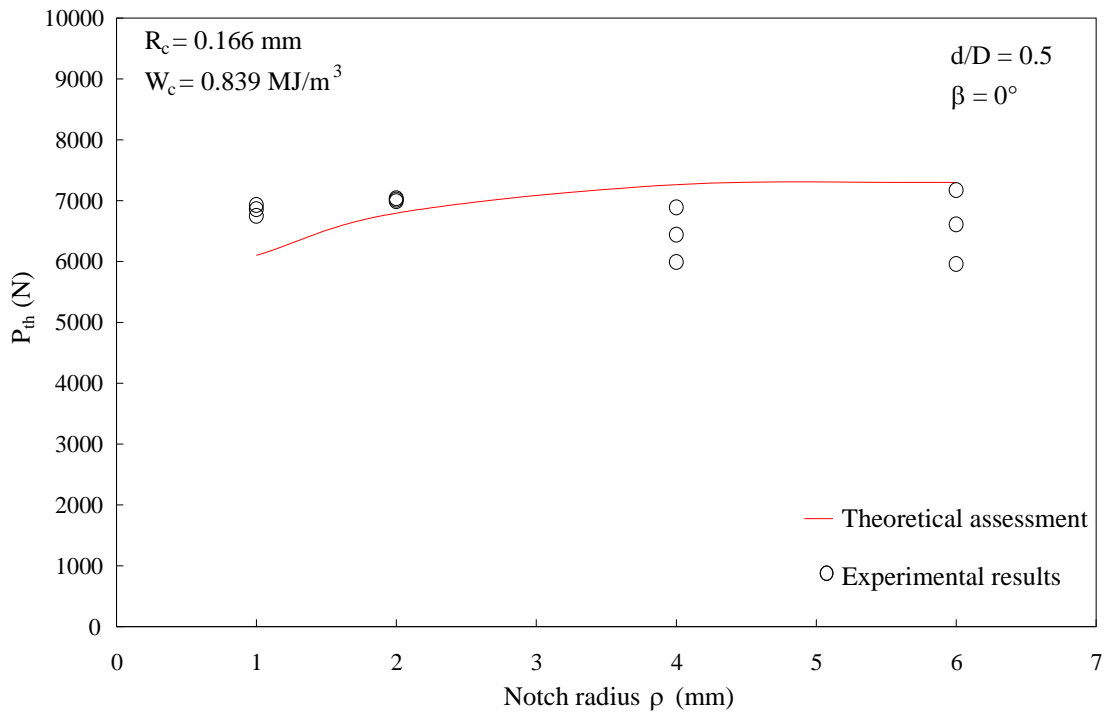


Figure 2.1.12. Fracture assessment by means of SED for the case $d/D=0.5$ and $\beta=0^\circ$

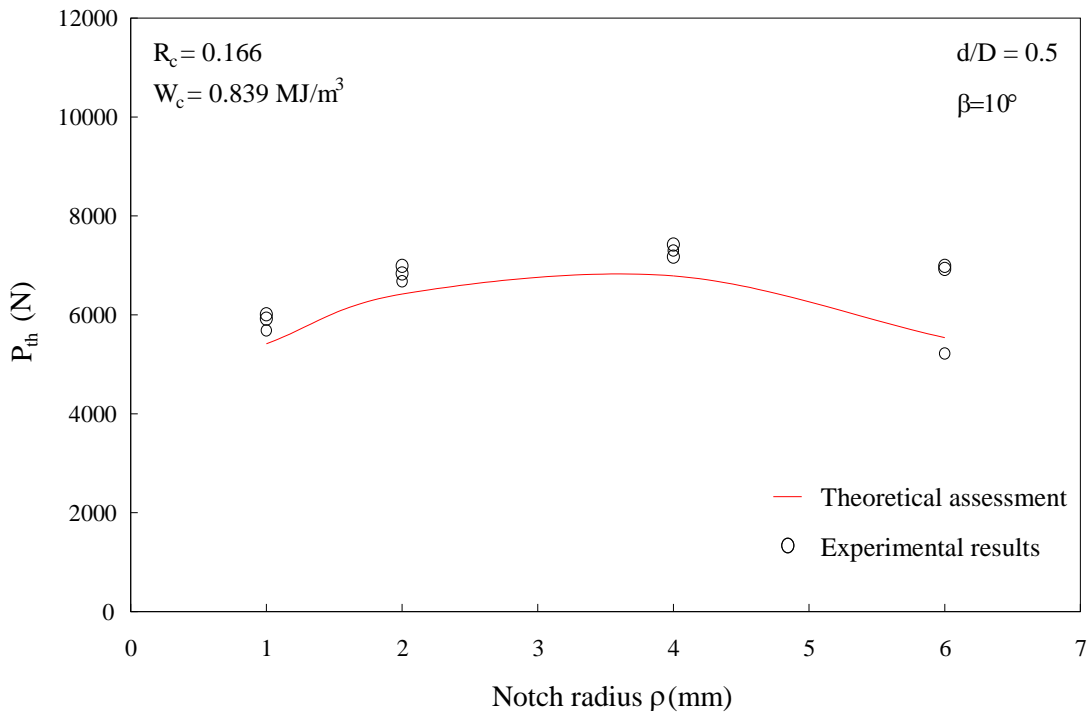


Figure 2.1.13. Fracture assessment by means of SED for the case $d/D=0.5$ and $\beta=10^\circ$

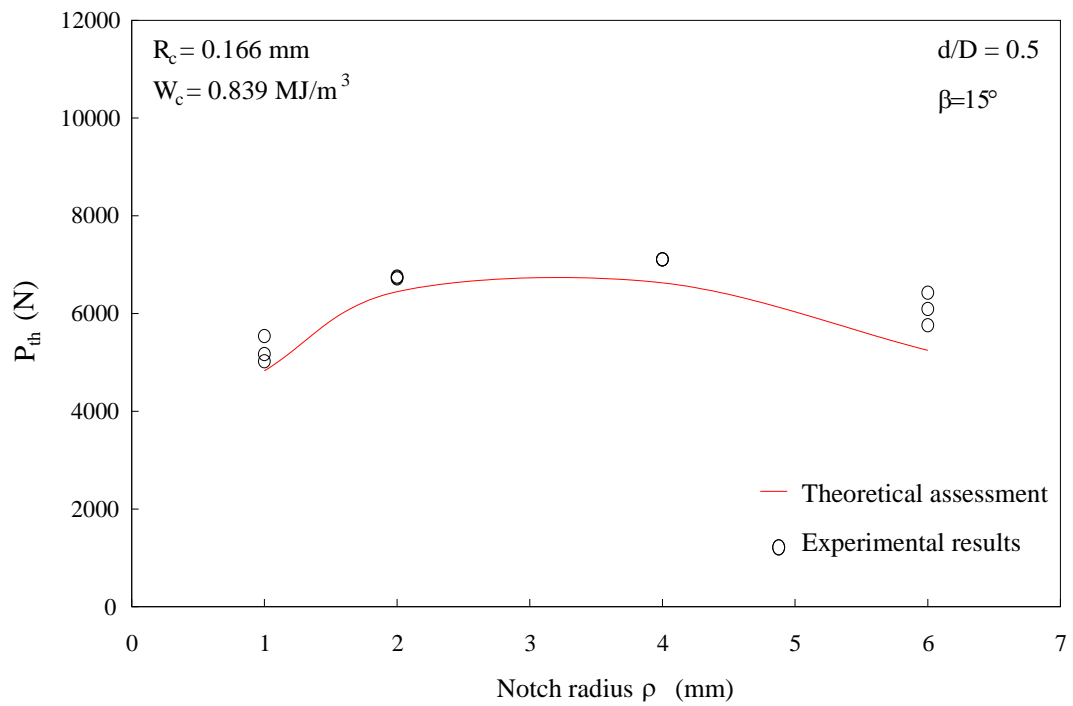


Figure 2.1.14. Fracture assessment by means of SED for the case $d/D=0.5$ and $\beta=15^\circ$

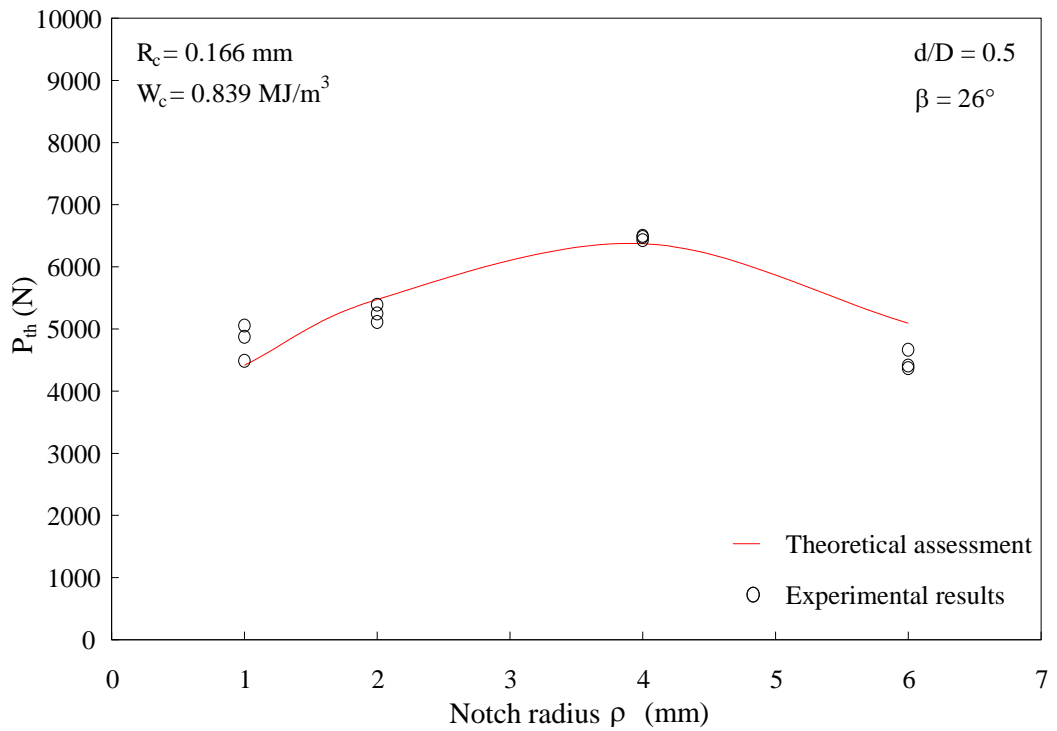


Figure 2.1.15. Fracture assessment by means of SED for the case $d/D=0.5$ and $\beta=26^\circ$

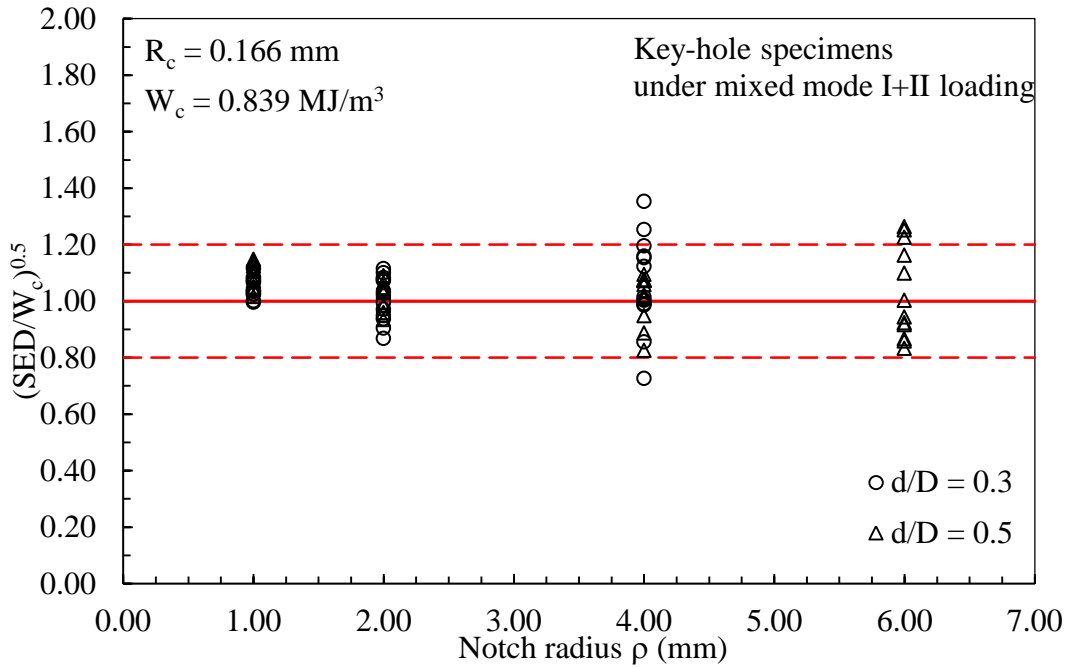


Figure 2.1.16. Synthesis of brittle failure data from PMMA specimens.

2.1.4.2 VO-notched specimens

The comparison between experimental values and theoretical estimations of the fracture loads for the PMMA notched components is reported in Table 2.1.5. The fracture loads obtained experimentally (P_i with $i = 1, 2, 3$) and the theoretical estimations (P_{th}) determined according to the SED approach are provided in the table with reference to each value of the notch tip radius ρ . The values of the averaged SED have been evaluated from the numerical analyses by applying to the FE model the mean value of the experimental loads $P = P_{av}$.

Table 2.1.5. Experimental fracture loads compared with theoretical loads evaluated by means of SED. The SED in the Table has been evaluated applying in the numerical model a load corresponding to the average experimental value, being $P=P_{av}$.

Specimen index	P_1 (N)	P_2 (N)	P_3 (N)	P_{av} (N)	SED (MJ/m ³)	P_{th} (N)		$\Delta\%$	
30-0.5-0	5635	5277	5724	5545	0.86	5468	-2.96	3.62	-4.47
30-0.5-10	4754	4332	4707	4597.7	0.74	4893	2.92	12.95	3.95
30-0.5-15	4395	4650	5203	4749.3	0.87	4645	5.69	-0.11	-10.72
30-0.5-25	3982	3988	4267	4079	0.86	4224	6.08	5.92	-1.01
30-1-0	5203	5612	5128	5314	0.67	5956	14.47	6.13	16.15
30-1-10	4395	5505	4651	4850.3	0.65	5501	25.16	-0.07	18.28
30-1-15	4127	4533	4949	4536.3	0.63	5227	26.65	15.31	5.62
30-1-25	4479	4589	4369	4479	0.67	4611	2.95	0.48	5.54
30-2-0	6497	6081	6389	6322	0.75	6679	2.80	9.83	4.54
30-2-10	6699	6082	6427	6402.7	0.85	6355	-5.14	4.49	-1.12
30-2-15	5203	4815	5308	5108.7	0.59	6075	16.76	26.17	14.45
30-2-25	5276	4904	5579	5253	0.75	5508	4.40	12.32	-1.27
30-4-0	6997	6530	6730	6752	0.72	7305	4.40	11.87	8.54
30-4-10	6261	6156	6208	6208.3	0.65	7050	12.60	14.52	13.56
30-4-15	5742	5456	6156	5784.7	0.63	6668	16.13	22.21	8.32
30-4-25	6369	6118	5203	5897	0.72	6462	1.46	5.62	24.20
60-0.5-0	3857	3790	3566	3738	0.83	3767	-2.33	-0.61	5.64
60-0.5-10	3857	3834	3620	3770.3	0.89	3651	-5.34	-4.77	0.86
60-0.5-20	3734	3935	3834	3834.3	0.83	3840	2.84	-2.41	0.16
60-0.5-28	5008	4815	4755	4859	0.83	4406	-12.02	-8.49	-7.34
60-1-0	4073	4089	4533	4232	0.77	4410	8.27	7.85	-2.71
60-1-10	4395	3834	4280	4169.7	0.81	4222	-3.94	10.12	-1.36
60-1-20	4357	4318	4280	4318.3	0.88	4215	-3.26	-2.39	-1.52
60-1-28	4395	4345	3857	4199	0.77	4470	1.71	2.88	15.89
60-2-0	5325	5440	4754	5173	0.77	5397	1.35	-0.79	13.53
60-2-10	4874	4993	4844	4903.7	0.80	4999	2.56	0.12	3.20
60-2-20	4228	4561	4693	4494.0	0.69	4953	17.15	8.59	5.54
60-2-28	5038	4859	4829	4909	0.77	5026	-0.24	3.44	4.08
60-4-0	5793	5866	5939	5866	0.68	6539	12.88	11.47	10.10
60-4-10	5758	5305	5686	5583.0	0.73	5978	3.82	12.69	5.14
60-4-20	5399	5686	5488	5524.3	0.67	6163	14.15	8.39	12.30
60-4-28	5776	5776	5054	5535	0.68	5993	3.76	3.76	18.58
90-0.5-0	2290	2481	2360	2377	0.99	2185	-4.59	-11.93	-7.42
90-0.5-10	2371	2353	2609	2444.3	0.90	2348	-0.97	-0.21	-10.00

90-0.5-20	2738	3013	2886	2879.0	0.77	3003	9.68	-0.33	4.05
90-0.5-34	4622	5901	6226	5583	0.99	5968	29.12	1.14	-4.14
90-1-0	2570	2473	2385	2476	0.74	2644	2.88	6.91	10.86
90-1-10	2722	2915	2907	2848.0	0.89	2763	1.51	-5.21	-4.95
90-1-20	3279	3279	2969	3175.7	0.82	3207	-2.20	-2.20	8.02
90-1-34	5159	5187	5173	5173	0.74	5175	0.31	-0.23	0.04
90-2-0	2827	3013	3013	2951	0.60	3486	23.31	15.70	15.70
90-2-10	3359	2862	2916	3045.7	0.61	3559	5.95	24.35	22.05
90-2-20	3319	3439	3445	3401.0	0.66	3835	15.55	11.51	11.32
90-2-34	5039	5309	4919	5089	0.60	5102	1.25	-3.90	3.72
90-4-0	3779	3947	3971	3899	0.54	4840	28.08	22.62	21.88
90-4-10	3700	3911	3947	3852.7	0.51	4904	32.54	25.39	24.25
90-4-20	3745	4071	3900	3905.3	0.51	4969	32.68	22.06	27.41
90-4-31	4485	5054	5171	4903	0.54	5493	22.47	8.69	6.23

The table also shows the percentage deviation ($\Delta\% = (P_{th} - P) \cdot 100/P$) between the theoretical estimation of the fracture load and each of the three experimental values, with reference to all geometries considered. As highlighted in other contributions [33,44], acceptable values from the engineering point of view are between -20% and +20%. It can be easily observed from Table 2.1.3 that this range is satisfied for the great majority of the present data with only a few exceptions falling outside the range from -20% and +20%.

The results reported in the table are also represented in the diagrams of Figs 2.1.17-19, in which the fracture loads experimentally determined (open dots) are compared with the theoretical estimations obtained according to the SED approach (solid line), with reference to a notch opening angle 2α equal to 30° , 60° and 90° , respectively. In particular the abscissa axis of the figures reports the value of the notch root radius ρ of each specimen. The figures show clearly a good agreement between theoretical predictions and experimental data, for all the different notch opening angles (2α) and loading angles (β) taken into consideration in this work.

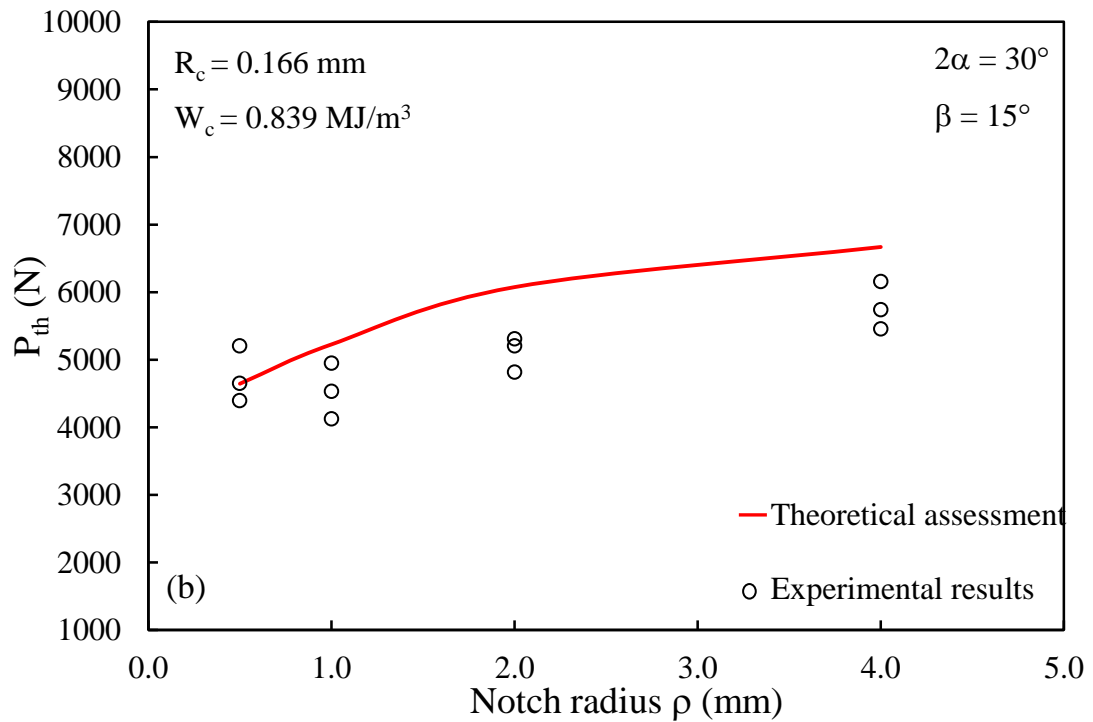
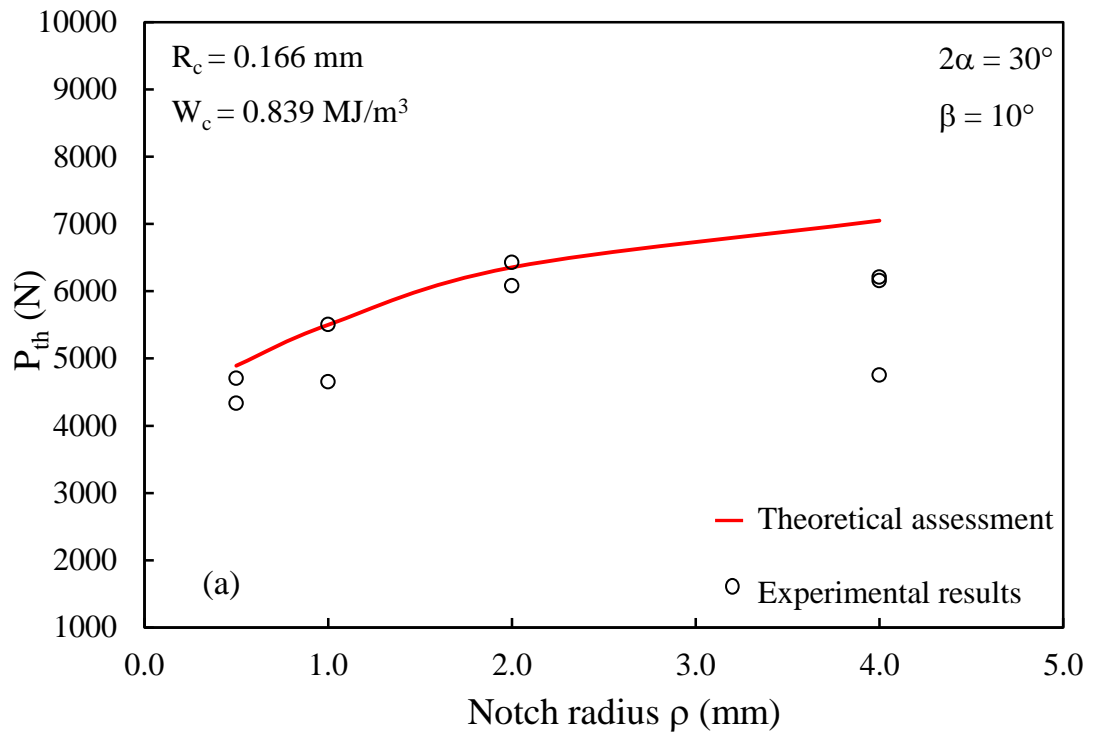


Figure 2.1.17. Comparison between theoretical fracture loads obtained by SED and experimental data for $2\alpha = 30^\circ$. (a) $\beta = 10^\circ$ and (b) $\beta = 15^\circ$.

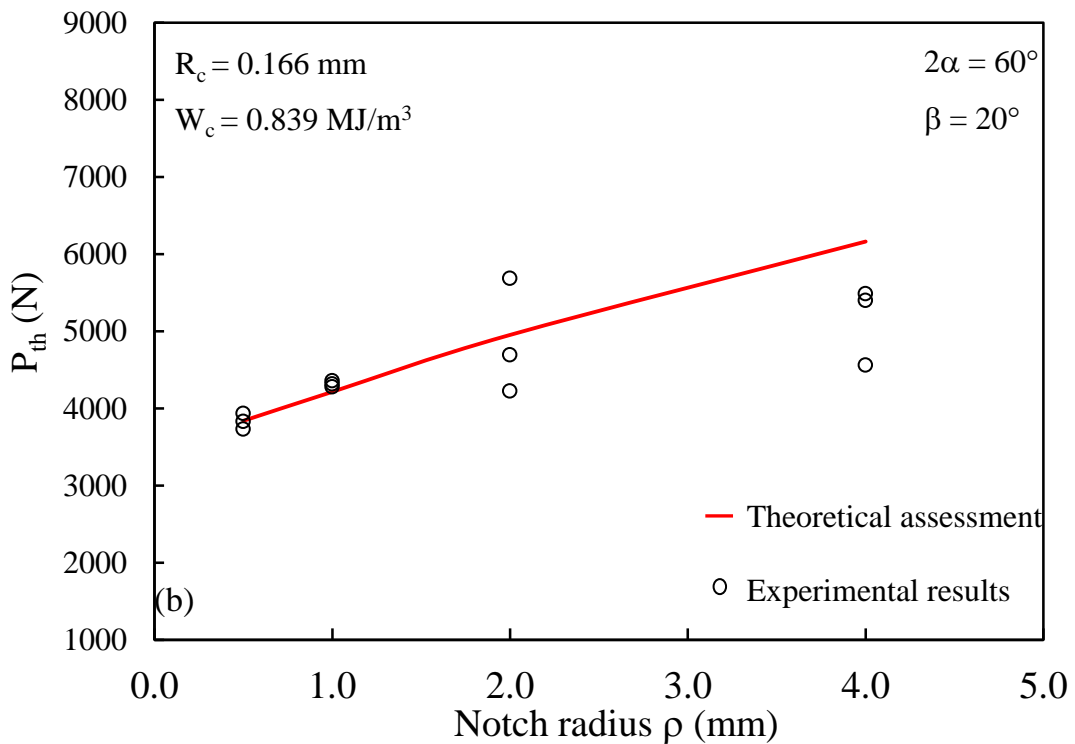
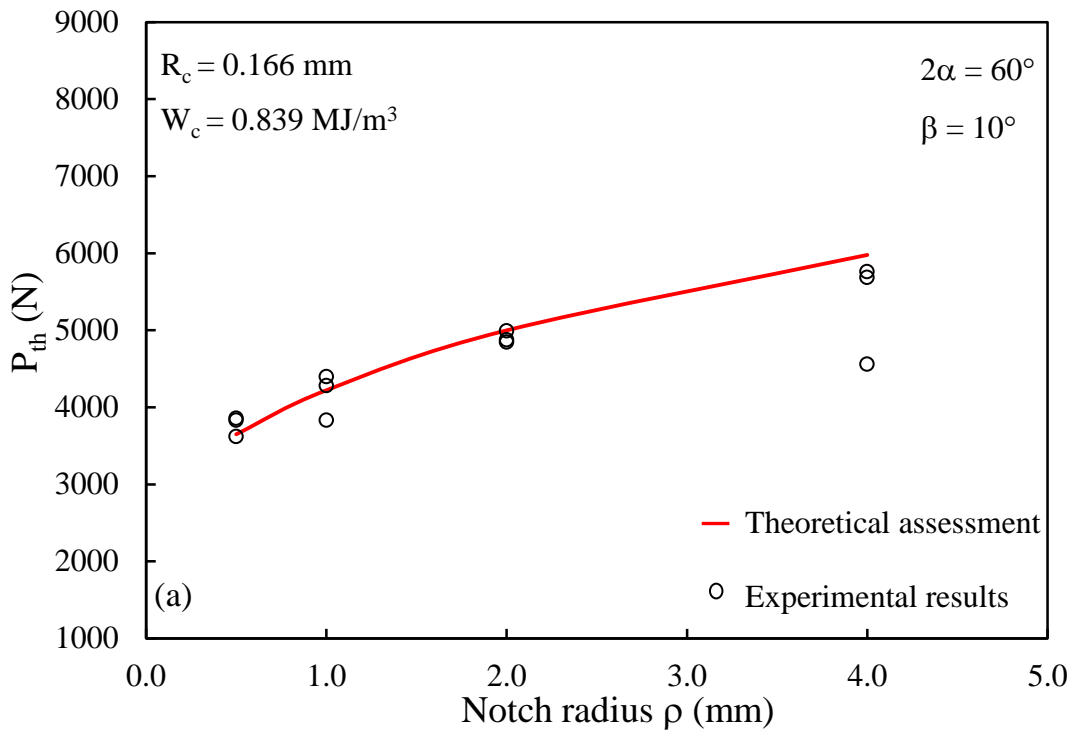


Figure 2.1.18. Comparison between theoretical fracture loads obtained by SED and experimental data for $2\alpha = 60^\circ$. (a) $\beta = 10^\circ$ and (b) $\beta = 20^\circ$.

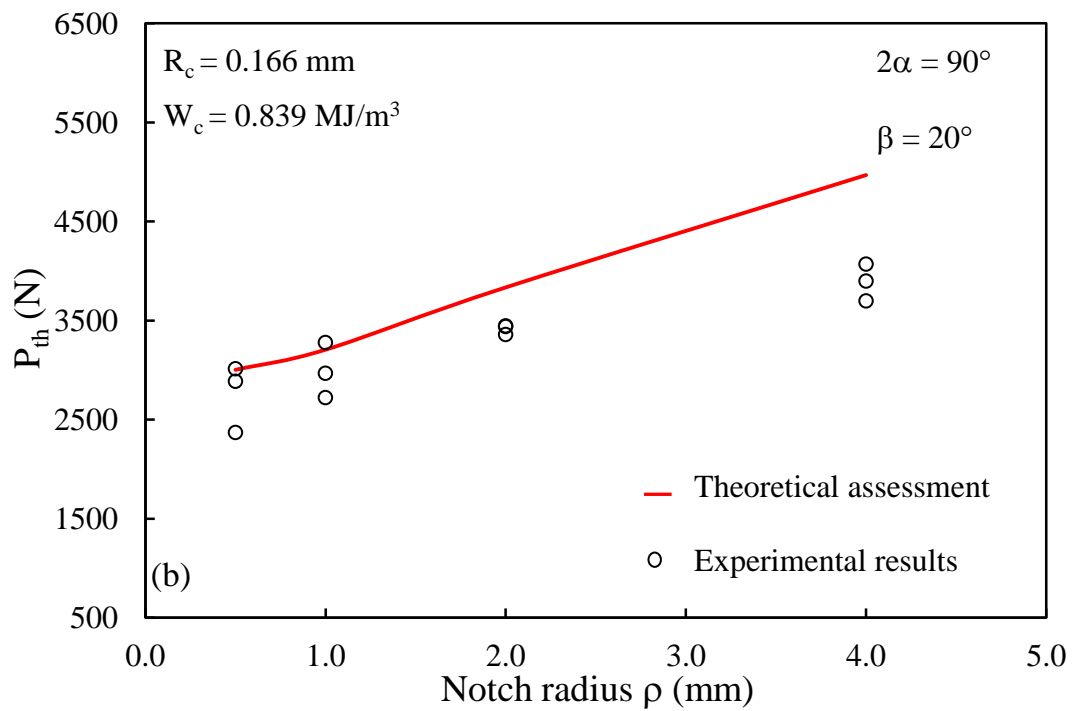
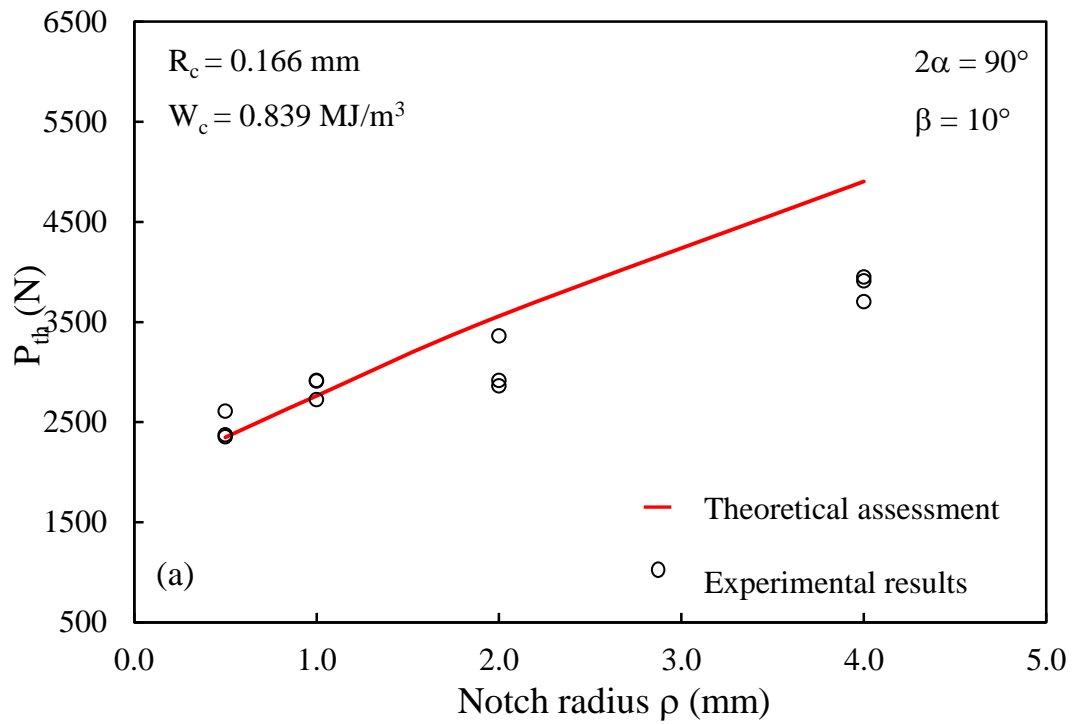


Figure 2.1.19. Comparison between theoretical fracture loads obtained by SED and experimental data for $2\alpha = 90^\circ$. (a) $\beta = 10^\circ$ and (b) $\beta = 20^\circ$.

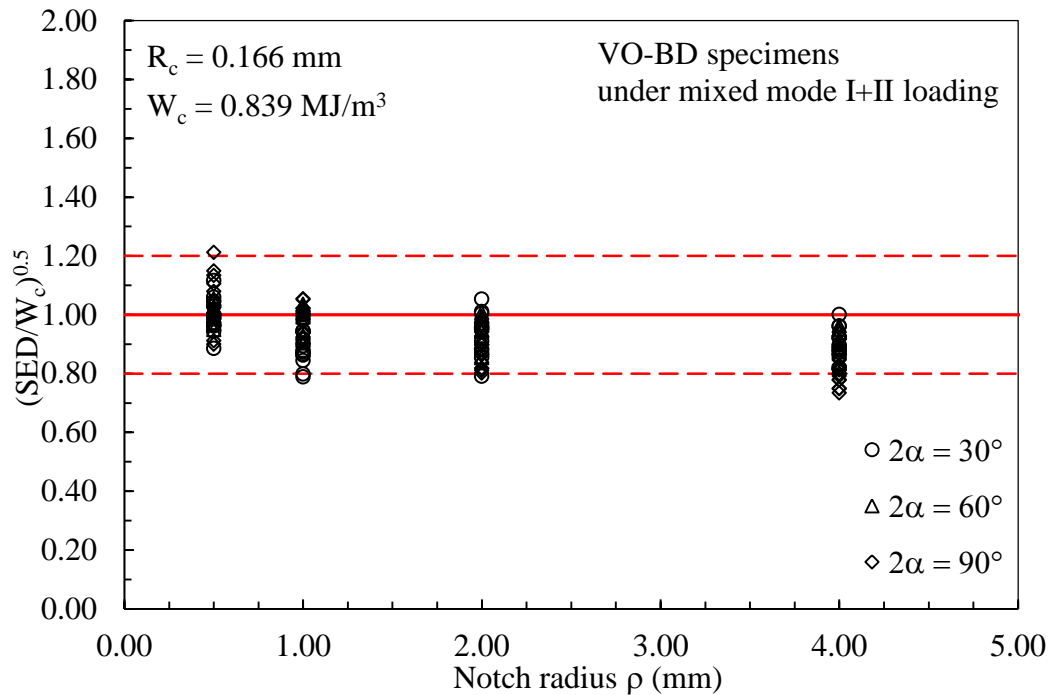


Figure 2.1.20. Synthesis of brittle failure data from PMMA specimens under mixed mode I+II loading.

Figure 2.1.20 shows the square root value of the ratio between the SED averaged over the control volume of radius R_c and the constant value of the critical energy of the material (0.839 MJ/m³) as a function of the notch radius ρ . Being the strain energy density proportional to the square of the applied load, the plotted parameter results to be proportional to the ratio between the experimental and the theoretical loads. The purpose is to evaluate the influence of the notch root radius and of the opening angle on the estimation of the critical loads according to the SED approach. From the diagram, it results to be clear that the scatter of the new data is very limited and almost independent of the notch geometries. In fact, the great majority of the experimental values obtained from the PMMA notched specimens fall inside a scatterband ranging from 0.8 to 1.2 with only a few values outside this range. One should also note that the majority of the results are inside a scatter ranging from 0.9 to 1.1.

These considerations along with the final synthesis diagram, reported in Fig. 2.1.21, underline the very good accuracy of the SED approach for the fracture assessment of notched components made of PMMA under mixed mode I+II loading conditions, once the control volume has been properly modeled.

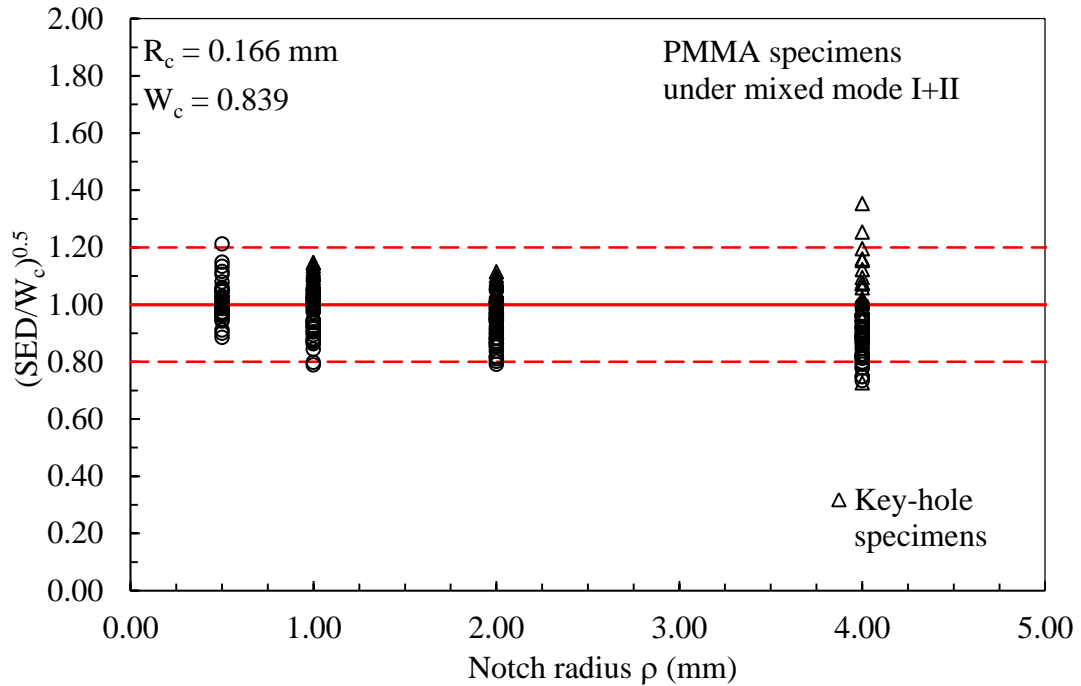


Figure 2.1.21. Synthesis of all brittle failure data from PMMA Key-BD and VO-BD specimens under mixed mode I+II loading.

2.1.5. Discussion

Some new experimental results regarding brittle fracture in Brazilian disk specimens weakened by keyholes and that weakened by V-notches with end holes, made of PMMA and subjected to mixed mode I+II loading have been provided.

First, static tests aimed at obtaining the fracture loads have been conducted on specimens characterized by different notch geometries, such as the notch opening angle 2α , the notch root radius ρ and the loading angle β .

Secondly the suitability of the well-established averaged strain energy density criterion (SED) in predicting the load-carrying capacity of PMMA notched specimens has been checked. It was found that the averaged SED criterion, used in combination with the equivalent local mode I concept, could predict successfully the static strength of PMMA notched specimens subjected to mixed mode loading and characterized by different notch opening angles, loading angles and various notch root radii. The scatter of the great majority of the data, that

represents the deviation between the experimental loads and the theoretical ones, was found to be very limited (within $\pm 20\%$) as a demonstration of the effectiveness of the SED approach.

From the synthesis based on SED criterion, it can be inferred that the choice of the crescent shape for the control volume is appropriate to characterize the PMMA behaviour under mixed mode I+II loading, and also that the critical SED W_c and the control radius R_c are both constant material properties.

2.2. Brittle Fracture of blunt notched components made of isostatic graphite under mixed mode I+III loading^(*)

Nomenclature

E	Young's modulus
G	Shear modulus
K_{Ic}	fracture toughness
K_{3c}	Mode III critical notch stress intensity factor
K_t	linear elastic stress concentration factor
M	mode mixity ratio
p	notch depth
r_0	distance between notch tip and origin of the reference system
R_{1c}	control radius under tensile loading
R_{3c}	control radius under torsion loading
\bar{W}	SED averaged over the control volumes
W_{1c}	critical SED value of the considered material under tensile loading
W_{3c}	critical SED value of the considered material under torsion loading

Symbols

2α	notch opening angle
ν	Poisson's ratio
ρ	notch tip radius
σ_{nom}	nominal tensile stress
σ_t	ultimate tensile strength
τ_{nom}	nominal torsion stress
τ_t	ultimate torsion strength

(*) See also:

Berto, F.; Campagnolo, A.; Ayatollahi, M. Brittle fracture of rounded V-notches in isostatic graphite under static multiaxial loading. *Physical Mesomechanics*; 18: 283-297 (2015)

2.2.1. Introduction

Isostatic graphite can be used in many industrial applications due to the good compromise between thermal and mechanical properties. The design of industrial products made of graphite is not focused only to structural applications. However, the large majority of components, although not thought as structural ones, is subjected to loads transferred by the other parts of the structure. For this reason, many studies in the past have been devoted to the investigation of the fracture strength of graphite. Brittle fracture is a typical behaviour for this material and usually happens after the initiation of micro-cracks in the most stressed parts of the structure, combined in some cases with a very limited amount of plasticity [53].

The majority of the studies focused on structural integrity of graphite components have been devoted to the investigation of cracked components by quantifying the fracture toughness under prevalent mode I loading [54–59]. Dealing with isotropic graphite, innovative techniques have been proposed with this aim [60,61]. Some researchers have also studied the fracture behaviour of composite materials reinforced by graphite fibres at room temperature [62–65]. The problem related to the mechanical behaviour at elevated temperature of graphite in presence of cracks is also a topic of active research [66–69]. Although the problem of brittle fracture of graphite components has been studied continuously for many years, only few predictive models have been proposed for the fracture assessment of cracked components. Some models are based on the microstructural properties [70–73]. A stress based criteria [74] has been recently proposed as an extension of the maximum tensile stress (MTS) criterion originally proposed in a pioneering study by Erdogan and Sih [75].

The papers briefly recalled in the first part of this introduction refer to the behaviour of graphite in the presence of cracks. A review of the recent and past literature shows that only very few papers are focused to the study of the notch sensitivity of graphite components. It is worth of mentioning here the pioneering study conducted by Bazaj and Cox [76] and Kawakami [77]. Only in the last years the topic of the fracture behaviour of blunt notches has been faced by other

researchers, who have investigated the case of pure mode I loading and in-plane mixed mode loading [6,31,32,35,36,39,51].

Dealing with static failure of notches under out-of-plane loading (i.e. pure torsion) the literature is very limited. There are few papers dealing with tension/torsion (mixed mode I/III) fracture in some other types of ceramics like Al_2O_3 [78] and inorganic glass [79].

Very recently Ayatollahi and Saboori [80] have proposed a new fixture for fracture tests under mixed mode I/III loading setting it with some PMMA specimens weakened by cracks.

Only one recent contribution by Berto et al. deals with V-notched specimens under pure torsion loading [38] while the case of static multiaxial loading (I+III) has never been investigated until now and no data are available for isostatic graphite. Due to this complete lack in the literature, the main aim of this research program is to systematically investigate the static behaviour of isostatic graphite subjected to multiaxial loadings obtained as a combination of tension and torsion with different values of the mode mixity ratio (i.e. the ratio between the nominal stress due to tension and that due to torsion loading): 0.40, 0.50 and 1.00. A new complete set of experimental data from cylindrical specimens subjected to combined tension and torsion loads is provided here, considering a large variety of geometrical configurations obtained by varying the notch opening angle and notch depth. More than 40 new data from graphite specimens are summarised here with reference to different geometric configurations and various notch acuties. The notch radius has been varied from 0.3 to 2 mm and the notch opening angle from 30° to 120° .

A fracture model based on the strain energy density (SED) averaged over a control volume is used for the first time for the fracture assessment of notched samples subjected to the multiaxial static loading case of tension and torsion applied in combination.

The SED based approach allows a sound fracture assessment of the critical load for the specific material under investigation and it can be potentially extended to other types of graphite subjected to different combinations of mode I and mode III loading conditions.

This paragraph is divided in two parts: in the first one the experimental activity is presented (sample geometry, test setting, details of experimental data). While the second part deals with the formulation and application of the averaged strain energy density criterion on the new data.

2.2.2. Fracture Experiments

The details of the graphite material, the test specimens and the fracture experiments are presented in this section.

2.2.2.1. Material properties of EG022A

The fracture tests were conducted on a grade of isostatic polycrystalline graphite with commercial name of EG022A. The basic material properties of the tested graphite are listed in Table 2.2.1: the mean grain size is of 300 μm , the porosity of 15%, the bulk density of 1830 kg/m^3 , the mean tensile strength of 30 MPa, the Young's modulus of 8.00 GPa and the shear modulus of 3.30 GPa.

Nonlinear deformation sometimes is observed in the mechanical behaviour of graphites, which makes the determination of Young's modulus rather complicated [81,82]. However, for simplicity the Young's modulus was obtained in this research from load-displacement graphs recorded by a universal tension-compression machine. The deviation observed from linear behaviour was less than 0.01% at failure for the specimen used in the test. Young's modulus has been measured at a load where the deviation from linear behaviour was less than 0.005%. The mean grain size was given in the material certify and measured by using the SEM technique while the density of the material was determined from the buoyancy method, submerging the tested graphite in a liquid of known density.

Table 2.2.1. Material properties.

Material property	Value
Elastic Modulus E [MPa]	8000
Shear Modulus G [MPa]	3300
Poisson's Ratio ν	0.2
Ultimate Tensile Strength [MPa]	30
Ultimate Torsion Strength [MPa]	37
Hardening [Shore]	53
Density [Kg/dm ³]	1.83
Average grain size [μm]	300
Resistivity [$\mu\text{ohm}\cdot\text{m}$]	10.8
Thermal Conductivity [W/(m·K)]	119

All tests were performed under displacement control on a servo-controlled MTS bi-axial testing device (± 100 kN/ ± 1100 Nm, ± 75 mm/ $\pm 55^\circ$). The load was measured by a MTS cell with ± 0.5 % error at full scale. A MTS strain gauge axial extensometer (MTS 632.85F-14), with a gage length equal to 25 mm was used for measuring the tensile elastic properties on plain specimens while a multi-axis extensometer MTS 632.80F-04 (with a gage length equal to 25 mm) was used for measuring the torsional elastic properties on unnotched specimens.

Some load-displacement curves were recorded to obtain the Young's modulus (E) of the graphite using an axial extensometer. The tensile strength (σ_t) was measured by means of axis-symmetric specimens with a net diameter equal to 12.5 mm on the net section and a diameter of 20 mm on the gross section (see Figure 2.2.1a). Due to the presence of a root radius equal to 40 mm, the theoretical stress concentration factor is less than 1.03.

The torque-angle graphs recorded by the MTS device were employed together with the bi-axis extensometer to obtain the shear modulus (G) and to measure the torsion strength (τ_t) of the tested graphite. The ultimate shear strength τ_t was found to be equal to 37 MPa.

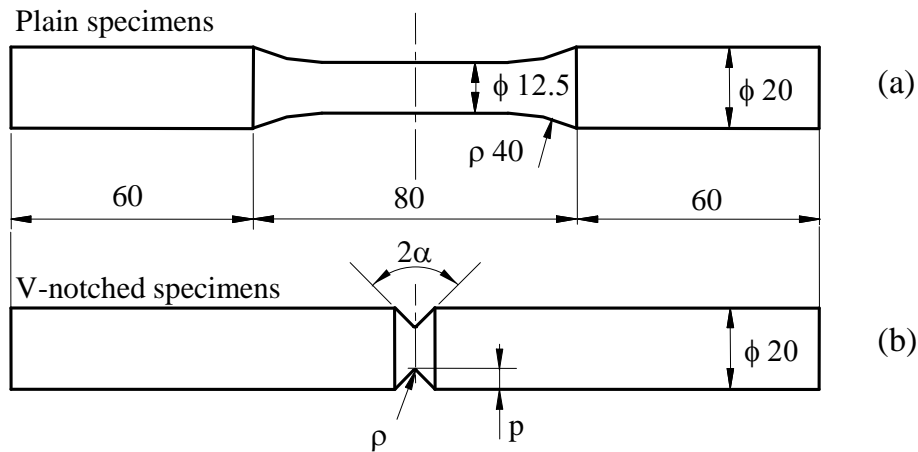


Figure 2.2.1. Geometry of plain (a) and notched (b) specimens used in the experimental tests.

2.2.2.2. Test specimens

As shown in Figure 2.2.1, different round bar specimens were used for multiaxial (tension and torsion) static tests: unnotched specimens (Fig. 2.2.1a) and cylindrical specimens with V-notches (Fig. 2.2.1b). This allows us to explore the influence of a large variety of notch shapes in the experiments.

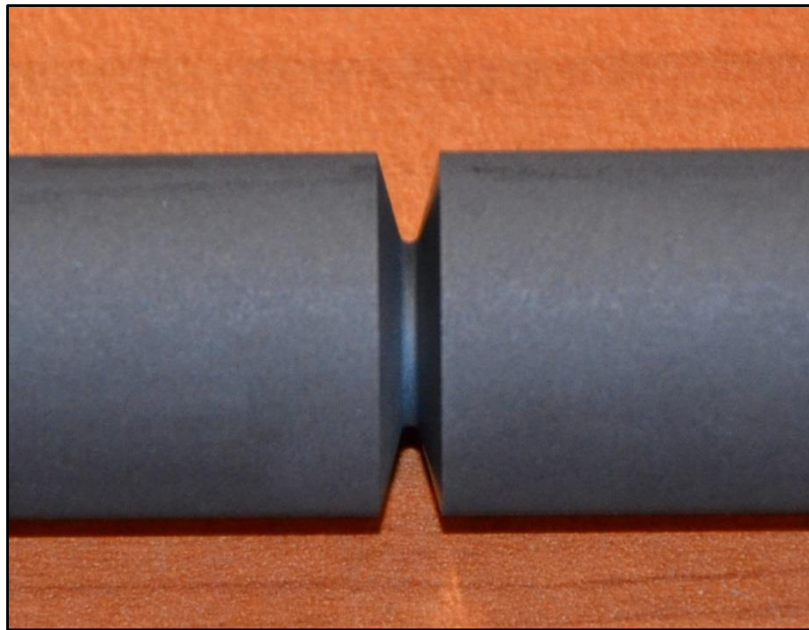
In more details:

- For V-notched graphite specimens with a notch opening angle $2\alpha = 120^\circ$ (Fig. 2.2.1b), notches with four different notch root radii were tested; $\rho = 0.3, 0.5, 1$ and 2.0 mm. The effect of net section area was studied by changing the notch depth p . Two values were used, $p = 3$ and 5 mm, while keeping the gross diameter constant (20 mm).
- For V-notched graphite specimens with a notch opening angle $2\alpha = 60^\circ$ (Fig. 2.2.1b), four different notch root radii were considered in the experiments: $\rho =$

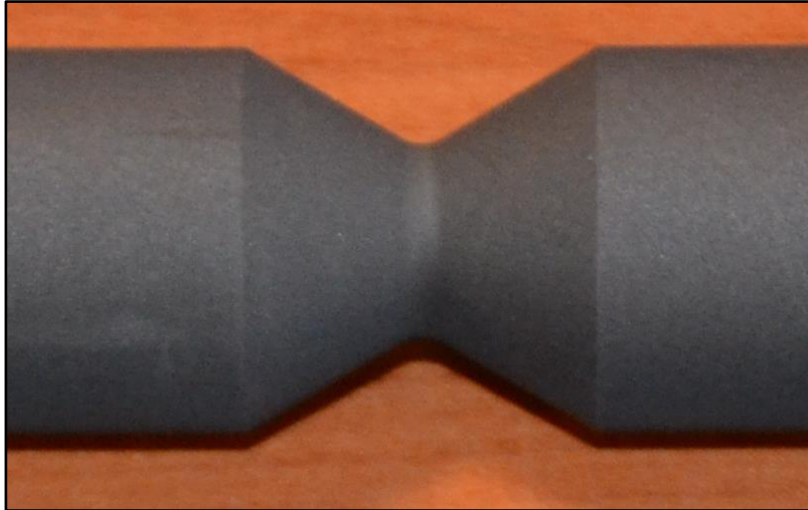
0.3, 0.5, 1.0 and 2.0 mm. With a constant gross diameter (20 mm), also the net section area was kept constant, such that $p = 5$ mm.

- For V-notched graphite specimens with a notch opening angle $2\alpha = 30^\circ$ (Fig. 2.2.1b), three different notch root radii were considered in the experiments: $\rho = 0.5, 1.0$ and 2.0 mm keeping constant the notch depth $p = 5$ mm.

At least three samples were prepared for each of the 15 specimen geometries described above, with a total number of 45 specimens. Figure 2.2.2a shows some samples used in the tension-torsion tests, whereas Figure 2.2.2b shows a typical fracture surface of a notched graphite component after failure under combined tension and torsion loading.

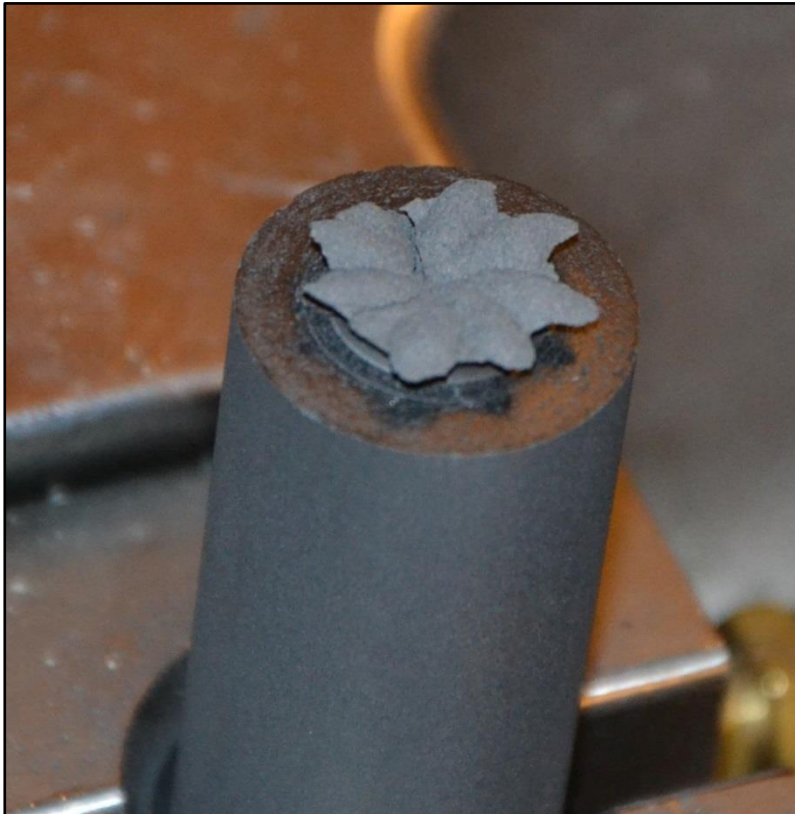


V-notch, $2\alpha = 30^\circ$



V-notch, $2\alpha = 120^\circ$

(a)



(b)

Figure 2.2.2. (a) Notched specimens used in combined tension-torsion tests and (b) a sample specimen broken after a combined tension-torsion test.

In order to prepare the specimens, first several thick plates were cut from a graphite block. Then, the specimens were precisely manufactured by using a 2-D CNC cutting machine. Before conducting the experiments, the cut surfaces of the graphite specimens were polished by using a fine abrasive paper to remove any possible local stress concentrations due to surface roughness.

The tests were conducted under three different combinations between the tensile and the torsional stresses, with the nominal mode mixity ratios of $\sigma_{\text{nom}}/\tau_{\text{nom}} = 0.4$, 0.5 and 1. The details of applied loads are given in Table 2.2.2 as well as the stress concentration factors of each specimen under tension and torsion loading conditions, obtained by means of FE analyses adopting very refined meshes. Different nominal mode mixity ratios have been achieved by properly setting the torsional loading rate with respect to the tensile loading rate. In particular the tensile loading rate was varied keeping constant the rotation control conditions with a loading rate of $1^\circ/\text{min}$.

Fig. 2.2.3 shows two example of load-angle (torque versus θ) diagrams corresponding to some V-notched specimens characterized by the same notch radius and different values of the notch depth ($p = 3$ mm, Fig. 2.2.3a and $p = 5$ mm, Fig. 2.2.3b). The load-angle curves recorded during the tests always exhibited an approximately linear trend up to the final failure, which occurred suddenly. Therefore, the use of a fracture criterion based on a linear elastic hypothesis for the material law is realistic. The same trend has been observed for the tensile curves plotting the load as a function of the axial displacement.

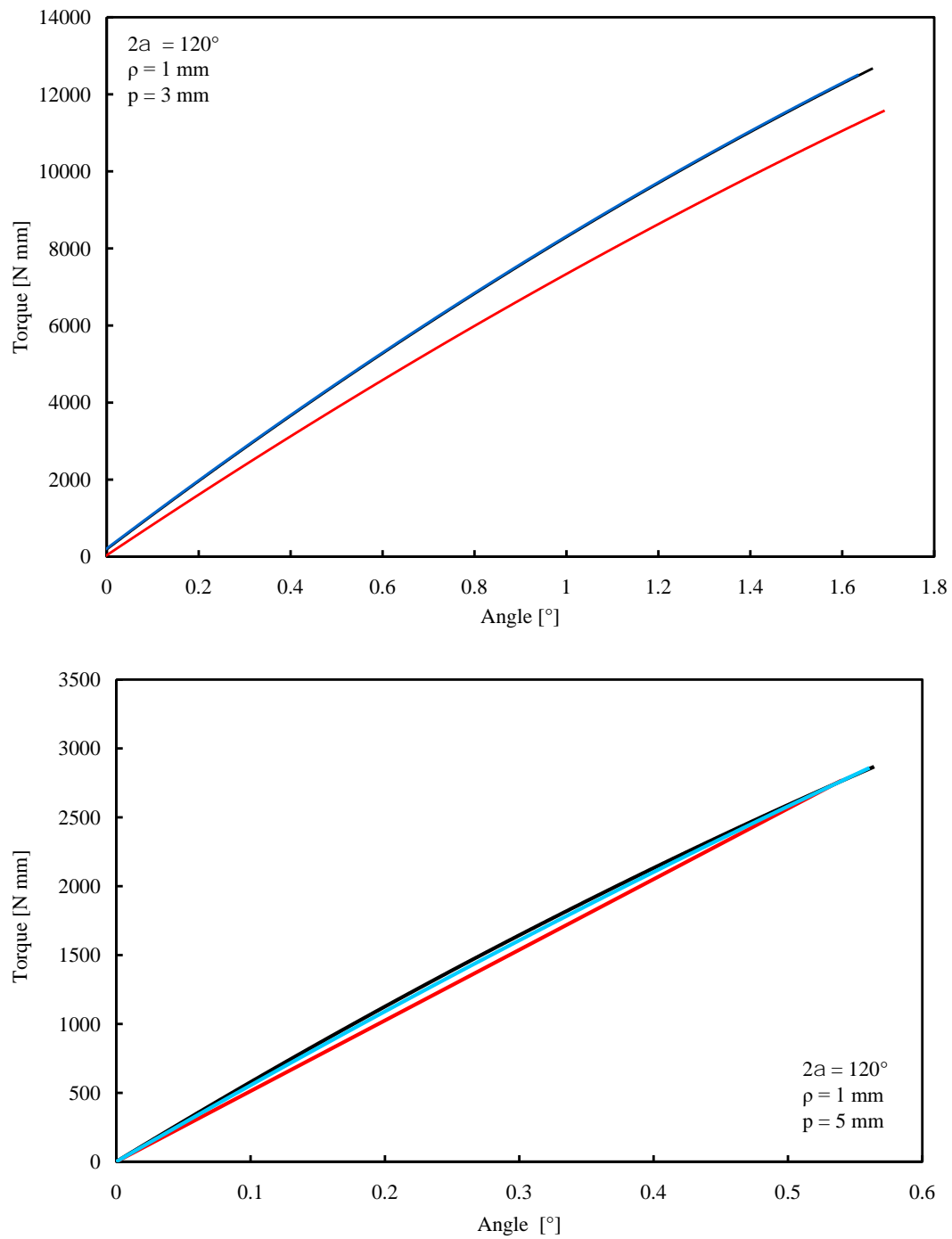


Figure 2.2.3. Torque-angle curves related to V-notched graphite specimens with a notch depth equal to (a) $p = 3 \text{ mm}$ and (b) $p = 5 \text{ mm}$.

Table 2.2.2. Geometrical parameters of the graphite specimens used in the tests.

Notch opening angle 2α (°)	Notch depth p (mm)	Notch radius ρ (mm)	K_t tension	K_t torsion	σ_{nom}/τ_{nom}
120	3	0.3	4.29	2.09	0.5
		0.5	3.54	1.85	0.5
		1	2.75	1.59	0.5
		2	2.14	1.38	0.5
	5	0.3	3.83	1.93	1
		0.5	3.15	1.72	1
		1	2.45	1.48	1
		2	1.91	1.30	1
60	5	0.3	4.46	2.25	1
		0.5	3.52	1.90	0.4
	1	2.59	1.55	0.4	
		2	1.96	1.32	0.4
30	5	0.5	3.53	1.94	1
	1	2.60	1.56	1	
		2	1.95	1.32	1

All loads to failure (tensile load and torque) are reported in Tables 2.2.3-2.2.5 for each notch configuration and loading conditions. In particular Table 2.2.3 reports the data for $\sigma_{nom}/\tau_{nom} = 1$ while Tables 2.2.4 and 2.2.5 summarize the data for the two ratios 0.4 and 0.5, respectively. As visible from the tables the imposed mode mixity ratio is almost fulfilled with a variation of approximately $\pm 10\%$ with respect to the imposed value.

The variability of the loads to failure as a function of the notch opening angle is weak although not negligible. For a constant notch radius, the fracture load slightly increases for larger notch opening angles, although this effect is very low. The main conclusion is that the stress concentration factors reported in Table 2.2.2 are not able to control the failure conditions due to a low notch sensitivity exhibited by the graphite specimens under combined tension and torsion loads.

Table 2.2.3. Experimental results in the case of $\sigma_{nom}/\tau_{nom} = 1.0$; notch depth $p = 5$ mm.

Specimen code	Notch opening angle 2α ($^{\circ}$)	Notch radius ρ (mm)	Tensile Load (N)	Torque (N mm)	σ_{nom} (MPa)	τ_{nom} (MPa)	σ_{nom}/τ_{nom}
1-01	120 $^{\circ}$	0.3	1193	2659	15.19	13.54	1.12
1-02			1025	2280	13.05	11.61	1.12
1-03			1114	2500	14.18	12.73	1.11
2-01		0.5	1190	2690	15.15	13.69	1.10
2-02			1234	2631	15.71	13.40	1.17
2-03			1200	2694	15.28	13.72	1.11
3-01		1	1302	2873	16.58	14.63	1.13
3-02			1251	2673	15.93	13.61	1.17
3-03			1283	2845	16.34	14.49	1.13
4-01		2	1497	3798	19.06	19.35	0.98
4-02			1451	3634	18.47	18.51	1.00
4-03			1532	3710	19.51	18.89	1.03
5-01	60 $^{\circ}$	0.3	1073	2632	13.66	13.40	1.02
5-02			1037	2867	13.20	14.60	0.90
5-03			1125	2883	14.32	14.68	0.98
6-01	30 $^{\circ}$	0.5	1097	2852	13.97	14.53	0.96
6-02			1157	2704	14.73	13.75	1.07
6-03			1213	2917	15.44	14.86	1.04
7-01		1	1178	3038	15.00	15.47	0.97
7-02			1112	2972	14.16	15.14	0.94
7-03			1214	3248	15.46	16.54	0.93
8-01		2	1302	3102	16.55	15.80	1.05
8-02			1319	3386	16.79	17.24	0.97
8-03			1486	3489	18.92	17.77	1.06

Table 2.2.4. Experimental results in the case of $\sigma_{nom}/\tau_{nom} = 0.4$; notch depth $p = 5$ mm.

Specimen code	Notch opening angle 2α (°)	Notch radius ρ (mm)	Tensile load (N)	Torque (N mm)	σ_{nom} (MPa)	τ_{nom} (MPa)	σ_{nom}/τ_{nom}
9-01	60	0.5	636	3923	8.10	19.98	0.41
9-02			600	4010	7.64	20.42	0.38
9-03			630	4009	8.02	20.42	0.39
10-01		1	645	4449	8.21	22.66	0.36
10-02			660	4634	8.40	23.60	0.36
10-03			631	4326	8.03	22.03	0.36
11-01		2	895	5164	11.40	26.30	0.43
11-02			811	5259	10.33	26.78	0.39
11-03			750	4700	9.55	23.94	0.40

Table 2.2.5. Experimental results in the case of $\sigma_{nom}/\tau_{nom} = 0.5$; notch depth $p = 3$ mm.

Specimen code	Notch opening angle 2α (°)	Notch radius ρ (mm)	Tensile load (N)	Torque (N mm)	σ_{nom} (MPa)	τ_{nom} (MPa)	σ_{nom}/τ_{nom}
12-01	120	0.3	1482	11606	9.63	21.54	0.45
12-02			1324	9657	8.60	17.92	0.48
12-03			1768	12129	11.49	22.51	0.51
13-01		0.5	1701	11768	11.05	21.84	0.51
13-02			1619	11196	10.52	20.78	0.51
13-03			1657	12005	10.76	22.28	0.48
14-01		1	1739	12150	11.30	22.55	0.50
14-02			1788	12756	11.62	23.68	0.49
14-03			1816	12611	11.80	23.41	0.50
15-01		2	2034	13891	13.21	25.78	0.51
15-02			1756	12500	11.41	23.20	0.49
15-03			1931	13452	12.54	24.97	0.50

2.2.3. Strain Energy Density averaged over a control volume: the fracture criterion

With the aim to assess the fracture load in notched graphite components, an appropriate fracture criterion is required which has to be based on the mechanical behaviour of material around the notch tip. In this section, a criterion proposed by Lazzarin and co-authors [31,32] based on the strain energy density (SED) is briefly described.

Dealing with cracked components, the strain energy density factor S was defined first by Sih in a pioneering contribution [43] as the product of the strain energy density by a critical distance from the point of singularity. Failure was suggested to be controlled by a critical value of S , whereas the direction of crack propagation was determined by imposing a minimum condition on S .

Different from Sih's criterion, which is a point-wise approach, the averaged strain energy density criterion (SED) as presented in Refs. [31–33,44] states that brittle failure occurs when the mean value of the strain energy density over a given control volume is equal to a critical value W_c . This critical value varies from material to material but it does not depend on the notch geometry and sharpness. The control volume, reminiscent of Neuber's concept of elementary structural volume [83], is considered to be dependent on the ultimate tensile strength σ_t and the fracture toughness K_{Ic} in the case of brittle or quasi-brittle materials subjected to static loads.

The method based on the averaged SED was formalised and applied first to sharp (zero radius) V-notches under mode I and mixed mode I+II loading [31] and later extended to blunt U- and V-notches [32,42,84–86]. Some recent developments and applications are summarized in Refs. [44,87–92] with some considerations also to three-dimensional effects [93–96], which have been widely discussed in Refs. [97,98].

When dealing with cracks, the control volume is a circle of radius R_c centred at the crack tip (Fig. 2.2.4a). Under plane strain conditions, the radius R_c can be evaluated according to the following expression [99]:

$$R_{1c} = \frac{(1+\nu)(5-8\nu)}{4\pi} \left(\frac{K_{Ic}}{\sigma_t} \right)^2 \quad (2.2.1)$$

where K_{Ic} is the fracture toughness, ν the Poisson's ratio and σ_t the ultimate tensile stress of a plain specimen.

For a sharp V-notch, the critical volume becomes a circular sector of radius R_c centred at the notch tip (Fig. 2.2.4b). When only failure data from open V-notches are available, R_c can be determined on the basis of some relationships reported in [36], where K_{Ic} is substituted by the critical value of the notch stress intensity factors (NSIFs) as determined at failure from sharp V-notches.

Dealing here with sharp notches under torsion loading, the control radius R_{3c} can be estimated by means of the following equation [100]:

$$R_{3c} = \left(\sqrt{\frac{e_3}{1+\nu}} \times \frac{K_{3c}}{\tau_t} \right)^{\frac{1}{1-\lambda_3}} \quad (2.2.2)$$

where K_{3c} is the Mode III critical notch stress intensity factor and τ_t is the ultimate torsion strength of the unnotched material. Moreover, e_3 is the parameter that quantifies the influence of all stresses and strains over the control volume and $(1-\lambda_3)$ is the degree of singularity of the linear elastic stress fields [101], which depends on the notch opening angle. Values of e_3 and λ_3 are 0.4138 and 0.5 for the crack case ($2\alpha = 0^\circ$).

For a blunt V-notch under mode I or mode III loading, the volume is assumed to be of a crescent shape shown in Fig. 2.2.4c, where R_c is the depth measured along the notch bisector line. The outer radius of the crescent shape is equal to R_c+r_0 , being r_0 the distance between the notch tip and the origin of the local coordinate system (Fig. 2.2.4c). Such a distance depends on the V-notch opening angle 2α , according to the expression [33,44]:

$$r_0 = \rho \frac{(\pi - 2\alpha)}{(2\pi - 2\alpha)} \quad (2.2.3)$$

For the sake of simplicity, complex theoretical derivations have deliberately been avoided in the present work and the SED values have been determined directly from the FE models.

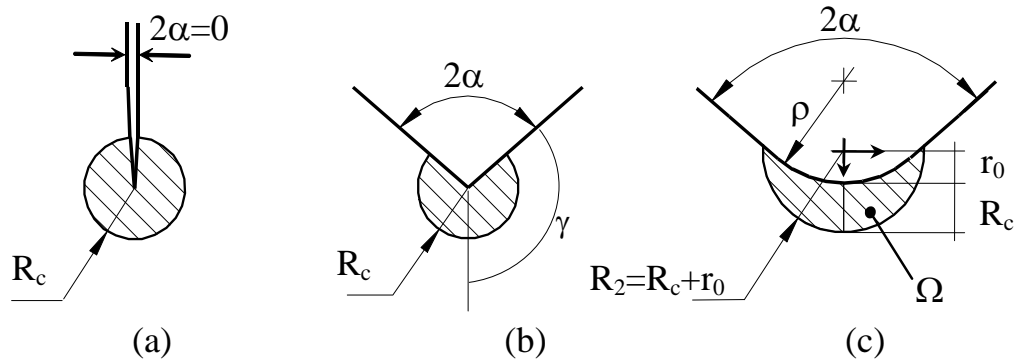


Figure 2.2.4. Control volume for (a) crack, (b) sharp V-notch and (c) blunt V-notch, under mixed mode I/III loading. Distance $r_0 = \rho \times (\pi - 2\alpha) / (2\pi - 2\alpha)$.

2.2.4. SED approach in fracture analysis of the tested graphite specimens

The fracture criterion described in the previous section is employed here to estimate the fracture loads obtained from the experiments conducted on the graphite specimens. In order to determine the SED values, first a finite element model of each graphite specimen was generated. A typical mesh used in the numerical analyses is shown in Fig. 2.2.5a. In addition, Fig. 2.2.5b shows the typical SED contour lines under combined tension and torsion loading condition.

As originally thought for pure modes of loading the averaged strain energy density criterion (SED) states that failure occurs when the mean value of the strain energy density over a control volume, \bar{W} , reaches a critical value W_c , which depends on the material but not on the notch geometry.

Under tension loads, this critical value can be determined from the ultimate tensile strength σ_t according to Beltrami's expression for the unnotched material:

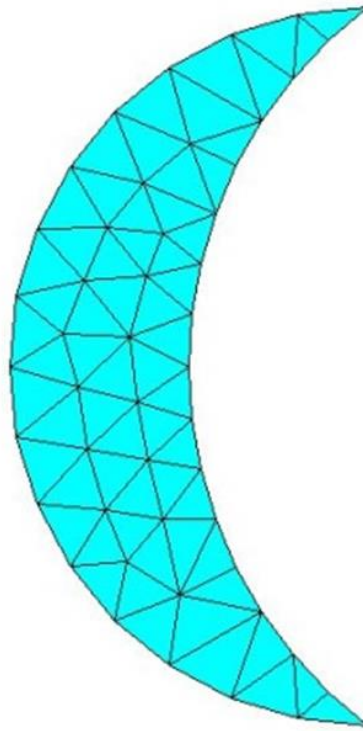
$$W_{1c} = \frac{\sigma_t^2}{2E} \quad (2.2.4)$$

By using the values of $\sigma_t = 30$ MPa and $E = 8000$ MPa, the critical SED for the tested graphite is $W_{1c} = 0.05625$ MJ/m³.

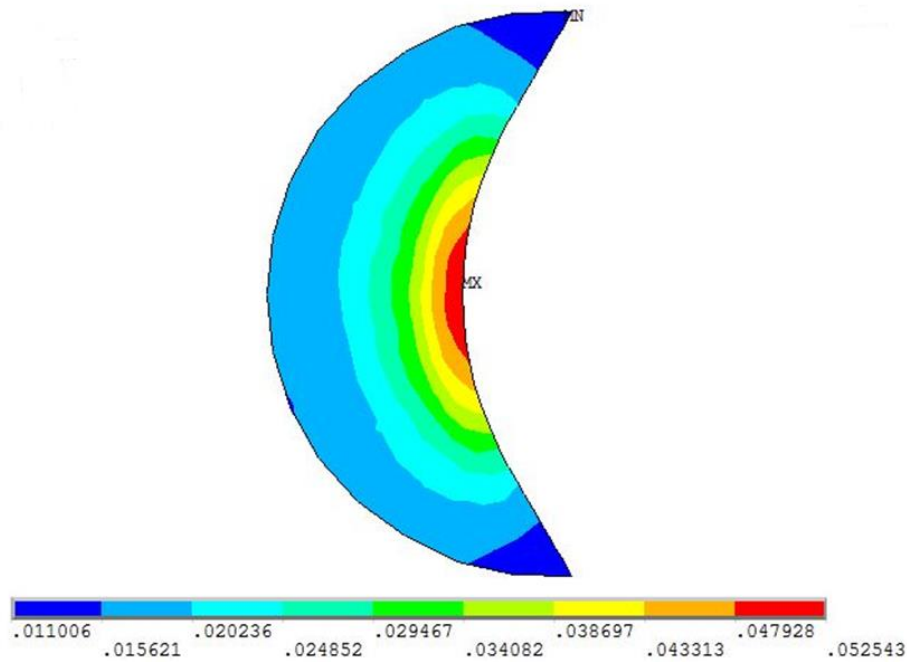
Under torsion loads, this critical value can be determined from the ultimate shear strength τ_t according to Beltrami's expression for the unnotched material:

$$W_{3c} = \frac{\tau_t^2}{2G} \quad (2.2.5)$$

By using the values of $\tau_t = 37$ MPa and $G = 3300$ MPa, the critical SED for the tested graphite is $W_{3c} = 0.2074$ MJ/m³.



(a)



(b)

Figure 2.2.5. Typical mesh used to evaluate the averaged SED for a V-notched specimen with $2\alpha = 120^\circ$, $\rho = 1$ mm, $p = 5$ mm, $R_c = 0.4$ mm. (a) FE mesh and (b) SED contour lines under combined tension and torsion loading.

In parallel, the control volume definition *via* the control radius R_c needs the knowledge of the mode I and mode III critical notch stress intensity factor K_{1c} and K_{3c} and the Poisson's ratio ν , see Eqs. (2.2.1) and (2.2.2). For the considered material K_{1c} and K_{3c} have been obtained from specimens weakened by sharp V-notches with an opening angle $2\alpha = 10^\circ$ and a notch radius less than 0.1 mm. A pre-crack was also generated with a razor blade at the notch tip. The resulting values are $K_{1c} = 1.06$ MPa m^{0.5} and $K_{3c} = 1.26$ MPa m^{0.5} which provide the control radii $R_{1c} = 0.405$ mm and $R_{3c} = 0.409$ mm, under pure tension and pure torsion, respectively. For the sake of simplicity, a single value of the control radius was kept for the synthesis in terms of SED setting $R_c = R_{1c} = R_{3c}$. As discussed in previous papers [33,44,102], the control radii under tension and torsion can be very different and this is particularly true when the material behaviour differs from a brittle behaviour: the difference is higher for materials

obeying a ductile behaviour. For this specific case, the values are so close to each other that a single value can be employed for the final synthesis. The SED criterion has been applied here for the first time to mixed mode I/III loading conditions. Two different methodologies have been proposed. The two procedures will be described below.

2.2.4.1 Total critical energy: criterion 1

The first proposal for the application of the local SED approach to the case of mixed mode I/III loading is based on the idea that the total critical SED, W_c , is a function of the nominal mode mixity ratio σ_{nom}/τ_{nom} and it can be evaluated according to the following equation valid for both unnotched and notched components:

$$W_c = f(\sigma_{nom,c}/\tau_{nom,c}) = W_1 + W_3 \quad (2.2.6)$$

For unnotched specimens Eq. (2.2.6) can be re-written as follows:

$$W_c = \frac{\sigma_{nom,c}^2}{2E} + \frac{\tau_{nom,c}^2}{2G} \quad (2.2.7)$$

where $\sigma_{nom,c}$ and $\tau_{nom,c}$ are the nominal critical stresses referred to the net area corresponding to different values of the mode mixity ratio. Then in this first criterion W_c is a function of the mode mixity ratio σ_{nom}/τ_{nom} .

Some tests on unnotched specimens have been made as a function of the nominal mode mixity ratio, Figure 2.2.6 reports the trend of the critical SED as obtained experimentally from plain specimens as a function of the nominal mode mixity ratio. When $\sigma_{nom}/\tau_{nom} = 0$, the case of pure torsion is achieved while when τ_{nom} tends to zero (σ_{nom}/τ_{nom} tends to $+\infty$) the case of pure tension is obtained. These two limits correspond to the left and right hand side limits of the diagram. By considering the critical energy as a function of the mode mixity ratio $M = 2/\pi \arctan(\sigma_{nom}/\tau_{nom})$, as reported in Figure 2.2.6, and numerically evaluating the SED for the notched graphite specimens tested in the present work, Table 2.2.6 was finally obtained. The values of the critical SED as a function the mode mixity

ratio are respectively 0.0833, 0.1173 and 0.1510 MJ/m³ for $\sigma_{\text{nom}}/\tau_{\text{nom}} = 1.0, 0.5$ and 0.4, respectively as indicated in Fig. 2.2.6.

The SED has been calculated numerically by using the FE code ANSYS 14.5[®]. All the analyses have been carried out by using eight-node harmonic elements (PLANE 83) under axis-symmetric conditions. Only one quarter of the geometry has been modelled in the positive quadrant. Being the SED value mesh independent [52,103], a free mesh was used for all models. Due to the fact that the SED is mesh insensitive, the similarity between the mesh patterns used to model different geometries would be unnecessary. The only point to consider is the correct definition of the control volume according to Figure 2.2.4b and 2.2.5. As stated above the size of the control volume is $R_c = 0.4$ mm for both tension and torsion loadings.

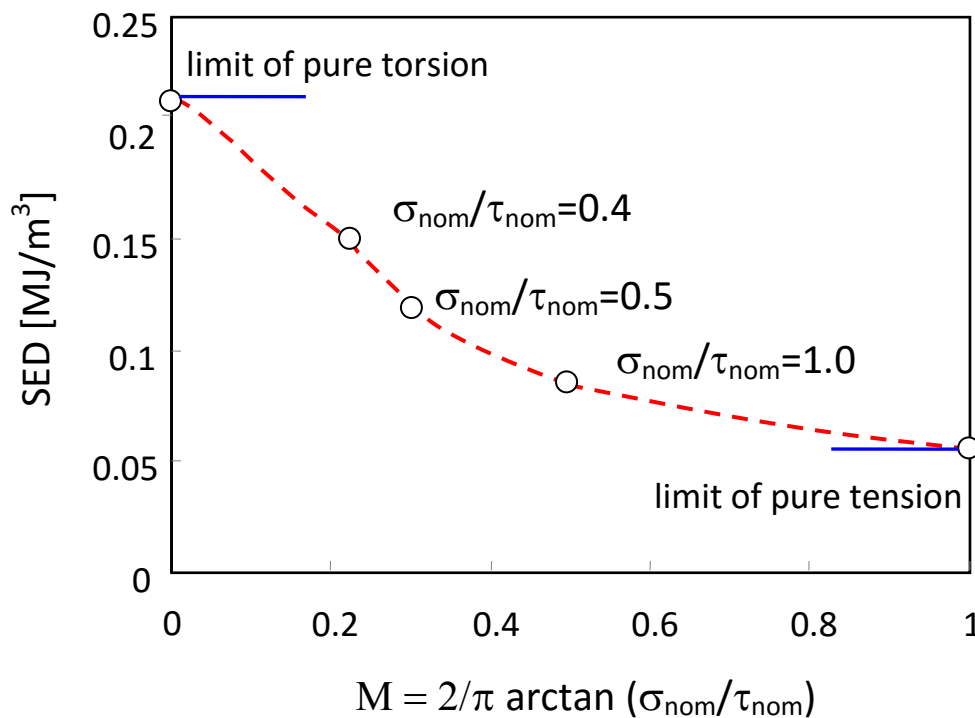


Figure 2.2.6. Trend of the critical SED as obtained experimentally from plain specimens as a function of the nominal mode mixity ratio.

Table 2.2.6 summarizes for each case, the contributions to SED due to mode I and due to mode III. The total SED as obtained by the simple sum of the two contributions has been reported in the tenth column of the table. The last column

presents the total SED normalized by its critical value, as obtained from plain specimens for a specific nominal mode mixity ratio $\sigma_{\text{nom}}/\tau_{\text{nom}}$ (Figure 2.2.6). The normalised values have been given in the form of the square root $(\text{SED}/W_c)^{0.5}$ being this ratio proportional to the values of the critical loads. This representation has been used by the same authors also in the past [44].

As it can be seen in Table 2.2.6 for the tested graphite samples, the agreement between the experimentally obtained critical loads and the theoretical values based on the constant value of the averaged SED, is satisfactory; with the relative deviation ranging from -15% to +15 %. However, for very few test data, the deviation is slightly higher than 15% but still comparable with previous findings under in plane mixed mode loading, where the acceptable scatter was about $\pm 20\%$.

The most significant results have also been given in graphical form in Figs. 2.2.7 and 2.2.8 where the *experimental* values of the critical loads (open dots) have been compared with the *theoretical* predictions based on the constancy of SED in the control volume (solid line). The plots of Figs. 2.2.7a,b are given for the notched graphite specimens as a function of the notch radius ρ for V-notches with $2\alpha = 30^\circ$ and $p = 5$ mm both for the critical tensile load (Fig. 2.2.7a) and for the critical torque (Fig. 2.2.7b). The theoretically predicted loads are in good agreement with the experimental results. This holds true also for the other specimens. The same plots are presented in Figs. 2.2.8a,b dealing with V-notches with $2\alpha = 120^\circ$ and $p = 3$ mm again divided in Figs. 2.2.8a and 2.2.8b with the aim to show the tensile fracture load and critical torque.

Fig. 2.2.9 shows a synthesis in terms of the square root value of the local energy averaged over the control volume of radius R_c , normalised with respect to the critical energy (as obtained from Figure 2.2.6) as a function of the notch radius ρ . Indeed, the ratio on the vertical axis is proportional to the fracture loads. The aim in this figure is to investigate the range of accuracy of all SED-based fracture assessments for the tested graphite specimens. It is clear that the scatter of the data is very limited and almost independent of the notch opening angle. All the experimental values fall inside a scatterband ranging from 0.80 to 1.20. Note that many of the results are inside a scatterband ranging from 0.85 to 1.15, which was

also typical for the notched graphite specimens tested under in-plane mixed tension-shear loading [36,51].

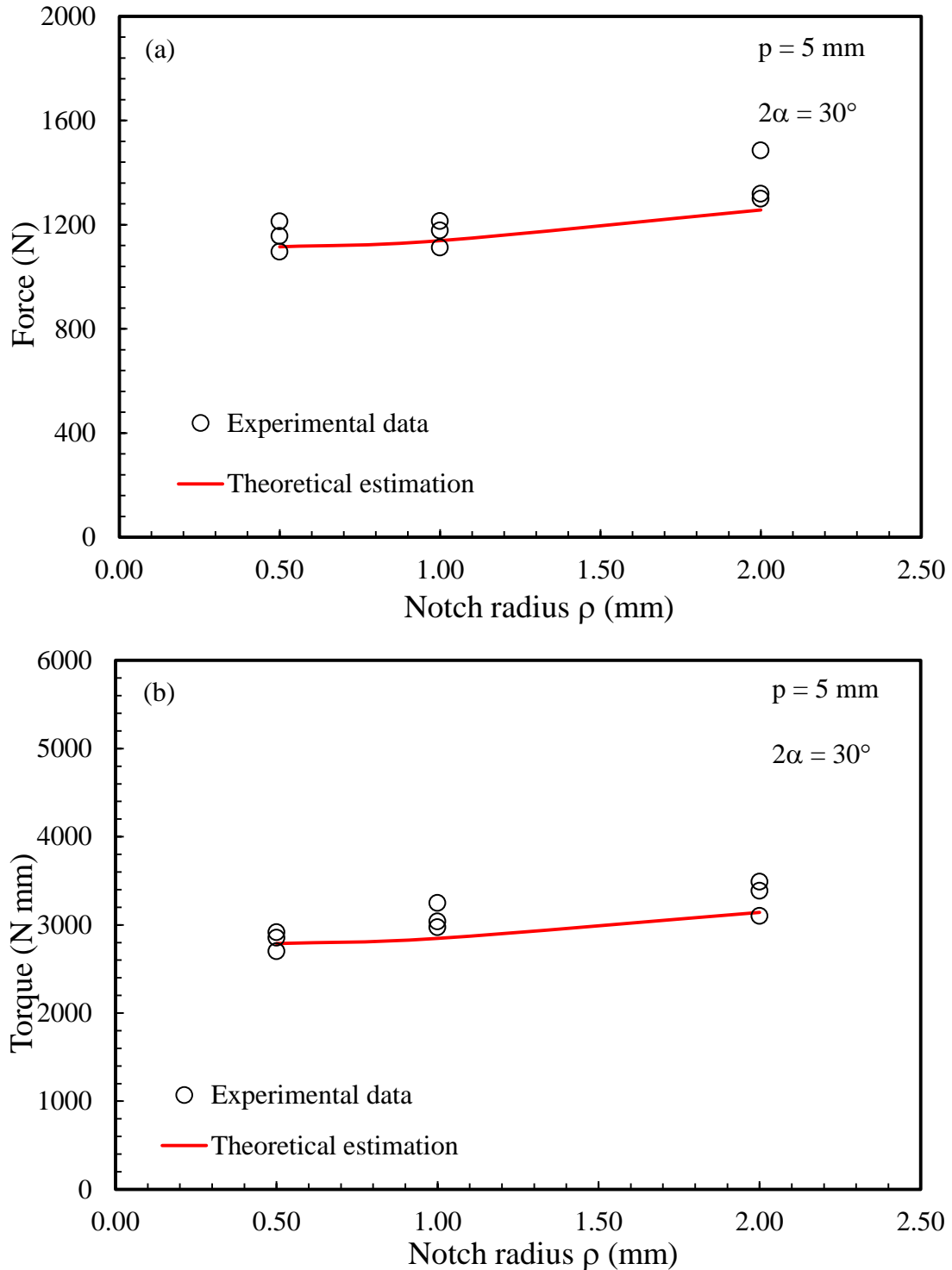


Figure 2.2.7. Comparison between experimental data and theoretical assessment for the graphite specimens V-shaped notches with $2\alpha = 30^\circ$ and $p = 5$ mm. Control radius $R_c = 0.4$ mm. (a) Tensile load and (b) torsion load.

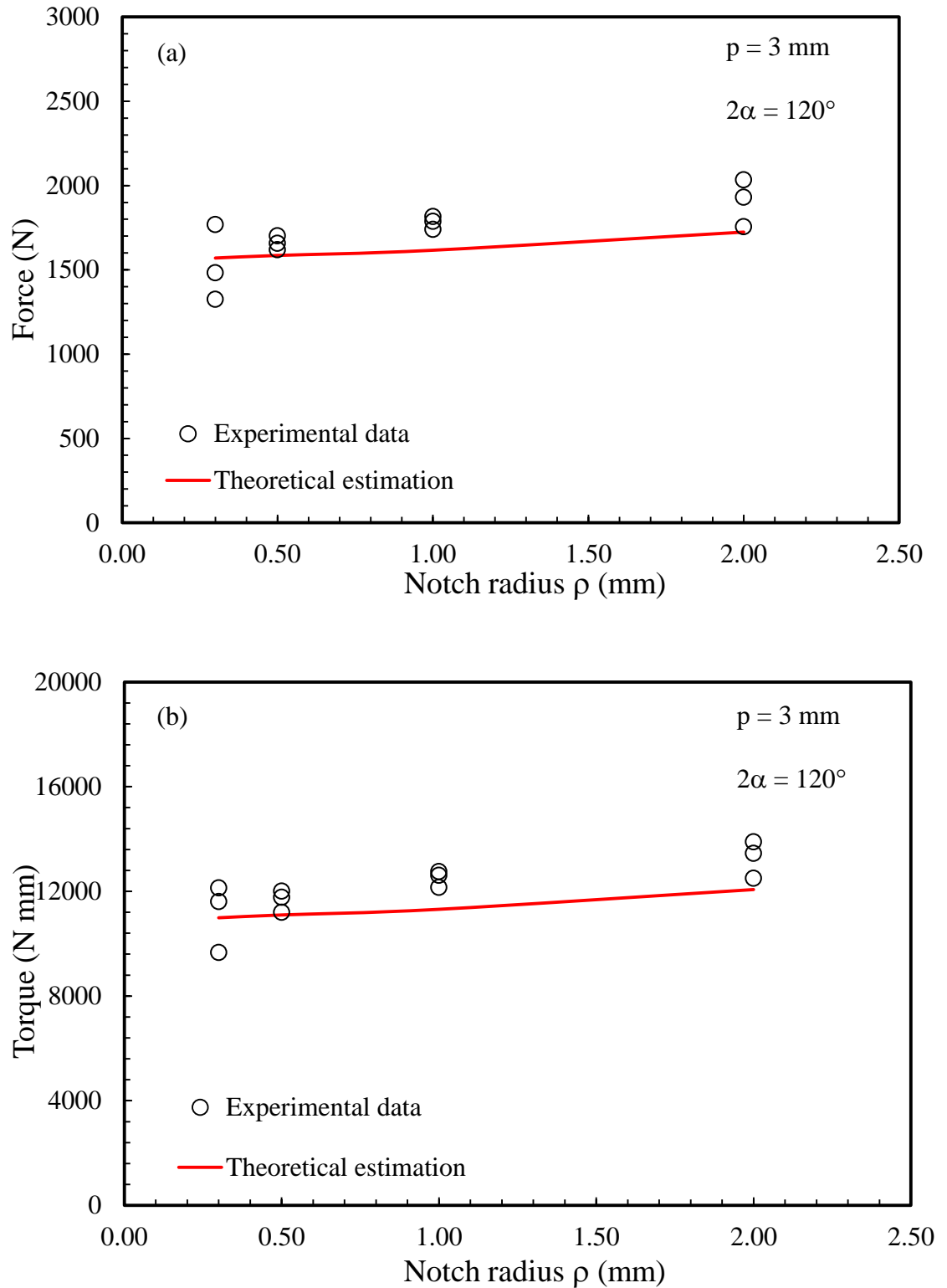


Figure 2.2.8. Comparison between experimental data and theoretical assessment for the graphite specimens V-shaped notches with $2\alpha = 120^\circ$ and $p = 3$ mm. Control radius $R_c = 0.4$ mm.

(a) Tensile load and (b) torsion load.

Table 2.2.6. Experimental results: overview of the data by using the method 1.

p (mm)	2α (°)	ρ (mm)	Tensile loading (N)	Torque (N mm)	W_1 (MJ/m ³)	W_3 (MJ/m ³)	SED $W_1 + W_3$ (MJ/m ³)	W_c (MJ/m ³)	$(SED/W_c)^{0.5}$
5	120	0.3	1193	2659	0.041	0.040	0.081	0.083	0.985
		0.3	1025	2280	0.030	0.029	0.060	0.083	0.846
		0.3	1114	2500	0.036	0.035	0.071	0.083	0.923
5	120	0.5	1190	2690	0.040	0.040	0.080	0.083	0.981
		0.5	1234	2631	0.043	0.038	0.082	0.083	0.989
		0.5	1200	2694	0.041	0.040	0.081	0.083	0.986
5	120	1	1302	2873	0.045	0.044	0.089	0.083	1.035
		1	1251	2673	0.042	0.038	0.080	0.083	0.979
		1	1283	2845	0.044	0.043	0.087	0.083	1.022
5	120	2	1497	3800	0.046	0.072	0.118	0.083	1.192
		2	1451	3634	0.043	0.066	0.109	0.083	1.145
		2	1532	3710	0.048	0.069	0.117	0.083	1.185
5	60	0.3	1073	2632	0.038	0.043	0.082	0.083	0.989
		0.3	1037	2867	0.036	0.051	0.087	0.083	1.023
		0.3	1125	2883	0.042	0.052	0.094	0.083	1.062
5	30	0.5	1097	2852	0.030	0.050	0.080	0.083	0.980
		0.5	1157	2700	0.034	0.045	0.078	0.083	0.969
		0.5	1213	2917	0.037	0.052	0.089	0.083	1.034
5	30	1	1178	3038	0.040	0.052	0.093	0.083	1.057
		1	1112	2972	0.036	0.050	0.086	0.083	1.018
		1	1214	3248	0.043	0.060	0.103	0.083	1.112
5	30	2	1300	3102	0.041	0.047	0.087	0.083	1.023
		2	1319	3386	0.042	0.056	0.097	0.083	1.081
		2	1486	3489	0.053	0.059	0.112	0.083	1.160
5	60	0.5	636	3923	0.011	0.097	0.108	0.151	0.845
		0.5	600	4010	0.010	0.101	0.111	0.151	0.857
		0.5	630	4009	0.011	0.101	0.112	0.151	0.861
5	60	1	645	4449	0.011	0.107	0.118	0.151	0.885
		1	660	4634	0.012	0.116	0.128	0.151	0.920
		1	631	4326	0.011	0.101	0.112	0.151	0.861
5	60	2	895	5164	0.020	0.132	0.152	0.151	1.005
		2	811	5259	0.017	0.137	0.154	0.151	1.009
		2	750	4700	0.014	0.110	0.124	0.151	0.905
3	120	0.3	1482	11606	0.021	0.118	0.139	0.117	1.089
		0.3	1324	9657	0.017	0.082	0.099	0.117	0.917
		0.3	1768	12129	0.030	0.129	0.159	0.117	1.164
3	120	0.5	1701	11768	0.027	0.120	0.148	0.117	1.121
		0.5	1619	11196	0.025	0.109	0.134	0.117	1.067
		0.5	1657	12005	0.026	0.125	0.151	0.117	1.135
3	120	1	1739	12150	0.027	0.124	0.151	0.117	1.134
		1	1788	12756	0.028	0.137	0.165	0.117	1.187
		1	1816	12611	0.029	0.134	0.163	0.117	1.179
3	120	2	2034	13891	0.027	0.156	0.182	0.117	1.247
		2	1756	12500	0.020	0.126	0.146	0.117	1.115
		2	1931	13452	0.024	0.146	0.170	0.117	1.200

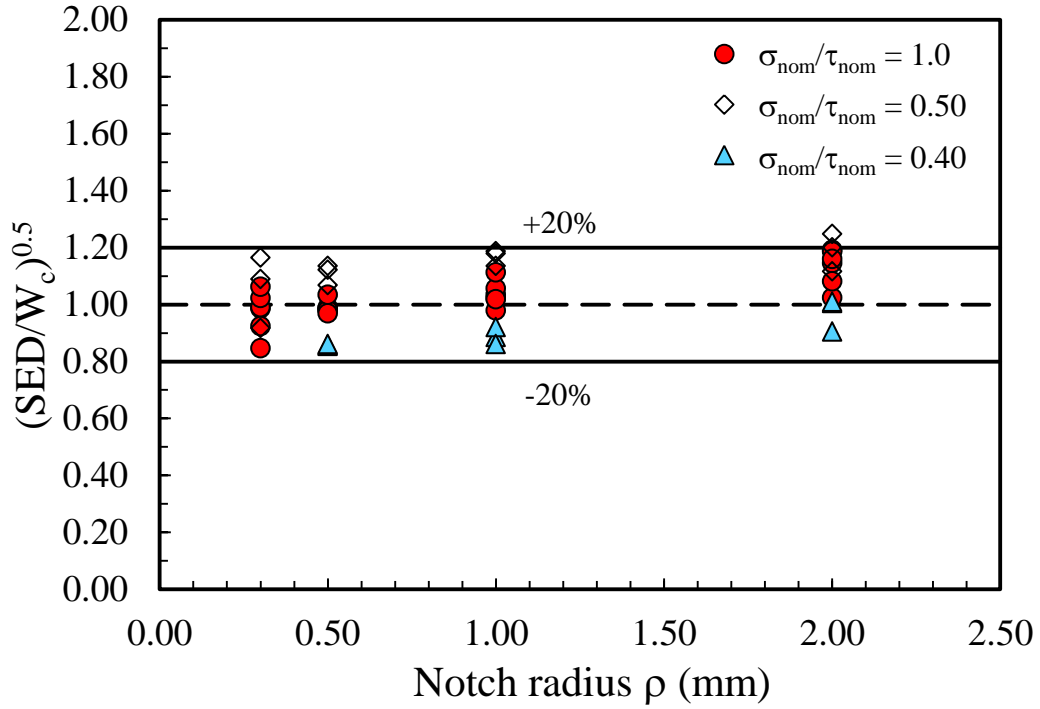


Figure 2.2.9. Synthesis based on SED of the results from combined tension and torsion tests: Method 1.

2.2.4.2 Normalized critical energies: criterion 2

The second proposed approach is a reminiscent of the work by Gough and Pollard [104] who proposed a stress-based expression able to summarize together the results obtained from bending and torsion. The criterion was extended in [105] in terms of the local SED to V-notches under fatigue loading in the presence of combined tension and torsion.

In agreement with [105] and extending the method to the static case, the following elliptic expression:

$$\frac{W_1}{W_{1c}} + \frac{W_3}{W_{3c}} = 1 \quad (2.2.8)$$

is obtained. In Eq. (2.2.8) W_{1c} and W_{3c} are the critical values of SED under pure tension and pure torsion. For the considered graphite, $W_{1c} = 0.05625 \text{ MJ/m}^3$ and $W_{3c} = 0.2074 \text{ MJ/m}^3$. The values of W_1 and W_3 have, instead, to be calculated as a function of the notch geometry and of the applied mode mixity ratio. Each specimen reaches its critical energy when the sum of the weighted contributions

of Mode I and Mode III is equal to 1, which represents the complete damage of the specimen.

The detailed calculations employing this second criterion are reported in Table 2.2.7. The square root of the left-hand side term of Eq. (2.2.8), which is, in fact, proportional to the critical load, is given in the last column of this table.

A synthesis in terms of the square root value of the considered parameter, that is the sum of the weighted energy contributions related to Mode I and Mode III loading, is shown in Figure 2.2.10 as a function of the notch root radius ρ . The obtained trend is very similar to that shown in Figure 2.2.9.

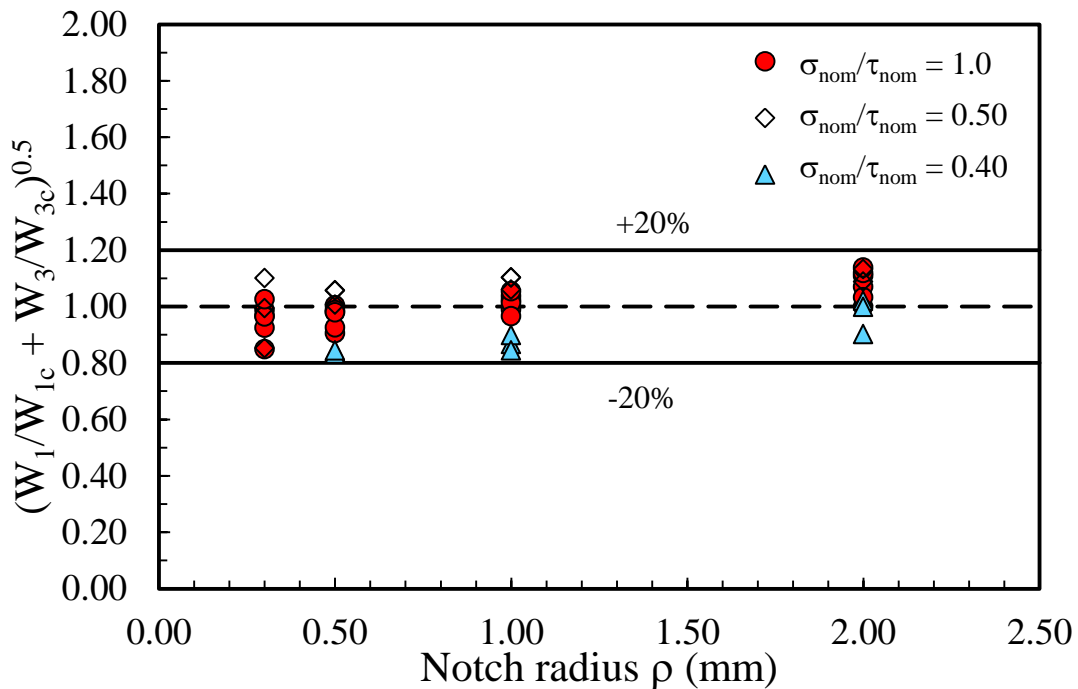


Figure 2.2.10. Synthesis based on SED of the results from combined tension and torsion tests:
Method 2.

Table 2.2.7. Experimental results: overview of the data by using the method 2.

p (mm)	2α (°)	ρ (mm)	Tensile loading (N)	Torque (N mm)	W_1 (MJ/m ³)	W_3 (MJ/m ³)	$W_1/W_{1c}+W_3/W_{3c}$	$(W_1/W_{1c}+W_3/W_{3c})^{0.5}$
5	120	0.3	1193	2659	0.041	0.039	0.935	0.967
		0.3	1025	2280	0.030	0.029	0.690	0.831
		0.3	1114	2500	0.036	0.035	0.818	0.904
5	120	0.5	1190	2690	0.040	0.040	0.919	0.959
		0.5	1234	2631	0.043	0.038	0.965	0.982
		0.5	1200	2694	0.041	0.040	0.932	0.965
5	120	1	1302	2873	0.045	0.044	1.028	1.014
		1	1251	2673	0.042	0.038	0.937	0.968
		1	1283	2845	0.044	0.043	1.001	1.000
5	120	2	1497	3800	0.046	0.072	1.181	1.087
		2	1451	3634	0.043	0.066	1.101	1.049
		2	1532	3710	0.048	0.069	1.203	1.097
5	60	0.3	1073	2632	0.038	0.043	0.899	0.948
		0.3	1037	2867	0.036	0.051	0.894	0.946
		0.3	1125	2883	0.042	0.052	1.010	1.005
5	30	0.5	1097	2852	0.030	0.050	0.789	0.888
		0.5	1157	2700	0.034	0.045	0.824	0.908
		0.5	1213	2917	0.037	0.052	0.921	0.960
5	30	1	1178	3038	0.040	0.052	0.985	0.993
		1	1112	2972	0.036	0.050	0.895	0.946
		1	1214	3248	0.043	0.060	1.068	1.033
5	30	2	1300	3102	0.041	0.047	0.958	0.979
		2	1319	3386	0.042	0.056	1.023	1.012
		2	1486	3489	0.053	0.059	1.241	1.114
5	60	0.5	636	3923	0.011	0.097	0.684	0.827
		0.5	600	4010	0.010	0.101	0.683	0.827
		0.5	630	4009	0.011	0.101	0.701	0.838
5	60	1	645	4449	0.011	0.107	0.739	0.860
		1	660	4634	0.012	0.116	0.794	0.891
		1	631	4326	0.011	0.101	0.701	0.838
5	60	2	895	5164	0.020	0.132	1.020	1.010
		2	811	5259	0.017	0.137	0.981	0.990
		2	750	4700	0.014	0.110	0.800	0.894
3	120	0.3	1482	11606	0.021	0.118	0.967	0.983
		0.3	1324	9657	0.017	0.082	0.709	0.842
		0.3	1768	12129	0.030	0.129	1.181	1.087
3	120	0.5	1701	11768	0.027	0.120	1.090	1.044
		0.5	1619	11196	0.025	0.109	0.987	0.993
		0.5	1657	12005	0.026	0.125	1.089	1.044
3	120	1	1739	12150	0.027	0.124	1.097	1.047
		1	1788	12756	0.028	0.137	1.188	1.090
		1	1816	12611	0.029	0.134	1.187	1.091
3	120	2	2034	13891	0.027	0.156	1.254	1.120
		2	1756	12500	0.020	0.126	0.985	0.992
		2	1931	13452	0.024	0.146	1.159	1.076

Many of the results are inside a scatterband ranging from 0.9 to 1.1 with only few exceptions. This second criterion is surely more advantageous with respect to the first one because for its application only the critical values W_{1c} and W_{3c} for the simpler cases of pure tension and pure torsion from plain specimens are required. The first criterion requires, instead, the knowledge of the total critical energy from unnotched specimens as a function of the mode mixity ratio.

The fracture models proposed here can be used for predicting the onset of brittle fracture in notched graphite components which are subjected to a combination of tension and torsion loading. Such criteria would be very useful for designers and engineers who should explore the safe performance of graphite components particularly under complex loading conditions.

2.2.5. Discussion

Brittle fracture in V-notched polycrystalline graphite specimens was investigated both experimentally and theoretically under combined tension and torsion loading. Fracture tests were conducted on notched round bar graphite specimens. Different notch depths, notch radii and opening angles were considered in the test specimens as well as different combinations of the mode mixity ratio σ_{nom}/τ_{nom} .

The new set of data provided here is unique because no previous papers have been devoted to similar topics dealing with graphite components.

The SED criterion was used for the first time in order to estimate the fracture load of notched graphite components under mixed mode I/III static loading. Two different approaches of the SED criterion were proposed showing the capabilities of the suggested methods to assess the fracture behaviour of polycrystalline graphite under the considered loading conditions.

The results estimated by the SED approach were found to be in good agreement with the experimental results. The second criterion based on the elliptic expression described above seems to be very advantageous because it requires, as experimental parameters, only the critical energies from unnotched graphite specimens under pure tension and pure torsion.

2.3. Brittle fracture of PMMA cracked components under mixed mode I+III loading ^(*)

Nomenclature

a	crack length
E	Young's modulus
G	Shear modulus
K_{Ic}	Mode I fracture toughness
K_{If}	Mode I critical stress intensity factor measured experimentally
K_{IIIc}	Mode III fracture toughness
K_{IIIf}	Mode III critical stress intensity factor measured experimentally
M	mode mixity ratio
P_c	fracture load
R_{1c}	control radius under tensile loading
R_{3c}	control radius under torsion loading
\bar{W}	SED averaged over the control volumes
W_{Ic}	critical SED value of the considered material under tensile loading
W_{IIIc}	critical SED value of the considered material under torsion loading

Symbols

α	loading angle
ν	Poisson's ratio
σ_t	ultimate tensile strength
τ_t	ultimate torsion strength

(*) See also:

Berto, F.; Ayatollahi, M.; Campagnolo, A. Fracture tests under mixed mode I/III loading: an assessment based on the local energy. *International Journal of Damage Mechanics* (Accepted);

2.3.1. Introduction

A large bulk of work has been dedicated to study brittle and ductile fracture under mixed mode loading both experimentally and theoretically. Numerous test specimens have been used by researchers for mixed mode I/II fracture experiments[85,106–111]. More recently other researchers have explored the same problem using different approaches[13,34,112–116].

However, there are relatively fewer results presented for experimental study of mixed mode I/III fracture[49,117–127]. By using different test configurations some results have been obtained in the past. In particular, the compact tension (CT) specimen with an angled crack[117–119], the three-point bend specimen with inclined crack through the thickness[120], the plate with an angled crack under a uniform far field tension[121], the three-point bend specimen with asymmetrically oriented crack[122], the circumferentially notched round bar[123], the loading fixture developed for thin sheets[124], the single edge cracked specimen[125,126] and the traditional CT specimen[127] subjected to combined tension-torsion are some of the specimens employed in the past for mixed mode I/III fracture tests on different engineering materials like metals, polymers and ceramics. Dealing with the specific case of blunt notches the only experimental results for PMMA samples under mixed mode (I + III) loading are provided in a work by Susmel and Taylor[49]. V-notched bars with a constant value of the opening angle ($2\alpha = 60^\circ$) and a root radius ranging from 0.2 to 1.2 mm have been considered. Some results from semicircular notches with a larger notch root radius (4.0 mm) have been also provided in that contribution.

In a recent paper[80], a new useful loading fixture was suggested for mixed mode I/III fracture experiments and a new set of data from mixed mode fracture tests conducted on PMMA was also provided. The mode mixity ratio ranged from pure mode I to pure mode III loading.

A fracture model based on the strain energy density (SED) averaged over a control volume is used for the first time for the fracture assessment of cracked samples made of PMMA subjected to the multiaxial static loading case of tension and torsion applied in combination. In previous studies the criterion has been applied to pure modes of loading and in particular to mode III[38,44,128,129] but

never extended to combined mode I+III loading conditions. The present work is aimed to partially fill this lack. The SED based approach is extended here to multiaxial static loading and this allows a sound fracture assessment of the critical load for the specific material under investigation. The criterion can be potentially extended to other types of materials subjected to different combinations of mode I and mode III loading conditions.

The paragraph is divided into two parts: in the first one the experimental activity is briefly re-called (sample geometry, test setting, details of experimental data). While the second part deals with the re-formulation and application of the averaged strain energy density criterion to the specific case of mode I and mode III loading applied in combination.

2.3.2. Mixed mode fracture experiments

The experimental activity performed in a recent contribution[80] is briefly recalled in this section.

2.3.2.1. Loading fixture and test configuration

The geometry of the loading fixture first proposed in a work by Ayatollahi and Saboori[80] and its test specimen used for mixed mode I/III fracture tests are shown schematically in Figs. 2.3.1 and 2.3.2. The test specimen is a plate of rectangular shape with an edge crack of length a . The loading fixture consists of two identical segments. There are five loading holes in each half of the loading fixture as shown in Fig. 2.3.1. The loading angle can be changed with respect to the crack plane by choosing proper holes on the loading fixture. The positions of loading holes on each half of the fixture are determined in a way to achieve an appropriate distribution of mixed modes between pure mode I and pure mode III. Depending on the loading angle α (see Fig. 2.3.1), pure mode I (0°), pure mode III (90°) and three intermediate mixed mode loading can be provided. The geometry and dimensions of the test specimen, shown in Fig. 2.3.2, are adopted according to the recommendations of the ASTM-E399-90 standard[130]. As presented in Fig.

2.3.1, the test specimen is fixed to the loading fixture through two devised holes (shown in Fig. 2.3.2) by bolt and nut.

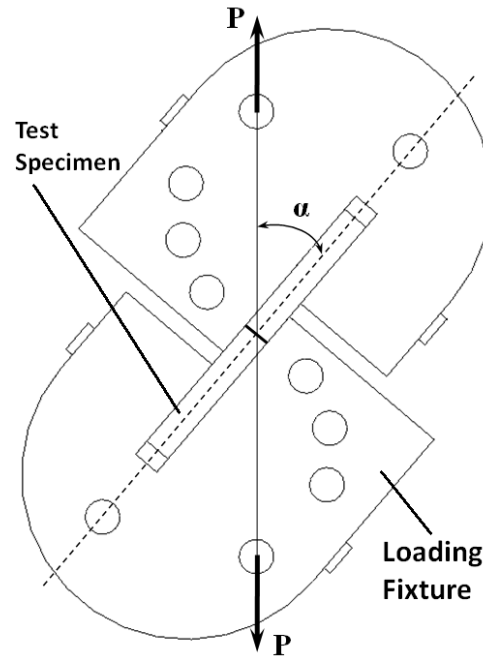


Figure 2.3.1. Test specimen and loading fixture for mixed mode I/III fracture experiments.

A review of the test specimens and loading fixtures suggested in the past for conducting mixed mode I/III fracture experiments shows that some of them can be utilized only for pure mode I fracture tests and some limited mixed mode I/III ones. The compact tension (CT) test specimen with an angled crack, the three-point bend specimen with inclined crack through the thickness, the angled cracked plate under tension and the three-point bend specimen with asymmetrically oriented crack can provide only limited combinations of the fracture modes I and III while mode I is predominant. In particular, they cannot be used for pure mode III tests. Moreover, to conduct the fracture test in each specific fracture mode by some of the mentioned specimens, an angled crack with a different orientation should be created. However, in the test configuration proposed by Ayatollahi and Saboori[80] the crack doesn't need to be slanted. Another advantage of the fixture suggested[80] is that it can exert the required load to the test specimen just by using the conventional uniaxial tension machines. Because of the advantages

elaborated above, the proposed loading fixture and its associated test specimen can be recommended as a favorite test set-up for conducting mixed mode I/III fracture experiments on various engineering materials.

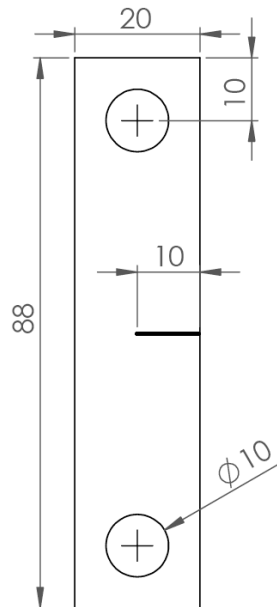


Figure 2.3.2. The test specimen containing an edge crack (dimensions in mm, thickness: 8mm).

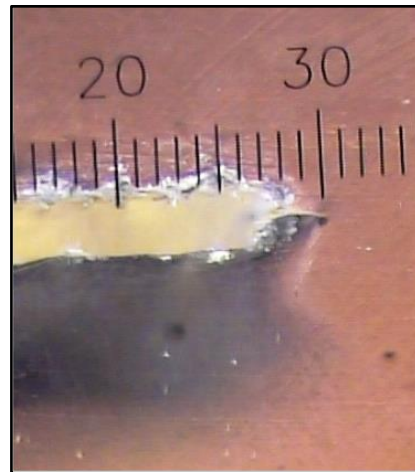
2.3.2.2. Mixed mode fracture experiments

A series of fracture tests on polymethyl-metacrylate (PMMA) were conducted by Ayatollahi and Saboori[80] to investigate and evaluate the applicability and efficiency of the proposed loading fixture for mixed mode I/III fracture experiments. As a transparent thermoplastic polymer, PMMA is relatively homogeneous and isotropic at room temperature and ambient pressure, and deforms with a linear elastic behavior[85]. According to ASTM-E399 standard[130], it is recommended replicating each fracture test at least three times. Consequently, a total number of 15 test specimens were manufactured with the specifications given in Fig. 2.3.2, from a PMMA sheet of 8 mm thickness for the five considered loading modes. A laser cutting machine was utilized to cut the specimens from the PMMA sheet, to prepare the two connection holes and to generate a notch in the middle of specimen (with the initial depth slightly less than 10 mm). Based on the measurement by an optical microscope, the width of

created notches didn't exceed 0.4 mm in all the specimens. Then, a sharp pre-crack was introduced by pressing a razor blade carefully to the notch tip. The depth of this pre-crack was also measured by the microscope for determining the total crack length of each specimen (given in Table 2.3.1). Fig. 2.3.3a illustrates a sample PMMA specimen prepared for the test while Fig. 2.3.3b shows a sharpened notch tip magnified under the microscope.



(a)



(b)

Figure 2.3.3. The PMMA test specimen with a single edge crack (a). A sample sharpened notch tip under an optical microscope (scale: 0.1 mm) (b).

Table 2.3.1. Summary of mixed mode I/III fracture tests conducted on PMMA specimens.

K_{Iff} (MPa·m ^{0.5})	K_{IIIff} (MPa·m ^{0.5})	P_c (N)	a (mm)	Loading Mode
1.673	0.0007	451.3	10.4	$\alpha = 0$ (Mode I)
1.713	0.0007	502.8	10.0	$\alpha = 0$ (Mode I)
1.777	0.0007	505.2	10.2	$\alpha = 0$ (Mode I)
1.816	0.397	488.0	10.2	$\alpha = 40$
1.785	0.393	480.4	10.2	$\alpha = 40$
1.570	0.366	443.9	10.0	$\alpha = 40$
1.838	1.066	597.1	10.1	$\alpha = 65$
1.817	1.060	577.5	10.3	$\alpha = 65$
1.700	1.020	571.6	10.0	$\alpha = 65$
0.882	1.617	656.1	10.3	$\alpha = 78$
0.879	1.615	661.1	10.2	$\alpha = 78$
0.924	1.662	693.7	10.0	$\alpha = 78$
0.013	1.893	741.9	10.0	$\alpha = 90$ (Mode III)
0.012	1.766	686.7	10.1	$\alpha = 90$ (Mode III)
0.014	1.993	781.1	10.0	$\alpha = 90$ (Mode III)

**Figure 2.3.4.** The test configuration used for fracture tests on PMMA.

The test specimens were loaded at a constant rate of 0.4 mm/min up to its final fracture. The experiments were conducted by means of a screw-driven tensile test machine having a capacity of 150 kN (Figure 2.3.4). The load and displacement data were recorded during the tests. All the tested PMMA specimens fractured suddenly from the crack tip and with negligible non-linear deformation showing a

brittle fracture behavior (see the example in Figure 2.3.5). Figure 2.3.5 reports a typical load–displacement curve obtained for a PMMA specimen fractured under pure mode III loading.

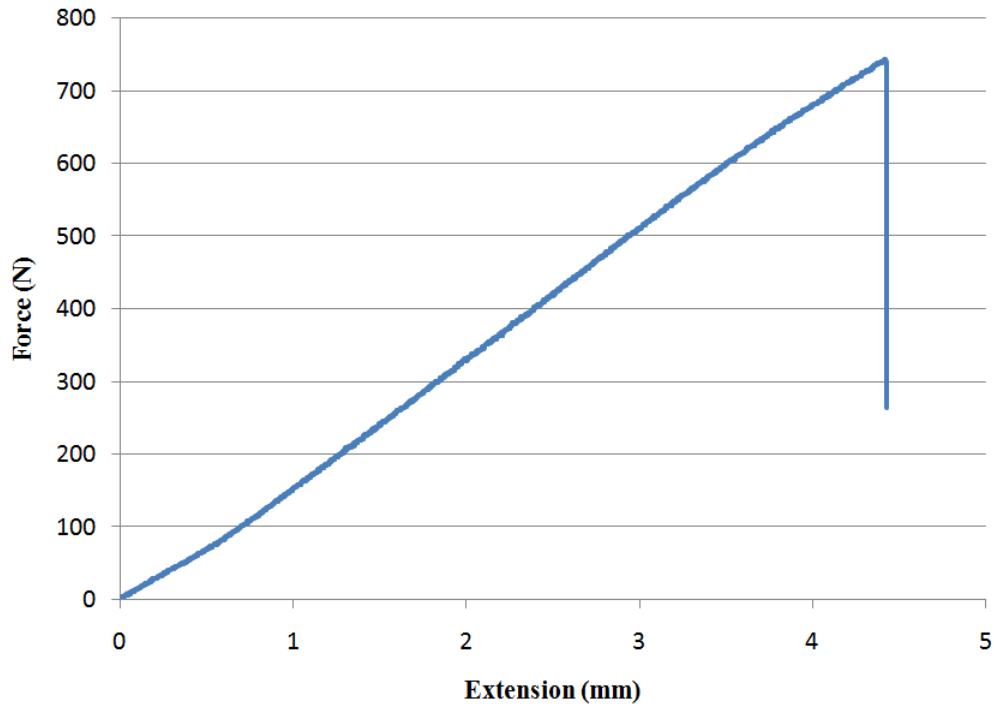


Figure 2.3.5. A sample load–displacement curve obtained for a PMMA sample fractured under pure mode III loading.

The fracture load obtained from each specimen was used to calculate its critical stress intensity factors. Since there are no analytical equations to calculate K_{If} and $K_{III f}$ of the tested samples, the fracture parameters were obtained from a series of finite element (FE) analyses. In the FE analyses, the elastic material properties of PMMA were considered as $E = 2.95$ GPa and $\nu = 0.34$. The details of test results including the fracture loads and the critical stress intensity factors are listed in Table 2.3.1. The fracture patterns of all the specimens fractured under different mixed mode I/III loading conditions can be observed in Fig. 2.3.6.

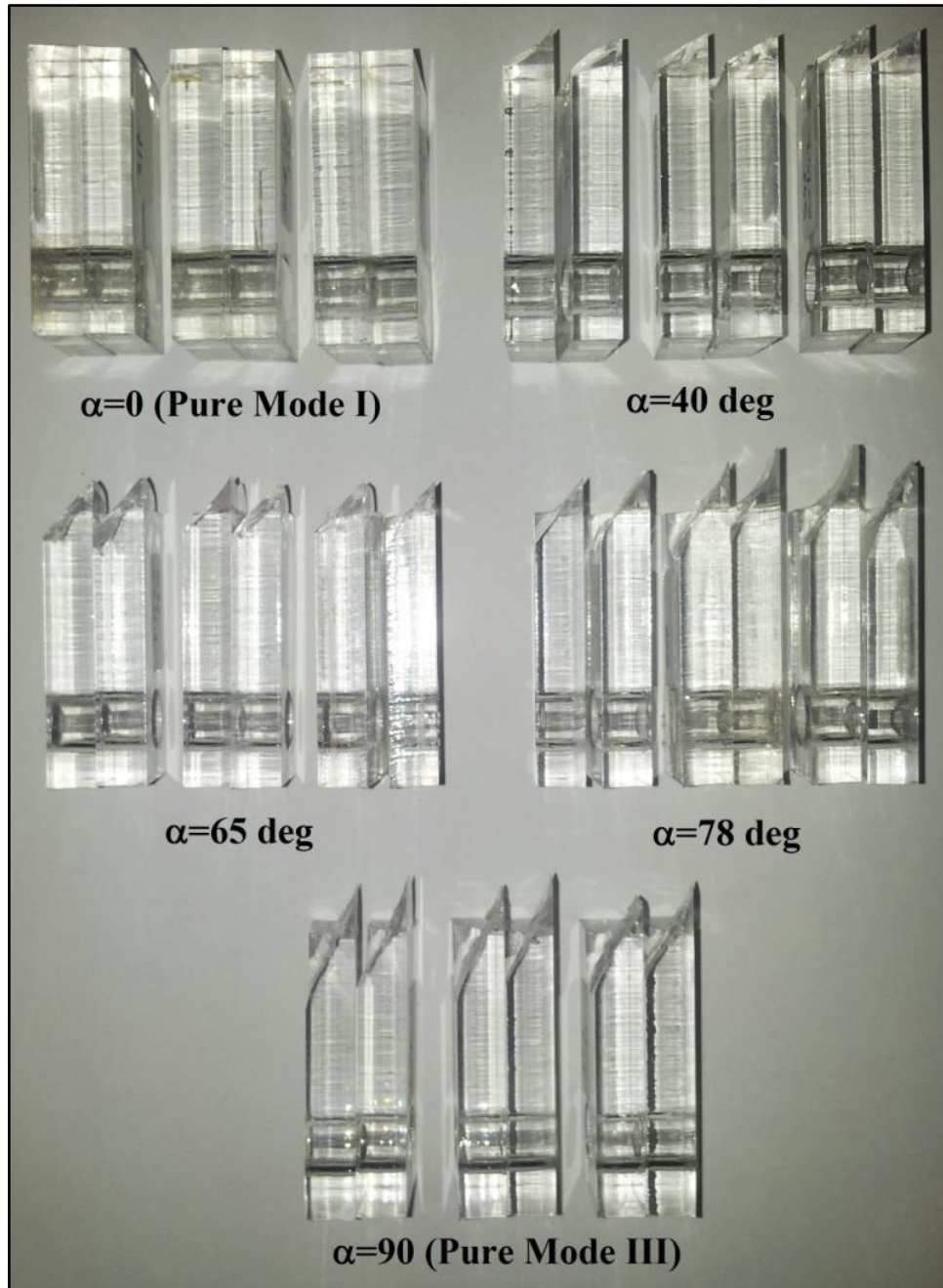


Figure 2.3.6. PMMA specimens fractured under different combinations of mode I and mode III loading.

The average value of mode I fracture toughness (K_{Ic}) obtained from the specimens tested at $\alpha = 0^\circ$ is $1.72 \text{ MPa}\cdot\text{m}^{0.5}$. This magnitude is in the range of $1 \div 2 \text{ MPa}\cdot\text{m}^{0.5}$ reported in previous papers for fracture toughness of PMMA[34,85,110,112]. The average value of mode III fracture toughness (K_{IIIc}) obtained from pure mode III tests is $1.88 \text{ MPa}\cdot\text{m}^{0.5}$ which is about 10% higher

than K_{Ic} . The ultimate tensile strength of the material, σ_t is equal to 70 MPa while under torsion the critical value of the shear stress, τ_t is equal to 43 MPa.

The tested specimens can be classified in terms of a mixity parameter M defined as:

$$M = \frac{2}{\pi} \arctan\left(\frac{K_{III}}{K_I}\right) \quad (2.3.1)$$

Based on the above definition, M varies between 0 (for pure mode I loading) and 1 (for pure mode III loading).

2.3.3. Strain Energy Density averaged over a control volume: the fracture criterion

With the aim to assess the fracture load in notched or cracked components, an appropriate fracture criterion is required which has to be based on the mechanical behaviour of material around the notch/crack tip. In this section, a criterion proposed by Lazzarin and co-authors[31] based on the averaged strain energy density (SED) is briefly described.

Dealing with cracked components, the strain energy density factor S was defined first by Sih in a pioneering contribution[43] as the product of the strain energy density by a critical distance from the point of singularity. Failure was suggested to be controlled by a critical value of S , whereas the direction of crack propagation was determined by imposing a minimum condition on S .

Different from Sih's criterion, which is a point-wise approach, the averaged strain energy density criterion[31] (SED) states that brittle failure occurs when the mean value of the strain energy density over a given control volume is equal to a critical value W_c . This critical value varies from material to material but it does not depend on the notch geometry and sharpness.

The method based on the averaged SED was formalised and applied first to sharp (zero radius) V-notches under mode I and mixed mode I+II loading[31] and later extended to blunt U- and V-notches[32,33,87,131].

When dealing with cracks, the control volume is a circle of radius R_c centred at

the crack tip (Fig. 2.3.7a). Under plane strain conditions, the radius R_c can be evaluated according to the following expression:

$$R_{Ic} = \frac{(1+\nu)(5-8\nu)}{4\pi} \left(\frac{K_{Ic}}{\sigma_t} \right)^2 \quad (2.3.2)$$

where K_{Ic} is the mode I fracture toughness, ν the Poisson's ratio and σ_t the ultimate tensile stress of a plain specimen.

For a sharp V-notch, the critical volume becomes a circular sector of radius R_c centred at the notch tip (Fig. 2.3.7b). When only failure data from open V-notches are available, R_c can be determined on the basis of some relationships reported in previous contributions[32,33,88], where K_{Ic} is substituted by the critical value of the notch stress intensity factors (NSIFs) as determined at failure from sharp V-notches.

Dealing here with cracks under torsion loading, the control radius R_{3c} can be estimated by means of the following equation[38,128,129]:

$$R_{3c} = \frac{e_3}{1+\nu} \cdot \left(\frac{K_{IIIc}}{\tau_t} \right)^2 \quad (2.3.3)$$

where K_{IIIc} is the mode III fracture toughness and τ_t is the ultimate torsion strength of the unnotched material. Moreover, e_3 is the parameter that quantifies the influence of all stresses and strains over the control volume. The value of e_3 is 0.4138 for the case of a sharp crack ($2\alpha = 0^\circ$).

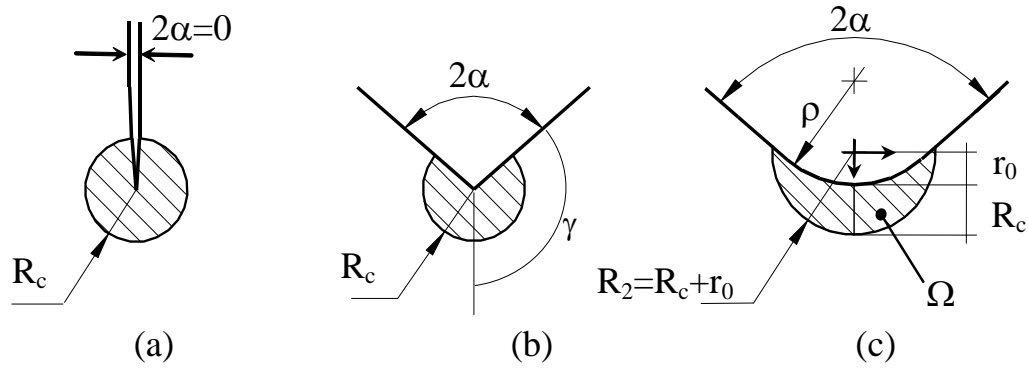


Figure 2.3.7. Control volume for (a) crack, (b) sharp V-notch and (c) blunt V-notch, under mixed mode I/III loading. Distance $r_0 = \rho \times (\pi - 2\alpha) / (2\pi - 2\alpha)$.

2.3.4. SED approach in fracture analysis of the tested specimens

The fracture criterion described in the previous section is employed here to estimate the fracture loads obtained from the experiments conducted on the PMMA specimens. As originally thought for pure modes of loading, the averaged strain energy density criterion (SED) states that failure occurs when the mean value of the strain energy density over a control volume, \bar{W} , reaches a critical value W_c , which depends on the material but not on the notch geometry.

Under tension loads, this critical value can be determined from the ultimate tensile strength σ_t according to Beltrami's expression for the unnotched material:

$$W_{lc} = \frac{\sigma_t^2}{2E} \quad (2.3.4)$$

By using the values of $\sigma_t = 70$ MPa and $E = 2950$ MPa, the critical SED under mode I for the tested PMMA is $W_{lc} = 0.8305$ MJ/m³.

Under torsion loads, this critical value can be determined from the ultimate shear strength τ_t according to Beltrami's expression for the unnotched material:

$$W_{llc} = \frac{\tau_t^2}{2G} \quad (2.3.5)$$

By using the values of $\tau_t = 43$ MPa and $G = 1100$ MPa, the critical SED under mode III for the tested PMMA is $W_{IIIc} = 0.8481 \text{ MJ/m}^3$.

In parallel, the control volume definition *via* the control radius R_c needs the knowledge of the mode I and mode III fracture toughness K_{Ic} and K_{IIIc} and the Poisson's ratio ν , see Eqs. (2.3.2) and (2.3.3). The resulting values are $K_{Ic} = 1.72$ MPa $\text{m}^{0.5}$ and $K_{IIIc} = 1.88$ MPa $\text{m}^{0.5}$ which provide the control radii $R_{Ic} = 0.147$ mm and $R_{3c} = 0.590$ mm, under pure tension and pure torsion, respectively. The SED criterion has been applied here to mixed mode I/III loading conditions.

The proposed approach is a reminiscent of the work by Gough and Pollard[104] who proposed a stress-based expression able to summarize together the results obtained from bending and torsion loading. The criterion was extended by Lazzarin et al. [105] in terms of the local SED to V-notches under fatigue loading in the presence of combined tension and torsion.

In agreement with Lazzarin et al. [105] and extending the method to the static case, the following elliptic expression is obtained:

$$\frac{W_I}{W_{Ic}} + \frac{W_{III}}{W_{IIIc}} = 1 \quad (2.3.6)$$

In Eq. (2.3.6), W_{Ic} and W_{IIIc} are the critical values of SED under pure tension and pure torsion. For the considered PMMA, $W_{Ic} = 0.8305 \text{ MJ/m}^3$ and $W_{IIIc} = 0.8481 \text{ MJ/m}^3$. The values of W_I and W_{III} have, instead, to be calculated as a function of the applied load and of the mode mixity ratio M . Each specimen reaches its critical energy when the sum of the weighted contributions of mode I and mode III is equal to 1, which represents the complete damage of the specimen.

W_I and W_{III} can be expressed as functions of the stress intensity factors of mode I and mode III accordingly to the following expressions:

$$W_I = \frac{e_1}{R_{Ic}} \frac{K_I^2}{E} \quad (2.3.7)$$

$$W_{III} = \frac{e_3}{R_{3c}} \frac{K_{III}^2}{E} \quad (2.3.8)$$

Functions e_1 and e_3 are 0.119 and 0.414, respectively, for $2\alpha = 0^\circ$ and $\nu = 0.34$.

The detailed calculations employing this criterion are reported in Table 2.3.2.

A synthesis in terms of the square root value of the considered parameter, that is the sum of the weighted energy contributions related to mode I and mode III loading, is shown in Figure 2.3.8 as a function of the mode mixity ratio M .

Many of the results are inside a scatterband ranging from 0.9 to 1.1 with only few exceptions. This criterion is surely advantageous because for its application, only the critical values W_{Ic} and W_{IIIc} for the simplest cases of pure tension and pure torsion from plain specimens are required.

The fracture model proposed here can be used for predicting the onset of brittle fracture in notched and cracked components which are subjected to a combination of tension and torsion loadings. Such criterion would be very useful for designers and engineers who should explore the safe performance of cracked and notched components particularly under complex loading conditions.

Table 2.3.2. Overview of the main results applying the SED criterion

M	K_I (MPa·m ^{0.5})	K_{III} (MPa·m ^{0.5})	W_I (MJ/m ³)	W_{III} (MJ/m ³)	$W_I/W_{Ic} + W_{III}/W_{IIIc}$	$(W_I/W_{Ic} + W_{III}/W_{IIIc})^{0.5}$
0.0003	1.673	0.001	0.766	0.000	0.923	0.961
0.0003	1.713	0.001	0.803	0.000	0.967	0.984
0.0003	1.777	0.001	0.864	0.000	1.041	1.020
0.1371	1.816	0.397	0.903	0.038	1.132	1.064
0.1380	1.785	0.393	0.872	0.037	1.094	1.046
0.1459	1.570	0.366	0.675	0.032	0.850	0.922
0.3348	1.838	1.066	0.925	0.273	1.435	1.198
0.3364	1.817	1.060	0.904	0.270	1.406	1.186
0.3442	1.700	1.020	0.791	0.250	1.247	1.117
0.6825	0.882	1.617	0.213	0.627	0.996	0.998
0.6830	0.879	1.615	0.212	0.626	0.993	0.996
0.6773	0.924	1.662	0.234	0.663	1.063	1.031
0.9961	0.013	1.893	0.000	0.860	1.014	1.007
0.9962	0.012	1.766	0.000	0.748	0.882	0.939
0.9960	0.014	1.993	0.000	0.953	1.124	1.060

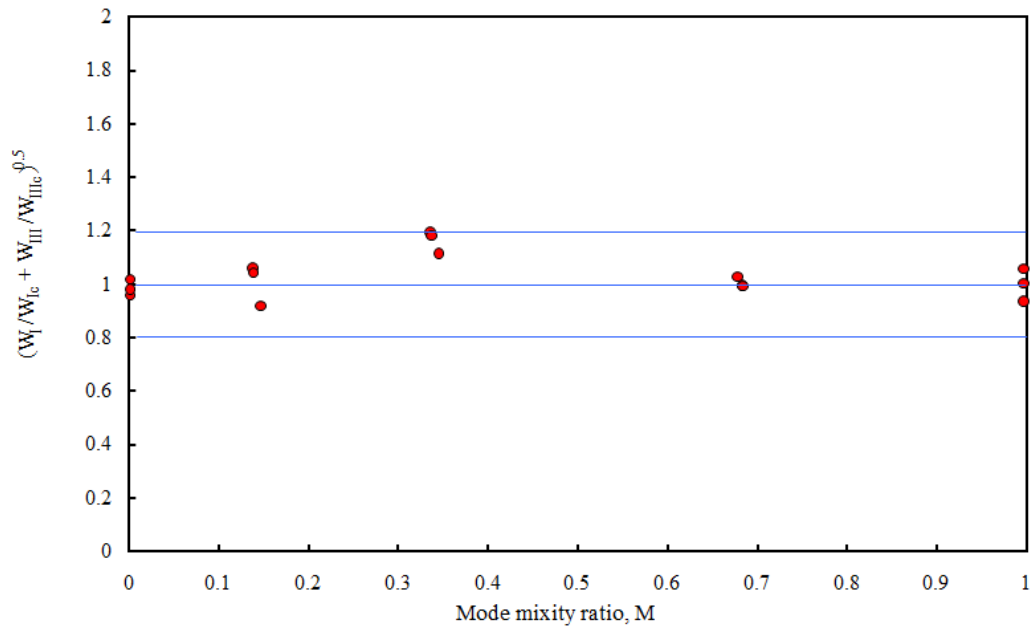


Fig. 2.3.8. Synthesis of the data obtained for PMMA by means of the SED approach.

2.3.5. Discussion

Brittle fracture in cracked PMMA specimens was investigated both experimentally and theoretically under combined tension and torsion loadings. A recent series of mixed mode I/III fracture tests carried out by means of pre-cracked specimens made of PMMA was re-analysed here. A loading fixture was employed for mixed mode I/III fracture studies. Fracture loads and out-of-plane fracture angles were briefly described. The set of data is unique because only few previous papers have been devoted to similar topics dealing with PMMA components. By taking advantage of this complete set of data ranging from pure mode I to pure mode III it has been possible to propose and validate a criterion for the specific case of tension and torsion loadings applied in combination.

The SED criterion has been used here for the first time in order to estimate the fracture load of cracked PMMA components under mixed mode I/III static loading. The criterion is based on an elliptic expression that is reminiscent of Gough and Pollard criterion for multiaxial fatigue loading. The capabilities to assess the fracture behaviour of PMMA cracked components under the considered loading conditions have been investigated. The results estimated by the SED

approach have been found to be in good agreement with the experimental results. The proposed fracture criterion seems to be very advantageous because it requires, as experimental parameters, only the critical energies from unnotched PMMA specimens under pure tension and pure torsion.

References

- [1] Gómez FJ, Elices M. A fracture criterion for sharp V-notched samples. *Int J Fract* 2003;123:163–75.
- [2] Gomez FJ, Elices M, Valiente A. Cracking in PMMA containing U-shaped notches. *Fatigue Fract Eng Mater Struct* 2000;23:795–803.
- [3] Gómez FJJ, Elices M. A fracture criterion for blunted V-notched samples. *Int J Fract* 2004;127:239–64.
- [4] Planas J, Elices M, Guinea G., Gómez F., Cendón D., Arbilla I. Generalizations and specializations of cohesive crack models. *Eng Fract Mech* 2003;70:1759–76.
- [5] Ayatollahi MR, Torabi AR. Brittle fracture in rounded-tip V-shaped notches. *Mater Des* 2010;31:60–7.
- [6] Ayatollahi MRR, Torabi ARR. Tensile fracture in notched polycrystalline graphite specimens. *Carbon N Y* 2010;48:2255–65.
- [7] Torabi AR. Fracture Assessment of U-Notched Graphite Plates Under Tension. *Int J Fract* 2013;181:285–92.
- [8] Torabi AR, Fakoor M, Pirhadi E. Tensile fracture in coarse-grained polycrystalline graphite weakened by a U-shaped notch. *Eng Fract Mech* 2013;111:77–85.
- [9] Torabi AR. Estimation of tensile load-bearing capacity of ductile metallic materials weakened by a V-notch: The equivalent material concept. *Mater Sci Eng A* 2012;536:249–55.
- [10] Torabi AR. On the use of the Equivalent Material Concept to predict tensile load-bearing capacity of ductile steel bolts containing V-shaped threads. *Eng Fract Mech* 2013;97:136–47.
- [11] Torabi AR. Ultimate Bending Strength Evaluation of U-Notched Ductile Steel Samples Under Large-Scale Yielding Conditions. *Int J Fract* 2013;180:261–8.
- [12] Ayatollahi MR, Torabi AR. Determination of mode II fracture toughness for U-shaped notches using Brazilian disc specimen. *Int J Solids Struct* 2010;47:454–65.
- [13] Torabi A, Fakoor M, Darbani M. Pure shear fracture study in a brittle graphite material containing a U-notch. *Int J Damage Mech* 2013;23:839–54.
- [14] Ayatollahi MR, Torabi AR. A criterion for brittle fracture in U-notched components under mixed mode loading. *Eng Fract Mech* 2009;76:1883–96.
- [15] Ayatollahi MR, Torabi AR. Investigation of mixed mode brittle fracture in rounded-tip V-notched components. *Eng Fract Mech* 2010;77:3087–104.
- [16] Ayatollahi MRR, Torabi ARR. Failure assessment of notched polycrystalline graphite under tensile-shear loading. *Mater Sci Eng A* 2011;528:5685–95.

- [17] Ayatollahi MR, Torabi AR. Experimental verification of RV-MTS model for fracture in soda-lime glass weakened by a V-notch. *J Mech Sci Technol* 2011;25:2529–34.
- [18] Ayatollahi MR, Torabi ARR, Azizi P. Experimental and Theoretical Assessment of Brittle Fracture in Engineering Components Containing a Sharp V-Notch. *Exp Mech* 2010;51:919–32.
- [19] Torabi AR. Sudden Fracture from U-Notches in Fine-Grained Isostatic Graphite Under Mixed Mode I/II Loading. *Int J Fract* 2013;181:309–16.
- [20] Torabi AR, Fakoor M, Pirhadi E. Fracture analysis of U-notched disc-type graphite specimens under mixed mode loading. *Int J Solids Struct* 2014;51:1287–98.
- [21] Livieri P. A new path independent integral applied to notched components under mode I loadings. *Int J Fract* 2003;123:107–25.
- [22] Matvienko YUG, Morozov EM. Calculation of the energy J -integral for bodies with notches and. *Int J Fract* 2004;125:249–61.
- [23] Berto F, Lazzarin P. Relationships between J-integral and the strain energy evaluated in a finite volume surrounding the tip of sharp and blunt V-notches. *Int J Solids Struct* 2007;44:4621–45.
- [24] Livieri P. Use of J-integral to predict static failures in sharp V-notches and rounded U-notches. *Eng Fract Mech* 2008;75:1779–93.
- [25] Barati E, Alizadeh Y, Aghazadeh J, Berto F. Some new practical equations for rapid calculation of J-integral in plates weakened by U-notches under bending. *Mater Des* 2010;31:2964–71.
- [26] Barati E, Alizadeh Y. A numerical method for evaluation of J-integral in plates made of functionally graded materials with sharp and blunt V-notches. *Fatigue Fract Eng Mater Struct* 2011;34:1041–52.
- [27] Becker TH, Mostafavi M, Tait RB, Marrow TJ. An approach to calculate the J-integral by digital image correlation displacement field measurement. *Fatigue Fract Eng Mater Struct* 2012;35:971–84.
- [28] Carpinteri A, Cornetti P, Pugno N, Sapora A, Taylor D. A finite fracture mechanics approach to structures with sharp V-notches. *Eng Fract Mech* 2008;75:1736–52.
- [29] Sapora A, Cornetti P, Carpinteri A. A Finite Fracture Mechanics approach to V-notched elements subjected to mixed-mode loading. *Eng Fract Mech* 2013;97:216–26.
- [30] Susmel L, Taylor D. The Theory of Critical Distances to estimate lifetime of notched components subjected to variable amplitude uniaxial fatigue loading. *Int J Fatigue* 2011;33:900–11.
- [31] Lazzarin P, Zambardi R. A finite-volume-energy based approach to predict the static and fatigue behavior of components with sharp V-shaped notches. *Int J Fract* 2001;112:275–98.
- [32] Lazzarin P, Berto F. Some expressions for the strain energy in a finite

-
- volume surrounding the root of blunt V-notches. *Int J Fract* 2005;135:161–85.
- [33] Berto F, Lazzarin P. A review of the volume-based strain energy density approach applied to V-notches and welded structures. *Theor Appl Fract Mech* 2009;52:183–94.
- [34] Lazzarin P, Berto F, Elices M, Gómez J. Brittle failures from U- and V-notches in mode I and mixed, I + II, mode: a synthesis based on the strain energy density averaged on finite-size volumes. *Fatigue Fract Eng Mater Struct* 2009;32:671–84.
- [35] Ayatollahi MRR, Berto F, Lazzarin P. Mixed mode brittle fracture of sharp and blunt V-notches in polycrystalline graphite. *Carbon N Y* 2011;49:2465–74.
- [36] Berto F, Lazzarin P, Marangon C. Brittle fracture of U-notched graphite plates under mixed mode loading. *Mater Des* 2012;41:421–32.
- [37] Berto F, Ayatollahi MRR. Fracture assessment of Brazilian disc specimens weakened by blunt V-notches under mixed mode loading by means of local energy. *Mater Des* 2011;32:2858–69.
- [38] Berto F, Lazzarin P, Ayatollahi MR. Brittle fracture of sharp and blunt V-notches in isostatic graphite under torsion loading. *Carbon N Y* 2012;50:1942–52.
- [39] Berto F, Lazzarin P, Ayatollahi MRR. Brittle fracture of sharp and blunt V-notches in isostatic graphite under pure compression loading. *Carbon N Y* 2013;63:101–16.
- [40] Berto F, Campagnolo A, Elices M, Lazzarin P. A synthesis of Polymethylmethacrylate data from U-notched specimens and V-notches with end holes by means of local energy. *Mater Des* 2013;49:826–33.
- [41] Lazzarin P, Campagnolo A, Berto F. A comparison among some recent energy- and stress-based criteria for the fracture assessment of sharp V-notched components under Mode I loading. *Theor Appl Fract Mech* 2014;71:21–30.
- [42] Torabi AR, Campagnolo A, Berto F. Mode II Brittle Fracture Assessment of Key-Hole Notches by Means of the Local Energy. *J Test Eval* 2016;44.
- [43] Sih GC. Strain-energy-density factor applied to mixed mode crack problems. *Int J Fract* 1974;10:305–21.
- [44] Berto F, Lazzarin P. Recent developments in brittle and quasi-brittle failure assessment of engineering materials by means of local approaches. *Mater Sci Eng R Reports* 2014;75:1–48.
- [45] Torabi AR, Berto F. Notch Fracture Toughness Evaluation for a Brittle Graphite Material. *Mater Perform Charact* 2014:MPC20130041.
- [46] Torabi AR, Berto F. Strain energy density to assess mode II fracture in U-notched disk-type graphite plates. *Int J Damage Mech* 2013.
- [47] Torabi AR, Berto F. Mixed mode fracture assessment of U-notched
-

- graphite Brazilian disk specimens by means of the local energy. *Struct Eng Mech* 2014;50:723–40.
- [48] Torabi AR, Berto F. Fracture Assessment of Blunt V-Notched Graphite Specimens by Means of the Strain Energy Density. *Strength Mater* 2013;45:635–47.
- [49] Susmel L, Taylor D. The theory of critical distances to predict static strength of notched brittle components subjected to mixed-mode loading. *Eng Fract Mech* 2008;75:534–50.
- [50] Torabi A, Amininejad S. Brittle fracture in V-notches with end holes. *Int J Damage Mech* 2014;1056789514538293 – .
- [51] Lazzarin P, Berto F, Ayatollahi MR. Brittle failure of inclined key-hole notches in isostatic graphite under in-plane mixed mode loading. *Fatigue Fract Eng Mater Struct* 2013;36:942–55.
- [52] Lazzarin P, Berto F, Zappalorto M. Rapid calculations of notch stress intensity factors based on averaged strain energy density from coarse meshes: Theoretical bases and applications. *Int J Fatigue* 2010;32:1559–67.
- [53] Sakai M, Urashima K, Inagaki M. Energy Principle of Elastic-Plastic Fracture and Its Application to the Fracture Mechanics of a Polycrystalline Graphite. *J Am Ceram Soc* 1983;66:868–74.
- [54] Awaji H, Sato S. Combined Mode Fracture Toughness Measurement by the Disk Test. *J Eng Mater Technol* 1978;100:175–82.
- [55] Li M, Tsujimura M, Sakai M. Crack-face grain interlocking/bridging of a polycrystalline graphite: The role in mixed mode fracture. *Carbon N Y* 1999;37:1633–9.
- [56] Yamauchi Y, Nakano M, Kishida K, Okabe T. Measurement of Fracture Toughness for Brittle Materials under Mixed-Mode Impact Loading Using Center-Notched Disk Specimen. *J Soc Mater Sci Japan* 2000;49:1324–9.
- [57] Yamauchi Y, Nakano M, Kishida K, Okabe T. Measurement of mixed-mode fracture toughness for brittle materials using edge-notched half-disk specimen. *Zair Soc Mater Sci Japan* 2001;50:229–34.
- [58] Shi L, Li H, Zou Z, Fok ASL, Marsden BJ, Hodgkins A, et al. Analysis of crack propagation in nuclear graphite using three-point bending of sandwiched specimens. *J Nucl Mater* 2008;372:141–51.
- [59] Mostafavi M, Marrow TJ. In situ observation of crack nuclei in polygranular graphite under ring-on-ring equi-biaxial and flexural loading. *Eng Fract Mech* 2011;78:1756–70.
- [60] Wang J-AJ, Liu KC. An innovative technique for evaluating fracture toughness of graphite materials. *J Nucl Mater* 2008;381:177–84.
- [61] Etter T, Kuebler J, Frey T, Schulz P, Löffler JF, Uggowitzer PJ. Strength and fracture toughness of interpenetrating graphite/aluminium composites produced by the indirect squeeze casting process. *Mater Sci Eng A* 2004;386:61–7.
-

-
- [62] Yum Y-JY-J, You H, You AH. Pure Mode I, II and Mixed Mode Interlaminar Fracture of Graphite/Epoxy Composite Materials. *J Reinf Plast Compos* 2001;20:794–808.
- [63] Choi S, Sankar B V. Fracture toughness of transverse cracks in graphite/epoxy laminates at cryogenic conditions. *Compos Part B Eng* 2007;38:193–200.
- [64] Wosu SN, Hui D, Dutta PK. Dynamic mixed-mode I/II delamination fracture and energy release rate of unidirectional graphite/epoxy composites. *Eng Fract Mech* 2005;72:1531–58.
- [65] Jurf RA, Pipes RB. Interlaminar fracture of composite materials. *J Compos Mater* 1982;16:386–94.
- [66] Latella BA, Liu T. The initiation and propagation of thermal shock cracks in graphite. *Carbon N Y* 2006;44:3043–8.
- [67] Kim JH, Lee YS, Kim DH, Park NS, Suh J, Kim JO, et al. Evaluation of thermal shock strengths for graphite materials using a laser irradiation method. *Mater Sci Eng A* 2004;387-389:385–9.
- [68] Sato S, Kawamata K, Awaji H, Osawa M, Manaka M. Thermal shock resistance and fracture toughness during the graphitization process. *Carbon N Y* 1981;19:111–8.
- [69] Sato S, Awaji H, Akuzawa H. Fracture toughness of reactor graphite at high temperature. *Carbon N Y* 1978;16:95–102.
- [70] Knibbs RH. Fracture in polycrystalline graphite. *J Nucl Mater* 1967;24:174–87.
- [71] Lomakin E V., Zobnin AI, Berezin A V. Finding the fracture toughness characteristics of graphite materials in plane strain. *Strength Mater* 1975;7:484–7.
- [72] Allard B, Rouby D, Fantozzi G, Dumas D, Lacroix P. Fracture behaviour of carbon materials. *Carbon N Y* 1991;29:457–68.
- [73] Burchell TD. A microstructurally based fracture model for polygranular graphites. *Carbon N Y* 1996;34:297–316.
- [74] Ayatollahi MR, Aliha MRM. Mixed mode fracture analysis of polycrystalline graphite – A modified MTS criterion. *Carbon N Y* 2008;46:1302–8.
- [75] Erdogan F, Sih GC. On the Crack Extension in Plates Under Plane Loading and Transverse Shear. *J Basic Eng* 1963;85:519.
- [76] Bazaj DK, Cox EE. Stress-concentration factors and notch-sensitivity of graphite. *Carbon N Y* 1969;7:689–97.
- [77] Kawakami H. Notch sensitivity of graphite materials for VHTR. *J At Energy Soc Japan / At Energy Soc Japan* 1985;27:357–64. doi:10.3327/jaesj.27.357.
- [78] Zheng X, Zhao K, Wang H, Yan J. Failure criterion with given
-

- survivability for ceramic notched elements under combined tension/torsion. *Mater Sci Eng A* 2003;357:196–202.
- [79] Zheng XL, Zhao K, Yan JH. Fracture and strength of notched elements of brittle material under torsion. *Mater Sci Technol* 2005;21:539–45.
- [80] Ayatollahi MR, Saboori B. A new fixture for fracture tests under mixed mode I/III loading. *Eur J Mech - A/Solids* 2015;51:67–76.
- [81] Losty HHW, Orchard JS. *The Strength of Graphite*. Fifth Conf. Carbon, Pennsylvania State University, Macmillan: 1962.
- [82] Greenstreet WL. *Mechanical Properties of Artificial Graphites – A Survey Report*. Oak Ridge, TN: 1968.
- [83] Neuber H. *Kerbspannungslehre*, 2nd Edition. Berlin: Springer-Verlag; 1958.
- [84] Berto F, Lazzarin P, Gómez FJ, Elices M. Fracture assessment of U-notches under mixed mode loading: two procedures based on the “equivalent local mode I” concept. *Int J Fract* 2007;148:415–33.
- [85] Gómez FJ, Elices M, Berto F, Lazzarin P. Local strain energy to assess the static failure of U-notches in plates under mixed mode loading. *Int J Fract* 2007;145:29–45.
- [86] Torabi ARR, Campagnolo A, Berto F. Tensile fracture analysis of V-notches with end holes by means of the local energy. *Phys Mesomech* 2015;18:194–202.
- [87] Torabi AR, Campagnolo A, Berto F. Experimental and theoretical investigation of brittle fracture in key-hole notches under mixed mode I/II loading. *Acta Mech* 2015;226:2313–22.
- [88] Berto F, Campagnolo A, Lazzarin P. Fatigue strength of severely notched specimens made of Ti-6Al-4V under multiaxial loading. *Fatigue Fract Eng Mater Struct* 2015;38:503–17.
- [89] Berto F. Some recent results on the fatigue strength of notched specimens made of 40CrMoV13.9 steel at room and high temperature. *Phys Mesomech* 2015;18:105–26.
- [90] Salavati H, Alizadeh Y, Berto F. Effect of notch depth and radius on the critical fracture load of bainitic functionally graded steels under mixed mode I + II loading. *Phys Mesomech* 2014;17:178–89.
- [91] Berto F, Lazzarin P, Gallo P. High-temperature fatigue strength of a copper-cobalt-beryllium alloy. *J Strain Anal Eng Des* 2013;49:244–56.
- [92] Berto F, Gallo P, Lazzarin P. High temperature fatigue tests of un-notched and notched specimens made of 40CrMoV13.9 steel. *Mater Des* 2014;63:609–19.
- [93] Pook LP, Campagnolo A, Berto F, Lazzarin P. Coupled fracture mode of a cracked plate under anti-plane loading. *Eng Fract Mech* 2015;134:391–403.
- [94] Pook LP, Berto F, Campagnolo A, Lazzarin P. Coupled fracture mode of a
-

-
- cracked disc under anti-plane loading. *Eng Fract Mech* 2014;128:22–36.
- [95] Berto F, Lazzarin P, Marangon C. The effect of the boundary conditions on in-plane and out-of-plane stress field in three dimensional plates weakened by free-clamped V-notches. *Phys Mesomech* 2012;15:26–36.
- [96] Marangon C, Campagnolo A, Berto F. Three-dimensional effects at the tip of rounded notches subjected to mode-I loading under cyclic plasticity. *J Strain Anal Eng Des* 2015;50:299–313.
- [97] Pook LP. A 50 year retrospective review of three-dimensional effects at cracks and sharp notches. *Fatigue Fract Eng Mater Struct* 2013;36:699–723.
- [98] He Z, Kotousov A, Berto F. Effect of vertex singularities on stress intensities near plate free surfaces. *Fatigue Fract Eng Mater Struct* 2015;n/a – n/a.
- [99] Yosibash Z, Bussiba A, Gilad I. Failure criteria for brittle elastic materials. *Int J Fract* 2004:307–33.
- [100] Berto F, Lazzarin P. Fatigue strength of structural components under multi-axial loading in terms of local energy density averaged on a control volume. *Int J Fatigue* 2011;33:1055–65.
- [101] Qian J, Hasebe N. Property of eigenvalues and eigenfunctions for an interface V-notch in antiplane elasticity. *Eng Fract Mech* 1997;56:729–34.
- [102] Campagnolo A, Berto F, Lazzarin P. The effects of different boundary conditions on three-dimensional cracked discs under anti-plane loading. *Eur J Mech - A/Solids* 2015;50:76–86.
- [103] Lazzarin P, Berto F, Gomez F, Zappalorto M. Some advantages derived from the use of the strain energy density over a control volume in fatigue strength assessments of welded joints. *Int J Fatigue* 2008;30:1345–57.
- [104] Gough HJ, Pollard H V. Properties of some materials for cast crankshafts, with special reference to combined stresses. *Arch Proc Inst Automob Eng* 1906-1947 (vols 1-41) 1936;31:821–93.
- [105] Lazzarin P, Sonsino CM, Zambardi R. A notch stress intensity approach to assess the multiaxial fatigue strength of welded tube-to-flange joints subjected to combined loadings. *Fatigue Fract Eng Mater Struct* 2004;27:127–40.
- [106] Williams JG, Ewing PD. Fracture under complex stress - The angled crack problem. *Int J Fract Mech* 1972;8.
- [107] Ewing PD, Swedlow JL, Williams JG. Further results on the angled crack problem. *Int J Fract* n.d.;12:85–93.
- [108] Richard HA, Benitz K. A loading device for the creation of mixed mode in fracture mechanics. *Int J Fract* 1983;22:R55–8.
- [109] Shetty DK, Rosenfield AR, Duckworth WH. Mixed-mode fracture in biaxial stress state: Application of the diametral-compression (Brazilian disk) test. *Eng Fract Mech* 1987;26:825–40.
-

- [110] Bhattacharjee D, Knott JF. Effect of mixed mode I and II loading on the fracture surface of polymethyl methacrylate (PMMA). *Int J Fract* 1995;72:359–81.
- [111] Xeidakis GS, Samaras IS, Zacharopoulos DA, Papakaliatakis GE. Crack growth in a mixed-mode loading on marble beams under three point bending. *Int J Fract* 1996;79:197–208.
- [112] Ayatollahi MR, Aliha MRM. Analysis of a new specimen for mixed mode fracture tests on brittle materials. *Eng Fract Mech* 2009;76:1563–73.
- [113] Aliha MRM, Hosseinpour GR, Ayatollahi MR. Application of Cracked Triangular Specimen Subjected to Three-Point Bending for Investigating Fracture Behavior of Rock Materials. *Rock Mech Rock Eng* 2012;46:1023–34.
- [114] Aliha MRM, Ayatollahi MR. Rock fracture toughness study using cracked chevron notched Brazilian disc specimen under pure modes I and II loading – A statistical approach. *Theor Appl Fract Mech* 2014;69:17–25.
- [115] Torabi A, Berto F. Strain energy density to assess mode II fracture in U-notched disk-type graphite plates. *Int J Damage Mech* 2014;23:917–30. doi:10.1177/1056789513519349.
- [116] Ayatollahi M, Saboori B. Maximum tangential strain energy density criterion for general mixed mode I/II/III brittle fracture. *Int J Damage Mech* 2014;24:263–78.
- [117] Kamat S., Srinivas M, Rama Rao P. Mixed mode I/III fracture toughness of Armco iron. *Acta Mater* 1998;46:4985–92.
- [118] Petersen D, Kumar A, Hirth J, Hoagland R, Feng X. A Suggested Test Procedure to Measure Mixed Mode I–III Fracture Toughness of Brittle Materials. *J Test Eval* 1994;22:327.
- [119] Manoharan M, Hirth JP, Rosenfield AR. Combined mode I-mode III fracture toughness of a spherodized 1090 steel. *Acta Metall Mater* 1991;39:1203–10.
- [120] Pook LP. The fatigue crack direction and threshold behaviour of mild steel under mixed mode I and III loading. *Int J Fatigue* 1985;7:21–30.
- [121] Yukio U, Kazuo I, Tetsuya Y, Mitsuru A. Characteristics of brittle fracture under general combined modes including those under bi-axial tensile loads. *Eng Fract Mech* 1983;18:1131–58.
- [122] Lin B, Mear ME, Ravi-Chandar K. Criterion for initiation of cracks under mixed-mode I + III loading. *Int J Fract* 2010;165:175–88.
- [123] Chang J, Xu J, Mutoh Y. A general mixed-mode brittle fracture criterion for cracked materials. *Eng Fract Mech* 2006;73:1249–63.
- [124] Cho S, Nakamura Y, Mohanty B, Kaneko K. Study on control of crack-propagation in blasting. *Fragblast 8, Santiago (Chile): 2006*, p. 124–8.
- [125] Lan W, Deng X, Sutton MA, Cheng C-S. Study of slant fracture in ductile materials. *Int J Fract* 2006;141:469–96.
-

- [126] Sutton MA, Deng X, Reynolds A. Crack Growth and Stress Intensity Prediction Techniques. 2006.
- [127] Cooke ML, Pollard DD. Fracture propagation paths under mixed mode loading within rectangular blocks of polymethyl methacrylate. *J Geophys Res* 1996;101:3387.
- [128] Berto F, Elices M, Lazzarin P, Zappalorto M. Fracture behaviour of notched round bars made of PMMA subjected to torsion at room temperature. *Eng Fract Mech* 2012;90:143–60.
- [129] Berto F, Cendon DAA, Lazzarin P, Elices M. Fracture behaviour of notched round bars made of PMMA subjected to torsion at -60°C . *Eng Fract Mech* 2013;102:271–87.
- [130] ASTM E399-90(1997). Standard Test Method for Plane-Strain Fracture Toughness of Metallic Materials 1997.
- [131] Torabi AR, Campagnolo A, Berto F. Local strain energy density to predict mode II brittle fracture in Brazilian disk specimens weakened by V-notches with end holes. *Mater Des* 2014;69:22–9.

CHAPTER 3

MULTIAXIAL FATIGUE

LOADINGS

3.1 Notched components made of Ti-6Al-4V under multiaxial loading^(*)

Nomenclature

e_1, e_3	Angular functions for the SED evaluation
k	Wohler's curve inverse slope
K_1, K_3	Notch Stress Intensity Factors (NSIFs) referred to tension and torsion loadings
N	Counting of loading cycles
R	Load ratio applied nominally
R_1, R_3	Size of the Mode I and Mode III control volumes
T_σ	Scatter index for the normal stress
T_τ	Scatter index for shear stresses
T_W	SED scatter index
\overline{W}	SED measured over the control volumes

Symbols

2α	Opening angle for V-notches
Φ	Angle of phase between tension and torsion loadings
λ	Nominal ratio between the stress amplitudes, τ_a/σ_a
λ_1	Eigenvalue for Mode I loading
λ_3	Eigenvalue for Mode III loading
ρ	Radius at the notch apex
σ_a	Nominal tensile stress referred to the net area
τ_a	Nominal torsion stress referred to the net area
σ_A, τ_A	Fatigue strength at N_A loading cycles

(*) See also:

Berto, F.; Campagnolo, A.; Lazzarin, P. Fatigue strength of severely notched specimens made of Ti-6Al-4V under multiaxial loading. *Fatigue and Fracture of Engineering Materials and Structures*; 38: 503-517 (2015);

3.1.1 Introduction

Multiaxial fatigue of metallic materials is a topic of active research. For a comparison between different criteria here the recent overview by Fatemi and Shamsaei [1] and the report by Sonsino and Nieslony [2] based on a large body of experimental data from notched specimens are mentioned. A central position is occupied by the critical plane approach as formulated by Fatemi, Socie and Kurath [3,4] and by some interesting variants [5–7].

In this ambit, energy-based criteria find important applications [8]. Recently it has been proposed a multiaxial fatigue criterion based on a frequency-domain formulation of a stress invariant, called “Projection by Projection” (PbP) approach [9]. A frequency-domain formulation of the critical plane-based C-S criterion has recently been presented [10].

In 1923 Jasper [11] first used an energy-based parameter to analyse fatigue strength under tension–compression loadings. Afterwards dealing with multiaxial fatigue loading Ellyin [12,13] proposed an approach based on the combination of both the plastic and elastic strain work. A wide review of energy-based multiaxial fatigue life formulations was carried out in the past [14].

Theoretical and experimental problems tied to multiaxial fatigue were discussed by several researchers [15–21]. The mechanisms inducing shielding effects during fatigue crack propagation were classified by Ritchie [18]. Some other pioneering contributions are due to Yu *et al.* [19] and Tanaka *et al.* [20]. A mathematical model able to describe the stresses near the crack tip, which considers the effects of plasticity and shielding effects on the applied elastic field, was developed by Christopher *et al.* [22–24]. Ravi-Chandar *et al.* [25] have recently shown that the cracks propagate through an abrupt fragmentation or segmentation of the crack front.

The deviatoric strain energy density (SED) evaluated at the notch tip was used by Park and Nelson [26] to assess the fatigue behavior under multi-axial stresses of specimens weakened by blunt notches. That point-wise criterion cannot be applied to sharp notches. With the aim to overcome this problem, a volume-based SED approach originally proposed for sharp V-notches and cracks [27] has been extended to multiaxial fatigue loading [28–34].

With reference to different combinations of multiaxial loading, the average SED was used [30] to summarize about 300 fatigue data from sharply notched axis-symmetric specimens made of C40 steel as well as more than 120 fatigue data from notched specimens made of 40CrMoV13.9 steel [33]. The control volume under tensile and torsion loading was assumed constant for both materials. This assumption was found to be not valid for the 39NiCrMo3 steel weakened by circumferential quasi-sharp V-notches [28]. In that case strong dissipative phenomena occurred due to torsion loads even in the high-cycle fatigue regime. It was possible to draw a single SED-based scatterband only by using two different control volumes for tension and torsion, respectively. The volume-based SED approach was used also to 13 series of fatigue data from plain and notched specimens made of AISI 416 [32] and to 10 series of fatigue data from severely notched specimens made of the cast iron EN-GJS400 [34]. Also for these two materials, two distinct radii, one for each type of loading, of the control volume were used under torsion and tension loading due to presence of strong non-linear effects. The SED was named ‘apparent linear elastic SED’ to make evident that the evaluation of the strain energy was carried out in two different volumes (for tension and torsion, as determined from experimental data). This simplified procedure allows us to overcome the problem tied to shielding mechanisms by employing a linear elastic model [35].

Ti-6Al-4V alloy under combined tension and torsion loadings is investigated in the present work. This titanium alloy is widely used for advanced military, civil aerospace and naval applications. The in-service conditions are usually characterized by a complex stress state combined with aggressive environments. The Ti-6Al-4V titanium alloy has very good static and fatigue properties, an high strength-to-mass ratio, with an excellent wear resistance, also at high temperature and in corrosive environments. The uniaxial fatigue resistance of smooth and notched specimens made of Ti-6Al-4V has been extensively investigated in the recent literature [36–46].

The effects of high frequencies as well as those of increased specimen temperature due to internal damping on the tensile fatigue behavior of Ti-6Al-4V titanium alloy have been investigated considering smooth specimens tested under

various nominal load ratios R [36,37], and also considering both smooth and 0.3 mm-hole-notched specimens under different heat treatments [38].

The fatigue behavior of Ti-6Al-4V in the presence of notch effects has been extensively investigated by Nicholas *et al.* [39–42], also with reference to the fretting fatigue performance of this titanium alloy [43]. In particular, the notch effect on high-cycle fatigue with different nominal load ratios R has been investigated [39,40] considering, respectively, cylindrical V-notched and notched flat dog-bone specimens characterized by an opening angle equal to 60 degrees and by a notch tip radius ranging between 0.127 and 0.432 mm. All the tests were conducted under pure tensile loading.

Considering the same specimen geometry and nominal load ratios R of the previous works, also the effects of combined low-cycle fatigue (LCF) and high-cycle fatigue (HCF) loading have been investigated [41]. In particular the fatigue limit at 10^7 cycles after LCF loading was established using a step loading technique. A weak influence of the LCF loading on the subsequent HCF fatigue limit has been observed.

The effect of microstructure on pulsating four point bending fatigue of Ti-6Al-4V has been studied considering prismatic specimens with a central hole and double-edge-notched specimens [44,45]. The importance of the microstructure (phases α , β) on the material damage was highlighted and correlated to the crack growth rate. Fatigue crack initiation of Ti-6Al-4V titanium alloy has been studied using plane specimens under pure bending [46].

With regard to multiaxial loading, the low-cycle fatigue behaviour of tubular specimens made of Ti-6Al-4V has been investigated by Hoshide *et al.* [47], focusing the analyses on proportional loading and the effect of microstructure, and by Nakamura *et al.* [48], who analysed the effect of out-of-phase loading. Regarding the high-cycle fatigue, the resistance of smooth specimens made of Ti-6Al-4V under multiaxial loading, both proportional and non-proportional, has been studied by Kallmeyer *et al.* [49], who have also compared various multiaxial fatigue models to verify their suitability at estimating fatigue damage in this titanium alloy. The multiaxial fatigue behaviour of smooth and notched specimens under proportional loading has been investigated in a recent contribution [50]

where the Lemaitre and Chaboche's model [51] was applied for fatigue life assessments.

A complete set of data from sharply V-notched specimens under torsion and combined tension and torsion loadings, both in-phase and out-of-phase, is not available in the literature for Ti-6Al-4V. With the aim to fill this lack, a complete set of experimental data from a severely notched titanium alloy under multiaxial loading is provided. The actual research program is mainly focused on the definition of a methodology applicable for the fatigue design of severely notched structural components made of Ti-6Al-4V subjected to multiaxial fatigue loadings. The results from multiaxial tests are discussed in the following together with those obtained under pure tension and pure torsion loading from un-notched and V-notched specimens tested under different nominal load ratios.

The approach based on the Strain Energy Density (SED) averaged on a control volume embracing the highly stressed region is employed to summarise all the data in a single scatterband. This volume is found to be dependent on the loading mode, in agreement with previous works dealing with multiaxial fatigue behaviour of structural steel and cast iron components [28,32,34].

3.1.2 Material properties and geometry of the specimens

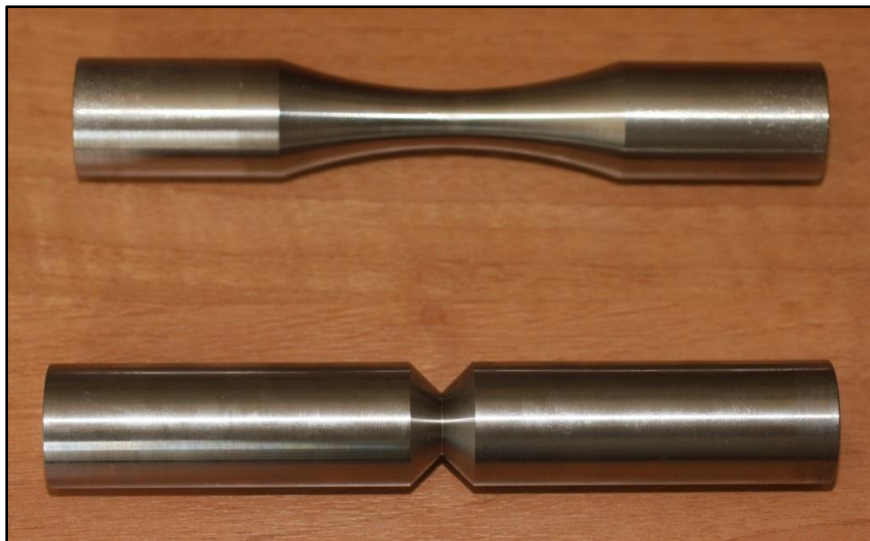
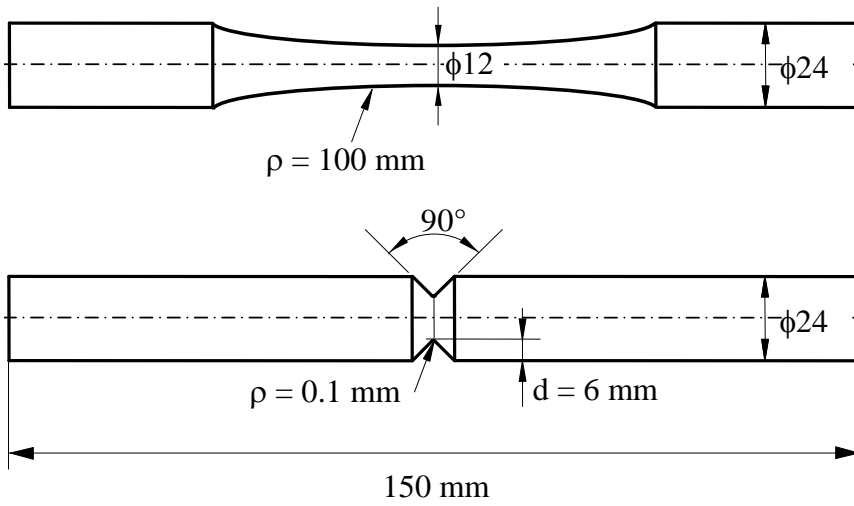
The material under investigation is a grade 5 titanium alloy, also known as Ti-6Al-4V. The mean values of the elastic and strength material properties determined by static tensile tests are listed in Table 3.1.1 whereas the chemical composition is shown in Table 3.1.2. The geometries of the un-notched and V-notched specimens are shown in Figure 3.1.1 together with some details of the notch tip.

Table 3.1.1. Mechanical properties of Ti6Al4V.

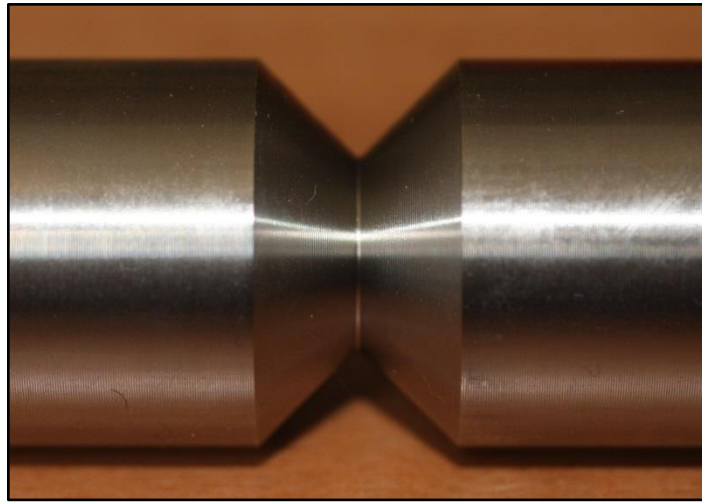
Ultimate tensile strength [MPa]	Yield stress [MPa]	Elongation to fracture [%]	Reduction of area [%]
978	894	16	36

Table 3.1.2. Chemical composition wt.%, balance Ti.

Fe	O	C	N	H	Al	V
0.057	0.15	0.015	0.021	0.001	6.06	4.18



(a)



(b)

Figure 3.1.1. Geometry of un-notched and V-notched specimens (a) and details of the notch tip (b).

The hourglass un-notched specimens (Figure 3.1.1a) were characterized by a diameter of the net transverse area equal to 12 mm and by a connecting radius ($\rho = 100$ mm) between the net and gross sections large enough to avoid any effect of stress concentration.

The cylindrical notched specimens (Figure 3.1.1b) were characterized by a V-notch depth $d = 6$ mm and an opening angle equal to 90 degrees, whereas the notch root radius, ρ , was always lower than 0.1 mm. The experimental measurements of the notch tip radius, carried out by means of an optical microscope and the dedicate software LAS (Leica Application Suite), have provided a mean value equal to 0.09 mm with a very reduced scatter. The precision ensured by the employed procedure is $\pm 5\%$ of the measured quantity. The typical notch geometry constituted by two rectilinear flanks tangent to the notch tip radius is shown in Figure 3.1.2, for one of the V-notched specimens.

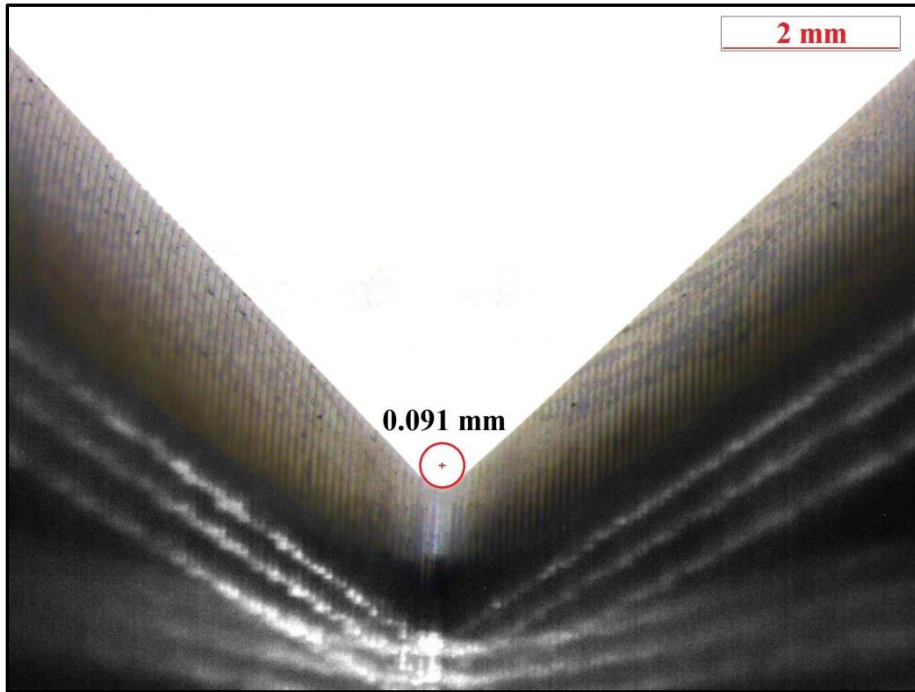


Figure 3.1.2. Measure of the notch tip radius.

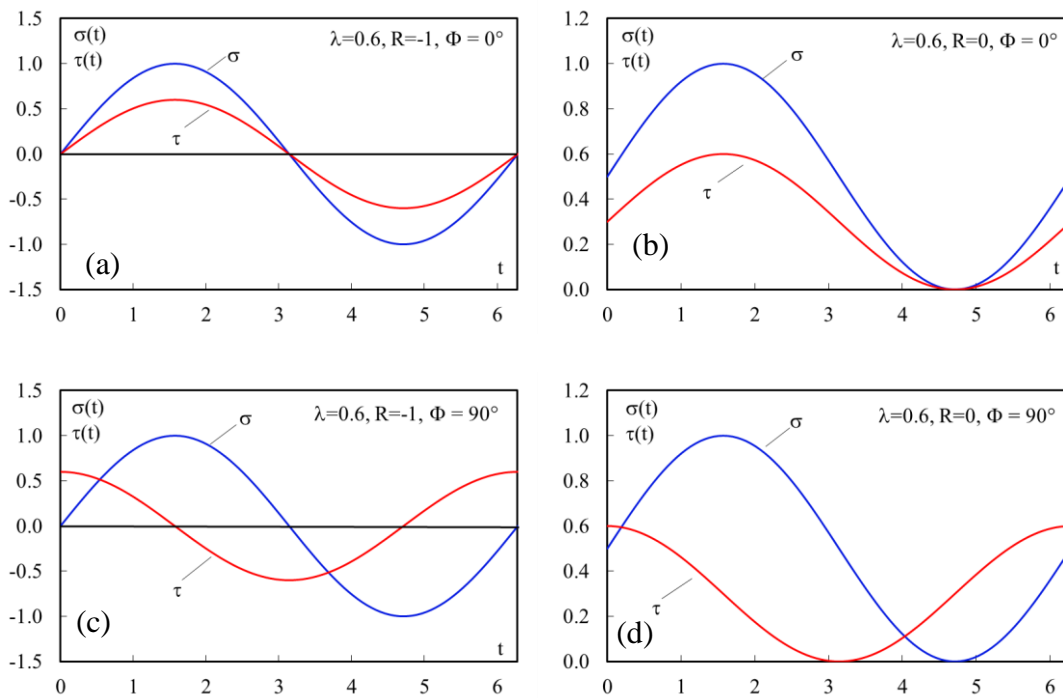


Figure 3.1.3. Wave forms for each multiaxial loading pattern. (a) in-phase loading at $R=-1$ and $\lambda=0.6$; (b) in-phase loading at $R=0$ and $\lambda=0.6$; (c) out-of-phase loading at $R=-1$ and $\lambda=0.6$; (d) out-of-phase loading at $R=0$ and $\lambda=0.6$.

The experimental tests have been performed on a MTS 809 servo-hydraulic bi-axial testing device (± 100 kN, ± 1100 Nm, ± 75 mm/ $\pm 55^\circ$) under load control. A MTS load cell with ± 0.5 % error at full scale has been used to measure the applied load. Altogether 15 different fatigue test series have been performed according to the parameters described below:

- Four series from plain and V-notched specimens under pure tension and pure torsion fatigue loading at $R = -1$;
- Four series from plain and V-notched specimens under pure torsion fatigue loading at $R = 0$ and 0.5 ;
- Three series from plain specimens under pure torsion fatigue loading at $R = 0.25$, -2 and -3 ;
- Four series from V-notched specimens under multiaxial loading, with a biaxiality ratio $\lambda = 0.6$. Two nominal load ratios, $R = 0$ and $R = -1$, and two phase angles, $\Phi = 0^\circ$ (in-phase loading) and $\Phi = 90^\circ$ (out-of-phase loading), have been adopted in these tests.

The time evolution of the different multiaxial loading conditions employed in the experimental tests is shown in Figure 3.1.3.

3.1.3 Results from the fatigue tests

All specimens have been polished with the aim of removing surface scratches and processing marks, before performing the tests. A MTS 809 servo-hydraulic biaxial machine with a 100 kN axial load cell and a torsion load cell of 1100 Nm has been used for fatigue tests. All tests have been conducted under load control at a frequency between 10 and 15 Hz as a function of the applied load.

The statistical analyses have been performed assuming a log-normal distribution. All data obtained from specimens characterized by fatigue life between 10^4 and $2 \cdot 10^6$ have been taken into account in the statistical analyses, excluding the run-outs. The nominal stress amplitudes for a probability of survival $P_s = 50\%$ at different number of loading cycles, $N_A = 10^6$ and $2 \cdot 10^6$, the inverse slope k of Wöhler curves and the scatter index T , which provides the width of the

scatterband between the curves with 10% and 90% probabilities of survival (with a confidence level equal to 95%) are shown in Table 3.1.3.

All fatigue strength data are shown in Figures 3.1.4-7, in terms of nominal stress amplitudes evaluated on to the net transverse area of the specimens. Fig. 3.1.4 shows the fatigue data from un-notched and V-notched specimens tested under pure tension at the same load ratio, $R = -1$. The reduction of the fatigue strength due to the notch effect is not so different in the low- and high-cycle fatigue regime; the slope of the two curves changes from 9.25 (smooth specimens) to 6.26 (notched specimens). At $2 \cdot 10^6$ loading cycles, the ratio between the mean stress amplitudes for un-notched and V-notched specimens is 4.75, see Table 3.1.3.

Figure 3.1.5 shows the fatigue data from un-notched and V-notched specimens tested under pure torsion considering two different values of load ratio ($R = -1$ and $R = 0$). There is an evident reduction of the fatigue strength as the load ratio increases from $R = -1$ to $R = 0$. At $2 \cdot 10^6$ loading cycles, the ratio between the mean stress amplitudes ($P_s = 50\%$), related to the $R = -1$ and $R = 0$ cases, is 1.35 for the un-notched specimens, 1.17 for the V-notched specimens (Table 3.1.3). For the same nominal load ratio R , it can be observed a reduction of the fatigue strength due to the stress concentration effect; at $2 \cdot 10^6$ loading cycles, the ratio between the mean stress amplitudes for smooth and V-notched specimens is found to be 1.34 for $R = -1$, reduced to 1.16 for $R = 0$.

Figure 3.1.6 shows the fatigue data from un-notched and V-notched specimens tested under pure torsion at different nominal load ratios. R ranges from 0.5 to -3 for the un-notched specimens, whereas R is 0.5 for the V-notched ones. With regard to the smooth specimens, the fatigue strength decreases when the load ratio increases from the minimum value, $R = -3$, to the maximum one, $R = 0.5$. At $2 \cdot 10^6$ loading cycles to failure, the maximum ratio between the stress amplitudes both for $R = -3$ and $R = 0.5$ is equal to 1.98. It is interesting to observe that, contrary to what was expected, the nominal load ratio $R = -2$ is found to be slightly beneficial with respect to $R = -3$ at the high-cycle regime (with the ratio between the mean stress amplitudes equal to 1.14 at $2 \cdot 10^6$ cycles), whereas the fatigue strength is almost the same at the low-cycle regime. With reference to the nominal load ratio $R = 0.5$, it can be observed that the fatigue strength reduction

due to the stress concentration effect induced by the V-notch effect is almost negligible, being the ratio at $2 \cdot 10^6$ loading cycles between the mean stress amplitudes relating to smooth and V-notched specimens equal to 1.06. Also the slope of all the curves is almost the same, see Table 3.1.3.

The fatigue data from V-notched specimens tested under combined tension and torsion loadings, both in-phase ($\Phi = 0^\circ$) and out-of-phase ($\Phi = 90^\circ$), are shown in Figures 3.1.7a,b considering two different values of the load ratio ($R = -1$ and $R = 0$). The corresponding shear stress amplitudes can be immediately derived from the biaxiality ratio $\tau_a = \lambda \sigma_a$, with λ constant and equal to 0.6. The four mean Wöhler curves at $P_s = 50\%$ related to multiaxial loadings are compared with the curve from pure tension ($R = -1$).

It is evident that the application of a multiaxial loading reduces the fatigue life compared to the pure tension loading case, with reference to the same normal stress amplitude (Fig. 3.1.7a), but the reduction is quite limited for the specific λ value. Stronger is the reduction of the multiaxial fatigue strength due to the nominal load ratio R . At $2 \cdot 10^6$ loading cycles the mean stress amplitudes for $R = -1$ and $R = 0$ are characterised by a ratio equal to 1.39 for the in-phase loading conditions and 1.21 for the out-of-phase ones.

The phase angle effect is found to be weak for $R = -1$, being the mean values of the normal stress amplitude about the same at $2 \cdot 10^6$ loading cycles: 96 MPa for out-of-phase loading, 94 MPa for in-phase loading.

More clear is the effect of the phase angle when $R = 0$; in this case the mean value of the normal stress amplitude increases from 68 MPa for in-phase loads to 80 MPa for out-of-phase loads. Then, for $R = 0$, the out-of-phase loading is slightly beneficial with respect to in-phase loading at high-cycle fatigue regime, whereas the fatigue strength is almost the same at low-cycle regime.

In conclusion, Figures 3.1.7a,b and Table 3.1.3 show that the sensitivity of this titanium alloy under multiaxial fatigue loading to the phase angle effect is quite limited, being lower than +15 percent for the $R = 0$ case, negligible for the $R = -1$ case. Some considerations on the effect of non-proportional loading on the fatigue behaviour of different structural steels can be found in a recent contribution [52].

Finally, the multiaxial fatigue data have shown that the influence of the nominal load ratio R on fatigue life is strong, confirming the trend found in both pure tension and pure torsion. A clear variation of the inverse slope k also occurred for $R = 0$ in the cases $\Phi = 0^\circ$ and $\Phi = 90^\circ$, whereas no evident change of slope occurred in the $R = -1$ case.

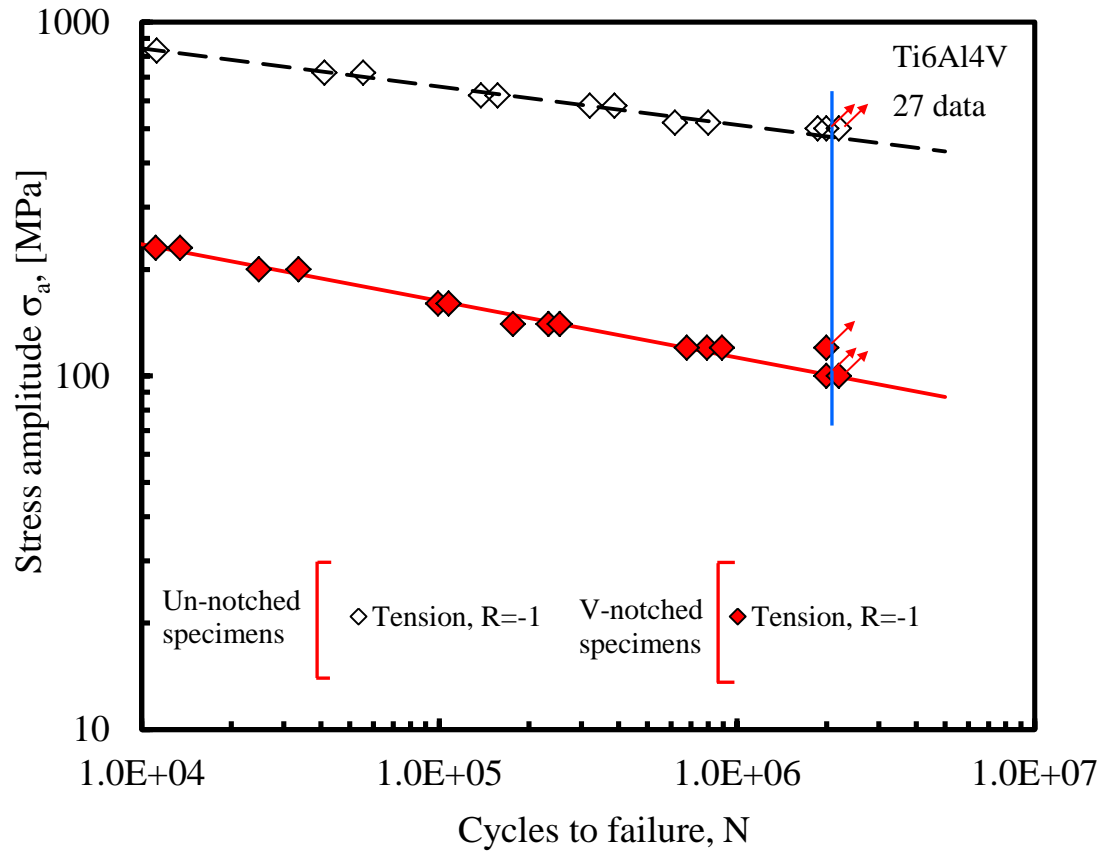


Figure 3.1.4. Data from un-notched and V-notched specimens under pure tension ($R = -1$).

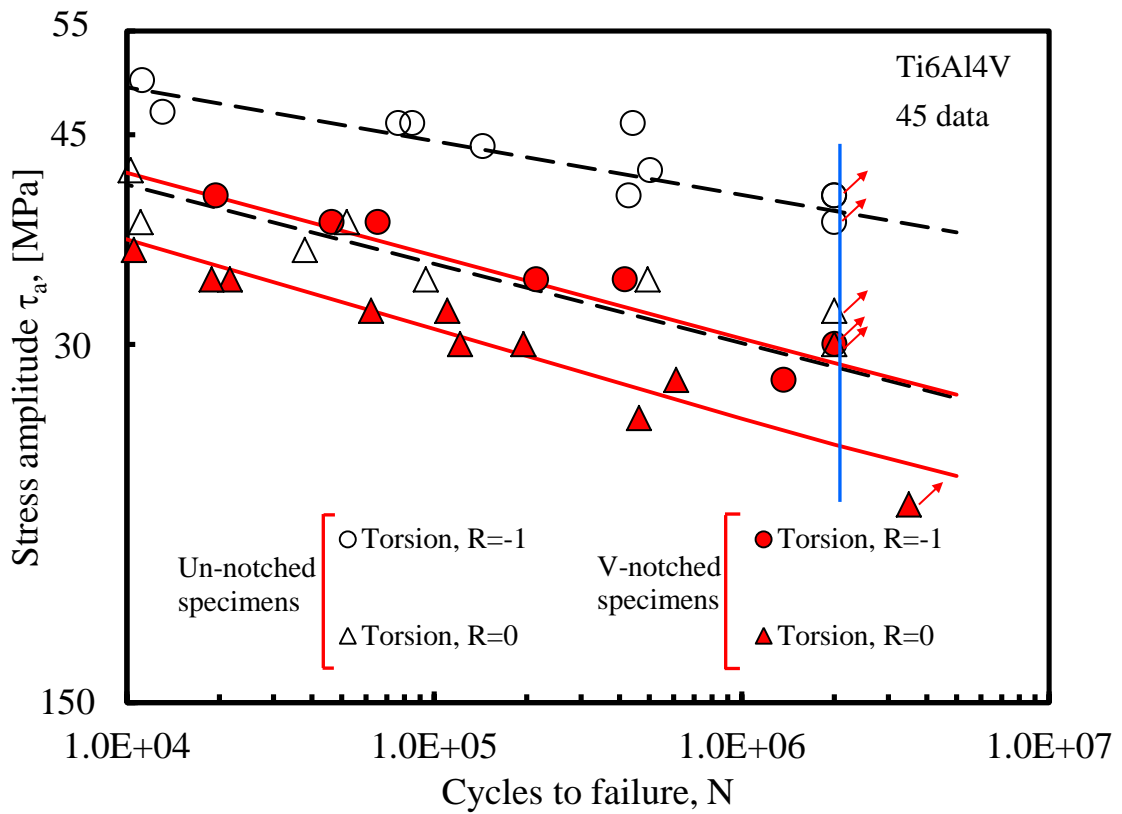


Figure 3.1.5. Data from un-notched and V-notched specimens under pure torsion ($R = -1$ and $R = 0$).

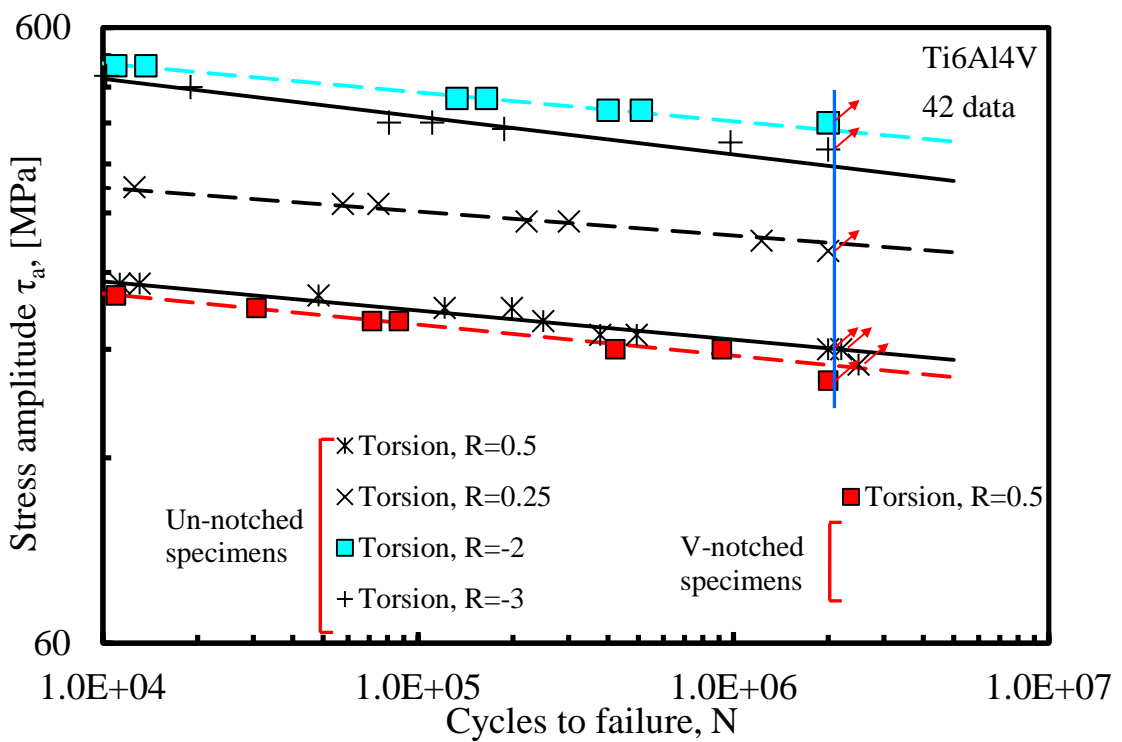


Figure 3.1.6. Data from un-notched and V-notched specimens under pure torsion (R ranging from 0.5 to -3).

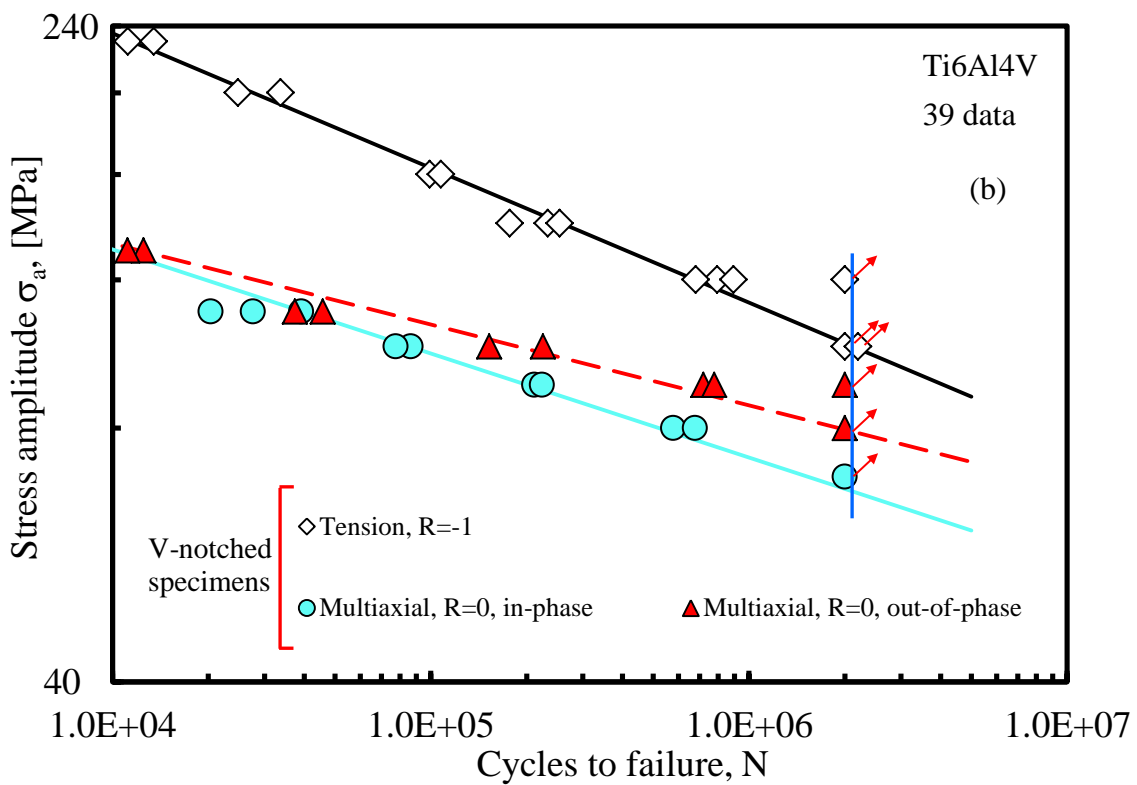
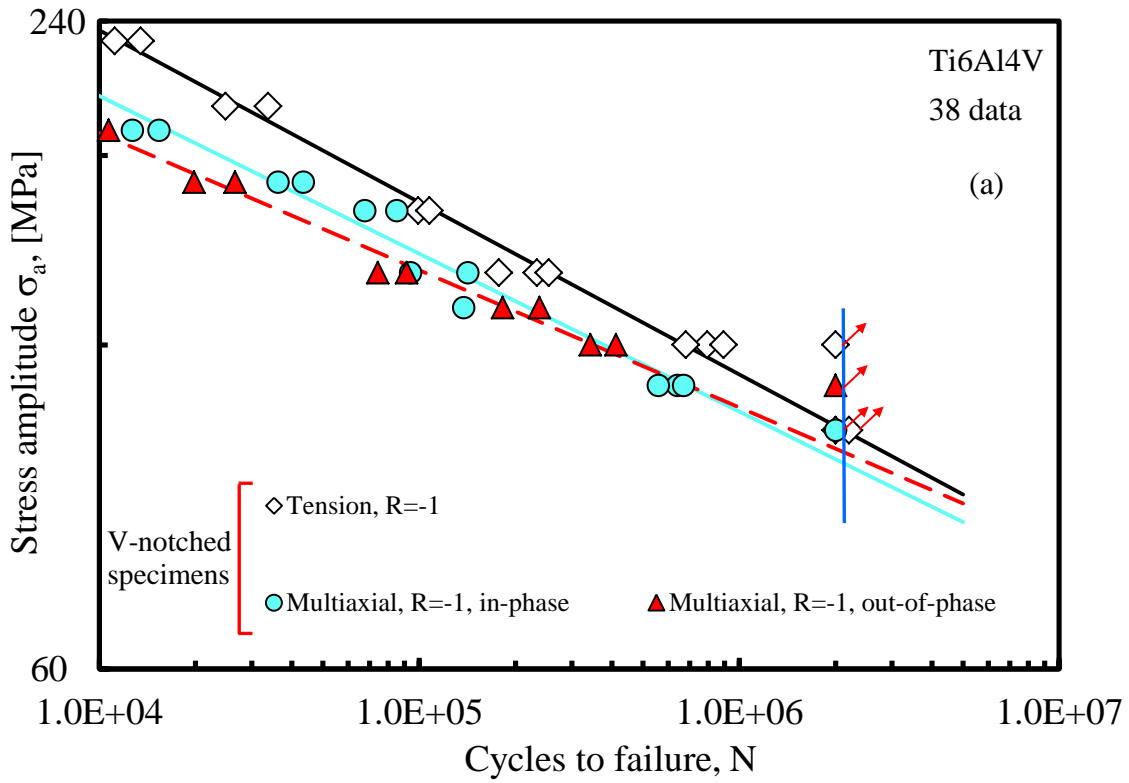


Figure 3.1.7. Data from V-notched specimens under multiaxial loading ($\lambda=0.6$) with R = -1 (a) and R = 0 (b). Comparison with pure tension.

Table 3.1.3. Results from fatigue tests. Mean values, $P_s=50\%$. Stresses referred to the net area.

Series	Load	N	k	T_σ or T_τ	σ_a or τ_a		
					10^6	$2 \cdot 10^6$	
1	Tension R = -1	12	σ	9.25	1.120	512.76	475.74
2	Torsion R = -1	16	τ	22.13	1.205	400.60	388.25
3	Torsion R = 0	9	τ	15.03	1.322	300.78	287.22
4	Tension R = -1, V-notch $2\alpha = 90^\circ$	15	σ	6.26	1.133	112.70	100.89
5	Torsion R = -1, V-notch $2\alpha = 90^\circ$	9	τ	14.59	1.229	303.39	289.31
6	Torsion R = 0, V-notch $2\alpha = 90^\circ$	11	τ	13.82	1.159	259.87	247.16
7	Torsion R = 0.5, V-notch $2\alpha = 90^\circ$	7	τ	19.91	1.080	175.91	169.89
8	Multiaxial R = -1, $\Phi = 0^\circ$, $\lambda = 0.6$, V-notch $2\alpha = 90^\circ$	13	σ	6.82	1.197	104.03	93.89
			τ			62.42	56.39
9	Multiaxial R = -1, $\Phi = 90^\circ$, $\lambda = 0.6$, V-notch $2\alpha = 90^\circ$	10	σ	7.84	1.124	104.99	96.11
			τ			63.00	57.67
10	Multiaxial R = 0, $\Phi = 0^\circ$, $\lambda = 0.6$, V-notch $2\alpha = 90^\circ$	12	σ	8.09	1.159	73.80	67.74
			τ			44.28	40.64
11	Multiaxial R = 0, $\Phi = 90^\circ$, $\lambda = 0.6$, V-notch $2\alpha = 90^\circ$	12	σ	10.43	1.158	85.12	79.65
			τ			51.07	47.79
12	Torsion R = 0.5	12	τ	21.19	1.134	186.74	180.73
13	Torsion R = 0.25	8	τ	25.67	1.078	275.46	268.12
14	Torsion R = -3	7	τ	16.25	1.178	373.13	357.55
15	Torsion R = -2	8	τ	21.32	1.042	422.53	409.01

3.1.4 Fracture surface analysis

After each fatigue test, the fracture surfaces of the specimen or the unbroken external surface have been analysed. Figure 3.1.8 shows a typical failure occurred in a plain specimen under torsion loading. It is characterized by micro-cracking in the longitudinal direction, in the central zone of the specimen corresponding to the minimum value of the transversal sectional area.

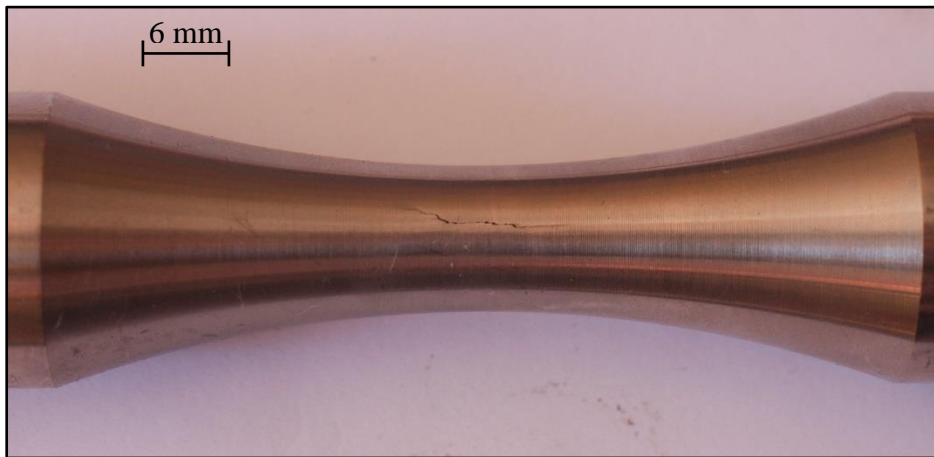


Figure 3.1.8. Typical crack propagating from an un-notched specimen under torsion loading.

Fracture surfaces of some V-notched specimens tested under torsion with nominal load ratios $R = 0$ and $R = 0.5$ are shown in Figure 3.1.9a and 3.1.9b, respectively. The outer diameter of the fracture surface is almost flat, particularly for $R = 0.5$. For both R values, the classical Mode I ‘factory roof’ morphology is also evident in large areas of the centre of the fracture surface where the effects due to abrasion are also clear. Generally, a limited but distinguishable quantity of debris and powder was emanated from the notch tip when a visible crack started to propagate.

Fracture surfaces of some specimens tested under multiaxial conditions with $R = -1$ are shown in Figure 3.1.10a and 3.1.10b considering low and high-cycle fatigue, respectively. These specimens were all tested with the same phase angle, $\Phi = 0^\circ$, and the same biaxiality ratio $\lambda = 0.6$. Clear is the presence of the ‘factory roof’

morphology, characterized by an inclination angle lower than 45° , extending from the initial notch tip. An analogous behaviour can be observed on the failure surfaces of the specimens tested under in-phase multiaxial loading with $R = 0$, as is shown in Figure 3.1.11(a,b) for low- and high-cycle fatigue, respectively.

As regards to out-of-phase multiaxial loading, the fracture surfaces of the specimens tested with a nominal load ratio R equal to -1 and 0 are shown in Figure 3.1.12a and 3.1.12b, respectively. The fracture surface morphology seem to be affected by the phase angle. Some signs of micro abrasions could be observed on all fracture surfaces and the extent to which the rubbing occurred depends on phase angle. Most visible is the abrasion for $\Phi = 90^\circ$ resulting in a smooth featureless fracture topography.

In the zone of crack initiation, micro-fusion zones due to the interference between the cracks surfaces are visible near the notch tip. During the tests, in fact, the two surfaces of the cracks scrape each other emanating some powder from the notch tip.

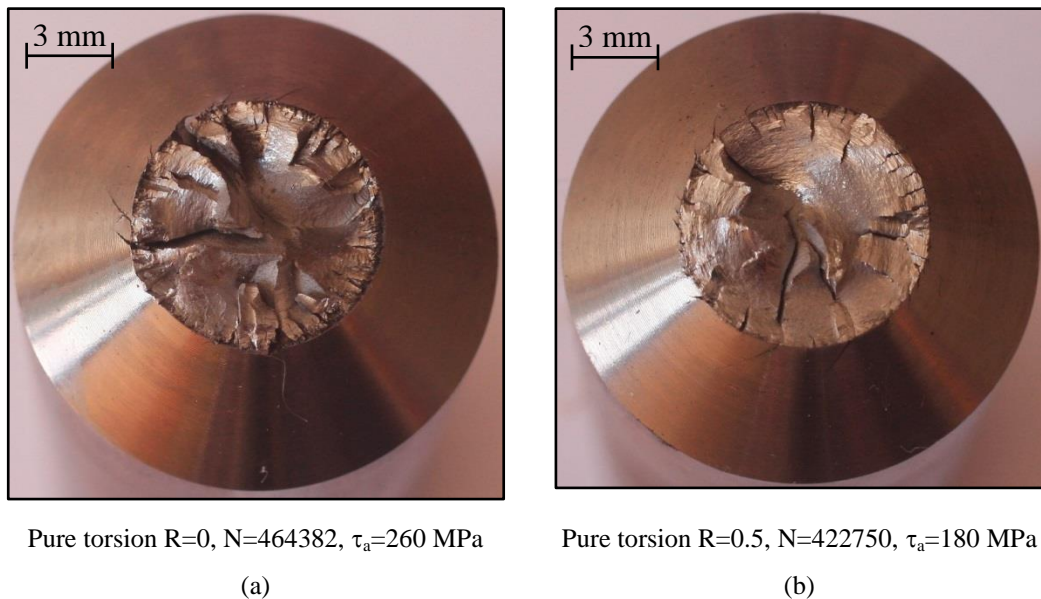
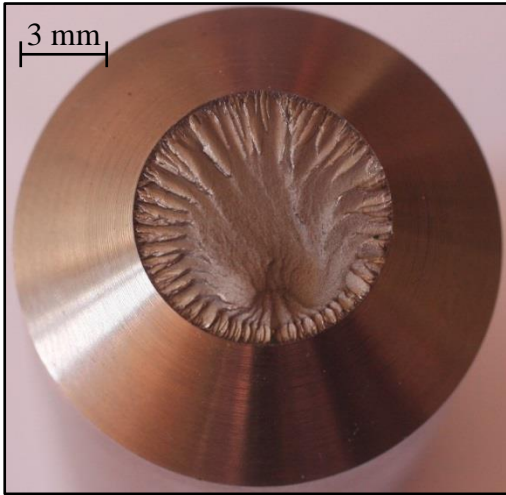
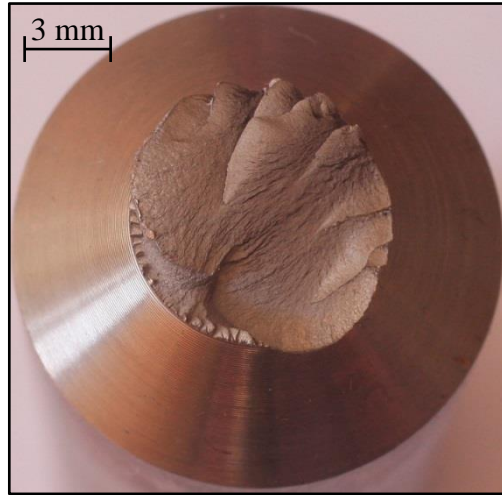


Figure 3.1.9. Fracture surfaces from V-notched specimens under pure torsion for $R=0$ (a) and $R=0.5$ (b).



Multiaxial fatigue, $N=12668$, $\sigma_a=190$ MPa

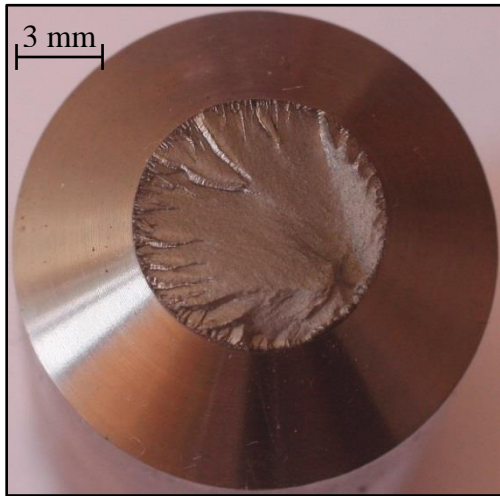
(a)



Multiaxial fatigue, $N=640874$, $\sigma_a=110$ MPa

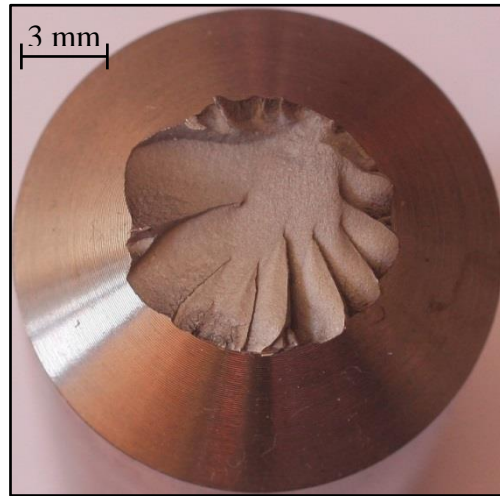
(b)

Figure 3.1.10. Fracture surfaces from V-notched specimens under in-phase multiaxial loading : $R=-1$, $\lambda=0.6$ and $\Phi=0^\circ$. Low (a) and high (b) cycle fatigue.



Multiaxial fatigue, $N=27588$, $\sigma_a=110$ MPa

(a)



Multiaxial fatigue, $N=577884$, $\sigma_a=80$ MPa

(b)

Figure 3.1.11. Fracture surfaces from V-notched specimens under in-phase multiaxial loading: $R=0$, $\lambda=0.6$ and $\Phi=0^\circ$. Low (a) and high (b) cycle fatigue.

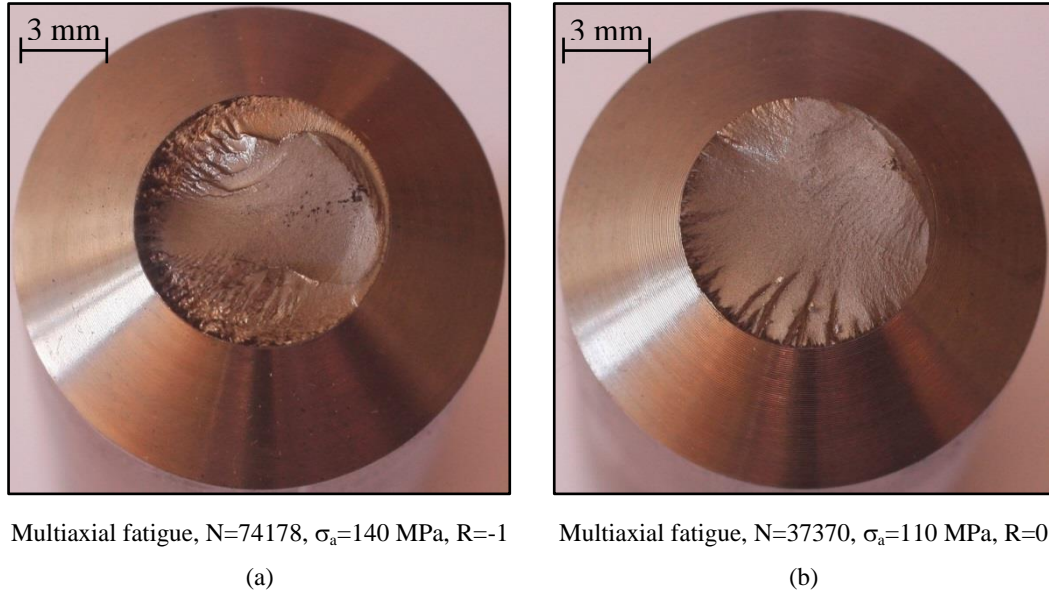


Figure 3.1.12. Fracture surfaces from V-notched specimens under out-of-phase multiaxial fatigue: $\lambda=0.6$ and $\Phi=90^\circ$. $R=-1$ (a) and $R=0$ (b).

3.1.5 A synthesis in terms of linear elastic SED averaged over a control volume

With regard to smooth specimens, all the experimental data are summarised here in terms of the strain energy density, which can be expressed under linear elastic hypothesis according to Beltrami's expression [53]. Under pure tension, it holds:

$$\Delta \bar{W} = \frac{\Delta \sigma_{\text{nom}}^2}{2E} \quad (3.1.1)$$

while under pure torsion it results:

$$\Delta \bar{W} = (1 + \nu) \frac{\Delta \tau_{\text{nom}}^2}{E} \quad (3.1.2)$$

where $\Delta \sigma_{\text{nom}}$ and $\Delta \tau_{\text{nom}}$ represent the range of the nominal stress components. For Ti-6Al-4V titanium alloy, the Young's modulus E is equal to 110 Gpa, while the Poisson's ratio ν is 0.3.

Also the experimental data related to V-notched specimens are summarised hereafter in terms of linear elastic strain energy density, but the SED calculation in this case is based on the local stress and strain state in a control volume

surrounding the notch tip. Being the radius at the notch tip very small (ρ less than 0.1 mm), the Mode I and Mode III notch stress intensity factors K_1 and K_3 can be used to re-analyse the fatigue strength data related to V-notched specimens in terms of SED.

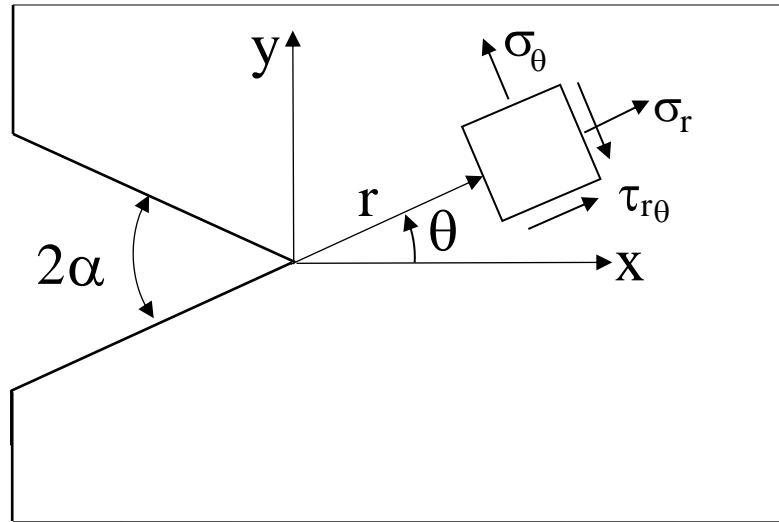


Figure 3.1.13. Polar coordinate system for V-shaped notches, with z normal to the plane; Mode I NSIF linked to the stress component σ_θ evaluated along the notch bisector line ($\theta=0$); under mode III the shear stress component $\tau_{z\theta}$ is oriented as σ_θ .

These field parameters were calculated by means of linear elastic FE analysis considering a sharp V-notch with $\rho = 0$, see Figure 3.1.13. In particular, considering a cylindrical coordinate system (r, θ, z) centered at the notch apex, where r is the radial coordinate, θ is the angle between a particular point and the notch bisector line while z is the longitudinal axis of the specimens, the Mode I and Mode III Notch Stress Intensity Factors (NSIFs) can be defined according to the following expressions [54,55]:

$$K_1 = \sqrt{2\pi} \lim_{r \rightarrow 0^+} r^{1-\lambda_1} \sigma_{\theta\theta}(r, \theta = 0) \quad (3.1.3)$$

$$K_3 = \sqrt{2\pi} \lim_{r \rightarrow 0^+} r^{1-\lambda_3} \tau_{\theta z}(r, \theta = 0) \quad (3.1.4)$$

In the case of a V-notch opening angle equal to 90 degrees, the eigenvalues λ_1 and λ_3 are equal to 0.545 and 0.667, respectively. On the other hand, in conditions of linear elasticity, the NSIFs can be linked to the nominal stress components according to the following expressions [29,55]:

$$\Delta K_1 = k_1 d^{1-\lambda_1} \Delta \sigma_{\text{nom}} \quad (3.1.5a)$$

$$\Delta K_3 = k_3 d^{1-\lambda_3} \Delta \tau_{\text{nom}} \quad (3.1.5b)$$

where d is the notch depth ($d = 6.0$ mm) while k_1 and k_3 are non-dimensional factors derived from FE analysis. They simply represent the shape factors, in analogy with the representation of Linear Elastic Fracture Mechanics.

The harmonic element solid plane 83 of the Ansys® code has been used in the finite element analysis. Taking advantage of the geometric and loading symmetry, it is possible to model only one quarter of the specimen. From the FE models, $k_1 = 1.000$ and $k_3 = 1.154$ have been obtained.

The trend of the Mode III shear stress field, normalized with respect to the nominal shear stress and plotted along the notch bisector line, is shown in Fig. 3.1.14 as a function of the distance from the notch tip. From this figure, it is evident that the stress field is controlled by the first singular term (NSIF) up to a distance from the notch tip equal to about 1.0 mm.

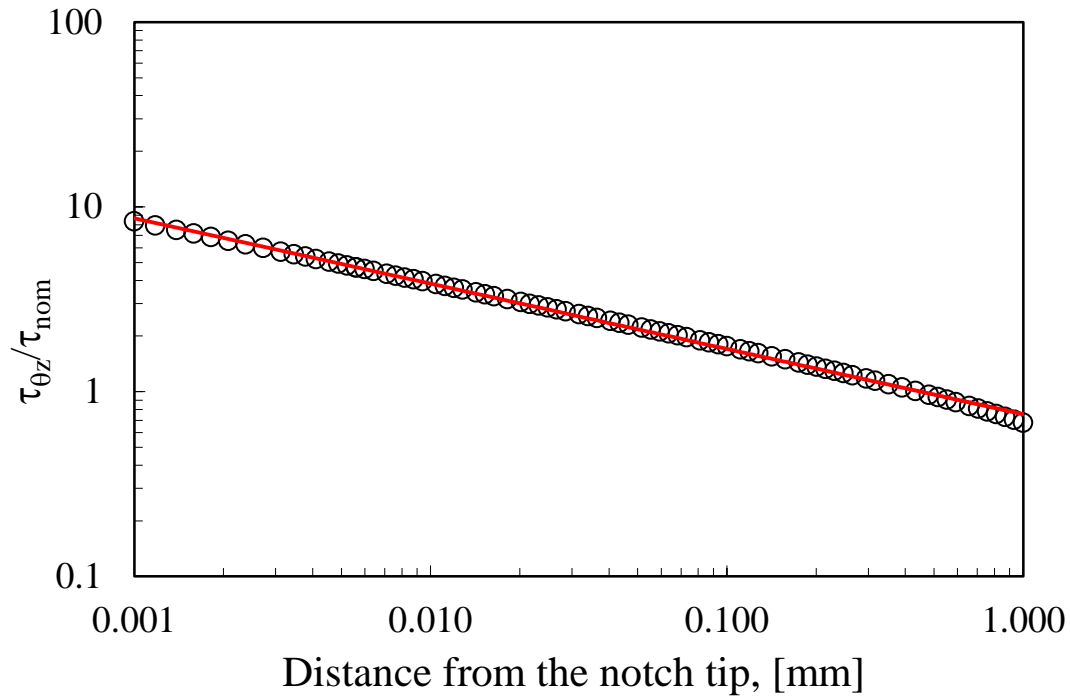


Figure 3.1.14. Local shear stress field along the notch bisector line (Mode III loading).

Substituting the notch depth of the specimens examined here, $d = 6$ mm, in Eqs (3.1.5a) and (3.1.5b), one can obtain:

$$\Delta K_1 = 2.260 \cdot \Delta \sigma_{nom} \quad (\text{in MPa} \cdot \text{mm}^{0.445}) \quad (3.1.6a)$$

$$\Delta K_3 = 2.096 \cdot \Delta \tau_{nom} \quad (\text{in MPa} \cdot \text{mm}^{0.333}) \quad (3.1.6b)$$

Taking into account the range of the nominal stresses at $N_A = 2 \cdot 10^6$ loading cycles relating to V-notched specimens tested under pure tension and pure torsion with a nominal load ratio $R = -1$ (Table 3) and substituting them into the Eqs (3.1.6a) and (3.1.6b), it can be obtained:

$$\Delta K_{1A} = 2.260 \cdot 200 = 452 \text{ MPa} \cdot \text{mm}^{0.445} \quad (3.1.7a)$$

$$\Delta K_{3A} = 2.096 \cdot 580 = 1216 \text{ MPa} \cdot \text{mm}^{0.333} \quad (3.1.7b)$$

In the case of a component weakened by a sharp V-notch and in conditions of linear elasticity, the SED averaged over a control volume, which embraces the notch tip, can be calculated by means of the following expression [29,30]:

$$\Delta\bar{W} = \frac{1}{E} \left[e_1 \cdot \frac{\Delta K_1^2}{R_1^{2(1-\lambda_1)}} + e_3 \cdot \frac{\Delta K_3^2}{R_3^{2(1-\lambda_3)}} \right] \quad (3.1.8)$$

where ΔK_1 and ΔK_3 represent the Mode I and Mode III NSIF ranges, R_1 and R_3 are the radii of the control volume related to Mode I and Mode III loadings, while e_1 and e_3 are two parameters that summarize the dependence on the V-notch geometry [27,29,31].

These parameters are directly linked to the integrals of the angular functions over the control volume, and they can be determined *a priori* by means of closed-form expressions once known the V-notch opening angle. Since the specimens examined here are characterized by a notch opening angle 2α equal to 90 degrees, e_1 and e_3 are equal 0.146 and 0.310, respectively, with the Poisson's ratio $\nu = 0.3$. The use of refined meshes in the close neighborhood of the stress singularity is necessary in the calculation of NSIFs. On the other hand, the SED averaged over a control volume is insensitive to the mesh refinement, and it can be accurately evaluated also by means of coarse meshes because it directly depends on nodal displacements [56,57].

It is possible to estimate the control volume radii described in Figure 3.1.15, R_1 and R_3 , considering separately the loading conditions of Mode I and Mode III. These radii are functions of the high-cycle fatigue strength of smooth specimens, $\Delta\sigma_{1A} = 950$ MPa, $\Delta\tau_{3A} = 776$ MPa, and of the mean values of the NSIFs, ΔK_{1A} and ΔK_{3A} , all referred to the same number of loading cycles, $N_A = 2 \cdot 10^6$:

$$R_1 = \left(\sqrt{2e_1} \cdot \frac{\Delta K_{1A}}{\Delta\sigma_{1A}} \right)^{\frac{1}{1-\lambda_1}} \quad (3.1.9a)$$

$$R_3 = \left(\sqrt{\frac{e_3}{1+\nu}} \cdot \frac{\Delta K_{3A}}{\Delta\tau_{3A}} \right)^{\frac{1}{1-\lambda_3}} \quad (3.1.9b)$$

Eqs 9a and 9b provide as a result: $R_1 = 0.051$ mm and $R_3 = 0.837$ mm. The obtained values are used to summarise all fatigue strength data by means of the averaged SED.

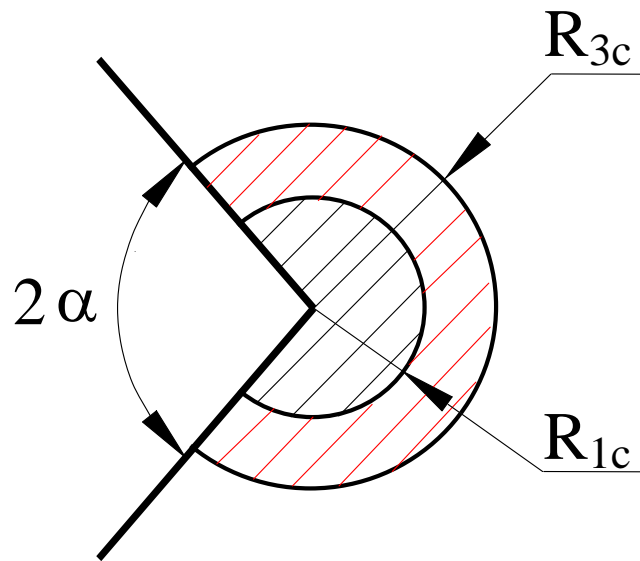


Figure 3.1.15. Control volumes for V-shaped notches under tension and torsion loading.

The expressions for estimating the control radii, thought of as material properties, have been obtained imposing (at N_A loading cycles) the constancy of the SED from smooth and V-notched specimens, which depends on the notch stress intensity factors and the radius of the control volume. Considering instead cracked specimens, the critical NSIFs should be replaced by the threshold values of the stress intensity factors.

In particular, a control volume of radius R_1 is used to evaluate the averaged contribution to local stress and strains due to tensile loading, whereas a radius R_3 is used to assess the averaged contribution due to torsion loading. The size of R_3 radius is highly influenced by the presence of larger plasticity under torsion loading with respect to tensile loading and by friction and rubbing between the crack surfaces, as was discussed extensively for different materials [19,28,34] and more recently investigated under linear elasticity by means of FE analyses taking advantage of free-clamped boundary conditions [58].

With the aim to unify in a single diagram the fatigue data related to different values of the nominal load ratio R , it is necessary to introduce a weighting factor c_w on the basis of mere algebraic considerations. The result of these observations [29,31] provides as master cases $c_w = 1.0$ for $R = 0$ and $c_w = 0.5$ for $R = -1$. The

expression of c_w as a function of the nominal load ratio R is:

$$\begin{cases} \frac{1 + R^2}{(1 - R)^2} & \text{for } -\infty \leq R < 0 \\ 1 & \text{for } R = 0 \\ \frac{1 - R^2}{(1 + R)^2} & \text{for } 0 < R \leq 1 \end{cases} \quad (3.1.10)$$

By applying the weighting factor c_w , the expressions for calculating the strain energy density under linear elasticity, for un-notched specimens (Eqs (3.1.1, 3.1.2)) and for V-notched ones (Eq. (3.1.8)), become:

$$\begin{aligned} SED &= c_w \cdot \overline{\Delta W} \\ &= \begin{cases} c_w \cdot \frac{\Delta \sigma_{nom}^2}{2E} & \text{un - notched specimens} \\ & \text{pure tension} \\ c_w \cdot (1 + \nu) \frac{\Delta \tau_{nom}^2}{E} & \text{un - notched specimens} \\ & \text{pure torsion} \\ \frac{c_w}{E} \left[e_1 \cdot \frac{\Delta K_1^2}{R_1^{2(1-\lambda_1)}} + e_3 \cdot \frac{\Delta K_3^2}{R_3^{2(1-\lambda_3)}} \right] & \text{V - notched specimens} \\ & \text{multiaxial loading} \end{cases} \quad (3.1.11) \end{aligned}$$

Figures 3.1.16 and 3.1.17 show the synthesis by means of local SED of all the experimental data from the fatigue tests at a nominal load ratio $R = 0$ and $R = -1$, respectively. The control radii are $R_1 = 0.051$ mm and $R_3 = 0.837$ mm. The scatterbands have been defined considering the range 10 to 90% for the probability of survival. It can be observed that the inverse slope k equals 5.44 for $R = 0$ case and 5.25 for $R = -1$ case, while the corresponding values of the strain energy density at $2 \cdot 10^6$ loading cycles are 2.72 MJ/m^3 and 2.60 MJ/m^3 . The SED-based scatter index T_w is 1.76 for $R = 0$ and 2.25 for $R = -1$ case, which would become equal to 1.33 and 1.50, respectively, once reconverted *a posteriori* into equivalent stress-based scatter indexes T_σ , by simply making the square root of the SED values. The values of the equivalent scatter index are satisfactory for engineering strength assessment, considering that each synthesis is performed on

fatigue data from un-notched and V-notched specimens under pure tension, pure torsion or combined tension-torsion loading, both in phase and out-of-phase.

Figures 3.1.18 and 3.1.19 show instead the synthesis by means of average SED of all the experimental data from the fatigue tests of un-notched specimens under pure torsion and V-notched samples, respectively. In the case of V-notches two control radii equal to $R_1 = 0.051$ mm and $R_3 = 0.837$ mm respectively have been used. It can be observed that the inverse slope k of the scatterbands equals 11.10 for un-notched specimens under pure torsion and 5.86 for V-notched ones, while the values of the strain energy density at $2 \cdot 10^6$ cycles are equal to 3.95 MJ/m^3 and 3.09 MJ/m^3 , respectively. In this case T_W equals 1.82 for un-notched specimens under pure torsion and 2.20 for V-notched ones, which would give 1.35 and 1.48, respectively, once reconverted *a posteriori* into equivalent stress-based scatter indexes T_σ . Also in this case the values of the scatter index are very satisfactory, given that each synthesis is based on fatigue data respectively from un-notched specimens under pure torsion with different values of the load ratio and from V-notched specimens under pure tension, pure torsion or combined tension-torsion loading, with different values both of the load ratio and the phase angle.

Finally, Figure 3.1.20 shows the synthesis in terms of SED of all the fatigue strength data presented here. Again two different control radii equal to $R_1 = 0.051$ mm and $R_3 = 0.837$ mm respectively have been adopted. The scatterband includes all the data from un-notched and V-notched specimens under pure tension, pure torsion and multiaxial loading, regardless of the load ratio and the phase angle. It is also characterized by an inverse slope k equal to 5.90, a scatter index $T_W = 2.5$ and a value of the strain energy density at the reference number of loading cycles, $N_A = 2 \cdot 10^6$, that equals 3.08 MJ/m^3 . The equivalent stress-based scatter index T_σ results to be 1.58, that is comparable with that observed in the Haibach scatterband ($T_\sigma = 1.50$).

From the comparison between Figure 3.1.20 and Figures 3.1.4-3.1.7, based on nominal stresses at the net area, the unifying capacity of the SED approach can easily be observed, in fact, it is capable of synthesize all the fatigue strength data in a single quite-narrow scatterband regardless of the loading mode and the specimens geometry.

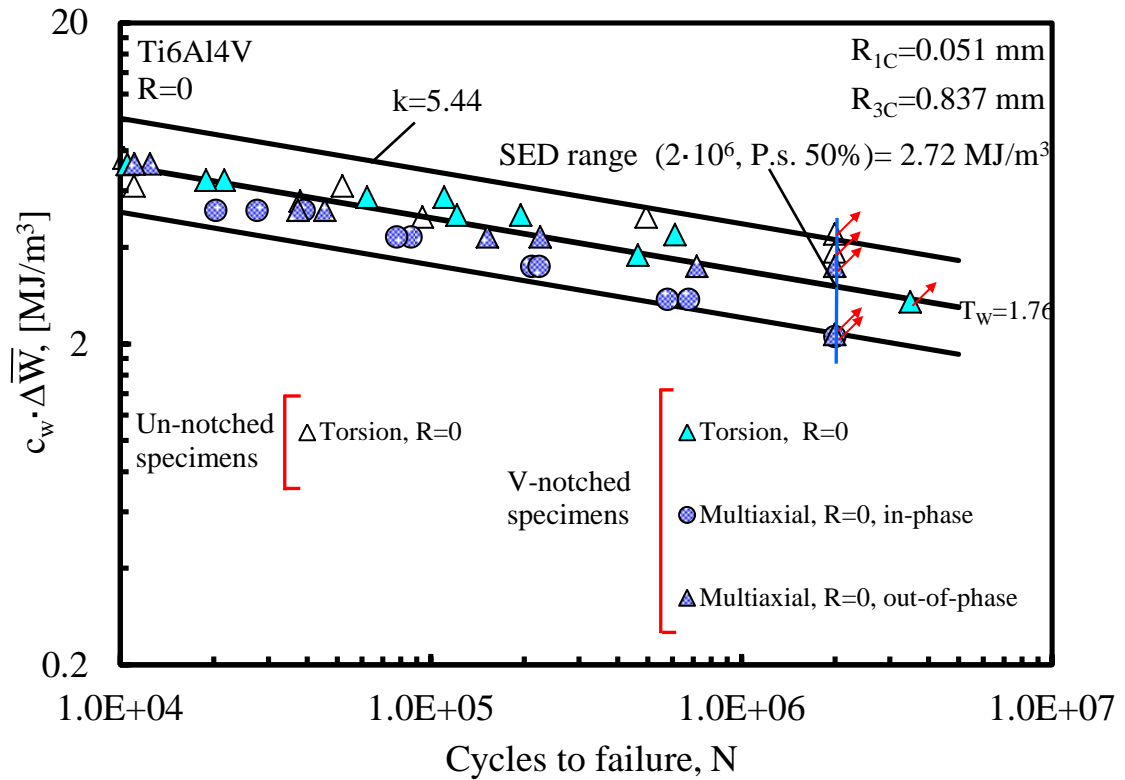


Figure 3.1.16. Synthesis by means of local SED of series data with R = 0.

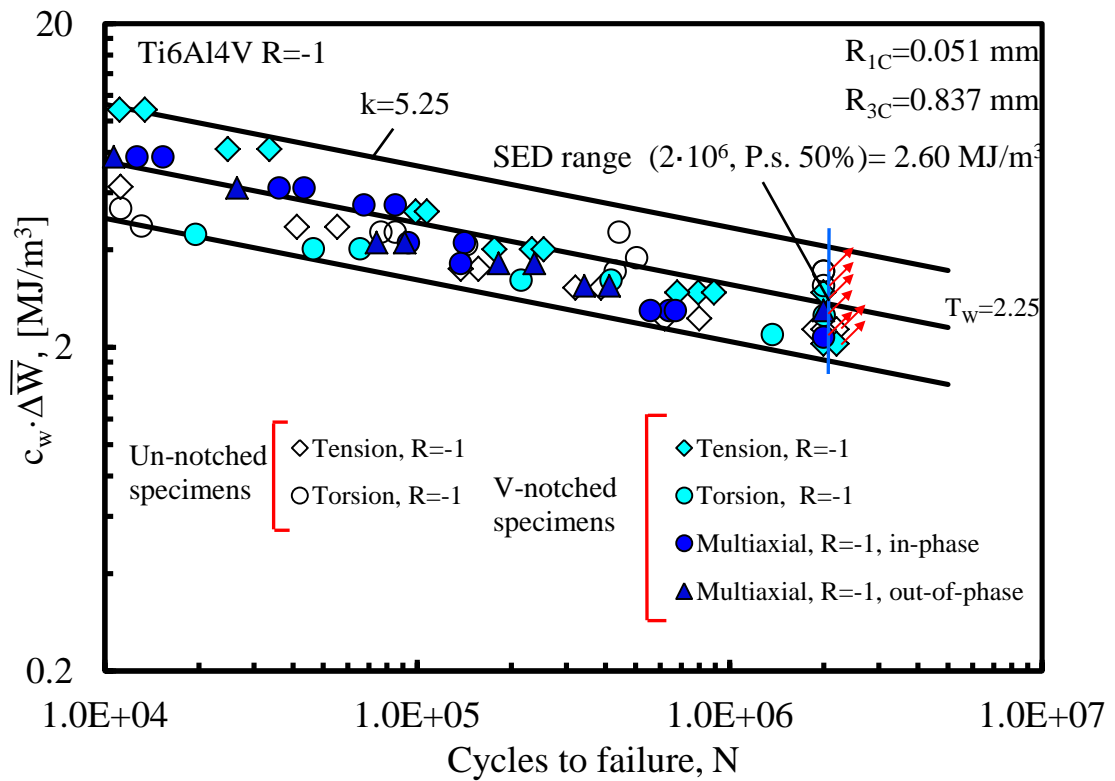


Figure 3.1.17. Synthesis by means of local SED of series data with R = -1.

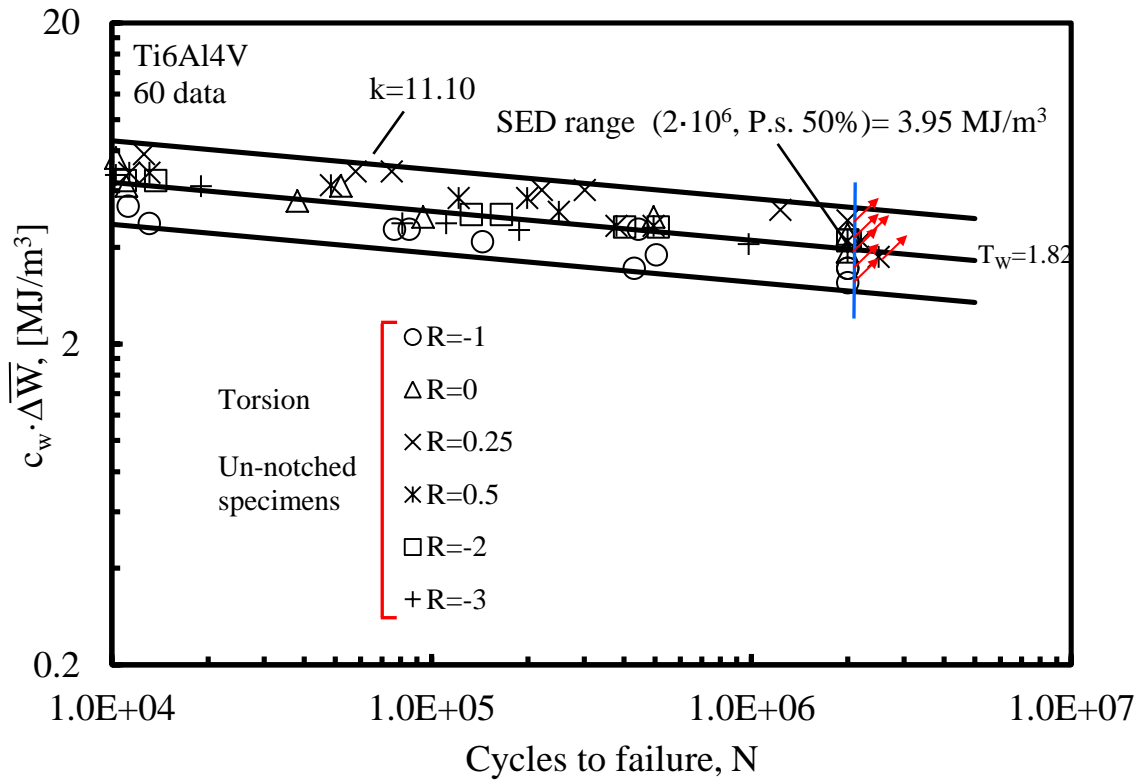


Figure 3.1.18. Synthesis by means of local SED of un-notched specimens data under pure torsion.

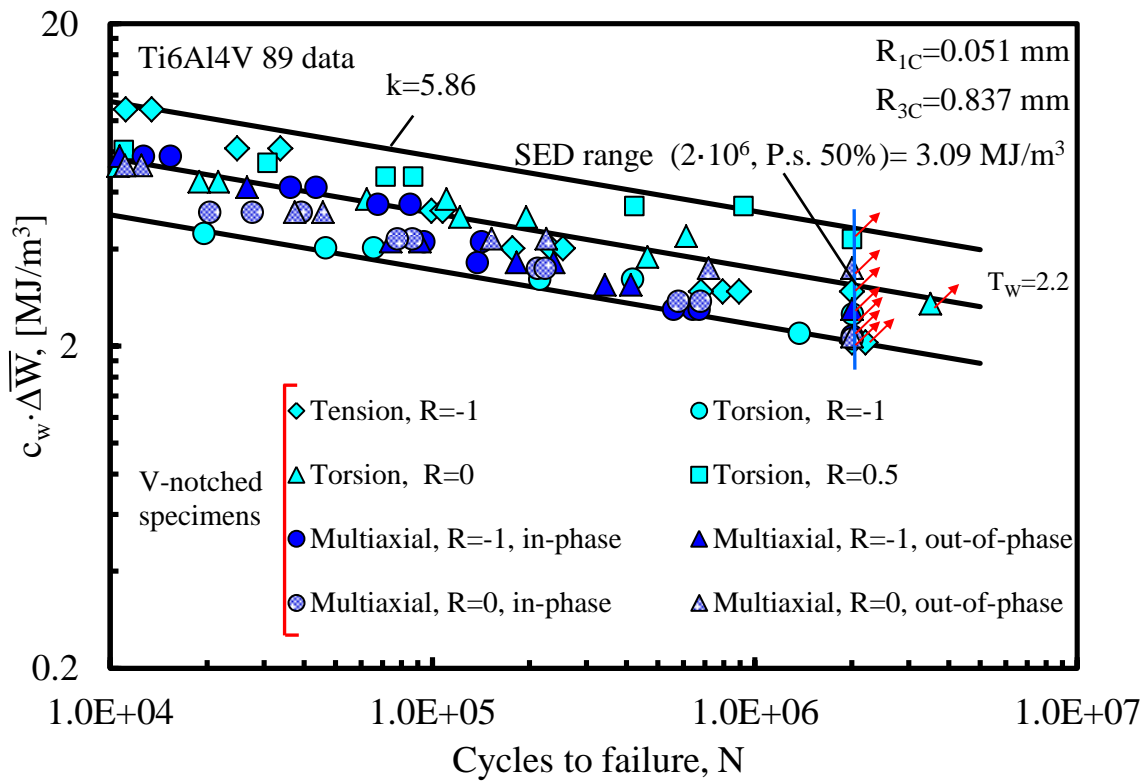


Figure 3.1.19. Synthesis by means of local SED of V-notched specimens data.

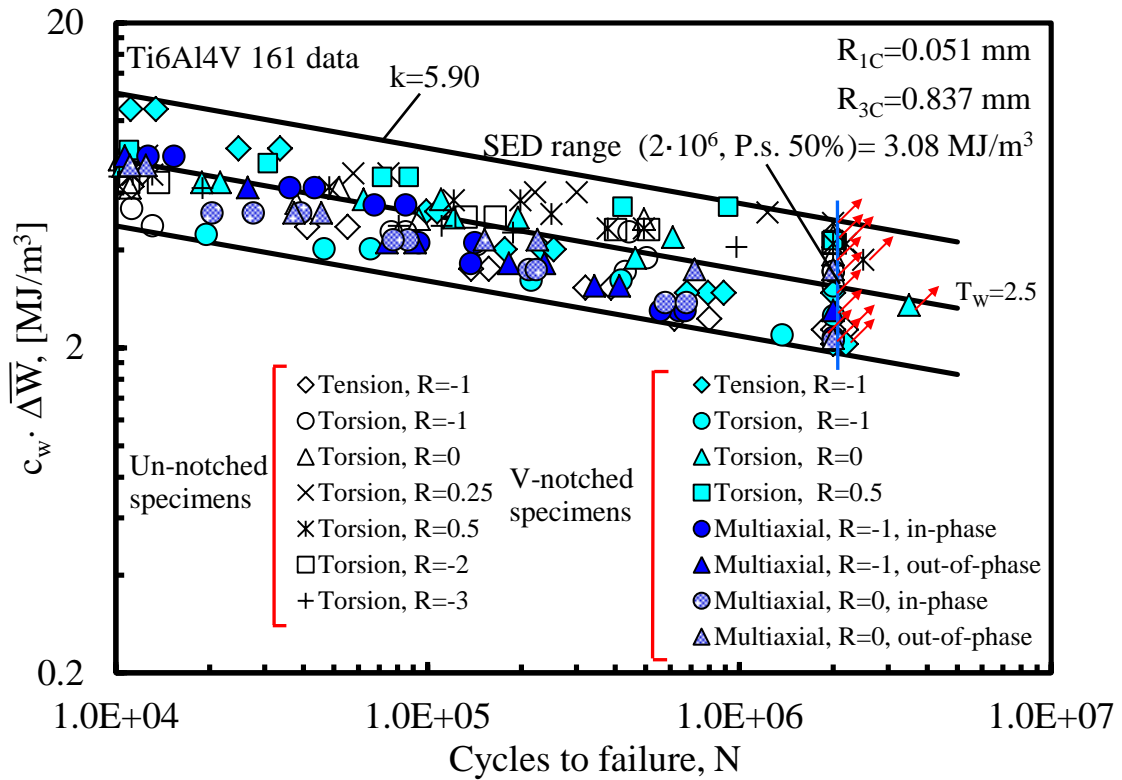


Figure 3.1.20. Synthesis by means of local SED of un-notched and V-notched specimens data.

3.1.6 Discussion

A complete experimental program has been carried out providing a large number of fatigue data referred to axis-symmetric V-notched specimens made of titanium alloy (Ti-6Al-4V, grade 5). The tests have been performed under combined Mode I and Mode III loadings with a proportional and non-proportional loading path. They have been compared with data from plain and V-notched samples under pure tension and pure torsion loading.

A total of over 160 new fatigue data (15 Wöhler curves) have been reported and discussed. First, all fatigue data have been plotted as a function of the nominal stress amplitudes and then reanalysed by using the local SED measured over a control volume embracing the notch flanks. For the titanium alloy Ti-6Al-4V, a different size of the control volume under Mode I and Mode III loadings has been found to be suitable to summarise the fatigue data.

The synthesis based on the local SED allows us to get a quite limited scatter-band ($T_w = 2.5$) considering all the data from V-notched and smooth samples under pure Mode I, pure Mode III and combined Mode I+III loadings, independent of the ratio, R , and the phase angle Φ .

3.2 Fatigue strength of welded joints – Industrial case study: steel rollers ^(*)

Nomenclature

c	length of the lack of penetration
e_1, e_2, e_3	parameters for the determination of the strain energy density (SED)
E	elastic modulus
k	inverse slope of the fatigue curves
K_1^N, K_2^N, K_3^N	mode I, mode II and mode III Notch Stress Intensity Factors (NSIFs)
ΔK_{IA}^N	NSIF-based fatigue strength of transverse non-load carrying fillet welded joints with $2\alpha = 135$ degrees at the weld toe
N_A	reference number of cycles
N_f	number of cycles to failure
R	load ratio (ratio between the minimum and the maximum applied load)
R_c	radius of the structural volume where local stresses are averaged
r, θ	polar coordinates
T_w	strain energy-based scatter index (for 2.3-97.7% probabilities of survival)
\bar{W}	Average Strain Energy Density (SED) over the control volumes

Symbols

2α	V-notch opening angle
Δ	range of the considered quantity
$\lambda_1, \lambda_2, \lambda_3$	mode I, mode II and mode III eigenvalues
ν	Poisson's ratio

$\Delta\sigma_A$	fatigue strength of butt ground welded joints at N_A cycles to failure
$\sigma_{\theta\theta}, \tau_{r\theta}$	normal and shear stress components in the polar frame of reference
σ_y	yield strength
$\tau_{z\theta}, \tau_{zr}$	mode III stress components in the polar frame of reference
ρ	radius at the weld root or toe
χ_1, χ_2	parameters for mode I and mode II stress distributions

(*) See also:

Berto, F.; Campagnolo, A.; Chebat, F.; Cincera, M.; Santini, M. Fatigue strength of steel rollers with failure occurring at the weld root based on the local strain energy values: modelling and fatigue assessment. *International Journal of Fatigue*; 82:643-657 (2016);

3.2.1. Introduction

Weld bead geometry cannot be precisely defined mainly because parameters such as bead shape, toe or root radius and length of lack of penetration vary from joint to joint even in well-controlled manufacturing operations [59,60]. It is, in fact well known that, the weld toe radius decreases with the local heat concentration of the welding process, i.e. it is extremely small for automated high-power processes, especially for laser beam welding. Since also conventional arc welding techniques result in small values of toe radius [61], in the Notch Stress Intensity Factor (NSIF) approach the weld toe region is modelled as a sharp notch and local stresses are given on the basis of the relevant mode I and mode II NSIFs [61,62]. When the opening angle at the weld toe is large enough to result in a non-singular contribution for stress components due to the mode II the fatigue behaviour can be correlated only to mode I NSIF [62]. A comparison among different steel welded joints can be performed on the basis of the relevant theoretical stress concentration factors, after having imposed a fictitious notch radius $\rho_f = 1.0$ mm. This value is valid only if the real radius at the weld toes and roots is thought of as zero [55]. Fatigue failure is generally characterized by the nucleation and growth

of cracks. As widely discussed in the previous literature, the differentiation of two stages is “qualitatively distinguishable but quantitatively ambiguous” [63]. In this context NSIFs are adequate to describe crack initiation at sharp corner notches, as stress intensity factors (SIFs) do at crack-like notches. However, it was observed experimentally that NSIFs can also be used to correlate the total fatigue life [64–67], due to cracks traversing the plate thickness of small size welded details. This is explained by the fact that a large amount of the fatigue life is spent for the initiation of a short crack in a zone governed by the V-notch singularity at the weld toe or root. Different set of experimental data proved this behaviour. Dealing with transverse non-load-carrying fillet welded joints Lassen [68] demonstrated that for various welding procedures, up to 40 percent of fatigue life was spent to nucleate a crack having a length of just 0.1 mm. Singh et al. [69,70] showed by testing load-carrying fillet joints in AISI 304L that the number of cycles required for the crack to grow by 0.5 mm in excess of the original lack of penetration reached 70 percent of the total life.

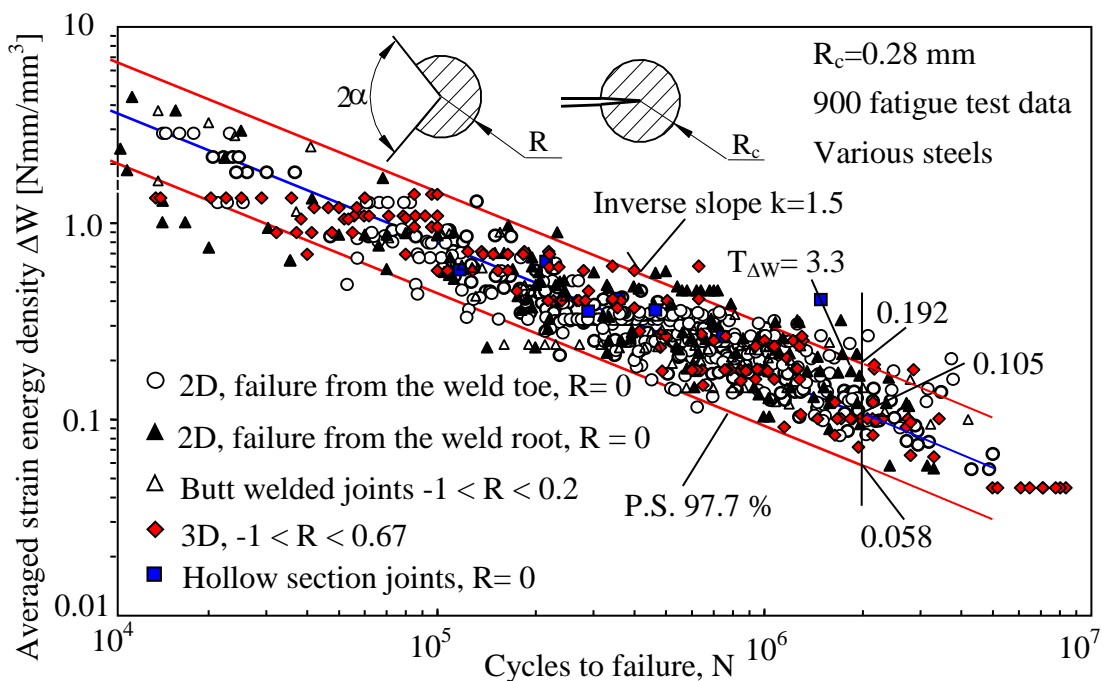


Figure 3.2.1. Fatigue strength of welded joints as a function of the averaged local strain energy density; R is the nominal load ratio.

From a theoretical point of view the NSIF-based approach cannot be applied to

joints characterized by weld flank angles very different from 135 degrees or for comparing failures at the weld root ($2\alpha = 0^\circ$) or weld toe ($2\alpha = 135^\circ$). That is simply because units for mode I NSIF are $\text{MPa}(\text{m})^\beta$, where the exponent β depends on the V-notch angle, according to the expression $\beta = 1 - \lambda_1$, λ_1 being Williams' eigenvalue [71]. This problem has been overcome by Lazzarin and co-authors in some recent papers [27,29,72] by using the mean value of the strain energy density range (SER) present in a control volume of radius R_c surrounding the weld toe or the weld root (see Figure 3.2.1). SER was given in closed form as a function of the relevant NSIFs, whereas R_c was thought of as dependent on welded material properties. The approach, reminiscent of Neuber "elementary volume" concept, was later applied to welded joints under multiaxial load conditions [29].

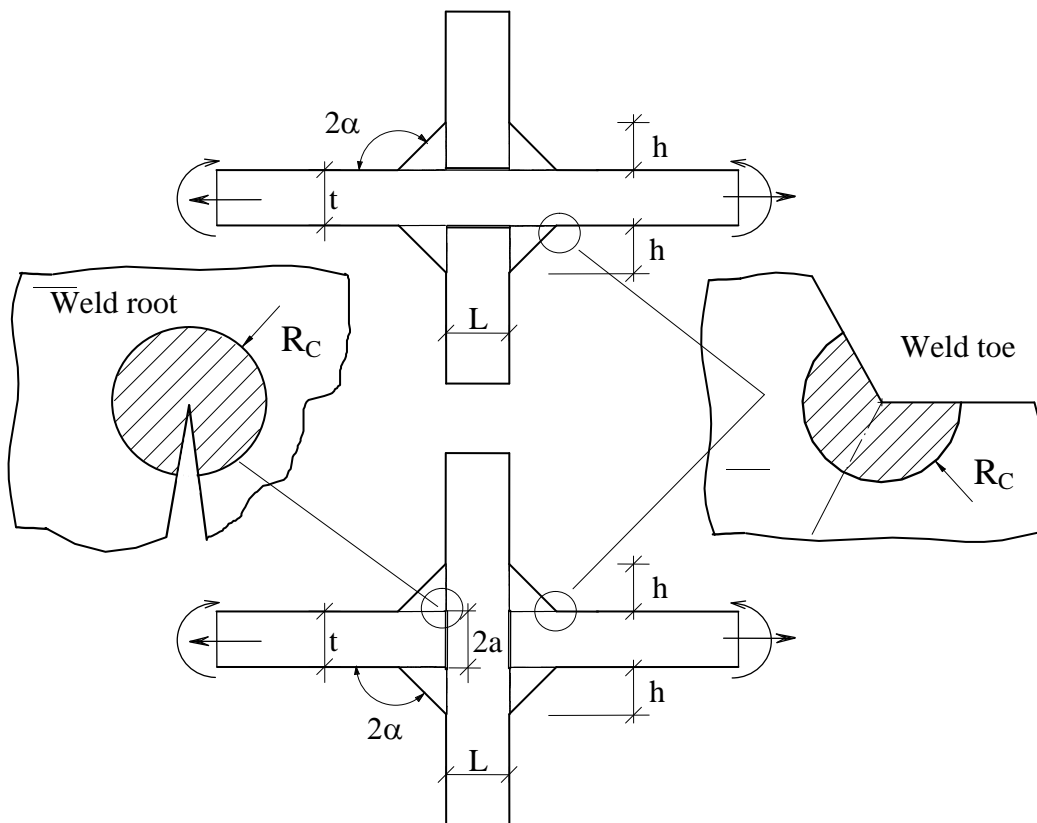


Figure 3.2.2. Geometrical parameters and critical volume (area) at the weld toes or roots.

The simple volume shown in Figure 3.2.2 is not so different from that already drawn by Sheppard [73] while proposing a volume criterion based on local

stresses to predict fatigue limits of notched components. Some analogies exist also with the highly stressed volume (the region where 90% of the maximum notch stress is exceeded) proposed by Sonsino dealing with high cycle strength of welded joints [74]. Finally it is useful to remember that the Theory of Critical Distances (TCDs) encloses some approaches, widely used in the literature and based again on Neuber “elementary volume” concept by using a characteristic material length parameter when performing fracture assessments on any kind of stress risers. The origins and the basis of the TCD can be found in Refs. [75–81]. Recently Susmel and Taylor have suggested and applied some critical distance methods, the ‘point method’, the ‘line method’ and the ‘area method’ for predicting high cycle fatigue of welded joints [60,82–85]. The three methods are to be seen as simplifications of a more generalized volume method, which coincides with the area method in plane problems. In the ‘area method’, Taylor uses the average stress in an area of circular form surrounding the point of maximum stress. With reference to welds fabricated from a low carbon steel, the local radius, evaluated experimentally by Taylor et al. [60], was 0.43 mm. For a given nominal load ratio, such a radius does depend only on the material.

The same based on energy approach has been employed here for the fatigue assessment of rollers (see for example Fig. 3.2.3) made by Rulmecca with failure occurring at the weld root.

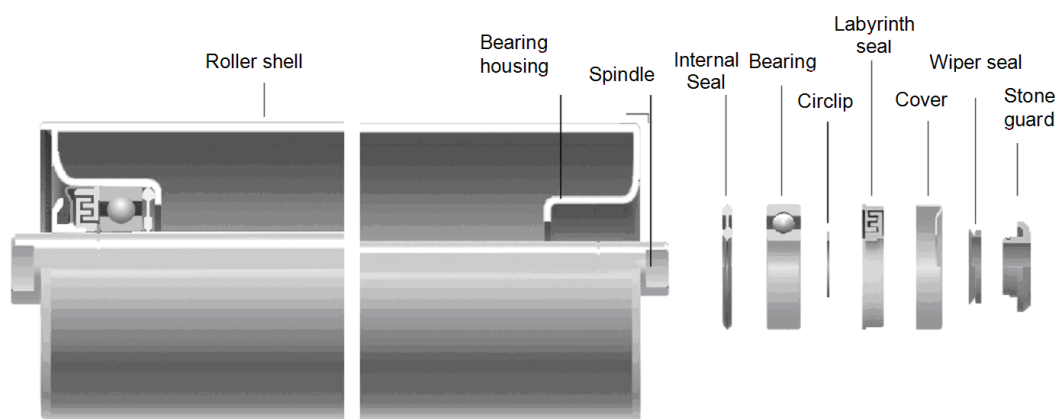


Figure 3.2.3. Typical roller assembly

The rollers considered in the present investigation belong to the category PSV which is particularly suited to conveyors that operate in very difficult conditions, where working loads are high, and large lump size material is conveyed; and yet, despite these characteristics, they require minimal maintenance. The bearing housings of the PSV series are welded to the tube body using auto-centralising automatic welding machines utilizing a continuous wire feed.

From the point of view of the fatigue behavior under load, the weakest point of the entire structure is the lack of penetration of the weld root. Therefore, if the roller is loaded well above its declared nominal admitted load [86] it would experience fatigue failure starting at the level of the weld root.

The aims of the present work are:

- to describe the procedure for modelling the roller by using the finite element method combined with three-dimensional analyses; the procedure will be shown in detail for a particular roller geometry named PSV4;
- to show the procedure for evaluating the local parameters in the zone close to the lack of penetration at the weld root;
- to describe the sensitivity of the model to the length of the lack of penetration;
- to show the procedure for evaluating the SED in a control volume surrounding the crack tip in a real component describing the trend of the SED in a three-dimensional model;
- to verify if a scatter band $\Delta\bar{W}$ -N (strain energy range – number of cycles to failure) summarising about 1200 fatigue data from welded joints with the majority of failures originated from the weld toes can be applied also to welded joints with failures from the weld roots and in particular to the considered rollers;
- with reference to the just mentioned point some preliminary fatigue tests from two different geometries belonging to the family of rollers called PSV4 and characterized by a different length, have been carried out and summarised here by means of local SED.

The main novelty of this work is related to the application of the SED approach to welded joints of small thickness, indeed the scatterband in terms of local strain energy density (SED) for welded joints made of structural steel, Fig. 3.2.1, has been calibrated in some previous works by fitting experimental data taken from the literature and relevant mainly to thick welded joints (thickness greater than 5 mm). Some new fatigue tests have been conducted on two different geometries of rollers, in order to compare the experimental results with the theoretical predictions based on the proposed SED approach.

3.2.2. Approach based on the local SED: analytical preliminaries

The degree of the singularity of the stress fields due to re-entrant corners was established by Williams both for mode I and mode II loading [71]. When the weld toe radius ρ is set to zero, NSIFs quantify the intensity of the asymptotic stress distributions in the close neighbourhood of the notch tip. By using a polar coordinate system (r, θ) having its origin located at the sharp notch tip, the NSIFs related to mode I and mode II stress distribution are [54]

$$K_1^N = \sqrt{2\pi} \lim_{r \rightarrow 0^+} r^{1-\lambda_1} \sigma_{\theta\theta}(r, \theta = 0) \quad (3.2.1)$$

$$K_2^N = \sqrt{2\pi} \lim_{r \rightarrow 0^+} r^{1-\lambda_2} \tau_{r\theta}(r, \theta = 0) \quad (3.2.2)$$

where the stress components $\sigma_{\theta\theta}$ and $\tau_{r\theta}$ have to be evaluated along the notch bisector ($\theta = 0$).

Dealing with mode III loading an extension of the definition proposed by Gross and Mendelson [54] has been carried out in [87,88]:

$$K_3^N = \sqrt{2\pi} \lim_{r \rightarrow 0^+} r^{1-\lambda_3} \tau_{\theta z}(r, \theta = 0) \quad (3.2.3)$$

By means of Eqs. (3.2.1, 3.2.2), it is possible to present Williams' formulae for stress components as explicit functions of the NSIFs. Then, mode I stress distribution is [89]:

$$\left. \begin{matrix} \sigma_{\theta\theta} \\ \sigma_{rr} \\ \tau_{r\theta} \end{matrix} \right|_{\rho=0} = \frac{1}{\sqrt{2\pi}} \frac{r^{\lambda_1-1} K_1^N}{(1+\lambda_1) + \chi_1(1-\lambda_1)} \cdot \left[\begin{matrix} (1+\lambda_1) \cos(1-\lambda_1)\theta \\ (3-\lambda_1) \cos(1-\lambda_1)\theta \\ (1-\lambda_1) \sin(1-\lambda_1)\theta \end{matrix} \right] + \chi_1(1-\lambda_1) \left[\begin{matrix} \cos(1+\lambda_1)\theta \\ -\cos(1+\lambda_1)\theta \\ \sin(1+\lambda_1)\theta \end{matrix} \right] \quad (3.2.4)$$

Mode II stress distribution is:

$$\left. \begin{matrix} \sigma_{\theta\theta} \\ \sigma_{rr} \\ \tau_{r\theta} \end{matrix} \right|_{\rho=0} = \frac{1}{\sqrt{2\pi}} \frac{r^{\lambda_2-1} K_2^N}{(1-\lambda_2) + \chi_2(1+\lambda_2)} \cdot \left[\begin{matrix} -(1+\lambda_2) \sin(1-\lambda_2)\theta \\ -(3-\lambda_2) \sin(1-\lambda_2)\theta \\ (1-\lambda_2) \cos(1-\lambda_2)\theta \end{matrix} \right] + \chi_2(1+\lambda_2) \left[\begin{matrix} -\sin(1+\lambda_2)\theta \\ \sin(1+\lambda_2)\theta \\ \cos(1+\lambda_2)\theta \end{matrix} \right] \quad (3.2.5)$$

Mode III stress distribution is:

$$\begin{aligned} \tau_{zr} &= \frac{K_3^N}{\sqrt{2\pi}} r^{\lambda_3-1} \sin(\lambda_3\theta) \\ \tau_{z\theta} &= \frac{K_3^N}{\sqrt{2\pi}} r^{\lambda_3-1} \cos(\lambda_3\theta) \end{aligned} \quad (3.2.6)$$

With reference to some typical V-notch angles, Table 3.2.1 gives the parameters λ and χ for mode I and mode II stress distributions [89]. Table 3.2.2 provides the main parameters [90] for the application of Eq. (3.2.6).

Table 3.2.1. Parameters as functions of the V-notch angle. Coefficients e_1 and e_2 for plane strain conditions and Poisson's ratio $\nu=0.3$.

2α [rad]	Mode I			Mode II		
	λ_1	χ_1	e_1	λ_2	χ_2	e_2
0	0.500	1.000	0.133	0.500	1.000	0.340
$\pi/6$	0.501	1.071	0.147	0.598	0.921	0.274
$\pi/4$	0.505	1.166	0.150	0.660	0.814	0.244
$\pi/3$	0.512	1.312	0.151	0.731	0.658	0.217
$\pi/2$	0.544	1.841	0.145	0.909	0.219	0.168
$2\pi/3$	0.616	3.003	0.129	1.149	-0.314	0.128
$3\pi/4$	0.674	4.153	0.118	1.302	-0.569	0.111
$5\pi/6$	0.752	6.362	0.104	1.486	-0.787	0.096

Table 3.2.2. Parameters as functions of the V-notch angle. Coefficients e_3 for axis-symmetric components.

2α [rad]	γ [rad]	λ_3	e_3
0	π	0.5000	0.41380
$\pi/12$	$23\pi/24$	0.5217	0.39659
$\pi/6$	$11\pi/12$	0.5455	0.37929
$\pi/3$	$5\pi/6$	0.6000	0.34484
$\pi/2$	$3\pi/4$	0.6667	0.31034
$2\pi/3$	$2\pi/3$	0.7500	0.27587
$3\pi/4$	$5\pi/8$	0.8000	0.25863

All stress and strain components in the highly stressed region are correlated to mode I, mode II and mode III NSIFs. Under plane strain hypothesis, the strain energy included in a semicircular sector shown in Figure 3.2.2 is [27,91]:

$$\Delta\bar{W} = \frac{e_1}{E} \left[\frac{\Delta K_1^N}{R_c^{1-\lambda_1}} \right]^2 + \frac{e_2}{E} \left[\frac{\Delta K_2^N}{R_c^{1-\lambda_2}} \right]^2 + \frac{e_3}{E} \left[\frac{\Delta K_3^N}{R_c^{1-\lambda_3}} \right]^2 \quad (3.2.7)$$

where R_c is the radius of the semicircular sector and e_1 , e_2 are functions that depend on the opening angle 2α and on the Poisson's ratio ν , while e_3 depends only on the notch opening angle (see Tables 3.2.1 and 3.2.2). A rapid calculation, with $\nu = 0.3$, can be made for e_1 and e_2 by using the following expressions [27]:

$$e_1 = -5.373 \cdot 10^{-6} (2\alpha)^2 + 6.151 \cdot 10^{-4} (2\alpha) + 0.1330 \quad (3.2.8)$$

$$e_2 = 4.809 \cdot 10^{-6} (2\alpha)^2 - 2.346 \cdot 10^{-3} (2\alpha) + 0.3400 \quad (3.2.9)$$

where 2α is in degrees.

Dealing with failures originated at the crack tip (i.e. weld root) Eq. (3.2.7) can be simplified as follows:

$$\Delta \bar{W} = \frac{1}{ER_c} [e_1 \Delta K_1^2 + e_2 \Delta K_2^2 + e_3 \Delta K_3^2] \quad (3.2.10)$$

The material parameter R_c can be estimated by using the fatigue strength $\Delta\sigma_A$ of the butt ground welded joints (in order to quantify the influence of the welding process, in the absence of any stress concentration effect) and the NSIF-based fatigue strength of welded joints having a V-notch angle at the weld toe constant and large enough to ensure the non singularity of mode II stress distributions.

A convenient expression is [27]:

$$R_c = \left(\frac{\sqrt{2e_1} \Delta K_{IA}^N}{\Delta\sigma_A} \right)^{\frac{1}{1-\lambda_1}} \quad (3.2.11)$$

where both λ_1 and e_1 depend on the V-notch angle. Eq. (3.2.11) will be applied in the next sections taking into account the experimental value ΔK_{IA}^N at 5 million cycles related to transverse non-load carrying fillet welded joints with $2\alpha = 135$ degrees at the weld toe.

The hypothesis of constancy of R_c under mixed mode loads had been validated by Lazzarin and Zambardi [27] by using experimental data mainly provided by Seweryn et al. [92] and Kihara and Yoshii [93].

From a theoretical point of view the material properties in the vicinity of the weld toes and the weld roots depend on a number of parameters as residual stresses and distortions, heterogeneous metallurgical micro-structures, weld thermal cycles, heat source characteristics, load histories and so on. To devise a model capable of predicting R_c and fatigue life of welded components on the basis of all these

parameters is really a task too complex. Thus, the spirit of this approach is to give a simplified method able to summarise the fatigue life of components only on the basis of geometrical information, treating all the other effects only in statistical terms, with reference to a well-defined group of welded materials and, for the time being, to arc welding processes. Eq. (3.2.11) makes it possible to estimate the R_c value as soon as ΔK_{IA}^N and $\Delta\sigma_A$ are known.

At $N_A = 5 \cdot 10^6$ cycles and in the presence of a nominal load ratio R equal to zero, a mean value ΔK_{IA}^N equal to $211 \text{ MPa mm}^{0.326}$ can be assumed [72]. For butt ground welds made of ferritic steels Atzori and Dattoma [94] found a mean value $\Delta\sigma_A = 155 \text{ MPa}$ (at $N_A = 5 \cdot 10^6$ cycles, with $R = 0$). That value is in very good agreement with $\Delta\sigma_A = 153 \text{ MPa}$ recently obtained by Taylor et al. [60] by testing butt ground welds fabricated of a low carbon steel. Then, by introducing the above mentioned value into Eq. (3.2.11), one obtains for steel welded joints with failures from the weld toe $R_c = 0.28 \text{ mm}$. The choice of 5 million cycles as a reference value is due mainly to the fact that, according to Eurocode 3, nominal stress ranges corresponding to 5 million cycles can be considered as fatigue limits under constant amplitude load histories. It is worth noting that the simplified hypothesis of a semicircular core of radius R_c led to the assessment of a fatigue scatter band that exactly agreed with that of Haibach's normalised S-N band [95].

In the case $2\alpha = 0$ and fatigue crack initiation at the weld root Eq. (3.2.11) gives $R_c = 0.36 \text{ mm}$, by neglecting the mode II contribution and using $e_1 = 0.133$, Eq. (3.2.8), $\Delta K_{IA}^N = 180 \text{ MPa mm}^{0.5}$ and, once again, $\Delta\sigma_A = 155 \text{ MPa}$. There is a small difference with respect to the value previously determined, $R_c = 0.28 \text{ mm}$. However, in the safe direction, the proposal is to use $R_c = 0.28 \text{ mm}$ also for the welded joints with failures from the weld roots which is the case considered here.

As opposed to the direct evaluation of the NSIFs, which needs very refined meshes, the mean value of the elastic SED on the control volume can be determined with high accuracy by using coarse meshes [56,57,96] and directly takes into account the three-dimensional effects well described in [97–100]. Very refined meshes are necessary to directly determine the NSIFs from the local stress distributions. Refined meshes are not necessary when the aim of the finite

element analysis is to determine the mean value of the local strain energy density on a control volume surrounding the points of stress singularity. The SED in fact can be derived directly from nodal displacements, so that also coarse meshes are able to give sufficiently accurate values for it. Some recent contributions document the weak variability of the SED as determined from very refined meshes and coarse meshes, considering some typical welded joint geometries and provide a theoretical justification to the weak dependence exhibited by the mean value of the local SED when evaluated over a control volume centred at the weld root or the weld toe. On the contrary singular stress distributions are strongly mesh dependent. This is a strong advantage of the SED approach in comparison with stress based criteria in particular when real three-dimensional structures have to be modeled.

3.2.3. Modelling of the rollers and evaluation of the local SED

3.2.3.1 Description of the rollers

The rollers considered in the present investigation belong to the series PSV which offer the highest quality and the maximum load capacity of Rulmeca's production (see Figure 3.2.3) [86].

Rollers PSV are particularly suited to conveyors that operate in very difficult conditions, where working loads are high, and large lump size material is conveyed; and yet, despite these characteristics, they require minimal maintenance. Typical types of application are: mines, caves, cement works, coal-fired electric utilities and dock installations. The effectiveness of the PSV roller sealing system provides the solution to the environmental challenges of dust, dirt, water, low and high temperatures.

Roller is made of the following main components:

- A mantel, constituted by a tube cut and machined using automatic numerically controlled machines, that guarantee and maintain the tolerances and the precision of the square cut.

- Two bearing housing made by a steel monolithic structure (in agreement with UNI EN 10111 characterized by a yield strength $170 < \sigma_y < 330$ MPa), deep drawn and sized to a forced fixed tolerance (ISO M7) at the bearing position. The thickness of the housings is proportional to the spindle diameter and to the bearing type, with thicknesses that are up to 5 mm, to guarantee the maximum strength for each application, including the heaviest.
- A spindle which sustains the roller when it is assembled into the troughing set supports. It is made from drawn steel, cut and machined by automatic numerically controlled machines. The spindle is ground to a precision tolerance, to guarantee a perfect match of bearings, seals. Spindle tolerance, together with bearing housing tolerances, functionally guarantees the autoalignment of the internal and outer bearing rings of the ball race resulting in a good performance even when the spindle deflection is extreme due to overloading.
- The seals components, which are meant to protect the bearing from harmful elements that may impinge from the outside or the inside of the roller, made of three main sections:
 - 1) external section: made of an external stone guard, a lip ring made from soft anti-abrasive rubber with a large contact surface onto a metal cover cap; that forms a self-cleaning stage of seal in that it centrifugally repels water and dust naturally towards the outside;
 - 2) outward bearing protection: triple lip labyrinth in nylon PA6 greased to give further bearing protection;
 - 3) inward bearing protection, made of a sealing ring in nylon PA6 is positioned that provides an ample grease reservoir and also retains the grease near to the bearing even when there is a depression due to an abrupt change in temperature (pumping effect).

- Locking system: provided by means of the correctly located cir-clip, which is the most effective and the strongest system implemented in heavy rollers for belt conveyors.

3.2.3.2 Feature and geometry under investigation

The feature under investigation is the joint between tube and bearing housing.

The bearing housings of the PSV rollers are welded to the tube body using autocentring automatic welding machines utilising a continuous wire feed. The weldments have been executed by applying the metal-arc inert gas (MIG) welding process with the shielding gas Ar + 8% CO₂. As filler material a 0.8 mm diameter wire has been used with an average wire feed rate equal to 18 mm/min. The welding voltage and the welding current have been set equal to 23 V and 240 A, respectively.

Tube and bearing housing form a monolithic structure of exceptional strength which itself reduces to the minimum any imbalance in the roller. This guarantees the alignment and concentricity with respect to the external diameter of the component parts of the sealing system. The optimum balance and concentricity thus obtained allows these rollers to be used at the highest speeds, eliminating harmful vibration to the conveyor structure and the “hammer effect” on the bearings of the rollers.

From the point of view of the fatigue behavior under loading, the weakest point of the entire structure is the lack of penetration of the weld root. Therefore, if the roller is loaded well above its declared nominal admitted load [86] it would experience fatigue failure starting at the level of the weld root. A detail of the weld root is shown in Figure 3.2.4, where the lack of penetration length is indicated as *c*.

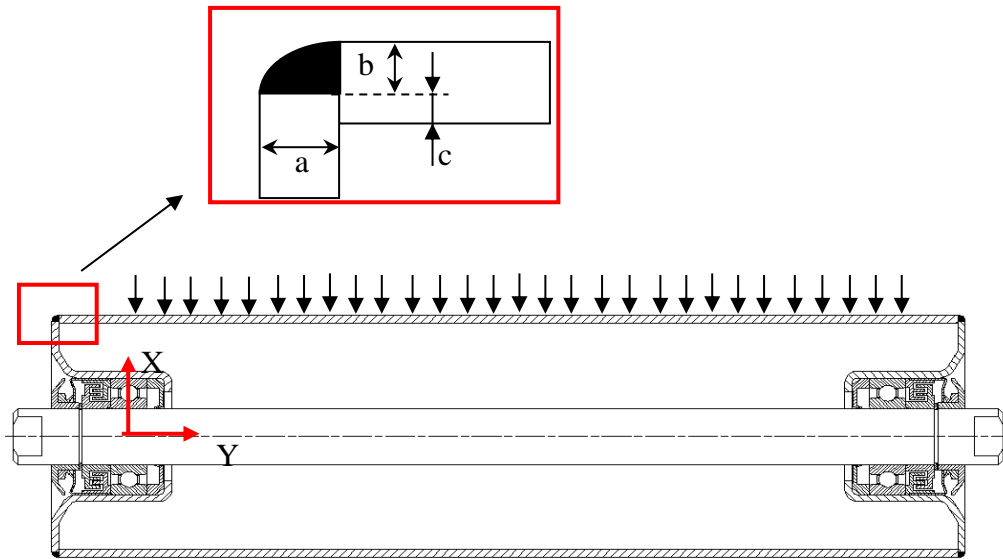
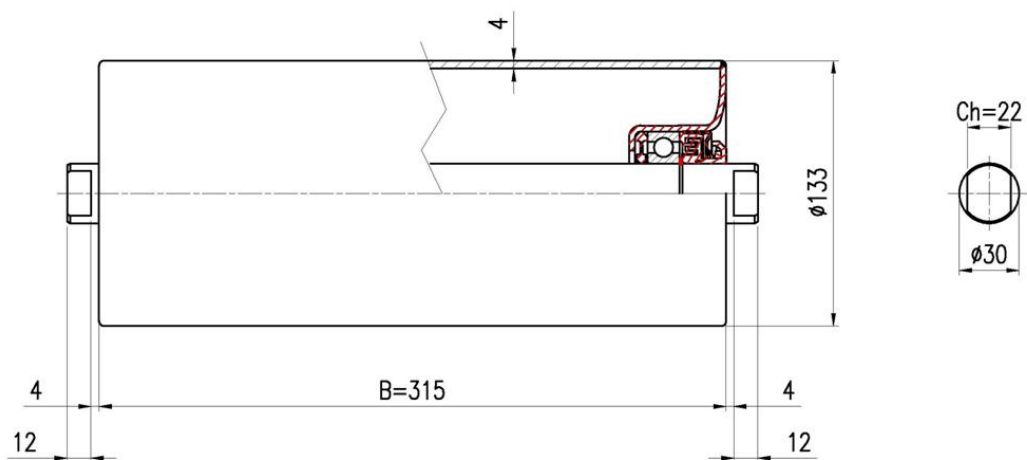


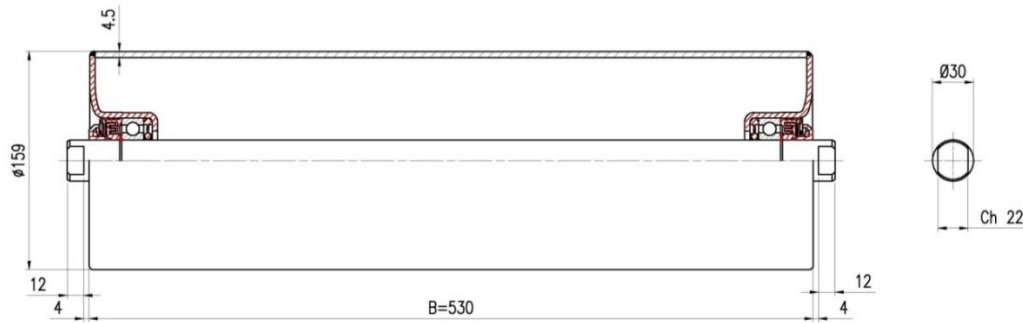
Figure 3.2.4. Scheme showing the main geometrical parameters at the weld root

The load on top of the roller is modelled typically as a uniformly distributed load on the longitudinal line of the roller [101], as reported in Figure 3.2.4.

Two geometries have been considered here and the details of the geometrical parameters are reported in Figure 3.2.5a and 3.2.5b for the two cases, named in the following as PSV4 133 315 and PSV4 159 530. For sake of brevity the modeling will be described step by step only for the first geometry.



(a)



(b)

Figure 3.2.5: Geometry of the rollers: PSV4 133 315 (a) PSV4 159 530 (b)

3.2.3.3 Finite element modelling

The analysis of the stress fields in these welded details needed 3D models, because of their variability along the circular path described by the weld root. The two considered geometries reported in Figure 3.2.5 have been modelled by means of 20-node 3D hexahedral finite elements (SOLID 186) implemented in the FE code ANSYS. The material has been assumed as linear elastic and isotropic. The values of Poisson's ratio ν and Young's modulus E typical for steels have been adopted in all FE analyses: accordingly ν and E have been set equal to 0.30 and 206 GPa, respectively. No other material property has been given as input to the FE code, indeed in the FE model the different zones of the welded joint (base material, heat-affected zone, weld metal) have been considered as made of a unique material with homogeneous mechanical properties.

Due to the symmetry of geometry and loading only one quarter of the geometry has been considered. The bearing has been considered of infinite stiffness and all the nodes of the bearing housing have been connected by means of rigid elements (links) to a master node. This special node has been placed on the symmetrical longitudinal axis of the roller in correspondence of the instantaneous rotation centre of the bearing. The rotation about the axis Z and the longitudinal displacement (direction Y in Figure 3.2.4) have been left unconstrained while all

the other displacements and rotations of the master node have been constrained. The load has been distributed along the longitudinal line as shown in Figure 3.2.6 [101].

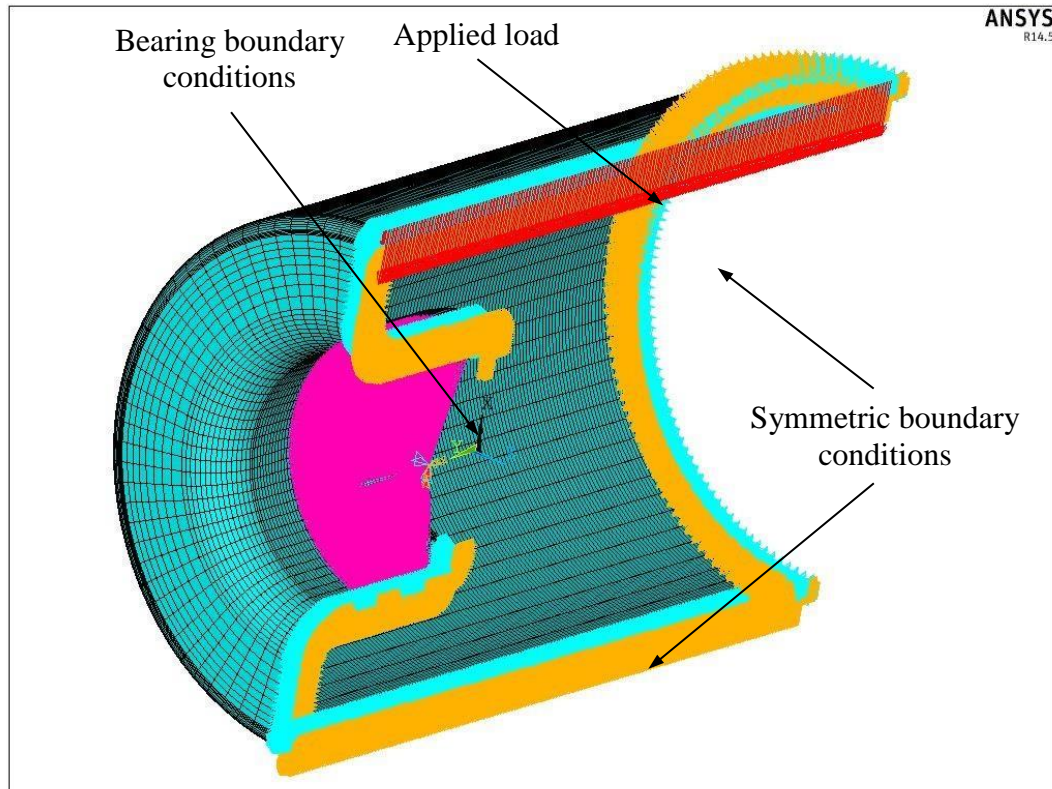
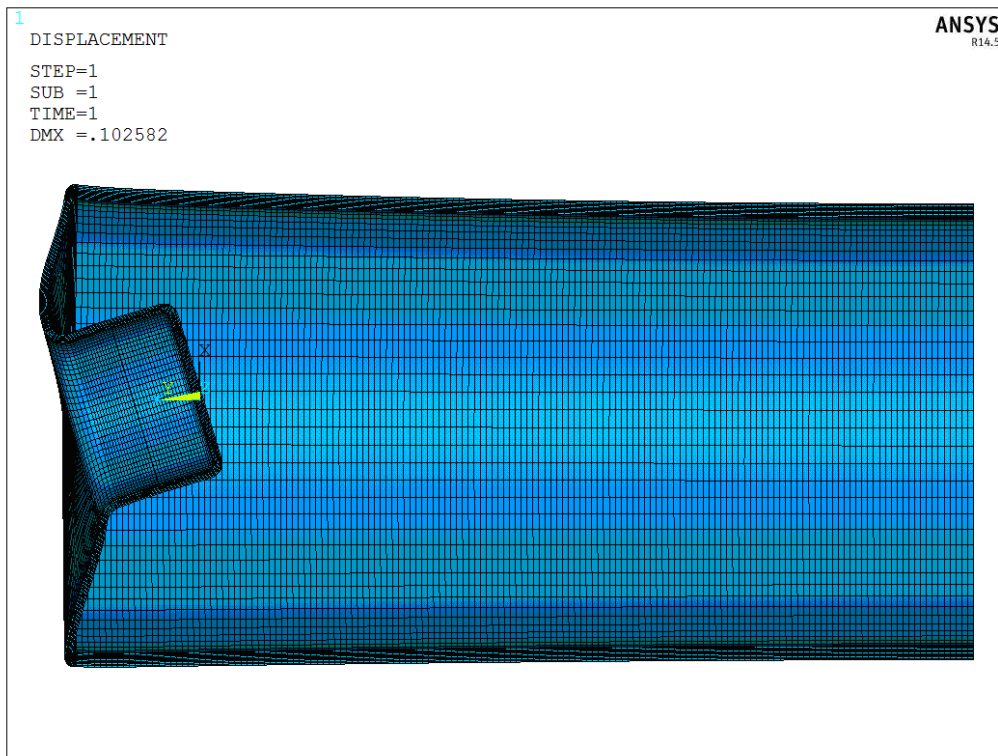


Figure 3.2.6. Typical boundary conditions applied in the numerical models.

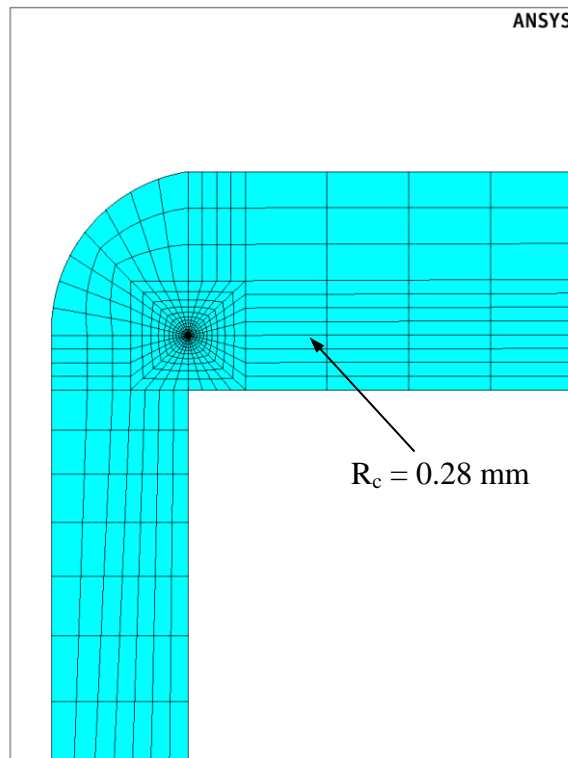
For each geometry two models were created: the first was mainly oriented to the determination of the point where the maximum principal stress and the maximum value of the strain energy density were located. Due to the complex geometry of the bearing housing in fact the point varies as a function of the geometry. In this case a regular fine mesh has been used with the aim also to determine the SIFs at the weld root (see Figure 3.2.7).

The second model was characterized by a coarse mesh but by an accurate definition of the control volume where the strain energy density should be averaged. As just stated the mesh used in that case was coarse with a regular increasing spacing ratio in the direction of the position of the control volume (see Figure 3.2.8) mainly aimed to a correct positioning of the volume itself in the

most critical region. All the analyses have been carried out by means of 20-node finite elements under linear-elastic hypotheses. A detail of the deformed shape (to which has been applied a displacement scaling factor to improve understanding) of the roller under the applied load and of the SED in the control volume around the most critical zone is shown in Figure 3.2.9a and 3.2.9b,c, respectively. The steps of the analyses will be shown here for sake of brevity only for the roller PSV 133 315 for which also the local SIFS have been determined.



(a)



(b)

Figure 3.2.7. Fine mesh for SIFs determination, global model (a) and detail at the weld root (b).

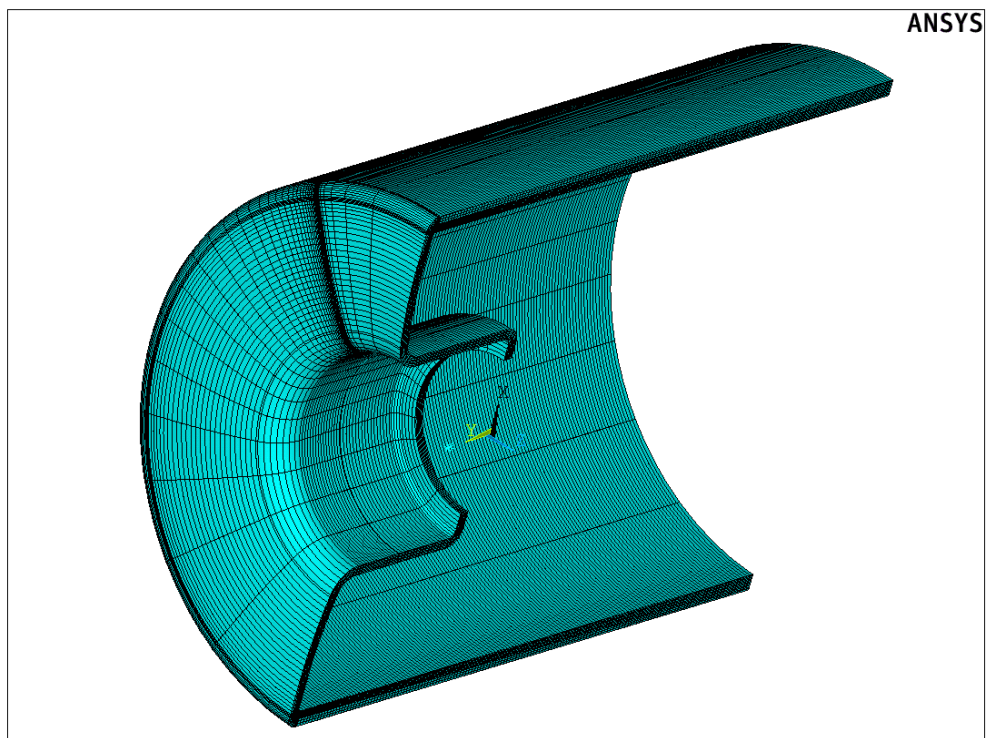
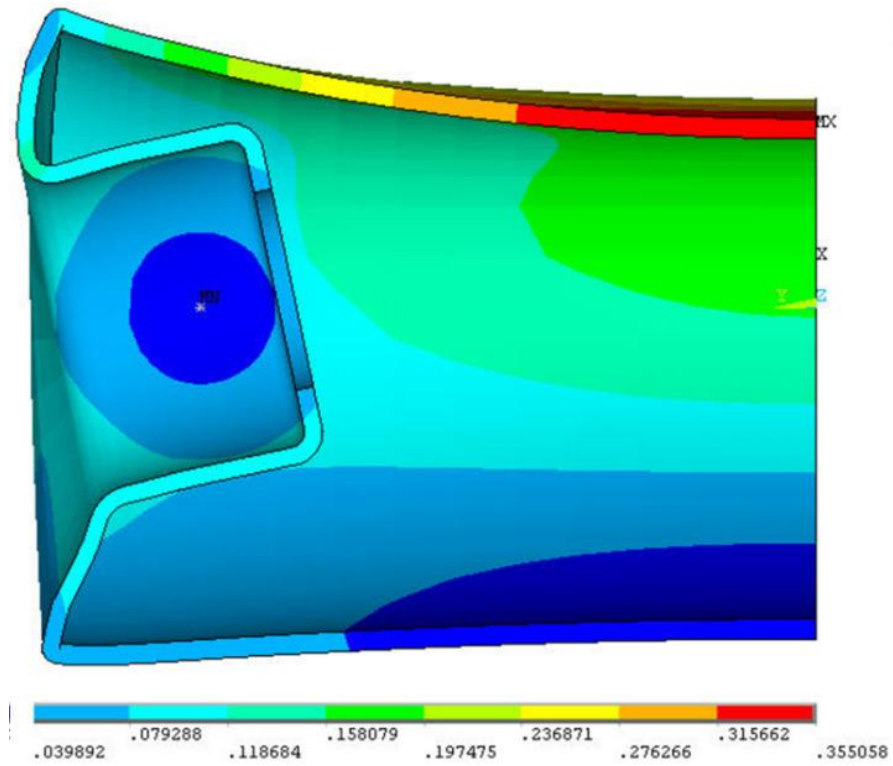
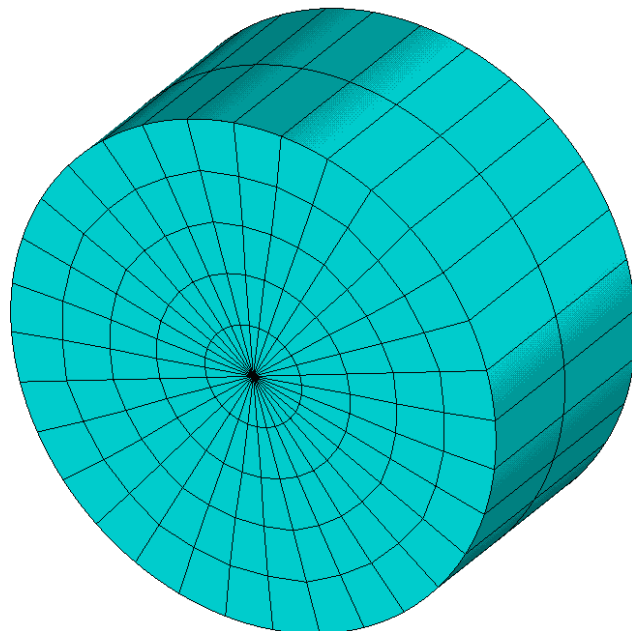


Figure 3.2.8. Relatively coarse mesh for SED determination.



(a)



(b)

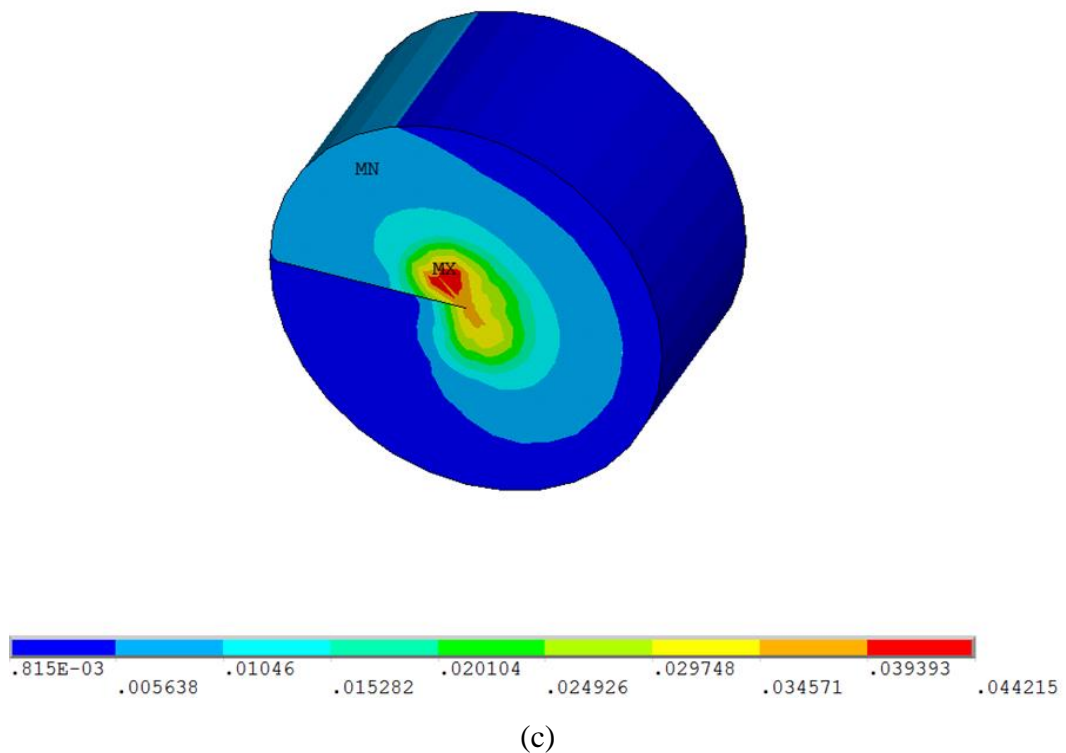


Figure 3.2.9. Deformed shape (a), mesh in the control volume (b) and SED contour lines (c).

3.2.3.4 Local parameters determination

By using the first model with a regular and very fine mesh the SED has been evaluated circumferentially all around the roller in the zone surrounding the weld root. The maximum SED value occurs outside the line of the application of the load. The angle of rotation is strongly dependent on the geometry of the bearing housing. In the case of the roller PSV 133 315 the maximum SED occurs at about 30 degrees from the line of load application as shown in Figure 3.2.10. In that point all the modes of failure are contemporary present as will be discussed in the following.

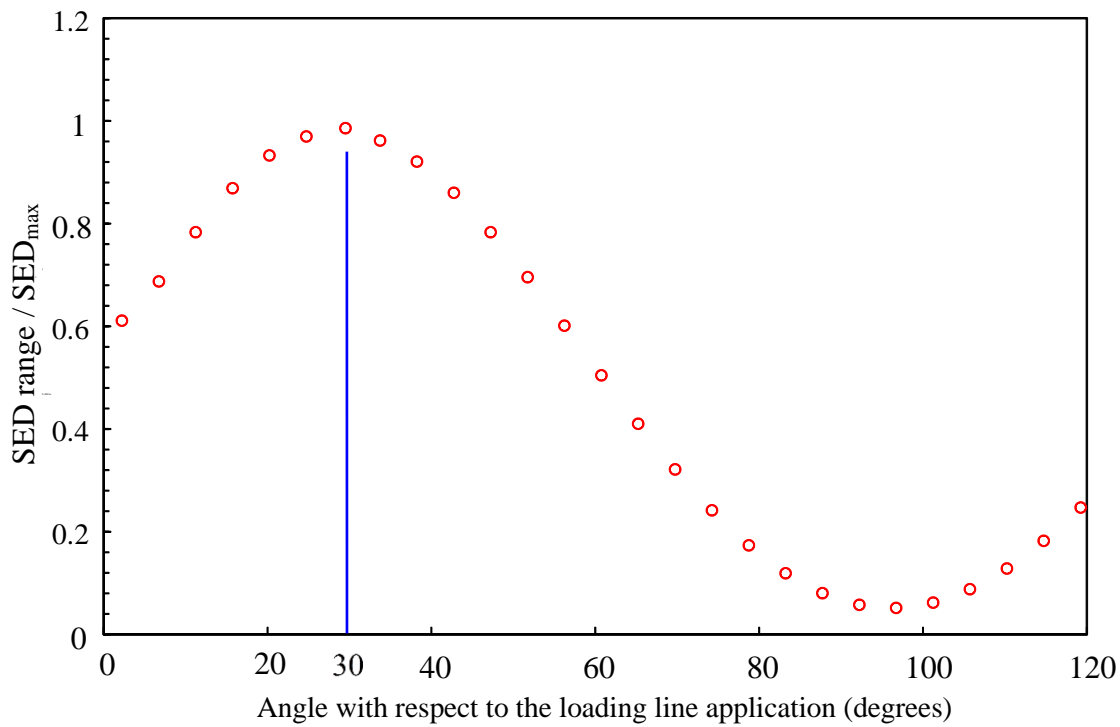
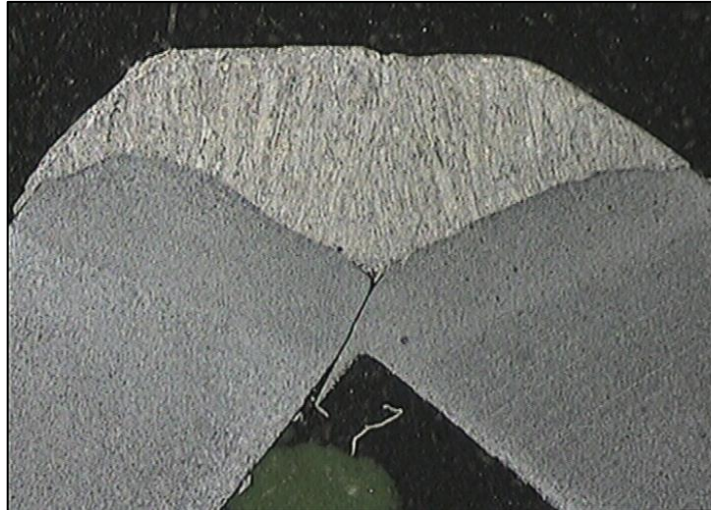


Figure 3.2.10. Angular distribution of the SED.

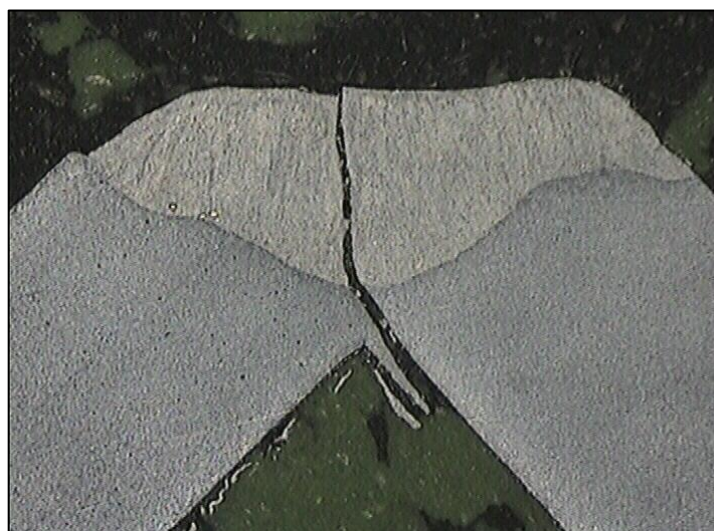
For this specific model an analysis of sensitivity of SED as a function of the length of the lack of penetration c has been carried out. From a micrographic analysis conducted on a large amount of welded rollers c has been found to vary in the range between 0.6 and 1.0 mm. A typical image of the weld root is shown in Figure 3.2.11a while Figure 3.2.11b shows a typical failure starting from the lack of penetration. Figure 3.2.11c shows the crack propagation through the weldment until the final failure of the roller. Finally Figure 3.2.11d reports a comparison between the real local geometry and the one considered in FE model, showing a very good agreement.



(a)



(b)



(c)

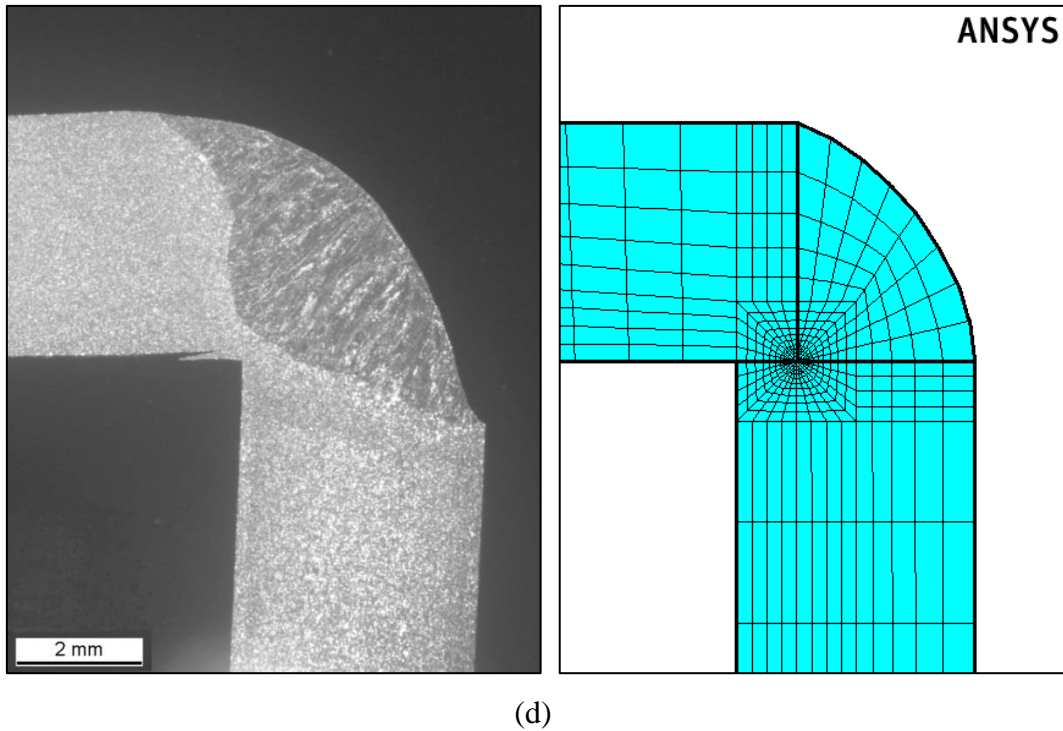


Figure 3.2.11. Lack of penetration at the weld root (a), typical structure failure (test load \gg nominal admitted load on the roller) (b) and a detail of the crack through the welded zone (c). Comparison between the real local geometry and the one considered in FE model (d).

The sensitivity analysis has been made varying the length of the lack of penetration and evaluating the SED in a control volume of radius $R_c = 0.28$ mm. The case considered corresponds to that reported in Table 3.2.3 for the roller PSV133 315. As visible from Figure 3.2.12 the variation of the SED is very limited in the range of c considered. The SED varies from 0.31 MJ/m^3 to 0.35 MJ/m^3 for a value of c corresponding to 0.6 and 1.0, respectively.

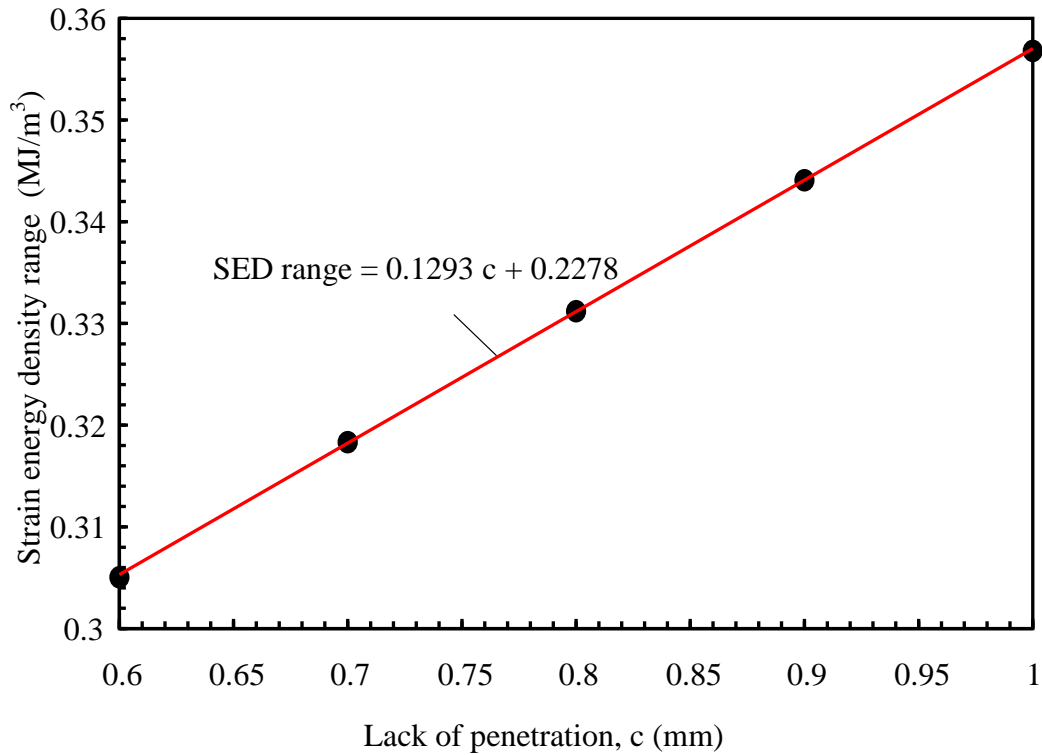


Figure 3.2.12. Sensitivity of the SED with respect to the lack of penetration.

Considering the low variation of the SED as a function of the initial lack of penetration, the length $c = 1$ mm has been set in all the analyses. This choice is in the safe direction because the worst configuration has been considered. In the specific case of the roller PSV 133, the first model, aimed to evaluate the angular position of the critical point with respect to the line of the loading application, has been very refined near the weld root with a high value of the spacing ratio as shown in Figure 3.2.7b. The mesh was also very refined but with a constant value of the spacing ratio circumferentially around the bearing housing, as shown in Figure 3.2.7a. The mesh employed allows not only to evaluate the SED but also the local stress field near the weld root in the most critical circumferential point determined by means of Figure 3.2.10. Figure 3.2.13 shows the local stress components plotted as a function of the distance from the crack tip. From the figure it is visible that, as anticipated before, the non-zero stress components confirm the presence not only of Mode I loading (opening mode) but also of Mode II (in-plane shear) and Mode III (out-of-plane shear) loadings. This is mainly due to the position of the point where the maximum SED occurs with

respect to the loading line which generates a complete three-dimensional stress field near the lack of penetration. The intensity of the stress components for the three different Modes is comparable although the prevalent mode is the opening one. By means of the local stress field determined in Figure 3.2.13 the stress intensity factor ranges have been determined as shown in Figure 3.2.14. The calculated values obtained for the loading case summarising in Table 3.2.3 for the roller PSV 133 315 are as following:

Mode I $\Delta K_I = 260 \text{ MPa mm}^{0.5}$

Mode II $\Delta K_{II} = 65 \text{ MPa mm}^{0.5}$

Mode III $\Delta K_{III} = 134 \text{ MPa mm}^{0.5}$

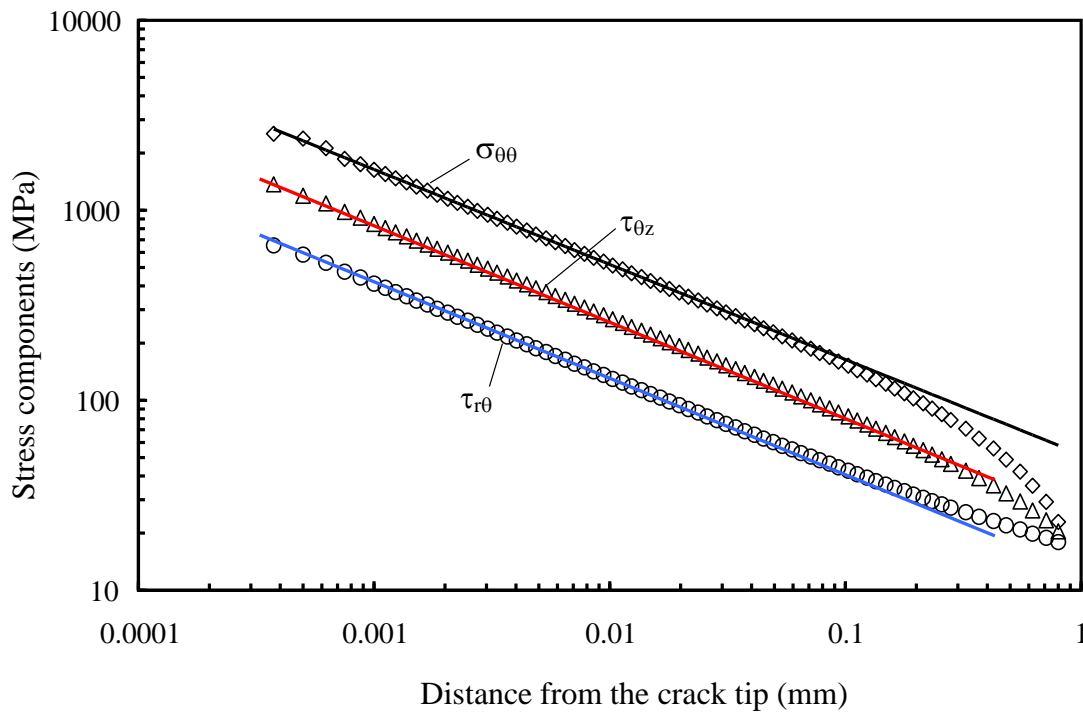


Figure 3.2.13. Stress field at the weld root tip.

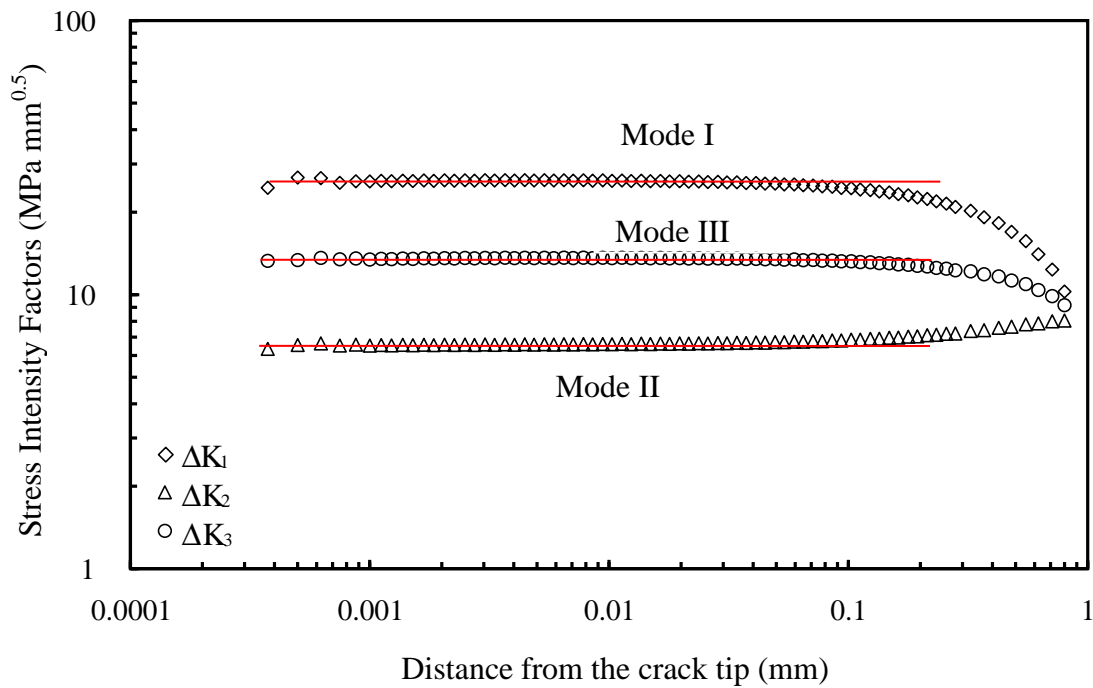


Figure 3.2.14. Typical trend of the stress intensity factors at the weld root.

Table 3.2.3. Main data of the two rollers considered in the present investigation

Reference load [N]	16300	12380
Model name	PSV4 133 315	PSV4 159 530
Length of the roller [mm]	315	530
Diameter of the roller [mm]	133	159
Tube thickness / Bearing housing thickness [mm]	4/3.5	4/3.5
Length of lack of penetration [mm]	1	1

By using Eq. (3.2.10) for a critical radius $R_c = 0.28$ mm and considering the values $e_1 = 0.13449$, $e_2 = 0.34139$ and $e_3 = 0.41380$ (see Tables 3.2.1 and 3.2.2) the SED range results to be 0.32 MJ/m^3 which is very close to that directly derived from the second FE model (0.34 MJ/m^3) where a ‘clever’ guided coarse mesh has been employed and the volume of radius $R_c = 0.28$ and of the same height (see Figure 3.2.9b,c) has been specifically modelled at the most critical point, previously determined with the first refined model. As visible from Figure 3.2.12, the SED evaluated from a very refined mesh was found to be 0.35 MJ/m^3 . The comparison between the values of SED obtained by using a coarse and a fine

mesh confirms the possibility to use a coarse mesh for the SED evaluation. Refined meshes are in fact not necessary when the aim of the finite element analysis is to determine the mean value of the local strain energy density on a control volume surrounding the points of stress singularity. The SED in fact can be derived directly from nodal displacements, so that also coarse meshes are able to give sufficiently accurate values for it. For this reason it is possible to avoid the direct evaluation of the stress intensity factor ranges which is a strong advantage from a computational point of view. After the deep preliminary analysis dedicated to the case study PSV133 315 the suggestion for implementing the SED approach to the other roller geometries is to employ two different models. The first is a coarse model only aimed to identify the most critical point along the bearing housing, the second is a ‘clever’ coarse model with the volume placed at the weld root in the most critical circumferential position determined by using the first model. The second model allows to determine the SED with a coarse mesh and with a degree of accuracy surely appropriate for practical applications.

3.2.4. Fatigue strength in terms of strain energy density averaged in a finite size volume

Some fatigue tests have been conducted on the two rollers shown in Figure 3.2.5. A test system has been created for reproducing the service conditions on the roller. Figure 3.2.15 shows a typical configuration of a test. The load has been applied by means of an external counter-roll which presses with a constant pressure the tested roller which rotates with a regular speed. Altogether 22 new tests have been carried out considering the two investigated geometries, under as-welded conditions. The details of the two fatigue series are reported in Tables 3.2.4 and 3.2.5 for the roller PSV 4 133 315 and PSV4 159 530, respectively. The experimental tests have been interrupted at about 10^7 cycles, accordingly the run-out specimens have been specified in the tables and in the diagram reported in Fig. 3.2.16. The new results reconverted in terms of the local SED have been compared with the scatterband proposed for structural welded steels [72]. That band, already reported in Figure 3.2.1, is shown in Figure 3.2.16 together with the new data. It is evident that the previous scatter band can be satisfactorily applied

also to the new data from failure at the weld root of rollers tested at different load levels.

Table 3.2.4. Fatigue data for the roller PSV4 133 315

Sample		Load [kg]	RPM	Cycles	Notes	Testing Time [h]	SED [Nmm/mm ³]
PSV4 133 315	1	1700	617	110000	-	2	0.439
	2	1675	617	155500	-	2	0.426
	3	1245	643	1680000	-	55	0.235
	4	1245	643	521658	-	14	0.235
	5	813	638	3687621	-	96	0.104
	6	752	638	13484745	runout	352	0.089
	7	760	638	10728361	runout	280	0.091
	8	752	638	10685583	runout	279	0.089
	9	713	638	10440417	runout	273	0.080
	10	647	638	10164948	runout	266	0.066
	11	610	638	11055235	runout	289	0.059
	12	553	646	10479312	runout	270	0.048
	13	510	646	10615367	runout	274	0.041
	14	404	646	11446934	runout	295	0.026

Table 3.2.5. Fatigue data for the roller PSV4 159 530

Sample		Load [kg]	RPM	Cycles	Notes	Testing Time [h]	SED [Nmm/mm ³]
PSV4 159 530	1	1262	541	363234	-	11	0.251
	2	1251	541	370432	-	11	0.247
	3	990	541	619344	-	19	0.155
	4	992	541	747548	-	23	0.155
	5	994	541	677279	-	21	0.156
	6	991	541	598390	-	18	0.155
	7	523	545	9962179	-	305	0.043
	8	708	545	2749333	-	84	0.079



(a)



(b)

Figure 3.2.15. Testing device for fatigue loading (a) and a detail of the roller during the test (b).

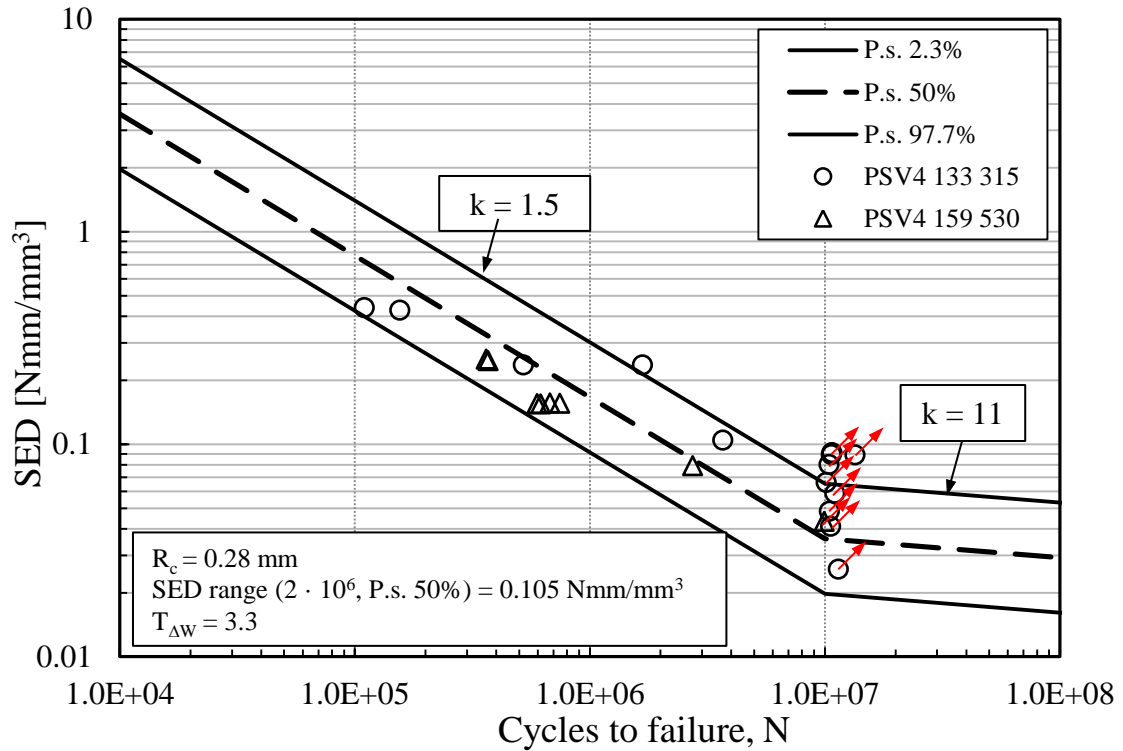


Figure 3.2.16. Synthesis of new data in terms of local SED and comparison with the scatterband shown in Figure 1.

3.2.5. Discussion

The present paragraph deals with a local energy based approach employed for the fatigue assessment of rollers with failure occurring at the weld root. The rollers considered in the present investigation are particularly suited to conveyors that operate in very difficult conditions, where working loads are high, and large lump size material is conveyed; and yet, despite these characteristics, they require minimal maintenance. The bearing housings are welded to the tube body using auto-centralising automatic welding machines utilizing a continuous wire feed.

From the point of view of the fatigue behavior under loading, the weakest point of the entire structure is the lack of penetration of the weld root. Therefore, if the roller is loaded well above its declared nominal admitted load (RULMECA Bulk Catalogue, 2015), it would experience fatigue failure starting at the level of the weld root. A detail of the weld root is shown in Figure 3.2.4, where the lack of penetration length is indicated as c .

The rollers have been modelled by using the finite element method combined with

three-dimensional analyses. The procedure for evaluating the local parameters in the zone close to the lack of penetration at the weld root has been described here showing the low sensitivity of the model to the length of the lack of penetration. The detailed procedure for evaluating the SED in the control volume surrounding the crack tip in the weakest point of the roller has been summarised. Some fatigue tests from two different geometries belonging to the family of rollers called PSV4 from Rulmeca production have been carried out and summarised here by means of local SED. It has been proved that the scatter band $\Delta W-N$ (strain energy range – number of cycles to failure), summarising about 1200 fatigue data from welded joints with the majority of failures originated from the weld toes, can be successfully applied also to welded joints with failures from the weld roots and in particular to the considered rollers geometry.

3.3 Sharp V-notches under multiaxial fatigue: analytical investigation of the phase angle effect^(*)

Nomenclature

I_1, I_2, I_3	Stress invariants
k_1, k_2, k_3	Shape factors associated to the NSIFs
K_1, K_2, K_3	Mode I, mode II and mode III notch stress intensity factors (NSIFs)
p, q	Auxiliary parameters used in Cardano's formulation
r	Radial coordinate
R	Load ratio
S_a	Nominal tensile amplitude
S_{nom}	Nominal sinusoidal tensile stress applied to the specimen
T_a	Nominal torsion amplitude
T_{nom}	Nominal sinusoidal torsion stress applied to the specimen
u, v, w	Auxiliary parameters used in Cardano's formulation

Symbols

2α	V-notch opening angle
β	Machine angle
χ_1, χ_2	Parameters used to describe the mode I and mode II stress fields
ϕ	Phase angle
η	Auxiliary parameter used in Cardano's formulation
$\lambda_1, \lambda_2, \lambda_3$	Eigenvalues related to Mode I, II and III respectively
Λ	Biaxiality ratio
ν	Poisson's ratio
θ	Angular coordinate
$\sigma_1, \sigma_2, \sigma_3$	Principal stress
$\bar{\tau}$	Maximum shear stress averaged over a loading cycle
$\bar{\tau}_{max}$	Maximum value of $\bar{\tau}$ by varying the phase angle and the biaxiality ratio

$\bar{\tau}_1, \bar{\tau}_2, \bar{\tau}_3$	First, second and third shear stresses averaged over a loading cycle
τ_1, τ_2, τ_3	Principal shear stresses
ξ	Auxiliary parameter used in Cardano's formulation

(*) See also:

Marangon, C.; Lazzarin, P.; Berto, F.; Campagnolo, A. Some analytical remarks on the influence of phase angle on stress fields ahead of sharp V-notches under tension and torsion loads. *Theoretical and Applied Fracture Mechanics*; 74:64-72 (2014).

3.3.1. Introduction

3.3.1.1 A brief review of some criteria for multiaxial fatigue loading

Several criteria have been proposed to assess the behaviour of unnotched or bluntly notched components subjected to multiaxial fatigue. It is well known that this type of loading condition induces the formation of surface cracks that usually nucleate on the plane characterized by the maximum shear.

After the pioneering works by Ewing and Humfrey [102] and Forsyth [103], many criteria take into account stress and strain components acting on the plane experiencing the maximum shear. The so called "critical plane approaches" use different damage parameters depending on the components of stress/strain thought of as critical on the maximum shear plane. Smith, Watson and Topper [104] considered the critical plane where the maximum principal strain acts, Brown and Miller considered both the shear and the normal strain acting on the critical plane [105]. Fatemi and Socie took in consideration the shear strain and the stress acting normal to the crack flanks [3]. Fatemi–Socie critical plane parameter [3] in terms of uniaxial fatigue properties was also used to correlate constant amplitude fatigue data [4]. The critical plane approach has been reviewed and modified by Carpinteri et al. [6,106], who correlated the critical plane orientation with the weighted mean principal stress directions. Accordingly, the fatigue failure assessment is performed considering a nonlinear combination of the maximum normal stress and the shear stress amplitude acting on the critical plane.

Developments of the Carpinteri-Spagnoli approach have been documented in a recent work [7].

The effects of multiaxial loading paths on the cyclic deformation behaviour, crack initiation and crack path have been investigated by Reis et al. in [107] considering plain specimens made of three structural steels (Ck45, medium carbon steel, 42CrMo4, low alloy steel and the AISI 303 stainless steel). Theoretical predictions of the damage plane were performed using some critical plane approaches, based on stress analysis or strain analysis (Findley, Smith–Watson–Topper, Fatemi–Socie, Wang–Brown–Miller, etc). Comparisons of the predicted crack orientation based on the critical plane approaches with the experimental observations were shown and discussed. Results showed the applicability of the critical plane approaches to predict the fatigue life and crack initial orientation in structural steels.

Some energy-based criteria have been also developed to face the problem of multiaxial loadings [108–111] on the basis of the strain energy density combined with a critical plane. Liu [108], Chu et al. [109], Glinka et al. [110] and Jiang [111]. Liu [108] considered two different energy failure modes and the collapse of the component was expected on the plane where the maximum virtual strain energy was reached. Chu et al. [109] used a similar approach in order to relate the work of shear and normal stress and strain components. Glinka et al. [110] modified Chu's criterion in order to better consider the effect of the mean stress in the case of non-proportional loading. Jiang [111] developed another multiaxial fatigue approach based on the cyclic plasticity and the plastic strain energy concept.

A wide review of the main multiaxial fatigue criteria is carried out in Refs [112–114]. It was shown in [114] that the effect of phase angle on the fatigue strength is still an open problem also dealing with plain specimens resulting in a non-conservative fatigue design rules.

To evaluate the different sensitivity of the unnotched materials to non-proportional cyclic loading, the non-proportional cyclic hardening coefficient is commonly employed [1,115]. This coefficient depends on the material microstructure and hardness level and has been related to uni-axial monotonic and

cyclic deformation properties by means of an empirical relationship. The exact determination would require as input data the in-phase equivalent stress amplitude and a second parameter from non-proportional tests, the out-of-phase equivalent stress amplitude at the same strain amplitude level.

3.3.1.2 Notched components under combined loadings: V-notches and holes

While these concepts are well consolidated for plain materials, the extension of the same concepts to sharp V-notches remains an open problem. In this case an additional complication is due to the fact that out-of-phase effect might be influenced by the microstructural properties of the material near the notch tip and by the shielding effects occurring during the initial crack propagation which are different under proportional and non-proportional loading.

The notch effect has been examined in some recent contributions dealing with blunt and sharp notches [28,30,32–34]. Different criteria have been used, which involve the strain energy density over a control volume when the notch tip radius is very small (0.1 mm), the J_2 invariant with stresses and strains at the notch root [116] or stress and strains at a given distance from it [117–119].

In the presence of blunt notches, the Fatemi–Socie critical plane parameter has been employed by Gladskyi and Fatemi for the fatigue strength assessment of tubular specimens made of a carbon steel, with or without a through thickness circular hole, subjected to axial and torsional loads [120].

Hertel and Vormwald [121] determined the fatigue lives of tubular and round shafts with blunt shoulder fillets (notch root radius equal to 1.4 mm) under combined tension/compression and torsion. A short crack model originally proposed for multiaxial constant amplitude loading is extended and applied to multiaxial variable amplitude loading [122]. The comparison between theoretical assessment and experimental results reveals that the proposed approach enables accurate estimations.

Shielding effects were accurately analysed by Tanaka et al. [20] who derived an elliptic equation for the threshold condition under mixed modes I and III. A novel mathematical model of the stresses around the tip of a fatigue crack was developed by Christopher et al. [22,23]. The model includes the T-stress and

considers the effects of plasticity through an analysis of their shielding effects on the applied elastic field. The ability of the CJP model to characterize plasticity-induced effects of cyclic loading on the elastic stress fields was demonstrated using full field photoelasticity. The CJP model can be seen as a modified linear elastic approach, to be applied outside the zone where nonlinear effects are prevailing. Two logarithmic terms are added to the Williams' solution and three new stress intensity factors K_F , K_R and K_S were proposed to quantify shielding effects ahead of the crack tip and on its back.

Recently Ohkawa I. and Ohkawa C. [123] investigated the notch effect under cyclic torsion with and without static tension using circumferentially severely notched solid round specimens of austenitic stainless and a low carbon steel. For the stainless steel they found that notched specimens had longer life than smooth specimens under torsion (with stresses referred to the net transverse area of the specimens). Tanaka [124] found independently the same results by investigating circumferentially notched bars of austenitic stainless and carbon steels with three different notch-tip radii subjected to cyclic torsion with and without static tension. The notch-strengthening behavior to delayed crack growth along the notch root due to rubbing or sliding contact of serrated factory-roof type crack faces under torsion and combined tension and torsion, both in-phase and out-of phase, was documented also by Berto et al. in [28] for 39NiCrMo3 steel and in [34] for cast iron.

3.3.1.3 Non proportional loadings in sharp V-notches

One of the more intriguing problems dealing with sharp notches is how to take into account the effect of non-proportional loading in the multiaxial fatigue strength assessment. The problem is really very complex because the sensitivity to the phase angle varies not only as a function of the material but also as a function of the notch acuity.

Dealing with welded joints, for example, it was shown that the out-of-phase loading results in a significant decrease of fatigue life of the steel joints [74,125], which is well known from investigations also with not welded ductile steels; conversely the non-proportional loading renders an indifferent (neutral) behaviour

of the welded aluminium connections [126], analogous to the behaviour exhibited by semi-ductile un-welded aluminium alloys.

Being conscious of the just above mentioned problems related to shielding effects, which are material dependent and being aware of the update literature dealing with non-proportional loadings, the main aim of the present investigation is to provide a simple linear elastic analytical frame applied to sharp, zero tip radius, V-notches. The proposed frame is based on the local maximum shear stress averaged over a single fatigue cycle evaluated at a certain distance from the notch tip. The model, which is based on Cardano's analytical formulation [127], is able to take into account not only the effect of the phase angle but also the effect of the notch opening angle, the nominal load ratio and the biaxiality ratio. The only analogy of the present model with the critical plane approaches is the consideration of a shear stress as a critical parameter. On the other hand substantial differences exist between the present approach and those based on critical planes. The main difference is due to the fact that only sharp notches are considered and for this reason the critical point and direction are not known a priori. Its determination is based on the maximization of the critical parameter. By applying the proposed frame to sharp V-notches under different loading configurations some interesting observations can be drawn and a possible explanation of the fatigue life reduction in sharply V-notched components due to phase angle can be provided.

3.3.2. Analytical frame

The aim of the present work is to analyze under linear elastic conditions the effect of the phase angle on axis-symmetric sharp V-notched components subjected to multiaxial loading. A schematic representation of a typical circumferentially V-notched specimen is shown in Figure 3.3.1. The attention is focused on the role played by the notch opening angle, the phase angle and the applied loads on the stress field.

The stress field ahead of the notch tip will be given in the polar coordinate system shown in Figure 3.3.1b. The origin is centered at the notch tip. The radial

coordinate is r while θ is the angle between a particular point and the notch bisector line.

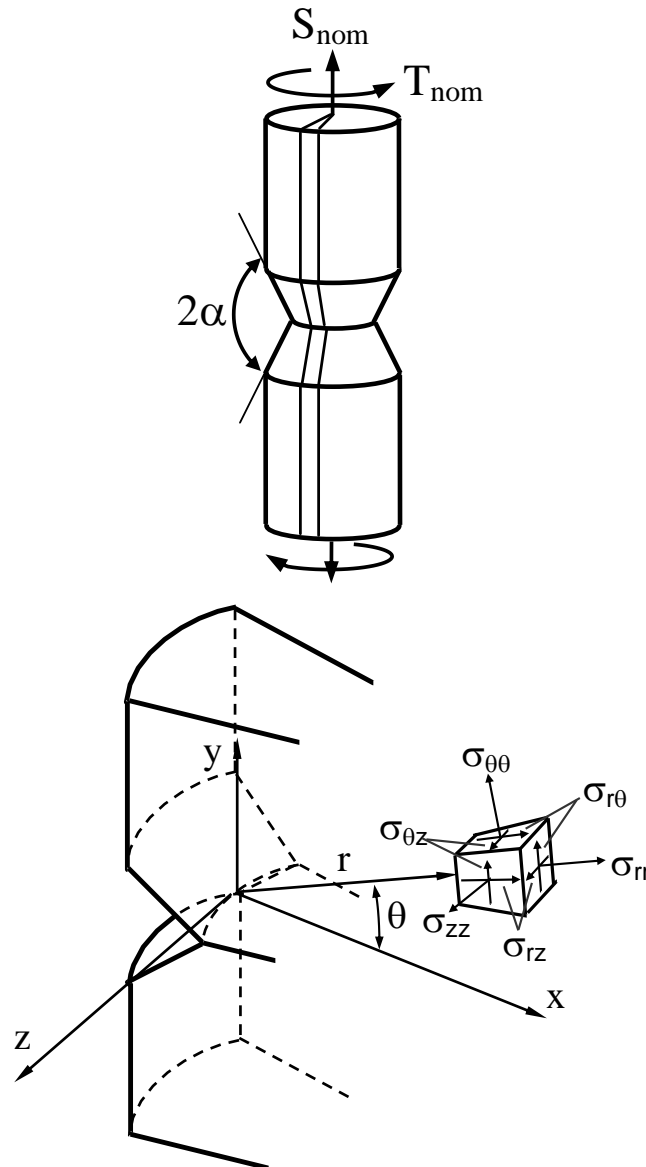


Figure 3.3.1. Component weakened by a sharp V-shaped notch subjected to multi-axial loading conditions (a). The centre of the polar coordinate system is located at the V-notch tip (b).

As it is well known the presence of a sharp V-notch and the application of a multiaxial loading induce a singular state of stress in the vicinity of the notch tip. Consider first the stress components linked to the Mode I and Mode II loading conditions [71,89]:

$$\begin{aligned}\sigma_{rr} = & \frac{K_1 \cdot r^{\lambda_1-1}}{\sqrt{2\pi} \cdot (1+\lambda_1) + \chi_1 \cdot (1-\lambda_1)} \cdot [(3-\lambda_1)\cos(1-\lambda_1)\theta + \chi_1 \cdot (1-\lambda_1) \cdot (-\cos(1+\lambda_1)\theta)] + \\ & + \frac{K_2 \cdot r^{\lambda_2-1}}{\sqrt{2\pi} \cdot (1-\lambda_2) + \chi_2 \cdot (1+\lambda_2)} \cdot [-(3-\lambda_2)\sin(1-\lambda_2)\theta + \chi_2 \cdot (1+\lambda_2) \cdot (\sin(1+\lambda_2)\theta)]\end{aligned}\quad (3.3.1)$$

$$\begin{aligned}\sigma_{\theta\theta} = & \frac{K_1 \cdot r^{\lambda_1-1}}{\sqrt{2\pi} \cdot (1+\lambda_1) + \chi_1 \cdot (1-\lambda_1)} \cdot [(1+\lambda_1)\cos(1-\lambda_1)\theta + \chi_1 \cdot (1-\lambda_1) \cdot (\cos(1+\lambda_1)\theta)] + \\ & + \frac{K_2 \cdot r^{\lambda_2-1}}{\sqrt{2\pi} \cdot (1-\lambda_2) + \chi_2 \cdot (1+\lambda_2)} \cdot [-(1+\lambda_2)\sin(1-\lambda_2)\theta + \chi_2 \cdot (1+\lambda_2) \cdot (-\sin(1+\lambda_2)\theta)]\end{aligned}\quad (3.3.2)$$

$$\begin{aligned}\sigma_{r\theta} = & \frac{K_1 \cdot r^{\lambda_1-1}}{\sqrt{2\pi} \cdot (1+\lambda_1) + \chi_1 \cdot (1-\lambda_1)} \cdot [(1-\lambda_1) \cdot \sin(1-\lambda_1)\theta + \chi_1 \cdot (1-\lambda_1) \cdot (\sin(1+\lambda_1)\theta)] + \\ & + \frac{K_2 \cdot r^{\lambda_2-1}}{\sqrt{2\pi} \cdot (1-\lambda_2) + \chi_2 \cdot (1+\lambda_2)} \cdot [(1-\lambda_2) \cdot \cos(1-\lambda_2)\theta + \chi_2 \cdot (1+\lambda_2) \cdot (\cos(1+\lambda_2)\theta)]\end{aligned}\quad (3.3.3)$$

The out-of-plane stress component σ_z of the stress field can be written by assuming plane strain conditions. This engineering approximation is generally well aligned with the real stress field near the notch tip in the case of axis-symmetric components weakened by sharp V-notches:

$$\sigma_{zz} = \nu \cdot (\sigma_{rr} + \sigma_{\theta\theta}) \quad (3.3.4)$$

In parallel the Mode III loading can be split in two tangential components as a function of the corresponding NSIF [90,128]:

$$\sigma_{rz} = \frac{K_3 \cdot r^{\lambda_3 - 1}}{\sqrt{2\pi}} \cdot \sin(\lambda_3 \cdot \theta) \quad (3.3.5)$$

$$\sigma_{\theta z} = \frac{K_3 \cdot r^{\lambda_3 - 1}}{\sqrt{2\pi}} \cdot \cos(\lambda_3 \cdot \theta) \quad (3.3.6)$$

Parameters K_1 , K_2 and K_3 in Eqs. (3.3.1-3, 3.3.5, 3.3.6) are the Notch Stress Intensity Factors (NSIFs) related to Mode I, Mode II and Mode III stress distributions respectively, λ_1 and λ_2 are Williams' eigenvalues [71], λ_3 is the Mode III eigenvalue [90,128] and, finally, χ_1 and χ_2 are auxiliary parameters which depend on the notch opening angle [89]. For example, when the V-notch opening angle is equal to 90° , the eigenvalues are $\lambda_1 = 0.5445$, $\lambda_2 = 0.9085$ and $\lambda_3 = 0.6667$ for Mode I, Mode II and Mode III respectively; in parallel, $\chi_1 = 1.841$ and $\chi_2 = 0.219$.

In order to better describe the behavior of every singular stress component during the cyclic loading, the notch stress intensity factors can be re-written in the form:

$$K_1 = k_1 \cdot d^{1-\lambda_1} \cdot S_{nom} \quad (3.3.7)$$

$$K_2 = k_2 \cdot d^{1-\lambda_2} \cdot S_{nom} \quad (3.3.8)$$

$$K_3 = k_3 \cdot d^{1-\lambda_3} \cdot T_{nom} \quad (3.3.9)$$

Here d is the V-notch depth (10 mm), k_1 , k_2 and k_3 are the shape factors, which can be obtained by a finite element analysis for a specific geometry. In the following, due to the applied loads and the polar symmetry conditions, k_2 can be set equal to zero. By means of a finite element analysis of the considered geometry (Fig. 3.3.1), the values of k_1 and k_3 resulted to be 5.40 and 5.88, respectively. S_{nom} and T_{nom} are the remote applied tension and torsion stresses (Fig. 3.3.1). Separating the stress amplitudes from the mean values, one obtains:

$$S_{nom} = S_a \cdot \sin(\beta) + S_a \cdot \frac{1+R}{1-R} \quad (3.3.10)$$

$$T_{\text{nom}} = T_a \cdot \sin(\beta - \phi) + T_a \cdot \frac{1+R}{1-R}$$

(3.3.11)

S_a and T_a are the nominal stress amplitude tied to the applied loads, β is the machine angle ranging from 0° and 360° to complete one cyclic loading, R is the nominal load ratio and ϕ is the phase angle. The ratio between T_a and S_a is the biaxiality ratio and it is named Λ .

In the following, due to singular stress field, the critical plane of maximum shear has not been determined, but the point outside a characteristic core region where the maximum shear stress averaged over one cycle of fatigue loading acts. The point is located to a given distance from the V-notch tip, thought of as a material's property at the conventional fatigue limit. In the volume-based strain energy density approach [27] the radius of the control volume varies from material to material and cannot be considered independent on the loading mode [29,33,64,129,130]. Here, for the sake of simplicity the distance r will be set equal to 0.28 mm, which matches the radius of the control volume used for high cycle fatigue assessments of steel welded joints, or 0.028 mm, which matches instead the radius typically used for high cycle fatigue assessments of high strength steels. By substituting Eqs. (3.3.7-3.3.9) into Eqs. (3.3.1-3.3.6) the trend of each stress component in a fatigue cycle can be obtained. The aim now is to find out the values of the three principal stresses acting during the cyclic loading and the values of the maximum shear stresses at a specific distance from V-notch tip. In the following the radial distance from the notch tip will be constant and equal to $r = 0.28$ mm or 0.028 mm, thought of as materials' characteristic lengths. Also the notch opening angle and the load ratio will be constant and equal to $2\alpha = 30, 90$ or 135 degrees and to $R = -1$ or 0 respectively. Doing so, the stress components depend on the machine angle β , the polar coordinate θ and the phase angle ϕ .

The stress tensor at point P can be written as follows:

$$[\mathbf{T}]_P = \begin{bmatrix} \sigma_{rr}(\beta, \theta, \phi) & \sigma_{r\theta}(\beta, \theta, \phi) & \sigma_{rz}(\beta, \theta, \phi) \\ \sigma_{r\theta}(\beta, \theta, \phi) & \sigma_{\theta\theta}(\beta, \theta, \phi) & \sigma_{\theta z}(\beta, \theta, \phi) \\ \sigma_{rz}(\beta, \theta, \phi) & \sigma_{\theta z}(\beta, \theta, \phi) & \sigma_{zz}(\beta, \theta, \phi) \end{bmatrix}_P \quad (3.3.12)$$

The secular equation giving the principal stresses is:

$$\sigma^3 - I_1 \cdot \sigma^2 - I_2 \cdot \sigma - I_3 = 0 \quad (3.3.13)$$

where I_1 , I_2 and I_3 are the stress invariants:

$$I_1 = \sigma_{rr} + \sigma_{\theta\theta} + \sigma_{zz} \quad (3.3.14)$$

$$I_2 = -\sigma_{rr} \cdot \sigma_{\theta\theta} - \sigma_{rr} \cdot \sigma_{zz} - \sigma_{\theta\theta} \cdot \sigma_{zz} + \sigma_{r\theta}^2 + \sigma_{\theta z}^2 + \sigma_{rz}^2 \quad (3.3.15)$$

$$I_3 = \sigma_{rr} \cdot \sigma_{\theta\theta} \cdot \sigma_{zz} - \sigma_{rr} \cdot \sigma_{\theta z}^2 - \sigma_{\theta\theta} \cdot \sigma_{rz}^2 - \sigma_{zz} \cdot \sigma_{r\theta}^2 + 2 \cdot \sigma_{r\theta} \cdot \sigma_{\theta z} \cdot \sigma_{rz} \quad (3.3.16)$$

Following Cardano's formulation [127], suitable for solving a generic cubic equation, the principal stresses, i.e. the stress tensor eigenvalues, assume the following form:

$$\sigma_1 = u + v + \frac{I_1}{3} \quad (3.3.17)$$

$$\sigma_2 = -\frac{u+v}{2} + i \cdot \frac{u-v}{2} \cdot \sqrt{3} + \frac{I_1}{3} \quad (3.3.18)$$

$$\sigma_3 = -\frac{u+v}{2} - i \cdot \frac{u-v}{2} \cdot \sqrt{3} + \frac{I_1}{3} \quad (3.3.19)$$

Parameters u and v of Eqs. (3.3.17-3.3.19) are linked to the invariants I_1 , I_2 and I_3 *via* the auxiliary parameters p and q :

$$u = \left(-\frac{q}{2} + \sqrt{\frac{q^2}{4} + \frac{p^3}{27}} \right)^{\frac{1}{3}} \quad (3.3.20)$$

$$v = \left(-\frac{q}{2} - \sqrt{\frac{q^2}{4} + \frac{p^3}{27}} \right)^{\frac{1}{3}} \quad (3.3.21)$$

where p and q are:

$$p = -\frac{I_1^2}{3} - I_2 \quad (3.3.22)$$

$$q = -\frac{2 \cdot I_1^3}{27} - \frac{I_1 \cdot I_2}{3} - I_3 \quad (3.3.23)$$

Being the stress tensor $[T]_p$ symmetrical (Eq. 3.3.12), due to the algebra's spectral theorem, the principal stresses (Eqs. 3.3.17-3.3.19) are always real. Consequently the following condition is always verified:

$$\frac{q^2}{4} + \frac{p^3}{27} \leq 0 \quad (3.3.24)$$

By operating now the following substitutions inside Eqs. (3.3.20, 3.3.21):

$$\eta = -\frac{q}{2} \quad (3.3.25)$$

$$\xi = \sqrt{-\frac{q^2}{4} - \frac{p^3}{27}} \quad (3.3.26)$$

it is possible to re-write the parameters u and v in the form:

$$u = (\eta + i\xi)^{1/3} = w^{1/3} \quad (3.3.27)$$

$$v = (\eta - i\xi)^{1/3} = \bar{w}^{1/3} \quad (3.3.28)$$

By using some well-known properties of complex variables, u and v become:

$$u = |w|^{1/3} \cdot \left[\cos\left(\frac{1}{3} \cdot \text{Arg}(w)\right) + i \cdot \sin\left(\frac{1}{3} \cdot \text{Arg}(w)\right) \right] \quad (3.3.29)$$

$$v = |w|^{1/3} \cdot \left[\cos\left(\frac{1}{3} \cdot \text{Arg}(w)\right) - i \cdot \sin\left(\frac{1}{3} \cdot \text{Arg}(w)\right) \right] \quad (3.3.30)$$

where:

$$|w| = \sqrt{\eta^2 + \xi^2} \quad (3.3.31)$$

$$\text{Arg}(w) = \begin{cases} \text{Arc tan}\left(\frac{\xi}{\eta}\right) & \text{if } \eta \geq 0 \\ \text{Arc tan}\left(\frac{\xi}{\eta}\right) + \pi & \text{if } \eta < 0 \end{cases} \quad (3.3.32)$$

The final expressions of the principal stresses are:

$$\sigma_1 = \frac{I_1}{3} + 2 \cdot |w|^{1/3} \cdot \cos\left[\frac{1}{3} \cdot \text{Arg}(w)\right] \quad (3.3.33)$$

$$\sigma_2 = \frac{I_1}{3} - |w|^{1/3} \cdot \cos\left[\frac{1}{3} \cdot \text{Arg}(w)\right] - \sqrt{3} \cdot |w|^{1/3} \cdot \sin\left[\frac{1}{3} \cdot \text{Arg}(w)\right] \quad (3.3.34)$$

$$\sigma_3 = \frac{I_1}{3} - |w|^{1/3} \cdot \cos\left[\frac{1}{3} \cdot \text{Arg}(w)\right] + \sqrt{3} \cdot |w|^{1/3} \cdot \sin\left[\frac{1}{3} \cdot \text{Arg}(w)\right] \quad (3.3.35)$$

Once known the principal stresses, it is straightforward to obtain the three related shear stresses:

$$\tau_1 = \frac{\sigma_1 - \sigma_3}{2} \quad (3.3.36)$$

$$\tau_2 = \frac{\sigma_1 - \sigma_2}{2} \quad (3.3.37)$$

$$\tau_3 = \frac{\sigma_2 - \sigma_3}{2} \quad (3.3.38)$$

Kept constant the notch opening angle 2α , the load ratio R and the distance r from the notch tip, the maximum shear stresses depend again on the polar coordinate θ , the machine angle β and the phase angle ϕ .

Now it is possible to determine the point, located along a circumferential path at a distance r from the notch tip, see Figure 3.3.2, where the integrals in one loading cycle of the three different shear stress functions reach their maximum values. As soon as the values of the three different integrals are known, the averaged values

of the three shear stresses can be calculated for a complete loading cycle. Finally, it has to be selected the maximum between the three averaged shear stresses, that corresponds to the maximum shear stress averaged on a loading cycle. The three averaged values of the shear stresses are obtainable as follows:

$$\bar{\tau}_1 = \frac{\int_0^{2\cdot\pi} \tau_1(\beta) \cdot d\beta}{2 \cdot \pi} \quad (3.3.39)$$

$$\bar{\tau}_2 = \frac{\int_0^{2\cdot\pi} \tau_2(\beta) \cdot d\beta}{2 \cdot \pi} \quad (3.3.40)$$

$$\bar{\tau}_3 = \frac{\int_0^{2\cdot\pi} \tau_3(\beta) \cdot d\beta}{2 \cdot \pi} \quad (3.3.41)$$

The maximum value between the three averaged shear stresses is finally called $\bar{\tau}$ ($\bar{\tau} = \max[(\bar{\tau}_1, \bar{\tau}_2, \bar{\tau}_3)]$).

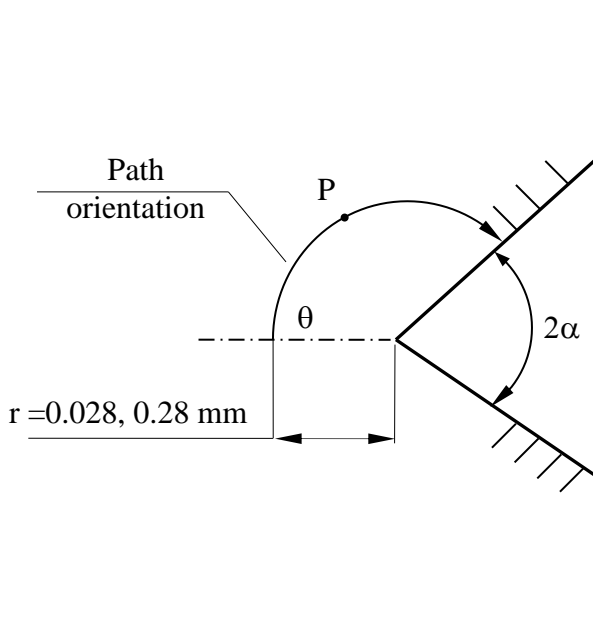


Figure 3.3.2. Definition of the circumferential path used to discover the critical point where the maximum averaged shear stress reaches its maximum value.

Once fixed the notch opening angle 2α , the load ratio R and the distance r from

the notch tip, the maximum value in each analysis has been compared considering different values of the phase angle ϕ and the biaxiality ratio $\Lambda = \frac{T_a}{S_a}$ (Eqs 3.3.10, 3.3.11). This analysis permits to understand if these two variables induce significant effects on the averaged shear stress and thus on the strength of a sharp V-notched component.

3.3.3. Results and discussions

In order to provide the value of the maximum shear stress averaged on a multiaxial fatigue cycle a dedicated software has been implemented on Wolfram Mathematica[®]. This software permits to compute $\bar{\tau}$ for different angles θ and to search the critical angle on which the maximum value of the averaged shear stress is reached. The angle θ has been varied between 0 and $180-\alpha$ degrees, being 2α the notch opening angle, with incremental steps of 1° .

All in all, considering all the varied parameters, more than 24000 different analyses have been carried out in order to investigate the effect of the phase angle. Only the most significant results are reported below.

Two different distances, $r = 0.28$ mm and $r = 0.028$ mm and three different notch opening angles, $2\alpha = 30^\circ$, 90° and 135° , have been considered. Then two different load ratios have been used, $R = 0$ and $R = -1$, while the biaxiality ratio has been set equal to $1/\sqrt{3}$, 0.6, 1, 1.6 and $\sqrt{3}$ and finally the phase angles taken into account were three: 0° (in phase loading), 45° , 90° .

The behavior of the maximum averaged shear stress along the circumferential path matching the increment of θ is investigated in Figures 3.3.3-3.3.4. Not all the studied cases are shown in the figures because a similar trend has been detected in the other cases.

Figure 3.3.3 shows the behavior of $\bar{\tau}$ normalized by the nominal tensile stress in the case of a notch opening angle $2\alpha = 90^\circ$, a load ratio R equal to -1, a distance $r = 0.28$ mm and a biaxiality ratio Λ equal to $1/\sqrt{3}$ for all the different phase angles. From the figure it can be seen that the averaged maximum shear stress assumes higher values moving from the in phase configuration to the out of phase

configuration (90°) for the whole circumferential path. The three curves tend to reach the maximum value in a range between 70° and 90° (see Table 3.3.1). This means that, according to the present analytical frame, the critical point for a V-notched specimen subjected to multiaxial loading is far from the notch bisector line. However it is worth mentioning that also on the notch bisector line the out of phase loading is more damaging.

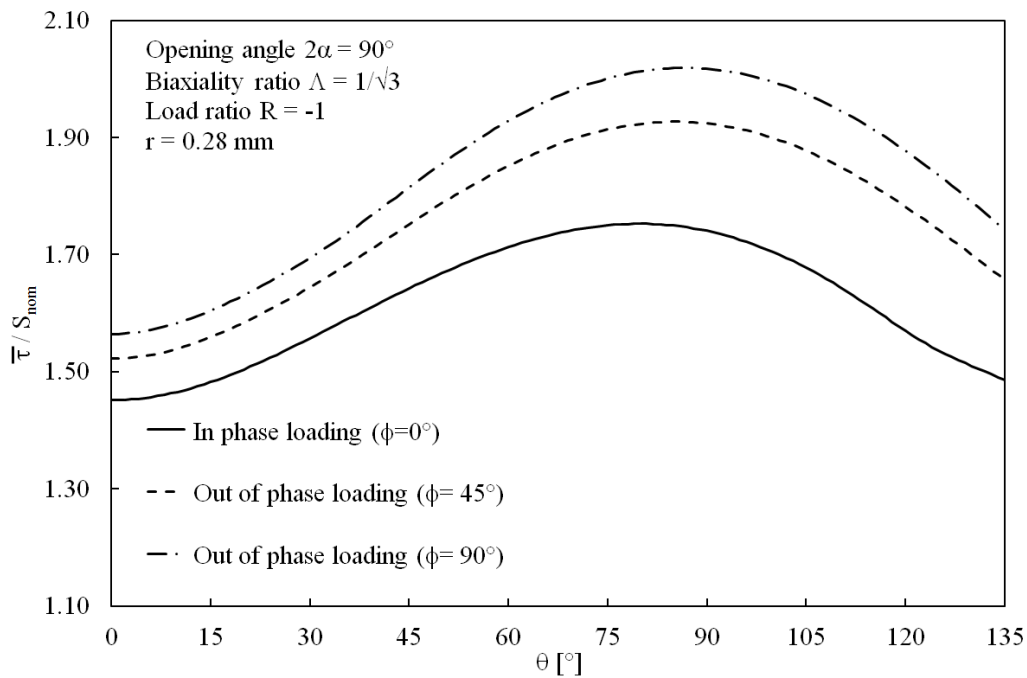


Figure 3.3.3. Behaviour of the averaged maximum tangential stress varying the polar coordinate θ and the phase displacement in the particular case of $2\alpha=90^\circ$, $\Lambda=1/\sqrt{3}$, $R=-1$ and $r=0.28$ mm.

The same diagram is provided also in the case of a load ratio $R = 0$. From Figure 3.3.4 it is evident that the results are close to those obtained in the case of $R = -1$. Also for this load ratio the maximum value is reached far from the notch bisector line at an inclination ranging from 70 to 90° .

The same behavior is noticed by varying the notch opening angle 2α , the distance r or the biaxiality ratio Λ .

In Table 3.3.1 all the values of the critical angle, θ , where the averaged shear stress reaches its maximum value are shown in the case of a notch opening angle $2\alpha = 90^\circ$ and a distance $r=0.28$ mm. It can be observed that the critical angle

increases reaching the maximum value for $\phi = 90^\circ$ both for $R = -1$ and for $R = 0$. Moreover, from all the analyses carried out, it is visible that at a fixed phase angle, the critical angle decreases when the biaxiality ratio increases (see again Table 3.3.1). These observations are also valid for the other values of the notch opening angle 2α and the distance r .

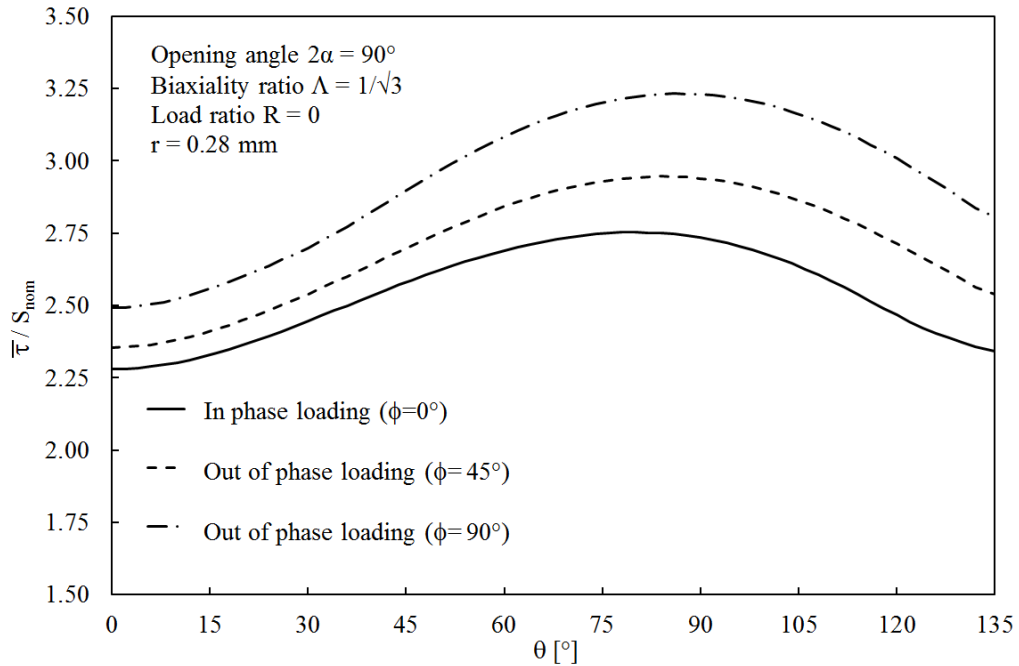


Figure 3.3.4. Behaviour of the averaged maximum tangential stress varying the polar coordinate θ and the phase displacement in the particular case of $2\alpha=90^\circ$, $\Lambda=1/\sqrt{3}$, $R=0$ and $r=0.28$ mm.

Table 3.3.1. Critical angles θ where the averaged maximum tangential stress is reached, in the case of $2\alpha = 90^\circ$ and $r = 0.28$ mm.

Load ratio, R	Phase angle, ϕ [°]	Biaxiality ratio, Λ				
		$1/\sqrt{3}$	0.6	1	1.6	$\sqrt{3}$
-1	0	80°	79°	73°	71°	71°
	45	85°	85°	82°	79°	79°
	90	87°	87°	84°	83°	82°
0	0	80°	79°	73°	71°	71°
	45	84°	84°	80°	77°	77°

90 87° 87° 85° 84° 83°

Figures 3.3.3-3.3.4 just commented above make it evident the trend of the averaged maximum shear stress by varying the polar coordinate θ . Figures 3.3.5-3.3.6 can justify that trend (of $\bar{\tau}$) by investigating the changing of the maximum shear stress over a single multiaxial fatigue cycle. The maximum shear stress, τ_{\max} , which is the maximum of the three different principal shear stresses, has been computed at the critical angle on which $\bar{\tau}$ reaches its maximum value.

Figure 3.3.5 plots $\tau_{\max}/S_{\text{nom}}$ in the case of a notch opening angle $2\alpha = 90^\circ$, a load ratio R equal to -1 , a distance $r = 0.28$ mm and a biaxiality ratio Λ equal to $1/\sqrt{3}$ for all the different phase angles. It can be noted that an in phase loading condition generates a maximum shear stress ranging between zero and an absolute maximum value. By increasing the phase angle from 0° to 90° it can be seen that the peak tends to decrease but, at the same time, the minimum assumes a value not much far from the maximum one, becoming almost constant in the case of a phase angle $\phi = 90^\circ$. This consideration leads to the conclusion that the mean effect just described is more effective by moving the phase angle from 0° to 90° .

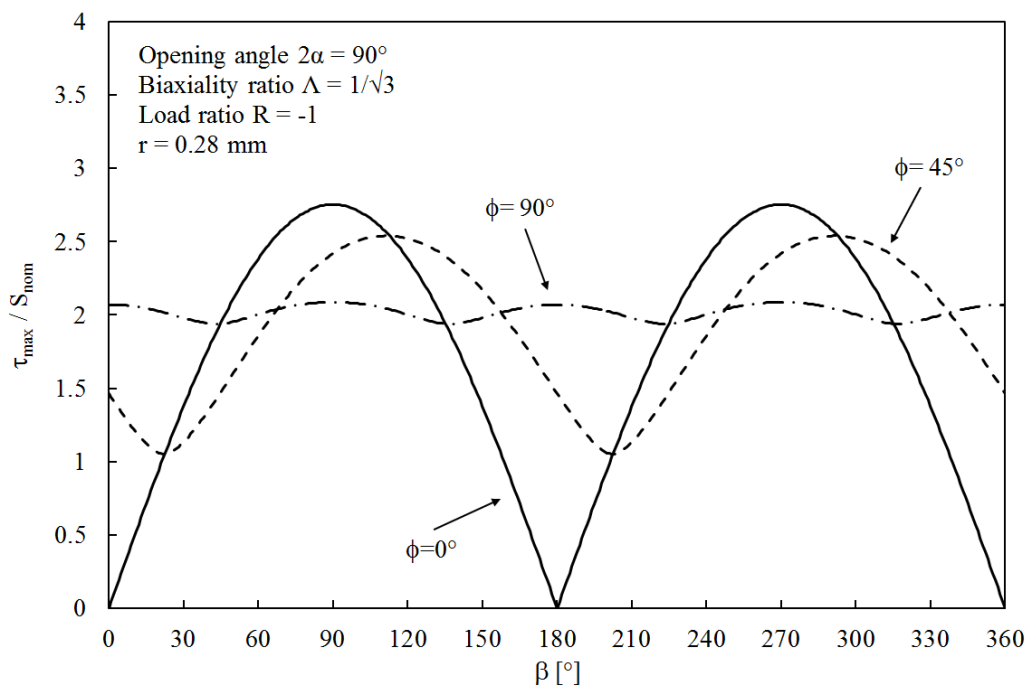


Figure 3.3.5. Variation of the maximum tangential stress on the critical coordinate θ during an entire loading cycle for different phase displacements. Case $2\alpha=90^\circ$, $\Lambda=1/\sqrt{3}$, $R=-1$ and $r=0.28$ mm.

In the case of a load ratio R equal to 0 (Figure 3.3.6), the maximum normalized shear stress for $\phi = 0^\circ$, ranges, once again, between 0 and an absolute maximum. By increasing the phase angle from 0° to 90° , the maximum value decreases and the minimum one increases. Unlike the previous case, however, it can be observed that the difference between the maximum value and the minimum one remains high also increasing the phase angle. Also for this load ratio, the phase angle generates a mean effect in terms of the averaged shear stress. This effect could be detrimental for the multiaxial fatigue strength of the component.

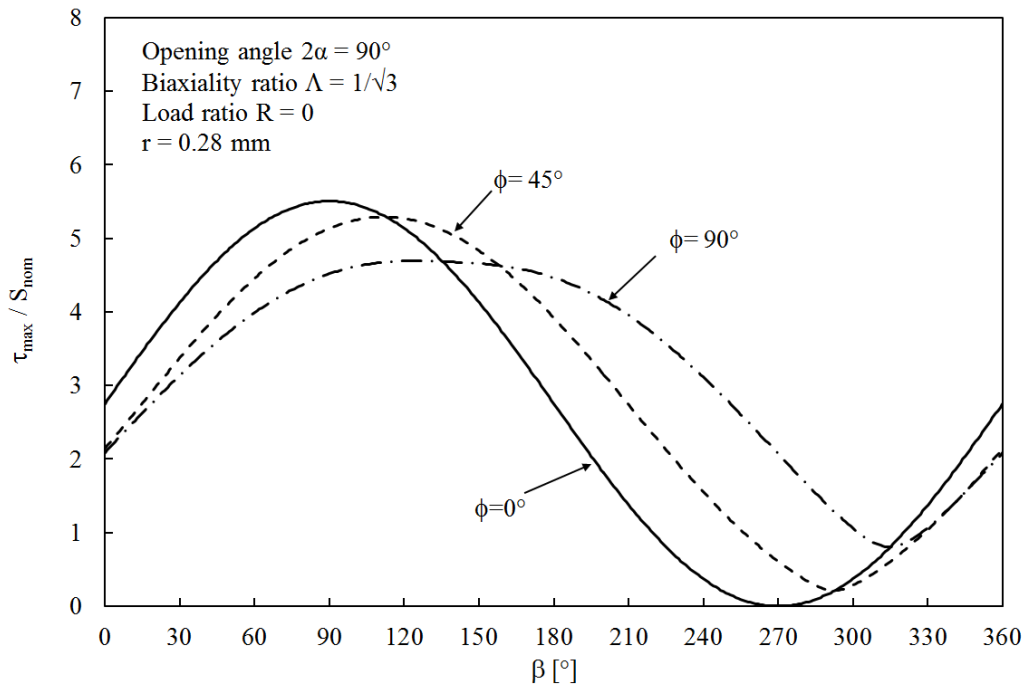


Figure 3.3.6. Variation of the maximum tangential stress on the critical coordinate θ during an entire loading cycle for different phase displacements. Case $2\alpha=90^\circ$, $\Lambda=1/\sqrt{3}$, $R=0$ and $r=0.28$ mm.

The same trends can be observed also for the other values of the notch opening angle 2α , the distance r and the biaxiality ratio Λ . The plots are not reported herein for sake of brevity.

Figures 3.3.7-3.3.11 represent the summary diagrams with the aim of quantifying the damaging effect due to the phase angle on a sharply V-notched component

subjected to multiaxial fatigue loading, by changing the notch opening angle 2α , the load ratio R and the distance from the notch tip r .

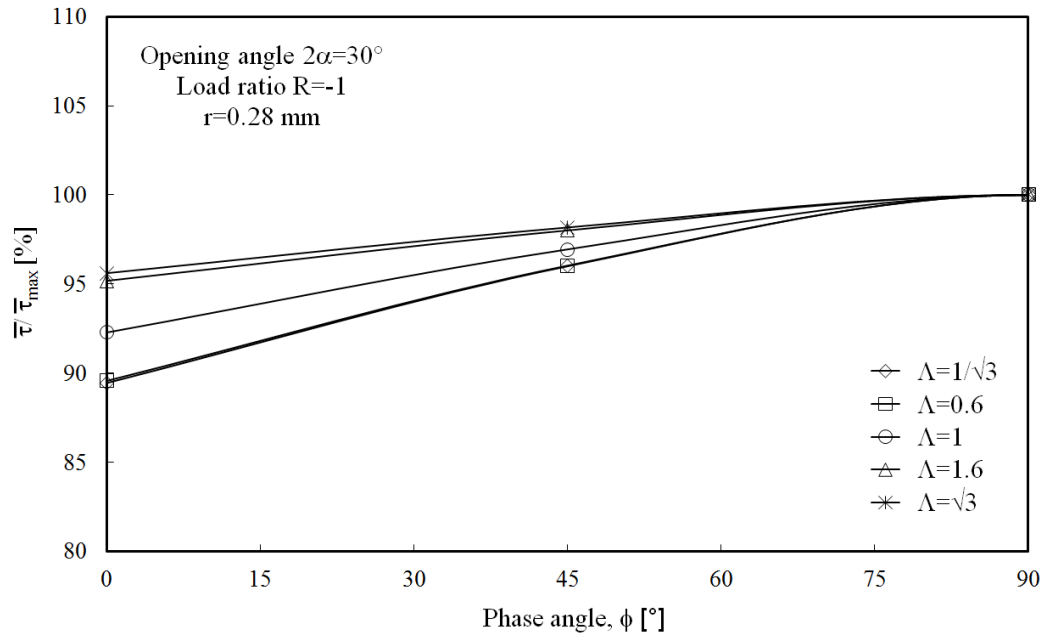


Figure 3.3.7. Summary of the phase angle effect for different biaxiality ratios in the case of $2\alpha=30^\circ$, $R=-1$ and $r=0.28$ mm.

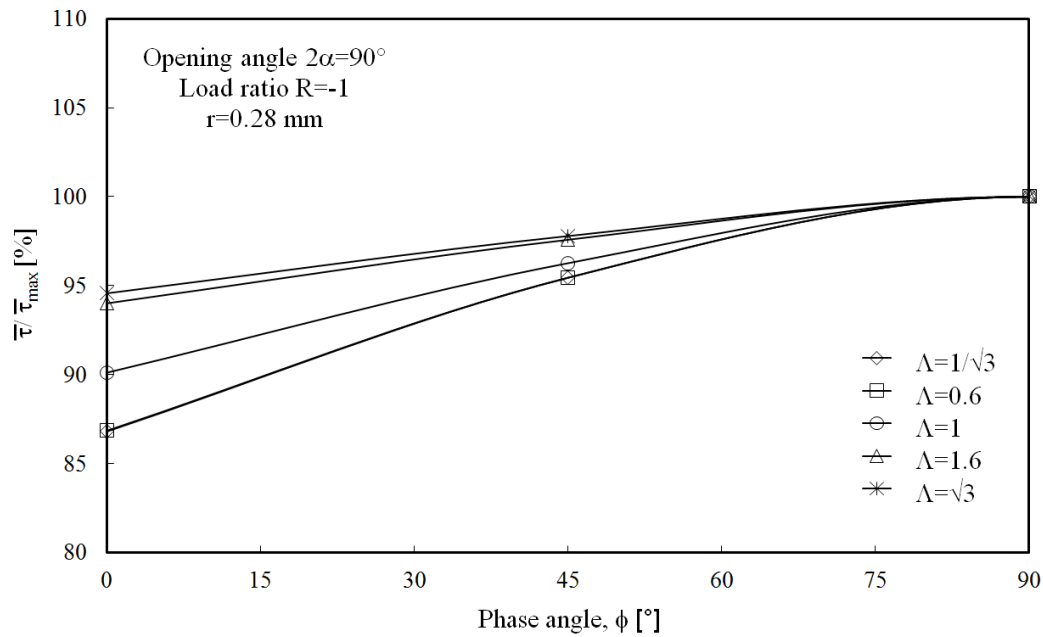


Figure 3.3.8. Summary of the phase angle effect for different biaxiality ratios in the case of $2\alpha=90^\circ$, $R=-1$ and $r=0.28$ mm.

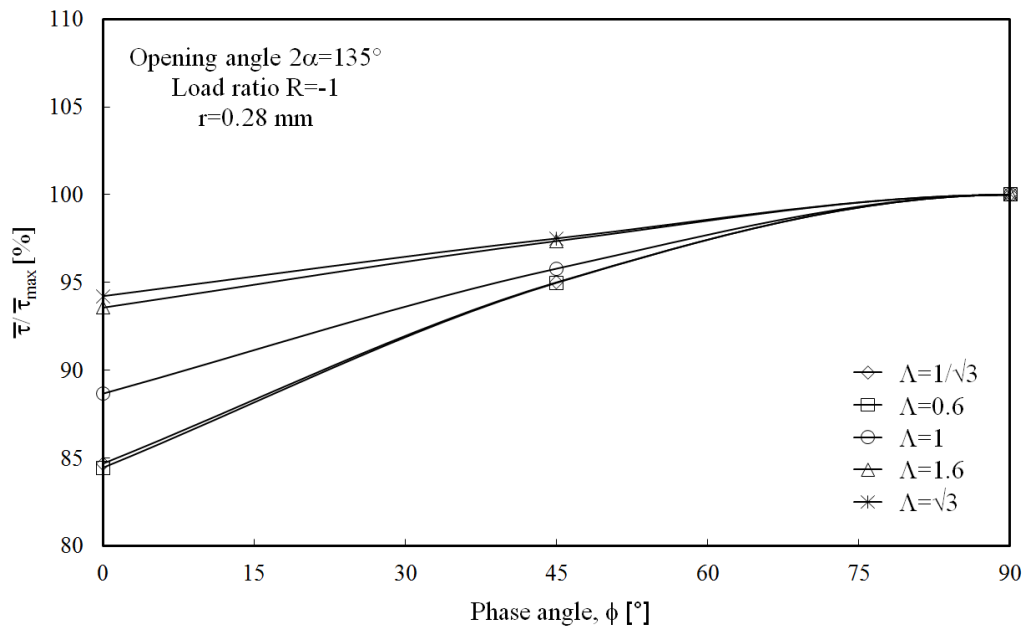


Figure 3.3.9. Summary of the phase angle effect for different biaxiality ratios in the case of $2\alpha = 135^\circ$, $R = -1$ and $r = 0.28$ mm.

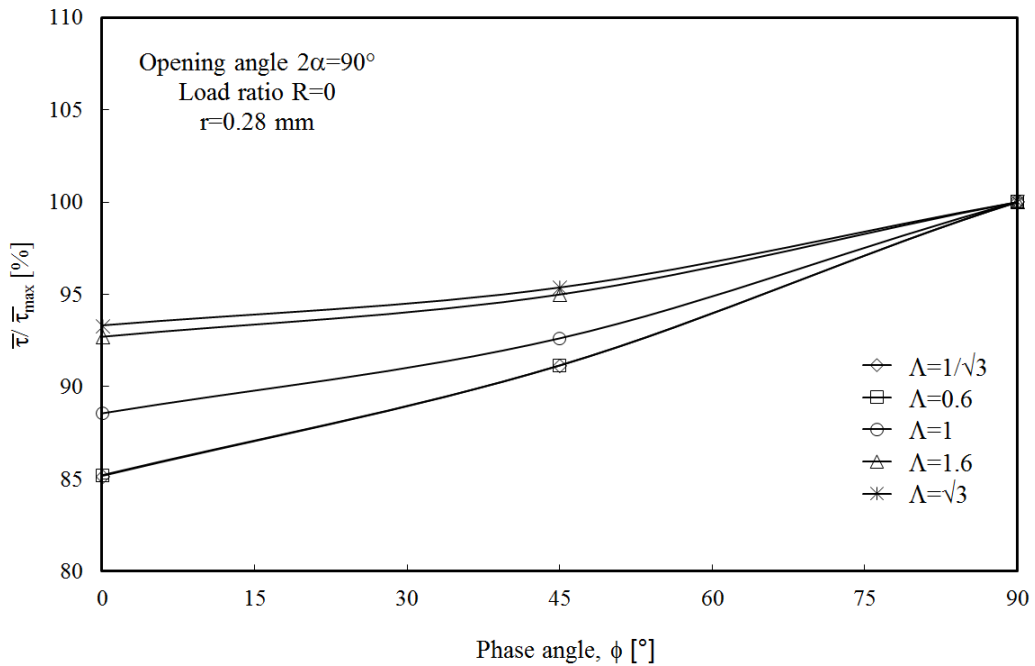


Figure 3.3.10. Summary of the phase angle effect for different biaxiality ratios in the case of $2\alpha = 90^\circ$, $R = 0$ and $r = 0.28$ mm.

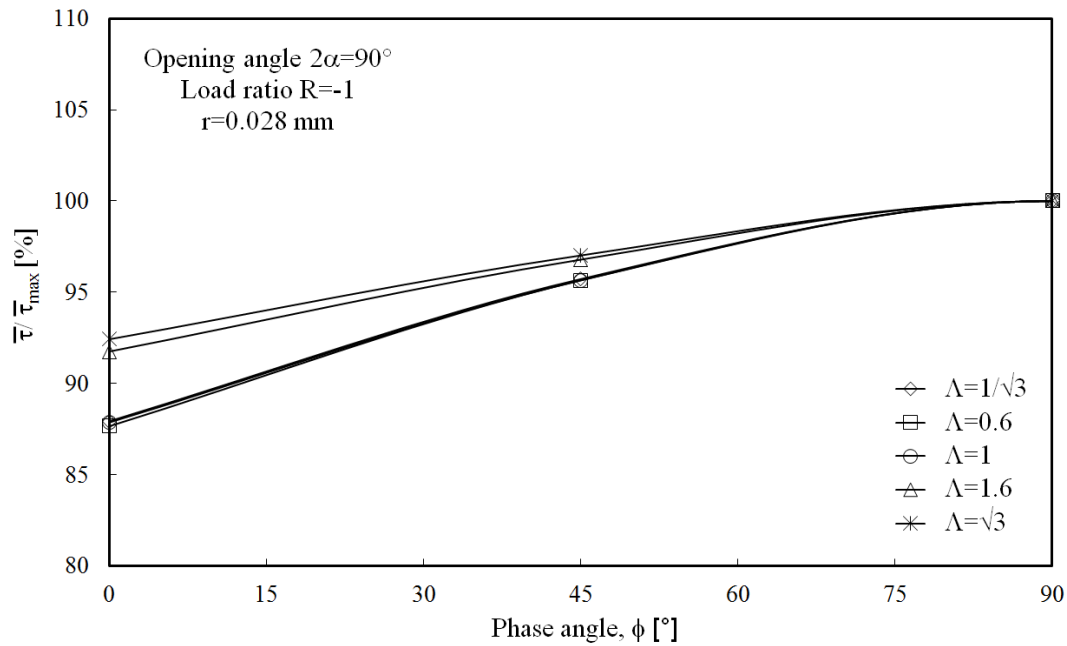


Figure 3.3.11. Summary of the phase angle effect for different biaxiality ratios in the case of $2\alpha=90^\circ$, $R=-1$ and $r=0.028$ mm.

Regarding the dependence on the notch opening angle, Figures 3.3.7-3.3.9 show the averaged maximum shear stress normalized by the maximum value computed for a fixed biaxiality ratio, in the case of three different notch opening angles, $2\alpha = 30^\circ$, 90° and 135° respectively, a load ratio $R = -1$ and a distance $r = 0.28$ mm from the notch tip for all the different biaxiality ratios. It can be seen that for all the five considered biaxiality ratios the critical configuration is reached for $\phi = 90^\circ$, independently from the notch opening angle. The in phase loading is always the less damaging configuration, however it becomes comparable to the case $\phi = 90^\circ$ when the biaxiality ratio increases. In the cases corresponding to lower values of Λ , the in phase loading is about 10, 13 and 16% less damaging with respect to the case $\phi = 90^\circ$ for a notch opening angle equal to $2\alpha = 30^\circ$, 90° and 135° respectively. The difference between in phase and out of phase loading reduces to 4, 6 and 7% respectively for higher values of the biaxiality ratio. According to the results it can be observed that the effect of the phase angle is weakly dependent on the notch opening angle, and this is more true for high values of the biaxiality ratio.

Figure 3.3.10, together with Figure 3.3.8, shows the effect of different load ratios

R, in the case of a notch opening angle $2\alpha = 90^\circ$ and a distance $r = 0.28$ mm from the notch tip for all the different biaxiality ratios. Dealing with a load ratio equal to 0, the critical phase angle, as visible from Figure 3.3.10, corresponds to the out of phase configuration ($\phi = 90^\circ$) while the in phase loading is about 15% less damaging in the case of low biaxiality ratios. The difference between in phase and out of phase loading reduces to 7% for higher values of Λ . Moving from $\phi = 0^\circ$ to $\phi = 90^\circ$ the effect of the phase angle becomes less detrimental but not negligible. The same trend can be observed for the other values of the notch opening angle considered herein. According to the results it can be observed that a variation of the load ratio R may induce only a modification of the concavity of the curves that slightly modify the normalized values of the averaged maximum shear stress.

Finally Figure 3.3.11, together with Figure 3.3.8, shows the effect of different distances r from the notch tip, in the case of a notch opening angle $2\alpha = 90^\circ$ and a load ratio $R = -1$ for all the different biaxiality ratios. Also considering a distance from the notch tip equal to 0.028 mm the critical phase angle, as visible from Figure 3.3.11, corresponds to the out of phase configuration ($\phi = 90^\circ$) while the in phase loading is about 12% less damaging in the case of low biaxiality ratios. The difference between in phase and out of phase loading reduces to 8% for higher values of Λ . The same trend has been observed for the other notch opening angles and load ratios considered herein. A variation of the distance r does not change substantially the trend but slightly modify the normalized values of the averaged maximum shear stress making the curves less spaced. It can be concluded that the effect of the phase angle is weakly sensitive to the material characteristic length.

3.3.4. Some experimental evidences

Being conscious that the out-of-phase loading is still an open problem in fatigue design, and that the proposed analytical frame is only a simplified method developed under linear elastic hypotheses, there are some recent experimental results which confirm the slight penalizing effect at least for severely notched specimens under multiaxial loading [28,32,33]. When the notch becomes blunt (see Refs [33]) the effect of out-of-phase is negligible. As explained above this is

a general tendency that could be influenced by the mechanical/fatigue properties of the tested material, by many non-linear effects which could be important in the crack nucleation and propagation under non-proportional loadings and also by the material characteristic length or control volume size with respect to the notch radius.

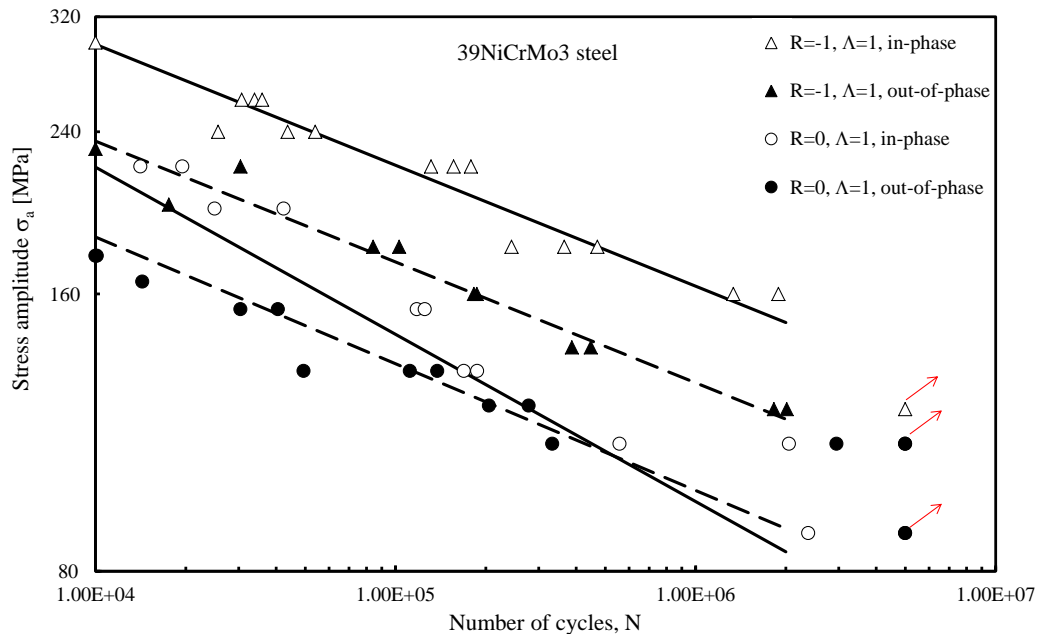


Figure 3.3.12. In-phase and out-of-phase fatigue data taken from Ref. [21]. The solid and dashed lines represent the Wohler curve (linear regression) with $P_s = 50\%$ relating to each data series.

Figures 3.3.12 and 3.3.13 report two examples taken from Refs [28] and [33], respectively. In Figure 3.3.12 data from 39NiCrMo3 steel under in-phase and out-of-phase loadings are summarized [28]. The notch tip radius was equal to 0.1 mm. In Figure 3.3.13 data from 40CrMoV13.9 notched specimens are summarized [33]. The notch tip radius was constant and equal to 1 mm, while the notch opening angle was equal to 90° . For both materials the penalizing effect due to out-of-phase loading is evident. It is also clear that for the same material the effect due to non-proportional loadings is affected by the nominal load ratio as well as by the biaxiality ratio ($\Lambda = \tau/\sigma$) in agreement with the analytical frame proposed here. These effects can be also different at low and high cycle fatigue due to the influence of the non-linear effects occurring during the tests and not considered in the proposed analytical formulation. From Figure 3.3.12 it is evident that the

effect of out-of-phase loading is more pronounced for $R = 0$ than for $R = -1$. This is in agreement with Figures 3.3.8 and 3.3.10 derived by using the analytical findings of the present work.

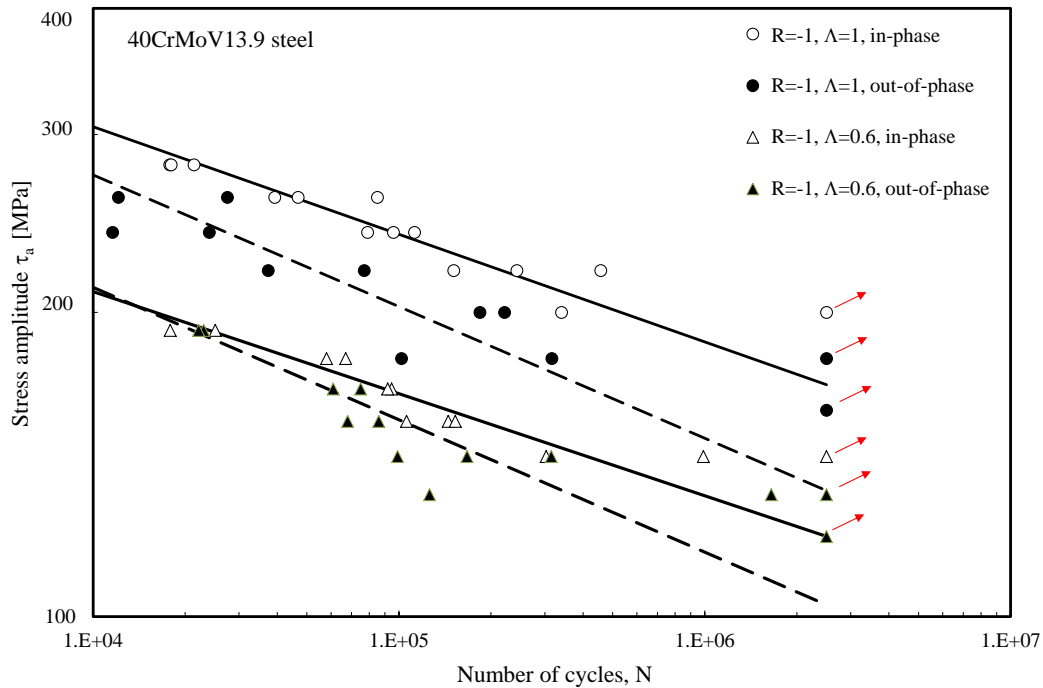


Figure 3.3.13. In-phase and out-of-phase fatigue data taken from Ref. [23]. The solid and dashed lines represent the Wohler curve (linear regression) with $P_s = 50\%$ relating to each data series.

To conclude, it can be also said that the complex fatigue response of metallic materials to multiaxial loading paths requires for calibration some information which can be obtained only by running the appropriate experiments [114]. Unfortunately, because of a lack of both time and resources, very often, structural engineers are requested to perform the multiaxial fatigue assessment by guessing the necessary fatigue properties. In this complex scenario, initially, the nowadays available empirical rules suitable for estimating fatigue strength under both pure axial and pure torsional fatigue loading have been reviewed. Under proportional loading, the empirical rules reviewed in [114] can confidently be used to perform the multiaxial fatigue assessment, this holding true in the presence of both zero and non-zero superimposed static stresses. On the contrary, under non-proportional loading, the use of such rules can result in a non-conservative fatigue design. Taking into account all these important considerations, this work is a first

trial to face the problem of non-proportional loadings dealing with pointed notches which is still a challenging and open problem.

3.3.5. Discussion

The present work deals with the investigation of the effect of the phase angle on sharp V-notched components subjected to multiaxial fatigue loading. The possible detrimental influence of the phase angle is often related to the arising of non-linear effects contemplated in the cyclic plasticity theory, as suggested by many papers in the literature.

Being conscious of the material dependent non-linear effects just mentioned and the simplified assumptions of the proposed frame, this work tries to explain the phase angle effect only focusing on the linear elastic stress field ahead of a pointed notch (i.e. notch radius equal to zero). The parameter considered as critical in the present study is the maximum shear stress averaged over an entire loading cycle. The analogy of the proposed approach with the critical plane approaches is only the consideration of a shear stress as a critical parameter. On the other hand substantial differences exist between the present approach and those based on critical planes. The main difference is that the present work is focused on sharp notches and the critical point is not known a priori being its determination based on the maximization of the chosen critical parameter.

All in all more than 24000 different analyses have been carried out considering different notch opening angles, load ratios, biaxiality ratios and phase angles. Different distances r have been considered, as well.

A dedicated software has been implemented in order to compute the averaged maximum shear stress on different inclinations with respect to the notch bisector line. It has been found that the location on which the averaged parameter reaches its maximum value is far from the notch bisector line and it acts at a circumferential coordinate ranging between 70° and 90° depending on the loading conditions. Considering an entire cycle on the critical angle, the maximum shear stress ranges from a value equal to zero to an absolute maximum in the case of in-phase loading. When the phase angle is different from zero it has been noted that the peak values decrease while the valley values increase, resulting in a mean

effect more damaging for the component.

In more detail, it has been shown that in the case of a fully reversed multiaxial fatigue loading the most damaging configuration is the 90° out-of-phase loading with a decreasing of the fatigue strength between 6 and 13% with respect to the in-phase loading, in the case of $2\alpha = 90^\circ$. The influence of the phase angle is more pronounced for lower values of the biaxiality ratio. A similar behavior has been observed for a load ratio equal to 0 being, also in this case, the most damaging configuration at $\phi = 90^\circ$. The reduction of the fatigue strength has been estimated between 7 and 15%, again for the master case $2\alpha = 90^\circ$. Also in this case, the influence of the phase angle is more pronounced for lower values of the biaxiality ratio.

In addition it has been observed that the effect of the phase angle depends weakly on the notch opening angle and on the material characteristic length.

References

- [1] Fatemi A, Shamsaei N. Multiaxial fatigue: An overview and some approximation models for life estimation. *Int J Fatigue* 2011;33:948–58.
- [2] Nieslony A, Sonsino CM. Comparison of some selected multiaxial fatigue assessment criteria. 2008.
- [3] Fatemi A, Socie DF. A critical plane approach to multiaxial fatigue damage including out-of-phase loading. *Fatigue Fract Eng Mater Struct* 1988;11:149–65.
- [4] Fatemi A, Kurath P. Multiaxial Fatigue Life Predictions Under the Influence of Mean-Stresses. *J Eng Mater Technol* 1988;110:380.
- [5] Lagoda T, Macha E, Bedkowski W. A critical plane approach based on energy concepts: application to biaxial random tension-compression high-cycle fatigue regime. *Int J Fatigue* 1999;21:431–43.
- [6] Carpinteri A, Spagnoli A. Multiaxial high-cycle fatigue criterion for hard metals. *Int J Fatigue* 2001;23:135–45.
- [7] Carpinteri A, Spagnoli A, Vantadori S, Bagni C. Structural integrity assessment of metallic components under multiaxial fatigue: the C-S criterion and its evolution. *Fatigue Fract Eng Mater Struct* 2013;36:870–83.
- [8] Ye D, Hertel O, Vormwald M. A unified expression of elastic–plastic notch stress–strain calculation in bodies subjected to multiaxial cyclic loading. *Int J Solids Struct* 2008;45:6177–89.
- [9] Cristofori A, Benasciutti D, Tovo R. A stress invariant based spectral method to estimate fatigue life under multiaxial random loading. *Int J Fatigue* 2011;33:887–99.
- [10] Carpinteri A, Spagnoli A, Vantadori S. Reformulation in the frequency domain of a critical plane-based multiaxial fatigue criterion. *Int J Fatigue* 2014;67:55–61.
- [11] Jasper TM. The value of the energy relation in the testing of ferrous metals at varying ranges of stress and at intermediate and high temperatures. *Philos Mag Ser 6* 1923;46:609–27.
- [12] Ellyin F. Cyclic strain energy density as a criterion for multiaxial fatigue failure. *Biaxial an. London: EGF Publication; 1989.*
- [13] Ellyin F. Fatigue damage, crack growth and life prediction. 1997.
- [14] Macha E, Sonsino CM. Energy criteria of multiaxial fatigue failure. *Fatigue Fract Eng Mater Struct* 1999;22:1053–70.
- [15] Pook LP, Sharples JK. The mode III fatigue crack growth threshold for mild steel. *Int J Fract* 1979;15:R223–6.
- [16] Pook LP. The fatigue crack direction and threshold behaviour of mild steel under mixed mode I and III loading. *Int J Fatigue* 1985;7:21–30.
- [17] Tong J, Yates JR, Brown MW. Some aspects of fatigue thresholds under

- mode III and mixed mode III and I loadings. *Int J Fatigue* 1996;18:279–85.
- [18] Ritchie RO. Mechanisms of fatigue crack propagation in metals, ceramics and composites: Role of crack tip shielding. *Mater Sci Eng A* 1988;103:15–28.
- [19] Yu H, Tanaka K, Akiniwa Y. Estimation of torsional fatigue strength of medium carbon steel bars with a circumferential crack by the cyclic resistance-curve method. *Fatigue Fract Eng Mater Struct* 1998;21:1067–76.
- [20] Tanaka K, Akiniwa Y, Yu H. The propagation of a circumferential fatigue crack in medium-carbon steel bars under combined torsional and axial loadings. In: *Mixed-Mode Crack Behaviour*. In: Miller K, McDowell D, editors. *Mix. Crack Behav.* ASTM 1359, PA: West Conshohocked; 1999, p. 295–311.
- [21] Pippin R, Zelger C, Gach E, Bichler C, Weinhandl H. On the mechanism of fatigue crack propagation in ductile metallic materials. *Fatigue Fract Eng Mater Struct* 2011;34:1–16.
- [22] Christopher CJ, James MN, Patterson EA, Tee KF. Towards a new model of crack tip stress fields. *Int J Fract* 2007;148:361–71.
- [23] Christopher CJ, James MN, Patterson EA, Tee KF. A quantitative evaluation of fatigue crack shielding forces using photoelasticity. *Eng Fract Mech* 2008;75:4190–9.
- [24] James MN, Christopher CJ, Lu Y, Patterson EA. Local crack plasticity and its influences on the global elastic stress field. *Int J Fatigue* 2013;46:4–15.
- [25] Lin B, Mear ME, Ravi-Chandar K. Criterion for initiation of cracks under mixed-mode I + III loading. *Int J Fract* 2010;165:175–88.
- [26] Park J, Nelson D. Evaluation of an energy-based approach and a critical plane approach for predicting constant amplitude multiaxial fatigue life. *Int J Fatigue* 2000;22:23–39.
- [27] Lazzarin P, Zambardi R. A finite-volume-energy based approach to predict the static and fatigue behavior of components with sharp V-shaped notches. *Int J Fract* 2001;112:275–98.
- [28] Berto F, Lazzarin P, Yates JR. Multiaxial fatigue of V-notched steel specimens: A non-conventional application of the local energy method. *Fatigue Fract Eng Mater Struct* 2011;34:921–43.
- [29] Lazzarin P, Sonsino CM, Zambardi R. A notch stress intensity approach to assess the multiaxial fatigue strength of welded tube-to-flange joints subjected to combined loadings. *Fatigue Fract Eng Mater Struct* 2004;27:127–40.
- [30] Atzori B, Berto F, Lazzarin P, Quaresimin M. Multi-axial fatigue behaviour of a severely notched carbon steel. *Int J Fatigue* 2006;28:485–93.
- [31] Lazzarin P, Livieri P, Berto F, Zappalorto M. Local strain energy density and fatigue strength of welded joints under uniaxial and multiaxial loading. *Eng Fract Mech* 2008;75:1875–89.
-

-
- [32] Berto F, Lazzarin P. Fatigue strength of structural components under multi-axial loading in terms of local energy density averaged on a control volume. *Int J Fatigue* 2011;33:1055–65.
- [33] Berto F, Lazzarin P, Marangon C. Fatigue strength of notched specimens made of 40CrMoV13.9 under multiaxial loading. *Mater Des* 2014;54:57–66.
- [34] Berto F, Lazzarin P, Tovo R. Multiaxial fatigue strength of severely notched cast iron specimens. *Int J Fatigue* 2014;67:15–27.
- [35] Lazzarin P, Berto F. Control volumes and strain energy density under small and large scale yielding due to tension and torsion loading. *Fatigue Fract Eng Mater Struct* 2008;31:95–107.
- [36] Morrissey R, McDowell DL, Nicholas T. Frequency and stress ratio effects in high cycle fatigue of Ti-6Al-4V. *Int J Fatigue* 1999;21:679–85.
- [37] Morrissey R, Nicholas T. Fatigue strength of Ti-6Al-4V at very long lives. *Int J Fatigue* 2005;27:1608–12.
- [38] Takeuchi E, Furuya Y, Nagashima N, Matsuoka S. The effect of frequency on the giga-cycle fatigue properties of a Ti-6Al-4V alloy. *Fatigue Fract Eng Mater Struct* 2008;31:599–605.
- [39] Haritos G, Nicholas T, Lanning DB. Notch size effects in HCF behavior of Ti-6Al-4V. *Int J Fatigue* 1999;21:643–52.
- [40] Lanning D, Haritos GK, Nicholas T. Influence of stress state on high cycle fatigue of notched Ti-6Al-4V specimens. *Int J Fatigue* 1999;21:87–95.
- [41] Lanning D, Haritos GK, Nicholas T, Maxwell DC. Low-cycle fatigue/high-cycle fatigue interactions in notched Ti-6Al-4V. *Fatigue Fract Eng Mater Struct* 2001;24:565–77.
- [42] Nicholas T. Step loading for very high cycle fatigue. *Fatigue Fract Eng Mater Struct* 2002;25:861–9.
- [43] Golden PJ, Nicholas T. The effect of angle on dovetail fretting experiments in Ti-6Al-4V. *Fatigue Fract Eng Mater Struct* 2005;28:1169–75.
- [44] Benedetti M, Bertini L, Fontanari V. Behaviour of fatigue cracks emanating from circular notches in Ti-6Al-4V under bending. *Fatigue Fract Eng Mater Struct* 2004;27:111–25.
- [45] Benedetti M, Fontanari V. The effect of bi-modal and lamellar microstructures of Ti-6Al-4V on the behaviour of fatigue cracks emanating from edge-notches. *Fatigue Fract Eng Mater Struct* 2004;27:1073–89.
- [46] Le Biavant K, Pommier S, Prioul C. Local texture and fatigue crack initiation in a Ti-6Al-4V titanium alloy. *Fatigue Fract Eng Mater Struct* 2002;25:527–45..
- [47] Hoshide T, Kakiuchi E, Hirota T. Microstructural effect on low cycle fatigue behaviour in Ti-alloys under biaxial loading. *Fatigue Fract Eng Mater Struct* 1997;20:941–50.
- [48] Nakamura H, Takanashi M, Itoh T, Wu M, Shimizu Y. Fatigue crack
-

- initiation and growth behavior of Ti-6Al-4V under non-proportional multiaxial loading. *Int J Fatigue* 2011;33:842-8.
- [49] Kallmeyer AR, Krgo A, Kurath P. Evaluation of Multiaxial Fatigue Life Prediction Methodologies for Ti-6Al-4V. *J Eng Mater Technol* 2002;124:229.
- [50] Marmi AK, Habraken AM, Duchene L. Multiaxial fatigue damage modelling at macro scale of Ti-6Al-4V alloy. *Int J Fatigue* 2009;31:2031-40.
- [51] Lemaitre J, Chaboche J-L. *Mechanics of solid materials*. New ed. Cambridge University Press; 1994.
- [52] Marangon C, Lazzarin P, Berto F, Campagnolo A. Some analytical remarks on the influence of phase angle on stress fields ahead of sharp V-notches under tension and torsion loads. *Theor Appl Fract Mech* 2014;74:64-72.
- [53] Beltrami E. Sulle condizioni di resistenza dei corpi elastici. *Il Nuovo Cimento* 18 (in Italian); 1885.
- [54] Gross B, Mendelson A. Plane elastostatic analysis of V-notched plates. *Int J Fract Mech* 1972;8:267-76.
- [55] Lazzarin P, Tovo R. A notch intensity factor approach to the stress analysis of welds. *Fatigue Fract Eng Mater Struct* 1998;21:1089-103.
- [56] Lazzarin P, Berto F, Zappalorto M. Rapid calculations of notch stress intensity factors based on averaged strain energy density from coarse meshes: Theoretical bases and applications. *Int J Fatigue* 2010;32:1559-67.
- [57] Lazzarin P, Berto F, Gomez F, Zappalorto M. Some advantages derived from the use of the strain energy density over a control volume in fatigue strength assessments of welded joints. *Int J Fatigue* 2008;30:1345-57.
- [58] Campagnolo A, Berto F, Lazzarin P. The effects of different boundary conditions on three-dimensional cracked discs under anti-plane loading. *Eur J Mech - A/Solids* 2015;50:76-86.
- [59] Radaj D. *Design and Analysis of Fatigue Resistant Welded Structures*. Cambridge: Abington Publishing; 1990.
- [60] Taylor D, Barrett N, Lucano G. Some new methods for predicting fatigue in welded joints. *Int J Fatigue* 2002;24:509-18.
- [61] Yakubovskii V V., Valteris IJ. Geometrical parameters of butt and fillet welds and their influence on the welded joints fatigue life. 1989.
- [62] Dunn ML, Suwito W, Cunningham S. Fracture initiation at sharp notches: Correlation using critical stress intensities. *Int J Solids Struct* 1997;34:3873-83.
- [63] Jiang Y, Feng M. Modeling of Fatigue Crack Propagation. *J Eng Mater Technol* 2004;126:77.
- [64] Berto F, Lazzarin P. Recent developments in brittle and quasi-brittle failure assessment of engineering materials by means of local approaches. *Mater*
-

-
- Sci Eng R Reports 2014;75:1–48.
- [65] Ferro P. The local strain energy density approach applied to pre-stressed components subjected to cyclic load. *Fatigue Fract Eng Mater Struct* 2014;37:1268–80.
- [66] Radaj D. State-of-the-art review on extended stress intensity factor concepts. *Fatigue Fract Eng Mater Struct* 2014;37:1–28.
- [67] Radaj D. State-of-the-art review on the local strain energy density concept and its relation to the J -integral and peak stress method. *Fatigue Fract Eng Mater Struct* 2015;38:2–28.
- [68] Lassen T. The effect of the welding process on the fatigue crack growth. *Weld Res Suppl* 1990;69:75S – 81S.
- [69] Singh PJ, Achar DRG, Guha B, Nordberg H. Fatigue life prediction of gas tungsten arc welded AISI 304L cruciform joints with different LOP sizes. *Int J Fatigue* 2003;25:1–7.
- [70] Singh PJ, Guha B, Achar DR. Fatigue life improvement of AISI 304L cruciform welded joints by cryogenic treatment. *Eng Fail Anal* 2003;10:1–12.
- [71] Williams ML. Stress singularities resulting from various boundary conditions in angular corners of plates in tension. *J Appl Mech* 1952;19:526–8.
- [72] Livieri P, Lazzarin P. Fatigue strength of steel and aluminium welded joints based on generalised stress intensity factors and local strain energy values. *Int J Fract* 2005;133:247–76.
- [73] Sheppard SD. Field Effects in Fatigue Crack Initiation: Long Life Fatigue Strength. *J Mech Des* 1991;113:188.
- [74] Sonsino C. Multiaxial fatigue of welded joints under in-phase and out-of-phase local strains and stresses. *Int J Fatigue* 1995;17:55–70.
- [75] Neuber H. Zur Theorie der technischen Formzahl. *Forsch Ing Wes* 1936;7:271–4.
- [76] Neuber H. *Theory of Notch Stresses*. Berlin: Springer-Verlag; 1958.
- [77] Peterson RE. *Notch sensitivity*. New York (USA): Metal fatigue, McGraw Hill; 1959.
- [78] Tanaka K. Engineering formulae for fatigue strength reduction due to crack-like notches. *Int J Fract* 1983;22:R39–46.
- [79] Lazzarin P, Tovo R, Meneghetti G. Fatigue crack initiation and propagation phases near notches in metals with low notch sensitivity. *Int J Fatigue* 1997;19:647–57.
- [80] Taylor D. Geometrical effects in fatigue: a unifying theoretical model. *Int J Fatigue* 1999;21:413–20.
- [81] Susmel L, Taylor D. Fatigue design in the presence of stress concentrations. *J Strain Anal Eng Des* 2003;38:443–52.
-

- [82] Crupi G, Crupi V, Guglielmino E, Taylor D. Fatigue assessment of welded joints using critical distance and other methods. *Eng Fail Anal* 2005;12:129–42.
- [83] Susmel L. The theory of critical distances: a review of its applications in fatigue. *Eng Fract Mech* 2008;75:1706–24.
- [84] Susmel L. Modified Wöhler curve method, theory of critical distances and Eurocode 3: A novel engineering procedure to predict the lifetime of steel welded joints subjected to both uniaxial and multiaxial fatigue loading. *Int J Fatigue* 2008;30:888–907.
- [85] Susmel L. The Modified Wöhler Curve Method calibrated by using standard fatigue curves and applied in conjunction with the Theory of Critical Distances to estimate fatigue lifetime of aluminium weldments. *Int J Fatigue* 2009;31:197–212.
- [86] Rulmeca Bulk Catalogue 2015. http://www.rulmeca.it/en/products_bulk/catalogue/1/trasporto_a_nastro/1/rollers.
- [87] Hasebe N, Kutanda Y. Calculation of stress intensity factor from stress concentration factor. *Eng Fract Mech* 1978;10:215–21.
- [88] Zappalorto M, Lazzarin P, Yates JR. Elastic stress distributions for hyperbolic and parabolic notches in round shafts under torsion and uniform antiplane shear loadings. *Int J Solids Struct* 2008;45:4879–901.
- [89] Lazzarin P, Tovo R. A unified approach to the evaluation of linear elastic stress fields in the neighborhood of cracks and notches. *Int J Fract* 1996;78:3–19.
- [90] Qian J, Hasebe N. Property of eigenvalues and eigenfunctions for an interface V-notch in antiplane elasticity. *Eng Fract Mech* 1997;56:729–34.
- [91] Berto F, Campagnolo A, Lazzarin P. Fatigue strength of severely notched specimens made of Ti-6Al-4V under multiaxial loading. *Fatigue Fract Eng Mater Struct* 2015;38:503–17.
- [92] Seweryn A, Poskrobko Sł, Mróz Z. Brittle Fracture in Plane Elements with Sharp Notches under Mixed-Mode Loading. *J Eng Mech* 1997;123:535–43.
- [93] Kihara S, Yoshii A. A strength evaluation method of a sharply notched structure by a new parameter, “the equivalent stress intensity factor”. *JSME Int J* 1991;34:70–5.
- [94] Atzori B, Dattoma V. A comparison of the fatigue behaviour of welded joints in steels and in aluminium alloys. *IIW Doc XXXIII-1089-1983* 1983.
- [95] Haibach E. *Service Fatigue-Strength – Methods and data for structural analysis*. Berlin: Springer Verlag; 2002.
- [96] Meneghetti G, Campagnolo A, Berto F, Atzori B. Averaged strain energy density evaluated rapidly from the singular peak stresses by FEM: cracked components under mixed-mode (I+II) loading. *Theor Appl Fract Mech* 2015;79:113–24.

-
- [97] He Z, Kotousov A, Berto F. Effect of vertex singularities on stress intensities near plate free surfaces. *Fatigue Fract Eng Mater Struct* 2015;n/a – n/a.
- [98] Pook LP. A 50 year retrospective review of three-dimensional effects at cracks and sharp notches. *Fatigue Fract Eng Mater Struct* 2013;36:699–723.
- [99] Pook LP, Berto F, Campagnolo A, Lazzarin P. Coupled fracture mode of a cracked disc under anti-plane loading. *Eng Fract Mech* 2014;128:22–36.
- [100] Marangon C, Campagnolo A, Berto F. Three-dimensional effects at the tip of rounded notches subjected to mode-I loading under cyclic plasticity. *J Strain Anal Eng Des* 2015;50:299–313.
- [101] Grabner K, Grimmer KJ, Kessler F. Research into normal-forces between belt and idlers at critical locations on the belt conveyor track. *Bulk Solids Handl* 1993;13:727–34.
- [102] Ewing JA, Humfrey JCW. The Fracture of Metals under Repeated Alternations of Stress. *Philos Trans R Soc A Math Phys Eng Sci* 1903;200:241–50.
- [103] Forsyth P. A two stage process of fatigue crack growth. *Crack Propag. Symp. - Cranf. Coll. Aeronaut.*, 1961, p. 76–94.
- [104] Smith R, Watson P, Topper T. A stress–strain function for the fatigue of metal. *J Mater* 1970;5:767–78.
- [105] Brown M, Miller K. A theory for fatigue under multiaxial stress–strain conditions. *Proc Inst Mech Eng* 1973;187:745–56.
- [106] Carpinteri A, Spagnoli A, Vantadori S. Multiaxial fatigue assessment using a simplified critical plane-based criterion. *Int J Fatigue* 2011;33:969–76.
- [107] Reis L, Li B, de Freitas M. Crack initiation and growth path under multiaxial fatigue loading in structural steels. *Int J Fatigue* 2009;31:1660–8.
- [108] Liu K. A Method Based on Virtual Strain-Energy Parameters for Multiaxial Fatigue Life Prediction. *Adv. Multiaxial Fatigue*, ASTM STP 1191, 100 Barr Harbor Drive, PO Box C700, West Conshohocken, PA 19428-2959: ASTM International; 1993, p. 67–84.
- [109] Chu C-C. Fatigue Damage Calculation Using the Critical Plane Approach. *J Eng Mater Technol* 1995;117:41.
- [110] Glinka G, Wang G, Plumtree A. Mean stress effects in multiaxial fatigue. *Fatigue Fract Eng Mater Struct* 2007;18:755–64.
- [111] Jiang Y. A fatigue criterion for general multiaxial loading. *Fatigue Fract Eng Mater Struct* 2000;23:19–32..
- [112] Gladskyi M, Fatemi A. Load sequence effects on fatigue crack growth in notched tubular specimens subjected to axial and torsion loadings. *Theor Appl Fract Mech* 2014;69:63–70.
- [113] Socie D, Marquis G. *Multiaxial fatigue*. Warrendale (PA): Society of Automotive Engineers; 2000.
-

- [114] Susmel L. On the estimation of the material fatigue properties required to perform the multiaxial fatigue assessment. *Fatigue Fract Eng Mater Struct* 2013;36:565–85.
- [115] Shamsaei N, Fatemi A. Effect of microstructure and hardness on non-proportional cyclic hardening coefficient and predictions. *Mater Sci Eng A* 2010;527:3015–24.
- [116] Capetta S, Tovo R, Taylor D, Livieri P. Numerical evaluation of fatigue strength on mechanical notched components under multiaxial loadings. *Int J Fatigue* 2011;33:661–71.
- [117] Susmel L. *Multiaxial notch fatigue*. Cambridge: Woodhead publishing; 2009.
- [118] Susmel L, Taylor D. A critical distance/plane method to estimate finite life of notched components under variable amplitude uniaxial/multiaxial fatigue loading. *Int J Fatigue* 2012;38:7–24.
- [119] Susmel L. Estimating fatigue lifetime of steel weldments locally damaged by variable amplitude multiaxial stress fields. *Int J Fatigue* 2010;32:1057–80.
- [120] Gladskyi M, Fatemi A. Notched fatigue behavior including load sequence effects under axial and torsional loadings. *Int J Fatigue* 2013;55:43–53.
- [121] Hertel O, Vormwald M. Short-crack-growth-based fatigue assessment of notched components under multiaxial variable amplitude loading. *Eng Fract Mech* 2011;78:1614–27.
- [122] Doring R, Hoffmeyer J, Seeger T, Vormwald M. Short fatigue crack growth under nonproportional multiaxial elastic–plastic strains. *Int J Fatigue* 2006;28:972–82.
- [123] Ohkawa C, Ohkawa I. Notch effect on torsional fatigue of austenitic stainless steel: Comparison with low carbon steel. *Eng Fract Mech* 2011;78:1577–89.
- [124] Tanaka K. Crack initiation and propagation in torsional fatigue of circumferentially notched steel bars. *Int J Fatigue* 2014;58:114–25.
- [125] Sonsino CM, Kueppers M. Multiaxial fatigue of welded joints under constant and variable amplitude loadings. *Fatigue Fract Eng Mater Struct* 2001;24:309–27.
- [126] SONSINO C. Multiaxial fatigue assessment of welded joints – Recommendations for design codes. *Int J Fatigue* 2009;31:173–87.
- [127] Cardano G. *Artis magnae sive de regulis algebraicis, liber unus*. Translated. Nuremberg: 1545.
- [128] Seweryn A, Molski K. Elastic stress singularities and corresponding generalized stress intensity factors for angular corners under various boundary conditions. *Eng Fract Mech* 1996;55:529–56.
- [129] Berto F, Lazzarin P. A review of the volume-based strain energy density approach applied to V-notches and welded structures. *Theor Appl Fract*

Mech 2009;52:183–94.

- [130] Lazzarin P, Berto F, Atzori B. A synthesis of data from steel spot welded joints of reduced thickness by means of local SED. *Theor Appl Fract Mech* 2013;63-64:32–9.

CHAPTER 4

THREE-DIMENSIONAL EFFECTS

4.1 Three-dimensional effects on cracked components ^(*)

Nomenclature

a	crack length
h	control volume height
K	stress intensity factor, subscripts I, II, III denote mode, superscript c indicates a coupled mode
K_λ	stress intensity measure
p	a given constant
R_0	control volume radius
r	radius of K-dominated region
r, θ	polar coordinates
r, θ , ϕ	spherical coordinates
s	distance from surface
t	thickness
U	displacement subscripts x, y, z denote direction
x, y, z	Cartesian coordinates

Symbols

β	crack surface intersection angle
γ	crack front intersection angle
λ	parameter defining stress intensity measure
ν	Poisson's ratio
ρ	profile tip radius
σ	stress, subscripts x, y, z denote direction
τ	shear stress, subscripts xy, yz, xz denote direction

(*) See also:

Pook, L. P.; Campagnolo, A.; Berto, F. Coupled fracture modes of discs and plates under anti-plane loading and a disc under in-plane shear loading. *Fatigue and Fracture of Engineering Materials and Structures* (In press);

4.1.1. Introduction

Displacements are of fundamental importance in the understanding of the mechanics of materials in general [1–5]. In fracture mechanics the interest is in what happens in the vicinity of the crack tip, so it is sometimes referred to as crack tip surface displacement [1]. Notation used is shown in Figure 4.1.1. If a load is applied to a cracked body, then the crack surfaces move relative to each other. For points on opposing crack surfaces that were initially in contact there are three possible modes of crack surface displacement (mode I, mode II, mode III). By superimposing the three modes, it is possible to describe the most general case of crack tip surface displacement.

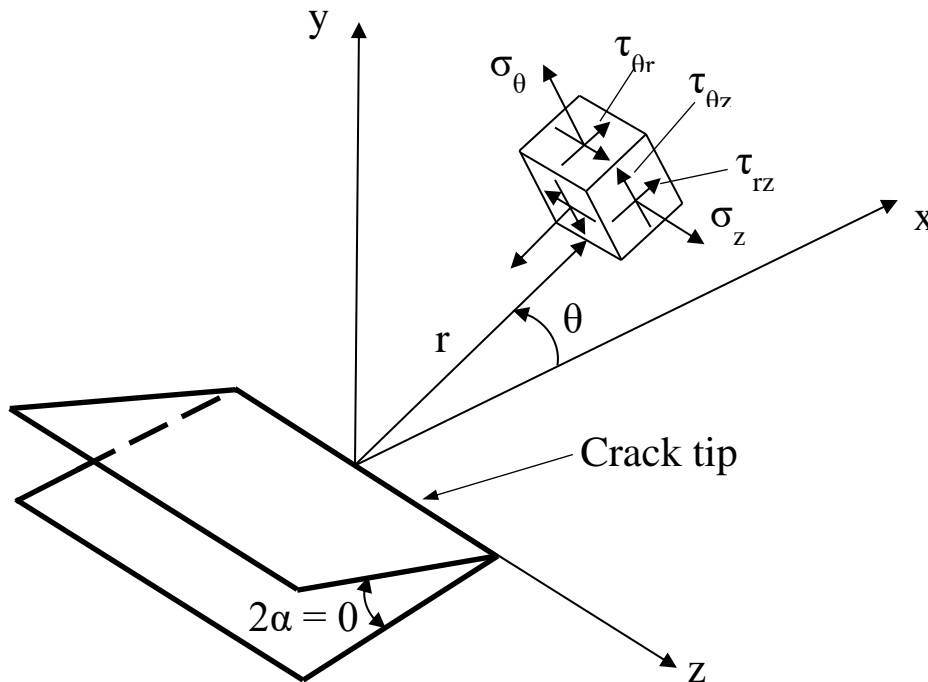


Figure 4.1.1. Notation for crack tip stress field.

If a crack surface is considered as consisting of points then the three modes of crack surface displacement provide an adequate description of the movements of crack surfaces when a load is applied. However, if the surface is regarded as consisting of infinitesimal elements, then element rotations must also be described, and Volterra distorsioni (distortions) are appropriate [6,7]. The crack

surfaces may be moved relative to each other in 6 different ways, so there are 6 distinct Volterra distortions. These are summarised in Table 4.1.1. Elements A and B are on opposite surfaces of a crack and are connected by a ring element around the crack tip (Figure 4.1.2). Modes I, II and III Volterra dislocations correspond to modes I, II and III crack tip surface displacements. The three Volterra disclinations are relative crack surface rotations.

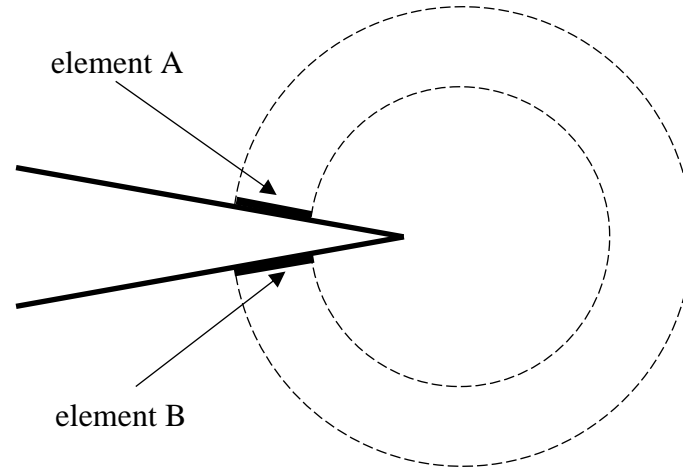


Figure 4.1.2. Ring element around crack tip.

Table 4.1.1. Volterra distortions.

Volterra distorsione	Relative motion of elements A and B
Mode I dislocation	Along y axis
Mode II dislocation	Along x axis
Mode III dislocation	Along z axis
Mode I disclination	Rotation about y axis
Mode II disclination	Rotation about x axis
Mode III disclination	Rotation about z axis

Crack tip surface displacements in the vicinity of a corner point in which a crack front intersects a surface are often of practical interest. Assuming that Poisson's ratio, $\nu > 0$, for the special case in which the crack surface intersection angle, γ (Figure 4.1.3) and the crack front intersection angle, β (Figure 4.1.4) are both 90°

then kinematics considerations for an antisymmetric loading [8–11] show that modes II and III crack tip surface displacements cannot exist in isolation [12,13]. Mode II induces mode III^c and mode III induces mode II^c. These induced modes are sometimes called coupled modes, indicated by the superscript c.

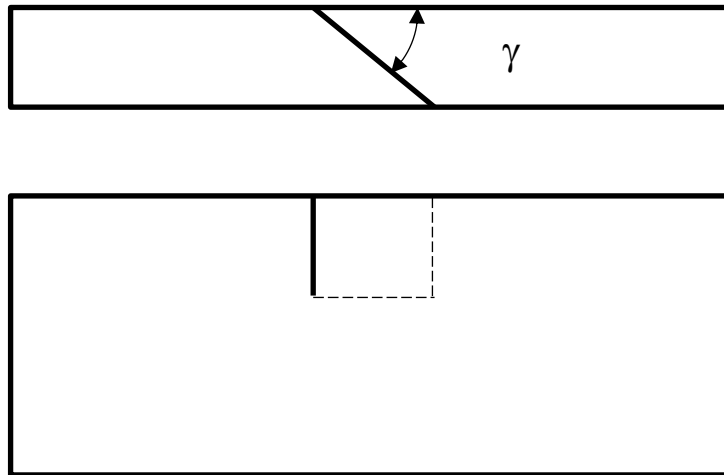


Figure 4.1.3. Definition of crack surface intersection angle, γ .

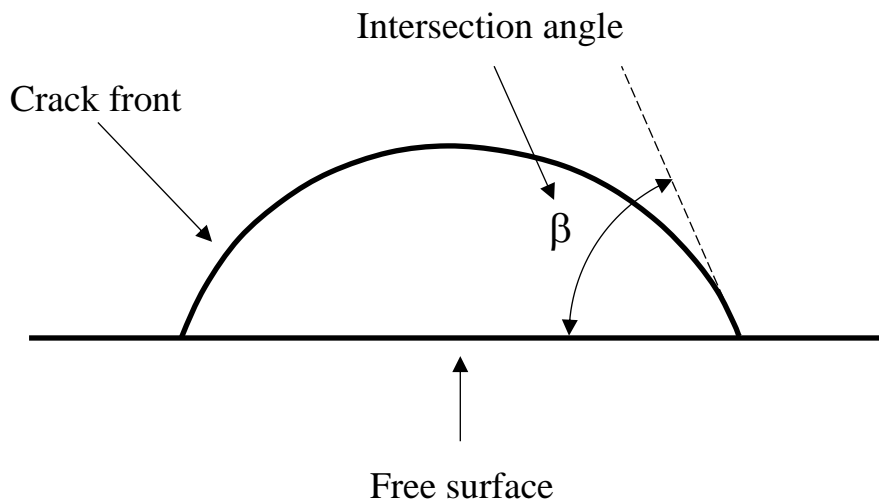


Figure 4.1.4. Definition of crack front intersection angle, β .

Within the framework of linear elastic fracture mechanics [1] the stress field in the vicinity of a crack tip is dominated by the leading term of a series expansion of the stress field [14]. This leading term is the stress intensity factor, K . A particular type of elastic crack tip stress field is associated with each mode of crack tip

surface displacement [15] and subscripts I, II and III are used to denote mode. Individual stress components are proportional to K/\sqrt{r} where r is the distance from the crack tip (Figure 4.1.1). Displacements are proportional to $K\sqrt{r}$. A stress intensity factor provides a reasonable description of the crack tip stress field in a K -dominated region at the crack tip, radius $r \approx a/10$ where a is crack length, [1] as shown in Figure 4.1.5.

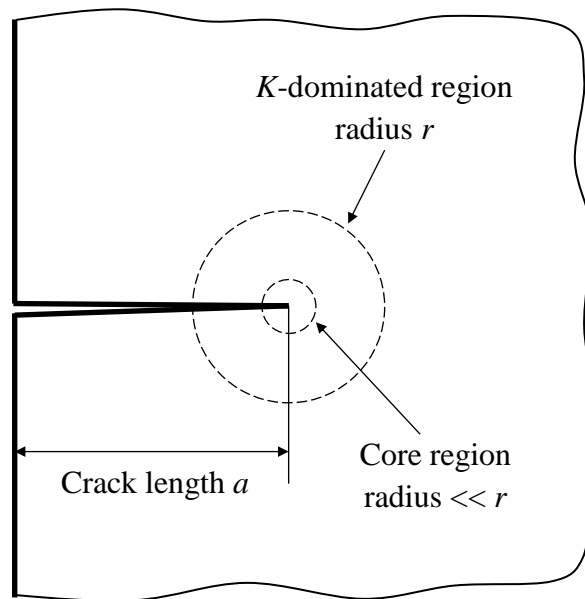


Figure 4.1.5. K -dominated region and core region at a crack tip.

Simplifying assumptions have become conventional in much present day linear elastic fracture mechanics, for example see Reference 2, and these are satisfactory for many purposes. The material is assumed to be a homogeneous isotropic continuum, and its behaviour is assumed to be linearly elastic. Crack surfaces are assumed to be smooth, although on a microscopic scale they are generally very irregular. Modifications are made to basic linear elastic fracture mechanics theory to allow for the actual behaviour of real materials. In considering practical aspects of linear elastic fracture mechanics, scales of observation need to be taken into account since the scale chosen can make a considerable difference to the appearance of an object [16]. Scales of observation for metallic materials [6,17,18]

are summarised in Table 4.1.2. The three largest are usually described as macroscopic, and the smaller scales as microscopic.

Table 4.1.2. Scales of observation for metallic materials.

Scale (mm)	Feature
10^{-6}	Ions, electron cloud
10^{-5}	Dislocations
10^{-4}	Subgrain boundary precipitates
10^{-3}	Subgrain slip bands
10^{-2}	Grains, inclusions, voids
10^{-1}	Large plastic strains
1	Stress intensity factor
10	Component, test piece

An apparent objection to the use of the stress intensity factor approach is the violation, in the immediate vicinity of the crack tip, of the initial linear elastic assumptions, in that strains and distortions are not small. However, as the assumptions are violated only in a small core region the general character of the K -dominated region is, to a reasonable approximation, unaffected. Similarly, by this small scale argument, small scale non-linear effects due to crack tip yielding, microstructural irregularities, internal stresses, irregularities in the crack surface, the actual fracture process, etc, may be regarded as within the core region. The idea of a core region within a K -dominated region was first used by Irwin in his analysis of crack tip plasticity [19]. The idea is the basis of the successful application of stress intensity factors to a wide range of practical engineering problems.

The existence of three-dimensional effects at cracks has been known for many years [4–6], but understanding has been limited, and for some situations still is. Understanding improved when the existence of corner point singularities [20] and their implications became known [21]. Despite increased understanding, three-dimensional effects are sometimes ignored in situations where they may be

important. Discussion here is restricted to cases in which the crack surface intersection angle, γ (Figure 4.1.3) and the crack front intersection angle β (Figure 4.1.4) are both 90° .

In three dimensional geometries, the derivation of stress intensity factors makes the implicit assumption that a crack front is continuous. This is not the case in the vicinity of a corner point, and the nature of the crack tip singularity changes. The resulting corner point singularities were described in detail in 1979 by Bažant and Estenssoro [20]. Some additional results were given by Benthem in 1980 [22]. For corner point singularities, the polar coordinates in Figure 4.1.1 are replaced by spherical coordinates (r, θ, ϕ) with origin at the corner point. The angle ϕ is measured from the crack front.

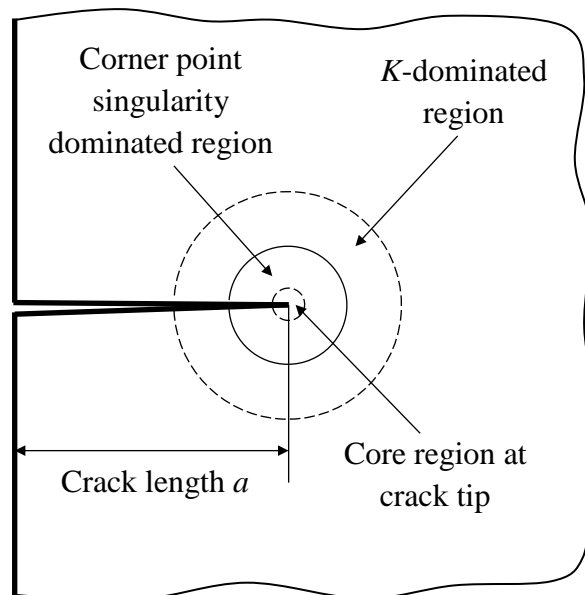


Figure 4.1.6. *K*-dominated region, corner point singularity dominated region and core region at a surface plane.

There do not appear to be any exact analytic solutions for corner point singularities. In their analysis Bažant and Estenssoro [20] assumed that all three modes of crack tip surface displacement are of the form $r^\lambda \rho^p F(\theta, \phi)$, where ρ is distance from the crack tip, and p is a given constant. They then calculated λ

numerically for a range of situations: λ is a function of Poisson's ratio, ν . For the antisymmetric mode, $\lambda = 0.598$ for $\nu = 0.3$. Benthem [22] made an equivalent assumption but used a different numerical method to calculate λ . The stress intensity measure, K_λ , may be used to characterise corner point singularities, where λ can be regarded as a parameter defining the corner point singularity. However, expressions for numerical values of K_λ , and associated stress and displacement fields, do not appear to be available. It follows from the initial assumption that stresses are proportional to K_λ/r^λ and displacements to $K_\lambda r^{1-\lambda}$, where r is measured from the corner point. Hence, stress and displacement plots are straight lines when plotted using logarithmic scales, and such plots obtained from finite element analysis can be used to determine values of λ . At the present state of the art the extent of a corner point singularity dominated region has to be determined numerically. However, it is usually small and at a surface plane can often be regarded as lying within a K -dominated region, as shown in Figure 4.1.6 [23]. When $\lambda = 0.5$ stress intensity factors are recovered.

At a corner point stresses are a singularity. They must be either infinite or zero, λ is indeterminate, and it is reasonable to speak of stress intensity factors in an asymptotic sense [4,5]. In the limit, as a crack front is approached, displacement fields must be those of a stress intensity factor [22]. Hence, there is an infinitesimal K -dominated region within the core region of a corner point singularity. The stress intensity factors are proportional to $s^{0.5 - \lambda}$ where s is distance from the surface along the z axis [22]. Hence, for the antisymmetric mode K_{II} and K_{III} both tend to infinity as a corner point is approached. Further, as a corner point the ratio K_{III}/K_{II} tends to a limiting value which is a function of ν . For $\nu = 0.3$ the limiting ratio is 0.5 [22]. Benthem points out that K_{II} and K_{III} lose their meaning at a corner point [22]. Dhondt suggests that modes II^c and III^c might not be singular [24]. The predicted tendency to infinity is reasonable for K_{II} since relevant stresses are in plane and disclinations are zero [4,5]. From a linear elastic viewpoint the predicted tendency of K_{III} to infinity cannot be correct [6]. At a surface shear stresses perpendicular to the surface are zero, which implies that K_{III} tends to zero as the surface is approached. Mode III is a torsion problem [15]. Under mode III (anti-plane) loading initially plane cross sections, including the

surface at a corner point, do not remain plane under load [6,7] and disclinations appear. It is well known that serious error can arise if warping of non circular cross sections under torsion is not taken into account in stress analyses [3]. Warping of the surface under mode III means that τ_{yz} at the surface does not have to be zero, and finite values of K_{III} are possible. The implication is that the non linearities cannot be regarded as being in a core region within a corner point singularity dominated region and that Bažant and Estenssoro's prediction that K_{III} tends to infinity as a corner point is correct. The alternative view, which is supported by a large body of evidence [6], is that apparent values of K_{III} decrease towards the surface in the z direction. This implies that K_{III} tends to zero as a corner point is approached, which is intuitively correct. It also implies that non linearities can be regarded as being within a core region, but does not explain why Bažant and Estenssoro's analysis does not give the correct limit. Nevertheless, this alternative view may well be adequate when considering practical implications. This paradox needs to be resolved so that the results of finite element analysis can be interpreted correctly.

The nature of finite element analysis means that stress intensity factors have to be calculated indirectly, and possible methods have been described by Hellen [25]. Finite element analysis of three dimensional configurations started in the late 1980 and confirmed the existence of coupled modes. However, results for K_{III} were erratic: sometimes K_{III} appeared to tend to infinity as a corner point was approached and sometimes appeared to tend to zero. For some time these erratic results were ascribed to the use of meshes that were too coarse [26]. Resolution of the paradox of the value of K_{III} at a corner point reduces to determining the correct method of proceeding to the limit as the corner point is approached.

There does not appear to have been a systematic investigation of the extent to which Bažant and Estenssoro's initial assumption is justified. Their assumption does appear to be satisfactory for the symmetric mode (mode I) in that their analysis leads to useful results [6].

Due to the uncertainties in the definition of the stress intensity factors on the free surfaces, as stated above, the strain energy averaged in a control volume (SED) [27] has been employed in the present investigation to quantify the stress intensity

through the thickness of the plate. For a review of the SED the reader can refer to [28,29]. This parameter has been successfully used by Lazzarin and co-authors to assess the fracture strength of a large bulk of materials, characterized by different control volumes, subjected to wide combinations of static loading [30–32] and the fatigue strength of welded joints [33] and notched components [34,35]. As described in [29] an intrinsic advantage of the SED approach is that it permits automatically to take into account higher order terms and three-dimensional effects. The parameter is easy to calculate in comparison with other well-defined and suitable 3D parameters [36,37] and can be directly obtained by using coarse meshes [29,38]. Another advantage of the SED is that it is possible to easily understand whether the through-the-thickness effects are important or not in the fracture assessment for a specific material characterized by a control volume depending on the material properties. Some brittle materials are characterized by very small values of the control radius and are very sensitive to stress gradients also in a small volume of material [29]. On the other hand more ductile materials have the capability of stress averaging in a larger volume and for this reason are less sensitive to the variations of the stress field through the thickness of the plate. The SED, once the control volume is properly modeled through the thickness of the plate, is able to quantify the 3D effects in comparison with the sensitivity of the specific material so providing precious information for the fracture assessment. Although only the crack case is considered here the SED could be easily applied also to V-notches.

4.1.2. Finite element modelling

4.1.2.1. Cracked discs under nominal Mode III loading

Stresses, stress intensity factors and displacements are examined in detail for 100 mm diameter discs of various thicknesses under anti-plane (nominal mode III) loading [4]. One half of the disc geometry used is shown in Figure 4.1.7a. The disc radius, r , is 50 mm, and the thickness is t . A through thickness crack has its tip at the centre of the disc, so its length, a , is 50 mm. Calculations are carried out using ANSYS 11 for $t/a = 0.25, 0.5, 0.75, 1, 1.25, 1.5, 1.75, 2, 2.25, 2.5, 2.75$ and 3. One

quarter of the disc is modelled. An overall view of the finite element mesh is shown in Figure 4.1.8a. Details of the mesh at the outer surface and crack tip are shown in Figures 4.1.8b and 4.1.8c. The crack tip element size in a radial direction, and the thicknesses of surface layers of elements are shown in Table 4.1.3.

The scale of the crack tip elements is of the same order as subgrain slip bands (Table 4.1.1), and the scale of surface layer thicknesses is of the same order as grains, inclusions and voids. Poisson's ratio is taken as 0.3 and Young's modulus as 200 GPa. Displacements corresponding to $K_{III} = 1 \text{ MPa}\cdot\text{m}^{0.5}$ ($31.62 \text{ N}\cdot\text{mm}^{0.5}$) are applied to the cylindrical surface. These boundary conditions mean that the disc is a core region within a virtual K -dominated region. Stress intensity factors are calculated from stresses on the crack surface near the crack tip using standard equations [1,15]. The strain energy density is calculated from a control volume at the crack tip.

4.1.2.2. Cracked plates under nominal Mode III loading

In the present calculations, stresses, stress intensity factors and displacements are examined in detail for 100 mm square plates of various thicknesses under anti-plane (nominal mode III) loading [5]. One half of the plate geometry used is shown in Figure 4.1.7b. The thickness is t . A through thickness crack has its tip at the centre of the plate, so its length, a , is 50 mm. Calculations are carried out using ANSYS 11 for $t/a = 0.25, 0.5, 0.75, 1, 1.25, 1.5, 1.75, 2, 2.25, 2.5, 2.75$ and 3. Poisson's ratio is taken as 0.3 and Young's modulus as 200 GPa. A displacement of 10^{-3} mm is applied to the edge of the plate. Stress intensity factors are calculated from stresses on the crack surface near the crack tip using standard equations [1,15]. The strain energy density is calculated from a control volume at the crack tip. One quarter of the plate is modelled. An overall view of the finite element mesh is shown in Figure 4.1.8a. Details of the mesh at the outer surface and crack tip are shown in Figures 4.1.8b and 4.1.8c. The crack tip element size in a radial direction, and the thicknesses of surface layers of elements are shown in Table 4.1.3. The scale of the crack tip elements is of the same order as subgrain slip bands (Table 4.1.1), and the scale of surface layer thicknesses is of the same order as grains, inclusions and voids.

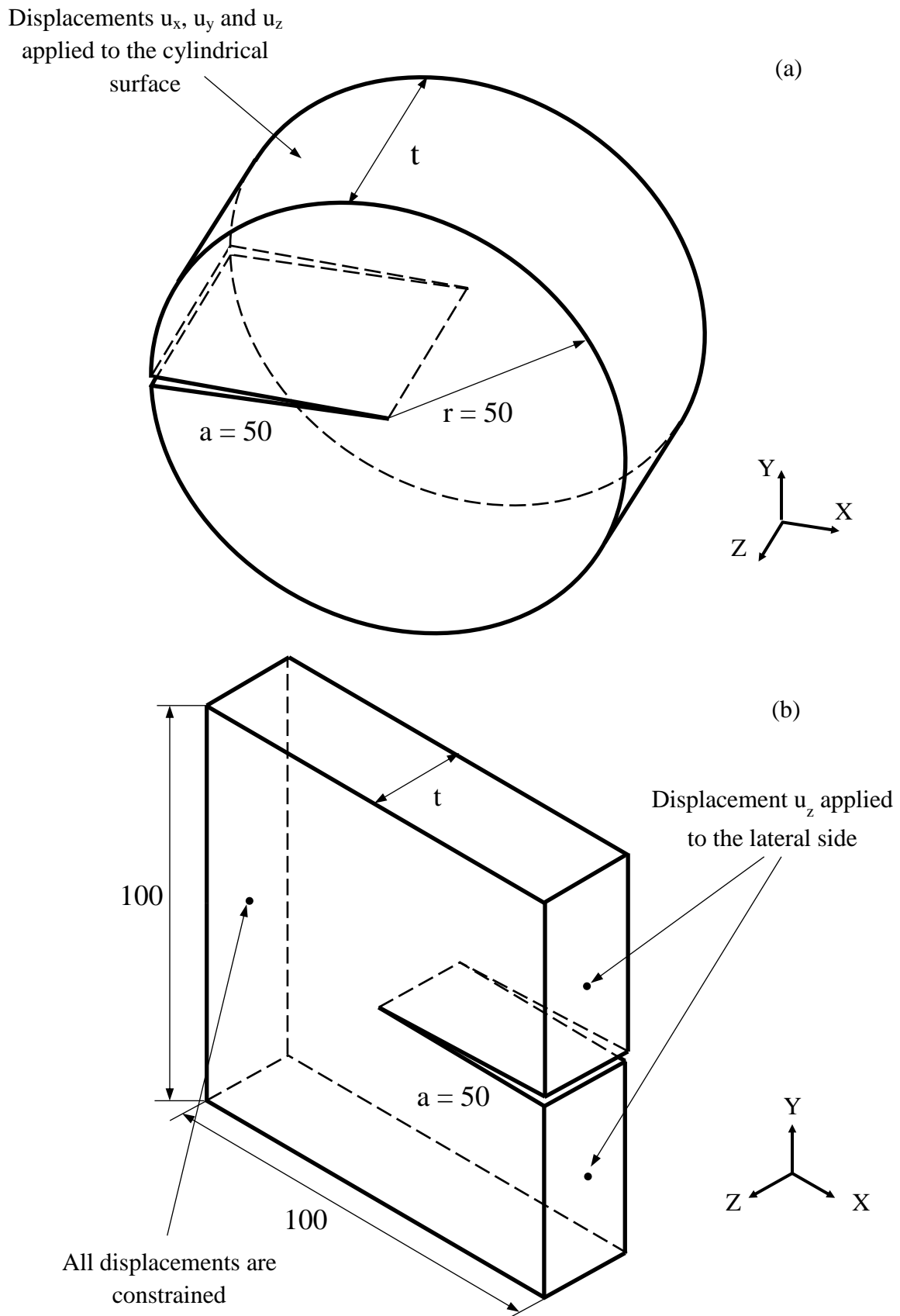


Figure 4.1.7. (a) Disc and (b) plate geometry.

4.1.2.3. Cracked discs under nominal Mode II loading

Stresses, stress intensity factors and displacements were examined in detail also for 100 mm diameter discs of various thicknesses under nominal mode II loading, Figure 4.1.7a and 4.1.8. In plane displacements were applied on the cylindrical surface, corresponding to a nominal mode II stress intensity factor $K_{II} = 1 \text{ MPa}\cdot\text{m}^{0.5}$ ($31.62 \text{ MPa}\cdot\text{mm}^{0.5}$). With these conditions the disc represents a core region completely dominated by the leading terms linked to the stress intensity factors.

Table 4.1.3. Element sizes.

t/a	Crack tip element size in radial direction (mm)	Surface layer thickness (mm)
0.25	10^{-3}	$1.11 \cdot 10^{-2}$
0.50	10^{-3}	$1.46 \cdot 10^{-2}$
0.75	10^{-3}	$1.75 \cdot 10^{-2}$
1.00	10^{-3}	$1.94 \cdot 10^{-2}$
1.25	10^{-3}	$2.15 \cdot 10^{-2}$
1.50	10^{-3}	$2.29 \cdot 10^{-2}$
1.75	10^{-3}	$2.47 \cdot 10^{-2}$
2.00	10^{-3}	$2.59 \cdot 10^{-2}$
2.25	10^{-3}	$2.74 \cdot 10^{-2}$
2.50	10^{-3}	$2.82 \cdot 10^{-2}$
2.75	10^{-3}	$2.93 \cdot 10^{-2}$
3.00	10^{-3}	$3.03 \cdot 10^{-2}$

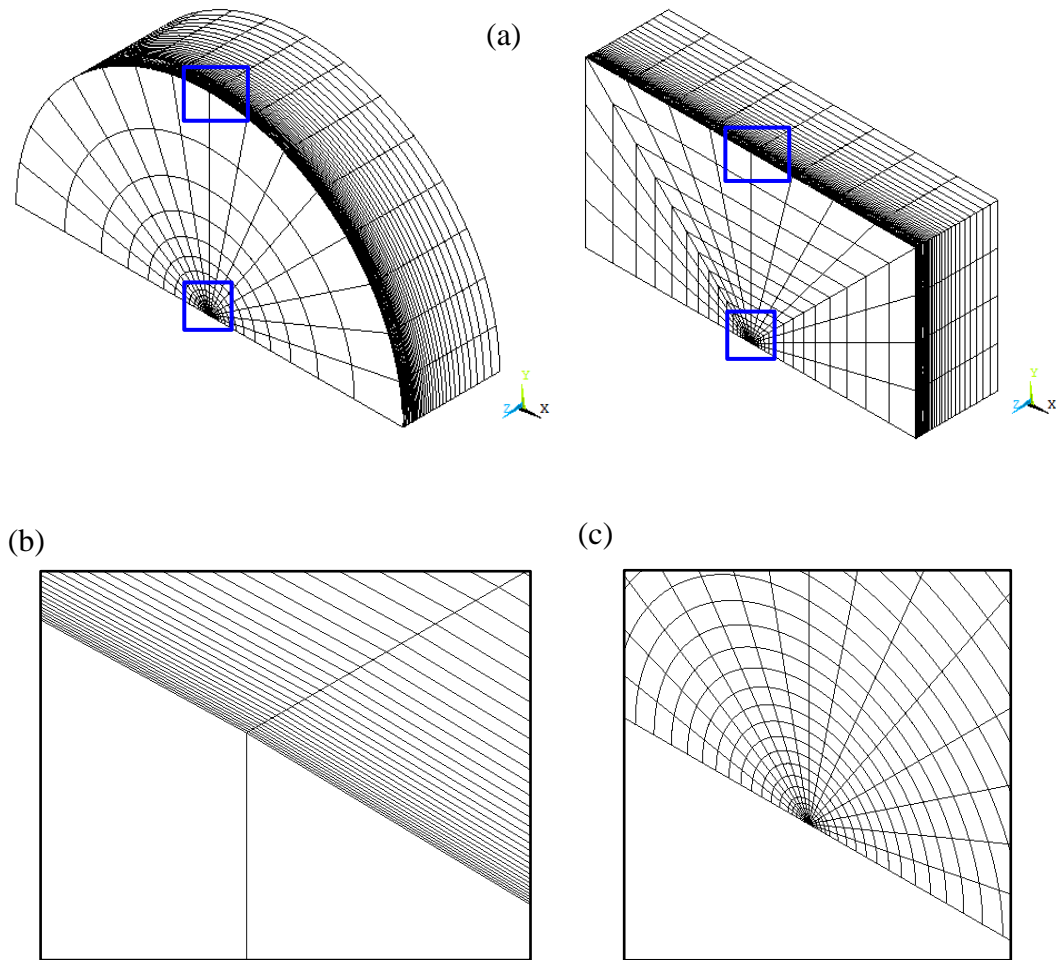


Figure 4.1.8. (a) Overall view of finite element mesh. (b) Detail of finite element mesh at outer surface. (c) Detail of finite element mesh at crack tip.

4.1.3. Results

4.1.3.1. Cracked discs under nominal Mode III loading

Crack surface stresses, τ_{yz} and τ_{xy} were extracted from the finite element results at distances, s , from the disc surfaces of 0 mm, 0.25 mm, 1 mm and 2 mm. Results for $t/a = 1$, plotted on logarithmic scales, are shown in Figures 4.1.9-4.1.12. Results for other values of t/a are generally similar, but with some differences in detail. When the plot is a straight line its slope is $-\lambda$. Values of λ taken from straight line plots are shown in Tables 4.1.4 and 4.1.5. Where no value is shown the plot could not be regarded as a straight line.

For $s = 0.25$ mm, 1 mm and 2 mm λ calculated from τ_{xy} is close to the theoretical value of 0.5 for a stress intensity factor singularity. Hence, realistic values of K_{II} can be calculated. For $s = 0$ mm λ is close to 0.5 for $t/a = 0.25$, and a realistic value of K_{II} can be calculated. However, λ increases with t/a to a maximum of 0.559 at $t/a = 2.25$, and then decreases slightly. The values of λ are all significantly less than the theoretical value of 0.598 for a corner point singularity. For $t/a > 0.25$ realistic values of K_{II} cannot be calculated.

Realistic values of K_{III} can be calculated from τ_{yz} for $s = 1$ mm and 2 mm. For $s = 0.25$ mm there is a straight line portion, parallel to the τ_{xy} plot, extending up a distance $x = 0.004$ mm from the crack tip. This suggests that realistic values of K_{III} can only be calculated for $x < 0.004$ mm, which is within the microscopic range. In other words there is a K -dominated region, radius ≈ 4 mm within the core region of the corner point singularity. The results for $s = 0$ show that τ_{yz} is slightly lower than τ_{xy} for small x , and decreases as x increases. The corresponding stress intensity factor plot (Figure 4.1.13) shows that the apparent value of K_{III} is a strong function of x . Realistic values of K_{III} cannot be calculated. The presence of apparent values of K_{III} is due to finite values of τ_{yz} . These appear because of the appearance of mode I disclinations, which are rotations about the y axis. Differentiating the expression for U_z gives the amount of this rotation which increases towards the crack tip, with a concomitant increase in τ_{yz} at a surface. This accounts qualitatively for the observed distributions of τ_{yz} at a surface.

Through thickness distributions of K_{II} and K_{III} for $t/a = 0.25, 0.5, 1, 2$ and 3 are shown in Figures 4.1.14-4.1.18. From Tables 4.1.4 and 4.1.5 the values of K_{II} are not realistic for $s < 0.25$ mm and the values of K_{III} are not realistic for $s < 1$ mm.

Maximum values of K_{III} are at the centreline. For $t/a > 1$ these correspond to K_{III} for the applied displacements. The influence of plate bending means that maxima steadily decrease as t/a decreases. Maximum values of K_{III} tend to zero as t/a tends to zero. This is to be expected because K_{III} is not possible in two dimensions. For the thicker discs K_{III} is nearly constant for $s > 50$ mm, and then decreases steadily towards the surface, with an abrupt drop close to the surface. However, this is within the region where calculated K_{III} values are not realistic. For thinner discs

behaviour is similar except that there is no constant K_{III} region. Hence, there is clear evidence of an end effect.

Plate bending theory [10] suggests that K_{II} should be zero on the centre line, with a linear increase towards a surface. For the thicker discs K_{II} is essentially zero for $s > 40$ mm. This shows that there is no significant plate bending effect, and is further evidence of an end effect, although its size does not quite match that deduced from the K_{III} values. The influence of plate bending increases as t/a decreases, and for $t/a = 0.25$ the distribution of K_{II} is nearly linear with a greater increase towards the surface (Figure 4.1.14). Intermediate values of t/a show intermediate behaviour (Figures 4.1.15-4.1.17). Maximum values of K_{II} are at the surface (Figure 4.1.13). This is within the region where calculated K_{II} values are not realistic so caution is needed in the interpretation of results.

The effect of plate bending means that a mixed mode loading is being applied. Hence, at a surface, both K_{III} and K_{II} are to be expected, even before coupled modes are considered in which K_{II}^c is induced by K_{III} and vice versa. At the present state of the art it is impossible to separate the coupled modes from the applied modes.

The through thickness distributions of displacements in the z direction, U_z , for $x = 0.3$ mm are shown in Figure 4.1.19. Values of K_{III} calculated from displacements at disc centre lines coincide with those calculated from stresses. The plots are on logarithmic scales, and for s up to about 4 mm they are of similar shape. The increasing effect of plate bending for $t/a < 1$ is to shift the curves downwards without significant change of shape. The curves all show clear minima at $s \approx 1.5$ mm. This is evidence that the change in the nature of the singularity from a stress intensity factor singularity to a corner point singularity is a boundary layer effect. The only available characteristic dimension is the crack length, a . A standard equation shows that K_{III} is proportional to U_z so corresponding K_{III} plots would have corresponding minima. These do not appear in K_{III} plots calculated using τ_{yz} . This is confirmation that K_{III} values for $s < 2$ mm are not realistic. The form of the curves suggests that a curve is the sum of two different distributions, one corresponding to a stress intensity factor singularity, and the other to a corner point singularity.

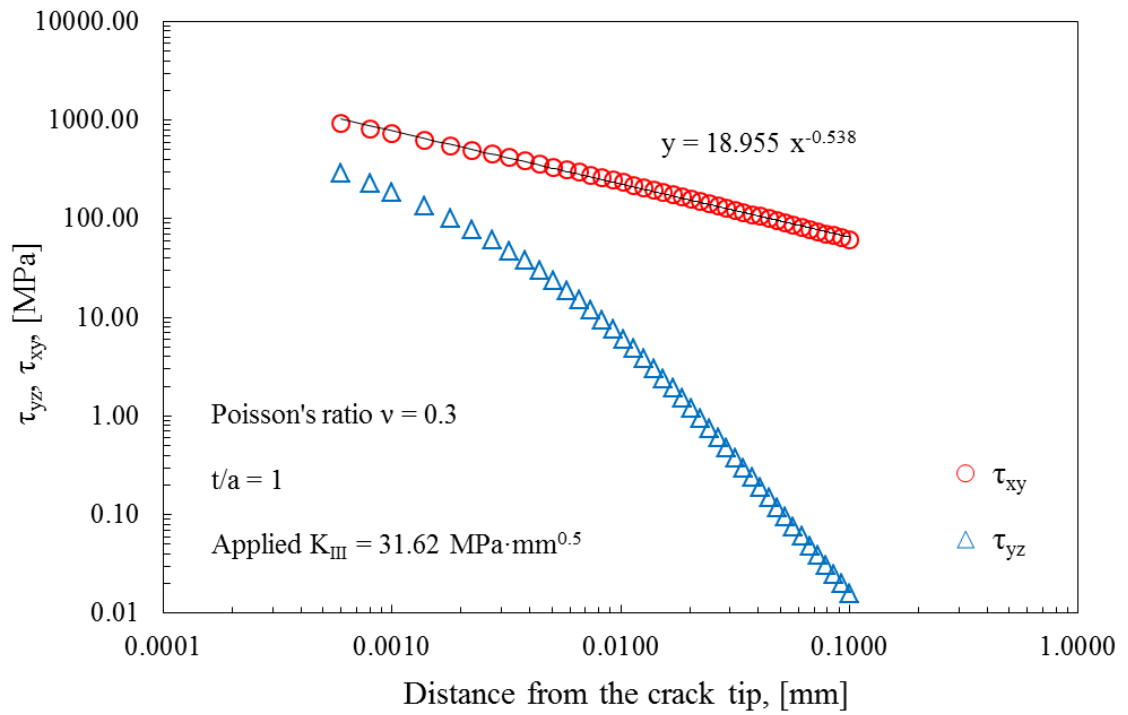


Figure 4.1.9. Stresses τ_{yz} and τ_{xy} on crack surface at $s = 0$ mm from disc surface, $t/a = 1$.

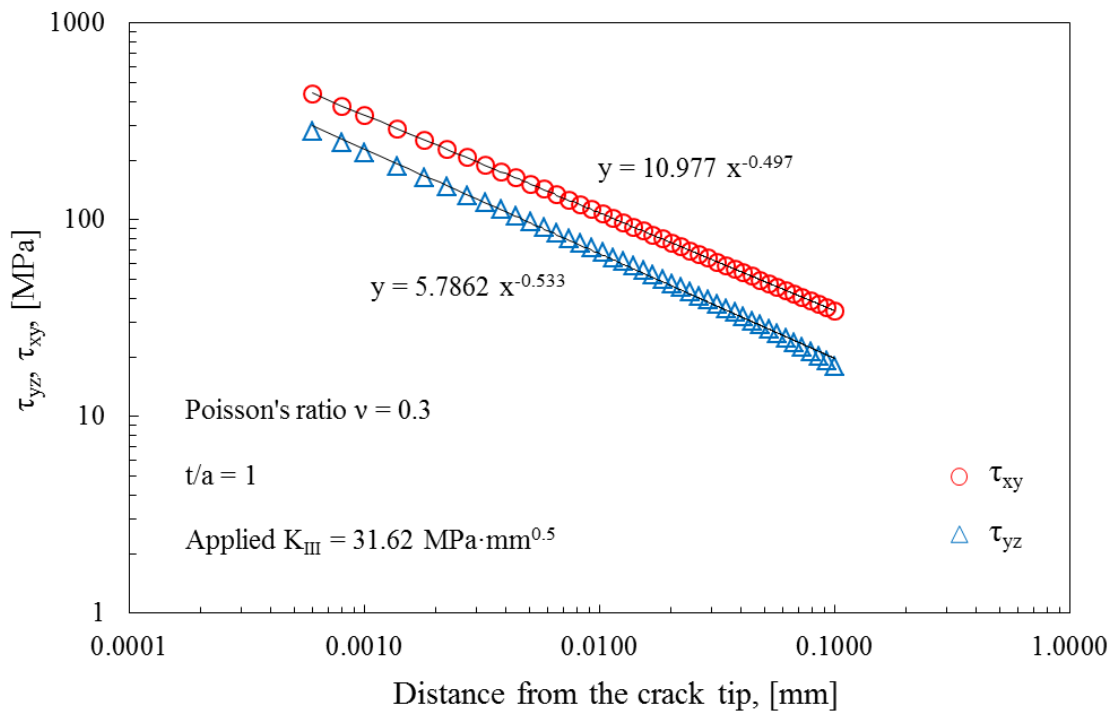


Figure 4.1.10. Stresses τ_{yz} and τ_{xy} on crack surface at $s = 0.25$ mm from disc surface, $t/a = 1$.

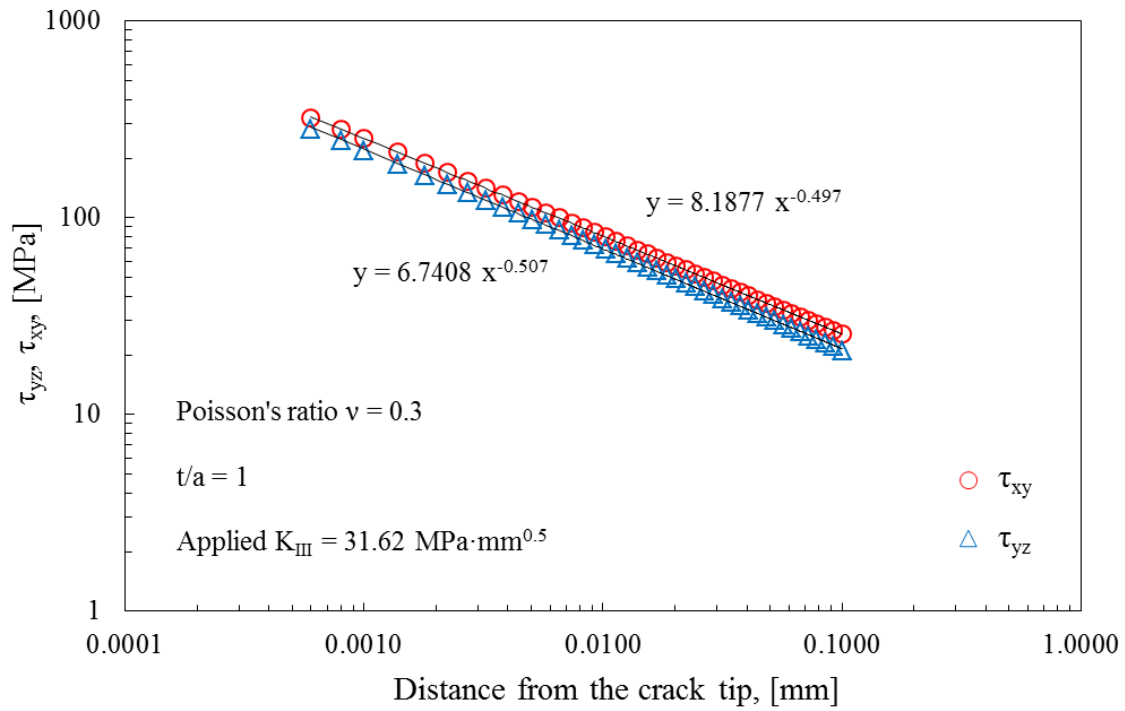


Figure 4.1.11. Stresses τ_{yz} and τ_{xy} on crack surface at $s = 1$ mm from disc surface, $t/a = 1$.

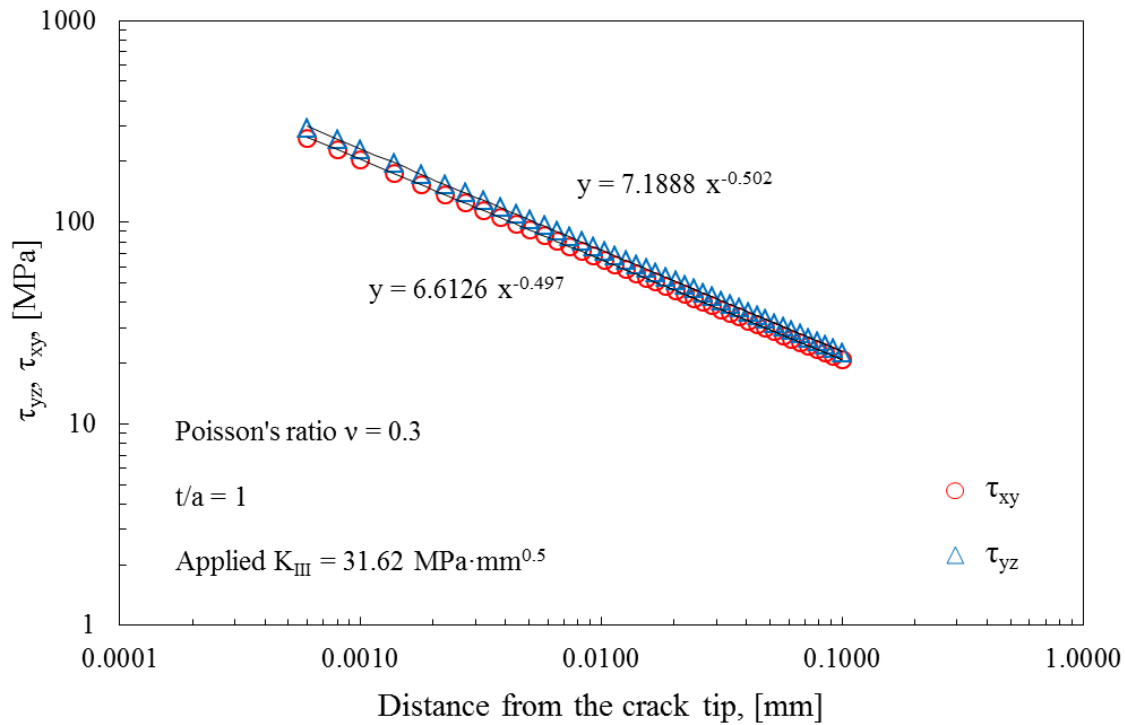


Figure 4.1.12. Stresses τ_{yz} and τ_{xy} on crack surface at $s = 2$ mm from disc surface, $t/a = 1$.

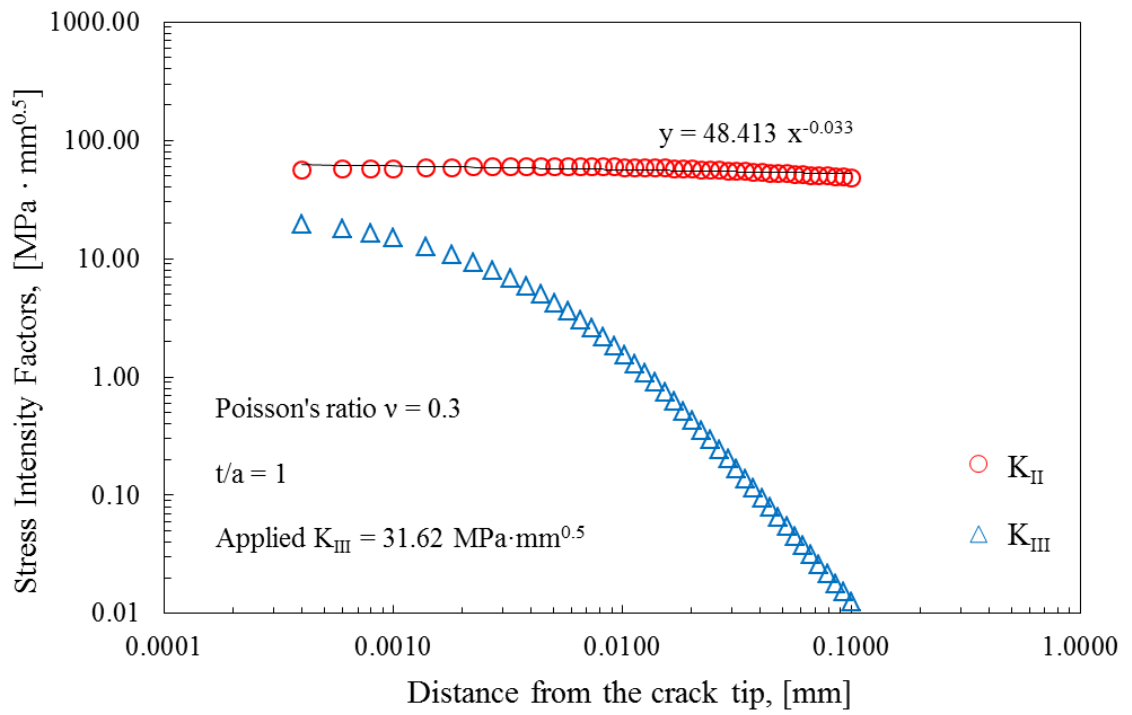


Figure 4.1.13. K_{II} and K_{III} at $s = 0$ mm from disc surface, $t/a = 1$.

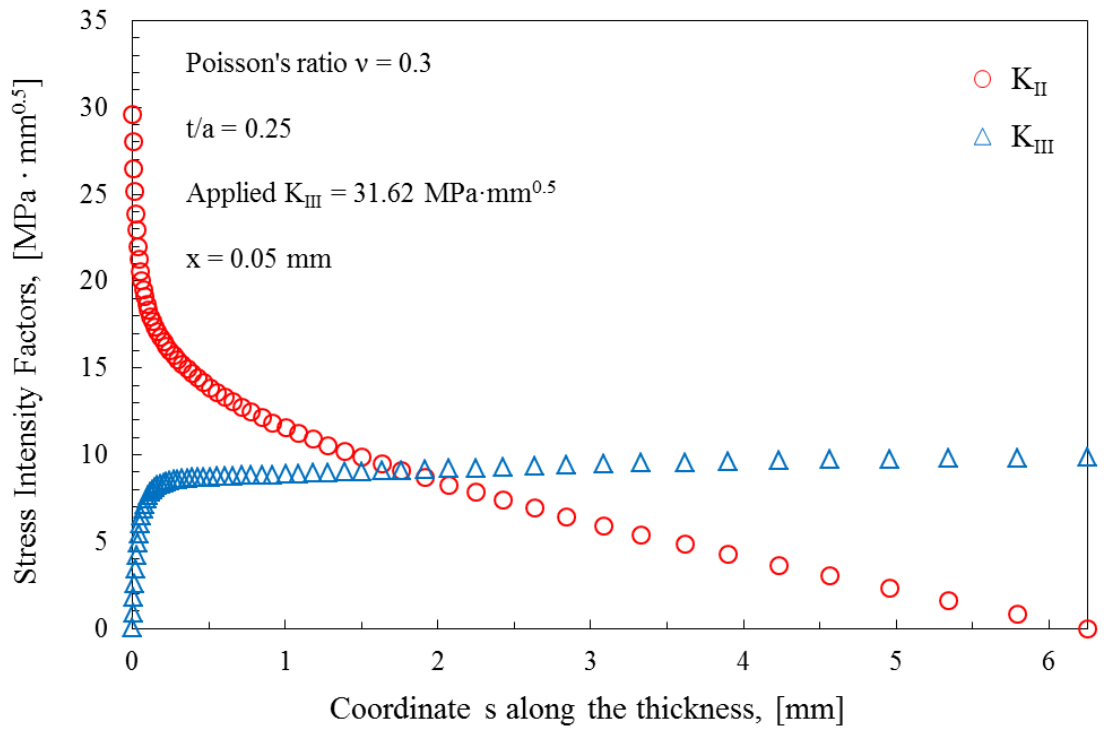


Figure 4.1.14. Through thickness distribution of K_{II} and K_{III} for $t/a = 0.25$, $x = 0.05$ mm.

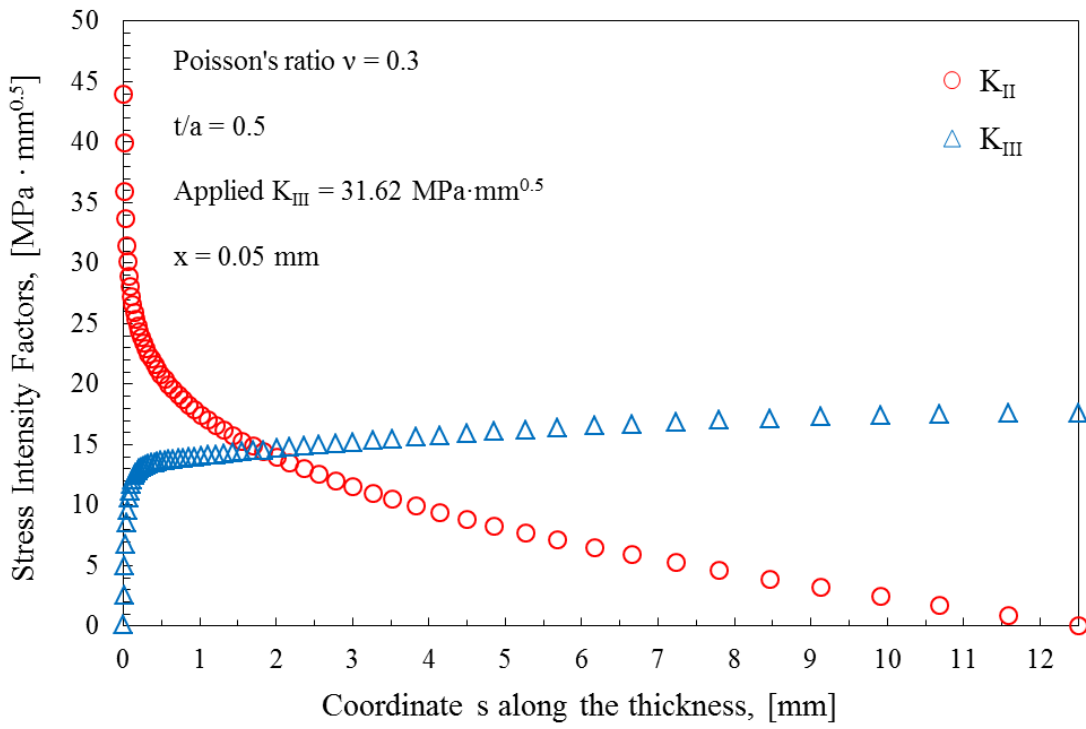


Figure 4.1.15. Through thickness distribution of K_{II} and K_{III} for $t/a = 0.5$, $x = 0.05$ mm.

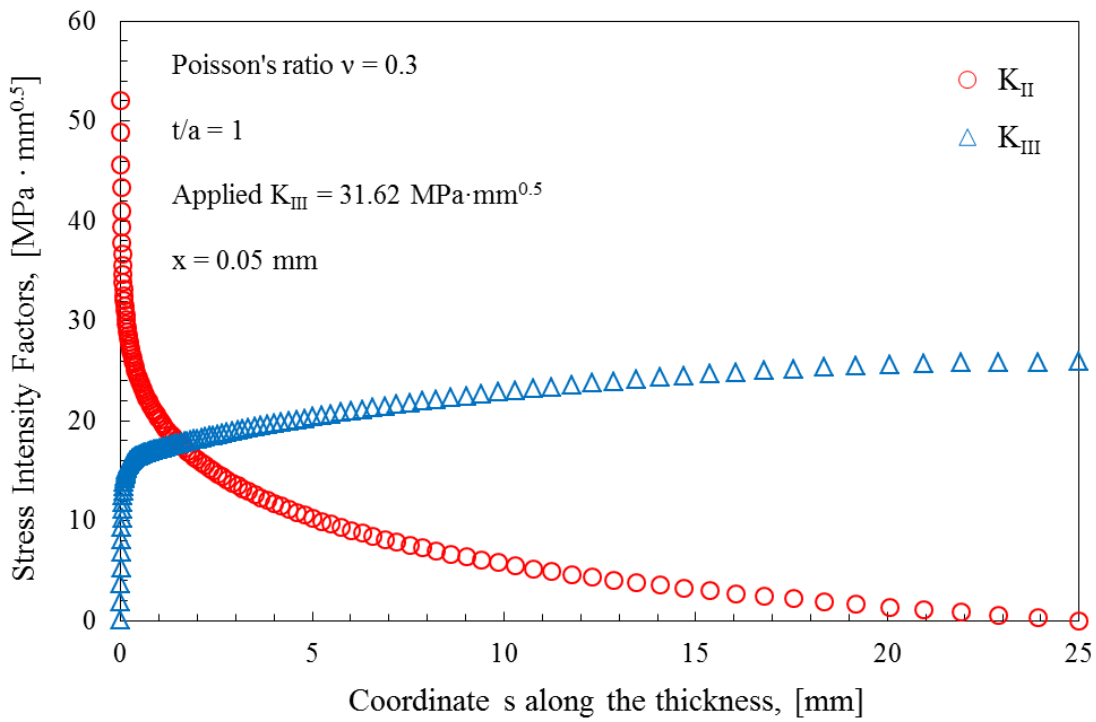


Figure 4.1.16. Through thickness distribution of K_{II} and K_{III} for $t/a = 1$, $x = 0.05$ mm.

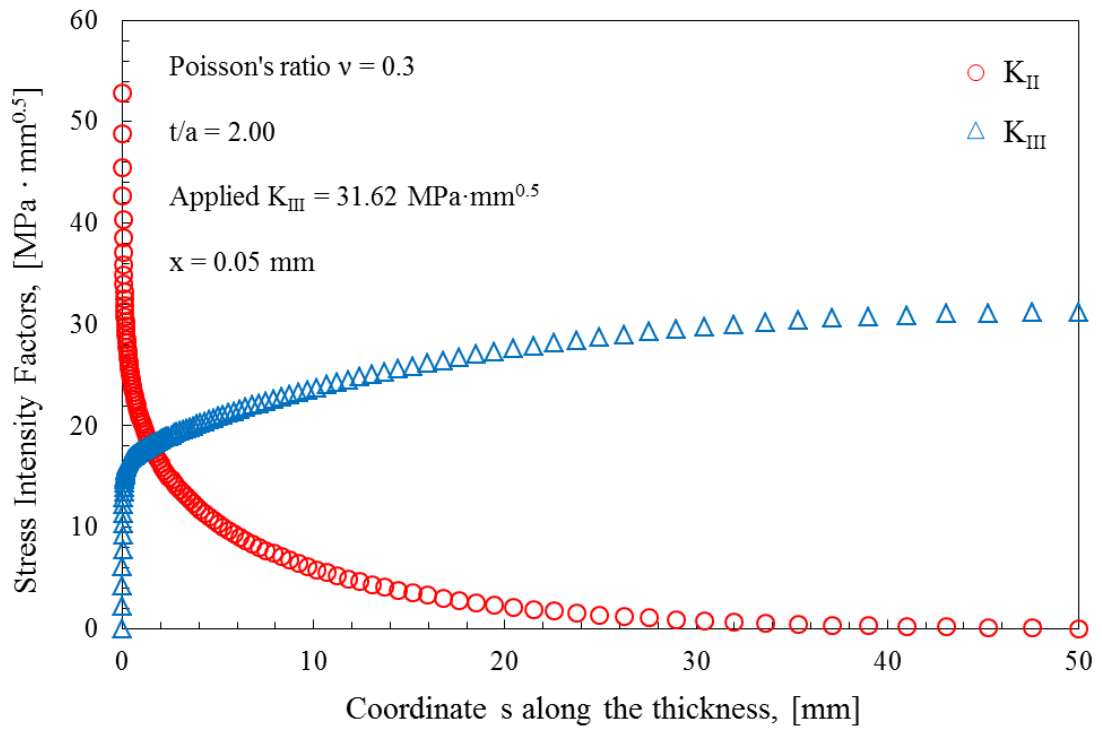


Figure 4.1.17. Through thickness distribution of K_{II} and K_{III} for $t/a = 2$, $x = 0.05 \text{ mm}$.

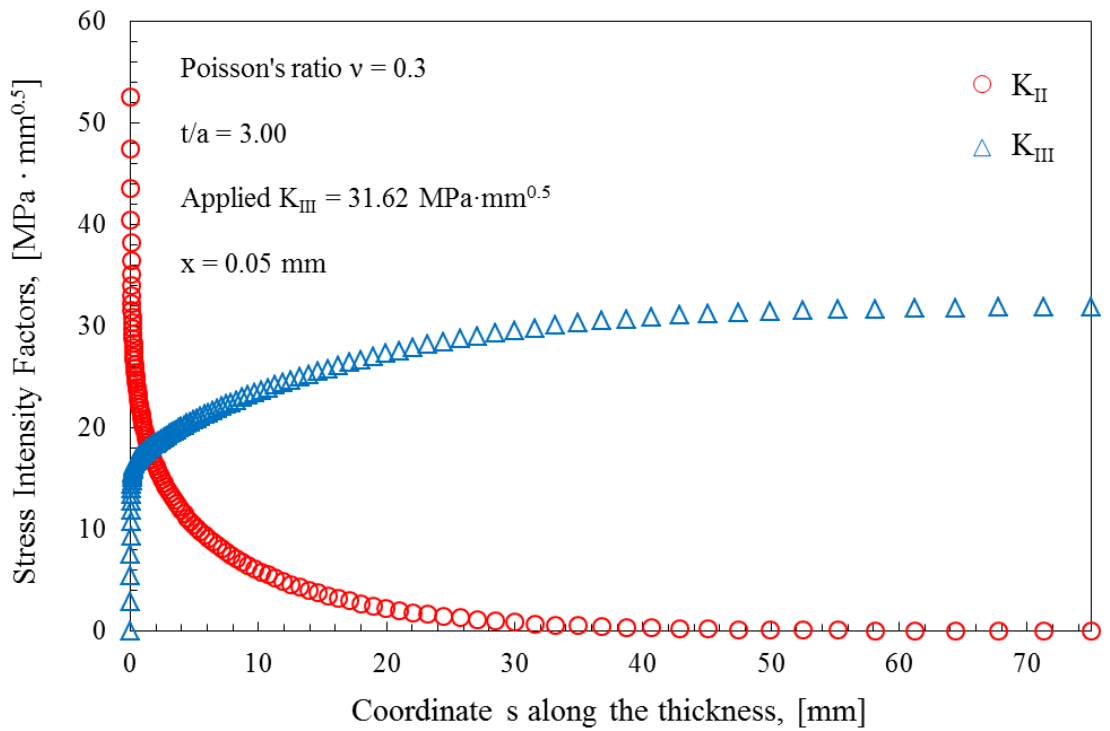


Figure 4.1.18. Through thickness distribution of K_{II} and K_{III} for $t/a = 3$, $x = 0.05 \text{ mm}$.

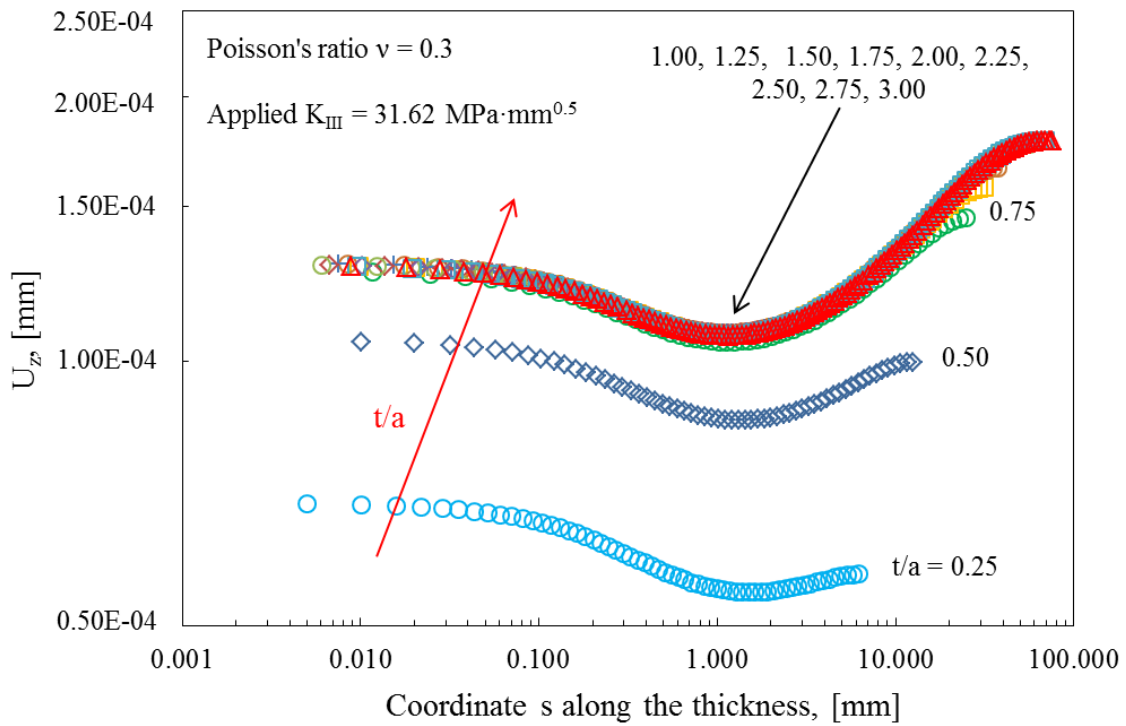


Figure 4.1.19. Through thickness distribution of U_z for $x = 0.3$ mm.

4.1.3.2. Cracked plates under nominal Mode III loading

Crack surface stresses, τ_{yz} and τ_{xy} were extracted from the finite element results at distances, s , from the plate surfaces of 0 mm, 0.25 mm, 1 mm and 2 mm. Results for $t/a = 1$, plotted on logarithmic scales, are shown in Figures 4.1.20-4.1.23. Results for other values of t/a are generally similar, but with some differences in detail. When the plot is a straight line its slope is $-\lambda$. Values of λ taken from straight line plots are shown in Tables 4.1.4 and 4.1.5. Where no value is shown the plot could not be regarded as a straight line.

Results are generally similar to those obtained for the discs. For $s = 0.25$ mm, 1 mm and 2 mm λ calculated from τ_{xy} is close to the theoretical value of 0.5 for a stress intensity factor singularity. Hence, realistic values of K_{II} can be calculated. For $s = 0$ λ has a maximum for $t/a = 0.25$, and decreases as t/a increases. The values of λ are all significantly less than the theoretical value of 0.598 for a corner point singularity. Realistic values of K_{II} can probably be calculated for $t/a > 2$. The

results are in contrast to the disc results where λ increases as t/a increases. Realistic values of K_{III} can be calculated from τ_{yz} for $s = 1$ mm and 2 mm.

The results for $s = 0$ (Figure 4.1.20) show that τ_{yz} is slightly lower than τ_{xy} for small x , and decreases as x increases. The corresponding stress intensity factor plot (Figure 4.1.24) shows that the apparent value of K_{III} is a strong function of x . Realistic values of K_{III} cannot be calculated. The presence of apparent values of K_{III} is due to finite values of τ_{yz} . These appear because of the appearance of mode I disclinations, which are rotations about the y axis. Differentiating the expression for U_z gives the amount of this rotation which increases towards the crack tip, with a concomitant increase in τ_{yz} at a surface. This accounts qualitatively for the observed distributions of τ_{yz} at a surface.

Through thickness distributions of K_{II} and K_{III} for $t/a = 0.25, 0.5, 1, 2$ and 3 are shown in Figures 4.1.25-4.1.29. From Tables 4.1.4 and 4.1.5 the values of K_{II} are not realistic for $s < 0.25$ mm and the values of K_{III} are not realistic for $s < 1$ mm.

The distributions of K_{III} are significantly different from those for disc results. There are maxima at the centre line but K_{III} then remains nearly constant for about half the distance to the plate surface. The influence of plate bending again means that maxima steadily decrease as t/a decreases. As a surface is approached K_{III} first decreases slightly then increases to a maximum at about 0.15 mm from the surface. There is then an abrupt drop which is within the region where realistic values of K_{III} cannot be calculated.

Plate bending theory [10] suggests that K_{II} should be zero on the centre line, with a linear increase towards a surface. For $t/a = 0.25$ K_{II} does indeed increase linearly for much of the thickness with a greater increase as the surface is approached. This is within the region where realistic values of K_{II} cannot be calculated. The extent of the linear portion, in terms of plate thickness, decreases as t/a increases but is still present when $t/a = 3$. This is in contrast with the disc results where linear portions are less extensive and K_{II} becomes essentially zero for $s > 40$ mm. Maximum values of K_{II} are at the surface. This is within the region where calculated K_{II} values are not realistic so caution is needed in the interpretation of results.

The effect of plate bending means that a mixed mode loading is being applied. Hence, at a surface, both K_{III} and K_{II} are to be expected, even before coupled

modes are considered in which K_{II}^c is induced by K_{III} and vice versa. At the present state of the art it is impossible to separate the coupled modes from the applied modes.

The through thickness distributions of displacements in the z direction, U_z , for $x = -0.3$ mm are shown in Figure 4.1.30. The plots are on logarithmic scales, and they are of similar shape. Unlike the disc results there are no pronounced minima indicating the change in the nature of the singularity from a stress intensity factor singularity to a corner point singularity.

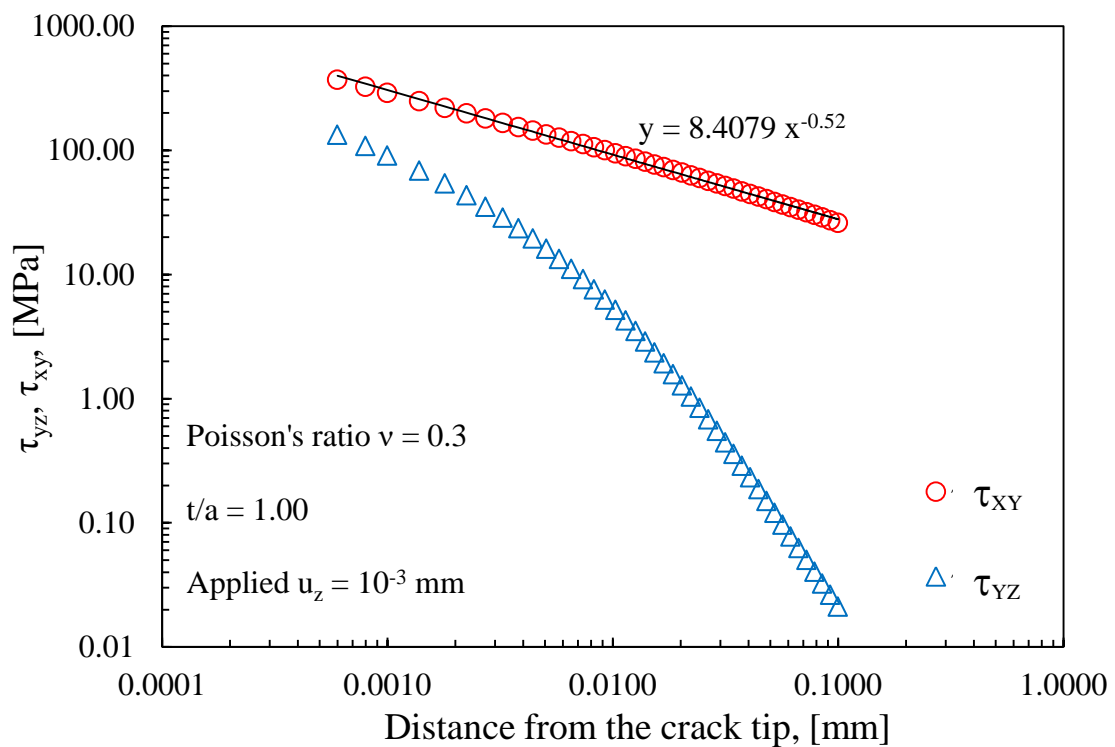


Figure 4.1.20. Stresses τ_{yz} and τ_{xy} on crack surface at $s = 0$ mm from plate surface, $t/a = 1$.

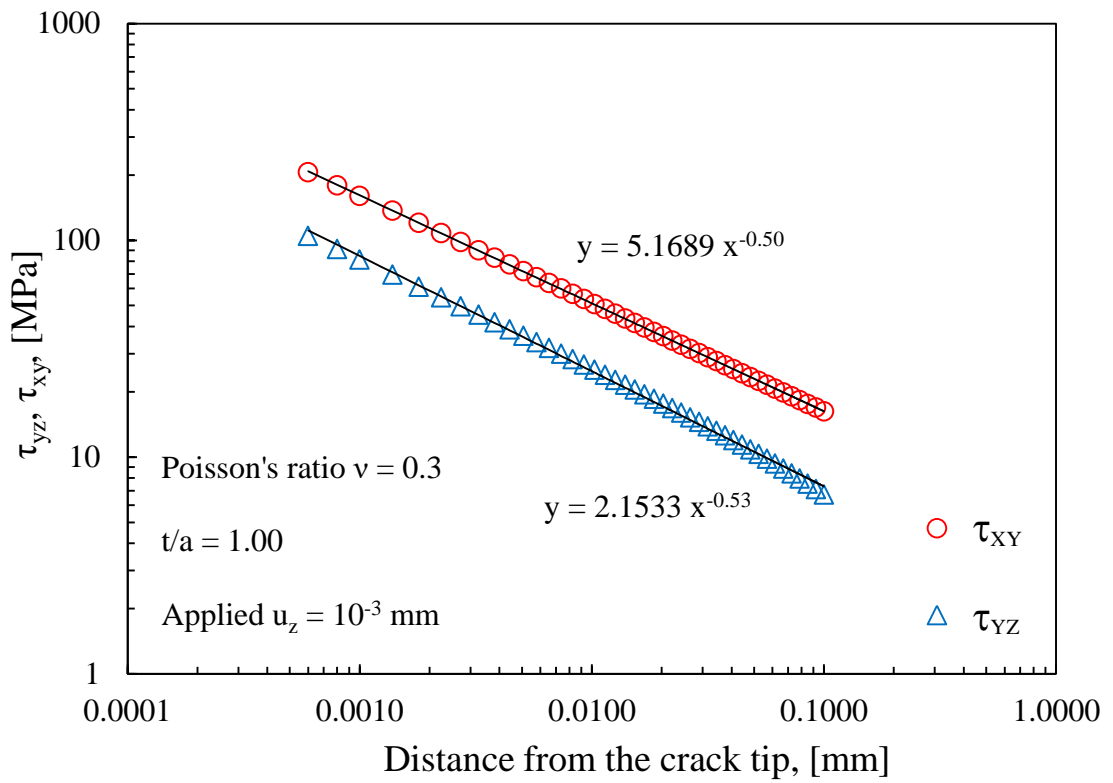


Figure 4.1.21. Stresses τ_{yz} and τ_{xy} on crack surface at $s = 0.25$ mm from plate surface, $t/a = 1$.

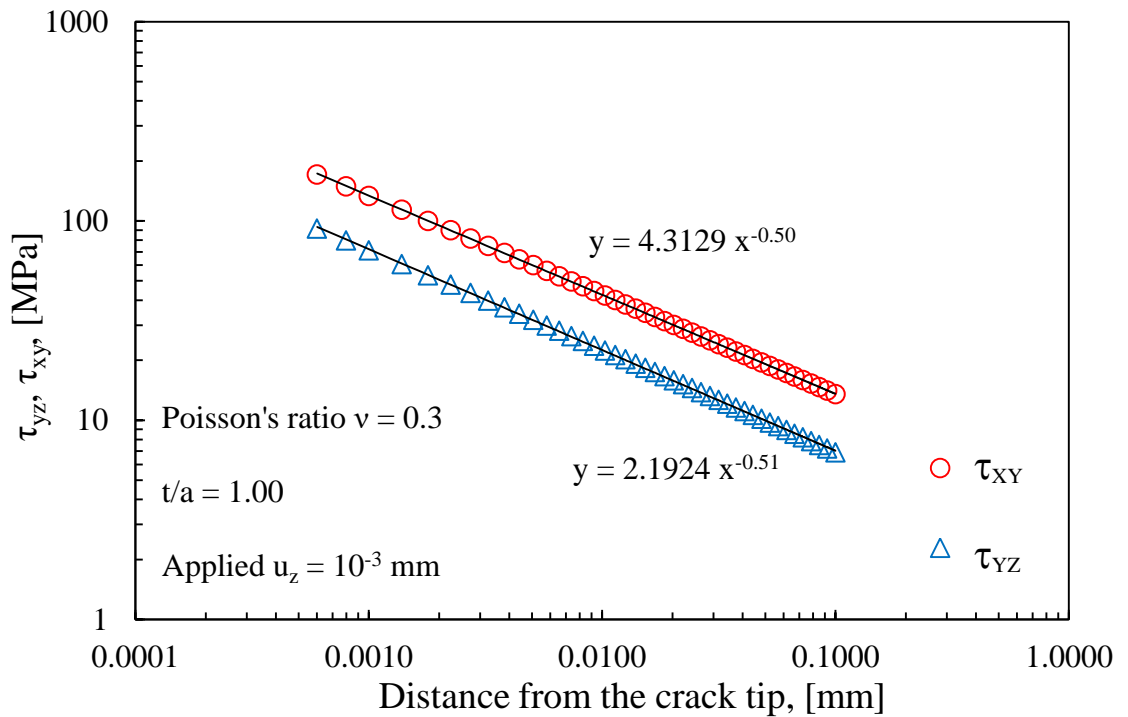


Figure 4.1.22. Stresses τ_{yz} and τ_{xy} on crack surface at $s = 1$ mm from plate surface, $t/a = 1$.

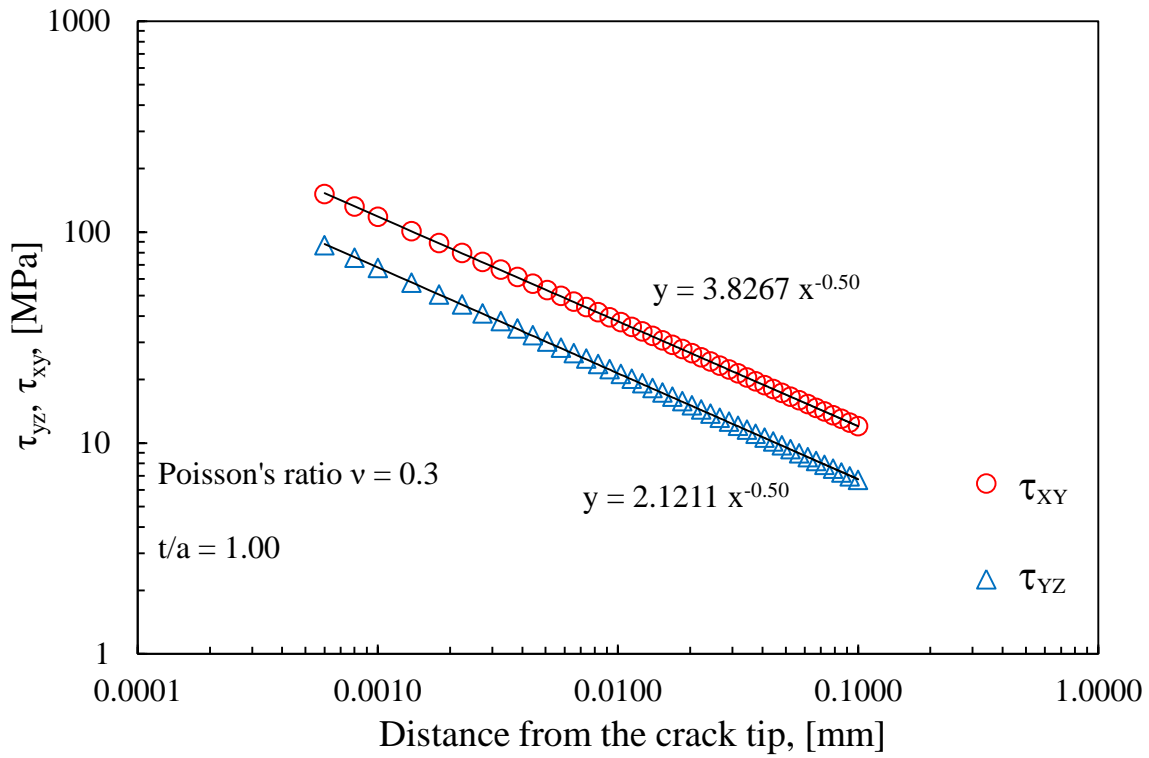


Figure 4.1.23. Stresses τ_{yz} and τ_{xy} on crack surface at $s = 2$ mm from plate surface, $t/a = 1$.

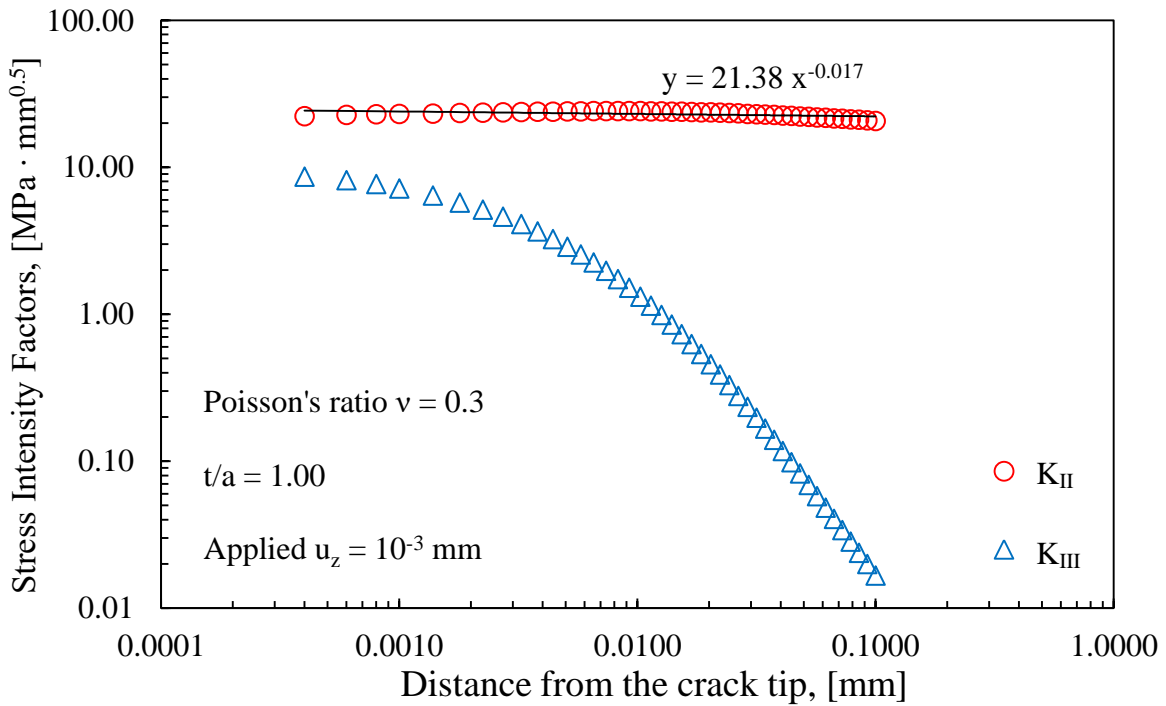


Figure 4.1.24. K_{II} and K_{III} at $s = 0$ mm from plate surface, $t/a = 1$.

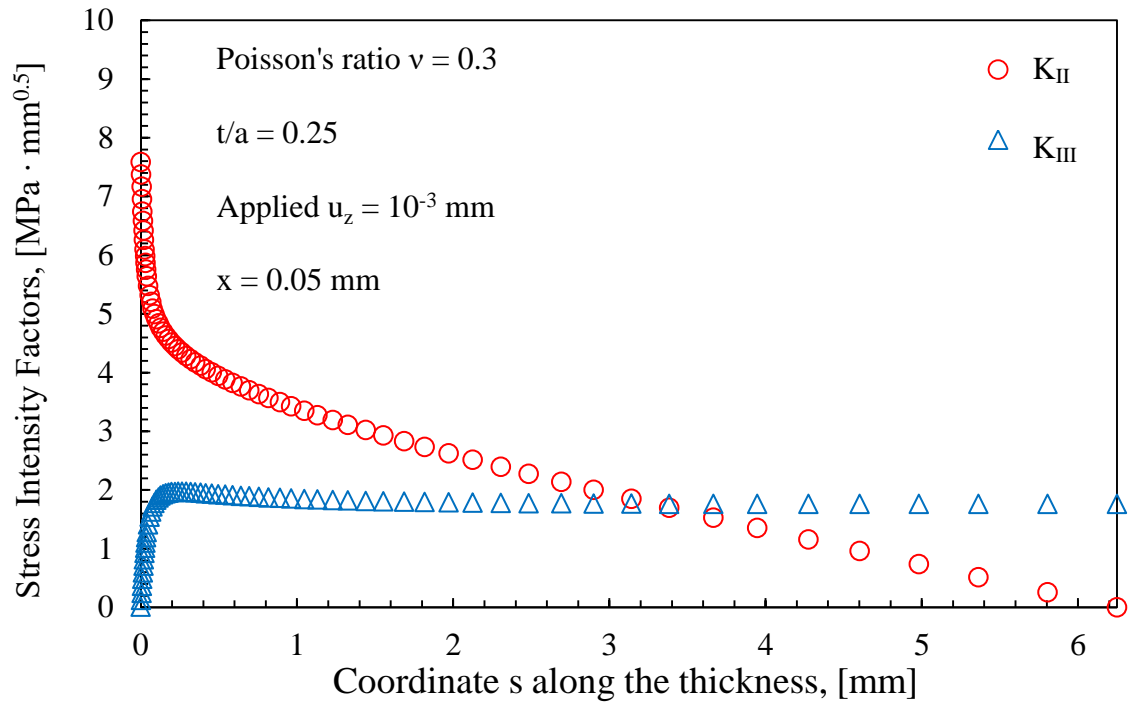


Figure 4.1.25. Through thickness distribution of K_{II} and K_{III} for $t/a = 0.25$, $x = 0.05$ mm.

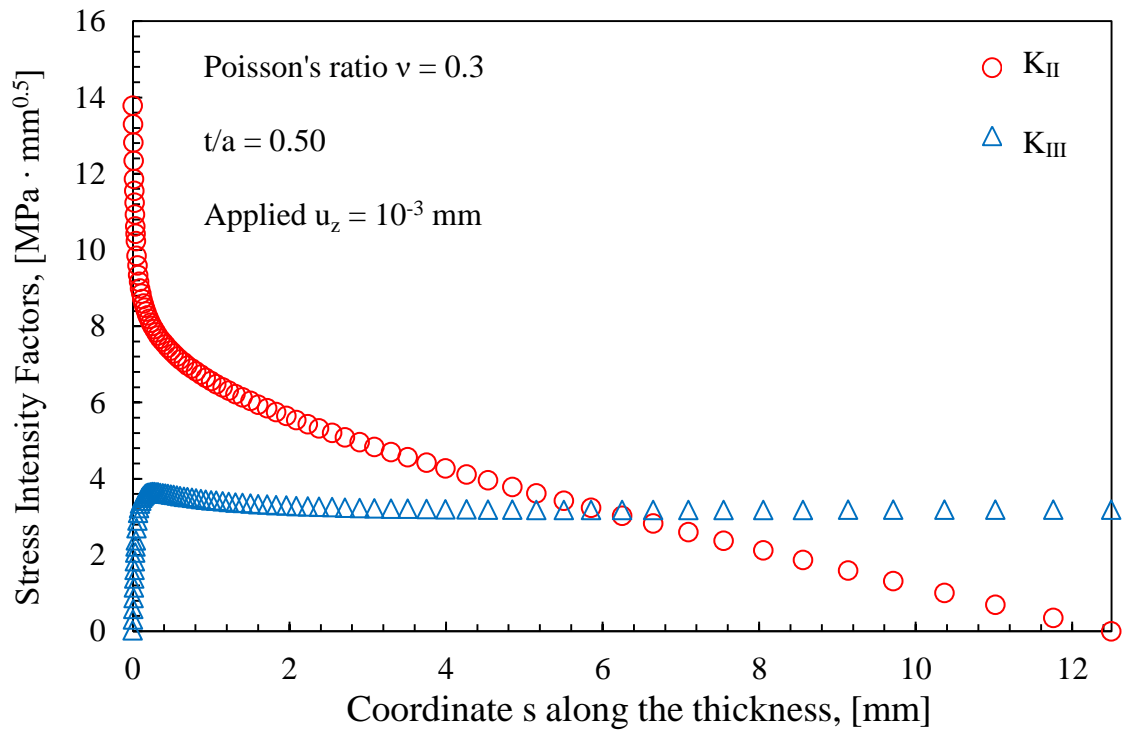


Figure 4.1.26. Through thickness distribution of K_{II} and K_{III} for $t/a = 0.50$, $x = 0.05$ mm.

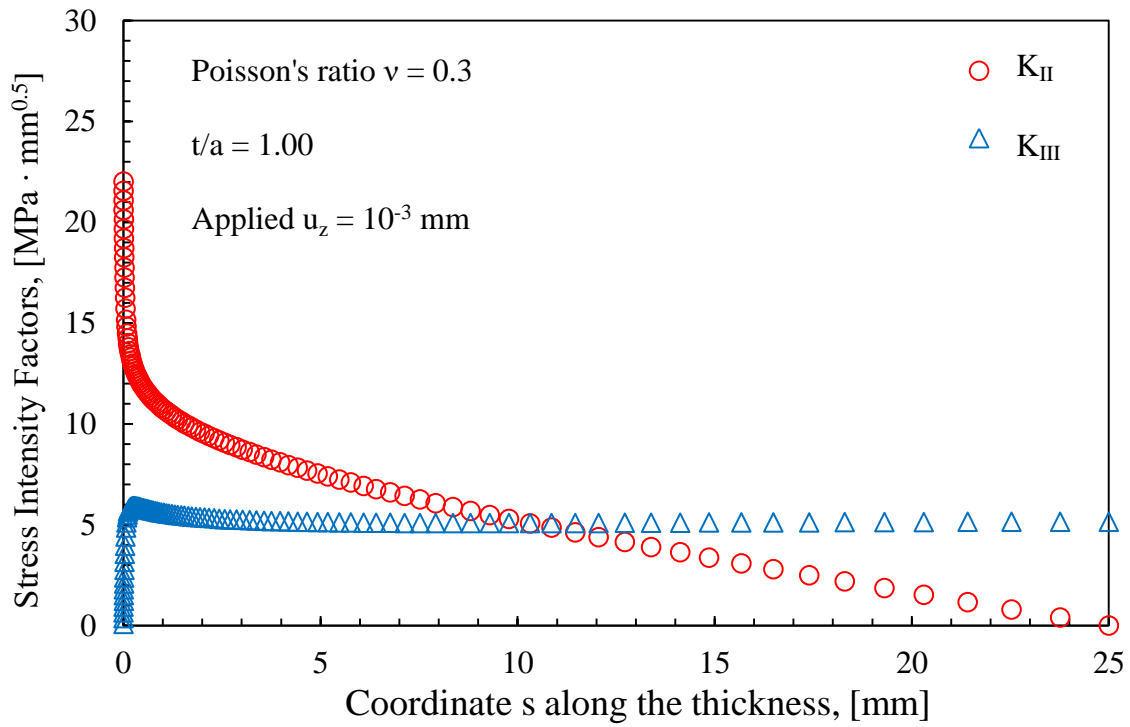


Figure 4.1.27. Through thickness distribution of K_{II} and K_{III} for $t/a = 1$, $x = 0.05$ mm.

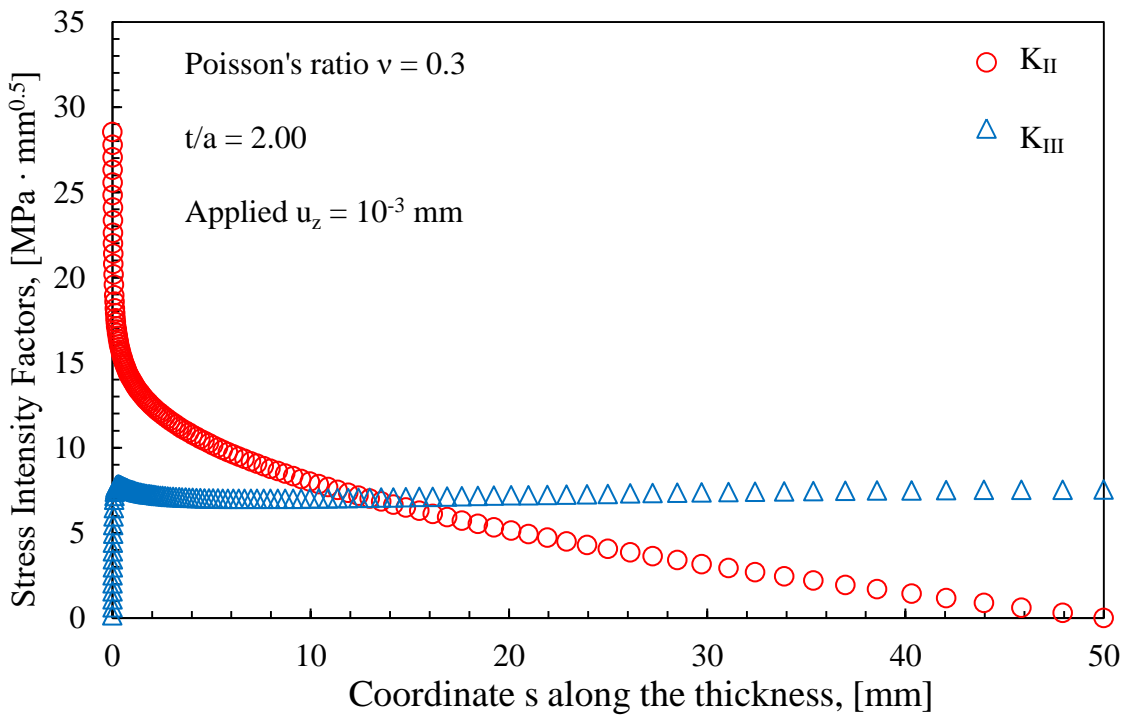


Figure 4.1.28. Through thickness distribution of K_{II} and K_{III} for $t/a = 2$, $x = 0.05$ mm.

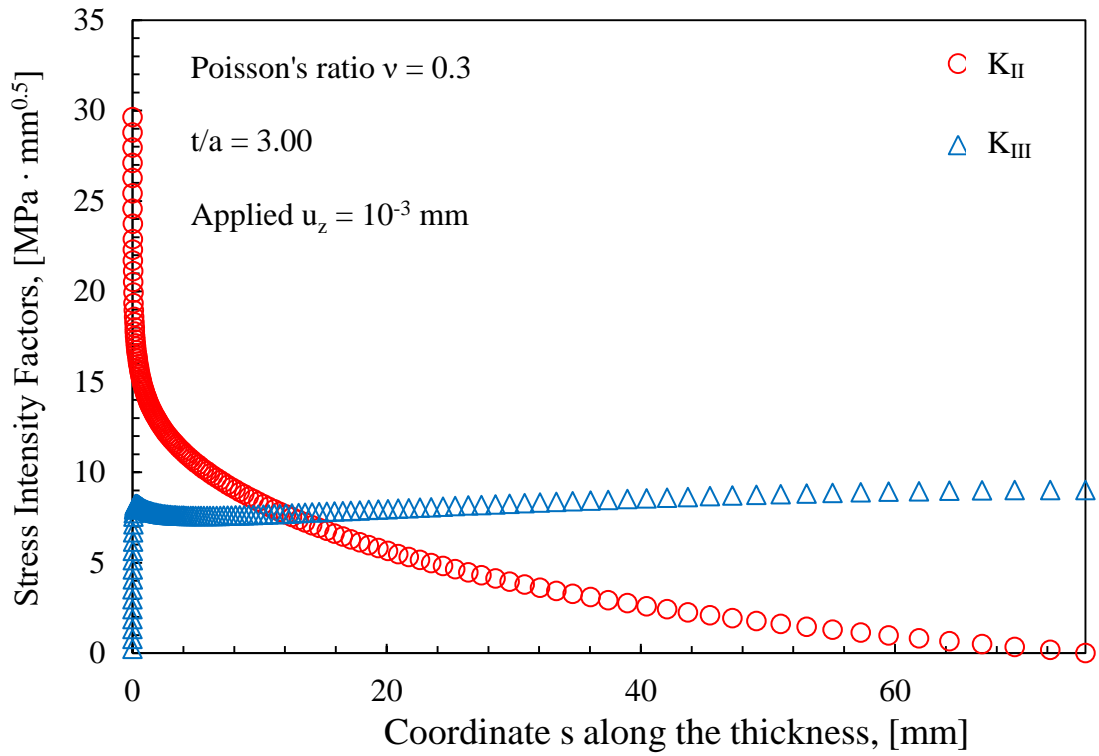


Figure 4.1.29. Through thickness distribution of K_{II} and K_{III} for $t/a = 3$, $x = 0.05$ mm.

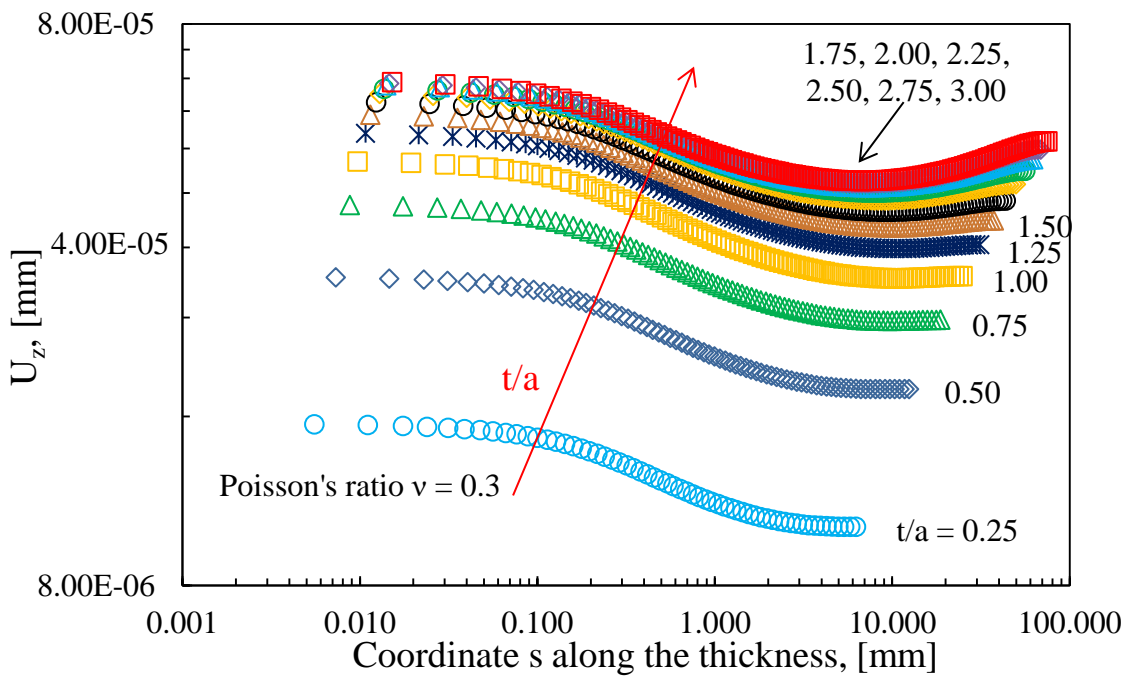


Figure 4.1.30. Through the thickness distribution of U_z for $x = -0.3$ mm.

Table 4.1.4. Values of λ for τ_{xy} , s is the distance from the surface in the z direction.

t/a	$s = 0 \text{ mm}$		$s = 0.25 \text{ mm}$		$s = 1 \text{ mm}$	
	disc	plate	disc	plate	disc	plate
0.25	0.505	0.538	0.497	0.498	0.497	0.497
0.50	0.520	0.527	0.497	0.498	0.497	0.497
0.75	0.530	0.523	0.497	0.498	0.497	0.497
1.00	0.538	0.520	0.497	0.498	0.497	0.497
1.25	0.544	0.517	0.497	0.498	0.497	0.497
1.50	0.549	0.515	0.497	0.498	0.497	0.497
1.75	0.553	0.513	0.497	0.498	0.497	0.497
2.00	0.556	0.512	0.497	0.498	0.497	0.497
2.25	0.559	0.510	0.497	0.498	0.497	0.497
2.50	0.542	0.510	0.497	0.498	0.497	0.497
2.75	0.545	0.509	0.497	0.498	0.497	0.497
3.00	0.547	0.508	0.497	0.498	0.497	0.497

Table 4.1.5. Values of λ for τ_{yz} , s is the distance from the surface in the z direction.

t/a	$s = 0 \text{ mm}$		$s = 0.25 \text{ mm}$		$s = 1 \text{ mm}$	
	disc	plate	disc	plate	disc	plate
0.25	-	-	-	-	0.508	0.507
0.50	-	-	-	-	0.506	0.506
0.75	-	-	-	-	0.507	0.506
1.00	-	-	-	-	0.507	0.506
1.25	-	-	-	-	0.506	0.506
1.50	-	-	-	-	0.506	0.506
1.75	-	-	-	-	0.506	0.506
2.00	-	-	-	-	0.506	0.506
2.25	-	-	-	-	0.507	0.506
2.50	-	-	-	-	0.506	0.505
2.75	-	-	-	-	0.506	0.506
3.00	-	-	-	-	0.507	0.506

4.1.3.3. Cracked discs under nominal Mode II loading

Stresses τ_{yz} and τ_{xy} on the crack surface at $s = 0$ mm from the disc surface are shown in Figure 4.1.31. These are similar to the stress distributions for nominal mode III loading, shown in Figure 4.1.9. The value of λ calculated from τ_{xy} , i.e. 0.541, is virtually the same as for nominal mode III loading.

Stresses τ_{yz} and τ_{xy} on the crack surface at $s = 1$ mm from the disc surface are shown in Figure 4.1.32. These are similar to the stress distributions for nominal mode III loading, shown in Figure 4.1.11. Values of λ , calculated from τ_{xy} and τ_{yz} , are 0.499 and 0.506, in excellent agreement with the nominal mode III results. Similarly, stresses τ_{yz} and τ_{xy} on the crack surface at $s = 2$ mm from the disc surface, shown in Figure 4.1.33, are similar to the stress distributions for nominal mode III loading, shown in Figure 4.1.12. Values of λ are in excellent agreement.

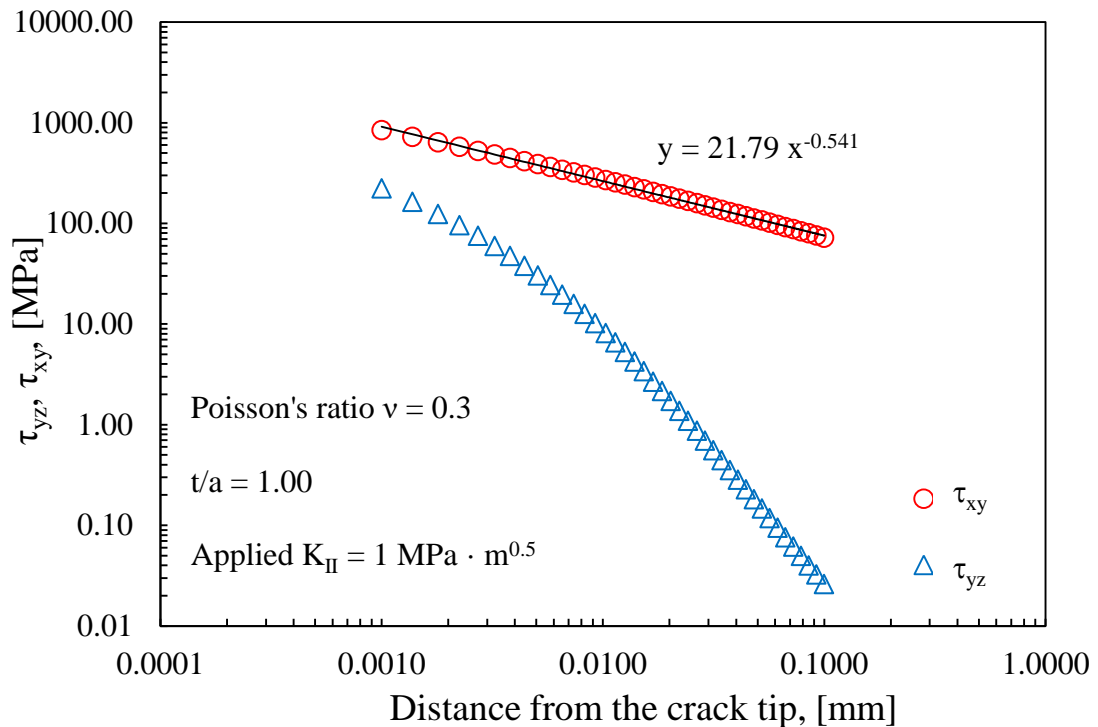


Figure 4.1.31. Stresses τ_{yz} and τ_{xy} on crack surface at $s = 0$ mm from disc surface, $t/a = 1$.

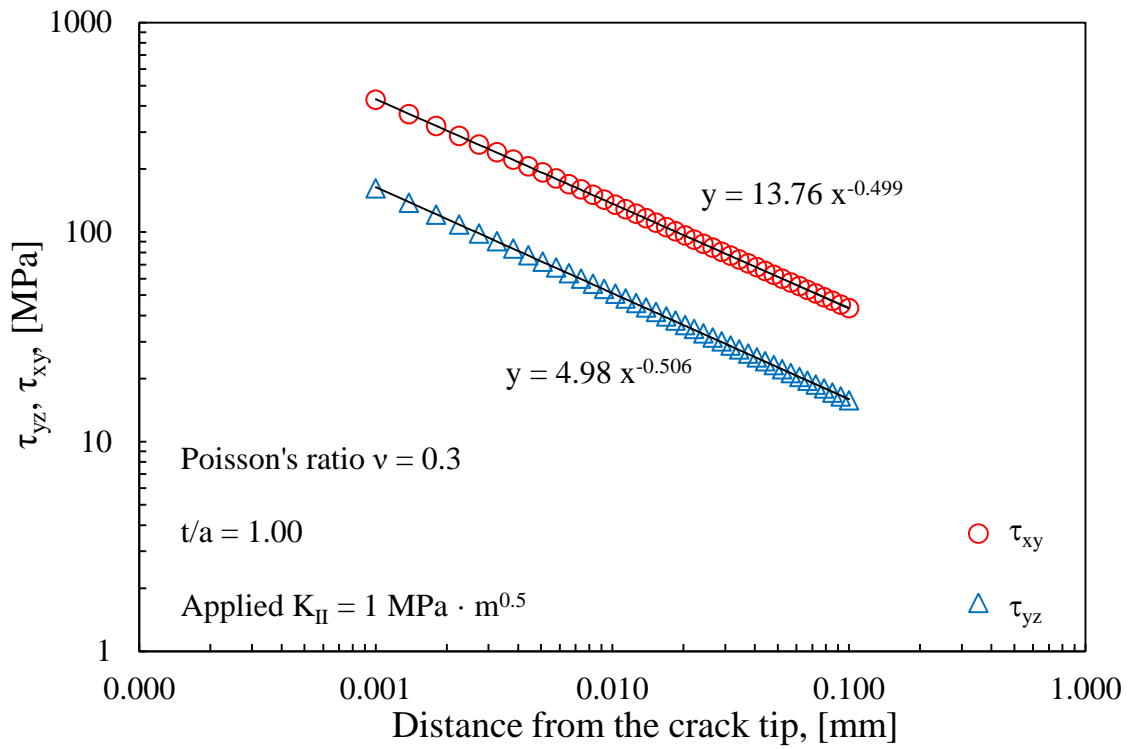


Figure 4.1.32. Stresses τ_{yz} and τ_{xy} on crack surface at $s = 1$ mm from disc surface, $t/a = 1$.

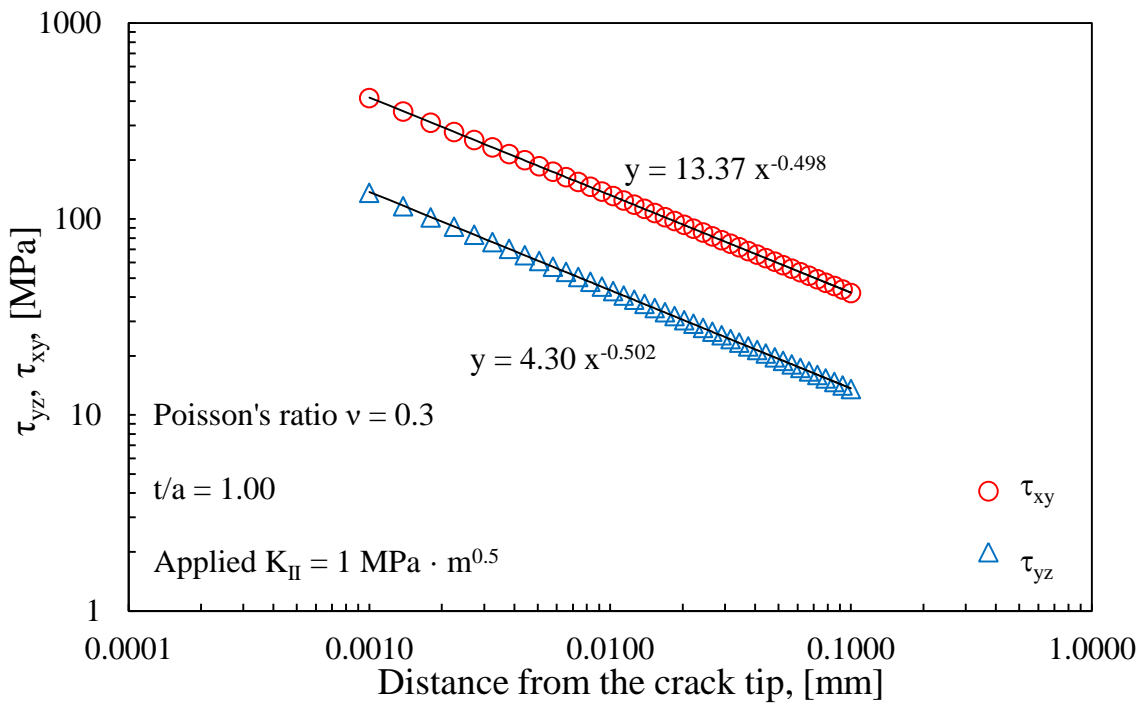


Figure 4.1.33. Stresses τ_{yz} and τ_{xy} on crack surface at $s = 2$ mm from disc surface, $t/a = 1$.

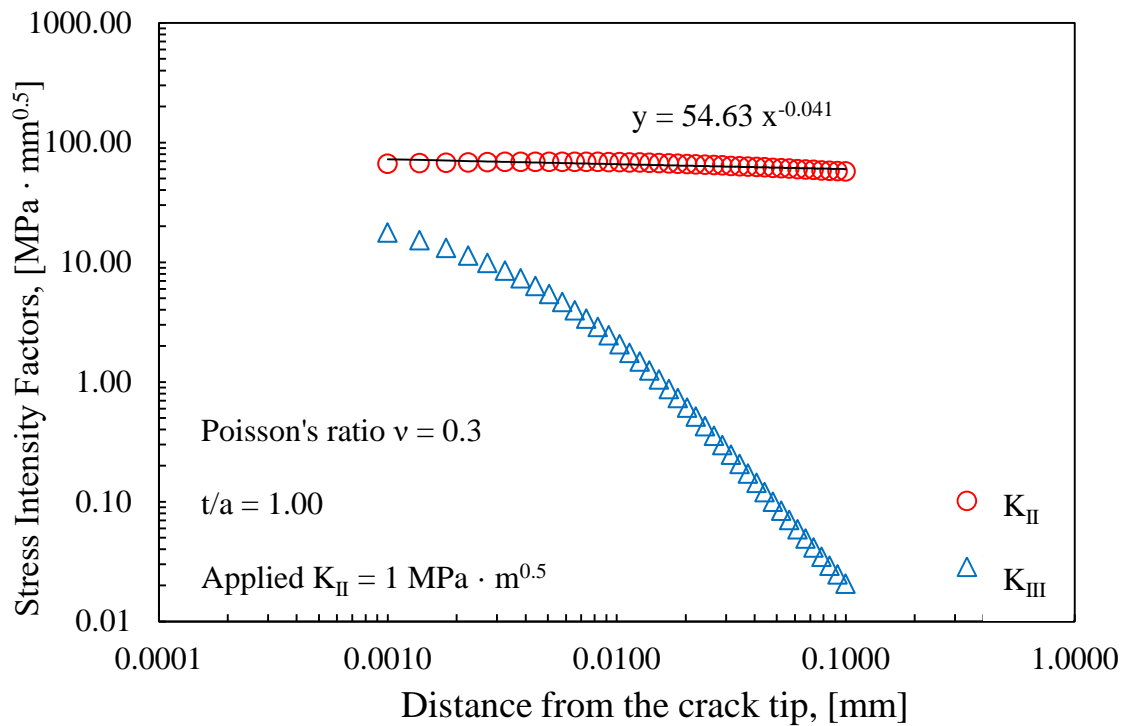


Figure 4.1.34. K_{II} and K_{III} at $s = 0$ mm from disc surface, $t/a = 1$.

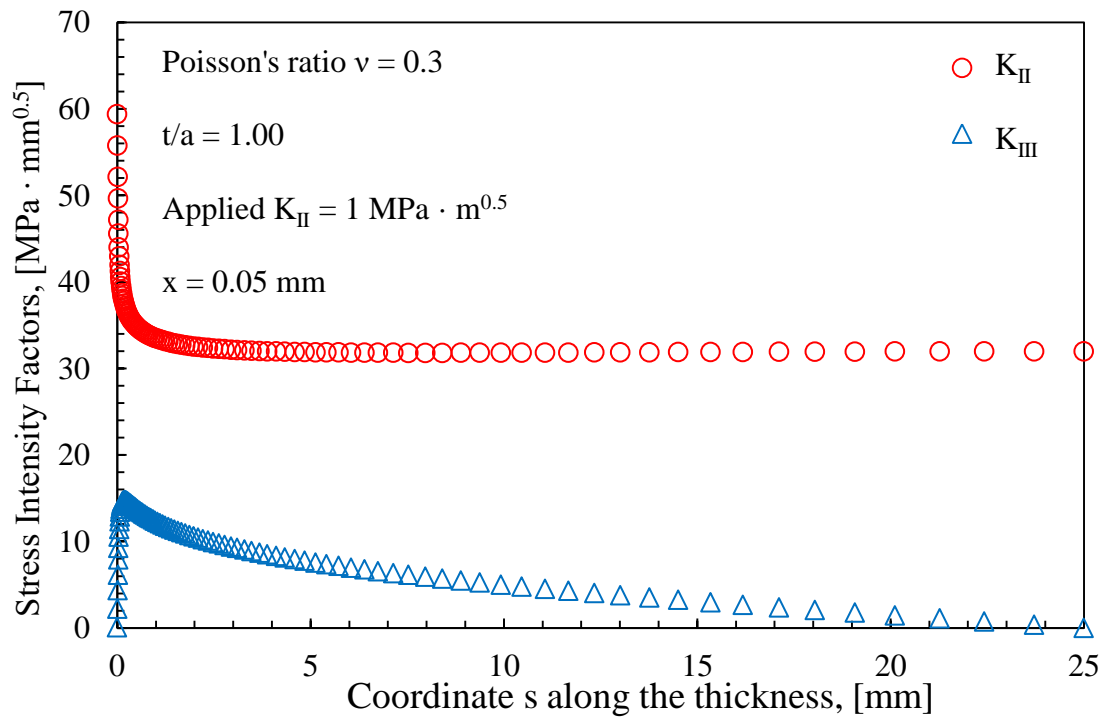


Figure 4.1.35. Through-thickness distribution of K_{II} and K_{III} for disc with $t/a = 1$, $x = 0.05$ mm.

Figure 4.1.34 shows that distributions of K_{II} and K_{III} at $s = 0$ mm from the disc surface are similar to those for nominal mode III loading, shown in Figure 4.1.13. However, through the thickness distribution of K_{II} and K_{III} , shown in Figure 4.1.35, differ from those for nominal mode III loading, shown in Figure 4.1.16. This difference is because the use of nominal mode II loading has eliminated disc bending.

4.1.4. Discussion

It is possible to base a linear elastic analysis of the stress field at a corner point on the following four ideas [4,5]. First, the corner point stress field can be expanded as a series in which the leading term is the stress intensity measure, K_λ , which is a singularity that dominates the stress field in the vicinity of the corner point. Higher order terms are non singular. This is not a new idea. The effect of the second term is discussed briefly by Glushkov et al [39]. Second, corner point stress fields are of two types corresponding to symmetric and antisymmetric modes of crack tip surface displacement. Third, there is a core region within a K_λ -dominated region in which non linearities can be neglected. In the present analysis elements at the corner point are small enough to be regarded as being within the core region. Fourth, the overall stress field for a crack tip which terminates in corner points is the sum of stress fields defined by stress intensity factors and stress intensity measures. Similarly, displacement fields are the sum of displacement fields defined by stress intensity factors and stress intensity measures. Use of these ideas means that previous difficulties in interpretation of results [6] can be avoided.

There has been a lot of discussion on whether K_{III} tends to zero or infinity as a corner point is approached [4,5]. When apparent K_{III} values are calculated from stresses at a constant distance from the crack tip then K_{III} appears to tend to zero as the model surface is approached (Figures 4.1.14-4.1.18, 4.1.25-4.1.29 and 4.1.35), in accordance with the linear elastic prediction. However, apparent values of K_{III} at the surface increase strongly as the distance from the crack tip at which they are calculated decreases (Figures 4.1.13, 4.1.24 and 4.1.34). These results can be interpreted as indicating that K_{III} tends to infinity at a corner point in accordance with Bažant and Estenssoro's prediction. The results in Figures 4.1.14-4.1.18,

4.1.25-4.1.29 and 4.1.35 also show that K_{II} does appear to tend to infinity as the surface is approached, in accordance with Bažant and Estenssoro's prediction. The discussion is futile because, as pointed out by Benthem [22], K_{III} is meaningless at a corner point and there is no paradox.

For $s \geq 0.2$ mm λ calculated from τ_{xy} is close to the theoretical value of 0.5 for a stress intensity factor singularity so K_{II} provides a reasonable description of the crack tip stress field. Similarly, K_{III} provides a reasonable description of the crack tip stress field for $s \geq 1$ mm. At the surface values of λ obtained from τ_{xy} are always less than the theoretical value for a corner point singularity. The distribution of τ_{yz} at the surface (Figures 4.1.13, 4.1.24 and 4.1.34) cannot be accounted for on the basis of Bažant and Estenssoro's analysis. There is clear evidence of a boundary layer effect whose extent is independent of the thickness. The only available characteristic dimension controlling the boundary layer thickness is the crack length, a .

Non linearities occur in the region close to the corner point for the following reasons. Under an anti-plane loading the distribution of mode III dislocations (U_z) at the intersection of the crack surface and model surface is approximately parabolic. Differentiating the distribution of U_z gives the distribution of mode I disclinations at the model surface: these are rotations about the y axis. The amount of rotation increases as the crack tip is approached. The limiting value is 90° at the crack tip. The shear stresses perpendicular to the rotated surface must be zero, but finite values of τ_{yz} appear, which means that finite values of apparent K_{III} appear. The distribution of finite values of τ_{yz} is the reason why apparent values of K_{III} increase as the distance from the crack tip at which they are calculated is reduced. Despite the very small elements in the vicinity of a corner point the present results do not confirm the existence of a corner point singularity dominated region within a K -dominated region. It appears that a new field parameter, probably a singularity, is needed to describe the stresses at the disc surfaces. The situation in the vicinity of the surface is clearly more complicated than predicted by Bažant and Estenssoro's analysis of corner point singularities. A possible alternative approach would be to take higher order terms need to be taken into account, in addition to the corner point singularity. It has to be concluded that, while Bažant

and Estenssoro's analysis works well for the symmetric mode (mode I) it is incomplete for the asymmetric mode (a combination of modes II and III). This unexpected finding suggested that further analysis was needed. Accordingly, the strain energy density was calculated for a control volume at the crack tip as described in the next section.

4.1.5. Strain energy density through the thickness

The intensity of the local stress and strain state through the plate thickness can be easily evaluated by using the strain energy density (SED) averaged over a control volume embracing the crack tip (see Ref. [28,29] for a review of the SED approach). The main advantage with respect to the local stress-based parameters is that it does not need very refined meshes in the close neighbourhood of the stress singularity [38]. In fact, contrary to some stress parameters integrated in the local criteria (e.g. maximum principal stress, hydrostatic stress, deviatoric stress), which are mesh-dependent, the SED averaged over a control volume is insensitive to the mesh refinement. The averaged SED can be accurately evaluated also by means of coarse meshes [38] because it directly depends on nodal displacements. As soon as the average SED is known, the notch stress intensity factors (NSIFs) quantifying the asymptotic stress distributions can be calculated *a posteriori* on the basis of very simple expressions linking the local SED and the relevant NSIFs. Furthermore the SED has been considered as a parameter able to control fracture and fatigue in some previous contributions [31–35] and can easily take into account also coupled three-dimensional effects [4,5].

With the aim to provide some numerical assessment of the contribution of the three-dimensional effects, specifically the coupled fracture mode, K_{II} , the local energy density through the thickness is evaluated and discussed in this section. Figures 4.1.36-4.1.38 show the local SED variation across the plate averaged over a cylindrical volume having radius R_0 and height h , with h about equal to R_0 . In Refs [28–35] R_0 was thought of as a material property which varies under static and fatigue loading but here, for the sake of simplicity, R_0 and h are simply set equal to 1.0 mm, only to quantify the three-dimensional effects through the disc thickness.

4.1.5.1. Cracked discs under nominal Mode III loading

The influence of the applied mode III loading combined with the induced singular mode II loading is shown in Figure 4.1.36. It is evident that the position of the maximum SED changes from case to case. It is close to the lateral surface (where the maximum intensity of the mode II takes place) for the two cases $t/a=0.5$ and 1.0 . For larger thicknesses, corresponding to the cases $t/a=2$ and 3 , the maximum value of the SED is at the mid-plane and its value is about 1.5 times the value at the lateral surface. The SED reaches a minimum under the free surface, due to the opposite trend exhibited by mode II and mode III. The change in the nature of the singularity just shown in Figure 4.1.19 is another possible reason of the minimum condition, at least for the cases with $t/a \geq 2$.

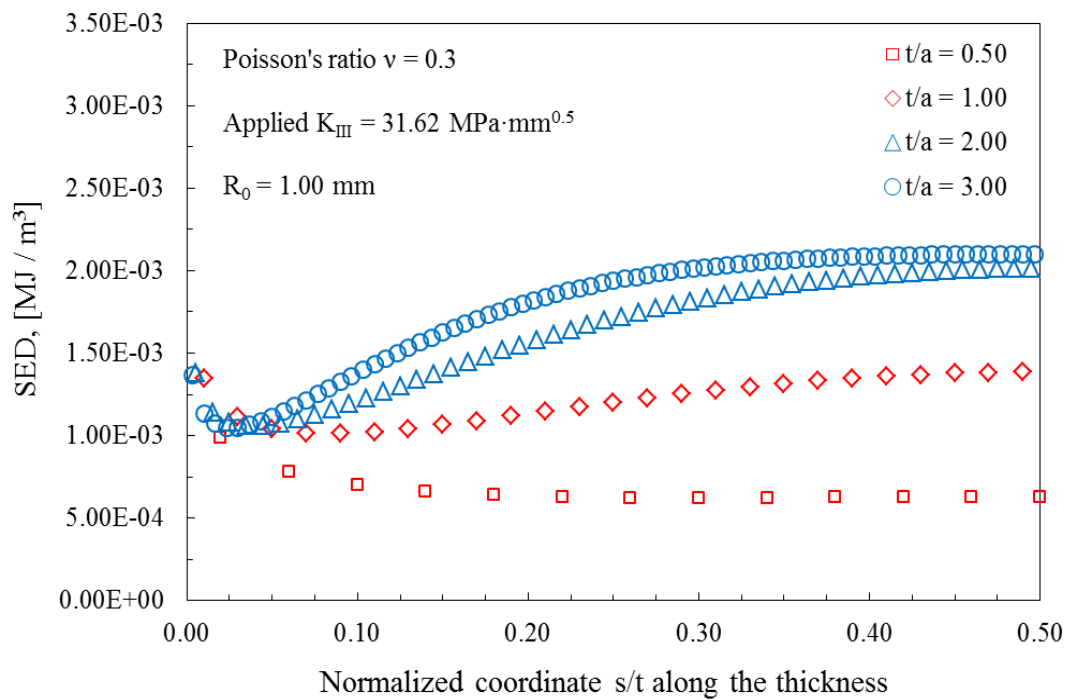


Figure 4.1.36. Through the thickness SED distribution for $t/a = 0.50, 1, 2, 3$. Control radius $R_0 = 1.00 \text{ mm}$.

4.1.5.2. Cracked plates under nominal Mode III loading

The influence of the applied mode III loading combined with the induced singular mode II loading is shown in Figure 4.1.37. It is evident that the position of the maximum SED is the same in all cases. It is close to the lateral surface, where the maximum intensity of the coupled mode II takes place, both for thin plates, $t/a=0.5$ and 1.0 , and for thick ones, $t/a=2$ and 3 . In fact, as can be seen from Figures 4.1.25-4.1.29 for the plate results the maximum contribution of the coupled mode II, at the lateral surface, is significantly higher (about 4 times) compared to the maximum contribution of the applied mode III, at the mid plane. For the disc results indeed the ratio between the maximum values of K_{II} and K_{III} was lower (about 2) as can be seen from Figures 4.1.14-4.1.18, so that the maximum contributions were not significantly different and the position of the maximum SED results to be a function of disc thickness.

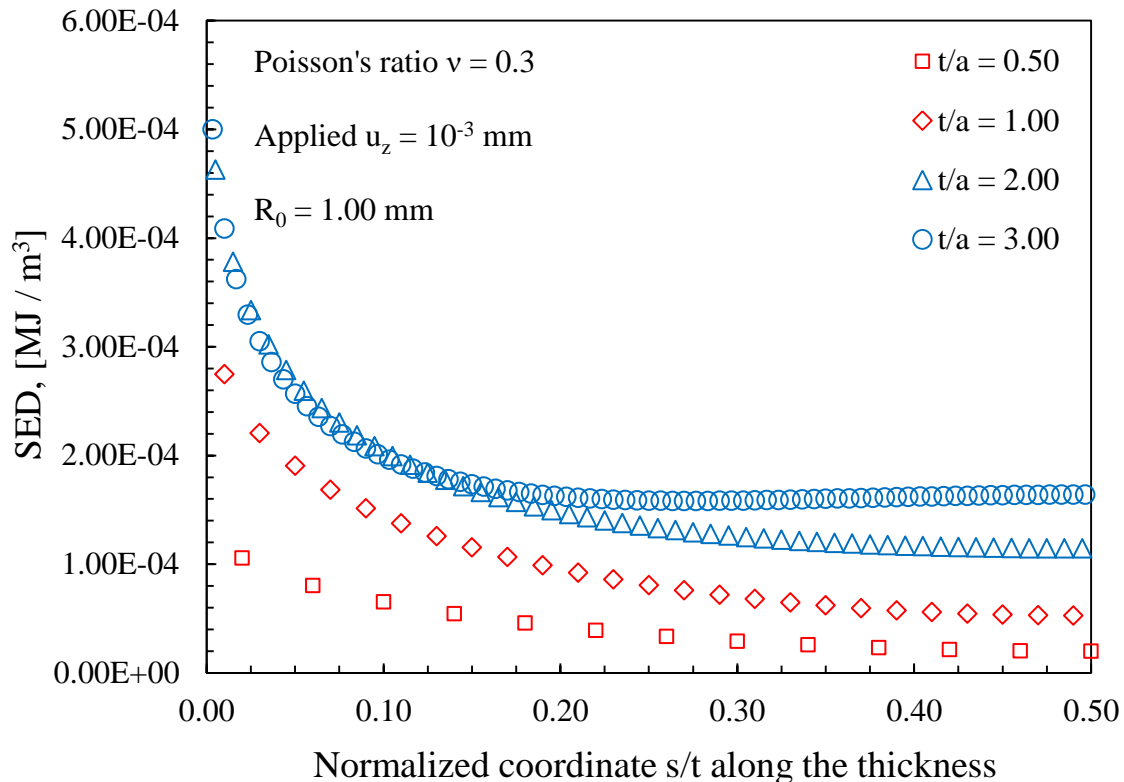


Figure 4.1.37. Through the thickness SED distribution for $t/a = 0.50, 1, 2, 3$. Control radius $R_0 = 1.00$ mm.

4.1.5.3. Cracked discs under nominal Mode II loading

Finally, Figure 4.1.38, compared with Figure 4.1.36, shows that through the thickness SED distributions, for $t/a = 0.50, 1, 2$ and 3 , have been altered by the elimination of disc bending.

The results show that the change of loading mode from nominal mode III to nominal mode II has had no effect on the distributions of τ_{yz} and τ_{xy} on and near the crack surface, but has significantly changed the through thickness distributions of K_{II} , K_{III} and SED .

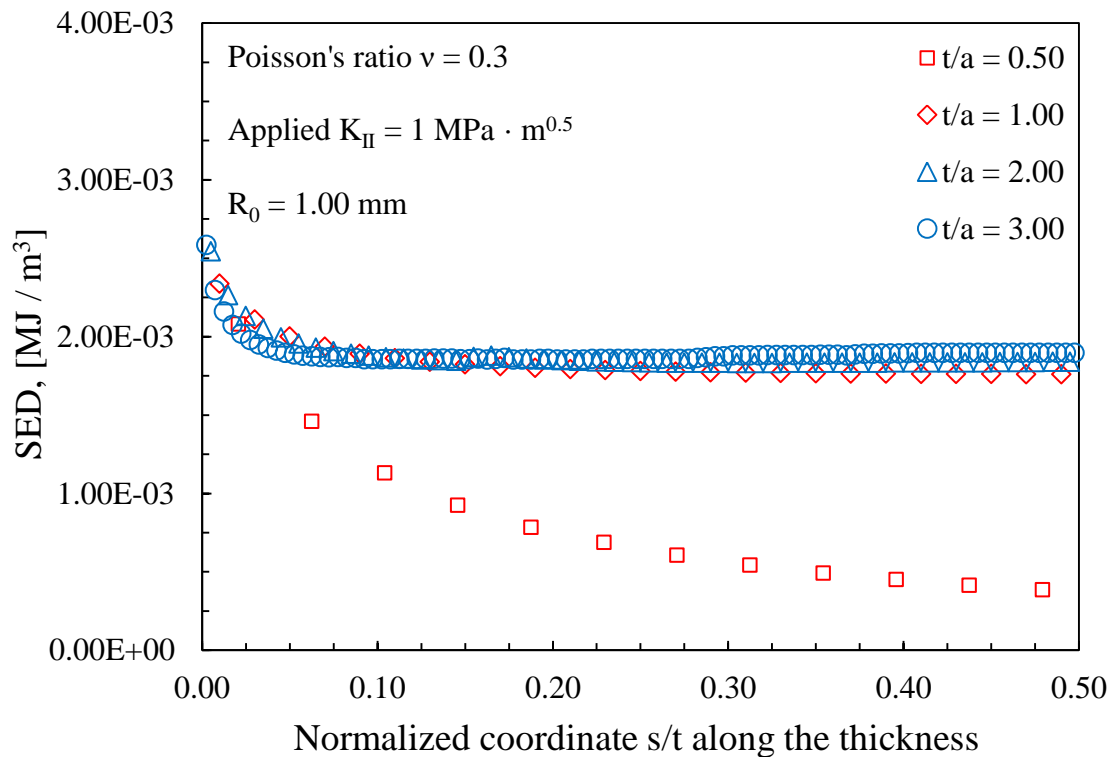


Figure 4.1.38. Through-the-thickness SED distribution for $t/a = 0.50, 1, 2, 3$. Control radius $R_0 = 1.00 \text{ mm}$.

4.1.6. Final discussion

The results obtained from the highly accurate finite element analyses of through cracked plates under anti-plane loading are broadly similar to results obtained for

discs under a different type of anti-plane loading. In particular, it is confirmed that mode III does induce coupled mode II^c.

The influence of plate bending is increasingly important as plate thickness decreases. The anti-plane loading used is a nominal mode III loading. For thin plate it is a mixed modes III and II loading, in which mode III induces mode II^c and vice versa. At the present state of the art it is not possible to separate the coupled modes from the applied modes.

Bažant and Estenssoro's analysis works well for the symmetric mode (mode I), but it is incomplete for the asymmetric mode (a combination of modes II and III).

Discussion on whether K_{III} tends to zero or infinity as a corner point is approached is futile because, as pointed out by Benthem, K_{III} is meaningless at a corner point.

Despite the very small elements in the vicinity of a corner point the present results do not confirm the existence of a corner point singularity dominated region within a K -dominated region. It appears that a new field parameter, probably a singularity, is needed to describe the stresses at the disc surfaces.

Calculation of the strain energy density (SED) in a control volume at the crack tip shows that the position of the maximum SED is independent of plate thickness, contrary to disc results. Both for thin plates and for thick ones the maximum SED is close to the lateral surface, where the maximum intensity of the coupled mode II takes place.

SED is promising as a means of characterizing the crack tip stress field under anti-plane loading, but the use of a control volume radius smaller than that adopted in the present work (1 mm) would be preferable.

Under the anti-plane loading used theoretical understanding of the stress field in the vicinity of a corner point is still incomplete.

4.2 Three-dimensional effects on cracked components: influence of boundary conditions ^(*)

Nomenclature

2α	notch opening angle
E	Young's modulus
G	shear modulus
K	stress intensity factor, subscripts I, II, III denote mode, subscript F-F indicates free-free, while F-C denotes free-clamped
R_0	control volume radius, subscripts I, II, III denote mode, subscript F-F indicates free-free, while F-C denotes free-clamped
r	disc radius
r, θ, z	cylindrical coordinates
s	distance from surface
u	displacement, subscripts x, y, z denote direction
x, y, z	Cartesian coordinates
W_c	material critical strain energy density
\overline{W}	Averaged Strain Energy Density (SED)

Symbols

κ_3	Mode III eigenvalue under free-clamped boundary condition
λ_3	Mode III eigenvalue under free-free boundary condition
ν	Poisson's ratio
σ	stress, subscripts x, y, z or r, θ , z denote normal stresses subscripts xy, yz, xz or r θ , θ z, rz denote shear stresses
τ_c	shear strength of the material

(*) See also:

Campagnolo, A.; Berto, F.; Lazzarin, P. The effects of different boundary conditions on three-dimensional cracked discs under anti-plane loading. *European Journal of Mechanics - A/Solids*; 50:76-86 (2015);

4.2.1. Introduction

Microscopic effects may play a significant role on the macroscopic behavior of materials as recently highlighted by Tang and Wei [40]. This is particularly true for micro electro mechanical systems [41,42] and not only under mechanical loading but also when the component is subjected to heat fluxes [43]. It is therefore pertinent to have a model that can couple the microscopic effects to those at the macroscopic scale. Examined, in particular, are the inhomogeneities at the microscale arising from uneven stiffness of the material microstructures which can vary the constraints on the micro-crack. These inhomogeneities are simulated by the free-free, fixed-fixed and free-fixed boundary conditions [44–46]. Dealing with the material microstructure an analytical multi-scale model has recently been developed by Tang and Sih [44]. Physically, the different orders of the stress singularities are related to the different constraints associated with the defect thought as a micro V-notch at the tip of the main crack. Irregularities of the material microstructure tend to torture the crack tip being the free-clamped boundary conditions the more realistic for a general representation of what occurs on the micro V-notch [44]. The approach by Tang and Sih [44] allows to overcome under linear elastic properties the problem tied to plasticity by considering different eigenvalues at different material scales. A multiscale damage model valid for anti-plane loading has been proposed by using the singularity representation method derived for plates under in-plane extension [44,45]. Different orders and strengths of singularity are uniquely associated with the boundary conditions, loadings and geometries of the defects under consideration. The stress and strain fields in the proximity of V-notch placed at the main crack tip are very complex. Some experimental and theoretical studies have been recently carried out on the fracture behavior of V-notches making clear the interest on this topic among the scientific community [47–51]. The degree of complexity usually arises if the complete three-dimensional elastic problem is investigated. For this reason it is of interest to study the behavior of a V-notch under a nominal anti-plane shear loading and the induced modes automatically generated near the notch tip due to different boundary conditions in a three-dimensional component. The problem of coupled modes generated by a primary

nominal applied mode has been extensively studied mainly dealing with cracks [10,11,52–55] but also with pointed and sharply radiused V-notches [7,12,13,21,56,57]. In those references it was shown that at a corner point Mode II and Mode III cannot exist in isolation. If one of these modes is applied then the other is always automatically induced. Moreover, if the free-clamped boundary conditions are applied to the edges of the notch, Mode I and II are always coupled each other also in a plane problem [44,45,58]. Their intensities are influenced by the shape of the notch and by the externally applied loads [44]. As explained above in three-dimensional pointed notches with free-clamped edges under nominal anti-plane shear loading all the Modes are locally present [44,46]. The degree of singularity of the different Modes is strongly influenced by the boundary conditions applied on the notch edges. Take for example the crack case that is generally characterized by a degree of singularity equal to 0.5 regardless of the loading mode according to Linear Elastic Fracture Mechanics. When the crack edges are characterized by free-clamped conditions different singularities can arise, depending on the considered loading Mode. This generates an odd dimensionality between the Stress Intensity Factors which are not directly comparable. Moreover there are some uncertainties in the definition of the stress intensity factors on the free surfaces, due to the corner point singularity generated by the intersection of the crack with the free surfaces of the model [4–6,22,24].

At the light of these considerations the present work is twofold. First some analytical expressions of the strain energy density (SED) averaged over a control volume embracing the V-notch tip with a generic opening angle 2α are derived in the case of Mode III loading, as a function of different boundary conditions on the notch edges. In particular free-free and free-clamped conditions are considered here combining the expressions of SED derived here for Mode III loading with those for coupled Modes obtained by extending to the specific case some previously derived expressions [27].

In the second part of the paragraph the specific case of three-dimensional cracked discs characterized by different thicknesses is investigated numerically. Free-free and free-clamped boundary conditions are applied to the FE models. The complex stress field is accurately investigated and the SED through the thickness of the

disc obtained by numerical analyses is compared with the theoretical trend derived by using the developed analytical frame. Due to the uncertainties in the definition of the stress intensity factors on the free surfaces, mentioned above, and the odd dimensionality of the SIFs due to the applied boundary conditions the strain energy averaged in a control volume (SED) is employed in the present investigation to quantify the stress intensity through the thickness of the disc. For a review of the SED the reader can refer to a recent paper [29]. This parameter has been successfully used by Lazzarin and co-authors to assess the fracture strength of a large bulk materials, characterized by different control volumes, subjected to wide combinations of static loading [27,29,31,32] and the fatigue strength of welded joints [33,59,60] and notched components [34,35,61]. As shown by Lazzarin et al. [62,38] an intrinsic advantage of the SED approach is that it permits automatically to take into account higher order terms and it is easy to calculate by using coarse meshes.

In the present work a careful comparison is carried out between free-free and free-clamped constraint conditions along the edges of the notch. Although the only aim of this work is to investigate the crack case, as visible from the developed analytical frame, the SED can be easily applied also to point V-notches and a direct comparison can be directly drawn between the crack case and the V-notch cases. This will be the subject of future works.

4.2.2. Analytical framework: stress and displacement fields under Mode III

This section summarises the analytical frame giving the expressions of the singular stress and displacement fields in the proximity of the V-notch tip. A Mode III loading condition is treated, by varying the boundary conditions of the notch edges. An isotropic and homogeneous material under linear elastic conditions is taken into account.

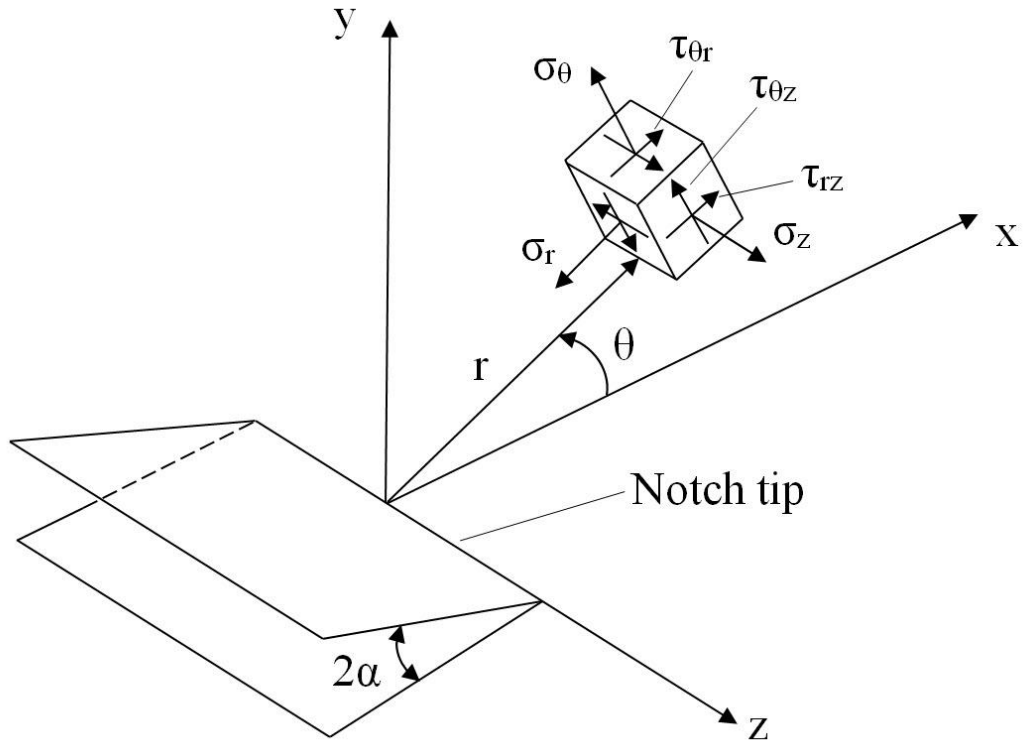


Figure 4.2.1. Cylindrical reference system for stress field.

4.2.2.1 Free-Free

In the presence of a sharp V-notch with stress free surfaces, named the free-free condition hereafter, the stress distributions due to anti-plane loading (Mode III) are [45,63,64]:

$$\sigma_{rz} = \frac{K_{3,F-F}}{\sqrt{2\pi}} 2\lambda_3 r^{\lambda_3-1} [\sin(\lambda_3\theta)] \quad (4.2.1a)$$

$$\sigma_{\theta z} = \frac{K_{3,F-F}}{\sqrt{2\pi}} 2\lambda_3 r^{\lambda_3-1} [\cos(\lambda_3\theta)] \quad (4.2.1b)$$

The only displacement component different from zero is:

$$u_z = \frac{K_{3,F-F}}{G} \sqrt{\frac{2}{\pi}} r^{\lambda_3} [\sin(\lambda_3\theta)] = 2(1+\nu) \frac{K_{3,F-F}}{E} \sqrt{\frac{2}{\pi}} r^{\lambda_3} [\sin(\lambda_3\theta)] \quad (4.2.2)$$

where G is the shear modulus, E the Young's modulus and ν the Poisson's ratio. The stress and displacement fields are given in a cylindrical coordinate system centered at the notch tip (Fig. 4.2.1); r is the radial coordinate, θ is the angle measured from the notch bisector line and z is the out-of-plane coordinate.

The parameter $K_{3,F-F}$ represents the Mode III Notch Stress Intensity Factor (NSIF), thought of as the natural extension of the Mode I and Mode II NSIFs first defined by Gross and Mendelson [65]. The degree of stress singularity depends on the Mode III eigenvalue λ_3 , which varies as a function of the notch opening angle 2α [45,66]. Under the free-free boundary condition, λ_3 is the lowest real eigenvalue of the following eigen-equation:

$$\cos \lambda_3 \gamma = 0 \quad \text{with} \quad \lambda_3 = \frac{\pi}{2\gamma} \quad (4.2.3)$$

where $\gamma = \pi - \alpha$.

4.2.2.2 Free-Clamped

In the presence of a sharp V-notch with one edge free and the other fixed from moving, named the free-clamped condition hereafter, the stress distributions due to an anti-plane loading (Mode III) are [45,66]:

$$\sigma_{rz} = \frac{K_{3,F-C}}{\sqrt{2\pi}} 2\kappa_3 r^{\kappa_3-1} [\sin(\kappa_3 \theta) + \cos(\kappa_3 \theta)] \quad (4.2.4a)$$

$$\sigma_{\theta z} = \frac{K_{3,F-C}}{\sqrt{2\pi}} 2\kappa_3 r^{\kappa_3-1} [\cos(\kappa_3 \theta) - \sin(\kappa_3 \theta)] \quad (4.2.4b)$$

The only displacement component different from zero is:

$$u_z = \frac{K_{3,F-C}}{G} \sqrt{\frac{2}{\pi}} r^{\kappa_3} [\sin(\kappa_3 \theta) + \cos(\kappa_3 \theta)] = 2(1 + \nu) \frac{K_{3,F-C}}{E} \sqrt{\frac{2}{\pi}} r^{\kappa_3} [\sin(\kappa_3 \theta) + \cos(\kappa_3 \theta)] \quad (4.2.5)$$

Also in this case the stress and displacement fields are given according to the polar coordinate system shown in Fig. 4.2.1.

The parameter $K_{3,F-C}$ represents again the Mode III Notch Stress Intensity Factor (NSIF) while κ_3 is the Mode III eigenvalue dependent on the notch opening angle 2α [45]. For the free-clamped condition, κ_3 is the lowest real eigenvalue of the following eigen-equation:

$$\cos 2\kappa_3\gamma = 0 \quad \text{with} \quad \kappa_3 = \frac{\pi}{4\gamma} \quad (4.2.6)$$

4.2.3. Strain energy density (SED) under Mode III

According to Beltrami [67], the total strain energy density W is equal to the total work done by the system. For a three-dimensional stress state the equation for W is:

$$W(r, \theta) = \frac{1}{2E} \left[\sigma_{\theta\theta}^2 + \sigma_{rr}^2 + \sigma_{zz}^2 - 2\nu(\sigma_{\theta\theta}\sigma_{rr} + \sigma_{\theta\theta}\sigma_{zz} + \sigma_{rr}\sigma_{zz}) + 2(1+\nu)(\sigma_{r\theta}^2 + \sigma_{rz}^2 + \sigma_{\theta z}^2) \right] \quad (4.2.7)$$

Under pure Mode III loading conditions, only σ_{rz} and $\sigma_{\theta z}$ stress components are different from zero and Eq. (4.2.7) becomes:

$$W_3(r, \theta) = \frac{1+\nu}{E} \cdot (\sigma_{rz}^2 + \sigma_{\theta z}^2) \quad (4.2.8)$$

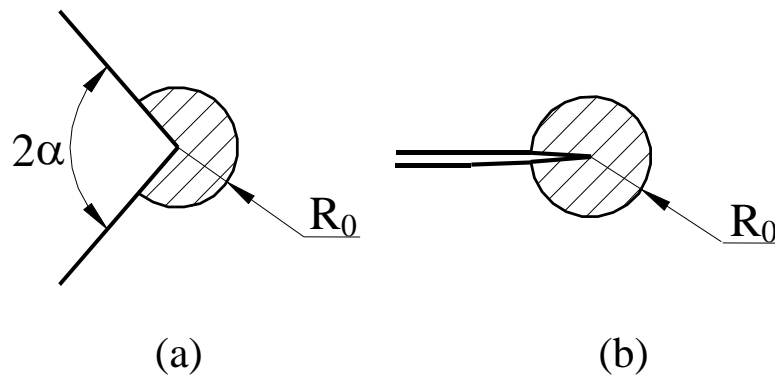


Figure 4.2.2. Control volume for sharp V-notches (a) and cracks (b).

4.2.3.1 SED for Free-Free boundary conditions

In the case of free-free V-notched components subjected to Mode III loading condition, the elastic energy $E(R_0)$ in a circular sector of radius R_0 surrounding the notch tip (Fig. 4.2.2) can be calculated by inserting Eqs (4.2.1a,b) into Eq. (4.2.8). Doing so, one obtains:

$$E(R_0) = \int_A W_3(r, \theta) dA = \frac{1}{E} \int_{-\gamma}^{\gamma} \int_0^{R_0} (1 + \nu)(\sigma_{rz}^2 + \sigma_{\theta z}^2) r dr d\theta = \frac{(1 + \nu)}{E} K_{3,F-F}^2 R_0^{2\lambda_3} \quad (4.2.9)$$

The average SED is simply given by the ratio between the elastic energy $E(R_0)$ and the area of the circular sector $A(R_0)$. Then:

$$\bar{W}_3 = \frac{E(R_0)}{A(R_0)} = \frac{(1 + \nu)}{E} \frac{K_{3,F-F}^2 R_0^{2\lambda_3}}{\gamma R_0^2} = \frac{1}{E} \frac{1 + \nu}{(\pi - \alpha)} \frac{K_{3,F-F}^2}{R_0^{2(1-\lambda_3)}} \quad (4.2.10)$$

According to Lazzarin and Zambardi [27] the brittle fracture of the material occurs when the average value of the strain energy density, calculated on a control volume of radius R_0 surrounding the notch tip (Fig. 4.2.2), is equal to the material critical value W_c . After Beltrami, Schleicher [68] was the first to consider W_c dependent not only on the material but also on the loading conditions. Under Mode III loading, it can be obtained:

$$W_c = \frac{\tau_c^2}{2G} = (1 + \nu) \frac{\tau_c^2}{E} \quad (4.2.11)$$

where τ_c is the shear strength of the material.

Under linear elastic conditions, by imposing at failure $\bar{W}_3 = W_c$, Eq. (4.2.10) and Eq. (4.2.11) in combination give:

$$\left(\frac{1}{\pi - \alpha} \right) K_{3c,F-F}^2 R_{0,F-F}^{2(\lambda_3-1)} = \tau_c^2 \quad (4.2.12)$$

Finally, by solving Eq. (4.2.12), the control radius R_0 for the free-free condition results to be:

$$R_{0,F-F} = \left(\frac{1}{\pi - \alpha} \cdot \frac{K_{3c,F-F}^2}{\tau_c^2} \right)^{\frac{1}{2(1-\lambda_3)}} \quad (4.2.13)$$

When the V-notch becomes a crack ($2\alpha = 0$, $\lambda_3 = 0.5$), the value of $K_{3c,F-F}$ coincides with the Mode III fracture toughness and the control radius becomes:

$$R_{0,F-F} = \frac{1}{\pi} \left(\frac{K_{IIIc,F-F}}{\tau_c} \right)^2 \quad (4.2.14)$$

4.2.3.2 SED for Free-Clamped boundary conditions

In the case of free-clamped V-notches under Mode III, the elastic energy $E(R_0)$ in a circular sector of radius R_0 surrounding the notch tip (Fig. 4.2.2) can be calculated by Eq. (4.2.8) and Eqs (4.2.4a,b):

$$E(R_0) = \int_A W_3(r, \theta) dA = \frac{1}{E} \int_{-\gamma}^{\gamma} \int_0^{R_0} (1 + \nu)(\sigma_{rz}^2 + \sigma_{\theta z}^2) r dr d\theta = \frac{(1 + \nu)}{E} K_{3,F-C}^2 R_0^{2\kappa_3} \quad (4.2.15)$$

Also in this case, the average strain energy density is given by the ratio between the elastic energy $E(R_0)$ and the area of the circular sector $A(R_0)$. Then:

$$\bar{W}_3 = \frac{E(R_0)}{A(R_0)} = \frac{(1 + \nu)}{E} \frac{K_{3,F-C}^2 R_0^{2\kappa_3}}{\gamma R_0^2} = \frac{1}{E} \frac{(1 + \nu)}{(\pi - \alpha)} \frac{K_{3,F-C}^2}{R_0^{2(1-\kappa_3)}} \quad (4.2.16)$$

As said above, according to the average SED approach [27], the fracture of the material under linear elastic conditions occurs when the average value of the SED, as calculated on a control volume of radius R_0 surrounding the notch tip (Fig. 4.2.2), is equal to the material critical value W_c (see Eq. 4.2.11). By imposing at failure $\bar{W}_3 = W_c$, Eq. (4.2.16) and Eq. (4.2.11) in combination give:

$$\left(\frac{1}{\pi - \alpha} \right) K_{3c,F-C}^2 R_{0,F-C}^{2(\kappa_3-1)} = \tau_c^2 \quad (4.2.17)$$

Finally the control radius R_0 for the free-clamped condition results in:

$$R_{0,F-C} = \left(\frac{1}{\pi - \alpha} \cdot \frac{K_{3c,F-C}^2}{\tau_c^2} \right)^{\frac{1}{2(1-\kappa_3)}} \quad (4.2.18)$$

When the V-notch becomes a crack ($2\alpha = 0$, $\kappa_3 = 0.25$), the value of $K_{3c,F-C}$ is that for the crack case and the control radius becomes:

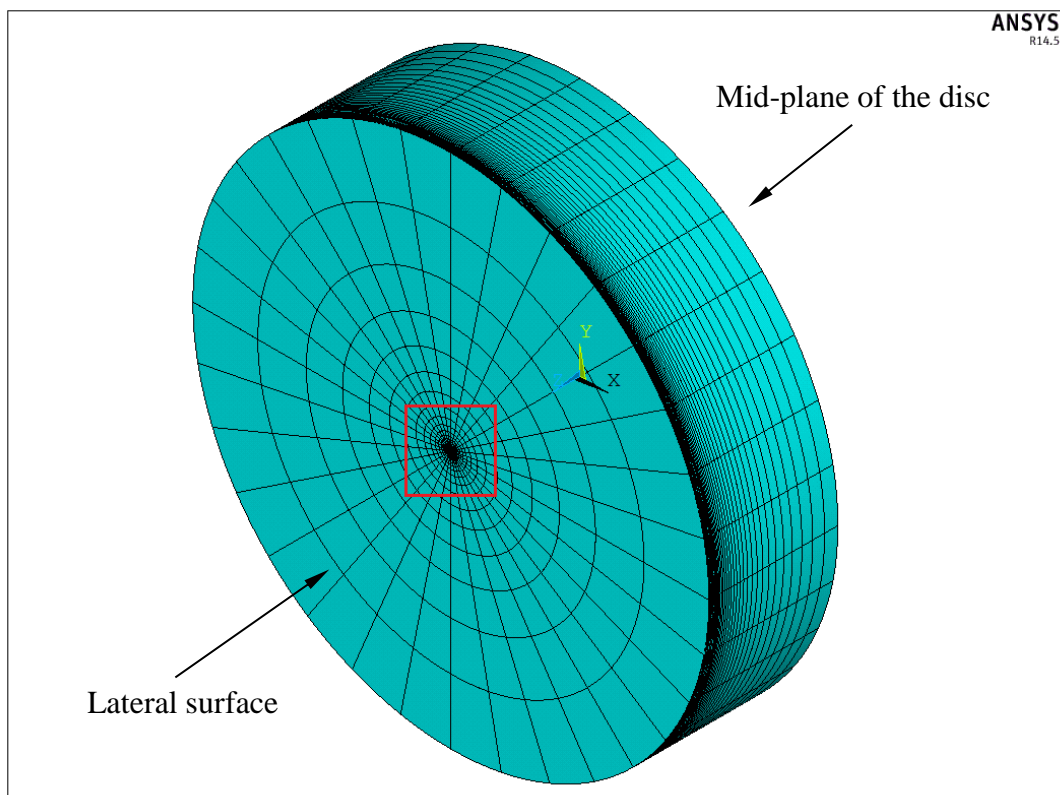
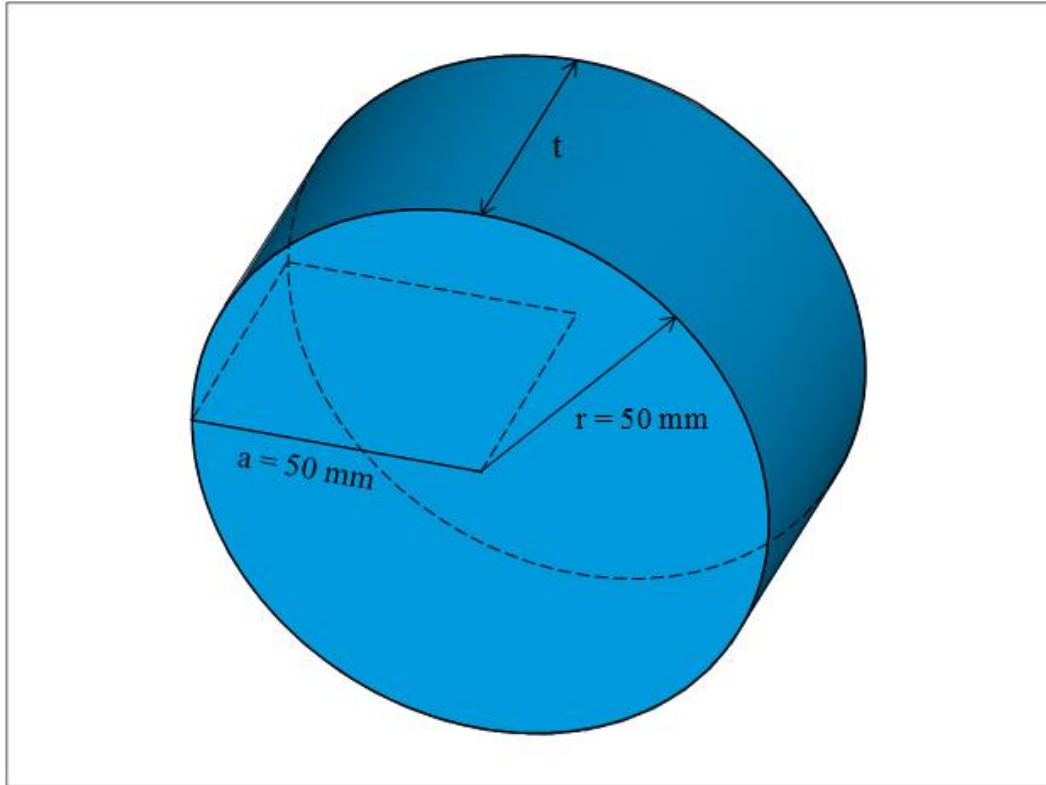
$$R_{0,F-C} = \left(\frac{1}{\pi} \right)^{\frac{2}{3}} \left(\frac{K_{IIIc,F-C}}{\tau_c} \right)^{\frac{4}{3}} \quad (4.2.19)$$

The developed analytical frame will be used in following for the crack case ($2\alpha = 0$), which will be analyzed also by a number of numerical analyses.

4.2.4. Finite element analysis of three-dimensional cracked discs

As anticipated in the introduction, to evaluate the effects of the boundary conditions the particular case corresponding to discs weakened by a crack ($2\alpha = 0$) is considered in the present work. Cracked discs subjected to anti-plane, nominal Mode III, loading have been modelled by using ANSYS code (version 14.5). Due to the out-of-plane u_z displacements, Eqs (4.2.2, 4.2.5), a three-dimensional FEM analysis has been carried out.

Stresses and stress intensity factors were determined for 100 mm diameter discs of varying thickness. The disc geometry is shown in Fig. 4.2.3a where the disc radius is constant, $r = 50$ mm, whereas the thickness t varies from case to case. The tip of the through-the-thickness crack is located at the centre of the disc, and its length, a , was set equal to 50 mm. Numerical models are characterised by a ratio $t/a = 0.5, 1, 2$ and 4 . The Poisson's ratio and the Young's modulus are kept constant and equal to 0.3 and 206 GPa, respectively.



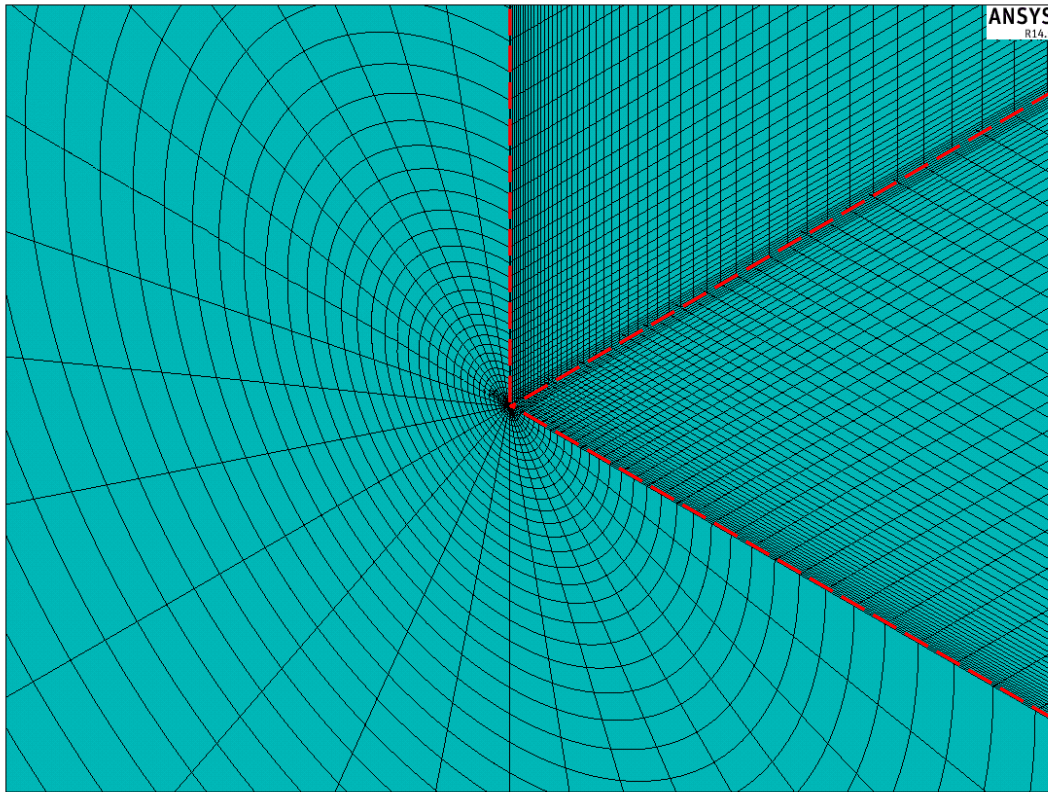


Figure 4.2.3. (a) Disc geometry. (b) Overall view of the finite element mesh. The number of elements used is equal to 360000, which corresponds to more than $4 \cdot 10^6$ degrees of freedom. (c) Detail of finite element mesh sectioned at crack tip. The minimum element size in radial direction is equal to $1.80 \cdot 10^{-4}$ mm while in z direction (along the disc thickness) is equal to $1.50 \cdot 10^{-4}$ mm.

In the case of free-free cracked elements one quarter of the disc was modelled, taking advantage of the antisymmetric boundary conditions with respect to the X-Y and X-Z planes (both crack edges are free). Conversely, in the case of free-clamped cracked components, one half of the disc was modelled, taking advantage of the antisymmetric boundary conditions with respect to the X-Y plane. With respect to the X-Z plane, in fact, there is no antisymmetric boundary condition, because one crack edge is free whereas the other is constrained in the z direction (Mode III-fixed with $u_z = 0$). An overall view of the finite element mesh used for modelling one half of the disc is shown in Fig. 4.2.3b; a detail of the mesh at the crack tip is shown in Fig. 4.2.3c. In the free-free case the mesh used is the same, with the only difference that one quarter of the disc was modelled

instead of one half of the disc. In both cases 20-node brick elements (BRICK 186) were used.

Taking advantage of Eq. (4.2.2) for the free-free case, and Eq. (4.2.5) for the free-clamped case, Mode III displacements have been applied to the cylindrical surface of the FE models as a function of the angular coordinate θ . The values of the applied stress intensity factors were $K_{3,F-F} = 1 \text{ MPa} \cdot \text{m}^{0.5}$ for the free-free case and $K_{3,F-C} = 0.67 \text{ MPa} \cdot \text{m}^{0.75}$ for the free-fixed case. Note that these values correspond to the same displacement range $\Delta u_z = 4.50 \cdot 10^{-3} \text{ mm}$, as measured with respect to the angular coordinates $\theta = -180$ and $+180$ degrees, as shown in Fig. 4.2.4. Thanks to these boundary conditions, the disc can be thought of as a K -dominated core region.

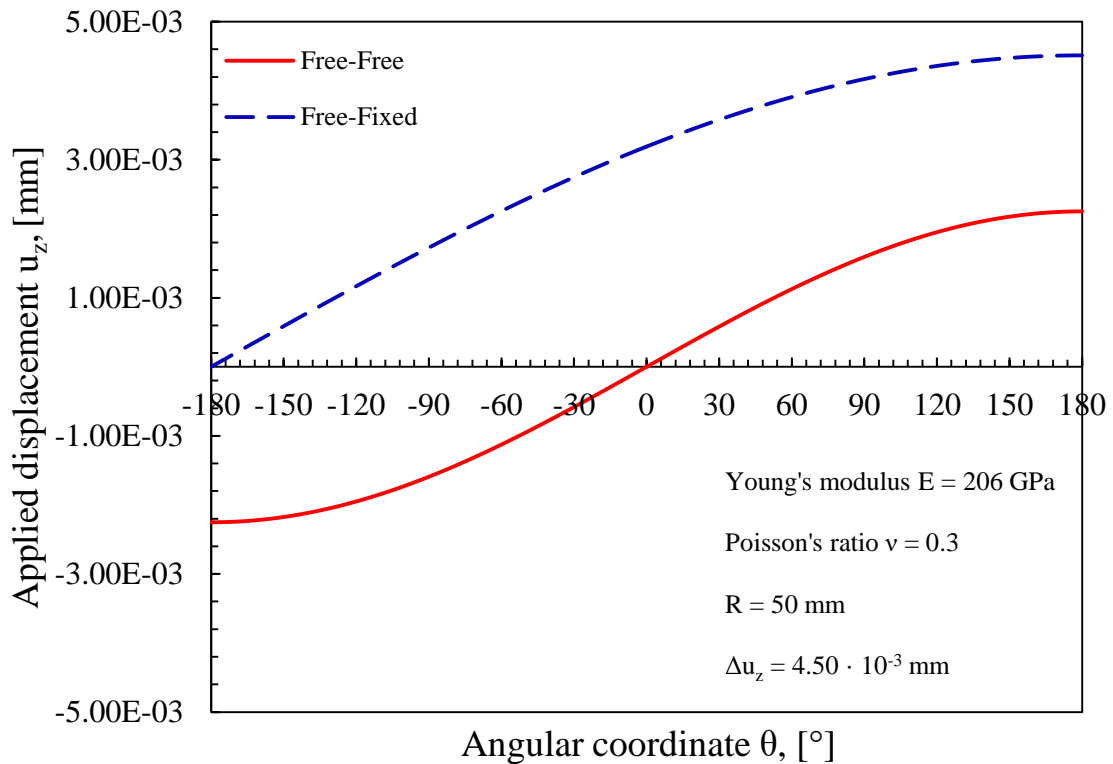


Figure 4.2.4. Applied displacement u_z as a function of the angular coordinate θ . Free-Free and Free-Clamped cases.

4.2.5. Results

Due to local three-dimensional effects, widely discussed by Pook [7,21] and Berto et al. [56,57], the application of a nominal Mode III loading condition via nodal displacements at a convenient distance from the crack tip results in induced modes, which depend on the boundary conditions. The induced modes are discussed in detail on the basis of the FE results.

4.2.5.1 Stress fields and Stress Intensity Factors

The stresses and the Stress Intensity Factors related to Mode I, II and III loading were extracted from the finite element results at the crack bisector line at distances s from the disc surfaces of 0, 0.25, 0.50, 1 and 2 mm. It can be observed that for the nodes belonging to the crack bisector line the cylindrical reference system r - θ - z coincides with the Cartesian system x - y - z , therefore $\sigma_\theta = \sigma_y$ (Mode I), $\tau_{r\theta} = \tau_{xy}$ (Mode II) and $\tau_{\theta z} = \tau_{yz}$ (Mode III).

Results for $t/a = 2$, with stress fields plotted on double logarithmic scales, are shown in Figs 4.2.5-7 for the free-free cases, in Figs 4.2.9-11 for the free-clamped cases. When the plot is according to a straight line, the slope will be reported explicitly. Otherwise no value of slope is shown. Plots for values of t/a different from 2.0 are analogous, with some differences in detail. Plots for t/a ranging from 0.5 to 4.0 will be presented only with reference to the average SED.

4.2.5.1.1 Stress analysis for Free-Free cases

In this case the stress components different from zero on the crack bisector line are τ_{xy} and τ_{yz} ; this means that in the free-free case the application of a nominal Mode III loading induces Mode II stress components.

Figure 4.2.5 shows that λ_2 calculated from τ_{xy} at the distance $s = 2$ mm from the crack tip coincides with the theoretical value of 0.50 [69,70]. This holds true also when this distance decreases to $s = 0.50$ mm, as shown in Fig. 4.2.6. Hence, realistic values of K_{II} can be calculated. For $s = 0$ mm, instead, λ_2 is found to depend on t/a . It decreases with t/a , to a minimum of 0.44 at $t/a = 2.00$ (Fig. 4.2.7) and then increases slightly. The values of λ_2 are all significantly greater than the

theoretical value of 0.40 due to the corner point singularity effect well described by Bazant and Estenssoro [20]. This means that exact values of K_{II} cannot be calculated.

Also λ_3 calculated from τ_{yz} matches or is very close to the theoretical value of 0.50, Eq. (4.2.3), both for $s = 2$ mm (Fig. 4.2.5) and for $s = 0.50$ mm (Fig. 4.2.6). Small variations of the slope have been detected at $s = 0.25$ mm, with $1 - \lambda_3 = 0.53$. Hence, in all models with $s \geq 0.25$ mm realistic values of K_{III} can be calculated from the τ_{yz} stress component. For $s = 0$ mm (see again Fig. 4.2.7) τ_{yz} has not a linear trend as a function of the distance x from the crack tip. Then it is not possible to exactly define the stress intensity factor K_{III} .

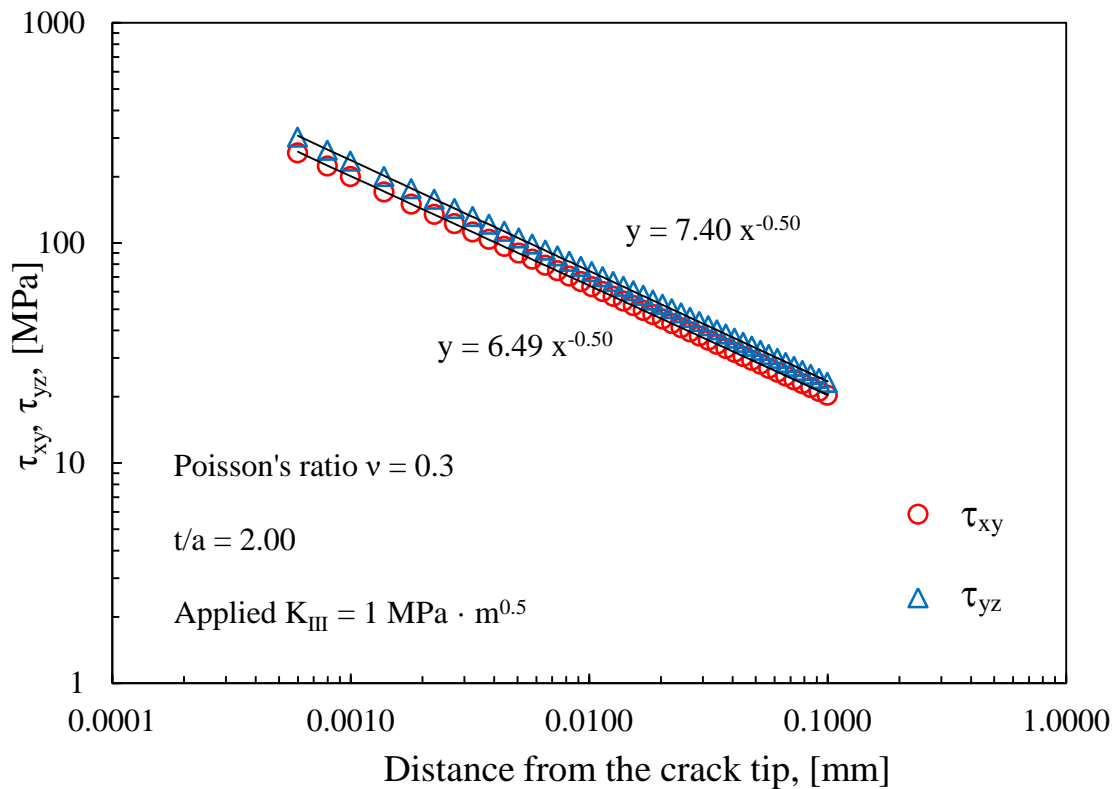


Figure 4.2.5. Free-Free: stresses τ_{xy} and τ_{yz} on crack surface at $s = 2$ mm from disc surface.

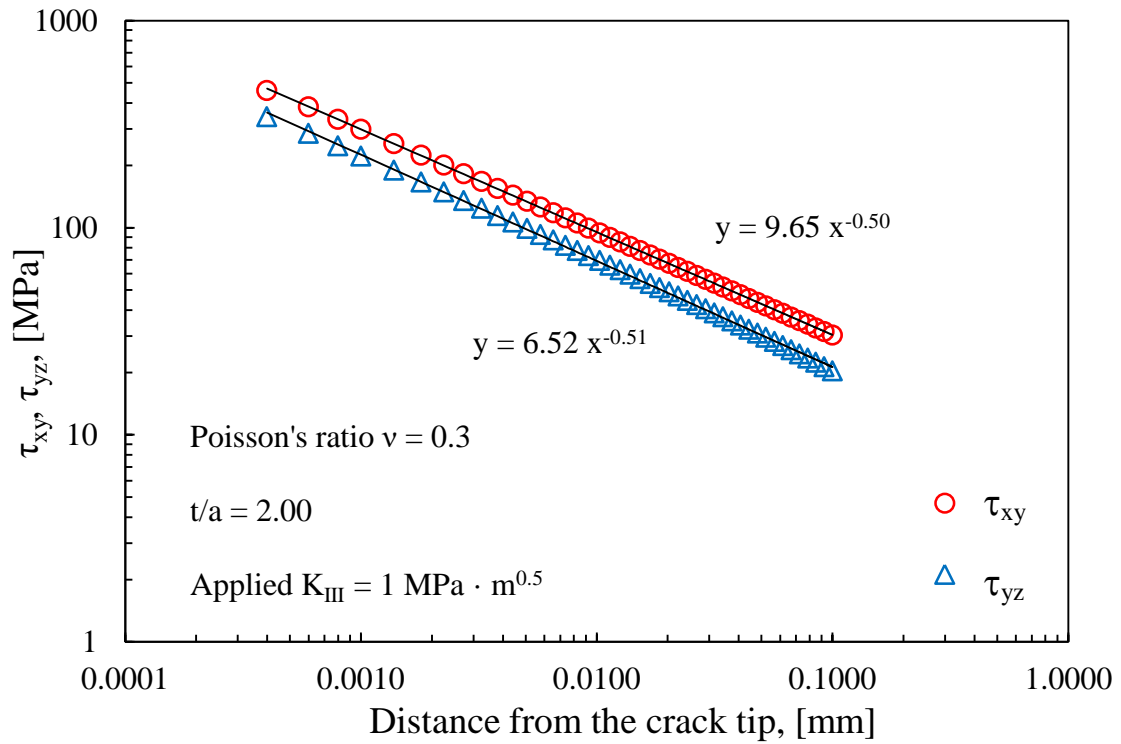


Figure 4.2.6. Free-Free: stresses τ_{xy} and τ_{yz} on crack surface at $s = 0.50$ mm from disc surface.

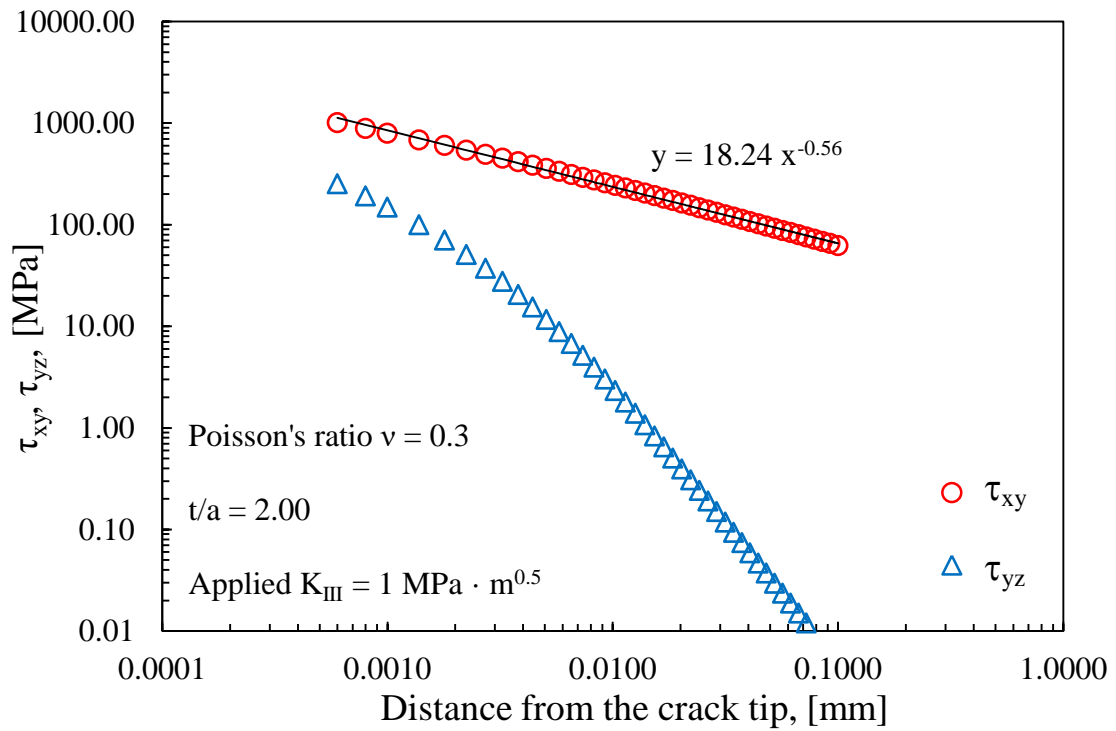


Figure 4.2.7. Free-Free: stresses τ_{xy} and τ_{yz} on crack surface at $s = 0$ mm from disc surface.

On the basis of the obtained results it is evident that only at a given distance from the free surfaces the slopes of the applied (τ_{yz}) and induced (τ_{xy}) stress distributions are consistent with those of the stress fields related to the free-free boundary conditions, which correspond to $\lambda_2 = \lambda_3 = 0.50$ ([14,69,70] and Eq. (4.2.3) respectively). For $s \geq 0.25$ mm, the stress intensity factors K_{II} and K_{III} can be directly calculated by means of the stresses evaluated at a small distance x from the crack tip, so that:

$$K_{II} = \sqrt{2\pi} \cdot \tau_{xy} \cdot x^{1-\lambda_2} = \sqrt{2\pi} \cdot \tau_{xy} \cdot x^{0.5} \quad (4.2.20)$$

$$K_{III} = \frac{\sqrt{2\pi}}{2\lambda_3} \cdot \tau_{yz} \cdot x^{1-\lambda_3} = \sqrt{2\pi} \cdot \tau_{yz} \cdot x^{0.5} \quad (4.2.21)$$

In our calculation a value of 0.05 mm has been used for x , since it falls within the region in which the SIFs can be defined and also it is the most convenient for the particular FE mesh adopted, being a node present at such a distance from the crack tip.

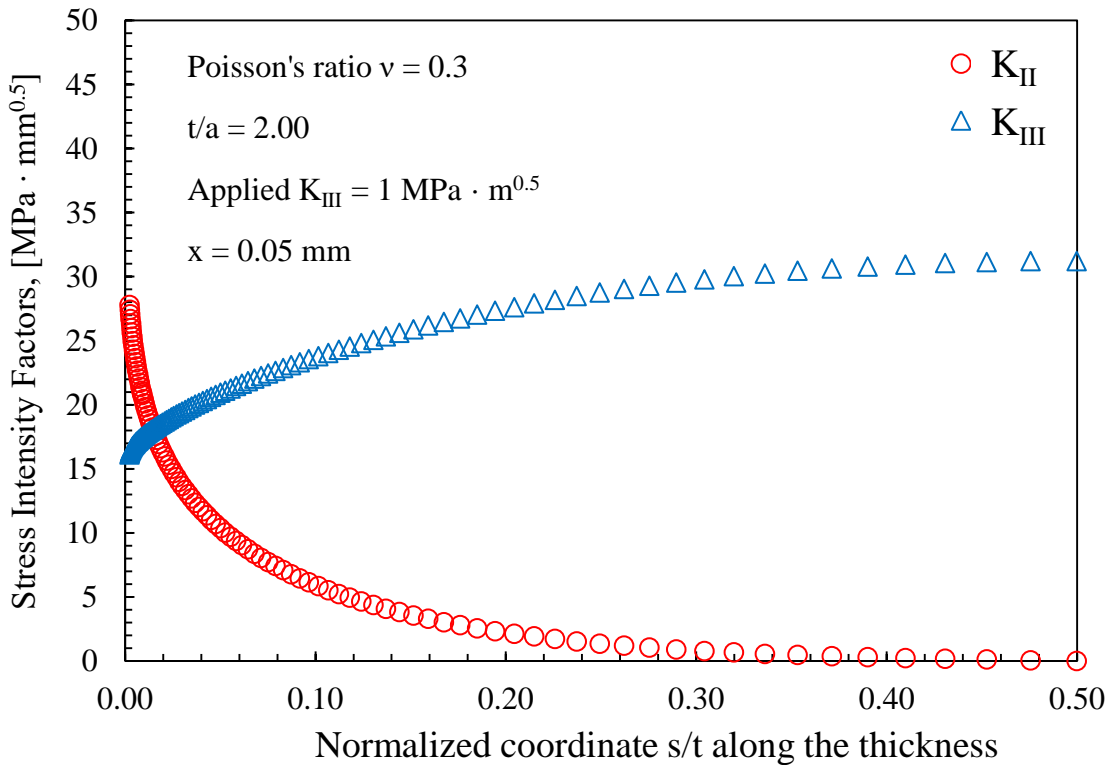


Figure 4.2.8. Free-Free: through thickness distribution of K_{II} and K_{III} for $t/a = 2$, $x = 0.05$ mm.

The through-the-thickness plots of K_{II} and K_{III} are shown in Figure 4.2.8 for $t/a = 2$; the values of K_{II} and K_{III} are not realistic for $s < 0.25$ mm due to the corner point singularity and for this reason are excluded.

For what concern the applied loading mode, the maximum value of K_{III} is at the centreline. For $t/a > 1$ this corresponds to K_{III} for the applied displacements (Eq. (4.2.2)). The influence of plate bending means that maxima steadily decrease as t/a decreases: maximum values of K_{III} tend to zero as the ratio t/a tends to zero, this is to be expected because K_{III} is not possible in two dimensions.

4.2.5.1.2 Stress analysis for Free-Clamped cases

In the presence of the free-clamped boundary conditions, the application of a nominal Mode III loading case induces in the vicinity of the crack tip not only Mode II but also Mode I local stress fields. In this case the stresses different from zero on the crack bisector line are σ_y , τ_{xy} and τ_{yz} .

Figures 4.2.9 and 4.2.10 show that for distances $s = 2$ mm and $s = 0.50$ mm, the eigenvalues λ_1 and λ_2 , calculated from σ_y and τ_{xy} , respectively, match the theoretical values of 0.50 [14,69,70]. In these cases realistic values of K_I and K_{II} can be calculated. For $s = 0$ mm, instead, λ_1 and λ_2 are found to be 0.31 and 0.44, respectively, as shown in Fig. 4.2.11. FE analyses showed that λ_1 and λ_2 decrease with t/a to the minimum values of 0.28 and 0.39 at $t/a = 1.00$ and then increase slightly with t/a . Realistic values of K_I and K_{II} cannot be calculated for $s = 0$ mm.

Also λ_3 calculated from τ_{yz} is close to the theoretical value of 0.25 given by Eq. (4.2.6), as shown in Fig. 4.2.9 for $s = 2$ mm and in Fig. 4.2.10 for $s = 0.50$ mm.

Small variations of λ_3 have been detected for $s = 0.25$ mm (0.23 against 0.25). Then for distances $s \geq 0.25$ mm, realistic values of K_{III} can be calculated from the τ_{yz} shear stress component. The results for $s = 0$, Fig. 4.2.11, show that τ_{yz} is close to τ_{xy} for small x values, but shows a stronger reduction as x increases. In the double logarithmic diagram, τ_{yz} has not a linear trend as a function of the distance x from the crack tip and therefore it is not possible to identify the stress intensity factor K_{III} .

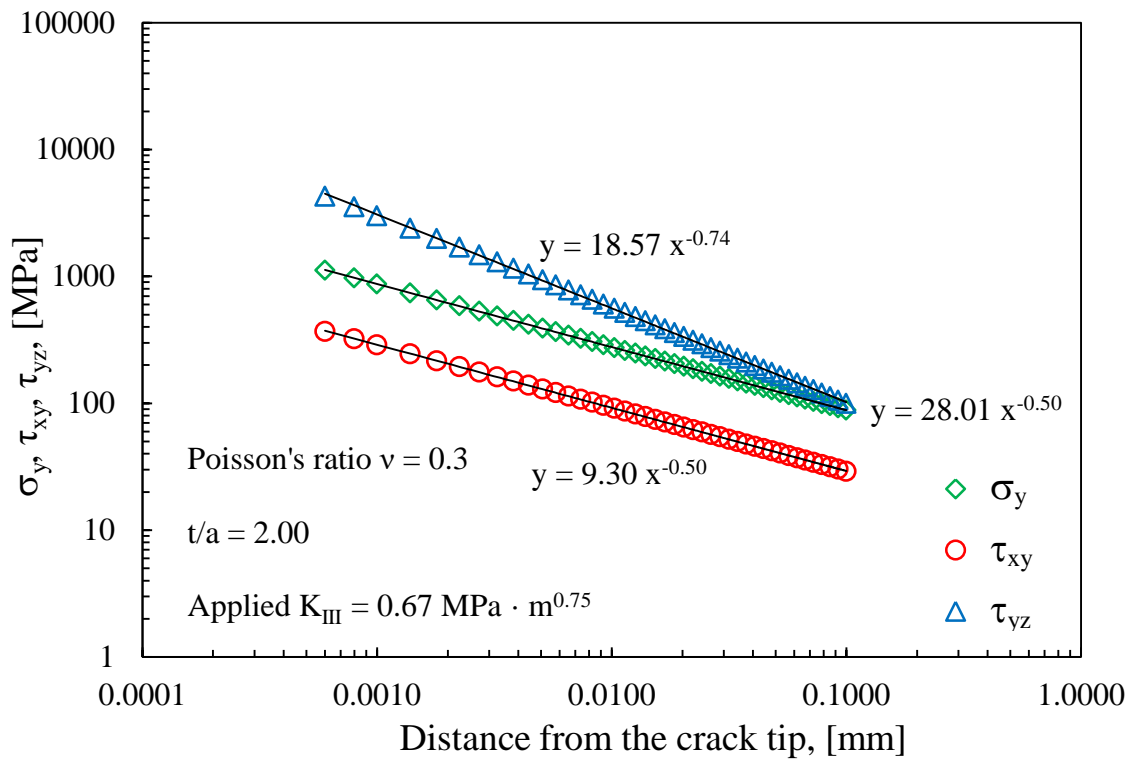


Figure 4.2.9. Free-Clamped: stresses σ_y , τ_{xy} and τ_{yz} on crack surface at $s = 2$ mm from disc surface.

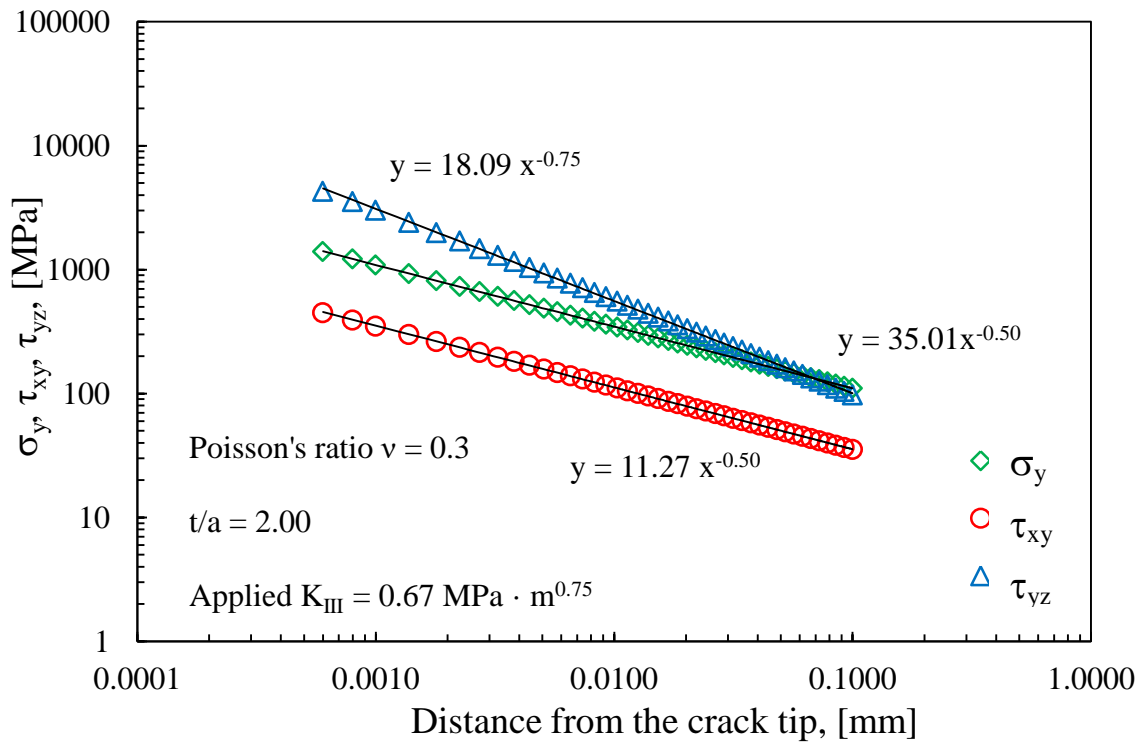


Figure 4.2.10. Free-Clamped: stresses σ_y , τ_{xy} and τ_{yz} on crack surface at $s = 0.50$ mm from surface.

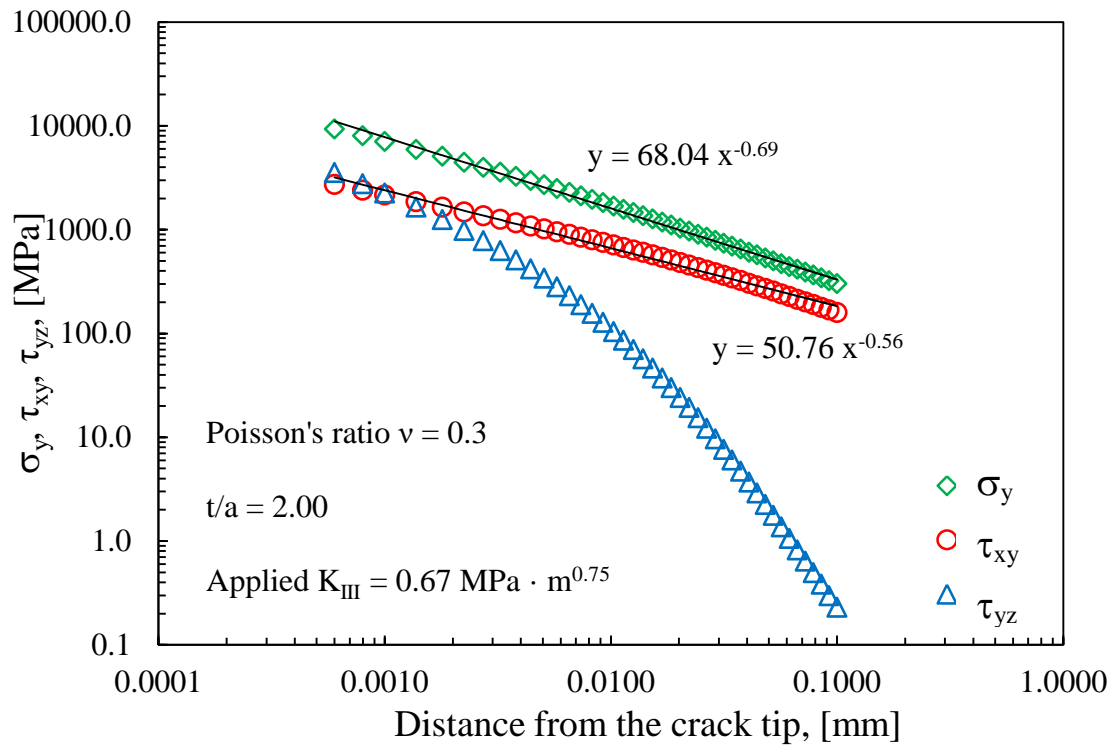


Figure 4.2.11. Free-Clamped: stresses σ_y , τ_{xy} and τ_{yz} on crack surface at $s = 0$ mm from disc surface.

It can be observed that at a convenient distance from free surfaces, the slopes of the applied (τ_{yz}) and induced (σ_y , τ_{xy}) stress fields are consistent with the boundary conditions applied to the crack edges: free-clamped for Mode III, that is $\lambda_3 = \kappa_3 = 0.25$ (Eq. (4.2.6)), and free-free for Mode I and II, that is $\lambda_1 = \lambda_2 = 0.5$ [14,69,70]. The through-the-thickness distributions of K_I , K_{II} and K_{III} for $t/a = 2$ are shown in Figure 4.2.12, where the values not realistic determined for $s < 0.25$ mm are excluded. The SIFs K_I , K_{II} and K_{III} were calculated according to the relationships:

$$K_I = \sqrt{2\pi} \cdot \sigma_y \cdot x^{1-\lambda_1} = \sqrt{2\pi} \cdot \sigma_y \cdot x^{0.5} \quad (4.2.22)$$

$$K_{II} = \sqrt{2\pi} \cdot \tau_{xy} \cdot x^{1-\lambda_2} = \sqrt{2\pi} \cdot \tau_{xy} \cdot x^{0.5} \quad (4.2.23)$$

$$K_{III} = \frac{\sqrt{2\pi}}{2\kappa_3} \cdot \tau_{yz} \cdot x^{1-\kappa_3} = 2\sqrt{2\pi} \cdot \tau_{yz} \cdot x^{0.75} \quad (4.2.24)$$

where the distance x from the crack was set constant and equal to 0.05 mm.

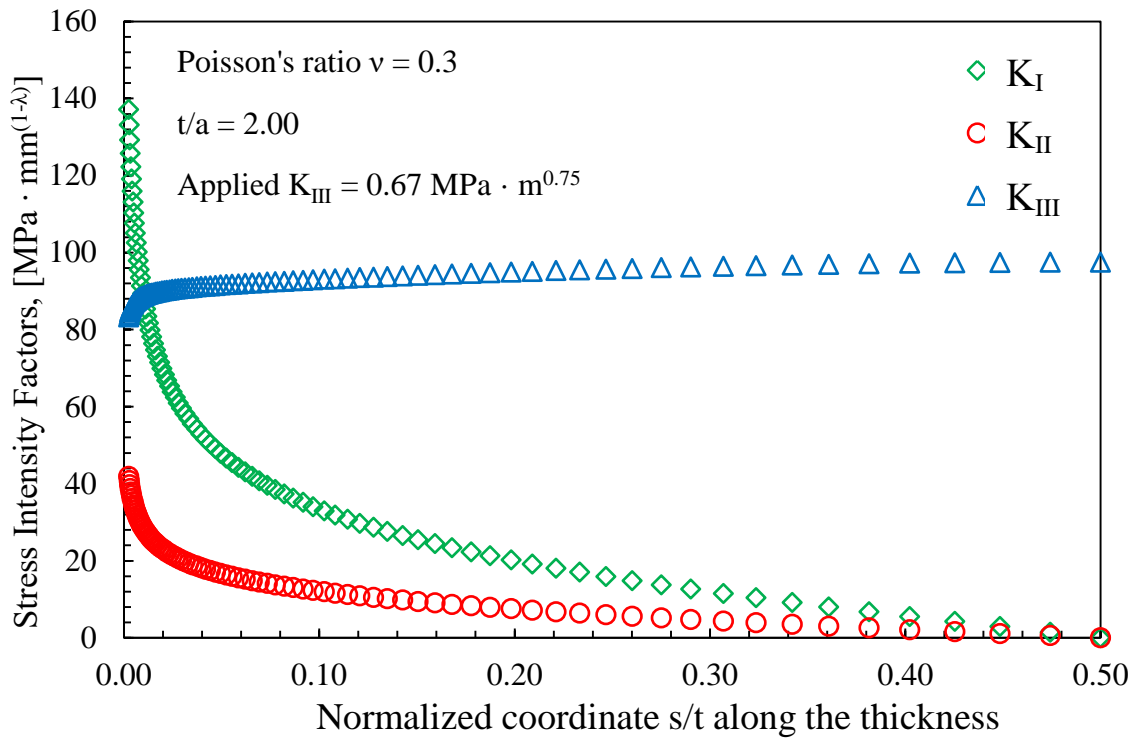


Figure 4.2.12. Free-Clamped: through thickness distribution of K_I , K_{II} and K_{III} for $t/a = 2.00$.

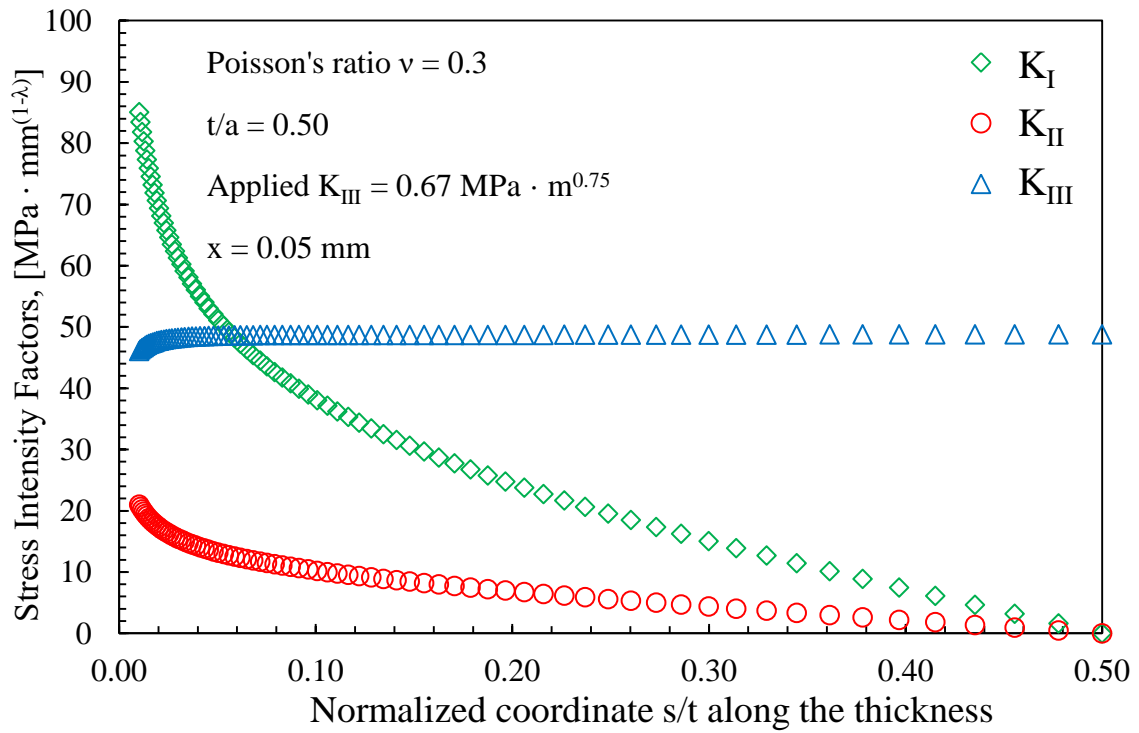


Figure 4.2.13. Free-Clamped: through thickness distribution of K_I , K_{II} and K_{III} for $t/a = 0.50$.

As far as the applied mode of loading is concerned, the maximum value of K_{III} is at the centreline. For $t/a > 1$ it tends to K_{III} corresponding to the applied displacements, see Eq. (4.2.5). Also in this case the influence of plate bending means that maxima steadily decrease as t/a decreases: maximum values of K_{III} tend to zero as t/a tends to zero. There is a constant K_{III} region for $s > 1$ mm in the thinner discs (see the example reported in Figure 4.2.13) and for $s > 5$ mm in the thicker ones (see the example reported in Figure 4.2.12), then K_{III} decreases steadily towards the surface, with an abrupt drop close to the surface.

As regards the induced modes of loading, both K_I and K_{II} are zero on the centre line, with an increase towards the surface. For all the considered geometries the distribution of K_I is nearly linear with a greater increase towards the surface, reaching very high values if compared to K_{II} ($K_{I,max}/K_{II,max} \approx 3$) and K_{III} , but in the last case it is impossible to define a ratio because of the different units. On the other hand for the thicker discs (see Figure 4.2.12) K_{II} is essentially zero for $s > 40$ mm, this means that there is no significant plate bending effect. The influence of plate bending increases as t/a decreases, and for $t/a = 0.50$ (see Figure 4.2.13) the distribution of K_{II} is nearly linear with a greater increase towards the surface. Intermediate values of t/a show intermediate behaviour. Maximum values of both K_I and K_{II} are at the surface, but it is within the region where calculated K_I and K_{II} values are not realistic so caution is needed in the interpretation of results.

4.2.5.2 Strain energy density through the disc thickness

Due to the uncertainties in the definition of the stress intensity factors on the free surfaces discussed in the previous sections, the strain energy density (SED) averaged in a control volume embracing the crack tip has been employed in the following to quantify the intensity of overall stress state through the thickness of the disc. The strain energy density plays a crucial role in the fracture process [71] and influences also the crack propagation under mode I [72] and mixed-mode (I+II) loadings [73].

Considering three-dimensional FE models, unlike Section 4.2.3 in which calculations involved a semicircular sector described by plane elements, the control volume is given by a cylinder with radius R_0 and height h , with h being

about equal to R_0 (Fig. 4.2.2). R_0 was thought of as a material property which varies under static and fatigue loading [27,29] but here, for the sake of simplicity, R_0 and h are simply set equal to 1.0 mm, small enough to quantify three-dimensional effects through the disc thickness.

The average SED, in contrast to the point-wise SED, can be easily calculated by using coarse meshes [38,62], because it directly depends on nodal displacements. Moreover, as soon as the average SED is known, the notch stress intensity factors (NSIFs) quantifying the asymptotic stress distributions can be calculated *a posteriori* on the basis of very simple expressions linking the local SED and the relevant NSIFs [38,62].

An advantage of the SED approach is that it is possible to easily understand whether the through-the-thickness effects are important or not in the fracture assessment of a specific material. Some brittle materials are characterized by very small control radius and then the stress gradient sensitivity is very strong. On the other hand more ductile materials have the capability of stress averaging in a larger volume and for this reason are less sensitive to any variation of the stress field through the thickness of the disc. The SED, once the control volume is properly modeled through the thickness of the disc, is able to quantify the 3D effects in comparison with the sensitivity of the specific material so providing precious information for fracture assessments. Another very fundamental point is that the SED is automatically sensitive to the different applied boundary conditions.

Although only the crack case is considered in this work, the SED-based approach can be easily applied also to pointed V-notches and a direct comparison can be directly drawn between the crack case and the V-notch cases. The SED is sensitive to the constraint variation on the crack or V-notch edges and some interesting conclusions can be drawn by observing the SED variation along the disc thickness when different boundary conditions are applied. This point will be investigated in the three following sub-sections.

With the aim to provide some numerical assessment of the contribution of the three-dimensional effects, specifically the induced fracture modes K_I and K_{II} , the local energy density through the disc thickness has been evaluated and discussed

in this section. The effect of different boundary conditions on strain energy density will be discussed in detail.

4.2.5.2.1 Three dimensional SED variations for Free-Free boundary conditions

The strain energy density averaged over a cylindrical volume embracing the crack tip was extracted from the finite element models of the free-free cracked discs. Figures 4.2.14-4.2.17 show the local SED variation through the disc thickness for $t/a = 0.5, 1, 2$ and 4 .

The influence of the applied Mode III loading combined with the induced singular Mode II loading is shown in the figures. It is evident that the position of the maximum SED changes from case to case. In thinner discs, that is for $t/a = 0.5$ and 1.0 , the maximum SED is close to the lateral surface, where the maximum intensity of the induced Mode II takes place. For larger thicknesses, corresponding to the cases $t/a = 2$ and 4 , the maximum value of the SED is at the mid-plane and its value is about 1.5 times the value at the lateral surface; moreover in these cases the SED reaches a minimum under the free surface, due to the opposite trend exhibited by Mode II and Mode III.

The local SED variation through the disc thickness obtained by FEM analysis can be compared with the theoretical estimations obtained by adding the Mode II and III contributions. For what concern the contribution given by Mode III, it is possible to use the Eq. (4.2.10) derived for a free-free Mode III loading. The Mode II contribution, instead, can be approximately calculated following the expression of \overline{W}_2 for cracked components reported by Lazzarin and Zambardi [27] being the stress field τ_{xy} consistent with a free-free boundary condition ($\lambda_2 = 0.50$), except for a small region close to the surface. The theoretical value of the SED averaged over a control volume having radius $R_0 = 1$ mm (Fig. 4.2.2), can be calculated as a function of K_{II} and K_{III} values through the disc thickness according to the following expression:

$$\overline{W}_{th} = \overline{W}_{II} + \overline{W}_{III} = \frac{1}{E} \left(\frac{I_2}{2\pi} \right) \frac{K_{II}^2}{R_0} + \frac{1}{E} \left(\frac{1+\nu}{\pi} \right) \frac{K_{III}^2}{R_0} \quad (4.2.25)$$

where I_2 is the integral of the angular stress functions, which depends on the notch opening angle 2α and the Poisson's ratio ν . For $\nu = 0.3$ and $2\alpha = 0$, it results $I_2 = 2.145$.

It can be seen from Figs 4.2.14-4.2.17 that FE results, represented by markers, are in good agreement with the theoretical prediction, represented by a solid line. It can be concluded that the expressions proposed for Mode III loading conditions (Eq. 4.2.10) coupled with the expressions for the induced modes [27] enable to predict well the three-dimensional effects and the position of the maximum values, which may be critical for the mechanical strength of the cracked components.

4.2.5.2.2 Three dimensional SED variations for Free-Clamped boundary conditions

As for the previous case, the strain energy density averaged over a cylindrical volume embracing the crack tip was extracted from the finite element models of the free-clamped cracked discs. Figures 4.2.14-4.2.17 show the local SED variation through the disc thickness for $t/a = 0.5, 1, 2$ and 4 .

The influence of the applied Mode III loading combined with the induced singular Modes I and II loading is shown in the figures. It is evident that the position of the maximum SED is the same for all the cases. Both for thinner and thicker discs the maximum SED is close to the lateral surface, where the maximum intensity of the induced Modes I and II takes place. Differently from the free-free case, in the thicker discs there is not a minimum of SED under the free surface.

Also in this case, the local SED variation through the thickness of the disc obtained by FEM analysis can be compared with the theoretical estimations obtained by adding the Mode I, II and III contributions. For what concern the contribution given by Mode III, it is possible to use Eq. (4.2.16) derived for a free-clamped Mode III loading. The Mode I and II contributions, instead, can be approximately calculated following the expressions of \bar{W}_1 and \bar{W}_2 for cracked components reported by Lazzarin and Zambardi [27], being the stress fields σ_y and τ_{xy} consistent with a free-free boundary condition ($\lambda_1 = \lambda_2 = 0.50$), except for a small region close to the surface. The theoretical value of the SED averaged over

a control volume having radius $R_0 = 1$ mm (Fig. 4.2.2), can be calculated as a function of K_I , K_{II} and K_{III} values through the thickness of the disc according to the following expression:

$$\overline{W}_{th} = \overline{W}_I + \overline{W}_{II} + \overline{W}_{III} = \frac{1}{E} \left(\frac{I_1}{2\pi} \right) \frac{K_I^2}{R_0} + \frac{1}{E} \left(\frac{I_2}{2\pi} \right) \frac{K_{II}^2}{R_0} + \frac{1}{E} \left(\frac{1+\nu}{\pi} \right) \frac{K_{III}^2}{R_0^{3/2}} \quad (4.2.26)$$

where I_1 and I_2 are the integrals of the angular stress functions, which depend on the notch opening angle 2α and the Poisson's ratio ν . For $\nu = 0.3$ and $2\alpha = 0$, $I_1 = 0.845$ and $I_2 = 2.145$.

It can be seen from Figs 4.2.14-4.2.17 that FE results, represented by markers, are in good agreement with the theoretical prediction, represented by a solid line. It can be concluded that the expressions proposed for Mode III loading conditions (Eq. 4.2.16) coupled with the expressions for the induced modes, extending here what previously made by Lazzarin and Zambardi [27], enable to predict well the three-dimensional effects and the position of the maximum values, which may be critical for the mechanical strength of the cracked components.

In addition from Figs 4.2.14-4.2.17 it can be observed that the SED in the free-clamped case is always higher than the SED in the free-free case. In fact the ratio $SED_{max,F-C}/SED_{max,F-F}$ increases with increasing t/a . The position of the maximum values of the SED as well as the ratio $SED_{max,F-C}/SED_{max,F-F}$ are summarized in Table 4.2.1. The ratio ranges between 9 and 15 for all the cases investigated. This means that in order to obtain the same value of the critical energy, thought as a material parameter, with an equal nominal applied displacement range, Δu_z , it is necessary to adopt a larger control radius in the free-clamped case. It is worth mentioning that for the crack case under free-free conditions all the SED contributions tied to Mode I, II and III are proportional to $1/R_0$ (Eq. 4.2.25) while under free-clamped conditions the contribution of SED tied to Mode III is proportional to $1/(R_0)^{3/2}$, Eq. (4.2.26). The ratio between the control radii $R_{0,F-C}/R_{0,F-F}$ is of the same order of the ratio $SED_{max,F-C}/SED_{max,F-F}$, that can be observed in Figs 4.2.14-4.2.17 and in Tab. 1 where $R_{0,F-C} = R_{0,F-F} = 1$ mm. For this reason very different values of the control radius are possible for free-free and free-clamped boundary conditions also for the same material. Under linear elastic

hypothesis and free-free conditions the same control radius, thought as an intrinsic characteristic of the material, is expected independently of the loading mode (I, II and III) resulting in $R_{I,F-F} = R_{II,F-F} = R_{III,F-F}$. Free-clamped conditions are usually achieved because of friction between the scratching surfaces or local plasticity that occurs in a non-negligible zone inside the control volume. This behaviour can sometimes be observed under torsion loading as described by Berto et al. [34,35] where very different values of the volume size were found to be necessary to uniform data from pure tension (thought as free-free) and pure torsion (thought as free-clamped) in terms of SED. Under free-free conditions the employed radius was $R_{I,F-F} = 0.32$ mm, whereas under free-clamped conditions $R_{III,F-C}$ was found to be 1.42 mm. At the light of the observations above, different local boundary conditions allow us to justify very different values of the control radius for the same material, as a function of the loading mode and of the specific local behaviour of the material depending on the external load. In fact different control volumes, for some specific materials characterized by a linear elastic behaviour under tension and a plastic or non-linear behaviour under torsion, make possible to re-compact the data in terms of a single SED scatterband.

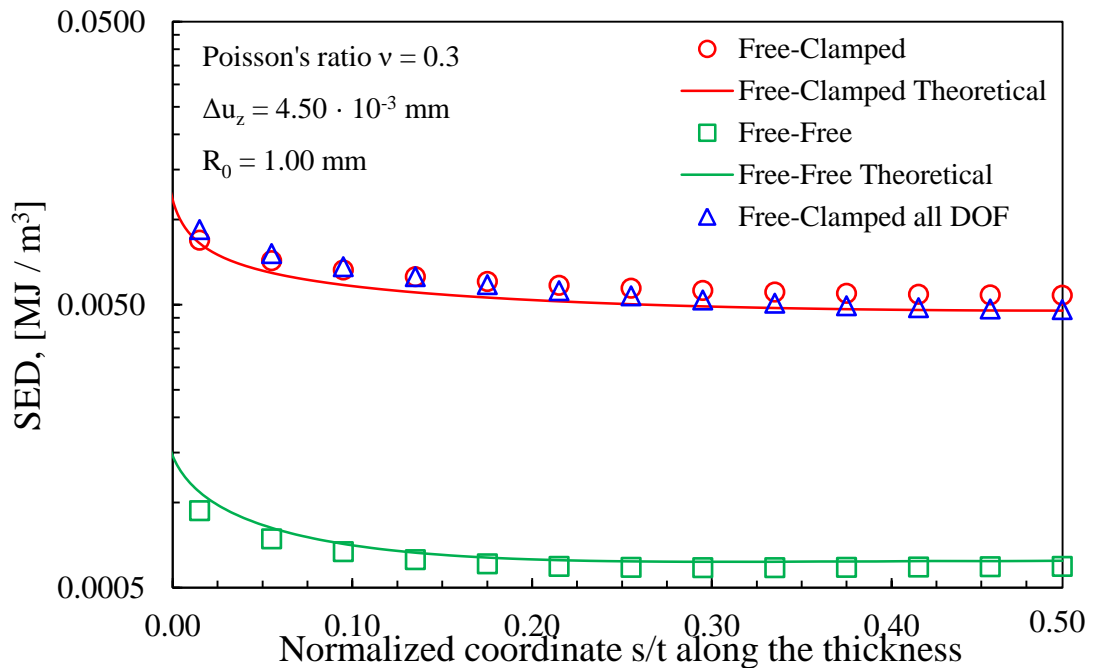


Figure 4.2.14. Through the thickness *SED* distribution for $t/a = 0.50$. Control radius $R_0 = 1.00$ mm. DOF stands for degrees of freedom in the FE model (displacement u_x , u_y , u_z).

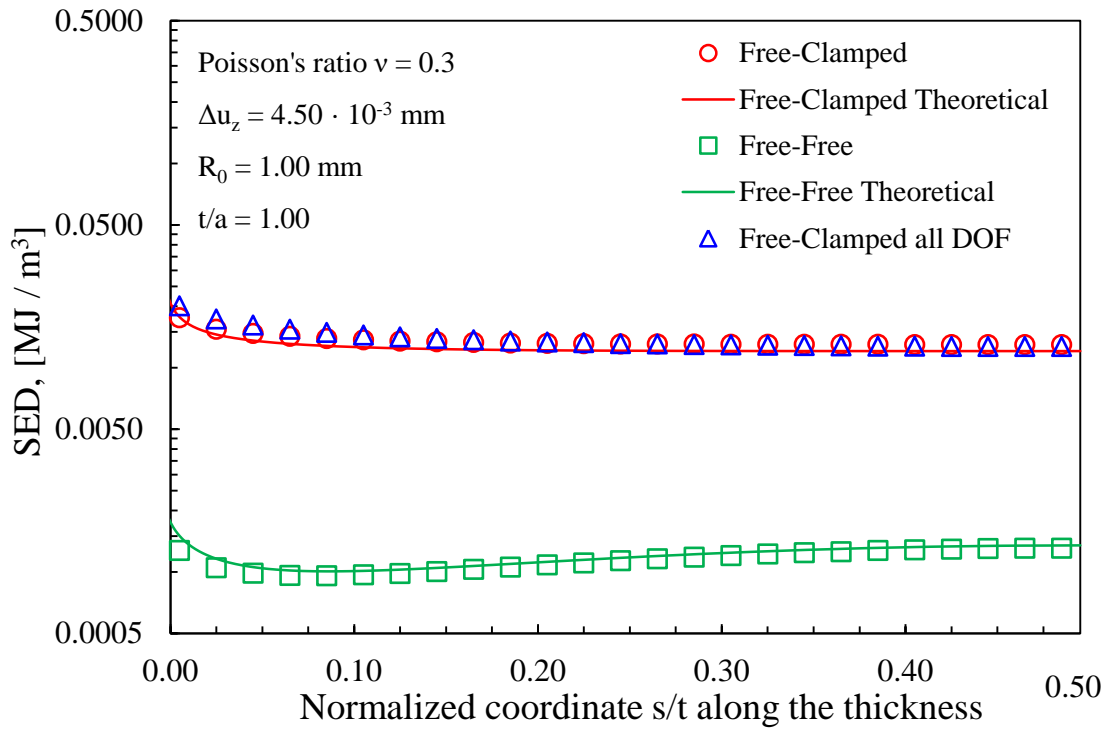


Figure 4.2.15. Through the thickness *SED* distribution for $t/a = 1$. Control radius $R_0 = 1.00$ mm. DOF stands for degrees of freedom in the FE model (displacement u_x, u_y, u_z).

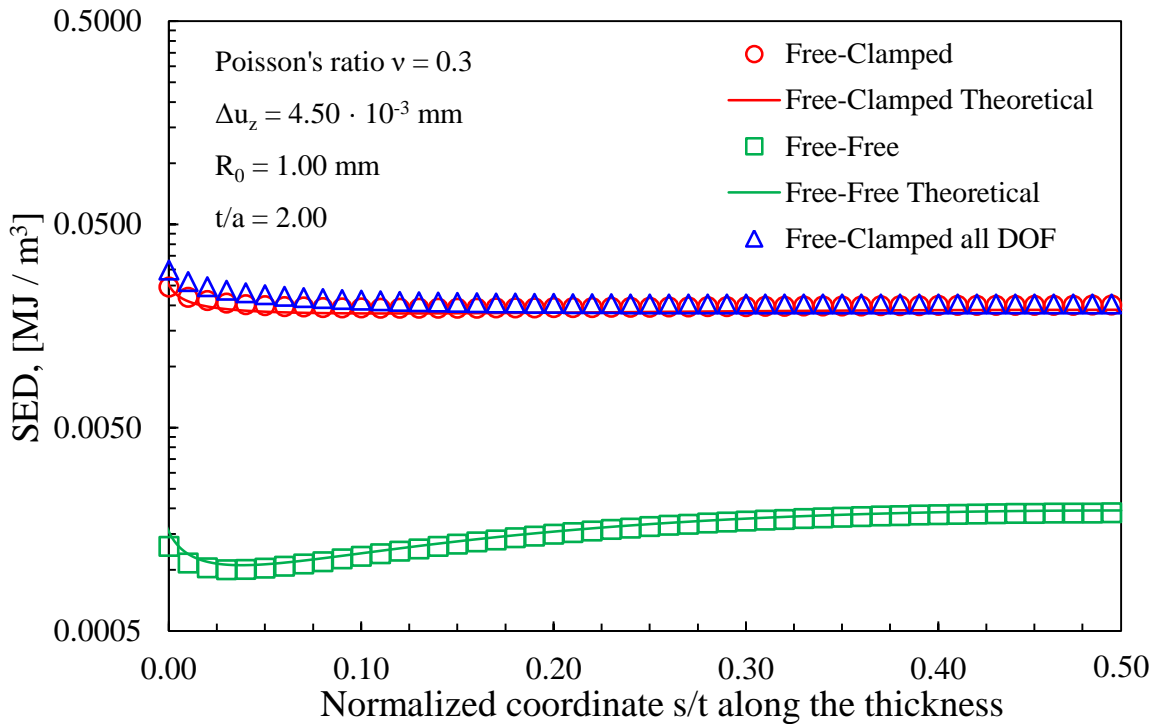


Figure 4.2.16. Through the thickness *SED* distribution for $t/a = 2$. Control radius $R_0 = 1.00$ mm. DOF stands for degrees of freedom in the FE model (displacement u_x, u_y, u_z).

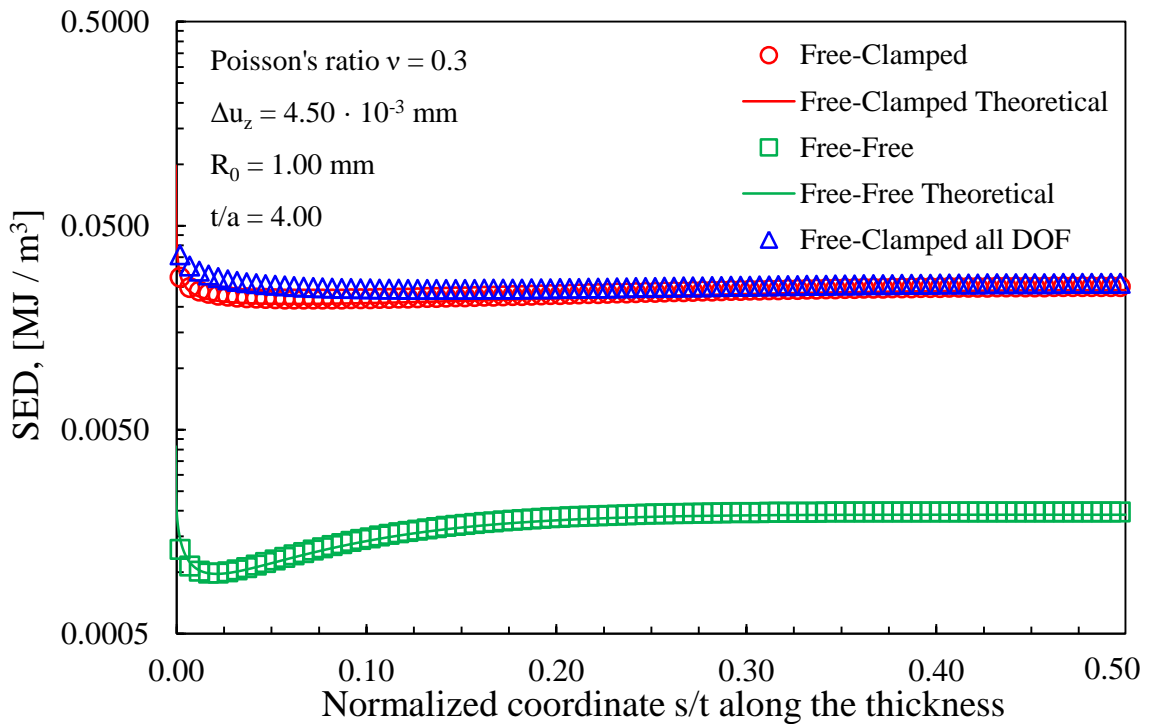


Figure 4.2.17. Through the thickness *SED* distribution for $t/a = 4$. Control radius $R_0 = 1.00$ mm. DOF stands for degrees of freedom in the FE model (displacement u_x, u_y, u_z).

Table 4.2.1. Values and positions of maximum *SED* in the free-free and free-clamped cases.

t/a	$SED_{\max,F-F}$		$SED_{\max,F-C}$		$SED_{\max,F-C}/SED_{\max,F-F}$
	position	10^{-3} MJ/m^3	position	10^{-3} MJ/m^3	
0.5	surface	0.94	surface	8.46	9.05
1		1.31		17.50	13.40
2	midplane	1.90	surface	24.52	12.92
4		1.97		27.85	14.13

4.2.5.2.3 Free-Clamped all displacements

In the previous section the effect of the boundary conditions on the crack edges on the strain energy density has been investigated. Free-free ($u_z \neq 0$ for both the crack edges) and free-clamped ($u_z \neq 0$ for one crack edge and $u_z = 0$ for the other) boundary conditions were applied to the Mode III displacement, u_z . As regards,

instead, the Mode I and Mode II displacements (u_y and u_x), a free-free condition ($u_y \neq 0$ and $u_x \neq 0$ for both the crack edges) was considered in all cases. For completeness, the aim here is to examine the local SED variation through the disc thickness when one crack edge is free ($u_z \neq 0$, $u_y \neq 0$ and $u_x \neq 0$) whereas the other edge has all the displacements clamped ($u_z = u_y = u_x = 0$), this represents a complete free-clamped condition.

The geometry described in Section 4.2.4 has been considered and the Mode III displacements corresponding to a free-clamped condition (Eq. 4.2.5 with $K_{3,F-C} = 0.67 \text{ MPa} \cdot \text{m}^{0.75}$) have been applied to the FE models.

As already observed in Section 4.2.5.1.2, the stresses different from zero on the crack bisector line are σ_y , τ_{xy} and τ_{yz} . For the sake of brevity, only the case $s = 1$ mm is shown in Fig. 4.2.18. The values of λ_1 and λ_2 , calculated from σ_y and τ_{xy} , are respectively greater and lower than the theoretical value of 0.25 [58] associated to the in-plane solution; this means that realistic values of K_I and K_{II} cannot be calculated. As regards, instead, the Mode III eigenvalue, λ_3 calculated from the shear stress component τ_{yz} is close to the theoretical value of 0.25 (Eq. 4.2.6). Hence, realistic values of K_{III} can be calculated from τ_{yz} .

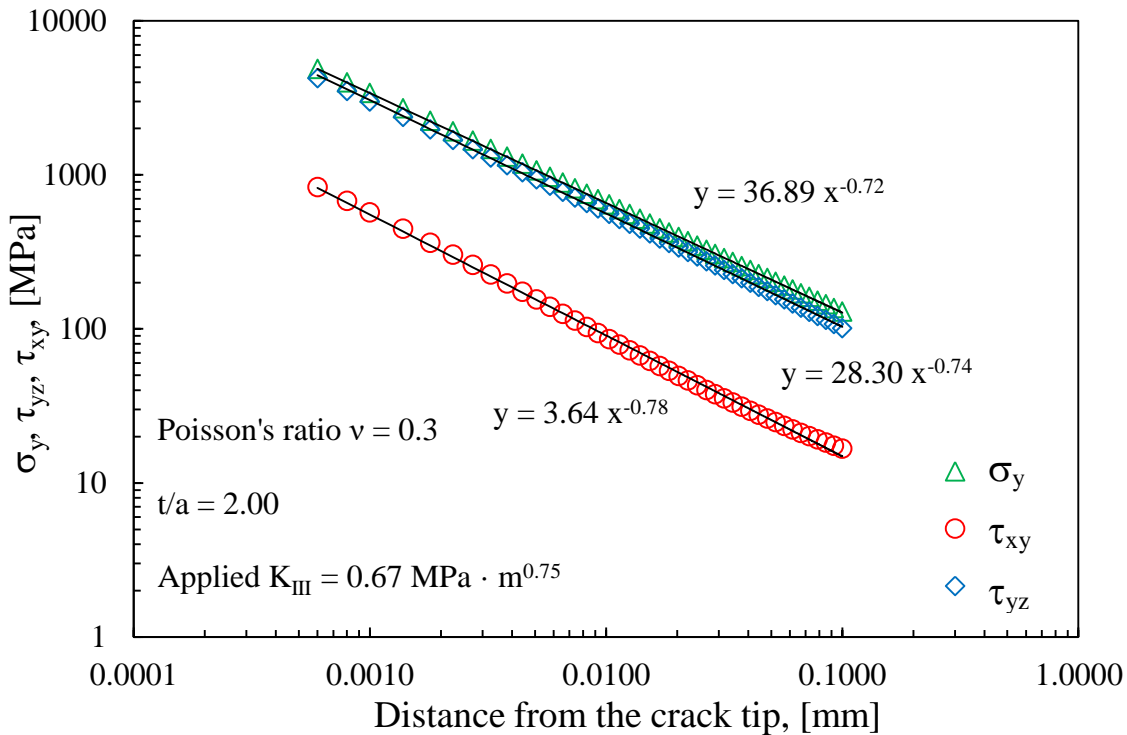


Figure 4.2.18. Free-Clamped all DOF: stresses σ_y , τ_{xy} and τ_{yz} on crack surface at $s = 1$ mm from disc surface, $t/a = 2$. DOF stands for degrees of freedom in the FE model (displacement u_x , u_y , u_z).

In this case the uncertainties in the definition of the stress intensity factors are even more marked, therefore the average strain energy density (SED) becomes a parameter necessary for quantifying the intensity of the local stress and strain state through the disc thickness. For this purpose the strain energy density averaged over a cylindrical control volume embracing the crack tip was extracted from the finite element models. Figures 4.2.14-4.2.17 show the local SED variation through the disc thickness for $t/a = 0.5, 1, 2$ and 4 . The figures show that for all the values of t/a considered in the present investigation, the local SED variation through the disc thickness in the complete free-clamped condition is nearly coincident with the SED variation in the Mode III free-clamped condition. In the thinner discs the maximum deviation occurs in the mid-plane of the disc. As t/a increases, it moves toward the lateral surface. In all cases the deviation is less than 15%, so it can be concluded that the different boundary conditions, free-free or free-clamped, applied to the Mode I and Mode II displacements have a limited effect on the average strain energy density.

Therefore the conclusions drawn in the previous section in regard to the control radius can be extended to the case of cracked elements subjected to Mode III loading in the presence of a complete free-clamped condition.

4.2.6. Discussion

Dealing with the local damage and the out-of-plane loading (Mode III), an analytical multi-scale model has recently been developed by Sih and Tang. Physically, the different orders of the stress singularities were linked to the different constraints associated with a micro-V-notch at the tip of the main crack. Starting from Sih and Tang's model, in the present work some analytical expressions have been proposed for the calculation of the strain energy density (SED) averaged over a control volume embracing the V-notch tip. The expressions vary as a function of the different boundary conditions.

The results from the analytical frame have been compared with those determined numerically under linear-elastic conditions, by applying the boundary conditions to the through-the-thickness crack edges in three dimensional discs. Free-free and free-clamped boundary conditions were applied to the crack displacements. For

the sake of simplicity, only the case of a cracked element has been examined, but the procedure drawn here can be easily extended to any notch opening angle 2α .

Due to three-dimensional effects, the application of a nominal Mode III loading results in induced modes, depending on the boundary conditions. In the free-free case the applied Mode III induces only Mode II, whereas in the free-clamped case it induces Mode II and Mode I in combination.

The Stress Intensity Factors related to Mode I, II and III stress distributions have been determined on the basis of the FE data. In a small region near the lateral surface of the disk, the eigenvalues λ are found to be significantly different from the theoretical values, this means that realistic values of K cannot be calculated.

The strain energy density (SED) averaged in a control volume embracing the crack tip has been employed to quantify the local stress and strain state through the thickness of the disc. The effect of different boundary conditions on strain energy density has been discussed in detail.

Results obtained by FE analysis have been compared with the theoretical predictions obtaining a good agreement. Calculation of the strain energy density (SED) shows that the position of the maximum SED is a function of the boundary condition on the crack edges and the disc thickness.

It was observed that the SED in the free-clamped case is always higher than the SED in the free-free case. This means that to have the same value of the critical energy, it is necessary to adopt a larger control radius in the free-clamped condition. This result is usually achieved because of friction between the scratching surfaces or local plasticity that occurs inside the control volume.

For completeness the local SED variation has been examined also in the case of a complete free-clamped condition. It was observed that the local SED variation in the complete free-clamped condition is nearly coincident with the SED variation in the Mode III free-clamped condition.

4.3 Three-dimensional effects on notched components under cyclic plasticity^(*)

Nomenclature

C_q	Energy dissipation coefficient
$c^{(i)}, r^{(i)}, \chi^{(i)}$	Material coefficients related to Jiang-Sehitoglu model
C_i, γ_i	Material coefficients related to Ansys [®] kinematic hardening material model, based on Chaboche plasticity model
E	Young's modulus
G	Shear modulus
h	Plastic modulus function
k	Yield stress in simple shear
K_t	Theoretical (elastic) stress concentration factor
K'	Parameter of Ramberg-Osgood representation of the material stabilized cyclic curve
n'	Strain hardening exponent
n_{ij}	Unit exterior normal to the yield surface
S_{ij}	Deviatoric stress
ΔW_q	Dissipated energy during one loading cycle
ΔW_p	Total plastic strain energy density during one loading cycle
R_c	Control radius for SED evaluation

Symbols

α_{ij}	Deviatoric backstress (center of the yield surface)
$\Delta\sigma_{nom}, \Delta\varepsilon_{nom}$	Remotely applied nominal stress and strain ranges
$\Delta\sigma, \Delta\varepsilon$	Notch-tip elastic plastic stress and strain ranges
$\Delta\sigma^e, \Delta\varepsilon^e$	Hypothetical notch-tip stress and strain ranges
δ	Small but finite increment in incremental cyclic plasticity
δ_{ij}	Kronecker delta
δp	Equivalent plastic strain increment
σ_{kk}	Sum of the normal stress components

σ^*	Yield stress
ν	Poisson's ratio

(*) *See also:*

- Campagnolo, A.; Berto, F.; Marangon, C. Cyclic plasticity in three-dimensional notched components under in-phase multiaxial loading at R=-1. *Theoretical and Applied Fracture Mechanics*; 81: 76-88 (2016);
- Marangon, C.; Campagnolo, A.; Berto, F. Three-dimensional effects at the tip of rounded notches subjected to mode-I loading under cyclic plasticity. *The Journal of Strain Analysis for Engineering Design*; 50: 299-313 (2015);

4.3.1. Introduction

Failure of engineering components under fatigue loading is often related to the presence of stress raisers like defects, cracks or different shaped notches. It is well known that the stress arising in the proximity of these points may exceed the yielding limit of the material. The full elastic-plastic stress and strain fields ahead of notches can be assessed by using complex non-linear finite element analyses that, however, are heavy in terms of time and resources required by engineers and industries.

For these reasons, simplified methods that approximate the actual elastic-plastic notch-tip material behaviour are frequently preferred in practical engineering applications. In a pioneering work Hardrath and Ohman [74] applied a generalisation of Stowell's relation [75] for the plastic stress concentration factor at notches in aluminium-alloy-sheet specimens obtaining a good agreement with experimental results. One of the most important works on the evaluation of the elastic-plastic stress state at the tip of a notch is due to Neuber [76], who proposed a general rule able to obtain the stress-strain concentration factors for uniaxial static and cyclic loading. Dealing with energy-based assumptions, Molski and Glinka [77] stated that the strain energy density distribution in the plastic zone ahead of a notch tip is the same as that determined under a pure elastic stress-strain solution, adopting this as the basis of the ESED criterion. During the last years extensions of the above mentioned criteria have been developed in order to

refine the assessment of the actual state of stress and strain ahead of a notch under simple and complex loading configurations, the most widely used approaches are: the modified Neuber's rules proposed in [78–80], the modified ESED methods [81–83], and new approaches reported in [84–86]. Other widely used methods are the stress field intensity model proposed by Weixing [87], the local stress-strain field intensity approach suggested by Shang et al. [88] and the volumetric approach based on the total strain energy density per cycle proposed by Bentachfine et al. [89].

In particular Ye et al. [86,90], making use of thermodynamics assumptions, considered the influence of the stored energy during a loading history as a fundamental parameter for the calculation of the actual stress-strain at the tip of a notch. With this aim a new modified approach, which confines the two milestones, Neuber's rule [76] and Molski-Glinka's approach [77], as limiting cases of the same problem, has been presented. Ye [90] proved that the two above mentioned methods turn out to be coincident when considering the plastic strain energy density as a negligible parameter.

A computational model for multiaxial stress-strain notch analysis has been recently proposed by Ince and Glinka [83] to evaluate the elasto-plastic notch-tip stress-strains by using results from linear elastic finite element analyses. The model has been applied and validated by comparing model-based results with experimental data of a steel notched shaft subjected to several loading conditions, obtaining good accuracy. The proposed model allows to estimate the fatigue life and fatigue damage in an efficient manner, in a simpler way compared to more complex and time-consuming elasto-plastic FE analyses.

Uniaxial and multiaxial fatigue loads generate a variable complex state of stress at the tip of a rounded notch. In order to take into account this effect, incremental approximate formulations [81,82,85,86,90] have been developed on the basis of energy equilibrium conditions between the stress and strain components acting at the notch tip.

The incremental approximate procedures make use of constitutive relations of the cyclic incremental plasticity theory that is composed of three main parts: 1) the von Mises yield criterion; 2) the flow rule (or normality condition) presented by

Drucker [91] which is used to combine the increment of plastic strain with the related increment of stress; 3) the hardening rule which specifies changes in the yield condition as a consequence of the applied load under elastic-plastic conditions. In the case of fatigue problems the kinematic hardening is the most used rule because of the inner ability to simulate the Bauschinger effect during cyclic loading. Prager [92] proposed the first linear hardening formulation able to take into account the above mentioned effect. This rule allows the yield surface to move into the stress space without changing in shape or size. Armstrong and Frederick [93] presented the first non-linear relation (A-F rule) introducing a recovery term associated to a strain memory effect. Different extensions of the A-F rule have been proposed in the last years (see among the others Bower [94], Bower and Johnson [95], Ohno-Wang [96]). Chaboche [97,98] expressed for the first time a non-linear kinematic hardening rule in the form of an expansion of M backstress parts, each one following the Armstrong-Frederick relation. Chaboche model has been adopted by many finite element codes in order to obtain the actual behaviour of the material subjected to fatigue loading. A new A-F type model has been presented by Jiang and Sehitoglu [99,100] aiming to account for the ratchetting effect during an asymmetric loading cycle.

Many contributions dealing with fatigue problems under plasticity conditions have been developed in the last years addressing different fields of applications. Jiang and Xu [101] studied the problem of a plate with a central hole and a shaft with a circumferential groove subjected to proportional and non-proportional loading, implementing an approximate incremental method and comparing the results with some cyclic FE analyses. Ye et al. [86,90] made use of an incremental procedure in order to develop a unified expression for elastic-plastic notch stress-strain calculations. The new approach was first calibrated with experimental results obtained by uniaxial fatigue tests on flat specimens weakened by different notch geometries [90] and then extended to the multiaxial fatigue of notched components [86]. Qiu et al. [102] made use of an incremental procedure in order to investigate the non-Masing behaviour of 16MnR steel. An accurate method for strain calculation of a notched specimen under axial-torsion loading was proposed by Firat in [103,104]. The method used a cyclic plasticity model aiming to obtain

the actual stress and strain state at the focal points of the components in exam. Gao et al. [105] conducted tension–compression, torsional, and axial-torsional fatigue experiments on notched shaft specimens made of 16MnR steel comparing the fatigue lives with those obtained by predictive analyses based on incremental cyclic plasticity.

As already mentioned, the incremental cyclic plasticity has been used in order to address plane or axis-symmetric problems but it has never been coupled with three dimensional effects arising at the tip of a notched component. An extended review on the 3D linear elastic stress distribution ahead of the notch tip can be found in a recent contribution [106] in which the developments leading up to the current state of the art are described. All the loading modes (I, II and III) have been addressed concluding that three-dimensional effects are sometimes ignored in situations where they might be important for the strength of components. In particular, the application of a nominal mode II loading to a notched component induces at the notch tip a coupled mode III, also known as mode O (out-of-plane), as highlighted by Harding et al. [9]. Those authors investigated the parameters influencing the intensity of this new singularity and demonstrated the relevance of this new singular mode to practical problems, as for example in welded lap joints. Dealing with rounded notches, Zappalorto and Lazzarin [12], Berto et al. [58] and Berto and Marangon [107], demonstrated that also when the notch root radius is different from zero, the out-of-plane mode still exists, and its intensity depends on the notch radius and the plate thickness. Some important aspects in bi-material notches were investigated in [108,109] highlighting the importance of higher order terms.

The main aim of the present work is to relate the incremental cyclic plasticity to three-dimensional effects arising in the close neighbourhood of the notch tip. The paragraph first focuses on the calibration of the incremental cyclic plasticity with bi-dimensional problems of notched members subjected to uniaxial, torsional and multiaxial (tension-torsion) in-phase cyclic loadings. Subsequently, the procedure will be extended for the first time to the investigation of in-plane and out-of-plane three-dimensional effects arising at the tip of a rounded notch by considering the presence of a small scale yielded area ahead of the notch tip. Three-dimensional

flat specimens weakened by different notch geometries and subjected to cyclic mode I loading as well as cyclic mode II loading will be investigated by comparing the analytical results obtained from a modification of the incremental routine with those obtained by means of cyclic elastic-plastic FE analyses.

Finally, a link between the averaged strain energy density (SED) criterion [27,29] and the area inside the hysteresis loops tied to the different stress-strain components acting at the notch tip, obtained by the incremental cyclic plasticity theory, has been investigated. The criterion based on the strain energy density averaged over a control volume surrounding the tip of a sharp or rounded notch has been successfully used to assess the fracture strength of a large bulk of materials subjected to wide combinations of static loading [32,110–112] and the fatigue strength of notched components [35,113], also under high-temperature conditions [114], as well as welded joints [115].

The control volume for SED evaluation adapts itself as a function of the notch geometry, in particular of the notch root radius ρ and the notch opening angle 2α . The control radius R_c , which is the size of the control volume, is thought of as dependent only on the material properties and not on the notch geometry [29].

As described in some recent contributions [4,5,116] an intrinsic advantage of the SED approach is that it permits automatically to take into account higher order terms and three-dimensional effects, moreover it can be directly obtained by using coarse meshes [29].

Several notched geometries subjected to different nominal load amplitudes have been analysed in order to evaluate the evolution of the ratio between the averaged SED and the area of the hysteresis loop acting at the notch tip (A_{hl}), which represents the plastic strain hysteretic energy, considered to be an index for fatigue damage in the literature [117–119].

4.3.2. Analytical frame

4.3.2.1 Unified expression for elastic-plastic stress-strain estimation

Recently Ye et al. [90] proposed a unified expression to estimate the elastic-plastic stress-strain state at the tip of a rounded notch both in the case of static and cyclic uniaxial loading. The general expression can be written as follows:

$$K_t^2 \Delta\sigma_{\text{nom}} \Delta\varepsilon_{\text{nom}} = \Delta\sigma \Delta\varepsilon + \Delta W_q(\Delta\sigma, \Delta\varepsilon) \quad (4.3.1)$$

where K_t is the theoretical (elastic) stress concentration factor, $\Delta\sigma_{\text{nom}}$ and $\Delta\varepsilon_{\text{nom}}$ are the remotely applied nominal stress and strain ranges, while $\Delta\sigma$ and $\Delta\varepsilon$ denote the notch-tip elastic-plastic stress and strain ranges. ΔW_q is, instead, the dissipated energy during one loading cycle. The approach considers the energy stored within the specimen during the loading as a damaging parameter. Ye et al. [86] also introduced the so called “energy dissipation coefficient” in order to obtain a physical relationship between the plastic strain energy density and the dissipated energy during one loading cycle:

$$C_q = \frac{\Delta W_q}{\Delta W_p} \cong \frac{1 - 2n'}{1 - n'} \quad (4.3.2)$$

where ΔW_p is the total plastic strain energy density during one loading cycle and n' is the strain hardening exponent of the material took into account. The Neuber’s rule [76] and the ESED approach [77] provide the bound limits of the above mentioned criterion, namely when the “energy dissipation coefficient” C_q is equal to 0 and 1, respectively. As highlighted by Ye et al. [86], the method of estimating the stored energy based on Eq. (4.3.2) is acceptable for engineering approximate calculations.

Moving from a uniaxial to a multiaxial state of stress-strain, the use of K_t is no longer sufficient because it is linked only to the normal stress component acting at the notch tip, thus a more general formulation of Eq. (4.3.1) is needed [86]. This problem can be overcome by introducing the “hypothetical notch tip stress and

strain” σ^e and ε^e , which can be obtained in the case of a perfect linear-elastic material [82,85]. The governing equation is:

$$\sum_{i,j=1}^3 \Delta\sigma_{ij}^e \Delta\varepsilon_{ij}^e = \sum_{i,j=1}^3 \left(\Delta\sigma_{ij} \Delta\varepsilon_{ij} + C_q \Delta W_p (\Delta\sigma_{ij}, \Delta\varepsilon_{ij}) \right) \quad (4.3.3)$$

The subscripts “ij” denote the different stress and strain components involved in the problem.

When the proposed expression is applied to estimate the notch-tip stress and strain due to a generic cyclic loading a proper incremental form should be developed. By substituting also the expression of ΔW_p [86], the following simplified equation can be obtained:

$$\sum_{i,j=1}^3 \left(\sigma_{ij}^e \delta\varepsilon_{ij}^e + \varepsilon_{ij}^e \delta\sigma_{ij}^e \right) = \sum_{i,j=1}^3 \left((1 + C_q) \sigma_{ij} \delta\varepsilon_{ij} + (1 - C_q) \varepsilon_{ij} \delta\sigma_{ij} \right) \quad (4.3.4)$$

The prefix δ denotes a small but finite increment.

Then assuming that the relative contribution of each elastic-plastic stress and strain component to the total SED and to ΔW_q at the notch tip is the same as the relative contribution of the analogous linear-elastic stress and strain components to the total SED at the notch tip, it is possible to define a unified expression for each stress-strain component acting at the tip of a rounded notch:

$$\sigma_{ij}^e \delta\varepsilon_{ij}^e + \varepsilon_{ij}^e \delta\sigma_{ij}^e = (1 + C_q) \sigma_{ij} \delta\varepsilon_{ij} + (1 - C_q) \varepsilon_{ij} \delta\sigma_{ij} \quad (4.3.5)$$

This assumption has been verified in the case of in-phase and out-of-phase multiaxial loadings [81,82]. Gao et al. [105] modified Eq. (4.3.5) by introducing, within the formulation, the reference state parameter defined by Chu [120]:

$$\left(\sigma_{ij}^e - \sigma_{ij}^{e(0)} \right) \delta\varepsilon_{ij}^e + \left(\varepsilon_{ij}^e - \varepsilon_{ij}^{e(0)} \right) \delta\sigma_{ij}^e = (1 + C_q) \left(\sigma_{ij} - \sigma_{ij}^{(0)} \right) \delta\varepsilon_{ij} + (1 - C_q) \left(\varepsilon_{ij} - \varepsilon_{ij}^{(0)} \right) \delta\sigma_{ij} \quad (4.3.6)$$

The superscripts “0” indicate the reference state of the particular component of stress-strain. When a reversal point of a component occurs, the reference states of

the components are updated to the corresponding stress and strain at the reversal point.

For the sake of simplicity, in the present work, all the equations taking the form of Eq. (4.3.6) will be named “energy equations”. Once the linear elastic stress and strain components are known, each energy equation presents two unknowns: the elastic-plastic stress component and the related elastic-plastic strain component. Thus each energy equation has to be coupled with the corresponding material constitutive equations.

According to the theory of small deformations, an incremental strain component can be written as the sum of an elastic part ($\delta\varepsilon_{ij,el}$) and a plastic contribution ($\delta\varepsilon_{ij,pl}$) as follows:

$$\delta\varepsilon_{ij} = \delta\varepsilon_{ij,el} + \delta\varepsilon_{ij,pl} \quad (4.3.7)$$

The elastic part of strain is governed by the well-known Hooke’s law:

$$\delta\varepsilon_{ij,el} = \frac{\delta\sigma_{ij}}{2G} - \frac{\nu}{E} \delta\sigma_{kk} \delta_{ij} \quad (4.3.8)$$

where G is the shear modulus, E is the Young’s modulus, ν the Poisson’s ratio, δ_{ij} the Kronecker delta and σ_{kk} is the sum of the normal stress components.

4.3.2.2 Material constitutive model under cyclic plasticity

The incremental plastic part of strain can be described by using the cyclic plasticity theory which can be comprehensively described by the introduction of a proper yield criterion, a flow rule and a hardening rule. In the following \tilde{A} represents a second order Cartesian tensor, A_{ij} its components and $\|\tilde{A}\|$ the

Frobenius matrix norm defined as $\|\tilde{A}\| = \sqrt{\sum_{i,j=1}^3 A_{ij} \cdot A_{ij}}$, finally “:” represents the inner product between tensors.

The yield function represents the locus of points that divides the linear-elastic behaviour (within the boundary) and the elastic-plastic behaviour (boundary

surface). In the case of cyclic loading the von Mises yield criterion is the most widely used in the literature [86,99,105]. The material is thought to follow the elastic behaviour with totally absence of plastic deformation until the stress components satisfy the yield condition:

$$f = \|\tilde{\mathbf{S}} - \tilde{\boldsymbol{\alpha}}\| - \sqrt{2}k = \sqrt{\sum_{i,j=1}^3 (\mathbf{S}_{ij} - \alpha_{ij}) \cdot (\mathbf{S}_{ij} - \alpha_{ij})} - \sqrt{2}k = 0 \quad (4.3.9)$$

where \mathbf{S}_{ij} is a deviatoric stress component, α_{ij} is the pertinent deviatoric backstress component (center of the yield surface) and k is the yield strength in simple shear. When the yield condition, Eq. (4.3.9), is satisfied, the normality flow rule, Eq. (4.3.10), has to be applied in order to describe the increment of plastic strain during a loading cycle.

$$\delta \varepsilon_{ij,pl} = \frac{1}{h} \left\langle \sum_{i,j=1}^3 \delta \mathbf{S}_{ij} \cdot \mathbf{n}_{ij} \right\rangle \mathbf{n}_{ij} \quad (4.3.10)$$

Where the symbol “ $\langle \rangle$ ” denotes the McCauley brackets (i.e. $\langle x \rangle = (x + |x|)/2$), h is the plastic modulus function that will be described later, while \mathbf{n}_{ij} represents the unit exterior normal to the yield surface calculated using the following expression:

$$\mathbf{n}_{ij} = \frac{\mathbf{S}_{ij} - \alpha_{ij}}{\|\tilde{\mathbf{S}} - \tilde{\boldsymbol{\alpha}}\|} = \frac{\mathbf{S}_{ij} - \alpha_{ij}}{\sqrt{\sum_{i,j=1}^3 (\mathbf{S}_{ij} - \alpha_{ij}) \cdot (\mathbf{S}_{ij} - \alpha_{ij})}} \quad (4.3.11)$$

Finally, the hardening rule deals with the definition of the translation/expansion of the boundary yield surface within the stress space. In engineering practice the kinematic hardening rule is the most used in the case of cyclic loading, being able to account for the Bauschinger effect. In particular, in the generic case of a multiaxial state of stress-strain, the non-linear kinematic hardening rule gives the most accurate results [93]. In this case, the yield surface is allowed only to move within the stress space but not to homotetically expand or contract. In this investigation the Jiang-Sehitoglu's [99] non-linear kinematic hardening rule has been adopted in the implementation of the incremental routine for the

determination of the elastic-plastic state of stress-strain. The formulation of the plastic modulus function and of the increment of the i-th part of the backstress can be written as follows:

$$\mathbf{h} = \sum_{i=1}^M \mathbf{c}^{(i)} \cdot \left(\mathbf{r}^{(i)} - \left(\frac{\|\tilde{\boldsymbol{\alpha}}^{(i)}\|}{\mathbf{r}^{(i)}} \right)^{\chi^{(i)}} \tilde{\boldsymbol{\alpha}}^{(i)} : \tilde{\mathbf{n}} \right) \quad (4.3.12)$$

$$\delta \tilde{\boldsymbol{\alpha}}^{(i)} = \mathbf{c}^{(i)} \cdot \mathbf{r}^{(i)} \left(\tilde{\mathbf{n}} - \left(\frac{\|\tilde{\boldsymbol{\alpha}}^{(i)}\|}{\mathbf{r}^{(i)}} \right)^{\chi^{(i)+1}} \frac{\tilde{\boldsymbol{\alpha}}^{(i)}}{\|\tilde{\boldsymbol{\alpha}}^{(i)}\|} \right) \delta p \quad (4.3.13)$$

where δp is the equivalent plastic strain increment which can be computed as:

$$\delta p = \sqrt{\sum_{i,j=1}^3 (\delta \varepsilon_{ij,pl} \cdot \delta \varepsilon_{ij,pl})} \quad (4.3.14)$$

Parameters $\mathbf{c}^{(i)}$, $\mathbf{r}^{(i)}$ and $\chi^{(i)}$ are “ad-hoc” material coefficients. The superscript “i” on $\boldsymbol{\alpha}$ denotes the i-th part of the incremental backstress. In fact, according to Chaboche [97], the total backstress can be thought of as composed by M additive parts:

$$\tilde{\boldsymbol{\alpha}} = \sum_{i=1}^M \tilde{\boldsymbol{\alpha}}^{(i)} \quad (4.3.15)$$

The Jiang-Sehitoglu’s model is able to take into account the non-constant ratchetting rate during an asymmetric cyclic loading [99,100]. In the case of cyclic loading with load ratio $R = -1$, taken into consideration in all the analyses, this phenomenon has been neglected being the applied load balanced as highlighted in previous works [99,100]. Thus the parameters $\chi^{(i)}$ in Eqs. (4.3.12) and (4.3.13), which control the non-constant ratchetting rate effect, can be set equal to zero [121]. This allows to obtain the initial Chaboche model [97] (which results in a constant ratchetting rate decay) by means of Jiang-Sehitoglu coefficients [122].

The procedure for the determination of the material coefficients $c^{(i)}$, $r^{(i)}$ and $\chi^{(i)}$ is extensively described in previous contributions [100,121]. In particular the determination of $c^{(i)}$ and $r^{(i)}$ is based on a multi-linearization of the plastic part of the material stabilised cyclic curve (SCC). When M couples of $(\sigma, \varepsilon_{pl})$ on the SCC are known, the evaluation of the i-th material parameters is straightforward and in accordance with the following expressions:

$$c^{(i)} = \sqrt{\frac{2}{3}} \frac{1}{\varepsilon_{pl}} \quad (4.3.16)$$

$$r^{(i)} = \frac{2}{3} \frac{H^{(i)} - H^{(i+1)}}{c^{(i)}} \quad (4.3.17)$$

being:

$$H^{(i)} = \frac{\sigma^{(i)} - \sigma^{(i-1)}}{\varepsilon_{pl}^{(i)} - \varepsilon_{pl}^{(i-1)}} \quad (4.3.18)$$

4.3.3. Case studies

Many contributions on this topic deal with axis-symmetric components weakened by circumferential rounded notches and subjected to a multiaxial remote loading [86,103–105], while few contributions deal with plane 2D specimens weakened by rounded notches [90,123].

In this work, the use of the incremental cyclic plasticity theory combined with the “energy equations” will be first calibrated considering bi-dimensional problems of notched members subjected to uniaxial, torsional and multiaxial (tension-torsion) in-phase cyclic loadings, and then extended to the evaluation of three-dimensional effects at the tip of rounded notches.

The new applied procedure will be used to analyse these phenomena under cyclic elastic-plastic behaviour, providing different hysteresis loops moving through-the-thickness of the specimen.

Six different groups of case studies have been taken into examination in the present work. In the following the elastic-plastic systems of equations, to be solved in order to obtain the full stress-strain state at the tip of a rounded notch during one loading cycle, are reported in detail.

4.3.3.1 Tensile loading – Plane stress

Consider the Cartesian coordinate system centred at the tip of a rounded notch (Fig. 4.3.1). In the case of a remote tensile loading applied to a very thin plate, four equations (three constitutive equation and one “energy equation”) are needed for the determination of the elastic-plastic stress-strain state at the tip of the notch:

$$\left\{ \begin{array}{l} (\sigma_{yy}^e - \sigma_{yy}^{e(0)})\delta\varepsilon_{yy}^e + (\varepsilon_{yy}^e - \varepsilon_{yy}^{e(0)})\delta\sigma_{yy}^e = (1 + C_q)(\sigma_{yy} - \sigma_{yy}^{(0)})\delta\varepsilon_{yy} + (1 - C_q)(\varepsilon_{yy} - \varepsilon_{yy}^{(0)})\delta\sigma_{yy} \\ \delta\varepsilon_{xx} = \delta\sigma_{yy} \left(-\frac{1}{3h} n_{xx}^2 + \frac{2}{3h} n_{xx} n_{yy} - \frac{1}{3h} n_{xx} n_{zz} - \frac{\nu}{E} \right) \\ \delta\varepsilon_{yy} = \delta\sigma_{yy} \left(-\frac{1}{3h} n_{xx} n_{yy} + \frac{2}{3h} n_{yy}^2 - \frac{1}{3h} n_{yy} n_{zz} + \frac{1}{E} \right) \\ \delta\varepsilon_{zz} = \delta\sigma_{yy} \left(-\frac{1}{3h} n_{xx} n_{zz} + \frac{2}{3h} n_{yy} n_{zz} - \frac{1}{3h} n_{zz}^2 - \frac{\nu}{E} \right) \end{array} \right. \quad (4.3.19)$$

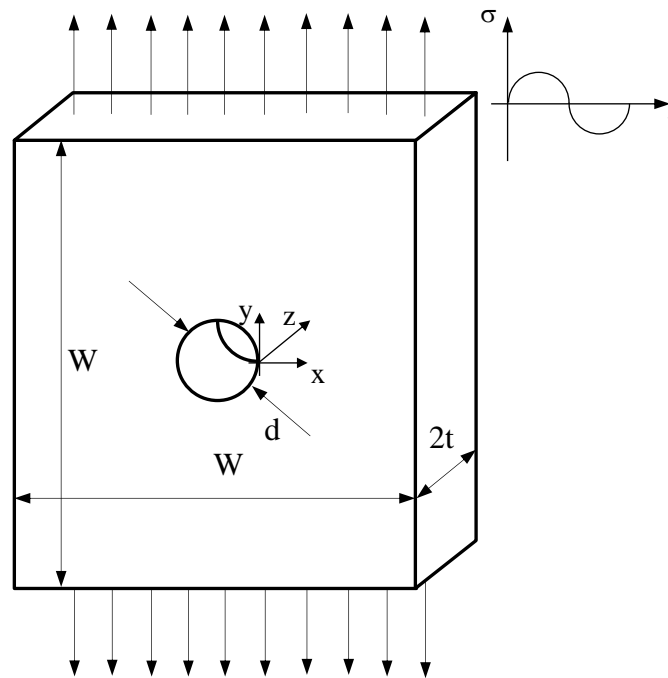
4.3.3.2 Tensile loading – Plane strain

In the case of plane strain conditions, the following four relations are needed for the determination of the elastic plastic stress-strain state:

$$\left\{ \begin{array}{l} (\sigma_{yy}^e - \sigma_{yy}^{e(0)}) \delta \varepsilon_{yy}^e + (\varepsilon_{yy}^e - \varepsilon_{yy}^{e(0)}) \delta \sigma_{yy}^e = (1 + C_q)(\sigma_{yy} - \sigma_{yy}^{(0)}) \delta \varepsilon_{yy} + (1 - C_q)(\varepsilon_{yy} - \varepsilon_{yy}^{(0)}) \delta \sigma_{yy} \\ \delta \sigma_{zz} = \nu_{pl} \cdot \delta \sigma_{yy} \\ \delta \varepsilon_{xx} = \delta \sigma_{yy} \left(-\frac{1 + \nu_{pl}}{3h} n_{xx}^2 + \frac{2 - \nu_{pl}}{3h} n_{xx} n_{yy} - \frac{1 - 2\nu_{pl}}{3h} n_{xx} n_{zz} - \frac{\nu}{E} (1 + \nu_{pl}) \right) \\ \delta \varepsilon_{yy} = \delta \sigma_{yy} \left(-\frac{1 + \nu_{pl}}{3h} n_{xx} n_{yy} + \frac{2 - \nu_{pl}}{3h} n_{yy}^2 - \frac{1 - 2\nu_{pl}}{3h} n_{yy} n_{zz} + \frac{1 - \nu \cdot \nu_{pl}}{E} \right) \end{array} \right.$$

(4.3.20)

Where ν_{pl} is equal to 0.5 and it is named plastic Poisson's ratio.



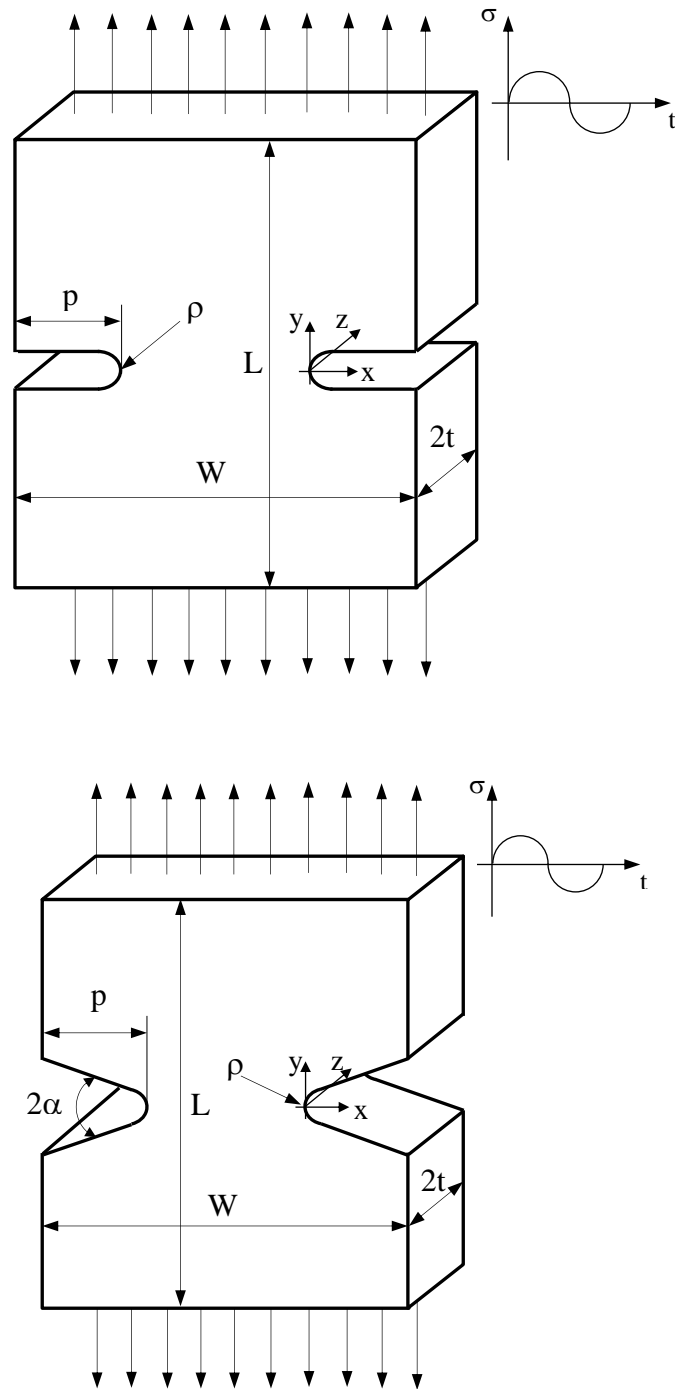


Figure 4.3.1. Specimens subjected to a tension-compression fatigue loading and weakened by: a) a circular hole, b) double symmetrical blunt U-notches and c) double symmetrical rounded V-notches ($2\alpha = 90^\circ$).

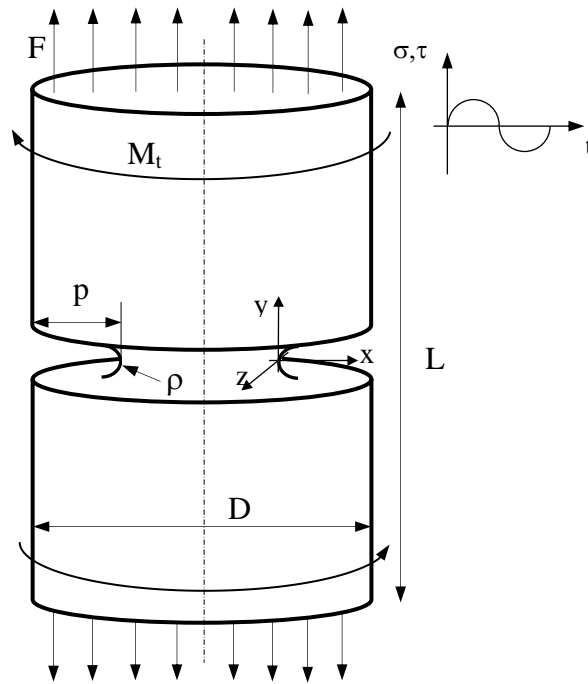


Figure 4.3.2. Cylindrical specimen subjected to torsion (Mode III) and tension-torsion (Mode I+III) in-phase fatigue loading and weakened by a blunt U-notch (radius ρ and depth p). Diameter of the net section $d = 20$ mm. F = tensile loading, M_t = torsion loading.

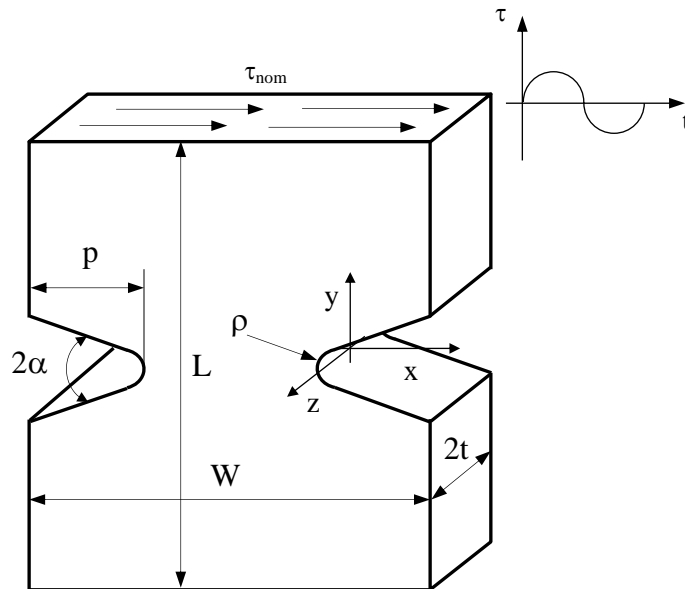


Figure 4.3.3. 3D specimen subjected to in-plane shear (Mode II) fatigue loading and weakened by double symmetrical rounded V-notch ($2\alpha = 120^\circ$, radius ρ and depth p). $W = 200$ mm, $2t = 40$ mm. The origin of the $Oxyz$ referential system is at the notch tip at the mid-plane.

4.3.3.3 Pure torsional loading – Axis-symmetric specimen

Consider the Cartesian coordinate system centred at the tip of a rounded notch (Fig. 4.3.2). In the case of a pure torsional loading applied to an axis-symmetric specimen (Fig. 4.3.2), two different equations (Eq. (4.3.21): one constitutive equation and one “energy equation”) are needed for the determination of the elastic-plastic stress-strain state at the tip of the notch. In fact, at the notch tip, only the “yz” component of stress-strain acts.

$$\begin{cases} (\sigma_{yz}^e - \sigma_{yz}^{e(0)}) \delta \varepsilon_{yz}^e + (\varepsilon_{yz}^e - \varepsilon_{yz}^{e(0)}) \delta \sigma_{yz}^e = (1 + C_q)(\sigma_{yz} - \sigma_{yz}^{(0)}) \delta \varepsilon_{yz} + (1 - C_q)(\varepsilon_{yz} - \varepsilon_{yz}^{(0)}) \delta \sigma_{yz} \\ \delta \varepsilon_{yz} = \left(\frac{2}{h} n_{yz}^2 + \frac{1 + \nu}{E} \right) \cdot \delta \sigma_{yz} \end{cases} \quad (4.3.21)$$

In this case the Cartesian coordinate system has been hold in order to simplify the calculation. It has been assumed that the notch tip belongs to the x-y plane.

4.3.3.4 Multiaxial loading – Axis-symmetric specimen

The general case of an axis-symmetric specimen subjected to multiaxial loading has been faced by many researchers [86,105]. In this case (Fig. 4.3.2), seven unknowns are present at the notch tip: three stress components (σ_{yy} , σ_{zz} and τ_{yz}) and four strain components (ε_{xx} , ε_{yy} , ε_{zz} and ε_{yz}), thus seven different equations are needed. For the sake of completeness the governing equations will be presented. In the following the shear stress tied to torsion loading will be indicated with σ_{yz} instead of τ_{yz} , with the aim to simplify and to make the equations uniform.

$$\left\{ \begin{aligned}
 &(\sigma_{yy}^e - \sigma_{yy}^{e(0)})\delta\varepsilon_{yy}^e + (\varepsilon_{yy}^e - \varepsilon_{yy}^{e(0)})\delta\sigma_{yy}^e = (1 + C_q)(\sigma_{yy} - \sigma_{yy}^{(0)})\delta\varepsilon_{yy} + (1 - C_q)(\varepsilon_{yy} - \varepsilon_{yy}^{(0)})\delta\sigma_{yy} \\
 &(\sigma_{zz}^e - \sigma_{zz}^{e(0)})\delta\varepsilon_{zz}^e + (\varepsilon_{zz}^e - \varepsilon_{zz}^{e(0)})\delta\sigma_{zz}^e = (1 + C_q)(\sigma_{zz} - \sigma_{zz}^{(0)})\delta\varepsilon_{zz} + (1 - C_q)(\varepsilon_{zz} - \varepsilon_{zz}^{(0)})\delta\sigma_{zz} \\
 &(\sigma_{yz}^e - \sigma_{yz}^{e(0)})\delta\varepsilon_{yz}^e + (\varepsilon_{yz}^e - \varepsilon_{yz}^{e(0)})\delta\sigma_{yz}^e = (1 + C_q)(\sigma_{yz} - \sigma_{yz}^{(0)})\delta\varepsilon_{yz} + (1 - C_q)(\varepsilon_{yz} - \varepsilon_{yz}^{(0)})\delta\sigma_{yz} \\
 &\delta\varepsilon_{xx} = \frac{n_{xx}}{3h} \left(-(\delta\sigma_{yy} + \delta\sigma_{zz})n_{xx} + (2\delta\sigma_{yy} - \delta\sigma_{zz})n_{yy} \right. \\
 &\quad \left. + (2\delta\sigma_{zz} - \delta\sigma_{yy})n_{zz} + 6\delta\sigma_{yz}n_{yz} \right) - \frac{\nu}{E}(\delta\sigma_{yy} + \delta\sigma_{zz}) \\
 &\delta\varepsilon_{yy} = \frac{n_{yy}}{3h} \left(-(\delta\sigma_{yy} + \delta\sigma_{zz})n_{xx} + (2\delta\sigma_{yy} - \delta\sigma_{zz})n_{yy} \right. \\
 &\quad \left. + (2\delta\sigma_{zz} - \delta\sigma_{yy})n_{zz} + 6\delta\sigma_{yz}n_{yz} \right) + \frac{1}{E}(\delta\sigma_{yy} - \nu\delta\sigma_{zz}) \\
 &\delta\varepsilon_{zz} = \frac{n_{zz}}{3h} \left(-(\delta\sigma_{yy} + \delta\sigma_{zz})n_{xx} + (2\delta\sigma_{yy} - \delta\sigma_{zz})n_{yy} \right. \\
 &\quad \left. + (2\delta\sigma_{zz} - \delta\sigma_{yy})n_{zz} + 6\delta\sigma_{yz}n_{yz} \right) + \frac{1}{E}(\delta\sigma_{zz} - \nu\delta\sigma_{yy}) \\
 &\delta\varepsilon_{yz} = \frac{n_{yz}}{3h} \left(-(\delta\sigma_{yy} + \delta\sigma_{zz})n_{xx} + (2\delta\sigma_{yy} - \delta\sigma_{zz})n_{yy} \right. \\
 &\quad \left. + (2\delta\sigma_{zz} - \delta\sigma_{yy})n_{zz} + 6\delta\sigma_{yz}n_{yz} \right) + \frac{1+\nu}{E}\delta\sigma_{yz}
 \end{aligned} \right.$$

(4.3.22)

4.3.3.5 Tensile loading – Three dimensional plates

In the case of a flat specimen with finite thickness and weakened by a rounded notch (Fig. 4.3.1), five unknowns are present at the notch tip, two components of stress (σ_{yy} and σ_{zz}) and three components of strain (ε_{xx} , ε_{yy} , ε_{zz}), thus five different equations should be used. In the present work the behaviour of each stress-strain component through the thickness of the plate has been evaluated, by providing the trend of the stress concentration factor K_t along the z coordinate (see Fig. 4.3.4) as input of the incremental procedure. In the case of 3D flat specimens subjected to tensile loading it is well known that the stress concentration factor decreases moving through the thickness of the specimen [124,125].

The problem is governed by the following equations:

$$\left\{ \begin{array}{l}
 (\sigma_{yy,(z)}^e - \sigma_{yy,(z)}^{e(0)}) \delta \varepsilon_{yy,(z)}^e + (\varepsilon_{yy,(z)}^e - \varepsilon_{yy,(z)}^{e(0)}) \delta \sigma_{yy,(z)}^e \\
 \quad = (1 + C_q)(\sigma_{yy,(z)} - \sigma_{yy,(z)}^{(0)}) \delta \varepsilon_{yy,(z)} + (1 - C_q)(\varepsilon_{yy,(z)} - \varepsilon_{yy,(z)}^{(0)}) \delta \sigma_{yy,(z)} \\
 (\sigma_{zz,(z)}^e - \sigma_{zz,(z)}^{e(0)}) \delta \varepsilon_{zz,(z)}^e + (\varepsilon_{zz,(z)}^e - \varepsilon_{zz,(z)}^{e(0)}) \delta \sigma_{zz,(z)}^e \\
 \quad = (1 + C_q)(\sigma_{zz,(z)} - \sigma_{zz,(z)}^{(0)}) \delta \varepsilon_{zz,(z)} + (1 - C_q)(\varepsilon_{zz,(z)} - \varepsilon_{zz,(z)}^{(0)}) \delta \sigma_{zz,(z)} \\
 \delta \varepsilon_{xx,(z)} = \frac{n_{xx}}{3h} (-(\delta \sigma_{yy,(z)} + \delta \sigma_{zz,(z)}) n_{xx} + (2\delta \sigma_{yy,(z)} - \delta \sigma_{zz,(z)}) n_{yy} \\
 \quad + (2\delta \sigma_{zz,(z)} - \delta \sigma_{yy,(z)}) n_{zz}) - \frac{\nu}{E} (\delta \sigma_{yy,(z)} + \delta \sigma_{zz,(z)}) \\
 \delta \varepsilon_{yy,(z)} = \frac{n_{yy}}{3h} (-(\delta \sigma_{yy,(z)} + \delta \sigma_{zz,(z)}) n_{xx} + (2\delta \sigma_{yy,(z)} - \delta \sigma_{zz,(z)}) n_{yy} \\
 \quad + (2\delta \sigma_{zz,(z)} - \delta \sigma_{yy,(z)}) n_{zz}) + \frac{1}{E} (\delta \sigma_{yy,(z)} - \nu \delta \sigma_{zz,(z)}) \\
 \delta \varepsilon_{zz,(z)} = \frac{n_{zz}}{3h} (-(\delta \sigma_{yy,(z)} + \delta \sigma_{zz,(z)}) n_{xx} + (2\delta \sigma_{yy,(z)} - \delta \sigma_{zz,(z)}) n_{yy} \\
 \quad + (2\delta \sigma_{zz,(z)} - \delta \sigma_{yy,(z)}) n_{zz}) + \frac{1}{E} (\delta \sigma_{zz,(z)} - \nu \delta \sigma_{yy,(z)})
 \end{array} \right.$$

(4.3.23)

In Eq. (4.3.23), the subscript (z) denotes the dependence of the stress and strain components on the through-the-thickness Cartesian coordinate.

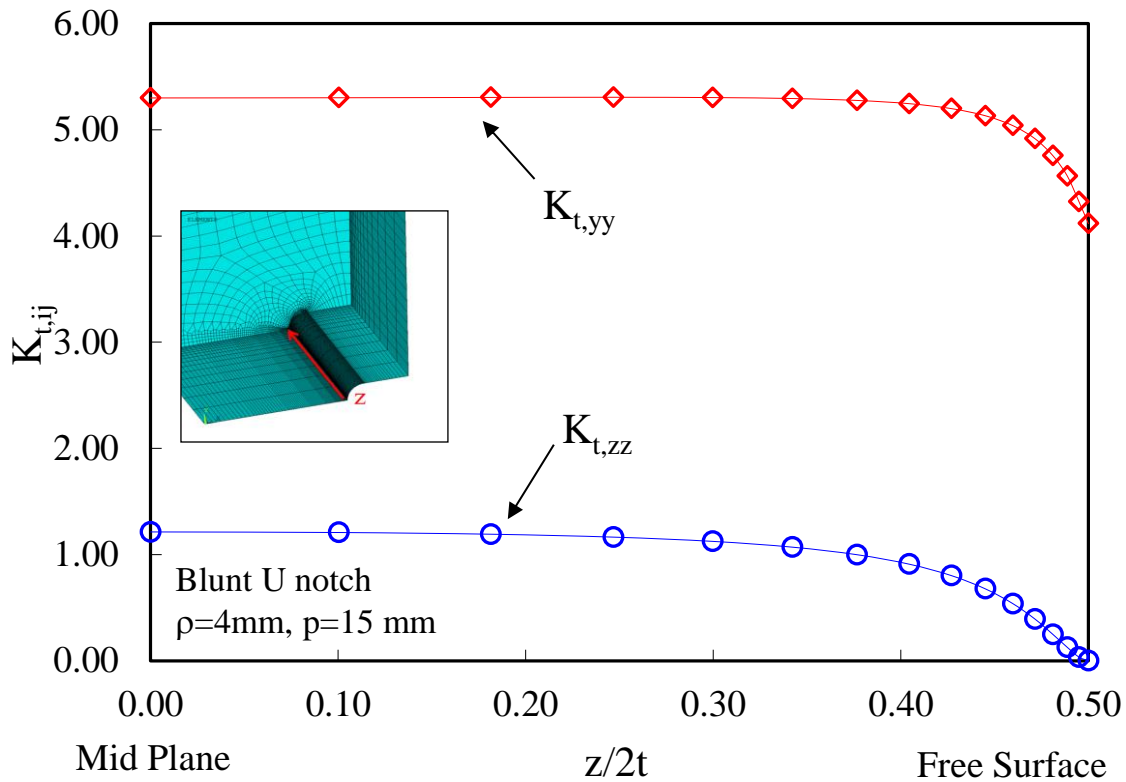


Figure 4.3.4. Example of K_t trend through the plate thickness for a blunt U-notch, $\rho=4\text{ mm}$ and $p=15\text{ mm}$.

4.3.3.6 Shear in-plane loading – Three dimensional V-notched plate

Consider the Cartesian coordinate system centred at the tip of a rounded notch at the mid-plane (Fig. 4.3.3). The application of a remote in-plane shear loading ($\tau_{nom} = \sigma_{xy}$) causes, at the notch tip, the presence of a non-negligible out-of-plane stress component (σ_{yz}) due to three-dimensional effects [9,106,107]. With the aim to emphasise this effect, in this work a flat specimen with finite thickness, weakened by double symmetrical rounded notches characterised by an opening angle equal to 120° , will be analysed. In the present work the behaviour of each stress-strain component through-the-thickness of the plate has been evaluated, by providing the trend of the stress concentration factor related to the O-mode ($K_{t,yz}$) along the z coordinate (see Fig. 4.3.5) as input of the incremental cyclic plasticity procedure.

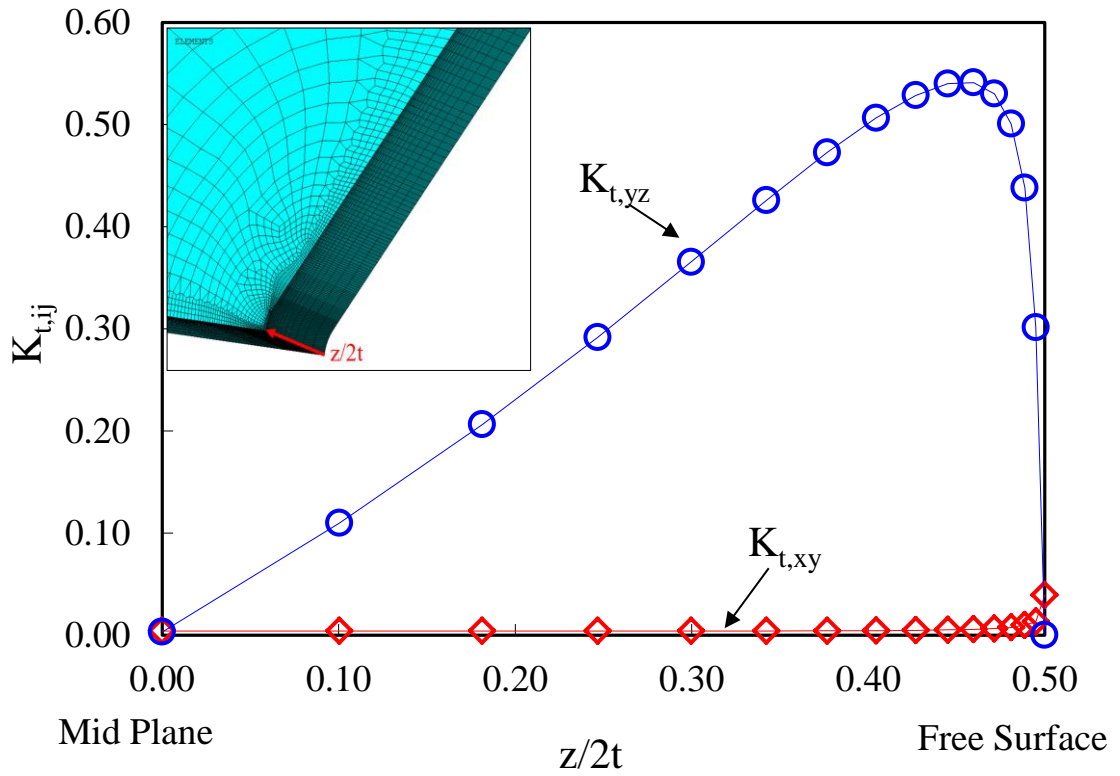


Figure 4.3.5. 3D specimen subjected to in-plane shear (Mode II) fatigue loading and weakened by double symmetrical rounded V-notch ($2\alpha = 120^\circ$, $\rho = 4$ mm, $p = 15$ mm): trend of the stress concentration factors $K_{t,ij}$ as functions of the normalized through-the-thickness coordinate.

The problem is governed by the following equations:

$$\left\{ \begin{aligned} & \left(\sigma_{yz,(z)}^e - \sigma_{yz,(z)}^{e(0)} \right) \delta \varepsilon_{yz,(z)}^e + \left(\varepsilon_{yz,(z)}^e - \varepsilon_{yz,(z)}^{e(0)} \right) \delta \sigma_{yz,(z)}^e \\ & = (1 + C_q) \left(\sigma_{yz,(z)} - \sigma_{yz,(z)}^{(0)} \right) \delta \varepsilon_{yz,(z)} + (1 - C_q) \left(\varepsilon_{yz,(z)} - \varepsilon_{yz,(z)}^{(0)} \right) \delta \sigma_{yz,(z)} \\ & \delta \varepsilon_{yz,(z)} = \left(\frac{2}{h} n_{yz,(z)}^2 + \frac{1+\nu}{E} \right) \cdot \delta \sigma_{yz,(z)} \end{aligned} \right.$$

(4.3.24)

where the subscripts (z) denote the dependence of the stress and strain components on the through-the-thickness Cartesian coordinate.

4.3.4. Incremental cyclic plasticity procedure

In order to represent the local behaviour of the stress-strain components acting at the tip of a rounded notch during one loading cycle, a numerical procedure based on the incremental cyclic plasticity has been implemented in Wolfram Mathematica[®]. The applied procedure accurately follows the chart presented by Gao et al. [105]. In the following only the fundamental steps are quoted:

- First of all, it is necessary to evaluate the material's parameters, $c^{(i)}$ and $r^{(i)}$, on the basis of Eqs. (4.3.16-4.3.18) once known the material constitutive law (see the next Section for more details);
- Then obtain the hypothetical linear-elastic stresses-strains at the notch tip at step i-th, σ^e and ε^e , by knowing the stress concentration factors $K_{t,ij}$ and the nominally applied loads;
- Get the increment of hypothetical linear-elastic stress-strain components, $\delta\sigma^e$ and $\delta\varepsilon^e$, between step i-th and i+1-th. The increments have to be small enough to well model the stress-strain behavior but at the same time a compromise has to be searched avoiding too much computational efforts. In the present investigation each loading cycle has been divided into $N = 1000$ steps, in order to obtain very small values of stress and strain increments without increasing too much the computational time;
- Evaluate the “energy dissipation coefficient” C_q on the basis of Eq. (4.3.2), once known the strain hardening exponent n' of the material taken into account;
- Obtain the tentative stresses and strains at the notch tip at step i+1-th by means of Eqs. (4.3.19-4.3.24) (depending on the case study), assuming no plastic deformations as a first attempt, that is $\delta\varepsilon_{ij} = \delta\varepsilon_{ij,el} + \delta\varepsilon_{ij,pl} = \delta\varepsilon_{ij,el}$;
- Check the yield condition, $f = 0$ (Eq. (4.3.9)), and the occurrence of a positive plastic strain increment, $\delta\varepsilon_{ij,pl} > 0$ (Eq. (4.3.10));
- Even if only one of the conditions is not satisfied, the tentative stresses and strains will be the true stresses and strains at the notch tip; the obtained solutions will be the i-th quantities at the next incremental step;

- If, instead, both the conditions are satisfied, plastic deformations will be induced at the notch tip;
- Compute the plastic modulus function h (Eq. (4.3.12));
- Compute the true stress-strain components by solving the elastic-plastic system of equations depending on the case studied (Eqs. (4.3.19-4.3.24)), the obtained solutions will be the i -th quantities at the next incremental step;
- Calculate the increment of equivalent plastic deformation δp (Eq. (4.3.14)) and then the tensor describing the incremental deviatoric backstress $\delta \tilde{\alpha}^{(i)}$ (Eq. (4.3.13));
- Update the input values of the M backstress parts on the basis of the incremental deviatoric backstress previously evaluated:

$$\tilde{\alpha}^{(i)} \rightarrow \tilde{\alpha}^{(i)} + \delta \tilde{\alpha}^{(i)};$$
- Return to begin and start the next step.

4.3.5. Finite Element modelling

The case studies presented in Section 4.3.3 will be analysed by means of the incremental cyclic plasticity procedure and the obtained results will be compared with a bulk of elastic-plastic numerical analyses carried out with the FE code Ansys[®] 14.5.

The Ansys[®] kinematic hardening material model, which is based on the Chaboche cyclic plasticity model [126], has been adopted in order to simulate the material cyclic behaviour (see the next Section for more details).

Then, aiming to simulate the cyclic fatigue loading applied to a specimen, a dedicated APDL routine has been implemented. This procedure permits to obtain also the stress-strain components acting at the notch tip that will be compared with the results obtained from the incremental cyclic plasticity frame.

In order to investigate the accuracy of the results obtained from the incremental cyclic plasticity procedure [86,105], several 2D and 3D FE analyses have been carried out with the software Ansys[®] 14.5, by using four node solid elements (PLANE 182) for 2D analyses with uniaxial loading, four node axisymmetric-

harmonic solid elements (PLANE 25) for 2D analyses with torsional or multiaxial loading and eight node solid elements (SOLID 185) for 3D models.

In more detail, the following notched geometries have been studied:

- 2D flat specimens weakened by a circular hole and by double symmetrical blunt U-notches subjected to tension-compression fatigue loading, both under plain stress and plain strain conditions (see Figs. 4.3.1a,b);
- an axis-symmetric specimen weakened by a circumferential semi-circular notch subjected to pure torsional and to multiaxial (tension-torsion) in-phase fatigue loading (Fig. 4.3.2);
- a flat specimen of finite thickness (3D analysis) weakened by a circular hole, by double symmetrical blunt U-notches and by double symmetrical rounded V-notches ($2\alpha = 90^\circ$) subjected to tension-compression fatigue loading (Figs. 4.3.1a,b,c);
- a flat specimen of finite thickness (3D analysis) weakened by double symmetrical rounded V-notches ($2\alpha = 120^\circ$) subjected to nominal in-plane shear ($\tau_{\text{nom}} = \sigma_{xy}$) fatigue loading (Fig. 4.3.3).

The nominal stress components have been applied to FE models by means of proper forces applied to the cross section of the specimens, far from the notch stress concentration zone. Then, the local elastic-plastic stress-strain components, which act at the notch tip and define the hysteresis loops compared in the following Sections, have been obtained directly from FE results.

4.3.6. Material parameters

The material parameters, required to simulate the cyclic material behaviour both in the incremental cyclic plasticity procedure (Section 4.3.4) and in the elastic-plastic FE analyses (Section 4.3.5), can be evaluated from the material mechanical properties on the basis of simple expressions.

The values of the mechanical properties of the material taken into account, an AISI 304L steel, are taken from a recent contribution by Meneghetti and Ricotta [127] and are given in Table 4.3.1. The stress defining the upper limit of purely

elastic strains on the material cyclic curve, based on the results of strain controlled fatigue tests, is named σ^* and it is equal to 160 MPa. Knowing this value, the quantification of the yield strength in simple shear, k , is straightforward. On the basis of the von Mises criterion, adopted in agreement with what was done in the cyclic plasticity model (see Eq. (4.3.9)), it can be obtained:

$$k = \frac{\sigma^*}{\sqrt{3}} = 92.4 \text{MPa} \quad (4.3.25)$$

In the case of cyclic loading the von Mises yield criterion is the most widely used in the literature as highlighted in [86,99,105]. However other yield criteria could be applied, defining accordingly also the yield function in the cyclic plasticity model (see Section 4.3.2.2).

As highlighted in Section 4.3.2.2, the knowledge of the stabilized cyclic curve (SCC) is required in order to obtain the necessary parameters for the application of the cyclic plasticity models. The aim of the present work is to compare the stabilized hysteresis loops obtained from the FE code (Ansys®) with those directly derived by means of a cyclic plasticity-based incremental procedure. No attention was paid here to initial material softening or hardening. In that case, mandatorily, the material monotonic curve should be the input both of FE analyses (Ansys® models) and of the incremental procedure implemented in Mathematica®.

The material under consideration has been thought to obey to a linear elastic behaviour up to σ^* and then to a Ramberg-Osgood representation (Fig. 4.3.6). Accordingly the stabilized cyclic curve (SCC) can be defined as:

$$\varepsilon = \begin{cases} \frac{\sigma}{E} & \text{when } \sigma < \sigma^* \\ \frac{\sigma}{E} + \left(\frac{\sigma - \sigma^*}{K'} \right)^{\frac{1}{n'}} & \text{when } \sigma \geq \sigma^* \end{cases} \quad (4.3.26)$$

The Ramberg-Osgood's parameters, reported in Table 4.3.1, have been determined in [127] by fitting the apex points of the hysteresis loops measured experimentally at 50% of the total fatigue life for different applied strain

amplitudes. Different constitutive formulations could be considered. In principle the method could be applied with similar accuracy also adopting other constitutive laws by setting the appropriate material parameters.

Table 4.3.1. Material properties of AISI 304L [127].

E	ν	K'	n'	σ^*	k
MPa		MPa		MPa	MPa
194700	0.3	2250	0.337	160	92.4

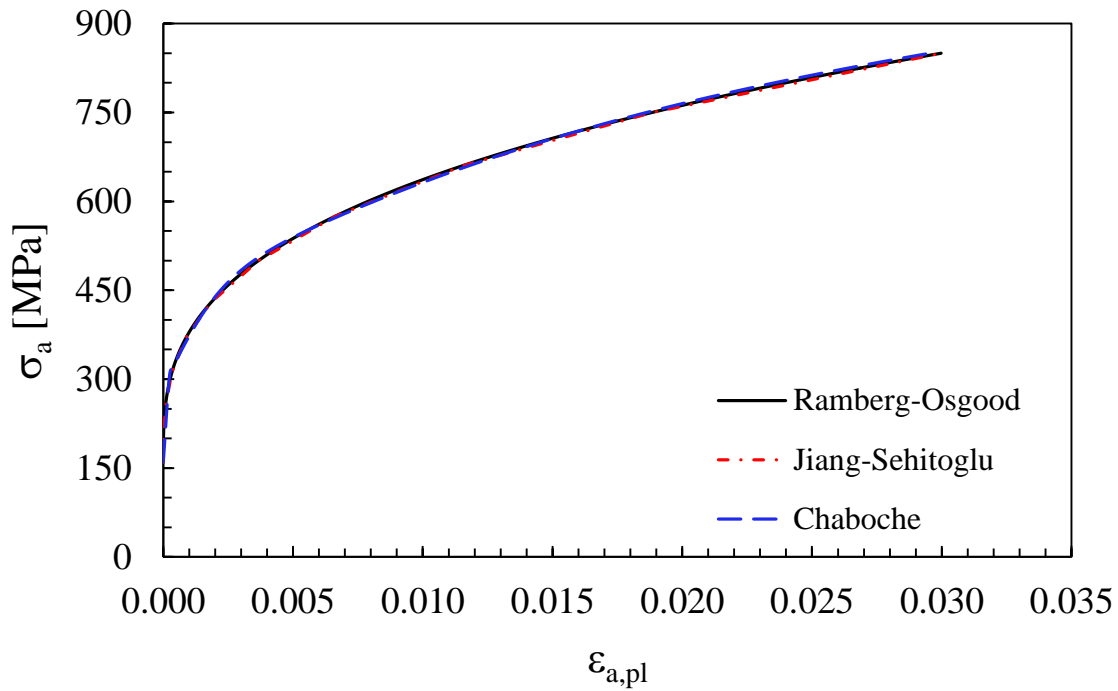


Figure 4.3.6. Plastic part of the stabilised cyclic curve related to AISI 304L [127]. Comparison between Ramberg-Osgood, Jiang-Sehitoglu's multi-linearization and Chaboche's multi-parametric function.

In the case of the incremental cyclic plasticity model (see Sections 4.3.2 and 4.3.4), the characterisation of the material behaviour is based on the parameters $c^{(i)}$ and $r^{(i)}$. The procedure for calculating them consists on a multi-linearization of the plastic part of the SCC (Fig. 4.3.6), following the guidelines explained by

Jiang and Sehitoglu [100] and by Jiang and Kurath [128]. The Jiang-Sehitoglu's material parameters (Table 4.3.2) have been determined using Eqs. (4.3.16-4.3.18), by means of $M = 10$ couples $(\sigma, \varepsilon_{pl})$ on the stabilised cyclic curve. As already remarked, the parameters $\chi^{(i)}$ have been set equal to zero, thus neglecting *a priori* variations of ratchetting rate decay.

In the case of the elastic-plastic FE analyses, instead, the Ansys[®] kinematic hardening material model, based on Chaboche plasticity model, has been adopted in order to simulate the material cyclic behaviour. Different from the incremental cyclic plasticity procedure, in this case the plastic part of the material SCC needs to be described using a multi-parametric function (Fig. 4.3.6) according to the following expression [129–131]:

$$\sigma - \sigma^* = \sum_{i=1}^j \frac{C_i}{\gamma_i} \cdot \tanh(\gamma_i \cdot \varepsilon_{pl}) \quad (4.3.27)$$

where C_i and γ_i (Table 4.3.3) are material parameters to be obtained by means of a dedicated fitting routine, applied to the plot of the material Ramberg-Osgood formulation (Eq. (4.3.26)). In this work, thirteen different parameters ($j = 5$) have been furnished to the FE software, namely five couples (C_i, γ_i) , the Young's modulus E , the Poisson's ratio ν and the yield strength σ^* .

In both cases the simplified material curves accurately match the actual behaviour of the considered material. All the parameters employed in the analyses are listed in Tables 4.3.2 and 4.3.3.

Table 4.3.2. Jiang-Sehitoglu's material parameters.

i	1	2	3	4	5	6	7	8	9	10
c_i	127408	9783	2523	930	441	223	123	71	43	27
r_i	29	33	32	33	35	39	43	48	51	220

Table 4.3.3. Material parameters employed in the Ansys® kinematic hardening routine, based on Chaboche plasticity model.

i	1	2	3	4	5
C_i	1398000	69860	13820	6002	600
γ_i	11000	449.6	60	10	0.5

4.3.7. Results and discussions

The aim of the present work is to estimate, by means of a cyclic plasticity-based incremental procedure, the hysteresis loops to which the material is subjected at the critical point when a fatigue loading is applied to a notched component, given the proper material stabilized cyclic curve (SCC), the geometry of the component and the nominally applied loading condition.

The different hysteresis loops obtained from the incremental cyclic plasticity procedure and from the cyclic elastic-plastic FE analyses will be compared hereafter, considering the two-dimensional cases above mentioned. Finally the three-dimensional stress and strain distribution effects arising at the tip of a rounded notch in a thick plate subjected to uniaxial and in-plane shear fatigue loadings will be investigated. The influence of the increase of the stress concentration factor and of the diminishing of the notch root radius, as well as the effects of the notch angle and depth on the accuracy of the method would be surely worth of investigation. However, due to the weight of numerical and computational efforts the present analysis has been limited to some specific geometries, characterized by blunt notches. To extend the procedure to sharp/pointed V-notches a new formulation would be required.

The applied nominal load amplitudes have been chosen in order to guarantee a state of small scale yielding on the neighbourhood of the notch tip. This condition is necessary to ensure the validity of the incremental procedure based on cyclic plasticity, being one of its basic hypothesis [86,90].

The load ratio R has been set equal to -1 for all the processed analyses. The method is able to take into account also non-zero mean stresses once defined the

material properties $\chi^{(i)}$ able to take into account the ratcheting effect. The complete set of material properties employed here [127] does not report parameters for different values of the nominal load ratio, not allowing thus to determine the parameters ($\chi^{(i)}$ in accordance with the procedure described in [100]) necessary to analyse asymmetric cyclic loading.

4.3.7.1. Stress-strain state at the tip of a rounded notch considering plane stress conditions

The attention has been initially focused on the case of a very thin flat specimen weakened by a circular hole or by double symmetrical blunt U notches (plane stress conditions).

For first a circular hole with diameter, d , equal to 10 mm in a plate of ligament $W = 200$ mm has been taken into account (see Fig. 4.3.1a). The nominal stress amplitude $\sigma_{a,nom}$ of the tension-compression loading cycle has been chosen equal to 0.8 times σ^* , namely 128 MPa.

In this case only one hysteresis loop, related to σ_{yy} and ε_{yy} , can be used as a term of comparison (see Fig. 4.3.7). From Fig. 4.3.7 it can be seen a very satisfactory agreement between the analytical incremental procedure and FE cyclic analyses. The transient behaviour of the material is substantially identical for both the cases, whereas an almost negligible distinction between the two curves can be observed on the lower and higher bounds of the hysteresis loops. This slight deviation can be thought of as due to a numerical inaccuracy of the incremental cyclic procedure induced by an increment of the hypothetical elastic stresses and strains not small enough.

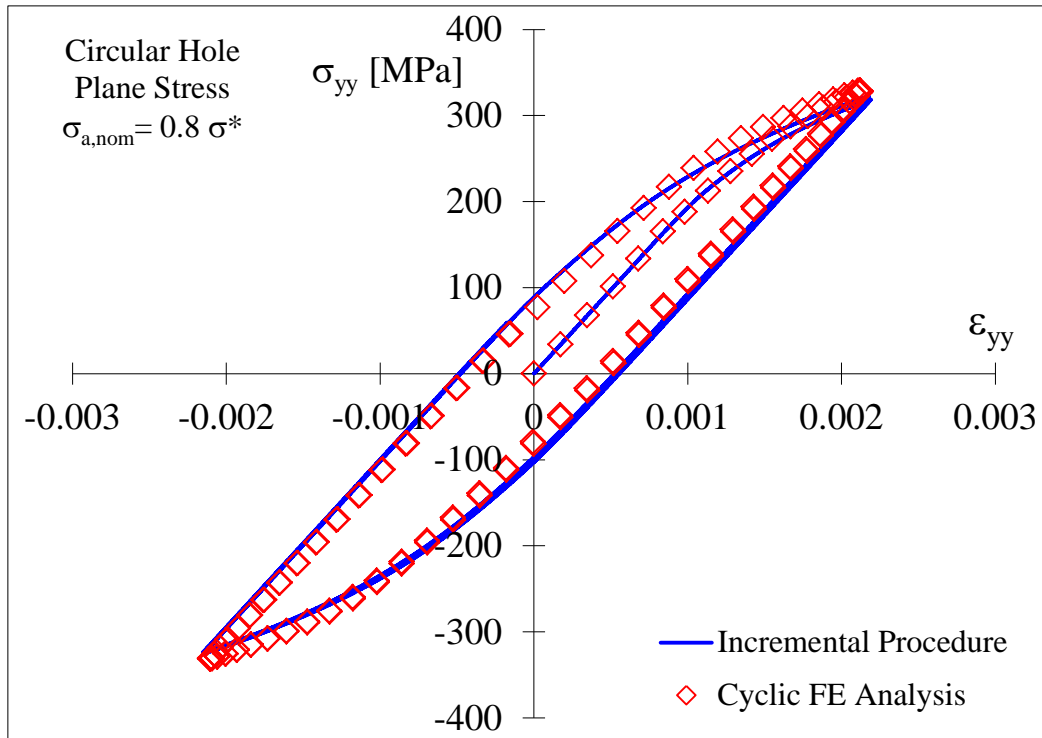


Figure 4.3.7. 2D flat specimen weakened by a circular hole subjected to a tension-compression fatigue loading under plane stress condition. Comparison between the hysteresis loops at the notch tip, obtained from the incremental procedure and the cyclic FE analyses. $\sigma_{a,nom} = 0.8 \sigma^*$.

In order to investigate the effect of the local notch geometry on the accuracy of the results, a flat specimen weakened by double symmetrical U-notches with different notch root radii (Fig. 4.3.1b) have been analysed ($\rho = 4$ and 1 mm). The notch depth, p , has been kept constant and equal to 15 mm.

As it can be seen from Fig. 4.3.8a, the agreement between analytical and numerical results is very satisfactory for a nominal stress amplitude equal to $0.8 \sigma^*$. Obviously, moving towards a sharper configuration ($\rho = 1$ mm), identical loading conditions result in an increase of the plastic zone ahead of the notch tip, the deviation between the results based on the two considered procedures slightly increases (Fig. 4.3.8b) because the small scale yielding conditions is no longer satisfied.

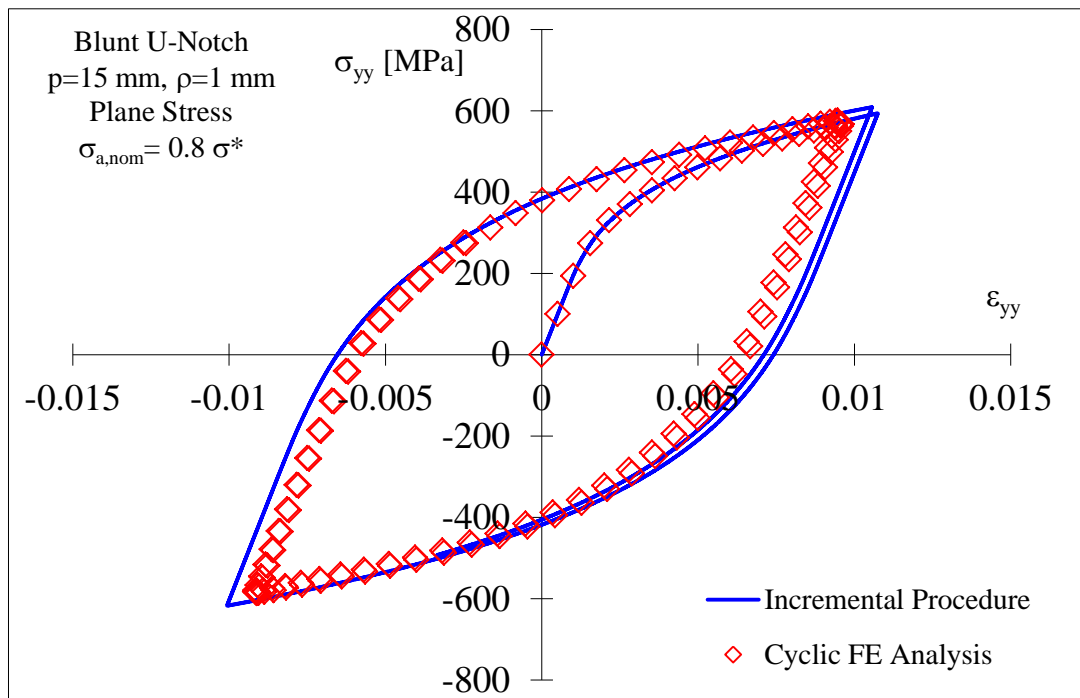
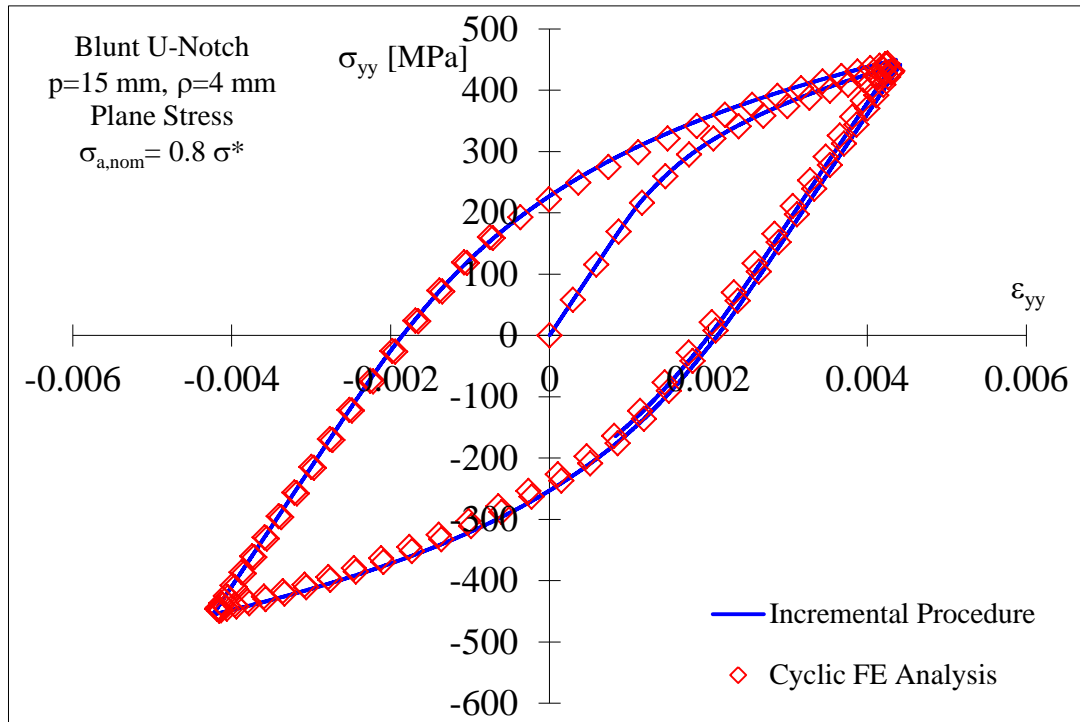


Figure 4.3.8. 2D flat specimen weakened by double symmetrical U-notches subjected to a tension-compression fatigue loading under plane stress condition. Comparison between the hysteresis loops at the notch tip, obtained from the incremental procedure and the cyclic FE analyses. (a) $\rho = 4$ mm; (b) $\rho = 1$ mm.

4.3.7.2. Stress-strain state at the tip of a rounded notch considering plane strain conditions

It is well known that under plane strain conditions the amount of plasticity at the notch tip neighbours is less pronounced than under plane stress. Accordingly, in this section the same geometries studied under plane stress have been analysed under plane strain conditions. The incremental system of equations (Eq. (4.3.20)) has been used in order to obtain the results from the incremental procedure. Results are presented in Figs. 4.3.9 and 4.3.10.

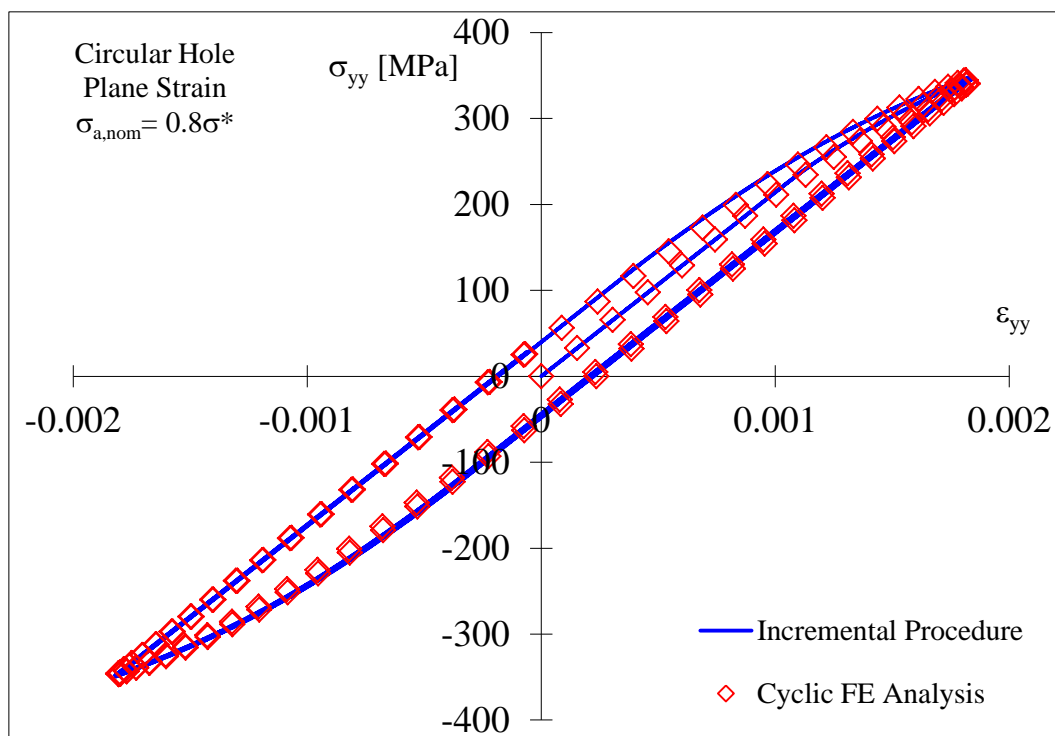


Figure 4.3.9. 2D flat specimen weakened by a circular hole subjected to a tension-compression fatigue loading under plane strain condition. Comparison between the hysteresis loops at the notch tip, obtained from the incremental procedure and the cyclic FE analyses. $\sigma_{a,nom} = 0.8 \sigma^*$.

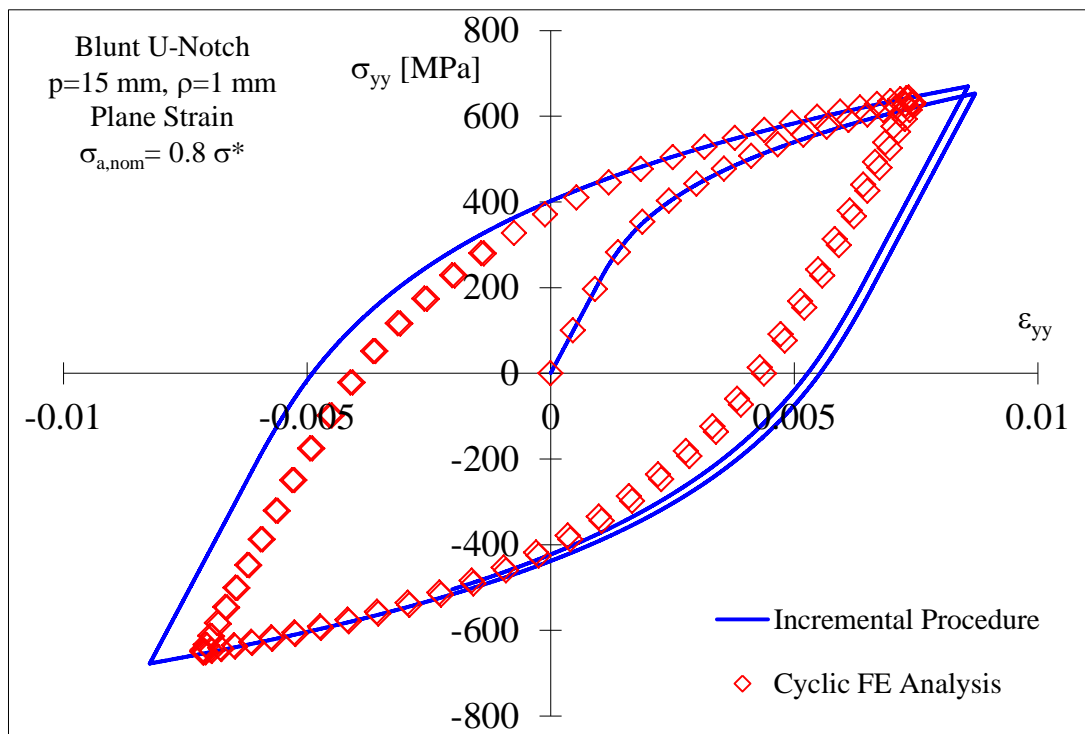
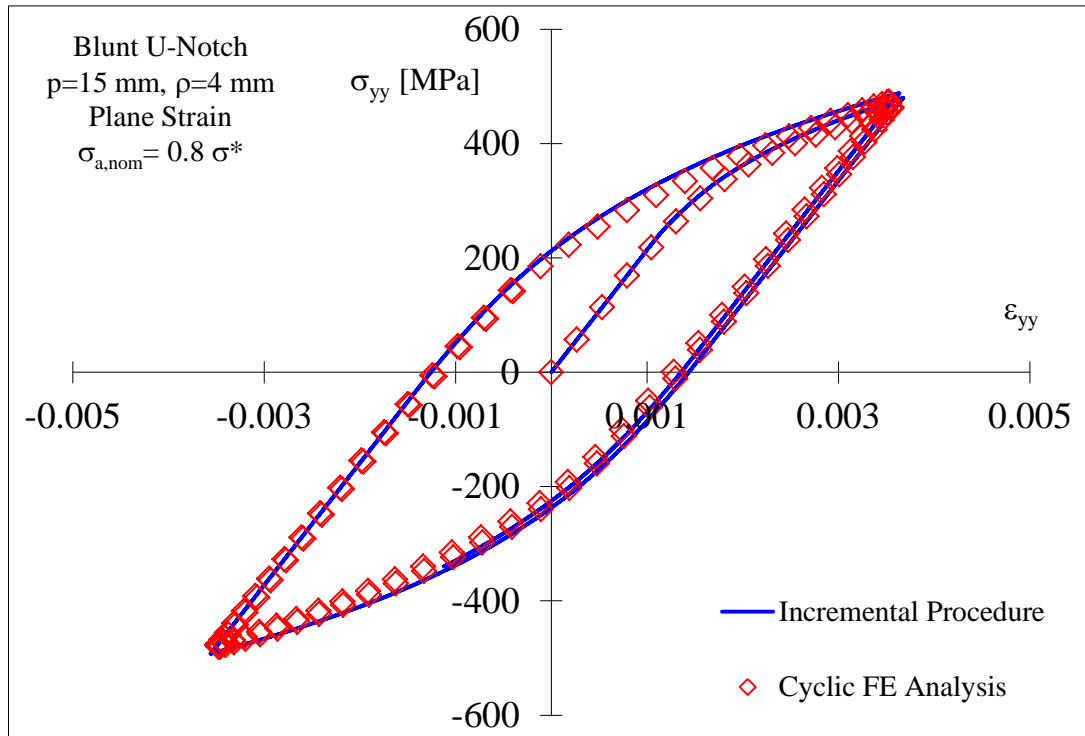


Figure 4.3.10. 2D flat specimen weakened by double symmetrical U-notches subjected to a tension-compression fatigue loading under plane strain condition. Comparison between the hysteresis loops at the notch tip, obtained from the incremental procedure and the cyclic FE analyses. (a) $\rho = 4 \text{ mm}$; (b) $\rho = 1 \text{ mm}$.

As it can be seen from Figs. 4.3.9 and 4.3.10a, the agreement between analytical and numerical results is very satisfactory for a nominal load stress amplitude equal to $0.8 \sigma^*$, being the deviation substantially zero also at the lower and higher bounds of the hysteresis loops. Also in the case of plane strain conditions, taking into consideration a sharper notch geometry ($\rho = 1 \text{ mm}$), the deviation between the results becomes higher (Fig. 4.3.10b). Moreover it is worth to be underlined that, with respect to the plane stress conditions, in this case the plastic hysteretic energies are slightly lower.

4.3.7.3. Stress-strain state at the tip of a rounded notch subjected to pure torsional fatigue loading

The attention has been initially focused on the case of an axis-symmetric specimen weakened by a circumferential semi-circular notch with $\rho = p = 4 \text{ mm}$ and with a net section characterized by a diameter $d = 20 \text{ mm}$. The overall geometry of the specimen is shown in Fig. 4.3.2.

The nominal stress amplitude remotely applied to the specimen has been set equal to 0.5 times the yield strength in simple shear, k . This choice is tied to the arising of a more extended plastic area ahead of the notch tip with respect to a tension-compression cyclic loading.

With reference to the Cartesian coordinate system shown in Fig. 4.3.2, only one hysteresis loop acts at the notch tip, that is tied to the “yz” stress and strain components. Dealing with the incremental plasticity procedure, the system of equations defined by Eq. (4.3.21) has been solved.

From Fig. 4.3.11 it can be observed a very satisfactory agreement between the results obtained from the analytical incremental cyclic plasticity procedure and those based on FE cyclic analyses, being the percentage deviation lower than 5% both for the stress range ($\Delta\sigma$, $\Delta\% = 3.70\%$) and the strain one ($\Delta\gamma$, $\Delta\% = 4.05\%$). The material transient behaviour is substantially identical for both the cases, whereas an almost negligible distinction between the two curves can be observed on the lower and higher bounds of the hysteresis loops. This slight deviation can be thought as being caused by a numerical inaccuracy of the incremental cyclic

procedure induced by an increment of the hypothetical elastic stresses and strains not small enough.

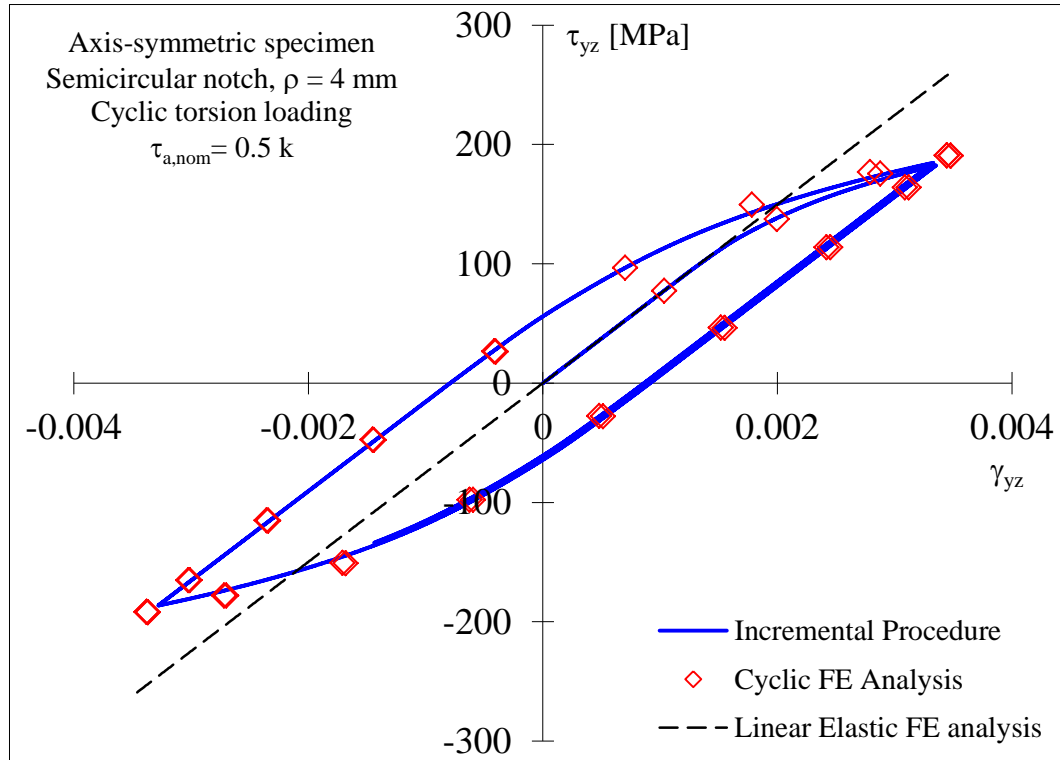


Figure 4.3.11. Cylindrical specimen weakened by a semi-circular notch ($\rho = p = 4$ mm, diameter of the net section $d = 20$ mm) subjected to torsion (Mode III) fatigue loading. Comparison between the hysteresis loop obtained from the incremental cyclic plasticity procedure and the cyclic FE analyses. Also the stress-strain curve obtained by perfectly elastic FE model has been reported for comparison.

4.3.7.4. Stress-strain state at the tip of a rounded notch subjected to multiaxial fatigue loading

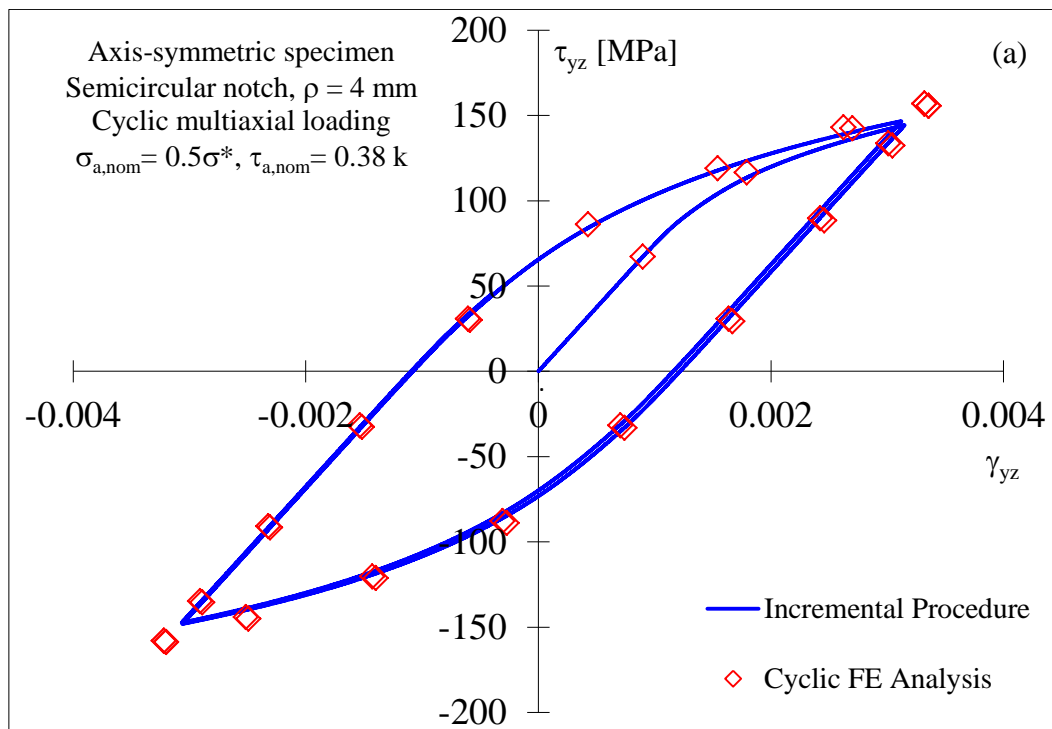
The same specimen's geometry considered in the previous case and subjected to a multiaxial tension-torsion in-phase loading has been taken into examination. Considering the Cartesian coordinate system shown in Fig. 4.3.2 three different hysteresis loops act at the notch tip: in fact the normal components “yy” and “zz” of stress-strain act simultaneously in addition to the shear “yz” component. However, the “zz” component is negligible and it has not been taken into

consideration. The nominal tensile stress amplitude and the torsional stress amplitude have been set equal to $0.5 \cdot \sigma^*$ and $0.38 \cdot k$ respectively. This choice ensures a small scale yielding condition at the notch tip.

The system of incremental equations (Eq. (4.3.22)) has been solved in order to obtain the results from the incremental cyclic plasticity procedure. The results are shown in Figs. 4.3.12a and 4.3.12b.

As it can be seen from Figs. 4.3.12a and 4.3.12b, the agreement between analytical and numerical results is very satisfactory. In particular in the case of the hysteresis loop tied to the normal stress σ_{yy} (Fig. 4.3.12b), the percentage deviation is very low both for the stress range ($\Delta\sigma$, $\Delta\% = 2.20\%$) and the strain one ($\Delta\varepsilon$, $\Delta\% = 0.35\%$), while higher values have been obtained in the case of the hysteresis loop related to the shear stress component τ_{yz} (Fig. 4.3.12a), both for the stress range ($\Delta\sigma$, $\Delta\% = 6.68\%$) and the strain one ($\Delta\gamma$, $\Delta\% = 5.46\%$).

Dealing with the computational time, the incremental cyclic plasticity procedure proved to be about 10 times faster than an elastic-plastic cyclic FE analysis with an average level of accuracy.



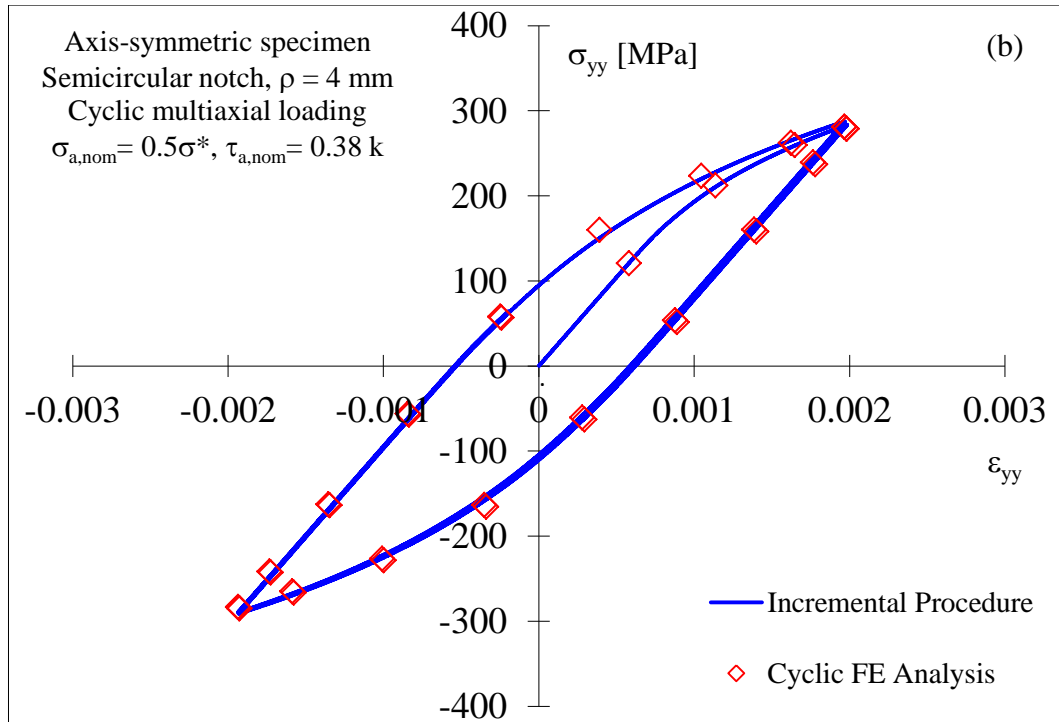


Figure 4.3.12. Cylindrical specimen weakened by a semi-circular notch ($\rho = p = 4$ mm, diameter of the net section $d = 20$ mm) subjected to tension-torsion (Mode I+III) in-phase fatigue loading. Comparison between the hysteresis loops obtained from the incremental cyclic plasticity procedure and the cyclic FE analyses.

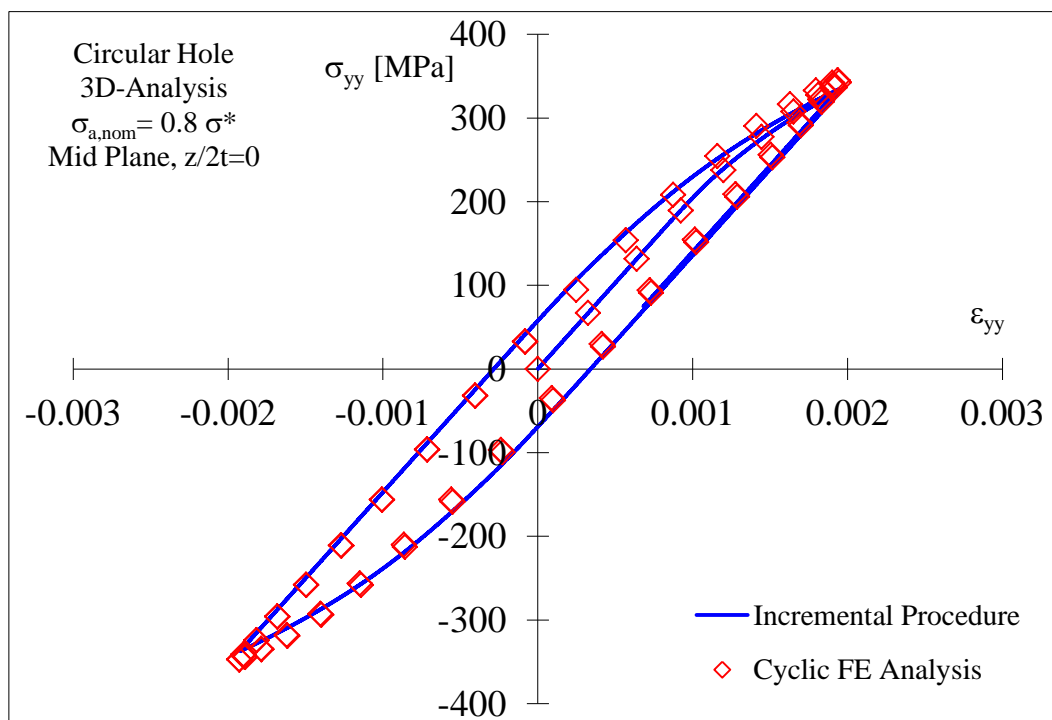
4.3.7.5. Stress-strain state at the tip of a rounded notch subjected to a uniaxial tension-compression loading considering a 3D analysis

Dealing with a three-dimensional thick plate weakened by different rounded notches and subjected to a cyclic tension-compression loading (Figs. 4.3.1a,b,c), a biaxial state of stress-strain is induced at the notch tip. In particular, through the plate thickness the stress concentration factors related to the acting stress components reduce while moving from the mid plane to the free surface (for example see Fig. 4.3.4 for the case of a blunt U-notch).

As stated above, in fact, the incremental procedure based on the cyclic plasticity theory has been extended for the first time in the present work with the aim to investigate the three dimensional effects arising at the notch tip. Starting from the through-the-thickness variations of the “yy” and “zz” linear-elastic stress

concentration factors K_t (obtainable with a 3D linear-elastic FE analysis), the new incremental routine allows us to obtain the whole elastic-plastic stress-strain state at the tip of the notch.

As a first case study, a three-dimensional flat specimen weakened by a circular hole has been considered, with $d = 10$ mm, $W = 200$ mm and thickness $2t$ equal to 40 mm (Fig. 4.3.1a). The applied nominal stress related to the uniaxial fatigue loading has been set equal to 0.8 times σ^* , in order to guarantee a small scale yielding condition at the notch tip. Figs. 4.3.13a-b show the “yy” hysteresis loop at different coordinates along the thickness: at the mid plane, at a coordinate $z/2t = 0.25$ mm and on the free surface of the specimen. A comparison has been performed with the results obtained from a 3D cyclic FE analysis as already done for the problems investigated in the previous sections. As expected, the hysteresis loop tends to become smaller moving from the mid plane to the free surface of the specimen, following the behaviour of the related stress concentration factor. The hysteresis loop tied to the “zz” component has not reported, being it negligible. As it can be seen from Figs. 4.3.13a-b, the agreement between analytical and numerical results is very satisfactory, being the deviation substantially zero with reference to all the different coordinates along the thickness of the plate.



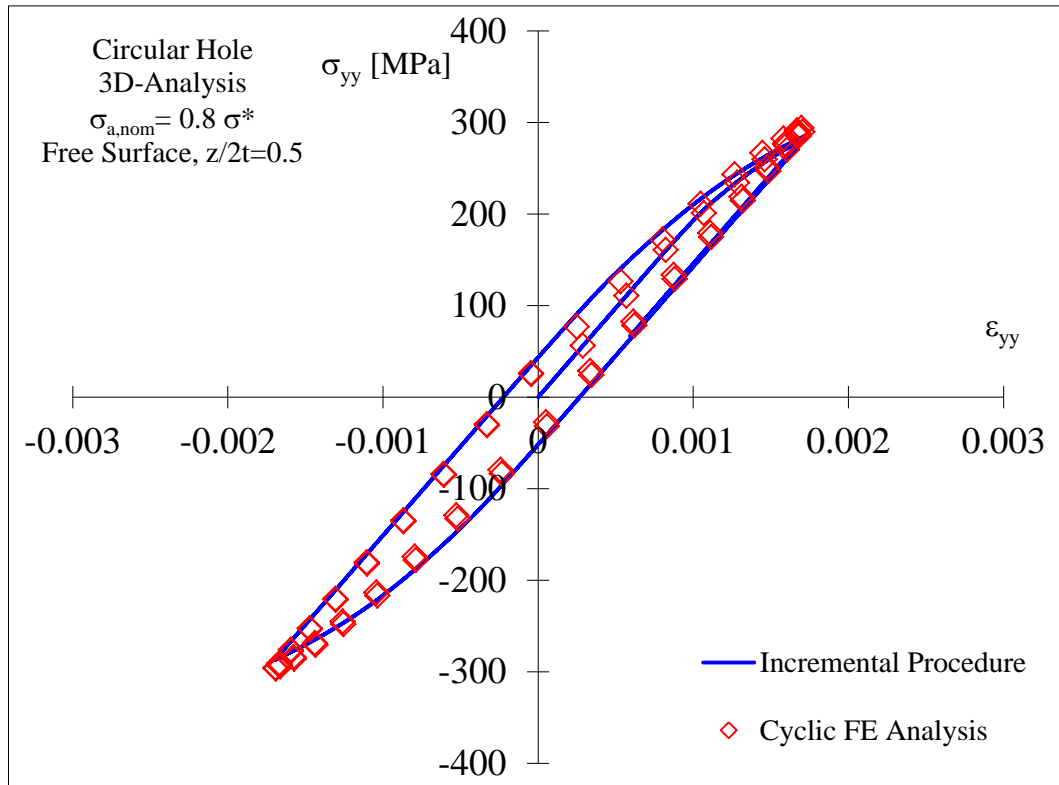


Figure 4.3.13. 3D specimen weakened by a circular hole subjected to a tension-compression fatigue loading. Comparison between the hysteresis loops at the notch tip, obtained from the incremental procedure and the cyclic FE analyses with reference to (a) mid plane; (b) free surface.

$$\sigma_{a,nom} = 0.8 \sigma^*.$$

The second case taken into consideration is a flat specimen with a thickness $2t$ equal to 40 mm weakened by double symmetrical blunt U-notches characterised by a notch tip radius equal to 4 mm and a notch depth of 15 mm (Fig. 4.3.1b). The load is the same applied in the previous investigation. Once again Figs. 4.3.14a-b demonstrate that the hysteresis loop related to “yy” component, follows the stress concentration factor behaviour. Also in this case a very good correlation has been obtained between analytical and numerical FE results.

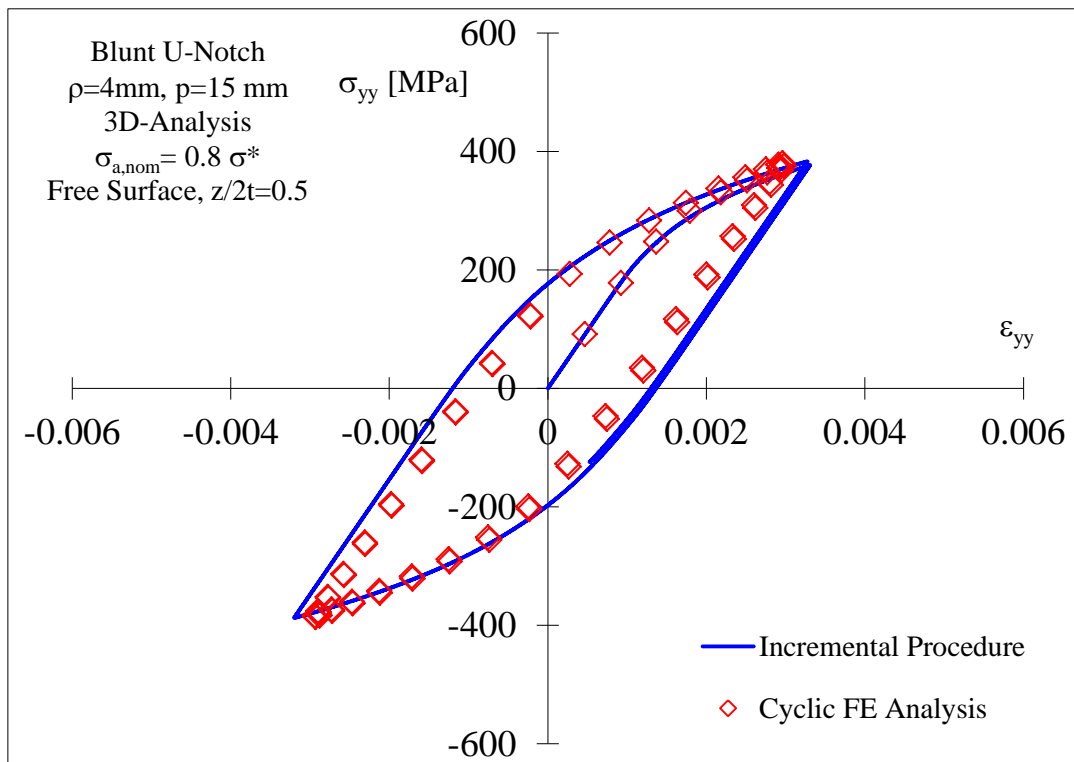
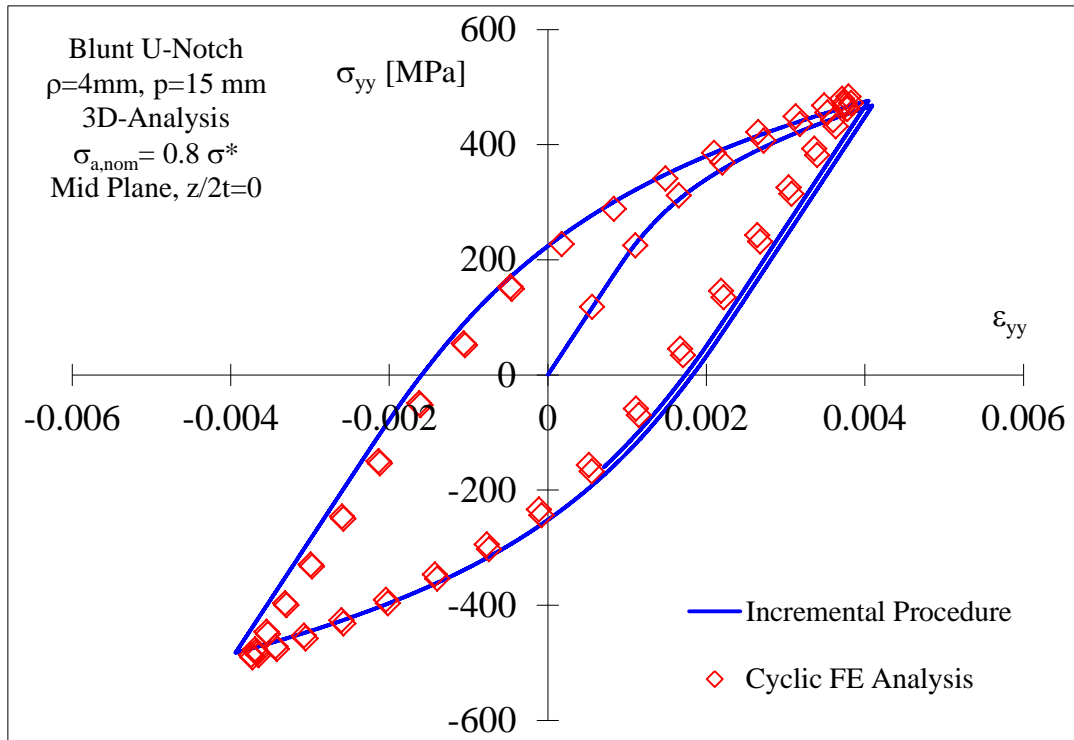


Figure 4.3.14. 3D specimen weakened by double symmetrical U-notches ($\rho = 4\text{ mm}$) subjected to a tension-compression fatigue loading. Comparison between the hysteresis loops at the notch tip, obtained from the incremental procedure and the cyclic FE analyses with reference to (a) mid plane, (b) free surface. $\sigma_{a,nom} = 0.8 \sigma^*$.

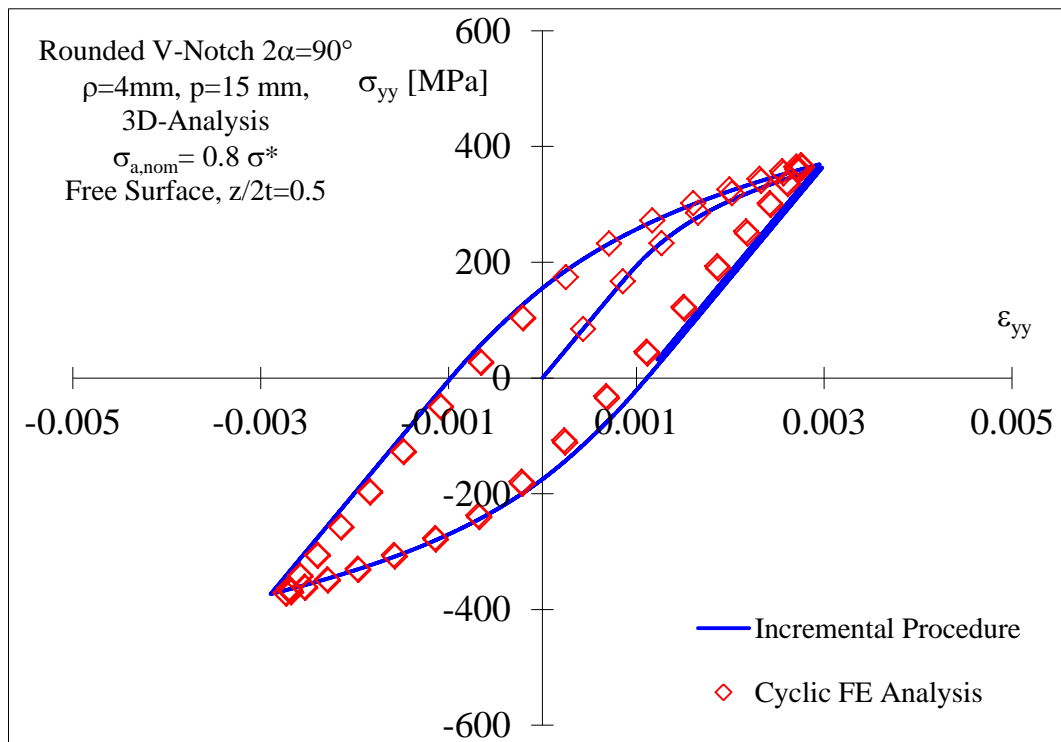
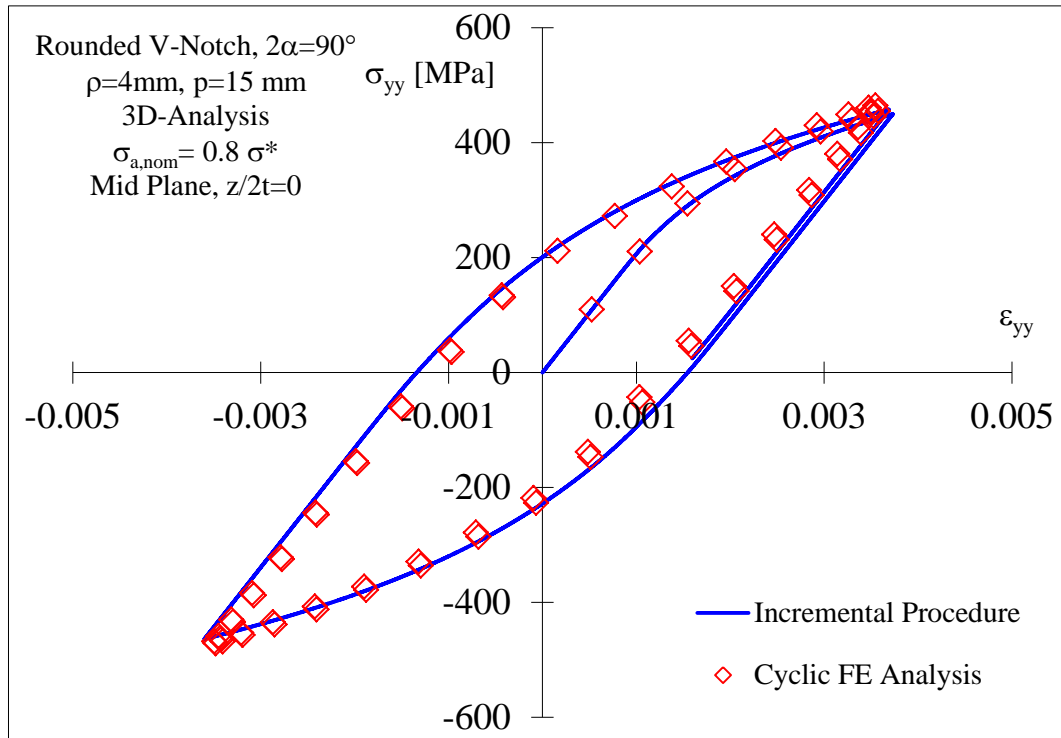


Figure 4.3.15. 3D specimen weakened by double symmetrical rounded V-notches ($\rho = 4 \text{ mm}$, $2\alpha = 90^\circ$) subjected to a tension-compression fatigue loading. Comparison between the hysteresis loops at the notch tip, obtained from the incremental procedure and the cyclic FE analyses with reference to (a) mid plane, (b) free surface. $\sigma_{a,nom} = 0.8 \sigma^*$.

Finally, a flat specimen weakened by double symmetrical rounded V-notches with an opening angle $2\alpha = 90^\circ$, a notch root radius $\rho = 4$ mm and a notch depth $p = 15$ mm has been studied (Fig. 4.3.1c). The specimen has been loaded with a uniaxial fatigue loading characterised by a nominal stress amplitude equal to 0.8 times σ^* . As in the previous cases, only the hysteresis loop tied to the prevailing component of stress and strain has been taken into account. Figs. 4.3.15a-b show, once again, a very good correlation between analytical results and cyclic FE analyses on different normalised “z” coordinates, in fact, approaching the free surface of the specimen the hysteresis loop becomes smaller than that related to the mid plane.

4.3.7.6. Stress-strain state at the tip of a rounded notch subjected to in-plane shear fatigue loading considering a 3D analysis

A three-dimensional thick plate weakened by double symmetrical rounded V-notches ($2\alpha = 120^\circ$), characterized by a notch root radius $\rho = 4$ mm and a notch depth $p = 15$ mm, and subjected to in-plane shear fatigue loading (Fig. 4.3.3) has been considered in order to extend the incremental procedure, based on the cyclic plasticity theory, to the study of the out-of-plane effects.

As already explained in the Introduction, if a notched component of finite thickness is subjected to a nominal mode II loading, an out-of-plane stress component (comparable to a mode III stress component) arises at the notch tip (for example see Fig. 4.3.5 for the case of a blunt V-notch). This effect is strictly related to the contraction/expansion of the specimen due to the Poisson’s ratio [9]. The so-called O-mode follows the through-the-thickness trend shown in Fig. 4.3.5. In particular, the out-of-plane effect ($K_{t,yz}$) does not act on the mid plane and on the free surface of the specimen, while it increases its intensity moving towards the free surface, reaching its maximum value at a normalized through-the-thickness coordinate $z/2t = 0.46$ (for the case taken into account) and then it drops to zero. The theoretical stress concentration factor $K_{t,yz}$ has been defined as the ratio between the stress component induced by the out-of-plane effect (σ_{yz}) through the plate thickness and the nominal in-plane shear stress applied to the model (τ_{nom}). Values of K_t lower than 1 have been obtained because they are linked to induced stresses.

In order to obtain a non-negligible yielded area at the notch tip, a very high nominal in-plane shear stress amplitude has been applied. As it can be noted from Fig. 4.3.5, the maximum intensity of the out-of-plane effect is close to 0.55 times the nominally applied load in a plane close to the free surface. For this reason the nominal in-plane shear stress amplitude has been set equal to $5 \cdot k$, with the aim to amplify the three-dimensional effect.

Starting from the through-the-thickness variation of the “yz” linear-elastic stress concentration factor K_t (obtainable with a 3D linear-elastic FE analysis), the new incremental routine allows us to obtain the whole elastic-plastic stress-strain state at the notch tip.

In particular, three different through-the-thickness normalized coordinates ($z/2t$) have been chosen to compare the results obtained by means of the incremental cyclic plasticity procedure and by means of 3D FE cyclic elastic-plastic analyses, as already done for the problems investigated in the previous sections. As it can be seen from Figs. 4.3.16a-c, the agreement between analytical and numerical results is very satisfactory, being the deviation limited with reference to all the different coordinates along the thickness of the plate. In particular in the case $z/2t = 0.25$ (Fig. 4.3.16a), the percentage deviation is good both for the stress range ($\Delta\sigma$, $\Delta\% = 6.12\%$) and the strain one ($\Delta\gamma$, $\Delta\% = 8.18\%$), while values even lower have been obtained in the case $z/2t = 0.46$ (Fig. 4.3.16b), both for the stress range ($\Delta\sigma$, $\Delta\% = 1.88\%$) and the strain one ($\Delta\gamma$, $\Delta\% = 4.39\%$), and also in the case $z/2t = 0.49$ (Fig. 4.3.16c), both for the stress range ($\Delta\sigma$, $\Delta\% = 1.94\%$) and the strain one ($\Delta\gamma$, $\Delta\% = 1.18\%$).

Fig. 4.3.16a shows the “yz” hysteresis loop at a coordinate $z/2t = 0.25$, in the increasing branch of the curve (Fig. 4.3.5) representing the through-the-thickness trend of the out-of-plane stress concentration factor $K_{t,yz}$. It is worth noting that, in this particular case, the yield condition has been just satisfied and the plastic strains are still very low.

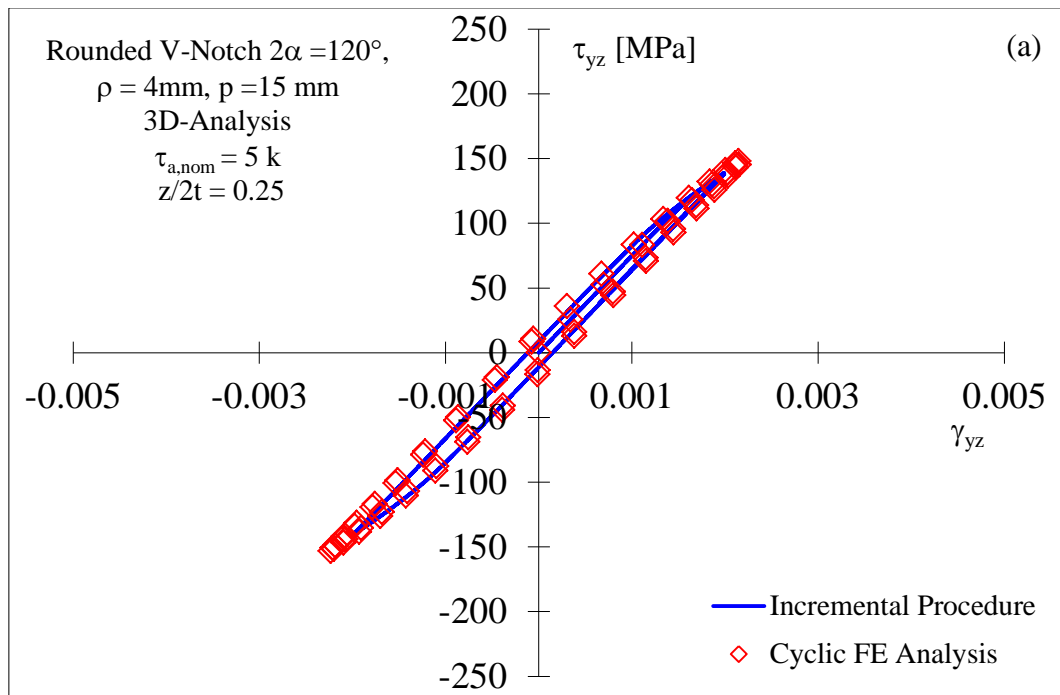
Moving from the mid plane to the free surface, the $K_{t,yz}$ reaches its maximum value at a normalized coordinate $z/2t = 0.46$ (see Fig. 4.3.5). In this case (Fig. 4.3.16b) a very dilated hysteresis loop is obtained, confirming the presence of a

more extended yielded area close to the notch tip. The agreement between analytical and numerical results remains very satisfactory.

Approaching the free surface, the out-of-plane stress concentration factor decreases, equating zero at $z/2t = 0.50$ (see Fig. 4.3.5). Accordingly, the area inside the “yz” hysteresis loop quickly decreases, as it can be observed from the comparison between Fig. 4.3.16b ($z/2t = 0.46$) and Fig. 4.3.16c ($z/2t = 0.49$), up to vanishing on the free surface.

On the basis of the obtained results, it can be stated that the modified incremental cyclic plasticity procedure is sensitive to the three-dimensional effects induced by the application of an in-plane cyclic shear loading.

The obtained results confirm what has already been observed in a recent contribution [132], in which the case of notched components subjected to uniaxial loadings has been analysed.



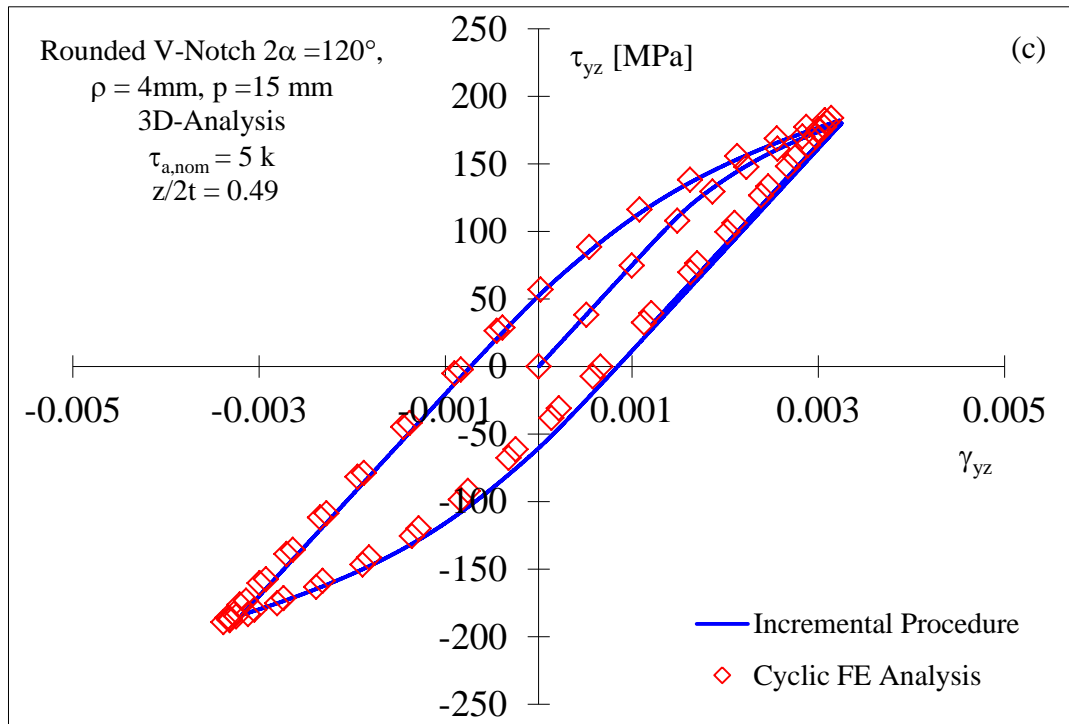
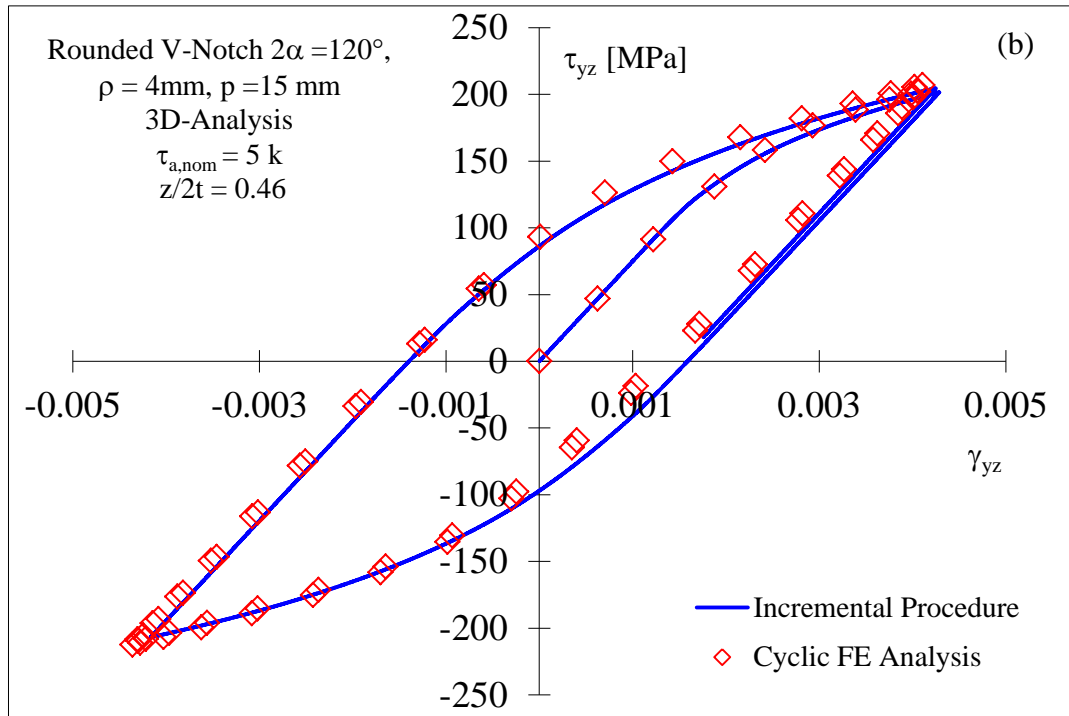


Figure 4.3.16. 3D specimen weakened by double symmetrical rounded V-notch ($\rho = 4$ mm, $2\alpha = 120^\circ$) subjected to in-plane shear (Mode II) fatigue loading. Comparison between the hysteresis loops obtained from the incremental cyclic plasticity procedure and the cyclic FE analyses with reference to (a) $z/2t = 0.25$, (b) $z/2t = 0.46$ and (c) $z/2t = 0.49$. $\tau_{a,nom} = 5$ k.

4.3.8. A link between cyclic plasticity and the averaged strain energy density criterion

In this section the link between the strain energy density (SED) averaged over a control volume surrounding the notch tip [27] and the area inside the hysteresis loops will be investigated. In the past, the SED criterion has been already used in order to find a correspondence between linear elastic and elastic-plastic behaviour. In this context the relation between linear elastic and elastic-plastic notch stress intensity factors has been obtained under plane stress and plane strain conditions [27].

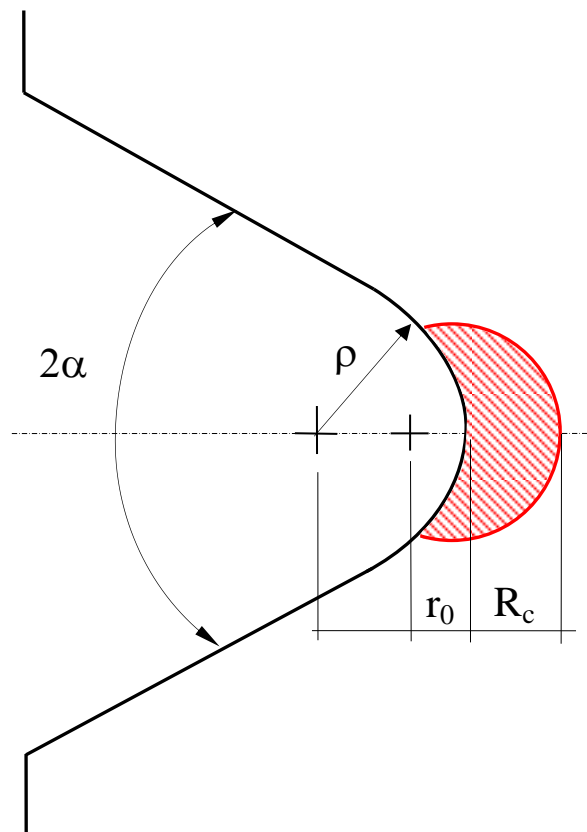


Figure 4.3.17. Control volume under multiaxial loading (tension and torsion) for specimens weakened by rounded V-notches; $r_0 = (q-1)\rho/q$ and $q = (2\pi-2\alpha)/\pi$.

The strain energy density, averaged over the control volume shown in Fig. 4.3.17, has been evaluated with some static FE elastic-plastic analyses performed in Ansys[®]. In all the cases taken into account the static applied load has been set equal to the nominal amplitude of the cyclic loading adopted in the incremental cyclic plasticity procedure. The values of the averaged SED have been obtained for three different control radius ($R_c = 0.1, 0.2$ and 0.3 mm) in order to investigate the influence of this fundamental parameter on the outputs and in addition to ensure the stability of the comparison. In the case of blunt V-notches [29], the control volume assumes the crescent shape shown in Fig. 4.3.17, where R_c is the size of the volume measured along the notch bisector line starting from the notch tip. The outer radius of the crescent shape is equal to $R_c + r_0$, where r_0 depends on the notch opening angle 2α and on the notch radius ρ according to the following expression [29]:

$$r_0 = \frac{q-1}{q} \rho \quad (4.3.28)$$

with q defined as:

$$q = \frac{2\pi - 2\alpha}{\pi} \quad (4.3.29)$$

The elastic-plastic averaged SED is defined as the ratio between the total elastic-plastic strain energy (E), related to the material inside the control volume, and the area of the control volume (A), both evaluated directly from the FE code:

$$SED = \frac{E}{A} \quad (4.3.30)$$

The area inside the hysteresis loops related to one loading cycle (A_{hl}) is defined by Eq. (4.3.31) and it has been evaluated by means of a numerical integration routine applied to the hysteresis loops obtained by means of the incremental cyclic plasticity procedure (see Figs. 4.3.7-4.3.16 for some examples).

$$A_{hl} = \oint \sigma \, d\varepsilon \quad (4.3.31)$$

In the present investigation, it has been thought that only the synergetic presence of a stress component with the related strain component causes a damaging effect. For instance this hypothesis leads to neglect the action of the “xx” strain component. In fact, because of equilibrium conditions, the related stress component holds zero value at the tip of a rounded notch (see Figs. 4.3.1-4.3.3).

In order to obtain a correlation between the averaged SED and the area inside the acting hysteresis loops, four different analyses have been performed. In particular, the problem of cyclic tension-compression loading under plain stress, plain strain and generic three-dimensional conditions as well as the problem of a cyclic multiaxial in-phase tension-torsion loading have been addressed. In the first case studies, a specimen weakened by double symmetrical blunt U-notches with a radius at the notch tip (ρ) equal to 1 mm has been considered. The notch depth p was set equal to 15 mm (see Fig. 4.3.1b). In the last case study, instead, an axis-symmetric specimen weakened by a circumferential blunt U-notch with a notch tip radius ρ equal to 1 mm has been considered. The notch depth p was set equal to 6 mm (see Fig. 4.3.2). The load ratio R has been taken always equal to -1. The material taken into account is the same used for the analyses in Section 4.3.6, namely AISI 304L steel [127].

Several analyses have been carried out by applying different nominal load amplitudes to the notched component, in order to evaluate the trend of the ratio SED/A_{hl} , defined as C_m , between the value of the averaged SED and the area inside the hysteresis loop acting at the notch tip (A_{hl}).

Initially the problem of a 2D flat specimen weakened by double symmetrical blunt U-notches and subjected to cyclic tension-compression loading has been addressed. The obtained results are shown in Fig. 4.3.18, with reference only to a plane strain state for the sake of brevity. From the figure it is evident that, for high values of the nominal applied stress, the parameter C_m tends to an asymptotic constant value. For low loads, instead, the link between the SED and the area inside the hysteresis loop is more complex. Accordingly, for high loads, the area inside the hysteresis loop can be directly determined from the SED value through a multiplicative factor. This behaviour holds true for all the three considered control volumes and, as it can be seen from Fig. 4.3.18, the ratio decreases with

increasing the value of the critical radius. Thus, by adopting the control radius R_c related to the properties of the material taken into account, the plastic strain hysteretic energy, considered to be an index for fatigue damage [117–119], can be easily estimated by means of a static FE analysis. The same analyses have been carried out for a very thin plate (plane stress conditions). Also in this case a plateau value exists at high applied loads, namely when a non-negligible amount of plasticity is present at the notch tip. This value, as expected, is similar to that obtained from the plane strain analysis.

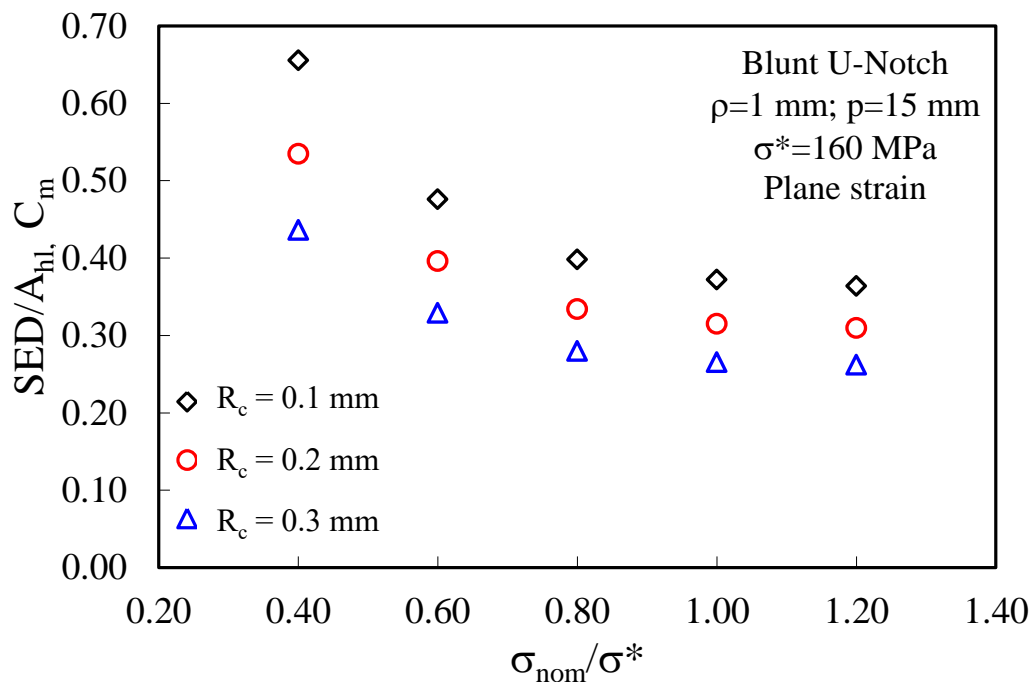


Figure 4.3.18. 2D specimen weakened by double symmetrical U-notches ($\rho = 1$ mm) subjected to a tension-compression fatigue loading. Ratio between the elastic-plastic averaged SED and the area inside the hysteresis loop at the notch tip. Under plane strain conditions.

Since plane stress and plane strain conditions are only “plane idealisations”, the investigation has been extended to the 3D problem of a thick plate weakened by double symmetrical U-shaped notches and subjected to a tension-compression cyclic loading (Fig. 4.3.1b). At the notch tip, two different couples of stress and strain components ($(\sigma_{yy}, \varepsilon_{yy})$ and $(\sigma_{zz}, \varepsilon_{zz})$) act. However, only the hysteresis loop area tied to the “yy” component has been taken into account, being that related to the “zz” component almost negligible (less than 1%).

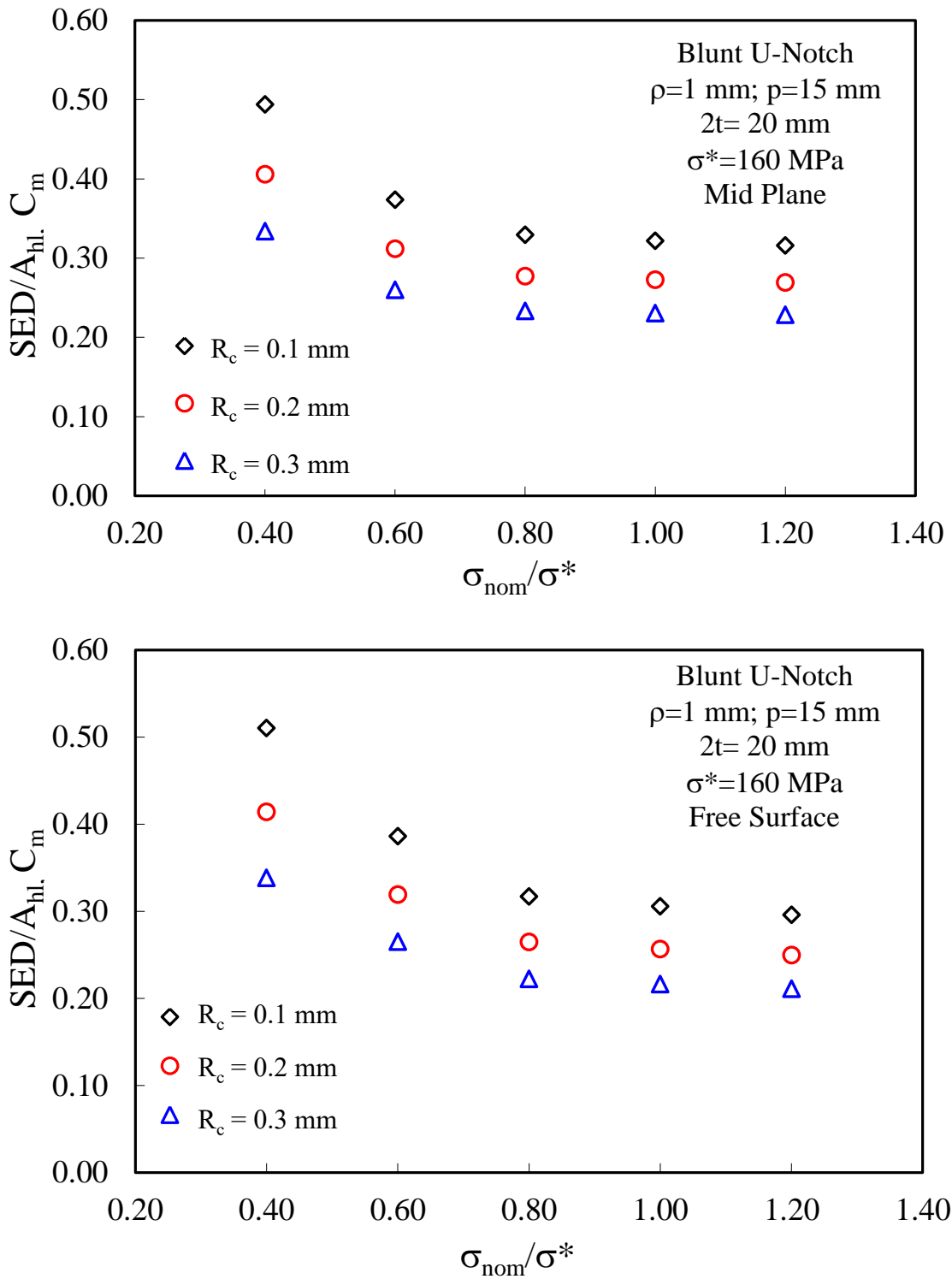


Figure 4.3.19. 3D specimen weakened by double symmetrical U-notches ($\rho = 1$ mm) subjected to a tension-compression fatigue loading. Ratio between the elastic-plastic averaged SED and the area inside the hysteresis loop at the notch tip, with reference to (a) mid plane and (b) free surface.

It is worth mentioning again that, in a thick plate weakened by a blunt notch, the maximum notch tip stress varies as a function of the through-the-thickness coordinate, as a result a variation of the ratio SED/A_{hl} might be present, as well. Accordingly, the correlation factor C_m has been determined on the mid plane ($z/2t = 0$) and on the free surface of the specimen ($z/2t = 0.5$), see Fig. 4.3.19a and 4.3.19b respectively. Also in this case, it is confirmed that the parameter C_m reaches an asymptotic value for high nominal applied stresses, in both locations taken into consideration.

It is also interesting to discuss the through-the-thickness variation of the correlation factor C_m with reference to a control radius R_c equal to 0.3 mm (Fig. 4.3.20). It can be observed that the parameter holds an almost constant value moving from the mid plane to the free surface of the specimen for all the different nominal applied loads.

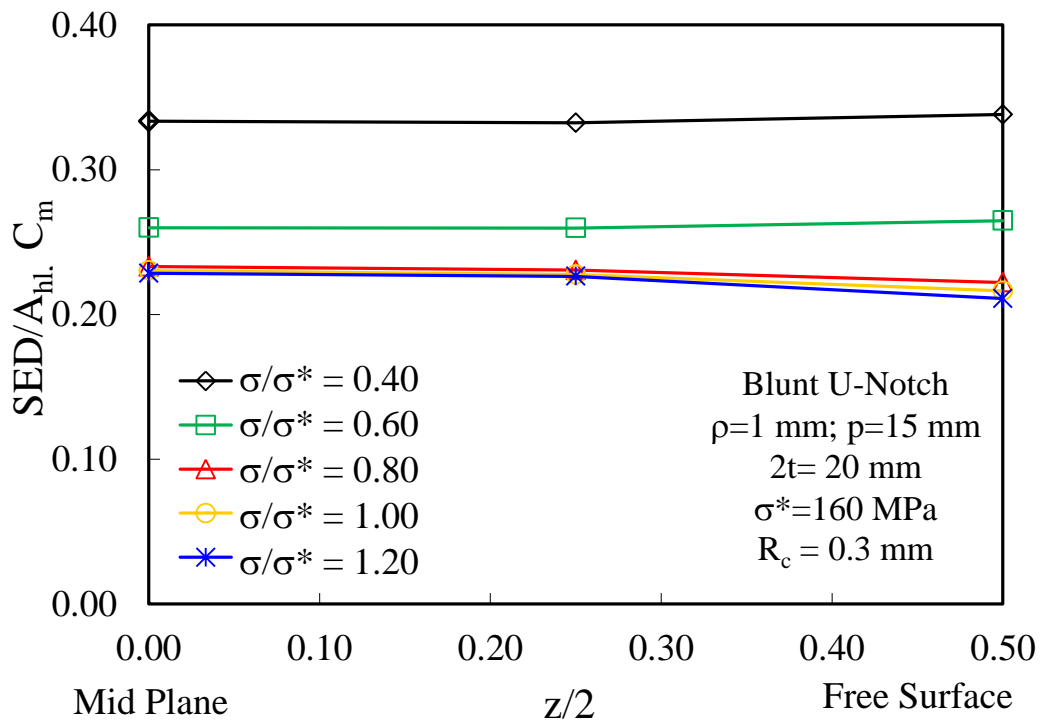


Figure 4.3.20. 3D specimen weakened by double symmetrical U-notches ($\rho = 1$ mm) subjected to a tension-compression fatigue loading. Through the thickness variability of the ratio between the elastic-plastic averaged SED and the area inside the hysteresis loop at the notch tip.

Finally the problem of an axis-symmetric specimen weakened by a circumferential blunt U-notch and subjected to cyclic multiaxial in-phase tension-torsion loading has been addressed (Fig. 4.3.2). Three couples of stress-strain components act at the notch tip, in particular the normal components “yy” and “zz” and the shear component “yz”. Being the hysteresis loop areas comparable, the total area has been thought as the sum of them. The obtained results are shown in Fig. 4.3.21 for different nominally applied loads, where σ_{eq} is the nominal equivalent von Mises stress. It is evident that, for high values of the nominally applied stress, the parameter C_m tends to an asymptotic constant value.

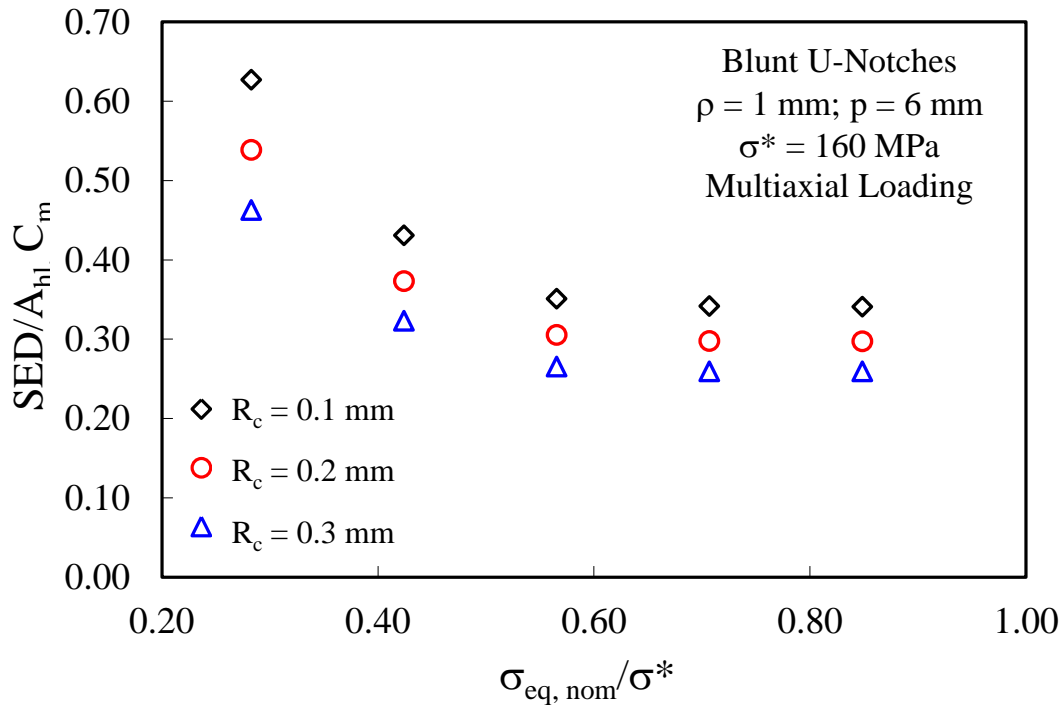


Figure 4.3.21. Cylindrical specimen weakened by a circumferential blunt U-notch ($\rho = 1$ mm and $p = 6$ mm) and subjected to multiaxial (Mode I+III) in-phase fatigue loading. Ratio between the elastic-plastic averaged SED and the area inside the hysteresis loop.

The presence of a plateau creates an interesting link between the hysteresis area and the SED averaged in the control volume, which could not be predicted *a priori*. In the case of low applied loads, instead, the link between the averaged SED and the area of the hysteresis loop is more complex. Accordingly, for high

loads, the total area inside the hysteresis loops can be directly determined by means of the averaged SED *via* a multiplicative factor. This behaviour holds true for all the three considered control volumes and, as it can be seen from Fig. 4.3.21, the ratio decreases with increasing the size of the control radius. Thus, by adopting the proper control radius R_c related to the mechanical properties of the material taken into account, the plastic strain hysteretic energy, considered to be an index for fatigue damage in the literature [117–119], can be easily estimated by means of a static FE analysis.

4.3.9. Discussion

In this work, the incremental cyclic plasticity procedure has been extended with the aim to investigate the three-dimensional effects arising at the tip of a rounded notch subjected to in-plane shear fatigue loading. The incremental cyclic plasticity procedure has been initially validated with a number of bi-dimensional analyses, considering torsional and multiaxial (tension-torsion) in-phase loading conditions. In both cases the theoretical predictions have been compared with FE elastic-plastic analyses showing a very good agreement.

Subsequently, the approach has been extended with the aim of studying three-dimensional effects arising at the notch tip considering plates of finite thickness subjected to in-plane shear fatigue loading and weakened by double symmetrical rounded V-shaped notches.

The through-the-thickness variation of the stress concentration factors, as obtained by a linear-elastic static FE analysis, has been included into the incremental cyclic procedure in order to consider the triaxial nature of the problem. By doing so, the actual stress-strain state on different through-the-thickness coordinates has been evaluated and compared with three-dimensional elastic-plastic FE analyses, obtaining a very good agreement. The results demonstrate that 3D effects related to the presence of a finite thickness in a notched component cannot be neglected *a priori* either in linear-elastic problems or in the presence of a yielded region ahead of the notch tip.

Finally, a link between the averaged strain energy density (SED) criterion and the area inside the hysteresis loops tied to the different stress and strain components

acting at the notch tip has been investigated. Several analyses have been carried out by applying different nominal stress amplitudes in order to evaluate the evolution of the ratio between the averaged SED and the area of the hysteresis loops acting at the notch tip. For high values of the nominally applied stress, the ratio tends to an asymptotic constant value. Accordingly, the plastic strain hysteretic energy, considered in the literature to be a parameter linked to the fatigue damage, can be directly determined by means of the averaged SED, obtained from a static FE analysis, *via* a multiplicative factor (C_m).

The results obtained with reference to notched components subjected to multiaxial loadings confirm those obtained in the case of uniaxial loadings.

References

- [1] Pook LP. Linear elastic fracture mechanics for engineers. Theory and applications. Southampton, UK: WIT Press; 2000.
 - [2] Pook LP. Metal fatigue: what it is, why it matters. vol. 145. Dordrecht: Springer Netherlands; 2007.
 - [3] Timoshenko SP, Goodier JN. Theory of elasticity. 3rd ed. New York, USA: McGraw-Hill Book Company; 1970.
 - [4] Pook LP, Berto F, Campagnolo A, Lazzarin P. Coupled fracture mode of a cracked disc under anti-plane loading. *Eng Fract Mech* 2014;128:22–36.
 - [5] Pook LP, Campagnolo A, Berto F, Lazzarin P. Coupled fracture mode of a cracked plate under anti-plane loading. *Eng Fract Mech* 2015;134:391–403.
 - [6] Pook LP. A 50 year retrospective review of three-dimensional effects at cracks and sharp notches. *Fatigue Fract Eng Mater Struct* 2013;36:699–723.
 - [7] Pook. Crack profiles and corner point singularities. *Fatigue Fract Eng Mater Struct* 2000;23:141–50.
 - [8] Kotousov A, Lazzarin P, Berto F, Harding S. Effect of the thickness on elastic deformation and quasi-brittle fracture of plate components. *Eng Fract Mech* 2010;77:1665–81.
 - [9] Harding S, Kotousov A, Lazzarin P, Berto F. Transverse singular effects in V-shaped notches stressed in mode II. *Int J Fract* 2010;164:1–14.
 - [10] Kotousov A, Berto F, Lazzarin P, Pegorin F. Three dimensional finite element mixed fracture mode under anti-plane loading of a crack. *Theor Appl Fract Mech* 2012;62:26–33.
 - [11] Kotousov A, Lazzarin P, Berto F, Pook LP. Three-dimensional stress states at crack tip induced by shear and anti-plane loading. *Eng Fract Mech* 2013;108:65–74.
 - [12] Zappalorto M, Lazzarin P. Three-dimensional elastic stress fields ahead of notches in thick plates under various loading conditions. *Eng Fract Mech* 2013;108:75–88.
 - [13] Lazzarin P, Zappalorto M. A three-dimensional stress field solution for pointed and sharply radiused V-notches in plates of finite thickness. *Fatigue Fract Eng Mater Struct* 2012;35:1105–19.
 - [14] Williams ML. On the stress distribution at the base of a stationary crack. *J Appl Mech* 1957;24:109–14.
 - [15] Paris PG, Sih GC. Stress analysis of cracks. *Fract. toughness Test. its Appl.* ASTM STP 381, Philadelphia, USA: American Society for Testing and Materials; 1965, p. 30–81.
 - [16] Mandelbrot BM. The fractal geometry of nature. New York, USA: W H Freeman and Company; 1983.
-

- [17] McClintock FA, Irwin GR. Plasticity aspects of fracture mechanics. *Fract. toughness Test. its Appl.* ASTM STP 381, Philadelphia, USA: American Society for Testing and Materials; n.d., p. 84–113.
- [18] Carpinteri A, Spagnoli A. A fractal analysis of size effect on fatigue crack growth. *Int J Fatigue* 2004;26:125–33.
- [19] Irwin GR. Crack-Extension Force for a Part-Through Crack in a Plate. *J Appl Mech* 1962;29:651.
- [20] Bažant ZP, Estenssoro LF. Surface singularity and crack propagation. *Int J Solids Struct* 1979;15:405–26.
- [21] Pook LP. Some implications of corner point singularities. *Eng Fract Mech* 1994;48:367–78.
- [22] Benthem JP. The quarter-infinite crack in a half space; Alternative and additional solutions. *Int J Solids Struct* 1980;16:119–30.
- [23] Pook LP. Crack paths. Southampton, UK: WIT Press; 2002.
- [24] Dhondt G. On corner point singularities along a quarter circular crack subject to shear loading. *Int J Fract* 1998;89:L13–8.
- [25] Hellen TK. How to undertake fracture mechanics analysis with finite elements. Hamilton, Scotland: NAFEMS; 2001.
- [26] Pook LP. A finite element analysis of cracked square plates and bars under antiplane loading. In: de Freitas M, editor. *Fatigue Fract. Eng. Mater. Struct.*, vol. 26, Instituto Superior Técnico, Lisbon, Portugal: 2001, p. 701–8.
- [27] Lazzarin P, Zambardi R. A finite-volume-energy based approach to predict the static and fatigue behavior of components with sharp V-shaped notches. *Int J Fract* 2001;112:275–98.
- [28] Berto F, Lazzarin P. A review of the volume-based strain energy density approach applied to V-notches and welded structures. *Theor Appl Fract Mech* 2009;52:183–94.
- [29] Berto F, Lazzarin P. Recent developments in brittle and quasi-brittle failure assessment of engineering materials by means of local approaches. *Mater Sci Eng R Reports* 2014;75:1–48.
- [30] Lazzarin P, Berto F, Elices M, Gómez J. Brittle failures from U- and V-notches in mode I and mixed, I + II, mode: a synthesis based on the strain energy density averaged on finite-size volumes. *Fatigue Fract Eng Mater Struct* 2009;32:671–84.
- [31] Berto F, Campagnolo A, Elices M, Lazzarin P. A synthesis of Polymethylmethacrylate data from U-notched specimens and V-notches with end holes by means of local energy. *Mater Des* 2013;49:826–33.
- [32] Lazzarin P, Campagnolo A, Berto F. A comparison among some recent energy- and stress-based criteria for the fracture assessment of sharp V-notched components under Mode I loading. *Theor Appl Fract Mech* 2014;71:21–30.

-
- [33] Livieri P, Lazzarin P. Fatigue strength of steel and aluminium welded joints based on generalised stress intensity factors and local strain energy values. *Int J Fract* 2005;133:247–76.
- [34] Berto F, Lazzarin P, Yates JR. Multiaxial fatigue of V-notched steel specimens: A non-conventional application of the local energy method. *Fatigue Fract Eng Mater Struct* 2011;34:921–43.
- [35] Berto F, Campagnolo A, Lazzarin P. Fatigue strength of severely notched specimens made of Ti-6Al-4V under multiaxial loading. *Fatigue Fract Eng Mater Struct* 2015;38:503–17.
- [36] Yosibash Z, Shannon S. Computing edge stress intensity functions (ESIFs) along circular 3-D edges. *Eng Fract Mech* 2014;117:127–51.
- [37] Omer N, Yosibash Z. On the Path Independency of the Point-wise J Integral in Three-dimensions. *Int J Fract* 2005;136:1–36.
- [38] Lazzarin P, Berto F, Zappalorto M. Rapid calculations of notch stress intensity factors based on averaged strain energy density from coarse meshes: Theoretical bases and applications. *Int J Fatigue* 2010;32:1559–67.
- [39] Glushkov E, Glushkova N, Lapina O. 3-D elastic stress singularity at polyhedral corner points. *Int J Solids Struct* 1999;36:1105–28.
- [40] Tang XS, Wei TT. Microscopic inhomogeneity coupled with macroscopic homogeneity: A localized zone of energy density for fatigue crack growth. *Int J Fatigue* 2015;70:270–7.
- [41] Corigliano A, Ghisi A, Langfelder G, Longoni A, Zaraga F, Merassi A. A microsystem for the fracture characterization of polysilicon at the micro-scale. *Eur J Mech - A/Solids* 2011;30:127–36.
- [42] Ardito R, Corigliano A, Frangi A, Rizzini F. Advanced models for the calculation of capillary attraction in axisymmetric configurations. *Eur J Mech - A/Solids* 2014;47:298–308.
- [43] Yang J, Jin X, Jin N. A penny-shaped crack in an infinite linear transversely isotropic medium subjected to uniform anti-symmetric heat flux: Closed-form solution. *Eur J Mech - A/Solids* 2014;47:254–70.
- [44] Tang XS, Sih GC. Weak and strong singularities reflecting multiscale damage: Micro-boundary conditions for free–free, fixed–fixed and free–fixed constraints. *Theor Appl Fract Mech* 2005;43:5–62.
- [45] Tang XS, Sih GC. Equilibrium mechanics model of multiscaling by segmentation: Asymptotic solution for macro-meso-micro damage in anti-plane shear deformation. *Theor Appl Fract Mech* 2005;44:1–15.
- [46] Sih GC, Tang XS. Scaling of volume energy density function reflecting damage by singularities at macro-, meso- and microscopic level. *Theor Appl Fract Mech* 2005;43:211–31.
- [47] Leguillon D. Strength or toughness? A criterion for crack onset at a notch. *Eur J Mech - A/Solids* 2002;21:61–72.
- [48] Murer S, Leguillon D. Static and fatigue failure of quasi-brittle materials at
-

- a V-notch using a Dugdale model. *Eur J Mech - A/Solids* 2010;29:109–18.
- [49] Ayatollahi MR, Dehghany M, Mirsayar MM. A comprehensive photoelastic study for mode I sharp V-notches. *Eur J Mech - A/Solids* 2013;37:216–30.
- [50] Torabi AR, Ayatollahi MR. Compressive brittle fracture in V-notches with end holes. *Eur J Mech - A/Solids* 2014;45:32–40.
- [51] Torabi AR, Pirhadi E. Stress-based criteria for brittle fracture in key-hole notches under mixed mode loading. *Eur J Mech - A/Solids* 2015;49:1–12.
- [52] Nakamura T, Parks DM. Three-Dimensional Stress Field Near the Crack Front of a Thin Elastic Plate. *J Appl Mech* 1988;55:805.
- [53] Nakamura T, Parks DM. Antisymmetrical 3-D stress field near the crack front of a thin elastic plate. *Int J Solids Struct* 1989;25:1411–26.
- [54] Pook L. A finite element analysis of cracked square plates and bars under antiplane loading. *Fatigue Fract Eng Mater ...* 2003:533–41.
- [55] Berto F, Lazzarin P, Kotousov A. On higher order terms and out-of-plane singular mode. *Mech Mater* 2011;43:332–41.
- [56] Berto F, Lazzarin P, Kotousov A, Harding S. Out-of-plane singular stress fields in V-notched plates and welded lap joints induced by in-plane shear load conditions. *Fatigue Fract Eng Mater Struct* 2011;34:291–304.
- [57] Berto F, Kotousov A, Lazzarin P, Pegorin F. On a coupled mode at sharp notches subjected to anti-plane loading. *Eur J Mech - A/Solids* 2013;38:70–8.
- [58] Berto F, Lazzarin P, Marangon C. The effect of the boundary conditions on in-plane and out-of-plane stress field in three dimensional plates weakened by free-clamped V-notches. *Phys Mesomech* 2012;15:26–36.
- [59] Radaj D, Lazzarin P, Berto F. Fatigue assessment of welded joints under slit-parallel loading based on strain energy density or notch rounding. *Int J Fatigue* 2009;31:1490–504.
- [60] Radaj D, Berto F, Lazzarin P. Local fatigue strength parameters for welded joints based on strain energy density with inclusion of small-size notches. *Eng Fract Mech* 2009;76:1109–30.
- [61] Berto F, Lazzarin P. Fatigue strength of structural components under multi-axial loading in terms of local energy density averaged on a control volume. *Int J Fatigue* 2011;33:1055–65.
- [62] Lazzarin P, Berto F, Gomez F, Zappalorto M. Some advantages derived from the use of the strain energy density over a control volume in fatigue strength assessments of welded joints. *Int J Fatigue* 2008;30:1345–57.
- [63] Qian J, Hasebe N. Property of eigenvalues and eigenfunctions for an interface V-notch in antiplane elasticity. *Eng Fract Mech* 1997;56:729–34.
- [64] Dunn ML, Suwito W, Cunningham S. Stress intensities at notch singularities. *Eng Fract Mech* 1997;57:417–30.
-

-
- [65] Gross B, Mendelson A. Plane elastostatic analysis of V-notched plates. *Int J Fract Mech* 1972;8:267–76.
- [66] Seweryn A, Molski K. Elastic stress singularities and corresponding generalized stress intensity factors for angular corners under various boundary conditions. *Eng Fract Mech* 1996;55:529–56.
- [67] Beltrami E. Sulle condizioni di resistenza dei corpi elastici. *Il Nuovo Cimento* 18 (in Italian); 1885.
- [68] Schleicher F. Der Spannungszustand an der Fließgrenze (Plastizitätsbedingung). *Z Angew Math Mech* 1926;6:199–216.
- [69] Williams ML. Stress singularities resulting from various boundary conditions in angular corners of plates in tension. *J Appl Mech* 1952;19:526–8.
- [70] Irwin GR. Analysis of stresses and strains near the end of a crack traversing a plate. *J Appl Mech* 1957;24:361–4.
- [71] Serpieri R, Sacco E, Alfano G. A thermodynamically consistent derivation of a frictional-damage cohesive-zone model with different mode I and mode II fracture energies. *Eur J Mech - A/Solids* 2015;49:13–25.
- [72] Marsavina L, Sadowski T, Knec M. Crack propagation paths in four point bend Aluminium–PMMA specimens. *Eng Fract Mech* 2013;108:139–51.
- [73] Marsavina L, Constantinescu DM, Linul E, Apostol DA, Voiconi T, Sadowski T. Refinements on fracture toughness of PUR foams. *Eng Fract Mech* 2014;129:54–66.
- [74] Hardrath F, Ohman L. A study of elastic and plastic stress concentration factors due to notches and fillets in flat plates. *NASA TC* 1117 1953.
- [75] Stowell EZ. Stress and strain concentration at a circular hole in an infinite plate. *NACA TN* 2073 1950.
- [76] Neuber H. Theory of Stress Concentration for Shear-Strained Prismatical Bodies With Arbitrary Nonlinear Stress-Strain Law. *J Appl Mech* 1961;28:544.
- [77] Molski K, Glinka G. A method of elastic-plastic stress and strain calculation at a notch root. *Mater Sci Eng* 1981;50:93–100.
- [78] Wetzel RM. Smooth specimen simulation of the fatigue behavior of notches. *J Mater Am Soc Test Mater* 1968;3:646–57.
- [79] Topper TH, Wetzel RM, Morrow J. Neuber's rule applied to fatigue of notched specimens. *J Mater* 1969;4:200.
- [80] Zappalorto M, Lazzarin P. A unified approach to the analysis of nonlinear stress and strain fields ahead of mode III-loaded notches and cracks. *Int J Solids Struct* 2010;47:851–64.
- [81] Moftakhar A, Buczynski A, Glinka G. Calculation of elasto-plastic strains and stresses in notches under multiaxial loading. *Int J Fract* 1995;70:357–73.
-

- [82] Singh MNK, Glinka G, Dubey RN. Elastic-plastic stress-strain calculation in notched bodies subjected to non-proportional loading. *Int J Fract* 1996;76:39–60.
- [83] Ince A, Glinka G. A numerical method for elasto-plastic notch-root stress-strain analysis. *J Strain Anal Eng Des* 2013;48:229–44.
- [84] Hoffmann M, Seeger T. A Generalized Method for Estimating Multiaxial Elastic-Plastic Notch Stresses and Strains, Part 1: Theory. *J Eng Mater Technol* 1985;107:250.
- [85] Ellyin F, Kujawski D. Generalization of notch analysis and its extension to cyclic loading. *Eng Fract Mech* 1989;32:819–26.
- [86] Ye D, Hertel O, Vormwald M. A unified expression of elastic–plastic notch stress–strain calculation in bodies subjected to multiaxial cyclic loading. *Int J Solids Struct* 2008;45:6177–89.
- [87] Weixing Y. On the notched strength of composite laminates. *Compos Sci Technol* 1992;45:105–10.
- [88] Shang D. Local stress–strain field intensity approach to fatigue life prediction under random cyclic loading. *Int J Fatigue* 2001;23:903–10.
- [89] Bentachfine S. Notch effect in low cycle fatigue. *Int J Fatigue* 1999;21:421–30.
- [90] Ye D, Matsuoka S, Suzuki N, Maeda Y. Further investigation of Neuber’s rule and the equivalent strain energy density (ESED) method. *Int J Fatigue* 2004;26:447–55.
- [91] Drucker DC. Plasticity in structural mechanics. In: Hoff G and, editor. *Proceeding First Symp. Nav. Struct. Mech.*, New York: Pergamon, Macmillan; 1960, p. 331–50.
- [92] Prager W. The theory of plasticity: a survey of recent achievements. *Arch Proc Inst Mech Eng 1847-1982 (vols 1-196)* 1955;169:41–57.
- [93] Armstrong P., Frederick CO. A mathematical representation of the multiaxial Bauschinger effect. Rep RD/B/N 731, Cent Electr Gener Board 1966.
- [94] Bower AF. Some aspects of plastic flow, residual stress and fatigue cracks due to rolling and sliding contact. University of Cambridge, 1987.
- [95] Bower AF, Johnson KL. The influence of strain hardening on cumulative plastic deformation in rolling and sliding line contact. *J Mech Phys Solids* 1989;37:471–93.
- [96] Ohno N, Wang JD. Non linear kinematic hardening rule: proposition and application to ratchetting problems. *Struct. Mech. React. Technol. Trans. 11th Int. Conf. Struct. Mech. React. Technol.*, Shibata: 1991.
- [97] Chaboche JL, Dang Van K, Cordier G. Modelization of the strain memory effect on the cyclic hardening of the 316 stainless steel. *Structural Mechanical in Reactor Technology. Struct. Mech. React. Technol. Trans. 5th Int. Conf. Struct. Mech. React. Technol.*, Berlin: 1979.

-
- [98] Chaboche JL. Cyclic plasticity modelling and ratchetting effects. Proc. Second Int. Conf. Const. laws Eng. Mater. Theory Appl., Tucson, Arizona: Elsevier Ltd; 1987, p. 47–58.
- [99] Jiang Y, Sehitoglu H. Modeling of Cyclic Ratchetting Plasticity, Part I: Development of Constitutive Relations. *J Appl Mech* 1996;63:720.
- [100] Jiang Y, Sehitoglu H. Modeling of Cyclic Ratchetting Plasticity, Part II: Comparison of Model Simulations With Experiments. *J Appl Mech* 1996;63:726.
- [101] Jiang Y, Xu B. Deformation analysis of notched components and assessment of approximate methods. *Fatigue Fract Eng Mater Struct* 2001;24:729–40.
- [102] Qiu B, Gao Z, Wang X. Fatigue Life Prediction of Notched Components Based on Multiaxial Local Stress-Strain Approach. Vol. 6 *Mater. Fabr. Parts A B*, ASME; 2009, p. 183–9.
- [103] Firat M. A notch strain calculation of a notched specimen under axial-torsion loadings. *Mater Des* 2011;32:3876–82.
- [104] Firat M. Cyclic plasticity modeling and finite element analyzes of a circumferentially notched round bar under combined axial and torsion loadings. *Mater Des* 2012;34:842–52.
- [105] Gao Z, Qiu B, Wang X, Jiang Y. An investigation of fatigue of a notched member. *Int J Fatigue* 2010;32:1960–9.
- [106] Pook LP. The linear elastic analysis of cracked bodies and crack paths. *Theor Appl Fract Mech* 2015.
- [107] Berto F, Marangon C. Three-dimensional effects in finite thickness plates weakened by rounded notches and holes under in-plane shear. *Fatigue Fract Eng Mater Struct* 2013;36:1139–52.
- [108] Ayatollahi MR, Mirsayar MM, Deghany M. Experimental determination of stress field parameters in bi-material notches using photoelasticity. *Mater Des* 2011;32:4901–8.
- [109] Mirsayar MM. On fracture of kinked interface cracks – The role of T-stress. *Mater Des* 2014;61:117–23
- [110] Torabi AR, Campagnolo A, Berto F. Experimental and theoretical investigation of brittle fracture in key-hole notches under mixed mode I/II loading. *Acta Mech* 2015;226:2313–22.
- [111] Torabi AR, Campagnolo A, Berto F. Local strain energy density to predict mode II brittle fracture in Brazilian disk specimens weakened by V-notches with end holes. *Mater Des* 2014;69:22–9.
- [112] Torabi AR, Campagnolo A, Berto F. Mode II Brittle Fracture Assessment of Key-Hole Notches by Means of the Local Energy. *J Test Eval* 2016;44.
- [113] Berto F, Lazzarin P, Marangon C. Fatigue strength of notched specimens made of 40CrMoV13.9 under multiaxial loading. *Mater Des* 2014;54:57–66.
-

- [114] Gallo P, Berto F, Lazzarin P. High temperature fatigue tests of notched specimens made of titanium Grade 2. *Theor Appl Fract Mech* 2015;76:27–34.
- [115] Lazzarin P, Berto F, Atzori B. A synthesis of data from steel spot welded joints of reduced thickness by means of local SED. *Theor Appl Fract Mech* 2013;63-64:32–9.
- [116] Campagnolo A, Berto F, Lazzarin P. The effects of different boundary conditions on three-dimensional cracked discs under anti-plane loading. *Eur J Mech - A/Solids* 2015;50:76–86.
- [117] Ellyin F, Kujawski D. Plastic Strain Energy in Fatigue Failure. *J Press Vessel Technol* 1984;106:342.
- [118] Feltner CE, Morrow JD. Microplastic Strain Hysteresis Energy as a Criterion for Fatigue Fracture. *J Basic Eng* 1961;83:15.
- [119] Ellyin F. A criterion for fatigue under multiaxial states of stress. *Mech Res Commun* 1974;1:219–24.
- [120] Chu C-C. Incremental Multiaxial Neuber Correction for Fatigue Analysis. SAE Tech Pap 1995.
- [121] Jiang Y, Kurath P. Characteristics of the Armstrong-Frederick type plasticity models. *Int J Plast* 1996;12:387–415.
- [122] Jiang Y. Cyclic plasticity with an emphasis on ratchetting. University of Illinois at Urbana Champagne, 1994.
- [123] Sethuraman R, Viswanadha Gupta S. Evaluation of notch root elasto-plastic stress–strain state for general loadings using an elastic solution. *Int J Press Vessel Pip* 2004;81:313–25.
- [124] Li Z, Guo W. Three-dimensional elastic stress fields ahead of blunt V-notches in finite thickness plates. *Int J Fract* n.d.;107:53–71.
- [125] Li Z, Guo W, Kuang Z. Three-dimensional elastic stress fields near notches in finite thickness plates. *Int J Solids Struct* 2000;37:7617–32.
- [126] Chaboche JL. On some modifications of kinematic hardening to improve the description of ratchetting effects. *Int J Plast* 1991;7:661–78.
- [127] Meneghetti G, Ricotta M. The use of the specific heat loss to analyse the low- and high-cycle fatigue behaviour of plain and notched specimens made of a stainless steel. *Eng Fract Mech* 2012;81:2–16.
- [128] Jiang Y, Kurath P. Nonproportional cyclic deformation: critical experiments and analytical modeling. *Int J Plast* 1997;13:743–63.
- [129] Sheldon I. Chaboche Nonlinear Kinematic Hardening Model. Memo Number STI0805A, ANSYS 2008. http://ansys.net/tips_sheldon/STI0805_Chaboche.pdf.
- [130] Chaboche JL. Time-independent constitutive theories for cyclic plasticity. *Int J Plast* 1986;2:149–88.
- [131] Chaboche JL. A review of some plasticity and viscoplasticity constitutive

theories. *Int J Plast* 2008;24:1642–93.

- [132] Marangon C, Campagnolo A, Berto F. Three-dimensional effects at the tip of rounded notches subjected to mode-I loading under cyclic plasticity. *J Strain Anal Eng Des* 2015;50:299–313.

CHAPTER 5

COMPARISON AMONG FRACTURE CRITERIA FOR SHARP V-NOTCHES

5.1 Comparison among energy-based criteria for fracture assessment of sharp V-notched components under Mode I loading ^(*)

Nomenclature

E	Young's modulus
G	Strain Energy Release Rate
K	scale factor dependent on the local geometry and the direction of fracture
K_I	Mode I Notch Stress Intensity Factor
k_I	NSIF according to Leguillon's definition
K_I^*	NSIF according to Carpinteri's definition
K_{Ic}	Mode I Notch Stress Intensity Factor at failure
K_{Ic}	fracture toughness
l_c	length of the incremental crack according to Leguillon
r, θ	polar coordinates
R_c	control radius for averaged SED evaluation
\bar{W}	SED averaged over the control volume
W_c	critical SED value of the considered material under tensile loading

Symbols

2α	notch opening angle
Δ_{SE}	length of the crack nucleated at the notch tip according to Carpinteri
λ_I	Mode I Williams' eigenvalue
ν	Poisson's ratio
$\bar{\theta}_c$	fracture direction
σ	stress, subscripts $rr, \theta\theta, zz$ denote normal stresses subscript $r\theta$ denote shear stresses
σ_c	ultimate tensile strength

(*) See also:

Lazzarin, P; Campagnolo, A.; Berto, F. A comparison among some recent energy- and stress-based criteria for the fracture assessment of sharp V-notched components under Mode I loading. *Theoretical and Applied Fracture Mechanics*; 71:21-30 (2014);

5.1.1. Introduction

A key issue in fracture mechanics is associated with the formulation of a sufficiently simple and accurate criterion for crack nucleation and propagation in structural elements under static and fatigue loading. For what concern structural elements weakened by cracks, the fracture initiation is generally determined by a critical value of the mode I stress intensity factor K_I , associated with the opening crack mode loading: under plane strain conditions the critical value to failure is the material fracture toughness K_{Ic} . This fracture criterion has been first formalised by Irwin [1]. For cracked elements subjected to mode I loading, a well-known link exists between the Irwin criterion and the Griffith criterion [2]. The latter assumes that failure occurs when the strain energy release rate G , defined as the derivative of the potential energy with respect to the crack surface area, reaches the critical value G_c , a material dependent parameter, which represents the energy needed to create a unit crack surface area.

Criteria able to assess the brittle failure of sharply notched components, with the notch tip radius being zero or close to zero, have received much interest in the last decades. To state a sufficiently simple and reliable condition to predict failure initiation in cases involving points of stress singularity remains a topic of active research. At such points local stresses tend to infinity under linear elastic hypotheses so that, in analogy to the crack case, it is necessary to introduce a stress field parameter, the notch stress intensity factor (NSIF), which depends on the loading mode, the notch opening angle and the geometry of the component. In the linear elastic Notch Mechanics, NSIFs are generally used to assess the static failure of brittle components weakened by sharp V-notches [3–11]. Among these references it is notable the investigation carried out by Leicester [3] who emphasized the scale effect in wood structures with V-notches in the ambit of a project financed by the Australian Forest Production Laboratory. Dealing with the

fatigue crack initiation conditions of components with V-notches other references are also available [12–15]. When fatigue life is consumed as microcrack initiation and propagation inside the zone governed by the V-notch singularity, NSIFs can be used also for total fatigue life assessments, as documented for welded joints [16–18].

For a better understanding of the V-notch problem, it is useful to remember some stress-based criteria proposed in the last twenty years. Starting from a previous work due to Novozhilov [19], Seweryn proposed a brittle fracture criterion based on the assumption that crack nucleation or propagation occurs when the mean value of normal stress over a specified segment d_0 reaches a limit value for the material (Seweryn, 1994 [7]). Afterwards, this criterion has been extended and applied also to structural elements subjected to mixed mode loading ([20,21]) by introducing a non local failure function combining normal and shear stress components, both normalized with respect to the relevant critical stresses of the material.

A group of methodologies is represented by the Theory of Critical Distances (TCD) [22,23], according to which a characteristic material length parameter has to be used when performing fracture assessments on any kind of stress risers. The TCD assumes as a fracture parameter the normal stress calculated on a point at a specified distance from the notch tip (Point-Method) or the same stress averaged over a specified segment (Line-Method).

By proceeding on parallel tracks, critical distance and line dimensions for notched components under fatigue limit conditions were correlated in [24,25] to the El-Haddad parameter a_0 [26]. The idea of stress averaging is the basis of Neuber's fictitious notch rounding (FNR) approach [27]. Recently, the influence of plane stress or plane strain conditions on the multiaxiality factor, s , was highlighted in Ref. [28,29], as well as the essential role played by the V-notch opening angle.

Worth mentioning is also the Cohesive Zone Model (CZM) sometimes called 'fictitious crack model'. First proposed for concrete, the CZM was later successfully extended to a number of brittle or quasi-brittle materials [30,31]. In these works both sharp and blunt U and V-notches were considered, under different loading conditions.

Finally, concluding this short review, some criteria based on the extension of J-integral to notches [32,33] and on the modified Maximum Tangential Stress criterion [34,35] able to take into account singular and non-singular stress terms of Williams' solution are mentioned.

In the present investigation, two recent failure criteria involving energy-based calculations are discussed in detail with reference to sharp V-notches, that based on the averaged SED [36–39] and that called Finite Fracture Mechanics criterion, according to two different version, the former due to Leguillon [40,41], the latter due to Carpinteri et al. [42], as extension to V-notches of the crack case solution [43]. Extensions to in-plane mixed mode loading have been reported in the recent literature [44,45].

The averaged SED criterion was first proposed in [36] and is based on the idea that the critical parameter for the material is the mean value of strain energy density evaluated over a control volume surrounding the notch tip. The method is reminiscent of Neuber's concept of elementary structural volume [27] and Sih's criterion based on factor S , which gives the strain energy density multiplied by a convenient distance from the crack or the V-notch tip [46,47]. It is obvious that any strain energy density approach cannot be used at the tip of a sharp V-notch since not only do stresses tend toward infinite but so does the strain energy density. On the contrary, in a small but finite volume of material close to the notch tip the energy always has a finite value and the main question is rather that of estimating the size of this characteristic volume as a function of the material and loading conditions [38,39].

The major advantage of the averaged SED approach with respect to the local stress-based criteria is the mesh independency. While some parameters integrated in the local criteria (e.g. maximum principal stress, hydrostatic stress, deviatoric stress) require the accurate stress field determination, the SED averaged over a control volume is substantially insensitive to the mesh refinement [48,49] and can easily take into account also coupled three-dimensional effects [50,51]. Other advantages of the total strain energy density have been underlined by other researchers. In [52], extending previous analyses [48,49], the SED approach has been used in combination with two separate volumes, located over and below the

crack or the V-notch bisector line, to compute the stress intensity factors (SIFs) and NSIFs for isotropic homogeneous and bi-material plates containing cracks and notches under mode I, II and III loading conditions. In [53] a novel contribution of an energy-based method has been provided for simulating 3D crack evolution on the basis of the first-order variation of energy release rate with respect to crack advance.

In the framework of Finite Fracture Mechanics, the criteria by Leguillon [40,41] and Carpinteri et al. [42] require the simultaneous verification of two separate conditions, the former based on stresses, the latter on an energy balance. Each condition is necessary but not sufficient to guarantee the fracture. When both conditions are simultaneously satisfied it is possible to get a sufficient condition for fracture. The governing idea is that at failure a finite incremental crack (or a finite crack advance) occurs at the notch tip.

Leguillon [40,41] proposed a failure criterion for components weakened by sharp V-notches based on a combination of the Griffith criterion (in the incremental form) and the stress criterion, in order to determine the incremental crack length and the critical value of the Notch Stress Intensity Factor as a function of the material properties and the V-notch opening angle. Also Carpinteri et al. [42], in analogy to Leguillon, proposed a fracture criterion based on a combination of the energy criterion (critical strain energy release rate) and the averaged stress criterion, which enables to determine the incremental crack length and the critical value of the Notch Stress Intensity Factor. One should note that the two criteria are based on the same energy balance calculated considering a finite incremental crack, the difference being in the stress calculations: the first involves a point-wise stress condition, the second considers an average stress condition.

After having briefly summarized the analytical frame in terms of singular stress fields at V-notch tip, strain energy density averaged in a finite size volume and strain energy release rate, the three published brittle fracture criteria are compared. The analytical comparison is performed on the basis of the different expressions proposed for the critical Notch Stress Intensity Factor.

Finally, the considered criteria are applied to components weakened by sharp V-notches under mode I loading conditions in order to investigate the predictive

capability of each approach. The comparison involves a number of experimental data taken from the literature and related to different materials.

5.1.2. Analytical frame

With the aim of clarifying the bases of the failure criteria analysed in this work, this section summarises the analytical frame giving the expressions of the singular stress fields at V-notch tip, the SED averaged in the control volume and the strain energy release rate. Only Mode I loading conditions are taken into account, considering an isotropic and homogeneous material under linear elastic conditions.

5.1.2.1. Singular stress fields at V-notch tip

In the presence of a sharp (zero notch tip radius) V-notch, the stress distributions (Fig. 5.1.1a) due to a symmetric loading with respect to the notch bisector (Mode I) are [54,55]:

$$\begin{aligned} & \begin{Bmatrix} \sigma_{\theta\theta} \\ \sigma_{rr} \\ \sigma_{r\theta} \end{Bmatrix} \\ &= \frac{K_1 \cdot r^{\lambda_1-1}}{\sqrt{2\pi}} \frac{1}{(1 + \lambda_1) + \chi_1(1 - \lambda_1)} \begin{Bmatrix} ((1 + \lambda_1) \cos(1 - \lambda_1)\theta) \\ (3 - \lambda_1) \cos(1 - \lambda_1)\theta \\ ((1 - \lambda_1) \sin(1 - \lambda_1)\theta) \end{Bmatrix} \\ &+ \chi_1(1 - \lambda_1) \begin{Bmatrix} \cos(1 + \lambda_1)\theta \\ -\cos(1 + \lambda_1)\theta \\ \sin(1 + \lambda_1)\theta \end{Bmatrix} = \frac{K_1 \cdot r^{\lambda_1-1}}{\sqrt{2\pi}} \begin{Bmatrix} \tilde{\sigma}_{\theta\theta}^{(1)} \\ \tilde{\sigma}_{rr}^{(1)} \\ \tilde{\sigma}_{r\theta}^{(1)} \end{Bmatrix} \end{aligned} \quad (5.1.1)$$

where the parameter K_1 represents the Mode I Notch Stress Intensity Factor (NSIF) according to Gross and Mendelson's definition [56], λ_1 is the Mode I Williams' eigenvalue [54], χ_1 is an auxiliary parameter dependent on the notch opening angle 2α [55] while $\tilde{\sigma}_{\theta\theta}^{(1)}$, $\tilde{\sigma}_{rr}^{(1)}$ and $\tilde{\sigma}_{r\theta}^{(1)}$ represent the angular stress

functions for Mode I loading. Plane stress and plane strain conditions result in $\sigma_{zz} = 0$ and $\sigma_{zz} = \nu(\sigma_{\theta\theta} + \sigma_{rr})$, respectively.

5.1.2.2. Strain energy density

According to Beltrami [57], the total strain energy density (SED) is equal to the total work done by the system and is given by the Eq. (5.1.2). For a three dimensional state of stress:

$$W(r, \theta) = \frac{1}{2E} [\sigma_{11}^2 + \sigma_{22}^2 + \sigma_{33}^2 - 2\nu(\sigma_{11}\sigma_{22} + \sigma_{11}\sigma_{33} + \sigma_{22}\sigma_{33})] \quad (5.1.2)$$

where σ_{11} , σ_{22} and σ_{33} are the principal stresses in a given reference system.

In the case of V-notched plate in Mode I, when only the contribution of the first singular term is significant, the SED can be directly linked to the NSIF, K_1 , by substituting into Eq. (5.1.2) the singular stress field given by Eq. (5.1.1):

$$\begin{aligned} W_1(r, \theta) = \frac{1}{2E} r^{2(\lambda_1-1)} K_1^2 & \left[\tilde{\sigma}_{\theta\theta}^{(1)2} + \tilde{\sigma}_{rr}^{(1)2} + \tilde{\sigma}_{zz}^{(1)2} \right. \\ & - 2\nu(\tilde{\sigma}_{\theta\theta}^{(1)}\tilde{\sigma}_{rr}^{(1)} + \tilde{\sigma}_{\theta\theta}^{(1)}\tilde{\sigma}_{zz}^{(1)} + \tilde{\sigma}_{rr}^{(1)}\tilde{\sigma}_{zz}^{(1)}) \\ & \left. + 2(1 + \nu)\tilde{\sigma}_{r\theta}^{(1)2} \right] \end{aligned} \quad (5.1.3)$$

The strain energy density, averaged in a circular sector of radius R_c surrounding the notch tip (Fig. 5.1.1b), is given by the ratio between the elastic strain energy $E(R_c)$ and the area of the circular sector $A(R_c)$:

$$\begin{aligned} \bar{W} = \frac{E(R_c)}{A(R_c)} &= \frac{\int_A W dA}{\int_A dA} = \frac{\int_0^{R_c} \int_{-\gamma}^{+\gamma} W_1(r, \theta) r dr d\theta}{\int_0^{R_c} \int_{-\gamma}^{+\gamma} r dr d\theta} = \frac{\frac{1}{E} \frac{I_1(\gamma)}{4\lambda_1} K_1^2 R_c^{2\lambda_1}}{R_c^2 \gamma} \\ &= \frac{1}{E} e_1 K_1^2 R_c^{2(\lambda_1-1)} \end{aligned} \quad (5.1.4)$$

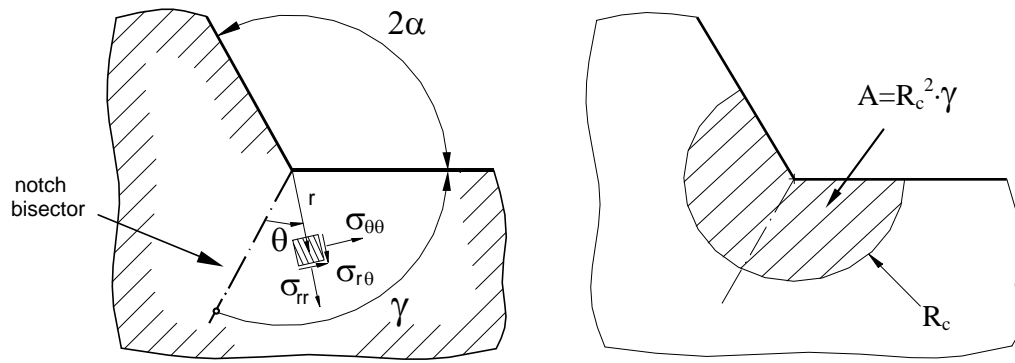


Figure 5.1.1 Polar coordinate system centred at the notch tip (a) and control volume (area) of radius R_c surrounding the V-notch tip.

where I_1 is the integral of the angular stress functions, which depends on the notch opening angle, $2\alpha = 2\pi - 2\gamma$, and the Poisson's ratio ν . I_1 changes under plane stress or plane strain conditions. Finally, e_1 is the parameter that summarizes the dependence from the notch geometry:

$$I_1(\gamma) = \int_{-\gamma}^{+\gamma} \left(\tilde{\sigma}_{\theta\theta}^{(1)2} + \tilde{\sigma}_{rr}^{(1)2} + \tilde{\sigma}_{zz}^{(1)2} - 2\nu \left(\tilde{\sigma}_{\theta\theta}^{(1)} \tilde{\sigma}_{rr}^{(1)} + \tilde{\sigma}_{\theta\theta}^{(1)} \tilde{\sigma}_{zz}^{(1)} + \tilde{\sigma}_{rr}^{(1)} \tilde{\sigma}_{zz}^{(1)} \right) + 2(1 + \nu) \tilde{\sigma}_{r\theta}^{(1)2} \right) d\theta \quad (5.1.5)$$

$$e_1(2\alpha) = \frac{I_1(\gamma)}{4\lambda_1\gamma} \quad (5.1.6)$$

Values of e_1 for plane strain conditions are given in Table 5.1.1 as a function of the V-notch opening angle [38,39]. The averaged value of the strain energy density needs the evaluation of a control radius value, which depends on the material, and varies under static and high cycle fatigue conditions loading [38,39].

Table 5.1.1 Values of the function $e_1(2\alpha, \nu)$.

2α (degrees)	λ	$e_1(\nu = 0.2)$	$e_1(\nu = 0.3)$	$e_1(\nu = 0.4)$
0	0.5000	0.1623	0.1345	0.1003
15	0.5002	0.1687	0.1400	0.1046
20	0.5004	0.1706	0.1417	0.1061
30	0.5014	0.1739	0.1448	0.1091
40	0.5035	0.1764	0.1475	0.1119
45	0.5050	0.1772	0.1485	0.1131
60	0.5122	0.1780	0.1504	0.1162
75	0.5247	0.1806	0.1498	0.1179
80	0.5304	0.1739	0.1490	0.1179
90	0.5445	0.1693	0.1462	0.1174
100	0.5628	0.1631	0.1421	0.1158
105	0.5739	0.1593	0.1394	0.1145
120	0.6157	0.1459	0.1296	0.1090
135	0.6736	0.1298	0.1172	0.1010
140	0.6972	0.1241	0.1127	0.0979
150	0.7520	0.1122	0.1030	0.0909
160	0.8187	0.1002	0.0930	0.0834
170	0.9000	0.0882	0.0828	0.0758
180	1.0000	0.0771	0.0730	0.0673

5.1.2.3. Strain energy release rate

Consider a loaded body initially in an equilibrium state: it is characterized by a potential energy W_p and a kinetic energy $W_k = 0$. After the nucleation of a new crack, or the propagation of a pre-existing crack, there is a change in the potential and kinetic energy of the body. A balance between the internal and external work gives:

$$dW_{\text{int}} = dU + dW_k + dW_s = dW_{\text{ext}} \quad \Rightarrow$$

$$d(U - W_{\text{ext}}) + dW_k + dW_s = 0 \quad (5.1.7)$$

$$dW_p + dW_k + G_c dS = 0 \quad (5.1.8)$$

where U is the elastic strain energy contained in the body, W_{ext} is the work done by the external forces, and W_p and W_k are the potential and kinetic energy, respectively. W_s represents indeed the energy available for crack formation, which can be expressed as a function of the new crack surface dS and fracture energy per unit surface G_c .

A condition for fracture can be derived from Eq. (5.1.8), being the kinetic energy always positive ($dW_k \geq 0$):

$$\frac{dW_p}{dS} + G_c \leq 0 \quad \Rightarrow \quad G = -\frac{dW_p}{dS} \geq G_c \quad (5.1.9)$$

The inequality obtained can be taken as a fracture criterion, in which G represents the Strain Energy Release Rate (SERR). When the equality is verified the change in kinetic energy is negligible ($dW_k \rightarrow 0$) and the crack propagation is stable; instead if G exceeds the critical value G_c then the crack propagation is unstable because the extra energy is transformed into kinetic energy of the crack itself ($dW_k \neq 0$).

For two-dimensional problems a relationship between the Strain Energy Release Rate (G) and the Mode I Stress Intensity Factor (K_I) has been demonstrated by Irwin [1]:

$$\begin{cases} G = \frac{K_I^2}{E} & \text{plane stress} \\ G = (1 - \nu^2) \cdot \frac{K_I^2}{E} & \text{plane strain} \end{cases} \quad (5.1.10)$$

Equation (5.1.9) represents the differential form of the Griffith fracture criterion [2], obtained by considering an infinitesimal increment of the crack surface $\delta S \rightarrow 0$. Considering indeed a finite increment of the crack surface δS , Leguillon [40,41] obtained the incremental form of the fracture criterion:

$$\frac{\delta W_p}{\delta S} + G_c \leq 0 \quad \Rightarrow \quad G = -\frac{\delta W_p}{\delta S} \geq G_c \quad (5.1.11)$$

This is the governing idea of the Finite Fracture Mechanics (FFM).

5.1.3. Failure criteria for sharp V-notches

In the literature the problem of the fracture assessment of components weakened by V-notches is typically treated with stress-based or energy-based approaches. In the present investigation, three different criteria are considered, in order of publication they are: the Strain Energy Density criterion (2001) [36], the Leguillon's criterion (2001) [40,41] and the Carpinteri et al. criterion (2008) [42].

5.1.3.1. Strain energy density (SED) criterion

According to Lazzarin-Zambardi [36] the brittle fracture of the material occurs when the average value of the strain energy density, calculated on a control volume of radius R_c surrounding the notch tip (Fig. 5.1.1b), is equal to the critical value W_c (Eq. (5.1.12)). According to Beltrami's hypothesis, it can be obtained:

$$W_c = \frac{\sigma_c^2}{2E} \quad (5.1.12)$$

where σ_c is the ultimate tensile strength and E the Young's modulus.

Under Mode I loading, by imposing $\overline{W} = W_c$, and combining Eq. (5.1.4) and Eq. (5.1.12) one obtains:

$$\frac{e_1}{E} \cdot \frac{K_{1c}^2}{R_c^{2(1-\lambda_1)}} = \frac{\sigma_c^2}{2E} \quad (5.1.13)$$

The critical value of the Notch Stress Intensity Factor at failure, K_{1c} , becomes:

$$K_{1c} = \frac{1}{\sqrt{2e_1}} \cdot \sigma_c \cdot R_c^{(1-\lambda_1)} \quad (5.1.14)$$

The radius R_c can be easily determined by using a set of experimental data giving the critical value of the NSIF from a specific V-notch angle. If the notch opening angle is zero, one can use the fracture toughness K_{Ic} , as made by Yosibash et al. [58], the final expression is:

$$R_c = \frac{(1 + \nu) \cdot (5 - 8\nu)}{4\pi} \cdot \left(\frac{K_{Ic}}{\sigma_c}\right)^2 \quad (5.1.15)$$

Substitution of Eq. (5.1.15) into Eq. (5.1.14) gives the NSIF at failure K_{Ic} (Eq. (5.1.17)) in the form:

$$K_{Ic} = \left[\left(\frac{(1 + \nu) \cdot (5 - 8\nu)}{4\pi} \right)^{(1-\lambda_1)} \cdot \frac{1}{\sqrt{2e_1}} \right] \cdot K_{Ic}^{2(1-\lambda_1)} \cdot \sigma_c^{2\lambda_1-1} \quad (5.1.16)$$

5.1.3.2. Leguillon's criterion

Leguillon [40,41] proposed a fracture criterion for components weakened by sharp V-notches based on the Finite Fracture Mechanics concept: at failure an incremental crack of length l_c nucleates at the notch tip.

According to Leguillon's criterion, two necessary conditions can be stated on stress and energy, but neither the one nor the other, taken separately, are sufficient. Only when they are simultaneously satisfied it is possible to get a condition sufficient for fracture.

According to the stress criterion the V-notched element failure occurs when the singular stress component normal to the fracture direction $\bar{\theta}_c$ exceeds the material tensile strength σ_c at a distance l_c from the notch tip, that is at the tip of the incremental crack.

According to the energy criterion, instead, the component failure occurs when the strain energy release rate G , that is the ratio between the potential energy variation in correspondence of the crack nucleation (δW_p) and the new crack surface created (δS), exceeds the critical material value G_c .

Therefore the simultaneous verification of the conditions formalized in Eqs. (5.1.17) and (5.1.18) provides a general criterion for the fracture of components weakened by sharp V-notches.

$$\text{Stress criterion :} \quad \sigma_\theta(l_c, \bar{\theta}_c) = k_1 \cdot l_c^{\lambda_1-1} \cdot s_\theta(\bar{\theta}_c) \geq \sigma_c \quad (5.1.17)$$

Energy criterion :
$$G = -\frac{\delta W_p}{\delta S} = \frac{k_1^2 \cdot K(2\alpha, \bar{\theta}_c) \cdot l_c^{2\lambda_1} \cdot d}{l_c \cdot d} \geq G_c \quad (5.1.18)$$

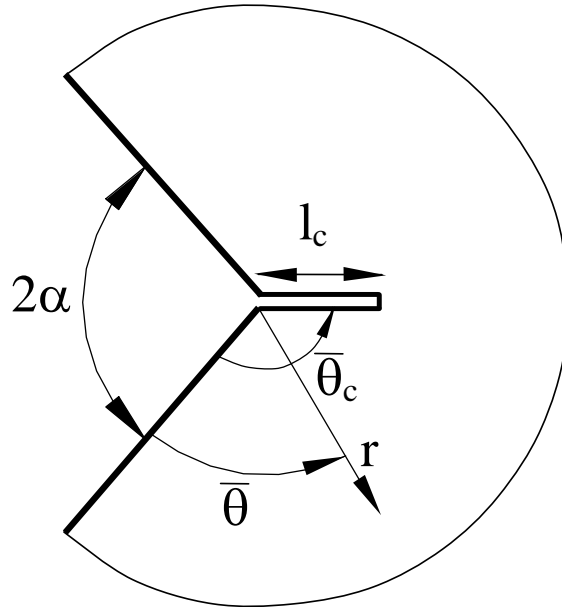


Figure 5.1.2 Leguillon's coordinate system, with incremental crack of length l_c .

In Eqs. (5.1.17, 5.1.18) l_c is the length of the incremental crack nucleated at the notch tip (see Fig. 5.1.2), λ_1 is the Mode I Williams' eigenvalue tied to the V-notch angle 2α , s_θ is a function of the angular coordinate $\bar{\theta}$, d is the thickness of the component. Finally, $K(2\alpha, \bar{\theta}_c)$ is a scale factor dependent on the local geometry (2α) and the direction of fracture ($\bar{\theta}_c$).

The parameter k_1 represents the NSIF according to Leguillon's definition, which is linked to Gross and Mendelson's definition [56] by means of Eq. (5.1.19).

$$k_1 = \lim_{r \rightarrow 0} \sigma_\theta \cdot r^{1-\lambda_1} = \frac{\lim_{r \rightarrow 0} \sigma_\theta \cdot \sqrt{2\pi} \cdot r^{1-\lambda_1}}{\sqrt{2\pi}} = \frac{K_1}{\sqrt{2\pi}} \quad (5.1.19)$$

In the following the lowercase letter will be used for the NSIFs defined according to Leguillon, capital letter instead for the NSIFs defined according to Gross and Mendelson.

The conditions (17) and (18) must be simultaneously satisfied. Solving the system in two unknowns, l_c and k_1 , it is possible to determine the length of the incremental crack:

$$l_c = \frac{G_c \cdot s_\theta(\bar{\theta}_c)^2}{K(2\alpha, \bar{\theta}_c) \cdot \sigma_c^2} \quad (5.1.20)$$

As soon as the incremental crack length l_c is introduced into Eq. (5.1.17) or Eq. (5.1.18), it is possible to give the failure criterion in terms of the classic Irwin's expression, $K_I \geq K_{Ic}$. Since the fracture direction for a V-notched component in a homogeneous and isotropic material subjected to a symmetric load (Mode I) is known a priori, $\bar{\theta}_c = \pi - \alpha$, the critical value of the Notch Stress Intensity Factor k_{Ic} can be defined as a function of the material mechanical properties (σ_c and G_c) and of the notch opening angle 2α , through $K(2\alpha)$ and λ_1 . Normalizing the angular function in such a way that $s_\theta(\bar{\theta}_c) = 1$, one obtains:

$$k_1 \geq \left(\frac{G_c}{K(2\alpha)} \right)^{1-\lambda_1} \cdot \sigma_c^{2\lambda_1-1} = k_{1c} \quad (5.1.21)$$

Under plane strain conditions G_c can be linked to the critical value k_{Ic} in the following form:

$$G_c = 2\pi \cdot k_{Ic}^2 \cdot \frac{1-\nu^2}{E} \quad (5.1.22)$$

The value of the scale factor K for the crack case ($2\alpha = 0$, $\lambda_1 = 0.5$) can be obtained from Eqs. (5.1.21) and (22) considering that $k_{Ic} = k_{Ic}$. In order to simplify the involved expressions, the dependence of k_{Ic} on the notch opening angle can be given defining a universal function $\gamma(2\alpha)$, calculated using an integration procedure described in [11]. Doing so, the general expression for the scale factor $K(2\alpha)$ is:

$$K(2\alpha) = K(2\alpha = 0) \cdot \frac{1}{\gamma(2\alpha)^{\frac{1}{1-\lambda_1}}} = 2\pi \cdot \frac{1-\nu^2}{E} \cdot \frac{1}{\gamma(2\alpha)^{\frac{1}{1-\lambda_1}}} \quad (5.1.23)$$

The universal function $\gamma(2\alpha)$ is plotted in Fig. 5.1.3 and its values listed in Table 5.1.2 [11].

Table 5.1.2 Values of the function $\gamma(2\alpha)$.

2α (degrees)	$\gamma(2\alpha)$	2α (degrees)	$\gamma(2\alpha)$
0	1.00	95	1.10
5	1.00	100	1.11
10	1.00	105	1.12
15	1.00	110	1.14
20	1.00	115	1.15
25	1.01	120	1.16
30	1.01	125	1.17
35	1.01	130	1.18
40	1.02	135	1.19
45	1.02	140	1.20
50	1.03	145	1.20
55	1.03	150	1.19
60	1.04	155	1.19
65	1.04	160	1.17
70	1.05	165	1.14
75	1.06	170	1.11
80	1.07	175	1.06
85	1.08	180	1.00
90	1.09		

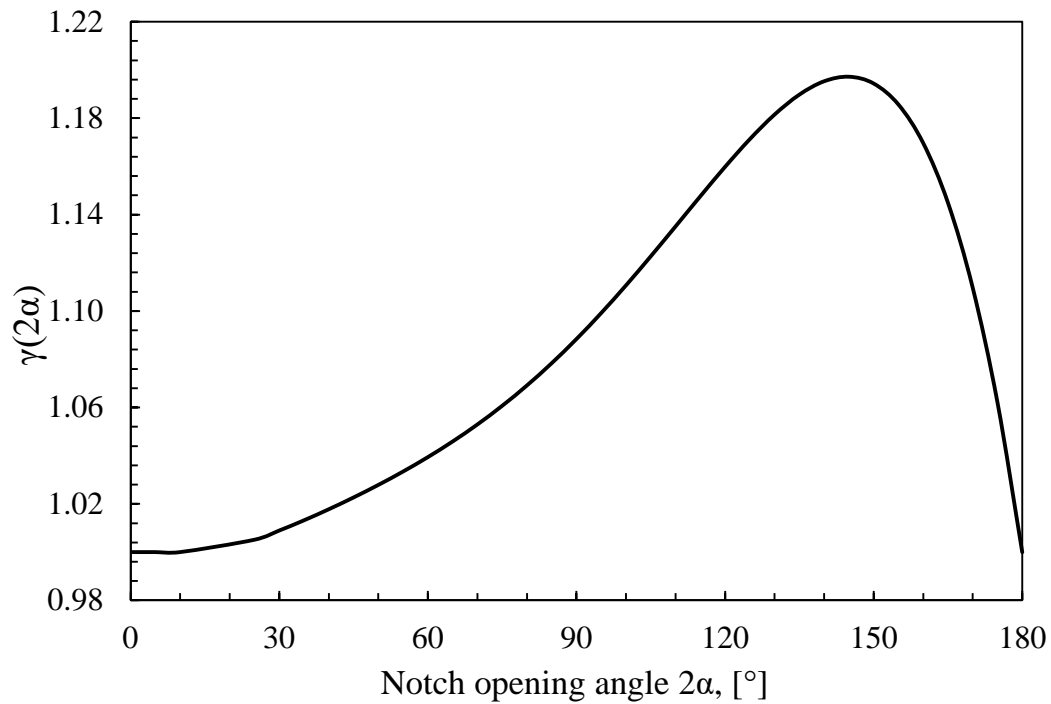


Figure 5.1.3 Leguillon's universal function $\gamma(2\alpha)$.

A simpler expression of the critical NSIF k_{1c} , as a function of the 'fracture toughness' k_{Ic} (defined according to Leguillon) and the material ultimate tensile strength σ_c , can be obtained substituting expressions (22) and (23) into Eq. (5.1.21). As a result:

$$k_{1c} = \gamma(2\alpha) \cdot k_{Ic}^{2(1-\lambda_1)} \cdot \sigma_c^{2\lambda_1-1} \quad (5.1.24)$$

A slightly different formulation of the criterion can be obtained by using Gross and Mendelson's definition for the critical NSIF K_{1c} and the fracture toughness K_{Ic} according to Eq. (5.1.19).

$$K_{1c} = \left[(2\pi)^{\left(\lambda_1 - \frac{1}{2}\right)} \cdot \gamma(2\alpha) \right] \cdot K_{Ic}^{2(1-\lambda_1)} \cdot \sigma_c^{2\lambda_1-1} \quad (5.1.25)$$

5.1.3.3. Carpinteri's formulation

Similarly to Leguillon, Carpinteri et al. [42] proposed a fracture criterion for components weakened by sharp V-notches based on Finite Fracture Mechanics

concept: at failure a crack of length Δ_{SE} nucleates at the notch tip. Also in this formulation, it is possible to obtain a sufficient condition for the fracture by satisfying simultaneously a stress criterion and an energy criterion.

According to the averaged stress criterion the V-notched element failure occurs when the notch singular stress component normal to the crack faces, averaged over the crack length Δ_{SE} , exceeds the material tensile strength σ_c .

According to the energy criterion, instead, the component failure occurs when the strain energy released at the nucleation of a crack of length Δ_{SE} exceeds the critical value of the material, which depends on G_c . A simplified formulation can be obtained by expressing the strain energy release rate G as a function of the Stress Intensity Factor K_I according to Irwin's relation valid under plane strain conditions.

Therefore the simultaneous verification of the conditions formalized in Eq. (5.1.26) and (5.1.27) provides a general criterion for the fracture of components weakened by sharp V-notches.

Averaged stress criterion :

$$\int_0^{\Delta_{SE}} \sigma_y(x) dx = \int_0^{\Delta_{SE}} \frac{K_I^*}{(2\pi x)^{1-\lambda_1}} dx \geq \sigma_c \cdot \Delta_{SE} \quad (5.1.26)$$

Energy criterion :

$$\int_0^{\Delta_{SE}} -\frac{dW_p}{da} da = \int_0^{\Delta_{SE}} G(a) da \geq G_c \cdot \Delta_{SE} \quad (5.1.27)$$

$$\int_0^{\Delta_{SE}} K_I^2(a) da = \int_0^{\Delta_{SE}} \left[\psi(2\alpha) \cdot \frac{K_I^*}{(2\pi)^{1-\lambda_1}} \cdot a^{\lambda_1 - \frac{1}{2}} \right]^2 da \geq K_{Ic}^2 \cdot \Delta_{SE}$$

where Δ_{SE} is the length of the crack nucleated at the notch tip (Fig. 5.1.4), λ_1 the Mode I Williams' eigenvalue [54], x the coordinate along the notch bisector line and a the generic crack length.

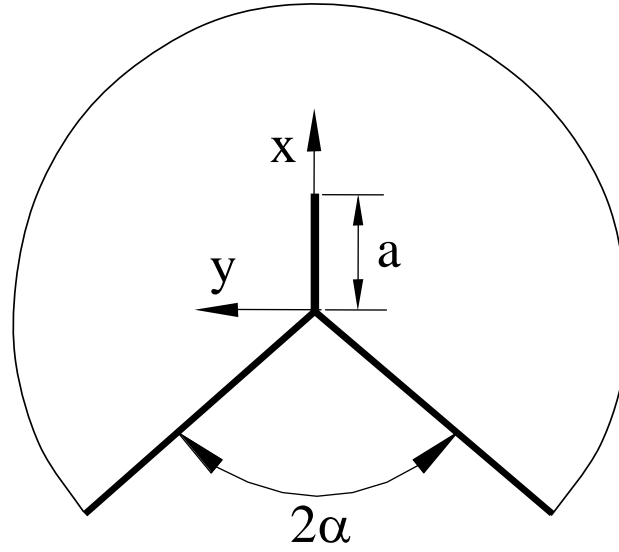


Figure 5.1.4 Carpinteri's coordinate system with crack of length a .

The parameter K_I^* represents again the NSIF according to Carpinteri's definition, which is slightly different from that given by Gross and Mendelson. In particular:

$$K_I^* = \lim_{x \rightarrow 0} \sigma_y \cdot (2\pi x)^{1-\lambda_1} = \frac{\lim_{x \rightarrow 0} \sigma_y \cdot \sqrt{2\pi} \cdot x^{1-\lambda_1}}{(2\pi)^{\lambda_1 - \frac{1}{2}}} = \frac{K_1}{(2\pi)^{\lambda_1 - \frac{1}{2}}} \quad (5.1.28)$$

In order to apply the energy criterion it is necessary to know the Stress Intensity Factor K_I of the crack nucleated at V-notch tip, as a function of the crack length a . For this purpose it is possible to use the expression by Tada et al. [59], which provides the SIF K_I as a function of the crack length a , the notch opening angle 2α and the NSIF K_I^* .

$$K_I(a) = \psi(2\alpha) \cdot \frac{K_I^*}{(2\pi)^{1-\lambda_1}} \cdot a^{\lambda_1 - \frac{1}{2}} \quad (5.1.29)$$

According to Carpinteri's criterion the failure of a V-notched component occurs when the stress and energy criteria given by Eqs. (5.1.26, 5.1.27) are both satisfied. Solving the system, it is possible to determine the length of the nucleated crack Δ_{SE} (Eq. (5.1.30)) and the critical NSIF K_{Ic}^* (Eq. (5.1.31)).

$$\Delta_{SE} = \frac{2}{\lambda_1 \cdot \psi^2} \cdot \left(\frac{K_{Ic}}{\sigma_c} \right)^2 \quad (5.1.30)$$

$$\begin{aligned} K_I^* &\geq \left[\lambda_1^{\lambda_1} \cdot \left(\frac{4\pi}{\psi^2} \right)^{1-\lambda_1} \right] \cdot K_{Ic}^{2(1-\lambda_1)} \cdot \sigma_c^{2\lambda_1-1} = \\ &= [\xi(2\alpha)] \cdot K_{Ic}^{2(1-\lambda_1)} \cdot \sigma_c^{2\lambda_1-1} = K_{Ic}^* \end{aligned} \quad (5.1.31)$$

The values of the auxiliary function $\xi(2\alpha)$ are plotted in Fig. 5.1.5 and listed in Table 5.1.3.

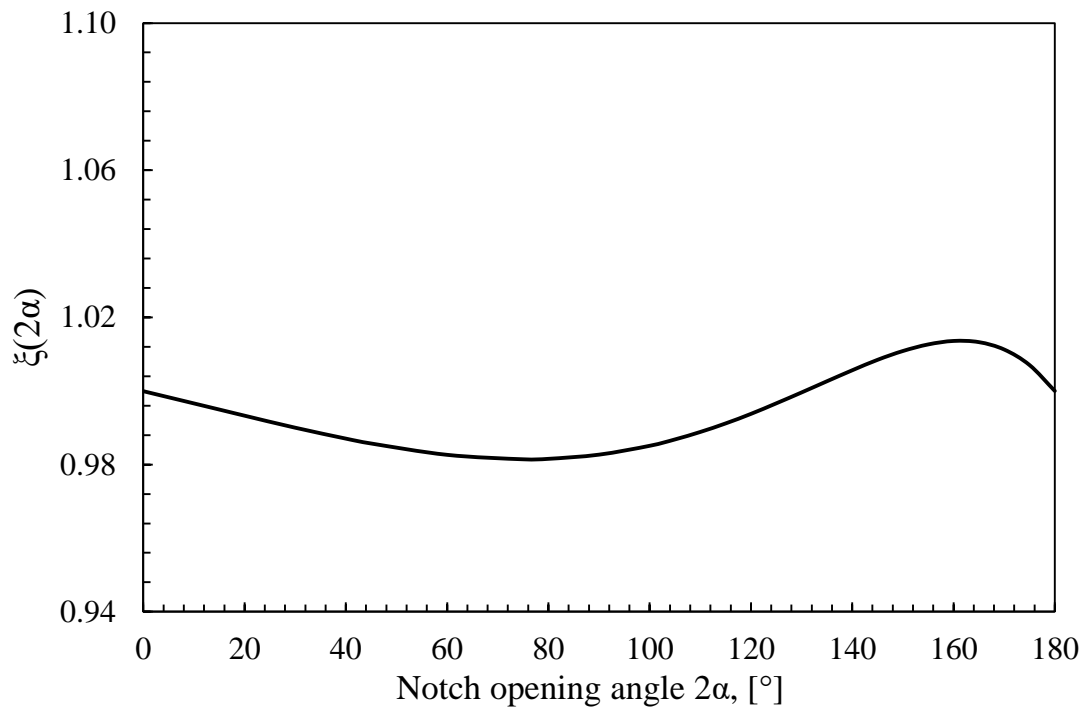


Figure 5.1.5 Plot of the function $\xi(2\alpha)$, according to Carpinteri et al. [42].

Table 5.1.3 Values of the functions $\psi(2\alpha)$ e $\xi(2\alpha)$.

2α (degrees)	$\psi(2\alpha)$	$\xi(2\alpha)$
0	2.5068	1.000
15	2.5192	0.995
20	2.5232	0.993
30	2.5306	0.990
40	2.5364	0.987
45	2.5384	0.986
60	2.5401	0.983
75	2.5326	0.981
80	2.5275	0.982
90	2.5127	0.983
100	2.4910	0.985
105	2.4771	0.987
120	2.4233	0.994
135	2.3486	1.003
140	2.3189	1.006
150	2.2516	1.011
160	2.1739	1.014
170	2.0863	1.011
180	1.9869	1.000

By using for the critical NSIF, K_{Ic} , the definition of Gross and Mendelson [56], see Eq. (5.1.28), the final result is:

$$K_{Ic} = \left[(2\pi)^{\left(\lambda_1 - \frac{1}{2}\right)} \cdot \xi(2\alpha) \right] \cdot K_{Ic}^{2(1-\lambda_1)} \cdot \sigma_c^{2\lambda_1-1} \quad (5.1.32)$$

5.1.4. Analytical comparison

Considering the three different formulations, it is possible to compare the final relationships of the critical NSIF according to Gross and Mendelson's definition:

SED:

$$K_{1c} = \left[\left(\frac{(1 + \nu) \cdot (5 - 8\nu)}{4\pi} \right)^{(1-\lambda_1)} \cdot \frac{1}{\sqrt{2e_1}} \right] \cdot K_{Ic}^{2(1-\lambda_1)} \cdot \sigma_c^{2\lambda_1-1} \quad (5.1.33)$$

Leguillon:

$$K_{1c} = \left[(2\pi)^{\left(\lambda_1 - \frac{1}{2}\right)} \cdot \gamma(2\alpha) \right] \cdot K_{Ic}^{2(1-\lambda_1)} \cdot \sigma_c^{2\lambda_1-1} \quad (5.1.34)$$

Carpinteri et al.:

$$K_{1c} = \left[(2\pi)^{\left(\lambda_1 - \frac{1}{2}\right)} \cdot \xi(2\alpha) \right] \cdot K_{Ic}^{2(1-\lambda_1)} \cdot \sigma_c^{2\lambda_1-1} \quad (5.1.35)$$

It can be observed that the three criteria give the same proportionality relation:

$$K_{1c} \propto K_{Ic}^{2(1-\lambda_1)} \cdot \sigma_c^{2\lambda_1-1} \quad (5.1.36)$$

The difference is given only by the proportionality factor. This factor depends only on the notch opening angle (2α) in Leguillon's and Carpinteri's criteria. In the SED criterion, instead, the proportionality factor depends on the opening angle 2α and the Poisson's ratio ν , as shown in Fig. 5.1.6.

The proportionality factors do not differ significantly in their trends, with the values of Leguillon's factor being always slightly greater than those assumed by the other two criteria for the same notch opening angle (2α), as shown in Fig. 5.1.7 and in Table 5.1.4. For $2\alpha=0^\circ$ and 180° Leguillon's and Carpinteri's criteria give the same proportionality factor, 1.0 and 2.507, respectively. The factor based on SED matches that of the other two criteria only for $2\alpha=0^\circ$, due to its dependence on the Poisson's ratio. However, Fig. 5.1.7 shows that the values of proportionality factors as a function of the notch opening angle (2α) are very similar for the SED and the Carpinteri's criterion, despite the different initial assumptions.

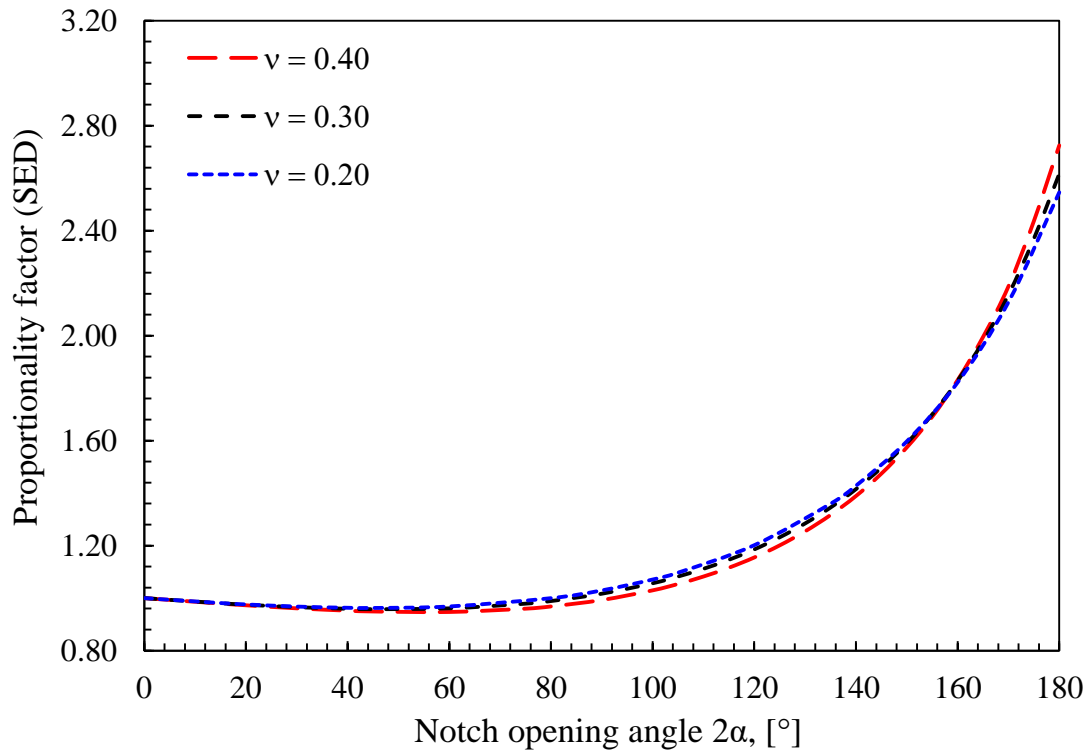


Figure 5.1.6 Variability of proportionality factor in the SED criterion, Eq. (5.1.33), as a function of the Poisson's ratio.

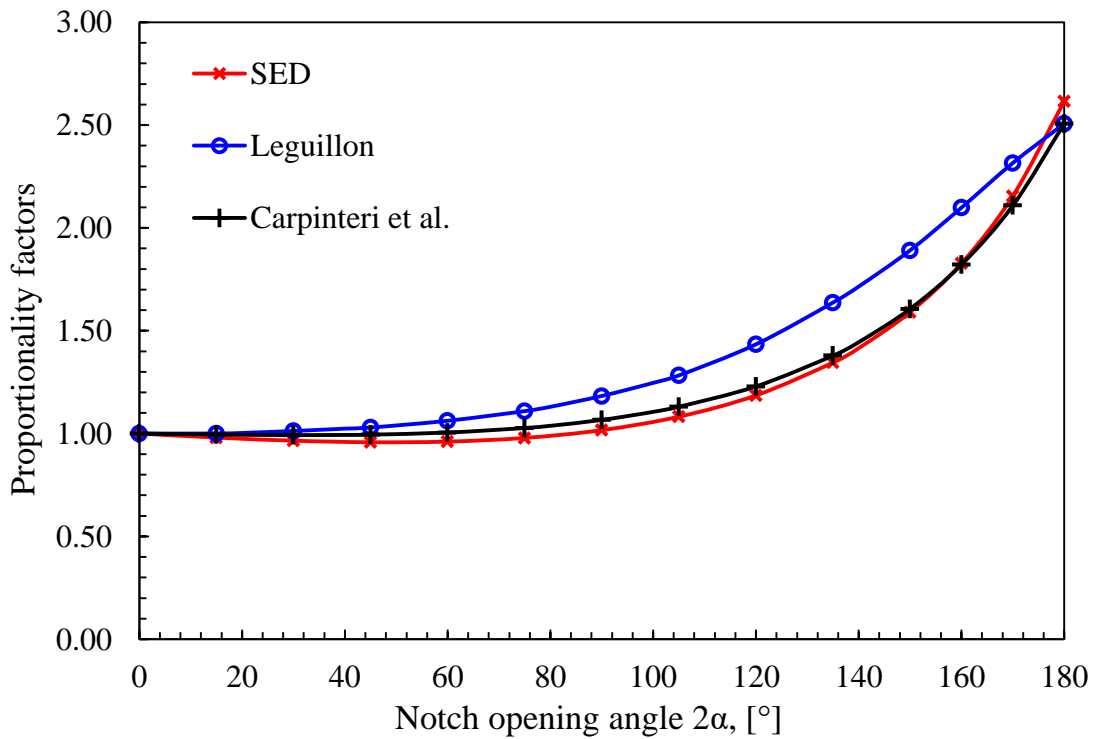


Figure 5.1.7 Comparison among proportionality factors given by Eqs. (5.1.33,5.1.34,5.1.35)

Table 5.1.4 Proportionality factors in Eqs. (5.1.33,5.1.34,5.1.35)

2α (degrees)	λ	SED ($\nu = 0.3$)	Leguillon	Carpinteri et al.
0	0.5000	1.000	1.000	1.000
15	0.5002	0.981	1.000	0.995
20	0.5004	0.975	1.003	0.994
30	0.5014	0.965	1.013	0.993
40	0.5035	0.959	1.024	0.993
45	0.5050	0.958	1.029	0.995
60	0.5122	0.961	1.062	1.005
75	0.5247	0.979	1.109	1.027
80	0.5304	0.989	1.130	1.038
90	0.5445	1.017	1.183	1.066
100	0.5628	1.056	1.247	1.106
105	0.5739	1.082	1.283	1.130
120	0.6157	1.186	1.434	1.229
135	0.6736	1.345	1.637	1.379
140	0.6972	1.416	1.715	1.444
150	0.7520	1.591	1.891	1.606
160	0.8187	1.828	2.099	1.821
170	0.9000	2.156	2.316	2.109
180	1.0000	2.616	2.507	2.507

5.1.5. Experimental validation

The predictive capability of the three different approaches is assessed by using a good number of experimental data taken from the literature. The analysed data are referred to V-notched specimens made of two materials: the polymer PMMA and the aluminium alloy Duraluminum. The mechanical properties of each tested material as well as the experimental procedures adopted are described below.

The comparison between the experimental data and the theoretical estimations based on Eqs. (5.1.33-5.1.35) is performed in terms of Notch Stress Intensity Factor K_{Ic} to failure as a function of the V-notch opening angle 2α . When not directly available, the values of the critical NSIF to failure K_{Ic} have been obtained by two-dimensional FEM analyses, by introducing into the models the experimental fracture loads. The finite element code ANSYS, version 14.5, has been used. In particular, the critical NSIF to failure K_{Ic} coincides with the Notch

Stress Intensity Factor K_1 calculated along the notch bisector line ($K_1 = \sigma_\theta \cdot \sqrt{2\pi} \cdot r^{1-\lambda_1}$ with $r \rightarrow 0$) when the final load to failure is applied to the FE model.

The first set of experimental data (Gomez and Elices [31]) was obtained from three-point bending and traction tests performed on PMMA V-notched specimens. The samples geometry was characterized by a length $l = 196$ mm for the traction specimens (SEN) and $l = 112$ mm for the three-point-bending specimens (TPB), width $D = 28$ mm, notch depth $a = 14$ mm and thickness $t = 14$ mm. Four values of the notch opening angle $2\alpha = 60^\circ, 90^\circ, 120^\circ, 150^\circ$ in the case of SEN specimens and six values $2\alpha = 15^\circ, 30^\circ, 60^\circ, 90^\circ, 120^\circ, 150^\circ$ in the case of TPB specimens have been considered.

The material properties were: Young's modulus $E = 3000$ MPa, Poisson's ratio $\nu = 0.4$, fracture toughness $K_{Ic} = 1$ MPa m^{0.5}. Furthermore the true curve σ - ϵ of unnotched specimens exhibited a non-linear behaviour whereas the notched specimens presented a brittle behaviour, with a linear trend up to the critical load, followed by a sudden failure. Under these circumstances the critical stress σ_c should be substituted by “the maximum normal stress existing at the edge at the moment preceding the cracking”, as underlined in Ref. [7] where it is also recommended to use tensile specimens with semicircular notches. Hence in order to apply the analysed criteria, the critical loads obtained experimentally on the specimens with the maximum notch root radius ($\rho = 2$ mm) have been used to estimate the critical strength σ_c . The value of the ‘critical tensile stress’ at the notch root was 136 MPa, in good agreement with other values reported in the literature for PMMA: for example Carpinteri [5] and Dunn et al. [9,10] gave 130 and 124 MPa, respectively.

The experimental values of the Notch Stress Intensity Factor K_{Ic} to failure are plotted for each specimen in Fig. 5.1.8 (SEN specimens) and Fig. 5.1.9 (TPB specimens) as a function of the notch opening angle 2α . In the same figures the theoretical curves of K_{Ic} obtained applying the three different formulations are given for comparison.

The second set of experimental data is due to Seweryn [7], who performed traction tests on specimens made of PMMA and Duraluminum.

The specimens geometry was characterized by a length $l = 192$ mm, width $W = 109$ mm and a notch depth $a = 27$ mm. The thickness of PMMA specimens was $t = 4$ mm, whereas the thickness of Duraluminum specimens was $t = 5$ mm. Nine values of the notch opening angle, $2\alpha = 0^\circ, 20^\circ, 40^\circ, 60^\circ, 80^\circ, 120^\circ, 140^\circ, 160^\circ, 180^\circ$ have been considered. Three PMMA and two Duraluminum specimens were tested for each opening angle.

The mechanical properties of PMMA were: Young's modulus $E = 3000$ MPa, Poisson's ratio $\nu = 0.3$, fracture toughness $K_{Ic} = 1.86 \text{ MPa m}^{0.5}$ and tensile strength $\sigma_c = 104.90$ MPa. In the case of Duraluminum, instead, the properties were: Young's modulus $E = 70000$ MPa, Poisson's ratio $\nu = 0.3$, fracture toughness $K_{Ic} = 50.56 \text{ MPa m}^{0.5}$ and tensile strength $\sigma_c = 705.27$ MPa.

The experimental values of the Notch Stress Intensity Factor K_{Ic} to failure are reported for each specimen in Fig. 5.1.10 for PMMA and in Fig. 5.1.11 for Duraluminum. In the same figures the theoretical curves of K_{Ic} as a function of the notch opening angle 2α are reported for comparison.

The third set of experimental data (Carpinteri [5]) was obtained from three-point bending tests performed on PMMA V-notched specimens.

The specimens geometry was characterized by a length $l = 190$ mm, width $b = 50$ mm and thickness $t = 50$ mm. Two values of the notch depth $a = 10, 20$ mm and six values of the notch opening angle $2\alpha = 0^\circ, 45^\circ, 90^\circ, 120^\circ, 150^\circ, 180^\circ$ have been considered. A total number of 36 specimens were tested, three specimens for each geometry.

The material properties were: Young's modulus $E = 3000$ MPa, Poisson's ratio $\nu = 0.3$, fracture toughness $K_{Ic} = 1.89 \text{ MPa m}^{0.5}$ and tensile strength $\sigma_c = 130.30$ MPa.

The experimental values of the Notch Stress Intensity Factor K_{Ic} to failure are shown for each specimen in Fig. 5.1.12 as a function of the notch opening angle 2α and the notch depth a .

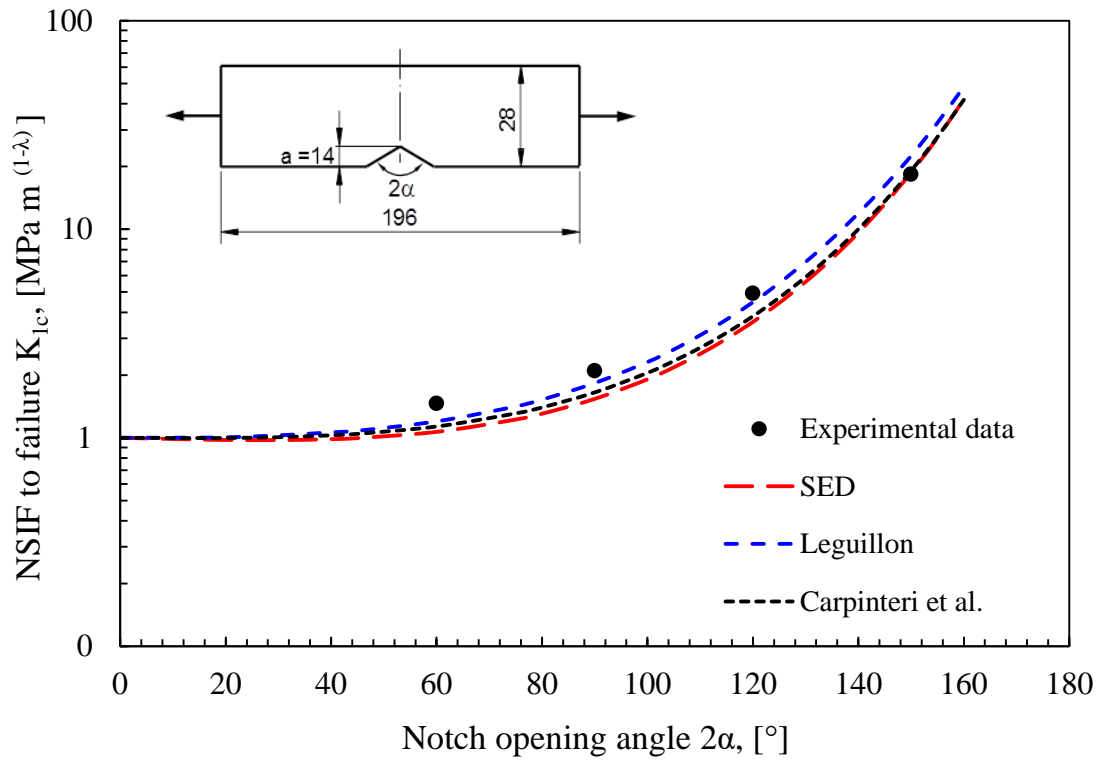


Figure 5.1.8 Plots of the NSIF to failure K_{Ic} (Log-scale) and comparison with the experimental data (mean values) from SEN specimens made of PMMA tested by Gomez and Elices [31].

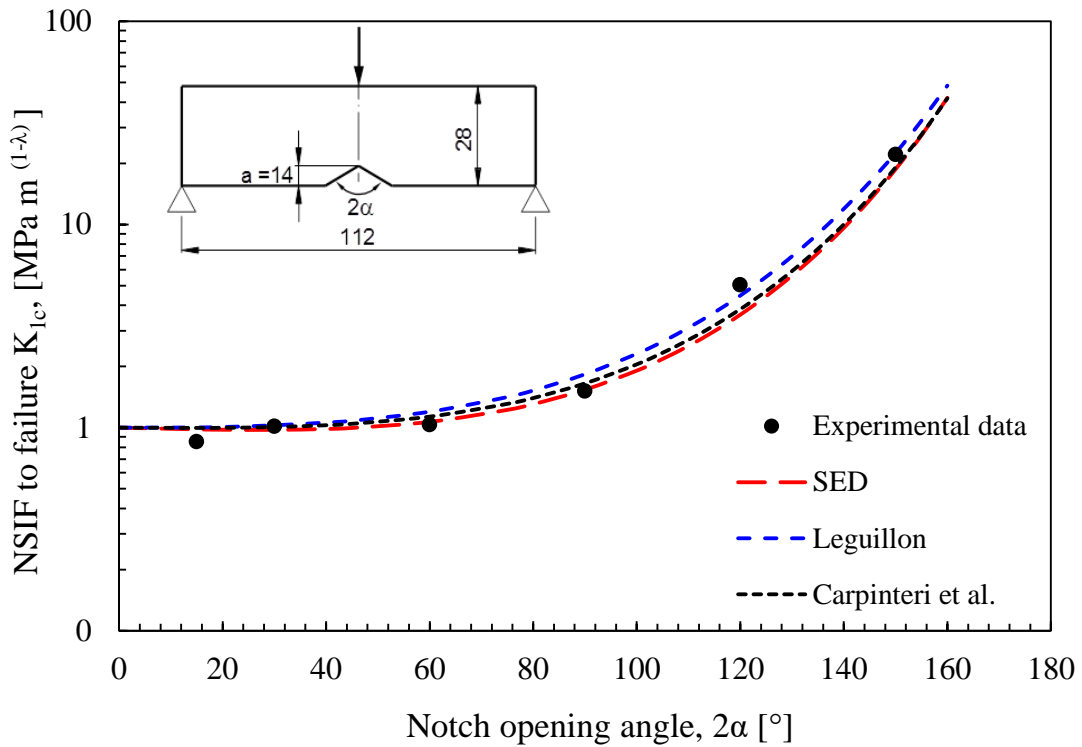


Figure 5.1.9 Plots of the NSIF to failure K_{Ic} (Log-scale) and comparison with the experimental data (mean values) from TPB specimens made of PMMA tested by Gomez and Elices [31].

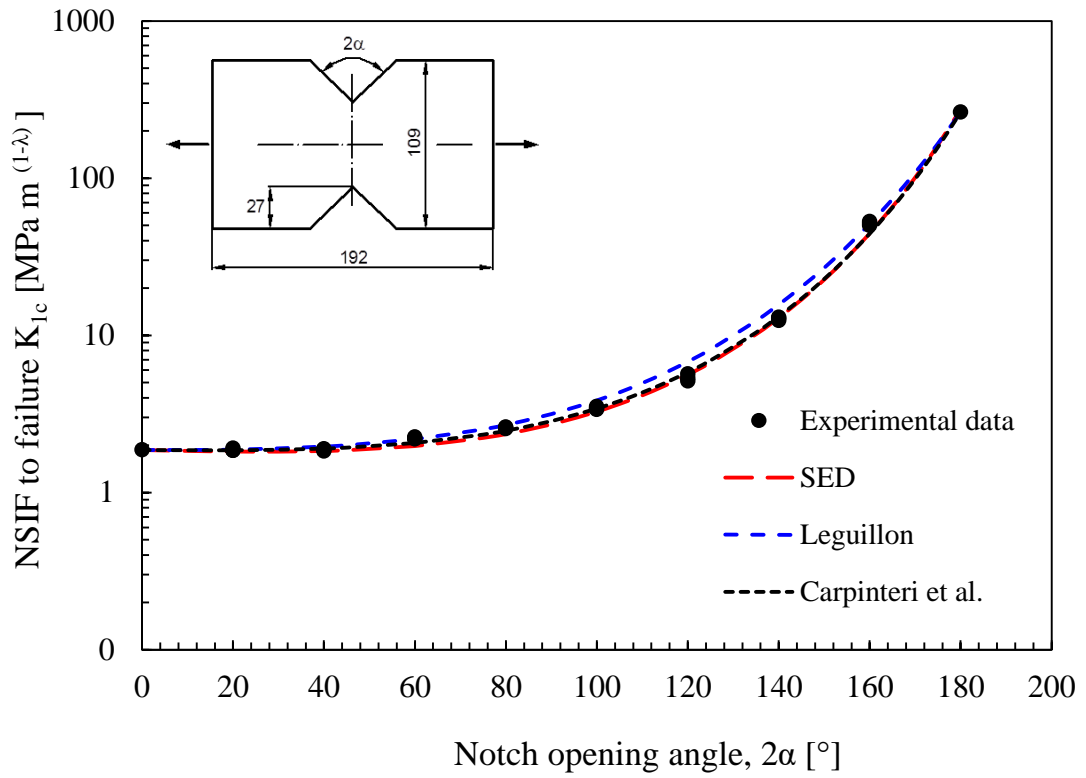


Figure 5.1.10 Plots of the NSIF to failure K_{1c} (Log-scale) and comparison with the experimental data (mean values) from PMMA specimens tested by Seweryn [7].

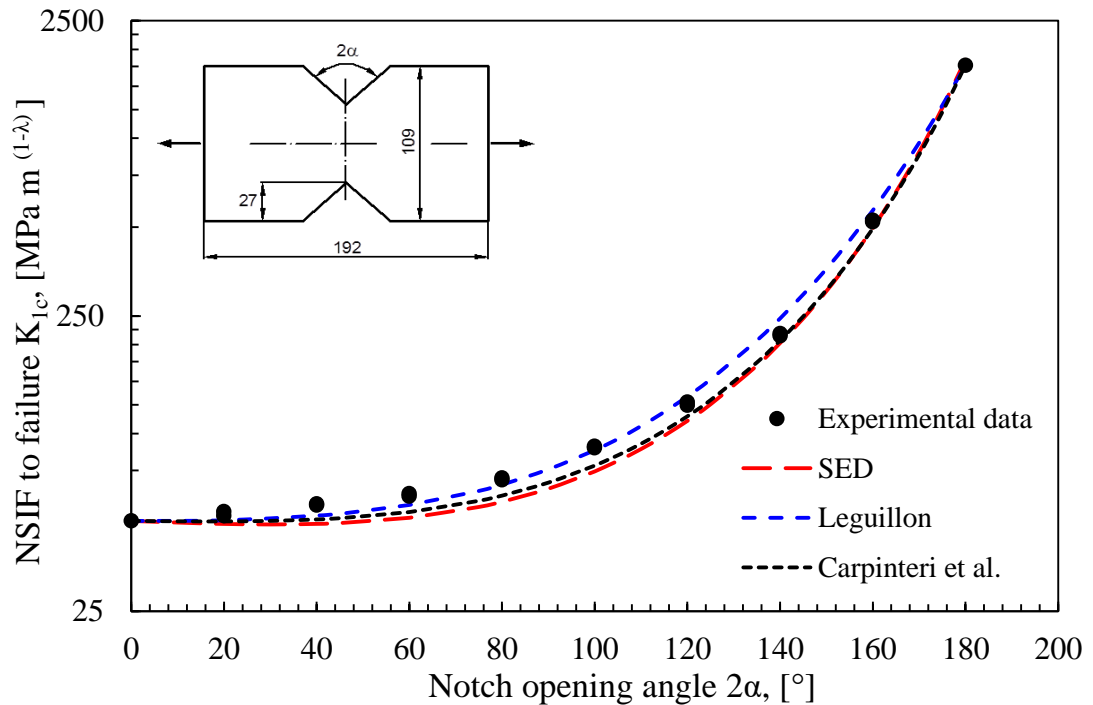


Figure 5.1.11 Plots of the NSIF to failure K_{1c} (Log-scale) and comparison with the experimental data (mean values) from Duraluminum specimens tested by Seweryn [7].

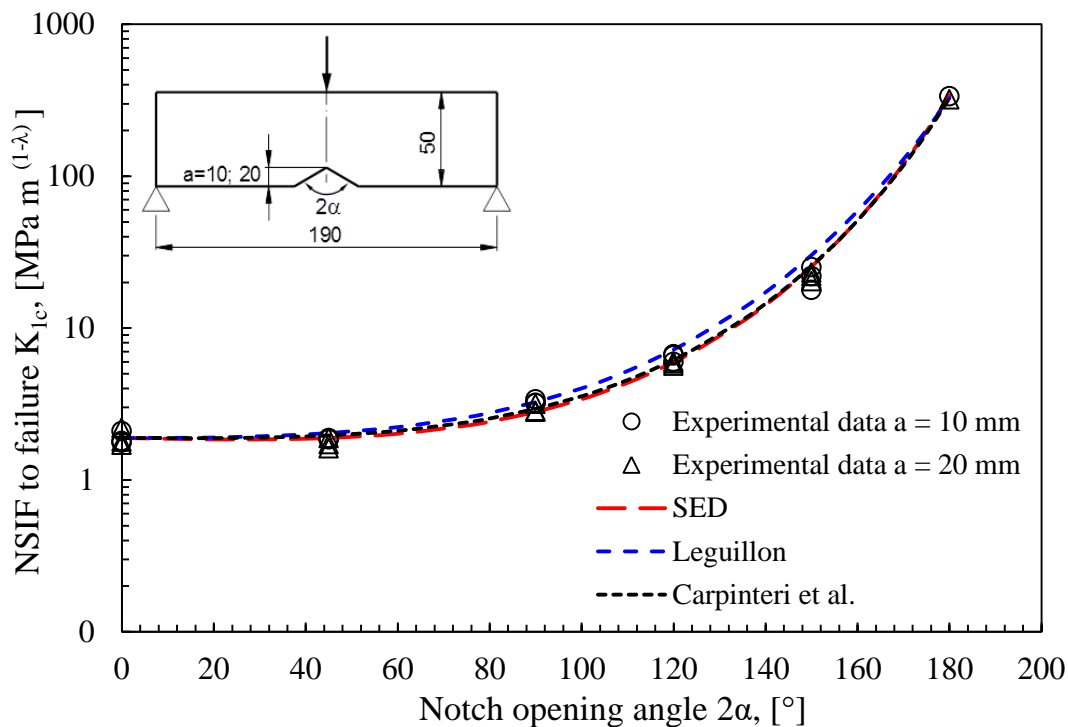


Figure 5.1.12 Plots of the NSIF to failure K_{1c} (Log-scale) and comparison with the experimental data from PMMA specimens tested by Carpinteri [5].

The plots of Figs. 5.1.8-5.1.12 shown that the agreement between the theoretical estimates and the experimental values of Notch Stress Intensity Factor K_{1c} to failure is good in all cases. For notch opening angles greater than 120° , the minimum deviation seems to be slightly reduced in the case of the averaged SED and the Carpinteri's criterion, which are substantially coincident although based on different assumptions. Furthermore it can be observed that theoretical assessments based on the averaged SED and the Carpinteri's criterion are always conservative with respect to those obtained by applying the Leguillon's criterion.

5.1.6. Discussion

A comparison between different fracture criteria for brittle components weakened by sharp V-notches has been presented considering Mode I loading conditions. The comparison has considered the averaged SED criterion, and two different formulations of the Finite Fracture Mechanics theory, according to Leguillon's or to Carpinteri et alii.

The analytical comparison has been performed on the basis of the different expressions for the critical value of the NSIF K_{1c} . The same proportionality relation exists between

K_{Ic} and two fundamental mechanical properties of the material: the fracture toughness K_{Ic} and the ultimate tensile strength σ_c . The difference is given by a proportionality factor, which depends only on the V-notch opening angle in Leguillon and Carpinteri's criteria, whereas it depends on the opening angle and the Poisson's ratio in the SED approach. The variability of the proportionality factors has been examined in detail.

Finally, the three criteria have been applied to components weakened by sharp V-notches under Mode I loading conditions in order to investigate the predictive capability of each approach. A number of experimental data taken from the literature have been used for the comparison. A good agreement in terms of critical values of the NSIF K_{Ic} has been found in all cases. It was observed that the static strength assessment based on the SED and the Carpinteri's criteria is always conservative with respect to the theoretical prediction based on the Leguillon's criterion.

5.2 Comparison among energy-based criteria for fracture assessment of sharp V-notched components under Mode II loading ^(*)

Nomenclature

E	Young's modulus
G	shear modulus
G_c	critical value of the Strain Energy Release Rate
H_{22}^*	geometrical factor dependent on the local geometry and the direction of fracture
K_I	Mode I Stress Intensity Factor
K_{Ic}	Mode I fracture toughness
K_2	Mode II Notch Stress Intensity Factor
k_2	NSIF according to Leguillon's definition
K_{II}^*	NSIF according to Carpinteri's definition
K_{2c}	Mode II Notch Stress Intensity Factor at failure
K_{II}	Mode II Stress Intensity Factor
K_{IIc}	Mode II fracture toughness
l_c	length of the incremental crack according to Leguillon
r, θ	polar coordinates
R_c	control radius for averaged SED evaluation, subscripts I, II denote mode
\bar{W}	SED averaged over the control volume
W_c	critical SED value of the considered material under shear loading

Symbols

2α	notch opening angle
Δ	length of the crack nucleated at the notch tip according to Carpinteri
ϕ	ratio between shear and tensile ultimate strength

λ_2	Mode II Williams' eigenvalue
ν	Poisson's ratio
$\bar{\theta}_c$	fracture direction
σ	stress, subscripts $rr, \theta\theta, zz$ denote normal stresses subscript $r\theta$ denote shear stresses
σ_c	ultimate tensile strength
τ_c	ultimate shear strength

(*) See also:

Campagnolo, A.; Berto, F; Leguillon, D. Mode II loading in sharp V-notched components: a comparison among some recent criteria. Theoretical and Applied Fracture Mechanics (under review);

5.2.1. Introduction

The formulation of a sufficiently simple and accurate criterion able to assess crack nucleation and propagation in structural components under static and fatigue loading is a key issue in fracture mechanics. Dealing with cracked components the fracture initiation phase is generally governed by a critical value of the Mode I stress intensity factor K_I that under plane strain conditions has to be compared with the material fracture toughness K_{Ic} . This fracture criterion has been first formalised by Irwin in his pioneering contribution [1]. A sound link exists between the Irwin criterion and the Griffith criterion [2] dealing with cracked elements subjected to Mode I loading. Griffith criterion considers as critical parameter the strain energy release rate G , defined as the derivative of the potential energy with respect to the crack surface area. This parameter becomes critical when it reaches the material critical value G_c , which represents the energy needed to create a unit crack surface area.

Dealing with sharply notched components, with the notch tip radius being zero or close to zero, several criteria have been proposed in the last decades. The definition of simple and reliable criteria to assess failures initiated at points of stress singularity is surely an active topic of research. Under linear elastic

hypotheses stresses tend to infinity at such points. For this reason, similarly to the crack case, the introduction of a stress field parameter is required. In the linear elastic Notch Mechanics, notch stress intensity factors (NSIFs) are generally used to assess the static failure of brittle components weakened by pointed V-notches [3–10]. Among these references it is surely worth of mentioning the investigation by Leicester [3] who studied the scale effect in wood components weakened by V-notches.

Sharp notches under fatigue loading have been investigated widely in [12,13,15]. When the fatigue life is mainly spent in the formation of micro-cracks and propagation inside the zone governed by the V-notch singularity, NSIFs can be used not only to predict the fatigue initiation life [60] but also for total fatigue life assessments [17].

For a better overview of the V-notch problem, it is useful here to mention some fundamental stress-based criteria developed by many researchers around the world in the last twenty years. Starting from a fundamental and pioneering work by Novozhilov [19], a brittle fracture criterion based on the mean value of normal stress over a material dependent parameter d_0 was proposed by Seweryn [7]. That criterion has been also successfully extended and applied to structural components under mixed mode loading [20,21]. A non-local failure function has been introduced which combines normal and shear stress components, both normalized with respect to the relevant critical stresses of the material.

The Theory of Critical Distances (TCD) [22,23], applicable to any kind of stress risers, has been developed due to the fundamental contribution by Taylor and Susmel. Neuber's fictitious notch rounding (FNR) approach [27] is also based on the idea of stress averaging. Recent studies have highlighted the influence of plane stress or plane strain conditions on the multiaxiality factor, s , as well as the influence of the V-notch opening angle [61].

Another worth mentioning approach is surely the Cohesive Zone Model (CZM) sometimes called 'fictitious crack model'. Initially proposed for concrete, the CZM was later successfully extended to a number of brittle or quasi-brittle materials [30,62].

To conclude this short review, some criteria based on the extension of J-integral to notches can be mentioned [32,33,63] as well as the modified Maximum Tangential Stress criterion [35,64], which is able to take into account singular and non-singular stress terms of Williams' solution.

In a recent contribution dealing with sharp V-notches under Mode I loading [65], two recent criteria involving energy-based calculations have been discussed in detail: that based on the averaged strain energy density (SED) [36,38,39] and that called Finite Fracture Mechanics (FFM) criterion, according to two different version, the former due to Leguillon [40,41], the latter due to Carpinteri et al. [42].

The main aim of the present investigation is to extend the comparison, performed in the previous work [65], also to pure Mode II loading. Dealing with the FFM criteria, the extensions to in-plane mixed mode and prevalent Mode II loading reported in the recent literature [44,45,66] will be taken into account. Instead, with reference to the SED criterion, a new expression for estimating the control radius under pure Mode II loading will be proposed and discussed in comparison with the expression valid for pure Mode I.

The averaged SED criterion [36] is reminiscent of Neuber's concept of elementary structural volume [27] and Sih's criterion based on factor S, which gives the strain energy density multiplied by a convenient distance from the crack or the V-notch tip [46]. The approach is based on the SED averaged over a material-dependent control volume surrounding the notch tip. The major advantage of the averaged SED approach with respect to the local stress-based criteria is the mesh independency [49,67] and that it can easily take into account also coupled three-dimensional effects [51,68,69].

In the framework of Finite Fracture Mechanics, the criteria by Leguillon et al. [41,44] and Carpinteri et al. [42,45,66] require the simultaneous verification of two separate conditions, the former based on stresses, the latter on an energy balance. Each condition is necessary but not sufficient to guarantee the fracture. When both conditions are simultaneously satisfied it is possible to get a sufficient condition for fracture. The governing idea is that at failure a finite incremental crack (or a finite crack advance) occurs at the notch tip. The two criteria are based

on the same energy balance calculated considering a finite incremental crack, the difference being in the stress calculations: the first involves a point-wise stress condition, the second considers an average stress condition.

Under mixed mode I+II loading providing a suitable fracture criterion is more complex than under Mode I loading because the crack path is out of the notch bisector line and its direction varies as a function of Mode I to Mode II stress distributions. For this reason, the problem of brittle or quasi-brittle fracture of notched components loaded under mixed mode (I+II) or prevalent Mode II loading requires further investigations. Another important reason is the scarcity of experimental results available in the literature, in particular dealing with V-notches under prevalent Mode II loading and, then, the possibility to set up an approach for the fracture assessment under the above mentioned conditions.

The proposal of Mode I dominance was first suggested by Erdogan and Sih (1963), when dealing with cracked plates under plane loading and transverse shear, where the crack grows in the direction almost perpendicular to the maximum tangential stress in radial direction from its tip [70]. Several criteria have been applied mainly to sharp V-notched samples but also to U-notches under mixed mode loading [36,44,45,66,71–75], showing a different degree of accuracy with respect to experimental results. The SED criterion, firstly proposed in [36] for sharp notches under Mode I and mixed mode I+II loading, has been extended also to rounded notches [71]. Seweryn and Lucaszewicz [76] reviewed the main criteria available under mixed mode loading. The Finite Fracture Mechanics criterion at re-entrant corners in brittle elastic materials validated for Mode I loading in [41,42] was extended to mixed mode loading and validated by experimental observations [44,45,72]. Chen and Ozaki [73] provided some interesting results under mixed mode loading, however, the prevalent mode during the test was Mode I.

After having briefly summarized the analytical frame in terms of singular stress fields at V-notch tip, strain energy density averaged in a finite size volume and strain energy release rate, the three published brittle fracture criteria [36,44,45,66] are compared considering Mode II loading conditions. The analytical comparison

is performed on the basis of the different expressions proposed for the critical Notch Stress Intensity Factor.

Finally, the considered criteria are applied to components weakened by sharp V-notches under pure Mode II loading in order to investigate the predictive capability of each approach. The comparison involves a number of experimental data taken from the literature and related to different materials.

5.2.2. Analytical frame

With the aim of clarifying the bases of the failure criteria analysed in this work, this section summarises the analytical frame giving the expressions of the singular stress fields at V-notch tip, the SED averaged in the control volume and the strain energy release rate. Only Mode II loading conditions are taken into account, considering an isotropic and homogeneous material under linear elastic conditions.

5.2.2.1. Mode II singular stress fields at V-notch tip

In the presence of a sharp (zero notch tip radius) V-notch, the stress distributions (Fig. 5.2.1a) due to a skew-symmetric loading with respect to the notch bisector line (Mode II) are [54,55]:

$$\begin{aligned} & \begin{Bmatrix} \sigma_{\theta\theta} \\ \sigma_{rr} \\ \sigma_{r\theta} \end{Bmatrix} \\ &= \frac{K_2 \cdot r^{\lambda_2-1}}{\sqrt{2\pi}} \frac{1}{(1-\lambda_2) + \chi_2(1+\lambda_2)} \begin{Bmatrix} (1+\lambda_2) \sin(1-\lambda_2)\theta \\ (3-\lambda_2) \sin(1-\lambda_2)\theta \\ (1-\lambda_2) \cos(1-\lambda_2)\theta \end{Bmatrix} \\ &+ \chi_2(1+\lambda_2) \begin{Bmatrix} \sin(1+\lambda_2)\theta \\ -\sin(1+\lambda_2)\theta \\ \cos(1+\lambda_2)\theta \end{Bmatrix} = \frac{K_2 \cdot r^{\lambda_2-1}}{\sqrt{2\pi}} \begin{Bmatrix} \tilde{\sigma}_{\theta\theta}^{(2)} \\ \tilde{\sigma}_{rr}^{(2)} \\ \tilde{\sigma}_{r\theta}^{(2)} \end{Bmatrix} \end{aligned} \quad (5.2.1)$$

where the parameter K_2 represents the Mode II Notch Stress Intensity Factor (NSIF) according to Gross and Mendelson's definition [56], λ_2 is the Mode II

Williams' eigenvalue [54], χ_2 is an auxiliary parameter dependent on the notch opening angle 2α [55], while $\tilde{\sigma}_{\theta\theta}^{(2)}$, $\tilde{\sigma}_{rr}^{(2)}$ and $\tilde{\sigma}_{r\theta}^{(2)}$ represent the angular stress functions for Mode II loading. Plane stress and plane strain conditions result in $\sigma_{zz} = 0$ and $\sigma_{zz} = \nu(\sigma_{\theta\theta} + \sigma_{rr})$, respectively.

It should be noted that the V-notch tip stress singularity $(1-\lambda_2)$, tied to Mode II loading, disappears for opening angles higher than 102° , according to Williams [54]. Therefore, in the following, only notch opening angles 2α included between 0° and about 100° will be taken into consideration.

5.2.2.2. Strain energy density

According to Beltrami [57], the total strain energy density (SED) is equal to the total work done by the system and it is given by Eq. (5.2.2). For a three dimensional state of stress:

$$W(r, \theta) = \frac{1}{2E} [\sigma_1^2 + \sigma_2^2 + \sigma_3^2 - 2\nu(\sigma_1\sigma_2 + \sigma_1\sigma_3 + \sigma_2\sigma_3)] \quad (5.2.2)$$

where σ_1 , σ_2 and σ_3 are the principal stresses in a given reference system.

In the case of a V-notched plate under Mode II loading, when only the contribution of the first singular term is significant, the SED can be directly linked to the NSIF, K_2 , by substituting into Eq. (5.2.2) the singular stress field given by Eq. (5.2.1):

$$\begin{aligned} W_2(r, \theta) = \frac{1}{2E} r^{2(\lambda_2-1)} K_2^2 & \left[\tilde{\sigma}_{\theta\theta}^{(2)2} + \tilde{\sigma}_{rr}^{(2)2} + \tilde{\sigma}_{zz}^{(2)2} \right. \\ & - 2\nu \left(\tilde{\sigma}_{\theta\theta}^{(2)} \tilde{\sigma}_{rr}^{(2)} + \tilde{\sigma}_{\theta\theta}^{(2)} \tilde{\sigma}_{zz}^{(2)} + \tilde{\sigma}_{rr}^{(2)} \tilde{\sigma}_{zz}^{(2)} \right) \\ & \left. + 2(1 + \nu) \tilde{\sigma}_{r\theta}^{(2)2} \right] \end{aligned} \quad (5.2.3)$$

The strain energy density, averaged in a circular sector of radius R_c surrounding the notch tip (Fig. 5.2.1b), is given by the ratio between the elastic strain energy $E(R_c)$ and the area of the circular sector $A(R_c)$:

$$\begin{aligned}\bar{W} &= \frac{E(R_c)}{A(R_c)} = \frac{\int_A W dA}{\int_A dA} = \frac{\int_0^{R_c} \int_{-\gamma}^{+\gamma} W_2(r, \theta) r dr d\theta}{\int_0^{R_c} \int_{-\gamma}^{+\gamma} r dr d\theta} = \frac{\frac{1}{E} \frac{I_2(\gamma)}{4\lambda_2} K_2^2 R_c^{2\lambda_2}}{R_c^2 \gamma} \\ &= \frac{1}{E} e_2 K_2^2 R_c^{2(\lambda_2-1)}\end{aligned}\quad (5.2.4)$$

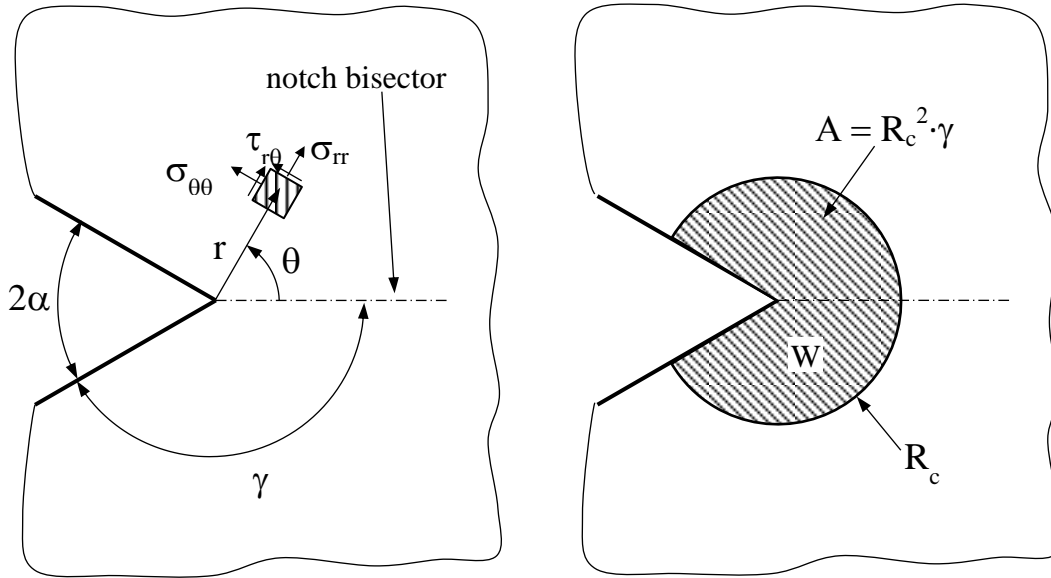


Figure 5.2.1. Polar coordinate system centred at the notch tip (a) and control volume (area) of radius R_c surrounding the V-notch tip.

where I_2 is the integral of the angular stress functions, which depends on the notch opening angle, $2\alpha = 2\pi - 2\gamma$, and the Poisson's ratio ν . I_2 changes under plane stress or plane strain conditions. Finally, e_2 is the parameter that summarizes the dependence from the notch geometry:

$$\begin{aligned}I_2(\gamma) &= \int_{-\gamma}^{+\gamma} \left(\tilde{\sigma}_{\theta\theta}^{(2)2} + \tilde{\sigma}_{rr}^{(2)2} + \tilde{\sigma}_{zz}^{(2)2} \right. \\ &\quad \left. - 2\nu \left(\tilde{\sigma}_{\theta\theta}^{(2)} \tilde{\sigma}_{rr}^{(2)} + \tilde{\sigma}_{\theta\theta}^{(2)} \tilde{\sigma}_{zz}^{(2)} + \tilde{\sigma}_{rr}^{(2)} \tilde{\sigma}_{zz}^{(2)} \right) \right. \\ &\quad \left. + 2(1 + \nu) \tilde{\sigma}_{r\theta}^{(2)2} \right) d\theta\end{aligned}\quad (5.2.5)$$

$$e_2(2\alpha) = \frac{I_2(\gamma)}{4\lambda_2\gamma} \quad (5.2.6)$$

Values of e_2 for plane strain conditions are given in Table 5.2.1 as a function of the V-notch opening angle [38,39]. The averaged value of the strain energy density needs the evaluation of a control radius value, which depends on the material, and varies under static and high cycle fatigue loading conditions [38,39].

Table 5.2.1. Values of the function $e_2(2\alpha, \nu)$.

2α (degrees)	λ_2	$e_2(\nu = 0.2)$	$e_2(\nu = 0.3)$	$e_2(\nu = 0.38)$
0	0.5000	0.3533	0.3414	0.3273
20	0.5620	0.3007	0.2946	0.2863
30	0.5982	0.2768	0.2730	0.2670
40	0.6382	0.2545	0.2525	0.2484
45	0.6597	0.2439	0.2428	0.2395
50	0.6823	0.2337	0.2333	0.2308
60	0.7309	0.2145	0.2153	0.2140
70	0.7844	0.1967	0.1984	0.1982
80	0.8434	0.1802	0.1827	0.1832
90	0.9085	0.1650	0.1679	0.1691
100	0.9805	0.1508	0.1542	0.1558
102.4	1.0000	0.1474	0.1508	0.1526

5.2.2.3. Strain energy release rate

Consider a loaded body initially in an equilibrium state: it is characterized by a potential energy W_p and a kinetic energy $W_k = 0$. After the nucleation of a new crack, or the propagation of a pre-existing crack, there is a change in the potential and kinetic energy of the body. A balance between the internal and external work gives:

$$dW_{\text{int}} = dU + dW_k + dW_s = dW_{\text{ext}} \quad \Rightarrow$$

$$d(U - W_{\text{ext}}) + dW_k + dW_s = 0 \quad (5.2.7)$$

$$dW_p + dW_k + G_c dS = 0 \quad (5.2.8)$$

where U is the elastic strain energy contained in the body, W_{ext} is the work done by the external forces, and W_p and W_k are the potential and kinetic energy, respectively. W_s represents indeed the energy necessary for crack formation, which can be expressed as a function of the new crack surface dS and fracture energy per unit surface G_c .

A condition for fracture can be derived from Eq. (5.2.8), being the kinetic energy always positive ($dW_k \geq 0$):

$$\frac{dW_p}{dS} + G_c \leq 0 \quad \Rightarrow \quad G = -\frac{dW_p}{dS} \geq G_c \quad (5.2.9)$$

The inequality obtained can be taken as a fracture criterion, in which G represents the Strain Energy Release Rate (SERR). When the equality is verified the change in kinetic energy is negligible ($dW_k \rightarrow 0$) and the crack propagation is stable; instead if G exceeds the critical value G_c then the crack propagation is unstable because the extra energy is transformed into kinetic energy of the crack itself ($dW_k \neq 0$).

For two-dimensional problems a relationship between the Strain Energy Release Rate (G) and the Stress Intensity Factors (K_I and K_{II}) can be derived [77] for a straight crack propagation:

$$\begin{cases} G = \frac{K_I^2}{E} + \frac{K_{II}^2}{E} & \text{plane stress} \\ G = (1 - \nu^2) \cdot \frac{K_I^2}{E} + (1 - \nu^2) \cdot \frac{K_{II}^2}{E} & \text{plane strain} \end{cases} \quad (5.2.10)$$

Under critical conditions, a relationship between the critical Strain Energy Release Rate (G_c) and the Mode I fracture toughness (K_{Ic}) can be derived according to Irwin [1]:

$$\begin{cases} G_c = \frac{K_{Ic}^2}{E} & \text{plane stress} \\ G_c = (1 - \nu^2) \cdot \frac{K_{Ic}^2}{E} & \text{plane strain} \end{cases} \quad (5.2.11)$$

Equation (5.2.9) represents the differential form of the Griffith fracture criterion [2], obtained by considering an infinitesimal increment of the crack surface $dS \rightarrow 0$. Considering indeed a finite increment of the crack surface δS , Leguillon [40,41] obtained the incremental form of the fracture criterion:

$$\frac{\delta W_p}{\delta S} + G_c \leq 0 \quad \Rightarrow \quad \tilde{G} = -\frac{\delta W_p}{\delta S} \geq G_c \quad (5.2.12)$$

This is the governing idea of the Finite Fracture Mechanics (FFM).

5.2.3. Failure criteria for sharp V-notches under pure Mode II loading

In the literature the problem of the fracture assessment of components weakened by V-notches is typically treated with stress-based or energy-based approaches. In the present investigation, three different criteria are considered, in order of publication they are: the Strain Energy Density criterion (2001) [36], the Leguillon et al. criterion (2002) [41,44] and the Carpinteri et al. criterion (2008) [42,45,66].

5.2.3.1. Strain energy density (SED) criterion

According to Lazzarin-Zambardi [36] the brittle fracture of the material occurs when the average value of the strain energy density, calculated on a control volume of radius R_c surrounding the notch tip (Fig. 5.2.1b), is equal to the critical value W_c (Eq. 5.2.13). In the case of a smooth component under nominal shear loading condition, according to Beltrami's hypothesis, it can be obtained:

$$W_c = \frac{\tau_c^2}{2G} = \frac{(1 + \nu) \cdot \tau_c^2}{E} \quad (5.2.13)$$

where τ_c is the ultimate shear strength, G the shear modulus and E the Young's modulus, while ν represents the Poisson's ratio.

Considering a V-notched plate subjected to nominal pure Mode II loading, the relationship $\bar{W} = W_c$ is verified under critical conditions. Therefore combining Eq. (5.2.4) and Eq. (5.2.13) one obtains:

$$\frac{e_2}{E} \cdot \frac{K_{2c}^2}{R_c^{2(1-\lambda_2)}} = \frac{(1 + \nu) \cdot \tau_c^2}{E} \quad (5.2.14)$$

The critical value of the Notch Stress Intensity Factor at failure, K_{2c} , becomes:

$$K_{2c} = \sqrt{\frac{(1 + \nu)}{e_2}} \cdot \tau_c \cdot R_c^{(1-\lambda_2)} \quad (5.2.15)$$

The control radius R_c can be easily determined by using a set of experimental data giving the critical value of the NSIF from a specific V-notch angle. If the notch opening angle is zero ($2\alpha = 0$, $\lambda_2 = 0.5$), the case of a cracked specimen under nominal pure Mode II loading is considered, so that under critical conditions K_{2c} coincides with the Mode II fracture toughness K_{IIc} . Then, taking advantage of Eq. (5.2.14), with $K_{2c} \equiv K_{IIc}$, and following the same procedure proposed by Yosibash et al. [58] for obtaining the control radius under Mode I loading condition, the final expression turns out to be:

$$\begin{aligned} R_{c,II} &= \frac{e_2(2\alpha = 0)}{(1 + \nu)} \cdot \left(\frac{K_{IIc}}{\tau_c}\right)^2 = \frac{(1 + \nu)(9 - 8\nu)}{4 \cdot 2\pi \cdot (1 + \nu)} \cdot \left(\frac{K_{IIc}}{\tau_c}\right)^2 \\ &= \frac{(9 - 8\nu)}{8\pi} \cdot \left(\frac{K_{IIc}}{\tau_c}\right)^2 \end{aligned} \quad (5.2.16)$$

Substitution of Eq. (5.2.16) into Eq. (5.2.15) gives the NSIF at failure K_{2c} (Eq. (5.2.17)) in the form:

$$K_{2c} = \left[\sqrt{\frac{1 + \nu}{e_2}} \cdot \left(\frac{9 - 8\nu}{8\pi}\right)^{(1-\lambda_2)} \right] \cdot K_{IIc}^{2(1-\lambda_2)} \cdot \tau_c^{2\lambda_2-1} \quad (5.2.17)$$

It is useful to express the NSIF at failure K_{2c} as a function of the Mode I material properties (K_{Ic} and σ_c), which are simpler to determine or to find in the literature than Mode II material properties. For this purpose, it is possible to approximately estimate the Mode II fracture toughness (K_{IIc}) as a function of K_{Ic} , according for example to Richard et al. [78]:

$$K_{IIc} \cong \frac{\sqrt{3}}{2} K_{Ic} \quad (5.2.18)$$

In the same manner, it is possible to approximately estimate the ultimate shear strength (τ_c) as a function of the tensile one (σ_c). Several failure criteria are shown in the literature (Guest-Tresca, von Mises and Beltrami among the others), but with reference to brittle materials with linear elastic behavior (as for example polymethylmethacrylate, graphite,...), it has been observed experimentally [39] that the most appropriate criterion is that of Galileo-Rankine:

$$\tau_c = \phi \cdot \sigma_c \quad \text{with} \quad \phi = 1 \quad (5.2.19)$$

Indeed, on the basis of experimental results on PMMA and graphite specimens [39], it has been observed that the ratio $\phi = \tau_c/\sigma_c$ varies a limited range, between 0.80 and 1.00. In the case of materials that exhibit a different behaviour, the criterion is still applicable once calibrated the value of the ratio ϕ . Finally, substitution of Eqs. (5.2.18) and (5.2.19) into Eq. (5.2.17) gives the NSIF at failure K_{2c} in a more useful form:

$$K_{2c} = \left[\sqrt{\frac{1+\nu}{e_2}} \cdot \left(\frac{3}{4} \cdot \frac{9-8\nu}{8\pi} \right)^{(1-\lambda_2)} \cdot \phi^{2\lambda_2-1} \right] \cdot K_{Ic}^{2(1-\lambda_2)} \cdot \sigma_c^{2\lambda_2-1} \quad (5.2.20)$$

It should be noted that the control radius R_c could be in principle different under Mode I and Mode II loading condition, this means that it depends on the material properties but also on the loading conditions, as recently highlighted in [79,80]. However, in previous contributions [81–84], the SED approach has been applied to notched components under mixed mode I+II and prevalent Mode II loading conditions, by adopting the control radius $R_{c,I}$ derived under Mode I loading [58].

This was possible mainly for two reasons: 1) the SED approach has been combined with the ‘equivalent local mode I’ concept [71], according to which under mixed mode loading the control volume is no longer centered at the notch tip, but rather at the point where the principal stress reaches its maximum value along the edge of the notch, following the Mode I dominance proposed by Erdogan and Sih [70]; 2) the application of SED approach has mostly involved blunt V-notched components, in which Mode II stresses are negligible in the close neighborhood of the notch tip compared to Mode I stresses.

Concerning instead sharp V-notched components under pure Mode II loading the ‘equivalent local mode I’ concept is not applicable and in addition Mode II stresses are singular at the notch tip, hence the need to adopt the proper control radius $R_{c,II}$ (Eq. 5.2.16).

Once known the expressions of $R_{c,I}$ [58] and $R_{c,II}$ (Eq. 5.2.16), it is possible to evaluate the ratio between the control radii $R_{c,I}/R_{c,II}$, adopting the approximate expressions (5.2.18) and (5.2.19) one obtains:

$$\frac{R_{c,I}}{R_{c,II}} = \frac{8 \cdot (1 + \nu) \cdot (5 - 8\nu)}{3 \cdot (9 - 8\nu)} \cdot \phi^2 \quad (5.2.21)$$

The trend of the ratio $R_{c,I}/R_{c,II}$, as a function of Poisson’s ratio ν , has been reported in Fig. 5.2.2. In the particular case of a material for which the expressions (18) and (19) result approximately verified (with $\phi = 1$), it can be observed from Fig. 5.2.2 that $R_{c,I}$ and $R_{c,II}$ are coincident for a Poisson's ratio ν about equal to 0.45.

Finally, it should be noted that the SED criterion does not allow to predict the fracture direction (θ_c), since the expression of K_{2c} reported in Eq. (5.2.17) is constant for a given notch opening angle and does not depend on the polar coordinate θ (Fig. 5.2.1).

Moreover, it is important to underline that according to SED criterion [36] only the nominal Mode II loading condition has been taken into account in Eq. (5.2.12), with reference to the ultimate strength τ_c of smooth specimens, and in Eqs. (5.2.14)-(5.2.16), with reference to the critical NSIF K_{2c} and to the fracture toughness K_{IIc} of notched and cracked components, respectively. This differentiates the SED criterion from the following FFM-based approaches, which

instead take into account that, even if the nominally applied load is Mode II, from the local point of view the crack initiates and grows in a direction such that it opens, in accordance with the concept of Mode I dominance proposed by Erdogan and Sih [70].

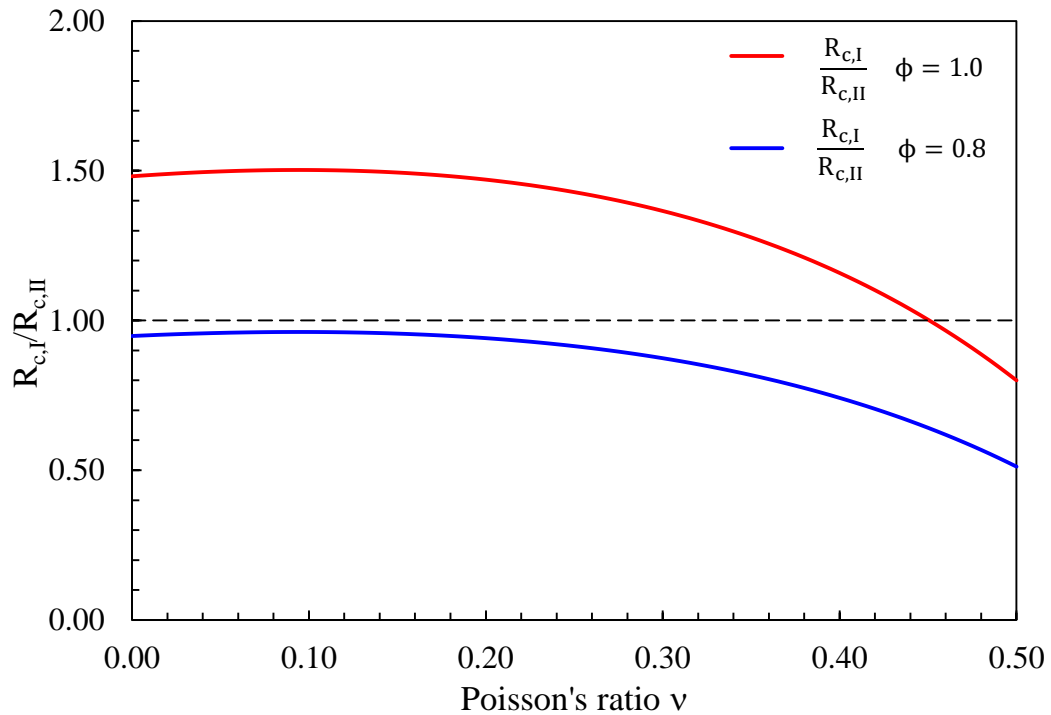


Figure 5.2.2. Trend of the ratio $R_{c,I}/R_{c,II}$, as a function of the Poisson's ratio ν , Eq. (5.2.21).

5.2.3.2. FFM: Leguillon's criterion

Leguillon et al. [41,44] proposed a fracture criterion for components weakened by sharp V-notches based on the Finite Fracture Mechanics concept: at failure an incremental crack of length l_c nucleates at the notch tip.

According to Leguillon's criterion, two necessary conditions can be stated on stress and energy, but neither the one nor the other, taken separately, are sufficient. Only when they are simultaneously satisfied it is possible to get a condition sufficient for fracture.

According to the stress criterion the V-notched element failure occurs when the singular stress component normal to the fracture direction $\bar{\theta}_c$ exceeds the material tensile strength σ_c all along the crack with length l_c just prior to fracture. It

amounts to a point-stress condition at a distance l_c since the tensile stress is a decreasing function of the distance to the notch root.

According to the energy criterion, instead, the component failure occurs when the strain energy release rate \tilde{G} , that is the ratio between the potential energy variation in correspondence of the crack nucleation (δW_p) and the new crack surface created (δS), exceeds the critical material value G_c .

Therefore the simultaneous verification of the conditions formalized in Eqs. (5.2.22) and (5.2.23) provides a general criterion for the fracture of components weakened by sharp V-notches.

Stress criterion :
$$\sigma_{\theta\theta}(l_c, \bar{\theta}_c) = k_2 \cdot l_c^{\lambda_2-1} \cdot \tilde{\sigma}_{\theta\theta}^{(2)}(\bar{\theta}_c) \geq \sigma_c \quad (5.2.22)$$

Energy criterion :
$$\tilde{G} = -\frac{\delta W_p}{\delta S} = \frac{k_2^2 \cdot H_{22}^*(2\alpha, \bar{\theta}_c) \cdot l_c^{2\lambda_2} \cdot d}{l_c \cdot d} \geq G_c \quad (5.2.23)$$

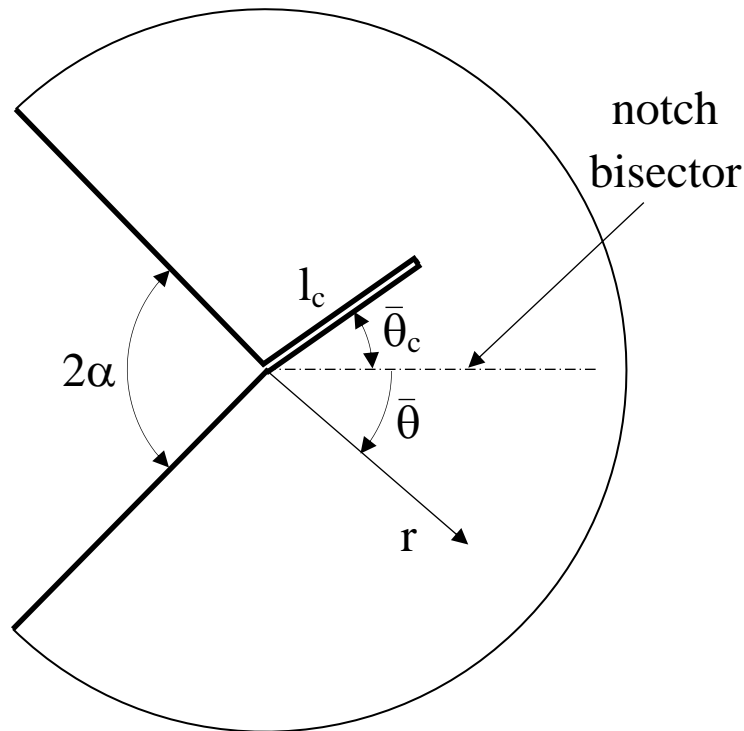


Figure 5.2.3. Leguillon's coordinate system [41,44], with incremental crack of length l_c .

In Eqs. (5.2.22, 5.2.23) l_c is the length of the incremental crack nucleated at the notch tip (see Fig. 5.2.3), λ_2 is the Mode II Williams' eigenvalue [54] tied to the V-notch angle 2α , $\tilde{\sigma}_{\theta\theta}^{(2)}(\bar{\theta})$ is a function of the angular coordinate $\bar{\theta}$, d is the thickness of the component. Finally, $H_{22}^*(2\alpha, \bar{\theta}_c)$ is a “geometrical factor” dependent on the local geometry (2α) and the direction of fracture ($\bar{\theta}_c$).

The parameter k_2 represents the NSIF according to Leguillon's definition, which is linked to Gross and Mendelson's definition [56] by means of Eq. (5.2.24).

$$k_2 = \lim_{r \rightarrow 0} \sigma_{r\theta} \cdot r^{1-\lambda_2} = \frac{\lim_{r \rightarrow 0} \sigma_{r\theta} \cdot \sqrt{2\pi} \cdot r^{1-\lambda_2}}{\sqrt{2\pi}} = \frac{K_2}{\sqrt{2\pi}} \quad (5.2.24)$$

In the following the lowercase letter will be used for the NSIFs defined according to Leguillon, capital letter instead for the NSIFs defined according to Gross and Mendelson.

The conditions (22) and (23) must be simultaneously satisfied. Solving the system in two unknowns, l_c and k_2 , it is possible to determine the length of the incremental crack:

$$l_c = \frac{G_c}{H_{22}^*(2\alpha, \bar{\theta}_c)} \cdot \left(\frac{\tilde{\sigma}_{\theta\theta}^{(2)}(\bar{\theta}_c)}{\sigma_c} \right)^2 \quad (5.2.25)$$

As soon as the incremental crack length l_c is introduced into Eq. (5.2.22) or Eq. (5.2.23), it is possible to give the failure criterion in terms of the classic Irwin's expression, $K_I \geq K_{Ic}$. The critical value of the Notch Stress Intensity Factor k_{2c} can be defined as a function of the material mechanical properties (σ_c and G_c), the notch opening angle 2α and the critical crack propagation angle $\bar{\theta}_c$.

$$k_2 \geq \left(\frac{G_c}{H_{22}^*(2\alpha, \bar{\theta}_c)} \right)^{1-\lambda_2} \cdot \left(\frac{\sigma_c}{\tilde{\sigma}_{\theta\theta}^{(2)}(\bar{\theta}_c)} \right)^{2\lambda_2-1} = k_{2c} \quad (5.2.26)$$

Under plane strain conditions G_c can be linked to the material fracture toughness K_{Ic} in the following form (see Eq. (5.2.11)):

$$G_c = K_{Ic}^2 \cdot \frac{1 - \nu^2}{E} \quad (5.2.27)$$

Yosibash et al. [44] have computed the function H_{22} for a range of values of the notch opening angle 2α and of the fracture direction $\bar{\theta}_c$, taking into account a material characterized by a Young's modulus $E = 1$ MPa and a Poisson's ratio $\nu = 0.36$. The function H_{22}^* for any other Young's modulus E and Poisson's ratio ν can be easily obtained according to the following expression:

$$H_{22}^*(2\alpha, \bar{\theta}_c) = H_{22}(2\alpha, \bar{\theta}_c) \cdot \frac{1 - \nu^2}{E} \cdot \frac{1}{1 - 0.36^2} \quad (5.2.28)$$

The values of H_{22} can be found in [44], with reference only to certain values of 2α and $\bar{\theta}_c$, or they can be evaluated according to the procedure described in the same contribution.

A simpler expression of the critical NSIF k_{2c} , as a function of the material fracture toughness K_{Ic} and the ultimate tensile strength σ_c , can be obtained substituting expressions (27) and (28) into Eq. (5.2.26). As a result:

$$k_{2c} = \left[\left(\frac{1 - 0.36^2}{H_{22}(2\alpha, \bar{\theta}_c)} \right)^{1-\lambda_2} \cdot \left(\frac{1}{\tilde{\sigma}_{\theta\theta}^{(2)}(\bar{\theta}_c)} \right)^{2\lambda_2-1} \right] \cdot K_{Ic}^{2(1-\lambda_2)} \cdot \sigma_c^{2\lambda_2-1} \quad (5.2.29)$$

The fracture direction $\bar{\theta}_c$, corresponding to the minimum failure load (i.e. the minimum value of k_{2c}), can be obtained by setting the $\bar{\theta}$ -derivative of k_{2c} equal to 0:

$$\frac{d}{d\bar{\theta}} \left[\left(H_{22}(2\alpha, \bar{\theta}) \right)^{1-\lambda_2} \cdot \left(\tilde{\sigma}_{\theta\theta}^{(2)}(\bar{\theta}) \right)^{2\lambda_2-1} \right] = 0 \quad (5.2.30)$$

The condition (30) provides the critical crack propagation angle $\bar{\theta}_c$ for each notch opening angle 2α . Different values of $\bar{\theta}_c$ for $0^\circ \leq 2\alpha \leq 100^\circ$ are reported in Table 5.2.2. Once known the fracture direction $\bar{\theta}_c$ as a function of the notch opening angle 2α , from Eq. (5.2.30), the expression of the critical NSIF k_{2c} can be simplified as follow:

$$k_{2c} = h_k(2\alpha) \cdot K_{Ic}^{2(1-\lambda_2)} \cdot \sigma_c^{2\lambda_2-1} \quad (5.2.31)$$

A slightly different formulation of the criterion can be obtained by using Gross and Mendelson's definition for the critical NSIF K_{2c} according to Eq. (5.2.24).

$$K_{2c} = [\sqrt{2\pi} \cdot h_k(2\alpha)] \cdot K_{Ic}^{2(1-\lambda_2)} \cdot \sigma_c^{2\lambda_2-1} \quad (5.2.32)$$

5.2.3.3. FFM: Carpinteri's formulation

Similarly to Leguillon, Carpinteri et al. [42,45,66] proposed a fracture criterion for components weakened by sharp V-notches based on Finite Fracture Mechanics concept: at failure a crack of length Δ nucleates at the notch tip. Also in this formulation, it is possible to obtain a sufficient condition for the fracture by satisfying simultaneously a stress criterion and an energy criterion.

According to the averaged stress criterion the V-notched element failure occurs when the notch singular stress component normal to the crack faces, averaged over the crack length Δ , exceeds the material tensile strength σ_c .

According to the energy criterion, instead, the component failure occurs when the strain energy released at the nucleation of a crack of length Δ exceeds the critical value of the material, which depends on G_c . A simplified formulation can be obtained by expressing the strain energy release rate G as a function of the Stress Intensity Factors K_I and K_{II} according to Eq. (5.2.10) valid under plane strain conditions for a straight crack propagation.

Therefore the simultaneous verification of the conditions formalized in Eq. (5.2.33) and (5.2.34) provides a general criterion for the fracture of components weakened by sharp V-notches.

Averaged stress criterion :

$$\int_0^\Delta \sigma_{\theta\theta}(r, \theta_c) dr = \int_0^\Delta \frac{K_{II}^*}{(2\pi r)^{1-\lambda_2}} \tilde{\sigma}_{\theta\theta}^{(2)}(\theta_c) dr \geq \sigma_c \cdot \Delta \quad (5.2.33)$$

Energy criterion :

$$\int_0^\Delta -\frac{dW_p}{da} da = \int_0^\Delta G(a, \theta_c) da \geq G_c \cdot \Delta \quad (5.2.34)$$

$$\begin{aligned} \int_0^\Delta [K_I^2(a, \theta_c) + K_{II}^2(a, \theta_c)] da \\ = \int_0^\Delta \left[K_{II}^{*2} \cdot a^{2\lambda_2-1} \cdot (\beta_{12}^2(2\alpha, \theta_c) + \beta_{22}^2(2\alpha, \theta_c)) \right] da \geq K_{Ic}^2 \cdot \Delta \end{aligned}$$

where Δ is the length of the crack nucleated at the notch tip (Fig. 5.2.4), λ_2 the Mode II Williams' eigenvalue [54], (r, θ) the polar coordinate system centred at the notch tip and a the generic crack length. The β_{ij} 's are defined later in Eq. (5.2.36).

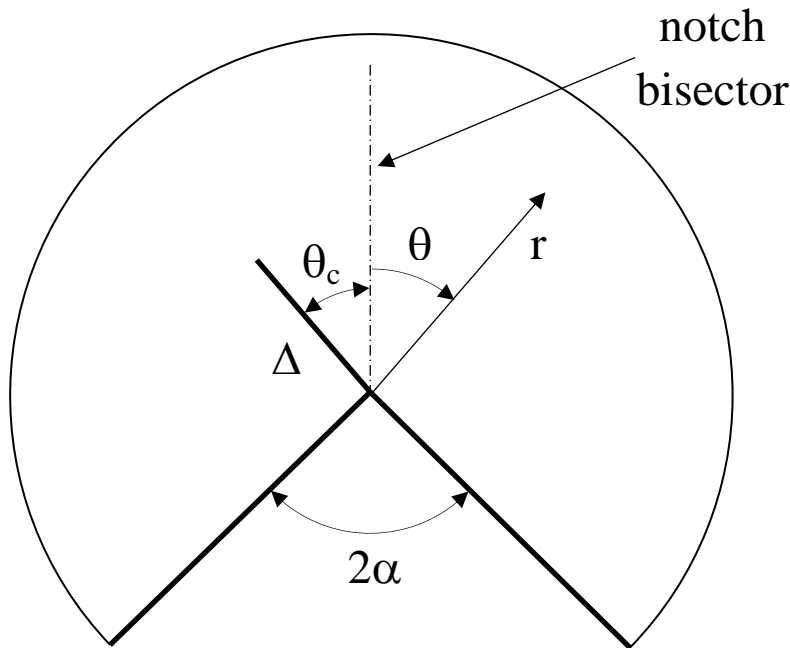


Figure 5.2.4. Carpinteri's coordinate system [42,45,66], with crack of length Δ .

The parameter K_{II}^* represents again the NSIF according to Carpinteri's definition, which is slightly different from that given by Gross and Mendelson [56]. In particular:

$$K_{II}^* = \lim_{r \rightarrow 0} \sigma_{r\theta} \cdot (2\pi r)^{1-\lambda_2} = \frac{\lim_{r \rightarrow 0} \sigma_{r\theta} \cdot \sqrt{2\pi} \cdot r^{1-\lambda_2}}{(2\pi)^{\lambda_2 - \frac{1}{2}}} = \frac{K_2}{(2\pi)^{\lambda_2 - \frac{1}{2}}} \quad (5.2.35)$$

In order to apply the energy criterion it is necessary to know the Stress Intensity Factors K_I and K_{II} of the tilted crack nucleated at V-notch tip, as a function of the crack length a . For this purpose it is possible to use the expressions of the SIFs K_I and K_{II} as a function of the crack length a , the notch opening angle 2α , the direction of fracture θ_c and the NSIF K_{II}^* derived by Beghini et al. [85], on the basis of approximate analytical weight functions.

$$K_I(a, \theta) = \beta_{12}(2\alpha, \theta) \cdot K_{II}^* \cdot a^{\lambda_2 - \frac{1}{2}} \quad (5.2.36a)$$

$$K_{II}(a, \theta) = \beta_{22}(2\alpha, \theta) \cdot K_{II}^* \cdot a^{\lambda_2 - \frac{1}{2}} \quad (5.2.36b)$$

The functions β_{ij} can be evaluated from the best fit expressions provided in Melin [86] for $2\alpha = 0^\circ$ and in Beghini et al. [85] for $2\alpha > 18^\circ$. It is useful to introduce a simplified notation according to Eq. (5.2.37), in which the relationship between the parameter $\bar{\beta}_{22}$ according to Sapora et al. [66] and the parameter H_{22} according to Yosibash et al. [44] is shown, as highlighted also in [45].

$$\bar{\beta}_{22}(2\alpha, \theta) = \frac{\beta_{12}^2(2\alpha, \theta) + \beta_{22}^2(2\alpha, \theta)}{2\lambda_2} = \frac{H_{22}(2\alpha, \theta) \cdot (2\pi)^{2\lambda_2 - 2}}{1 - 0.36^2} \quad (5.2.37)$$

According to Carpinteri's criterion the failure of a V-notched component occurs when the stress and energy criteria given by Eqs. (5.2.33, 5.2.34) are both satisfied. Solving the system, it is possible to determine the length of the nucleated crack Δ (Eq. (5.2.38)) and the critical NSIF K_{IIc}^* (Eq. (5.2.39)).

$$\Delta = \left[\left(\frac{1}{\bar{\beta}_{22}(2\alpha, \theta_c)} \right) \cdot \left(\frac{\tilde{\sigma}_{\theta\theta}^{(2)}(\theta_c)}{\lambda_2 \cdot (2\pi)^{1-\lambda_2}} \right)^2 \right] \cdot \left(\frac{K_{Ic}}{\sigma_c} \right)^2 \quad (5.2.38)$$

$$K_{II}^* \geq \left[\left(\frac{1}{\bar{\beta}_{22}(2\alpha, \theta_c)} \right)^{1-\lambda_2} \cdot \left(\frac{\lambda_2 \cdot (2\pi)^{1-\lambda_2}}{\tilde{\sigma}_{\theta\theta}^{(2)}(\theta_c)} \right)^{2\lambda_2-1} \right] \cdot K_{Ic}^{2(1-\lambda_2)} \cdot \sigma_c^{2\lambda_2-1}$$

$$= K_{IIc}^* \quad (5.2.39)$$

Following the procedure presented in the case of Leguillon et al. criterion, the fracture direction θ_c , corresponding to the minimum failure load (i.e. the minimum value of K_{IIc}^*), can be obtained by setting the θ -derivative of K_{IIc}^* equal to 0:

$$\frac{d}{d\theta} \left[\left(\bar{\beta}_{22}(2\alpha, \theta) \right)^{1-\lambda_2} \cdot \left(\tilde{\sigma}_{\theta\theta}^{(2)}(\theta) \right)^{2\lambda_2-1} \right] = 0 \quad (5.2.40)$$

The condition (40) provides the critical crack propagation angle θ_c for each notch opening angle 2α . Different values of θ_c for $0^\circ \leq 2\alpha \leq 100^\circ$ are reported in Table 5.2.2. Once known the fracture direction θ_c as a function of the notch opening angle 2α , from Eq. (5.2.40), the expression of the critical NSIF K_{IIc}^* can be simplified as follow:

$$K_{IIc}^* = g_k(2\alpha) \cdot K_{Ic}^{2(1-\lambda_2)} \cdot \sigma_c^{2\lambda_2-1} \quad (5.2.41)$$

Then, by using for the critical NSIF, K_{2c} , the definition of Gross and Mendelson [56], see Eq. (5.2.35), the final result is:

$$K_{2c} = \left[(2\pi)^{\left(\lambda_2 - \frac{1}{2}\right)} \cdot g_k(2\alpha) \right] \cdot K_{Ic}^{2(1-\lambda_2)} \cdot \sigma_c^{2\lambda_2-1} \quad (5.2.42)$$

Table 5.2.2. Crack propagation angles estimated according to Leguillon et al. criterion [41,44] and to Carpinteri et al. criterion [42,45,66], as a function of the notch opening angle 2α .

2α (degrees)	Crack propagation angle (degrees)	
	Leguillon et al.	Carpinteri et al.
0	75	76
20	71	71
30	68	68
40	66	66
50	64	63
60	61	61
70	59	59
80	57	56
90	54	54
100	52	52

5.2.4. Analytical comparison

Considering the three different formulations, it is possible to compare the final relationships of the critical NSIF according to Gross and Mendelson's definition:

SED:

$$K_{2c} = \left[\sqrt{\frac{1+\nu}{e_2}} \cdot \left(\frac{3 \cdot (9-8\nu)}{32\pi} \right)^{(1-\lambda_2)} \cdot \Phi^{2\lambda_2-1} \right] \cdot K_{Ic}^{2(1-\lambda_2)} \cdot \sigma_c^{2\lambda_2-1} \quad (5.2.43)$$

Leguillon et al.:

$$K_{2c} = [\sqrt{2\pi} \cdot h_k(2\alpha)] \cdot K_{Ic}^{2(1-\lambda_2)} \cdot \sigma_c^{2\lambda_2-1} \quad (5.2.44)$$

Carpinteri et al.:

$$K_{2c} = \left[(2\pi)^{\left(\lambda_2 - \frac{1}{2}\right)} \cdot g_k(2\alpha) \right] \cdot K_{Ic}^{2(1-\lambda_2)} \cdot \sigma_c^{2\lambda_2-1} \quad (5.2.45)$$

It can be observed that the three criteria give the same proportionality relation:

$$K_{2c} \propto K_{Ic}^{2(1-\lambda_2)} \cdot \sigma_c^{2\lambda_2-1} \quad (5.2.46)$$

The difference is given only by the proportionality factor. This factor depends only on the notch opening angle (2α) in Leguillon's and Carpinteri's criteria. In the SED criterion, instead, the proportionality factor depends on the opening angle 2α and the Poisson's ratio ν , as shown in Fig. 5.2.5. As pointed out above, the V-notch tip singularity ($1-\lambda_2$), tied to Mode II loading, disappears for opening angles higher than 102° , according to Williams [54]. Therefore the analytical comparison of Eqs. (5.2.43-5.2.45) has been carried out for notch opening angles 2α between 0° and about 100° .

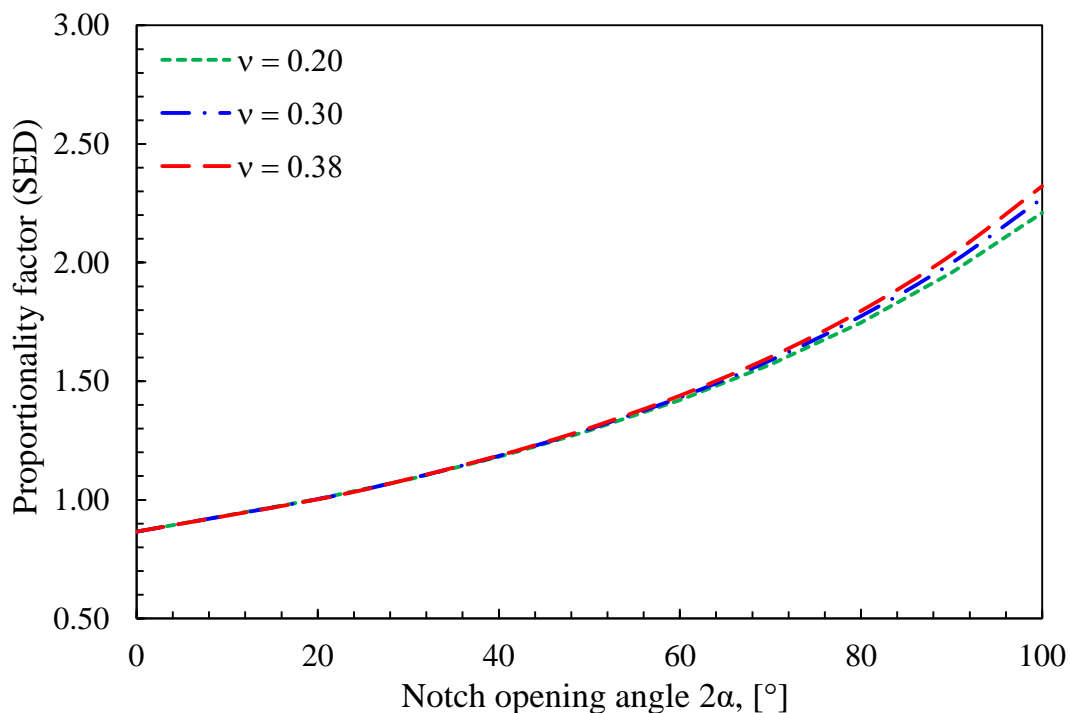
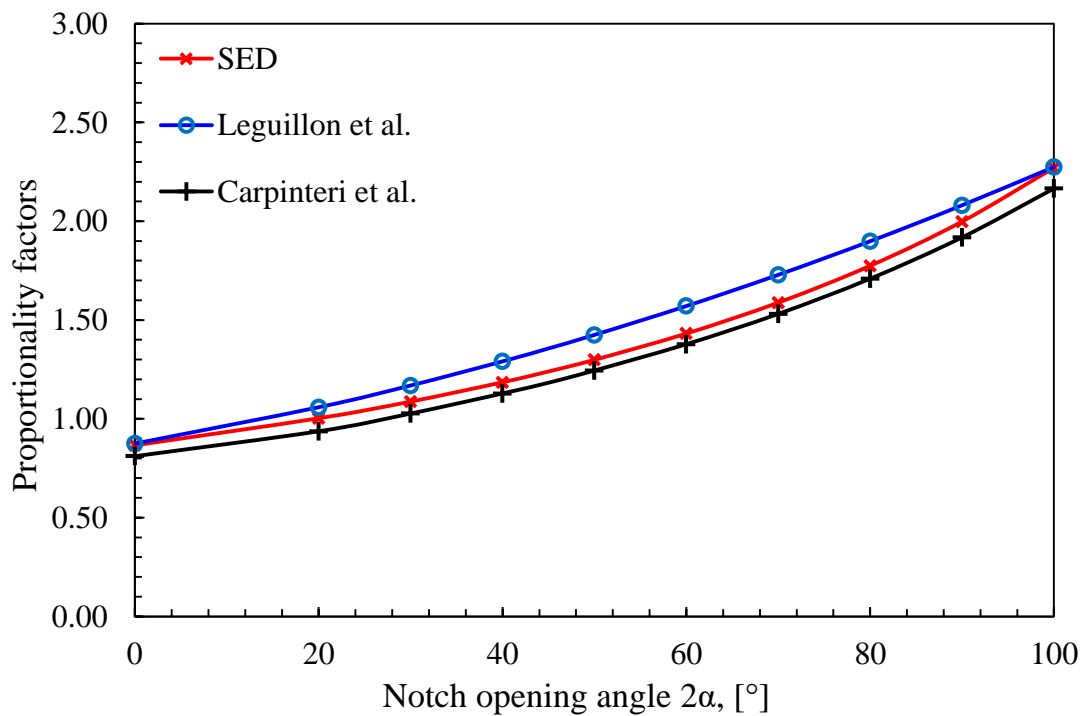


Figure 5.2.5. Variability of proportionality factor in the SED criterion, Eq. (5.2.43), as a function of the Poisson's ratio ν .

Table 5.2.3. Proportionality factors in Eqs. (5.2.43,5.2.44,5.2.45).

2α (degrees)	λ_2	SED ($\nu = 0.3$)	Leguillon et al.	Carpinteri et al.
0	0.5000	0.866	0.875	0.811
20	0.5620	1.003	1.059	0.937
30	0.5982	1.087	1.169	1.027
40	0.6382	1.185	1.291	1.128
45	0.6597	1.240	1.356	1.183
50	0.6823	1.299	1.425	1.245
60	0.7309	1.432	1.571	1.378
70	0.7844	1.588	1.729	1.531
80	0.8434	1.774	1.899	1.709
90	0.9085	1.998	2.081	1.918
100	0.9805	2.270	2.275	2.165

**Figure 5.2.6.** Comparison among proportionality factors given by Eqs. (5.2.43,5.2.44,5.2.45).

The proportionality factors do not differ significantly in their trends, with the values of Leguillon's factor being always slightly greater than those assumed by

the other two criteria for the same notch opening angle (2α), as shown in Fig. 5.2.6 and in Table 5.2.3. For $2\alpha = 0^\circ$ and 100° Leguillon's and SED criteria give the same proportionality factor, 0.87 and 2.27, respectively. The factor based on Carpinteri's criterion, instead, does not match that of the other two criteria for any value of 2α .

5.2.5. Experimental validation

The predictive capability of the three different approaches is assessed by using a good number of experimental data taken from the literature. The analysed data are referred to V-notched specimens made of two materials: polymethylmethacrylate (PMMA) and graphite. The mechanical properties of each tested material as well as the experimental procedures adopted are described below.

The comparison between the experimental data and the theoretical estimations based on Eqs. (5.2.43-5.2.45) is performed in terms of Notch Stress Intensity Factor K_{2c} to failure as a function of the V-notch opening angle 2α . When not directly available, the values of the critical NSIF to failure K_{2c} have been obtained by two-dimensional FEM analyses, by introducing into the models the experimental fracture loads. The finite element code ANSYS®, version 14.5, has been used. In particular, the critical NSIF to failure K_{2c} coincides with the Notch Stress Intensity Factor K_2 calculated along the notch bisector line ($K_2 = \sigma_{r\theta} \cdot \sqrt{2\pi} \cdot r^{1-\lambda_2}$ with $r \rightarrow 0$) when the final load to failure is applied to the FE model. The first set of experimental data is due to Ayatollahi and Torabi [87], who performed fracture tests on V-notched Brazilian disc (V-BD) made of graphite.

The specimens geometry was characterized by a disc diameter $D = 60$ mm, a notch depth $a = 15$ mm and a thickness $t = 8$ mm. Three values of the notch opening angle, $2\alpha = 30^\circ$, 60° and 90° , have been considered, being the loading angle to obtain pure Mode II loading equal to $\beta_{II} = 25^\circ$, 30° and 35° [87], respectively. Three graphite specimens were tested for each opening angle 2α .

The mechanical properties of the tested graphite were: Young's modulus $E = 8050$ MPa, Poisson's ratio $\nu = 0.20$, fracture toughness $K_{Ic} = 1.00$ MPa $m^{0.5}$ and tensile strength $\sigma_c = 27.50$ MPa.

The experimental values of the Notch Stress Intensity Factor K_{2c} to failure are reported for each specimen in Fig. 5.2.7 as a function of the notch opening angle 2α . In the same figure the theoretical curves of K_{2c} as a function of the notch opening angle 2α are reported for comparison.

The second set of experimental data (Seweryn et al. [21]) was obtained from Arcan tests performed on PMMA double V-notched specimens.

The samples geometry was characterized by a length $l = 200$ mm, width $w = 100$ mm, notch depth $a = 25$ mm and thickness $t = 5$ mm. Four values of the notch opening angle, $2\alpha = 20^\circ, 40^\circ, 60^\circ$ and 80° , have been considered, being the loading angle to obtain pure Mode II loading equal to $\psi = 90^\circ$ [21]. Three PMMA specimens were tested for each opening angle.

The material properties were: Young's modulus $E = 3000$ MPa, Poisson's ratio $\nu = 0.30$ and fracture toughness $K_{Ic} = 1.37$ MPa m^{0.5}. Furthermore the true curve σ - ϵ of unnotched specimens exhibited a non-linear behaviour whereas the notched specimens presented a brittle behaviour, with a linear trend up to the critical load, followed by a sudden failure. This is because the notch sufficiently weakens the specimens so that the experiments remain within the linear initial stage. Under these circumstances the critical stress σ_c should be substituted by "the maximum normal stress existing at the notch edge at the moment preceding the cracking", as underlined in Ref. [7] where it is also recommended to use tensile specimens with semicircular notches. Hence the critical loads obtained experimentally from tensile specimens characterized by semicircular notches with a root radius $\rho = 25$ mm have been used to estimate the critical strength σ_c . According to Seweryn et al. [21], the value of the 'critical tensile stress' at the notch root was 115 MPa, in fairly good agreement with other values reported in the literature for PMMA: for example Carpinteri [5] and Dunn et al. [9,10] gave 130 and 124 MPa, respectively.

The experimental values of the Notch Stress Intensity Factor K_{2c} to failure are plotted for each specimen in Fig. 5.2.8 as a function of the notch opening angle 2α . In the same figure the theoretical curves of K_{2c} obtained applying the three different formulations are given for comparison.

The third set of experimental data (Ayatollahi et al. [88]) was obtained from fracture tests conducted on V-notched Brazilian disc (V-BD) made of PMMA.

The specimens geometry was characterized by a disc diameter $D = 80$ mm, a notch depth $a = 20$ mm and a thickness $t = 10$ mm. Three values of the notch opening angle, $2\alpha = 30^\circ$, 60° and 90° , have been considered, being the loading angle to obtain pure Mode II loading equal to $\beta_{II} = 22.5^\circ$, 30.5° and 35° [88], respectively. A total number of 9 specimens were tested, three specimens for each geometry.

The material properties were: Young's modulus $E = 2960$ MPa, Poisson's ratio $\nu = 0.38$, fracture toughness $K_{Ic} = 1.96$ MPa m^{0.5} and tensile strength $\sigma_c = 70.5$ MPa. The experimental values of the Notch Stress Intensity Factor K_{2c} to failure are shown for each specimen in Fig. 5.2.9 as a function of the notch opening angle 2α . In the same figure the theoretical curves of K_{2c} as a function of the notch opening angle 2α are reported for comparison.

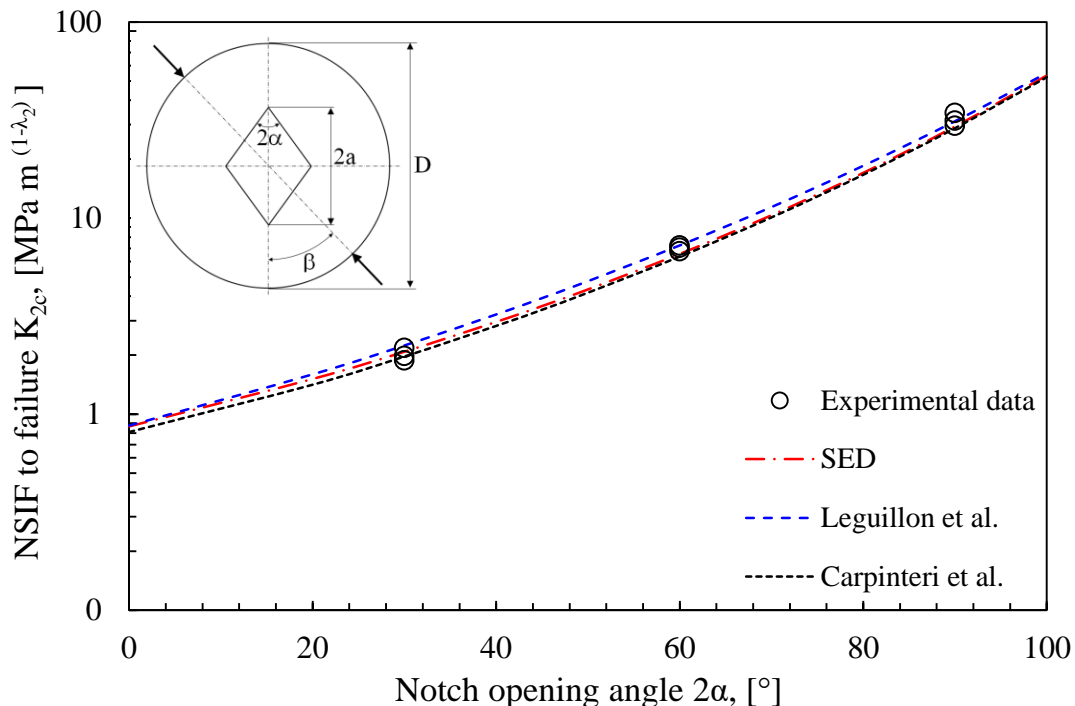


Figure 5.2.7. Plots of the NSIF to failure K_{2c} (Log-scale) and comparison with the experimental data from V-notched Brazilian disc (V-BD) specimens made of graphite tested by Ayatollahi and Torabi [87].

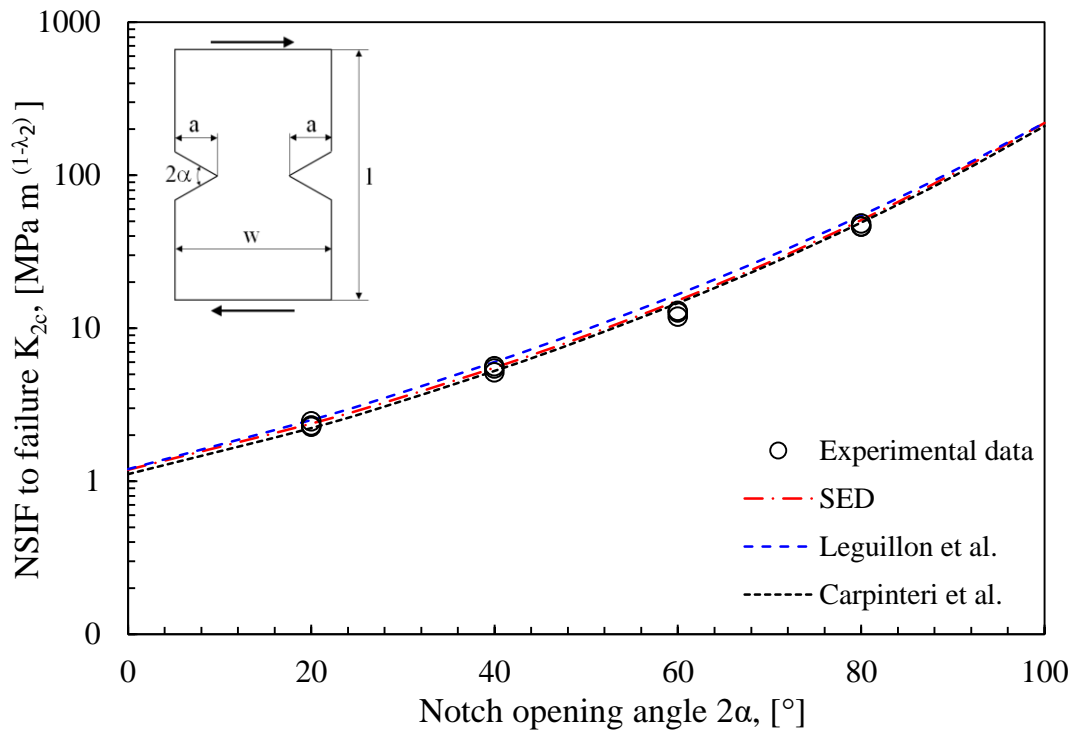


Figure 5.2.8. Plots of the NSIF to failure K_{2c} (Log-scale) and comparison with the experimental data from PMMA double V-notched specimens tested by Seweryn [21].

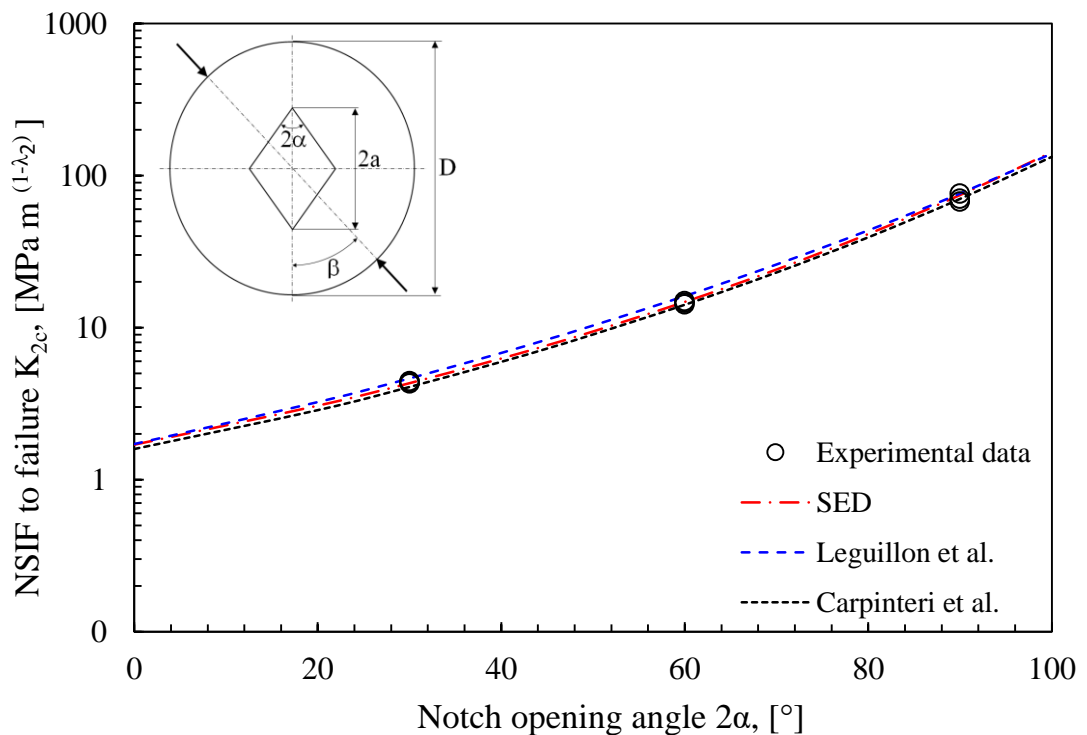


Figure 5.2.9. Plots of the NSIF to failure K_{2c} (Log-scale) and comparison with the experimental data from V-notched Brazilian disc (V-BD) specimens made of PMMA tested by Ayatollahi et al. [88].

The plots of Figs. 5.2.7-5.2.9 show that the agreement between the theoretical estimates and the experimental values of Notch Stress Intensity Factor K_{2c} to failure is very good in all cases. It can be observed that theoretical assessments based on the averaged SED and the Carpinteri's criterion are always fairly conservative with respect to those obtained by applying the Leguillon's criterion.

5.2.6. Discussion

A comparison between different fracture criteria for brittle components weakened by sharp V-notches has been presented considering Mode II loading conditions. The comparison has considered the averaged SED criterion, and two different formulations of the Finite Fracture Mechanics theory, according to Leguillon and to Carpinteri et alii.

With reference to the criterion based on the averaged SED, a new expression for estimating the control radius R_c under pure Mode II loading has been proposed and discussed in comparison with the expression valid for pure Mode I.

The analytical comparison has been performed on the basis of the different expressions for the critical value of the NSIF K_{2c} . The same proportionality relation exists between K_{2c} and two fundamental mechanical properties of the material: the fracture toughness K_{Ic} and the ultimate tensile strength σ_c . The difference is given by a proportionality factor, which depends only on the V-notch opening angle in Leguillon and Carpinteri's criteria, whereas it depends on the opening angle and the Poisson's ratio in the SED approach. The variability of the proportionality factors has been examined in detail.

Finally, the three criteria have been applied to components weakened by sharp V-notches under Mode II loading conditions in order to investigate the predictive capability of each approach. A number of experimental data taken from the literature have been used for the comparison. A very good agreement in terms of critical values of the NSIF K_{2c} has been found in all cases.

References

- [1] Irwin GR. Analysis of stresses and strains near the end of a crack traversing a plate. *J Appl Mech* 1957;24:361–4.
- [2] Griffith AA. The phenomena of rupture and flow in solids. *Philos Trans R Soc London A* 1921;221:163–98.
- [3] Leicester RH. Effect of size on the strength of structures. 1973.
- [4] Gradin A. A Fracture Criterion for Edge-Bonded Bimaterial Bodies. *J Compos Mater* 1982;16:448–56.
- [5] Carpinteri A. Stress-singularity and generalized fracture toughness at the vertex of re-entrant corners. *Eng Fract Mech* 1987.
- [6] Knesl Z. A criterion of V-notch stability. *Int J Fract* 1991;48:R79–83.
- [7] Seweryn A. Brittle fracture criterion for structures with sharp notches. *Eng Fract Mech* 1994;47:673–81.
- [8] Nui LS, Chehimi C, Pluvinage G. Stress field near a large blunted tip V-notch and application of the concept of the critical notch stress intensity factor (NSIF) to the fracture toughness of very brittle materials. *Eng Fract Mech* 1994;49:325–35.
- [9] Dunn ML, Suwito W, Cunningham S. Fracture initiation at sharp notches: Correlation using critical stress intensities. *Int J Solids Struct* 1997;34:3873–83.
- [10] Dunn ML, Suwito W, Cunningham S, May CW. Fracture initiation at sharp notches under mode I, mode II, and mild mixed mode loading. *Int J Fract* 1997;84:367–81.
- [11] Leguillon D, Yosibash Z. Crack onset at a v-notch. Influence of the notch tip radius. *Int J Fract* 2003;122:1–21.
- [12] Atzori B. Fracture mechanics or notch effect for fatigue design. XIII Natl. Congr. Ital. Soc. Strain Anal. (Edited by AIAS), Bergamo Italy (in Italian): 1985.
- [13] Boukharouba T, Tamine T, Niu L, Chehimi C, Pluvinage G. The use of notch stress intensity factor as a fatigue crack initiation parameter. *Eng Fract Mech* 1995;52:503–12.
- [14] Verreman Y, Nie B. Early development of fatigue cracking at manual fillet welds. *Fatigue Fract Eng Mater Struct* 1996;19:669–81.
- [15] Pluvinage G. Rupture and fatigue initiated from notches. Application of the notch intensity factor. *Rev Fr Mec* (in French) 1997:53–61.
- [16] Lazzarin P, Tovo R. A notch intensity factor approach to the stress analysis of welds. *Fatigue Fract Eng Mater Struct* 1998;21:1089–103.
- [17] Atzori B, Lazzarin P, Tovo R. From a local stress approach to fracture mechanics: a comprehensive evaluation of the fatigue strength of welded joints. *Fatigue Fract Eng Mater Struct* 1999;22:369–81.
- [18] Atzori B, Lazzarin P, Tovo R. Stress field parameters to predict the fatigue strength of notched components. *J Strain Anal Eng Des* 1999;34:437–53.
- [19] Novozhilov V. On a necessary and sufficient criterion for brittle strength. *J Appl Math Mech* (Translation PMM) 1969;33:201–10.
- [20] Seweryn A, Mróz Z. A non-local stress failure condition for structural elements

- under multiaxial loading. *Eng Fract Mech* 1995;51:955–73.
- [21] Seweryn A, Poskrobko Sł, Mróz Z. Brittle Fracture in Plane Elements with Sharp Notches under Mixed-Mode Loading. *J Eng Mech* 1997;123:535–43.
- [22] Taylor D. Geometrical effects in fatigue: a unifying theoretical model. *Int J Fatigue* 1999;21:413–20.
- [23] Susmel L, Taylor D. The theory of critical distances to predict static strength of notched brittle components subjected to mixed-mode loading. *Eng Fract Mech* 2008;75:534–50.
- [24] Tanaka K. Engineering formulae for fatigue strength reduction due to crack-like notches. *Int J Fract* 1983;22:R39–46.
- [25] Lazzarin P, Tovo R, Meneghetti G. Fatigue crack initiation and propagation phases near notches in metals with low notch sensitivity. *Int J Fatigue* 1997;19:647–57.
- [26] El Haddad MH, Topper TH, Smith KN. Prediction of non propagating cracks. *Eng Fract Mech* 1979;11:573–84.
- [27] Neuber H. *Theory of Notch Stresses*. Berlin: Springer-Verlag; 1958.
- [28] Berto F, Lazzarin P, Radaj D. Fictitious notch rounding concept applied to sharp V-notches: Evaluation of the microstructural support factor for different failure hypotheses. Part I: Basic stress equations. *Eng Fract Mech* 2008;75:3060–72.
- [29] Berto F, Lazzarin P, Radaj D. Fictitious notch rounding concept applied to sharp V-notches: Evaluation of the microstructural support factor for different failure hypotheses. *Eng Fract Mech* 2009;76:1151–75.
- [30] Elices M, Guinea GV, Gómez J, Planas J, Elices M, G J. The cohesive zone model: advantages, limitations and challenges. *Eng Fract Mech* 2002;69:137–63.
- [31] Gómez FJ, Elices M. Fracture of components with V-shaped notches. *Eng Fract Mech* 2003;70:1913–27.
- [32] Livieri P. Use of J-integral to predict static failures in sharp V-notches and rounded U-notches. *Eng Fract Mech* 2008;75:1779–93.
- [33] Barati E, Aghazadeh Mohandesi J, Alizadeh Y. The effect of notch depth on J-integral and critical fracture load in plates made of functionally graded aluminum–silicone carbide composite with U-notches under bending. *Mater Des* 2010;31:4686–92.
- [34] Ayatollahi MR, Aliha MRM. Mixed mode fracture analysis of polycrystalline graphite – A modified MTS criterion. *Carbon N Y* 2008;46:1302–8.
- [35] Saghafi H, Ayatollahi MR, Sistaninia M. A modified MTS criterion (MMTS) for mixed-mode fracture toughness assessment of brittle materials. *Mater Sci Eng A* 2010;527:5624–30.
- [36] Lazzarin P, Zambardi R. A finite-volume-energy based approach to predict the static and fatigue behavior of components with sharp V-shaped notches. *Int J Fract* 2001;112:275–98.
- [37] Lazzarin P, Berto F, Elices M, Gómez J. Brittle failures from U- and V-notches in mode I and mixed, I + II, mode: a synthesis based on the strain energy density averaged on finite-size volumes. *Fatigue Fract Eng Mater Struct* 2009;32:671–84.
- [38] Berto F, Lazzarin P. A review of the volume-based strain energy density
-

-
- approach applied to V-notches and welded structures. *Theor Appl Fract Mech* 2009;52:183–94.
- [39] Berto F, Lazzarin P. Recent developments in brittle and quasi-brittle failure assessment of engineering materials by means of local approaches. *Mater Sci Eng R Reports* 2014;75:1–48.
- [40] Leguillon D. A criterion for crack nucleation at a notch in homogeneous materials. *Comptes Rendus l'Académie Des Sci - Ser IIB - Mech* 2001;329:97–102.
- [41] Leguillon D. Strength or toughness? A criterion for crack onset at a notch. *Eur J Mech - A/Solids* 2002;21:61–72.
- [42] Carpinteri A, Cornetti P, Pugno N, Sapora A, Taylor D. A finite fracture mechanics approach to structures with sharp V-notches. *Eng Fract Mech* 2008;75:1736–52.
- [43] Cornetti P, Pugno N, Carpinteri A, Taylor D. Finite fracture mechanics: A coupled stress and energy failure criterion. *Eng Fract Mech* 2006;73:2021–33.
- [44] Yosibash Z, Priel E, Leguillon D. A failure criterion for brittle elastic materials under mixed-mode loading. *Int J Fract* 2006;141:291–312.
- [45] Sapora A, Cornetti P, Carpinteri A. A Finite Fracture Mechanics approach to V-notched elements subjected to mixed-mode loading. *Eng Fract Mech* 2013;97:216–26.
- [46] Sih GC. Strain-energy-density factor applied to mixed mode crack problems. *Int J Fract* 1974;10:305–21.
- [47] Sih GC. *Mechanics of Fracture Initiation and Propagation*. Dordrecht: Springer Netherlands; 1991.
- [48] Lazzarin P, Berto F, Gomez F, Zappalorto M. Some advantages derived from the use of the strain energy density over a control volume in fatigue strength assessments of welded joints. *Int J Fatigue* 2008;30:1345–57.
- [49] Lazzarin P, Berto F, Zappalorto M. Rapid calculations of notch stress intensity factors based on averaged strain energy density from coarse meshes: Theoretical bases and applications. *Int J Fatigue* 2010;32:1559–67.
- [50] Berto F, Lazzarin P, Kotousov A, Pook LP. Induced out-of-plane mode at the tip of blunt lateral notches and holes under in-plane shear loading. *Fatigue Fract Eng Mater Struct* 2012;35:538–55.
- [51] Pook LP, Campagnolo A, Berto F, Lazzarin P. Coupled fracture mode of a cracked plate under anti-plane loading. *Eng Fract Mech* 2015;134:391–403.
- [52] Treifi M, Oyadiji SO. Strain energy approach to compute stress intensity factors for isotropic homogeneous and bi-material V-notches. *Int J Solids Struct* 2013;50:2196–212.
- [53] Davis BR, Wawrzynek PA, Ingraffea AR. 3-D simulation of arbitrary crack growth using an energy-based formulation – Part I: Planar growth. *Eng Fract Mech* 2014;115:204–20.
- [54] Williams ML. Stress singularities resulting from various boundary conditions in angular corners of plates in tension. *J Appl Mech* 1952;19:526–8.
- [55] Lazzarin P, Tovo R. A unified approach to the evaluation of linear elastic stress fields in the neighborhood of cracks and notches. *Int J Fract* 1996;78:3–19.
-

- [56] Gross B, Mendelson A. Plane elastostatic analysis of V-notched plates. *Int J Fract Mech* 1972;8:267–76.
- [57] Beltrami E. Sulle condizioni di resistenza dei corpi elastici. *Il Nuovo Cimento* 18 (in Italian); 1885.
- [58] Yosibash Z, Bussiba A, Gilad I. Failure criteria for brittle elastic materials. *Int J Fract* 2004;307–33.
- [59] Tada H, Paris P, Irwin G. *The stress analysis of cracks, Handbook*. St Louis MO (USA): Paris Productions Incorporated; 1985.
- [60] Leguillon D, Murer S. Fatigue crack nucleation at a stress concentration point. 4th Int. Conf. Crack Paths (CP2012), Gaeta, Italy, Sept. 19-21, 2012.
- [61] Radaj D, Lazzarin P, Berto F. Generalised Neuber concept of fictitious notch rounding. *Int J Fatigue* 2013;51:105–15.
- [62] Planas J, Elices M, Guinea G., Gómez F., Cendón D., Arbilla I. Generalizations and specializations of cohesive crack models. *Eng Fract Mech* 2003;70:1759–76.
- [63] Berto F, Lazzarin P, Matvienko YG. J-integral evaluation for U- and V-blunt notches under Mode I loading and materials obeying a power hardening law. *Int J Fract* 2007;146:33–51.
- [64] Aliha MRM, Ayatollahi MR. Analysis of fracture initiation angle in some cracked ceramics using the generalized maximum tangential stress criterion. *Int J Solids Struct* 2012;49:1877–83.
- [65] Lazzarin P, Campagnolo A, Berto F. A comparison among some recent energy- and stress-based criteria for the fracture assessment of sharp V-notched components under Mode I loading. *Theor Appl Fract Mech* 2014;71:21–30.
- [66] Sapora A, Cornetti P, Carpinteri A. V-notched elements under mode II loading conditions. *Struct Eng Mech* 2014;49:499–508.
- [67] Meneghetti G, Campagnolo A, Berto F, Atzori B. Averaged strain energy density evaluated rapidly from the singular peak stresses by FEM: cracked components under mixed-mode (I+II) loading. *Theor Appl Fract Mech* 2015;79:113–24.
- [68] Marangon C, Campagnolo A, Berto F. Three-dimensional effects at the tip of rounded notches subjected to mode-I loading under cyclic plasticity. *J Strain Anal Eng Des* 2015;50:299–313.
- [69] Campagnolo A, Berto F, Marangon C. Cyclic plasticity in three-dimensional notched components under in-phase multiaxial loading at $R=-1$. *Theor Appl Fract Mech* 2015.
- [70] Erdogan F, Sih GC. On the Crack Extension in Plates Under Plane Loading and Transverse Shear. *J Basic Eng* 1963;85:519.
- [71] Gómez FJ, Elices M, Berto F, Lazzarin P. Local strain energy to assess the static failure of U-notches in plates under mixed mode loading. *Int J Fract* 2007;145:29–45.
- [72] Priel E, Yosibash Z, Leguillon D. Failure initiation at a blunt V-notch tip under mixed mode loading. *Int J Fract* 2008;149:143–73.
- [73] Chen DH, Ozaki S. Investigation of failure criteria for a sharp notch. *Int J Fract* 2008;152:63–74.
- [74] Tran V-X, Leguillon D, Krishnan A, Xu LR. Interface crack initiation at V-

- notches along adhesive bonding in weakly bonded polymers subjected to mixed-mode loading. *Int J Fract* 2012;176:65–79.
- [75] García IG, Leguillon D. Mixed-mode crack initiation at a v-notch in presence of an adhesive joint. *Int J Solids Struct* 2012;49:2138–49.
- [76] Seweryn A, Łukaszewicz A. Verification of brittle fracture criteria for elements with V-shaped notches. *Eng Fract Mech* 2002;69:1487–510.
- [77] Anderson TL. *Fracture Mechanics, Fundamentals and Applications*. 2nd ed. Boca Raton: CRC Press LLC; 1994.
- [78] Richard HA, Fulland M, Sander M. Theoretical crack path prediction. *Fatigue Fract Eng Mater Struct* 2005;28:3–12.
- [79] Berto F, Campagnolo A, Lazzarin P. Fatigue strength of severely notched specimens made of Ti-6Al-4V under multiaxial loading. *Fatigue Fract Eng Mater Struct* 2015;38:503–17.
- [80] Campagnolo A, Berto F, Lazzarin P. The effects of different boundary conditions on three-dimensional cracked discs under anti-plane loading. *Eur J Mech - A/Solids* 2015;50:76–86.
- [81] Torabi AR, Campagnolo A, Berto F. Experimental and theoretical investigation of brittle fracture in key-hole notches under mixed mode I/II loading. *Acta Mech* 2015;226:2313–22.
- [82] Torabi ARR, Campagnolo A, Berto F. Tensile fracture analysis of V-notches with end holes by means of the local energy. *Phys Mesomech* 2015;18:194–202.
- [83] Torabi AR, Campagnolo A, Berto F. Mode II Brittle Fracture Assessment of Key-Hole Notches by Means of the Local Energy. *J Test Eval* 2016;44.
- [84] Berto F, Campagnolo A, Gallo P. Brittle Failure of Graphite Weakened by V-Notches: A Review of Some Recent Results Under Different Loading Modes. *Strength Mater* 2015;47:488–506.
- [85] Beghini M, Bertini L, Di Lello R, Fontanari V. A general weight function for inclined cracks at sharp V-notches. *Eng Fract Mech* 2007;74:602–11.
- [86] Melin S. Accurate Data for Stress Intensity Factors at Infinitesimal Kinks. *J Appl Mech* 1994;61:467.
- [87] Ayatollahi MRR, Torabi ARR. Failure assessment of notched polycrystalline graphite under tensile-shear loading. *Mater Sci Eng A* 2011;528:5685–95.
- [88] Ayatollahi MR, Torabi ARR, Azizi P. Experimental and Theoretical Assessment of Brittle Fracture in Engineering Components Containing a Sharp V-Notch. *Exp Mech* 2010;51:919–32.

CHAPTER 6

LINK BETWEEN PEAK STRESS METHOD (PSM) AND STRAIN ENERGY DENSITY (SED)

6.1 Link between the Peak Stress Method (PSM) and the averaged Strain Energy Density (SED): long cracks under mixed mode (I+II) loading ^(*)

Nomenclature

2a	crack length
d	mean size of a finite element
e_1, e_2	parameters for averaged SED evaluation
E	elastic modulus
f_I, f_{II}	fitting functions for K_{FE}^* and K_{FE}^{**} convergence curves
K_I, K_{II}	mode I and II SIFs
K_{FE}^*, K_{FE}^{**}	non-dimensional K_I and K_{II} relevant to the peak stress method
MM	mode mixity ratio
R_0	radius of the control volume for the averaged SED evaluation
r, θ	polar coordinates
\overline{W}_{AN}	analytical, closed-form expression of the averaged SED, taking into account only SIFs contributions
\overline{W}_{FEM}	averaged SED calculated by FEM using very refined meshes (direct approach)
$\overline{W}_{FEM,coarse}$	averaged SED calculated by FEM using coarse meshes (direct approach with coarse mesh option)
\overline{W}_{PSM}	averaged SED calculated according to the PSM (only SIFs contributions are taken into account)

Symbols

2α	opening angle
ν	Poisson's ratio
σ_{nom}	nominal tensile stress

σ_{peak}	singular, linear elastic opening peak stress evaluated at the crack tip by FEM using the PSM
$\sigma_{\text{I,peak}}$	maximum elastic principal stress evaluated at the crack tip by FEM using the PSM
$\sigma_{\text{rr}}, \sigma_{\theta\theta}, \tau_{r\theta}$	normal and shear stress components in the polar frame of reference
τ_{peak}	singular, linear elastic sliding peak stress evaluated at the crack tip by FEM using the PSM

Abbreviations

FE	Finite element
FEM	Finite element method
NSIFs	Notch stress intensity factors
PSM	Peak stress method
SED	Strain energy density
SIFs	Stress intensity factors

(*) *See also:*

Meneghetti, G.; Campagnolo, A.; Berto, F.; Atzori, B. Averaged strain energy density evaluated rapidly from the singular peak stresses by FEM: cracked components under mixed-mode (I+II) loading. *Theoretical and Applied Fracture Mechanics*; 79: 113-124 (2015).

6.1.1. Introduction

Notch stress intensity factors (NSIFs) allow to quantify the intensity of the local stress distributions ahead of stress raisers. Nowadays, the analysis of the local stress distributions ahead of cracks and notches by means of numerical methods is widely adopted by engineers focused on safe designing of structural components against fracture and fatigue. A major drawback of numerical modelling stress concentration regions is that refined or extremely refined meshes are required to obtain reliable results in terms of local stresses and strains. Cracks can be modelled by special quarter-point elements which contain the crack tip stress singularity [1,2] and permit to obtain accurate results despite of the adopted relatively coarse meshes. Special singular finite elements and boundary elements have been developed to account for the appropriate singularity (see for example [3,4]) and to facilitate the evaluation of the generalized stress intensity factors [5,6]. Among the special finite elements, additional and commonly used numerical techniques include degenerated asymptotic finite elements [7,8], hybrid (or enriched) finite elements [9,10], extended finite element [11,12] and analytical finite elements [13].

Karihaloo and Xiao extended the hybrid crack element (HCE) originally introduced by Tong et al. [14] to calculate directly not only the SIF but also the coefficients of the higher-order terms of the crack tip asymptotic field [15]. Extensive studies have proved the versatility and accuracy of the element for pure mode I problems, but also for mode II and mixed mode cracks [16].

Special finite elements were presented in the literature also to capture the asymptotic nature of other stress singularities, like those arising from pointed V-shaped notches, see for example [17,18], but they are not available in commercial softwares. No special element exists for severe notches where the notch root is very small but different from zero.

Notch stress intensity factors (NSIFs) have a fundamental role in static strength estimation of V-notched structural elements made of brittle or quasi-brittle materials [19–23]. This also holds true for components made of structural materials undergoing high-cycle fatigue loading [23–25]. A valuable example of application of the NSIF approach to a practical problem is the fatigue design of

welded joints [26–29]. Local approaches based on N-SIFs extend the concepts of Linear Elastic Fracture Mechanics (LEFM), and play the same role the SIFs have in strength evaluations of cracked components.

In plane problems, the mode I and mode II NSIFs for sharp V-notches, which quantify the intensity of the asymptotic stress distributions in the close neighbourhood of the notch tip, can be expressed by means of the Gross and Mendelson definitions [30]:

$$K_I = \sqrt{2\pi} \cdot \lim_{r \rightarrow 0} [(\sigma_{\theta\theta})_{\theta=0} \cdot r^{1-\lambda_1}] \quad (6.1.1)$$

$$K_{II} = \sqrt{2\pi} \cdot \lim_{r \rightarrow 0} [(\tau_{r\theta})_{\theta=0} \cdot r^{1-\lambda_2}] \quad (6.1.2)$$

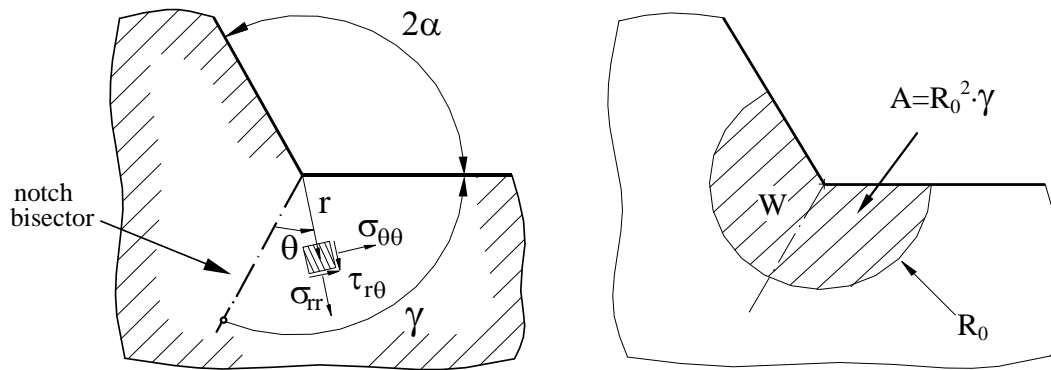


Figure 6.1.1: (a) Polar coordinate system centred at the notch tip. (b) Strain energy density

averaged over a control volume (area) of radius R_0 surrounding the V-notch tip, $\bar{W} = \frac{W}{A}$.

where (r, θ) is a polar coordinate system centred at the notch tip (Fig. 6.1.1a), $\sigma_{\theta\theta}$ and $\tau_{r\theta}$ are the stress components according to the above coordinate system, and λ_1 and λ_2 are the mode I and mode II first eigenvalues in William's equations [31], respectively. The condition $\theta = 0$ identifies the notch bisector line. When the V-notch angle 2α is equal to zero, λ_1 and λ_2 equal 0.5, and K_I and K_{II} match the conventional stress intensity factors, K_I and K_{II} , of a crack according to LEFM.

Structural strength problems of V-notches (with arbitrary opening angle 2α) subjected to mixed-mode loading can be treated using the linear elastic strain energy density averaged over a material-dependent structural volume (the SED parameter), which was idealised as a circular sector of radius R_0 , as illustrated in Fig. 6.1.1b, according to Lazzarin and Zambardi [23]. The SED approach has been extensively applied in static [23,32,33] as well as fatigue [23,29,34,35] strength assessments. With reference to plane strain conditions, the SED value can be evaluated analytically as a function of the NSIFs:

$$\bar{W}_{AN} = \frac{e_1}{E} \left[\frac{K_1}{R_0^{1-\lambda_1}} \right]^2 + \frac{e_2}{E} \left[\frac{K_2}{R_0^{1-\lambda_2}} \right]^2 \quad (6.1.3)$$

where e_1 and e_2 are two parameters that depend on the notch opening angle 2α and the Poisson's ratio ν [23]. Equation (6.1.3) is valid when the influence of the higher-order, non-singular terms can be neglected inside the control volume. Therefore, taking as an example the case of short cracks or thin welded lap joints, Eq. (6.1.3) is incomplete because the T-stress must be included in the local SED evaluation [36]. The main disadvantage in the practical application of Eq. (6.1.3) combined with (6.1.1) and (6.1.2) is that very refined meshes are needed to calculate the NSIFs by means of definitions (6.1.1) and (6.1.2) applied to the results of linear elastic finite element analyses. The reason is that the complete local stress distributions must be calculated accurately. The modelling procedure becomes particularly time-consuming for components that cannot be analysed by means of two-dimensional models and instead require three-dimensional FE analyses.

However, Lazzarin and co-workers [37] provided evidence that it is convenient to evaluate the SED parameter directly from the results of FE analyses, \bar{W}_{FEM} , by summing up the strain energies $W_{FEM,i}$ calculated for the i -th finite element located inside the control volume and subsequently by dividing by the total volume (A in Fig. 6.1.1b):

$$\bar{W}_{FEM} = \frac{\sum_A W_{FEM,i}}{A} \quad (6.1.4)$$

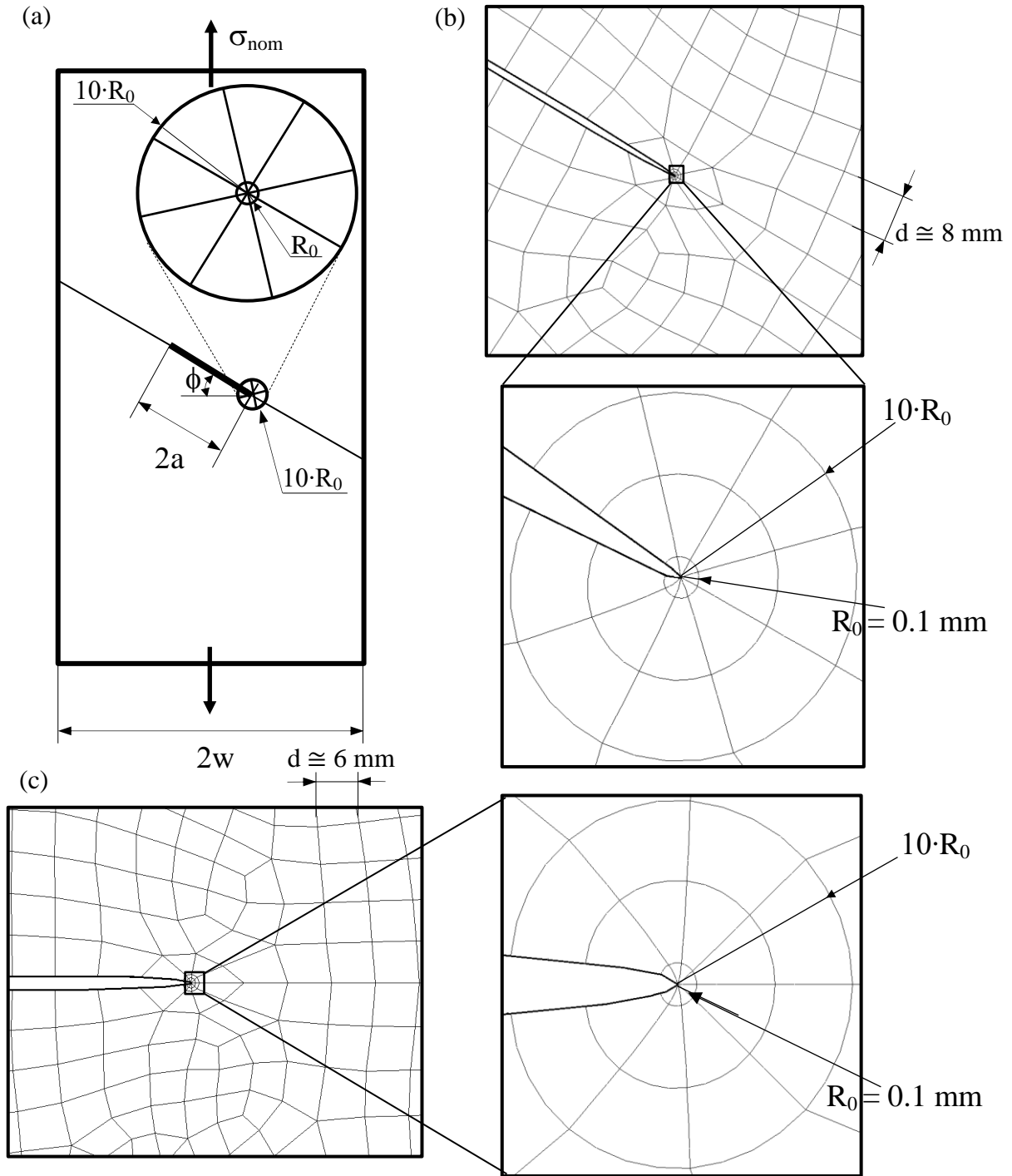


Figure 6.1.2: SED parameter evaluated according to the direct approach (Eq. (6.1.4)) with coarse mesh option, $\bar{W}_{FEM,coarse}$ [37]; (a) geometry and loading condition ($2w = 200$ mm). Coarse FE mesh (second order plane elements, PLANE 183 of Ansys Element Library) producing a 10% error in the cases: (b) $\phi = 30^\circ$, $2a = 46.19$ mm and (c) $\phi = 0^\circ$, $2a = 40$ mm. Control radius $R_0 = 0.1$ mm.

Equation (6.1.4) defines the so-called direct approach to evaluate the SED parameter. Additionally, it has been shown that the adopted FE meshes can be very coarse inside the control volume having radius R_0 [37]. More precisely, Figure 6.1.2a shows the required geometrical model, and Figures 6.1.2b and 6.1.2c report two examples of FE meshes (second order plane elements, PLANE 183 of the Ansys[®] element library) adopted to analyse a mixed-mode (I+II) and a pure mode I crack problem, respectively, according to the direct approach with coarse mesh option [37]. Figure 6.1.2 shows that only eight finite elements are generated inside the control volume, two concentric rings consisting of eight elements each are generated outside the control volume in the circular sector $R_0 < r < 10 \cdot R_0$, while a free mesh of elements having an average size d is generated outside. The average element size d must be input in Ansys[®] before running the free mesh generation algorithm. The FE meshes shown in Figures 6.1.2b and 6.1.2c are as coarse as possible to fulfil $0.9 \leq \bar{W}_{\text{FEM,coarse}}/\bar{W}_{\text{FEM}} \leq 1.1$, $\bar{W}_{\text{FEM,coarse}}$ and \bar{W}_{FEM} being evaluated from Eq. (6.1.4) by using the coarse mesh option and a very refined mesh (approximately 500 FE inside the control volume), respectively. Due to the adopted mesh refinement, \bar{W}_{FEM} represents the ‘exact’ reference value throughout the present paragraph.

A peculiar feature of the local SED is that it is able to capture three-dimensional effects of crack tip fields through the plate thickness that, in some cases, may play a significant role in fracture processes [38–40]. While it is not the aim of the present investigation to discuss this point in more detail, it is important to underline that such three-dimensional effects have to be considered case-by-case to understand their incidence on the simplifications adopted in fracture assessments.

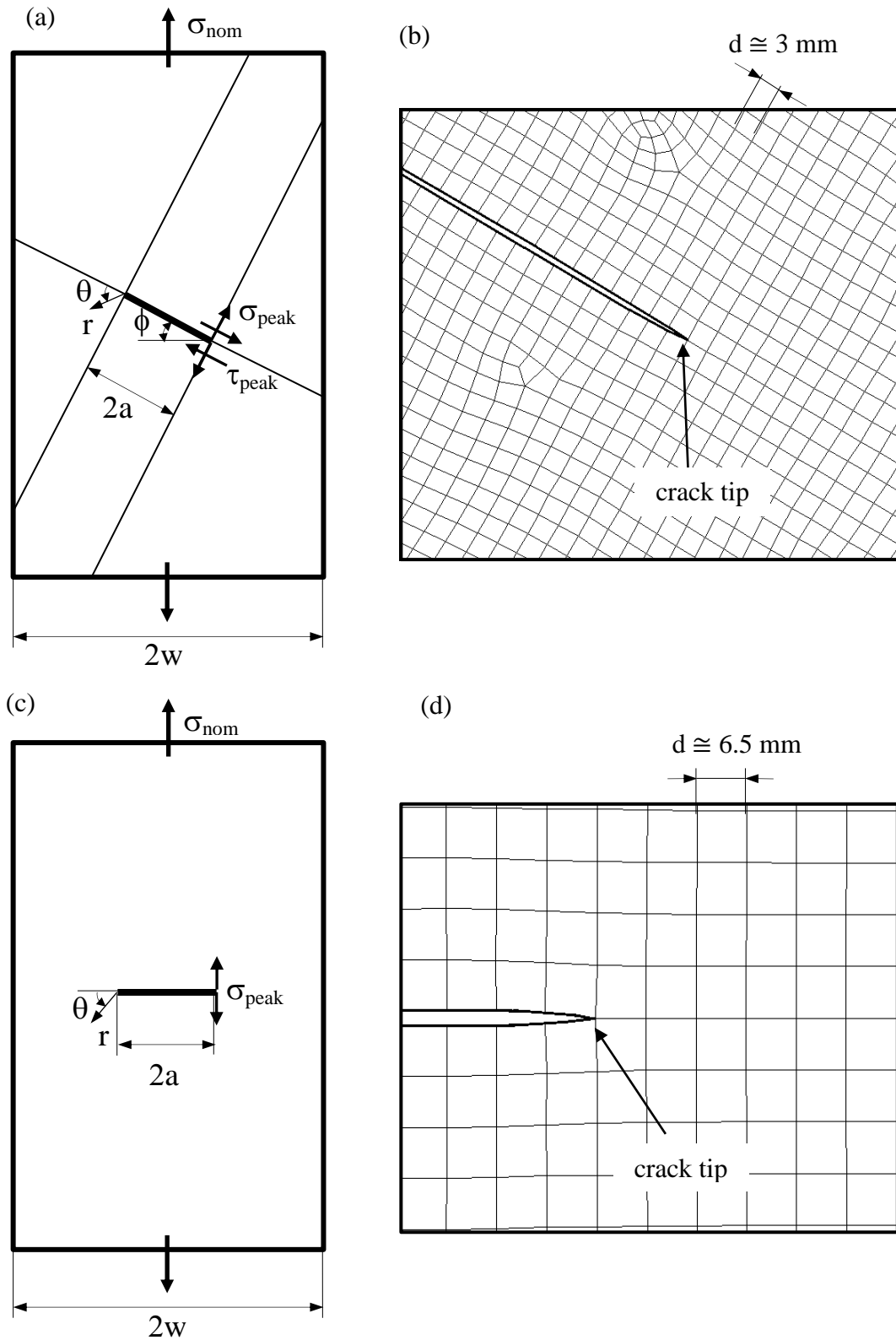


Figure 6.1.3: SED parameter evaluated according to the peak stress approach (Eq. (6.1.7)); geometry and loading condition ($2w = 200 \text{ mm}$): (a) mixed mode ($\phi > 0^\circ$) and (c) pure mode I ($\phi = 0^\circ$) loading. Coarse FE mesh (first order plane elements, PLANE 182 with K-option 1 set to 3) producing a 10% error in the cases: (b) $\phi = 30^\circ$, $2a = 46.19 \text{ mm}$ and (d) $\phi = 0^\circ$, $2a = 40 \text{ mm}$.

The numerical efficiency of the direct approach with the coarse mesh option has been illustrated in [37] and can be appreciated from Figure 6.1.2. Nonetheless, an alternative approach is put forward in the present paragraph, where modelling the circular sector-shaped structural volume is no longer necessary and the coarse mesh option is maintained. The method is referred to as the peak stress approach (PSM, Peak Stress Method) and the analysis technique is sketched in Figure 6.1.3, which reports the same crack problems examined in Figure 6.1.2. In particular, Figures 6.1.3b and 6.1.3d show the coarsest FE meshes (first-order plane elements, PLANE 182 of the Ansys[®] element library with K-option 1 set to 3) that can be adopted to comply with the conditions of applicability of the method. The level of mesh coarseness that can be adopted using the PSM depends on the crack length and mode mixity, such that more refined meshes are required if the crack size is reduced and the mode mixity is increased, as explained in the next section. The free mesh generation algorithm is again employed in Figures 6.1.3b and 6.1.3d by imposing an average element size d .

The PSM is briefly reviewed in the next section; here, it is important to underline that the method dates back to the technique introduced by Nisitani and Teranishi [41,42], who presented a new numerical procedure suitable to estimate K_I for a crack emanating from an ellipsoidal cavity. Such a procedure is based on the usefulness of the linear elastic peak stress σ_{peak} calculated at the crack tip by means of FE analyses characterized by a mesh pattern having a constant element size. In particular, Nisitani and Teranishi [41,42] were able to show that the ratio K_I/σ_{peak} depends only on the element size, such that σ_{peak} can be used to rapidly estimate K_I , provided that the adopted mesh pattern has previously been calibrated on geometries for which the exact K_I values are known. This approach has been theoretically justified and also extended to sharp V-shaped notches subject to mode I loading [43], giving rise to the Peak Stress Method, i.e., an approximate FE-based method to estimate the NSIFs. Later on, the PSM was extended to cracks subjected to mode I as well as mode II stresses [44]. The element size required to evaluate K_1 and K_2 from σ_{peak} and τ_{peak} , respectively, is several orders of magnitude greater than that required to evaluate the entire local stress field. The second advantage of using σ_{peak} and τ_{peak} is that a single stress value is sufficient

to estimate K_1 and K_2 , respectively, instead of a number of stress FE data, as is usually made by applying definitions (6.1.1) and (6.1.2).

Aims of the present investigation are as follows:

- to recall the fundamental concepts of the Peak Stress Method for pure modes of loading;
- to present the PSM applied to mixed mode (I+II) loading cases;
- to formulate the peak stress approach to calculate the SED parameter in the case of mixed mode (I+II) loading.

6.1.2. The Peak Stress Method for pure modes of loading

The PSM is a simplified numerical method to estimate the NSIFs parameters. It was originally formulated for cases where only mode I singular stresses exist (i.e., $K_2 = 0$ or mode II stresses are negligible). It has been based on a link between the exact value of the mode I NSIF K_1 (see Eq. (6.1.1)) and the linear elastic opening peak stress σ_{peak} calculated at the V-notch tip according to the following expression [43]:

$$K_{\text{FE}}^* = \frac{K_1}{\sigma_{\text{peak}} \cdot d^{1-\lambda_1}} \cong 1.38 \quad (6.1.5)$$

The PSM according to Eq. (6.1.5) was applied to correlate the fatigue strength of fillet- and full-penetration-welded joints subjected to mode I loading [45,46].

Recently, the Peak Stress Method has also been extended to mode II crack problems, linking the exact value of the mode II NSIF K_2 (Eq. (6.1.2) with $2\alpha = 0^\circ$ and $\lambda_2 = 0.5$) and the linear elastic sliding peak stress τ_{peak} calculated at the crack tip according to the following expression [44]:

$$K_{\text{FE}}^{**} = \frac{K_2}{\tau_{\text{peak}} \cdot d^{1-\lambda_2}} \cong 3.38 \quad (6.1.6)$$

In Eqs. (6.1.5) and (6.1.6), d is the so-called ‘global element size’ input when using the free mesh generation algorithm available in Ansys[®] numerical software.

Such a parameter controls the average element size of the FE pattern, as is reported for the example in Figs. 6.1.3b and d and then in Figs. 6.1.11a and b. There are no additional parameters to input or actions the FE analyst must take to generate the FE mesh according to the PSM. When Eqs. (6.1.5) and (6.1.6) were calibrated, K_1 and K_2 were obtained by using very refined FE mesh patterns in the numerical analyses and applying definitions (6.1.1) and (6.1.2) to the numerical results [43,44]. It is worth noting that FE sizes on the order of 10^{-5} mm were adopted; such refined meshes can hardly be adopted in practical design situations. Eqs. (6.1.5) and (6.1.6) are useful in practical applications because, if the mean element size d is kept constant, then the K_1/σ_{peak} and K_2/τ_{peak} ratios are also constant. Eqs. (6.1.5) and (6.1.6) are valid under the following conditions:

- use of 4-node quadrilateral finite elements with linear shape functions, as implemented in ANSYS[®] numerical software (PLANE 42 of the Ansys[®] element library or alternatively PLANE 182 with K-option 1 set to 3, which corresponds to a simplified enhanced strain formulation of the finite elements);
- the pattern of finite elements around a crack tip must be that shown in Figs. 6.1.3b and d (see also [43,44] when dealing with open V-notches); in particular, four elements share the node located at the crack tip;
- concerning Eq. (6.1.5), V-notches are characterised by an opening angle 2α ranging from 0° to 135° ;
- the ratio a/d must be greater than 3 to obtain $K_{\text{FE}}^* = 1.38 \pm 3\%$, with a being the semi-crack length (or the notch depth when dealing with open V-notches). When mode II (sliding) stresses are of interest, meshes must be more refined such that the ratio a/d must be greater than 14 to obtain $K_{\text{FE}}^{**} = 3.38 \pm 3\%$.

Recently, the PSM has also been combined with 3D numerical models and eight-node brick elements to assess the fatigue strength of steel-welded joints having complex geometry and characterised by toe as well as root cracking [47,48]. Finite element analyses performed using higher-order elements or significantly different

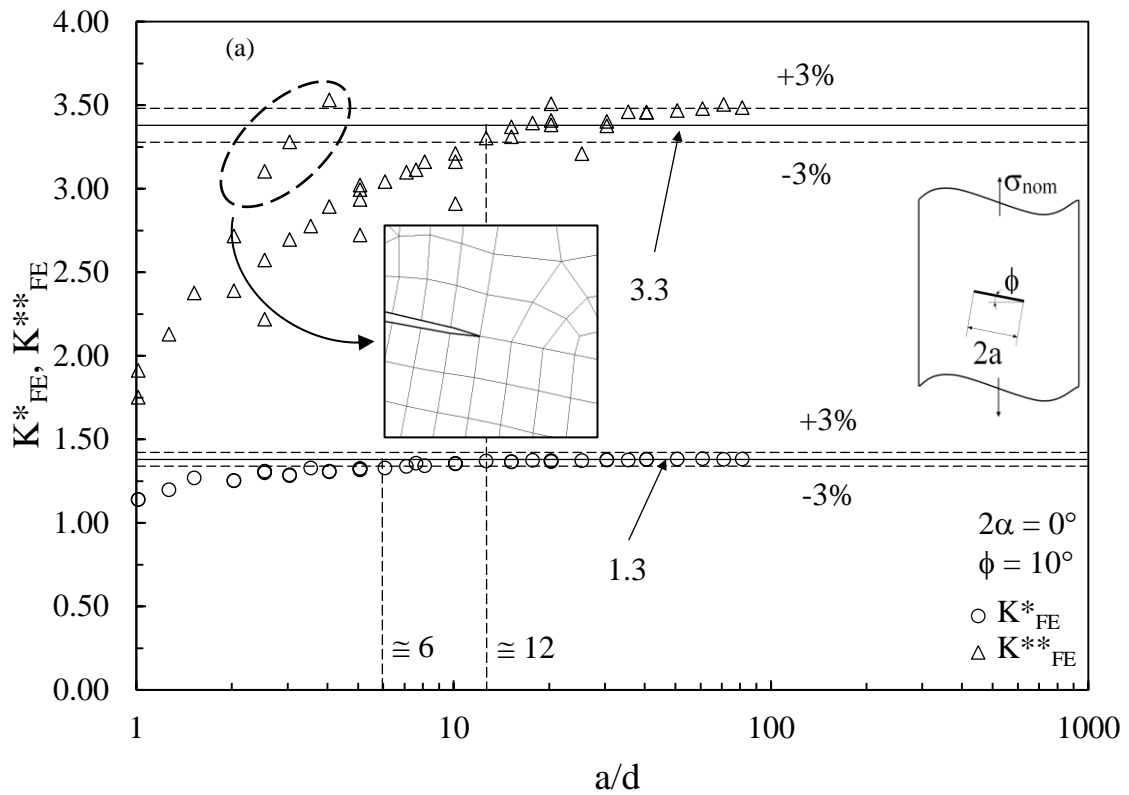
FE patterns imply that coefficients of Eqs. (6.1.5) and (6.1.6) should be recalculated.

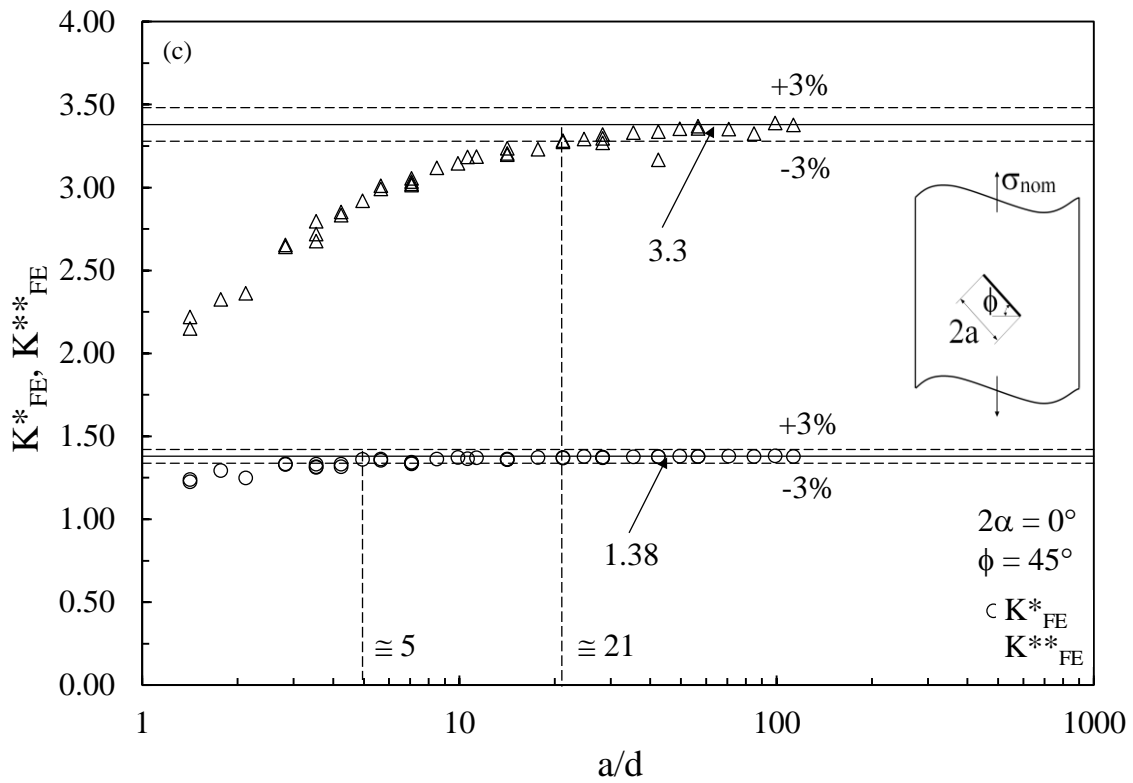
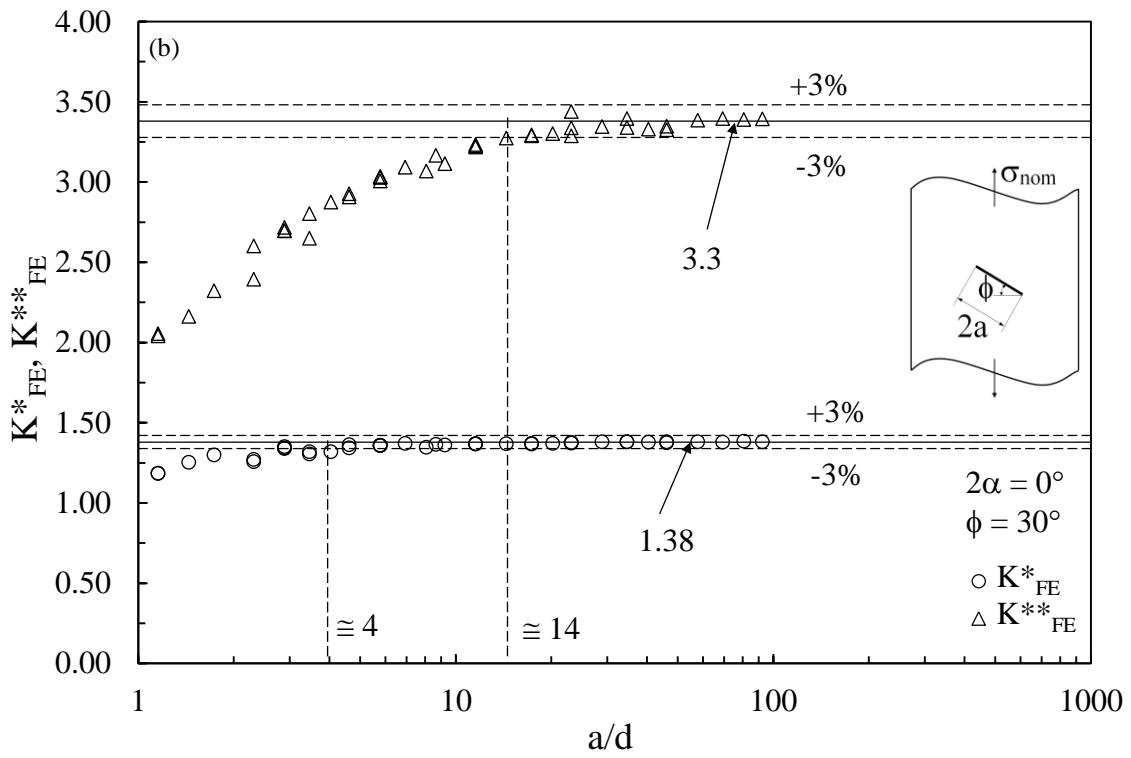
6.1.3. The Peak Stress Method for mixed mode (I+II) loading

In the present Section, the Peak Stress Method is extended to mixed mode (I+II) crack problems. Consider a crack ($2\alpha = 0^\circ$) centred in a plate having the geometry reported in Figs. 6.1.3a and c and subjected to tensile loading. By varying the inclination angle ϕ of the crack, it is possible to obtain different mode mixities, from pure mode I ($\phi = 0^\circ$) to mixed mode I+II ($\phi > 0^\circ$) loading. Different geometrical combinations are considered, varying the crack length $2a$ (from 5 to 160 mm) and the inclination ϕ (0° , 10° , 30° , 45° and 60°). The average size of the finite elements d (0.5, 1, 2, 5 and 10 mm) is also varied, with the aim of investigating to what extent the PSM holds true. Finite element analyses have been performed via the commercial software Ansys[®] and 4-node quadrilateral elements (PLANE 42 or equivalently PLANE 182 with K-option 1 set to 3). The free mesh algorithm has been used in all numerical analyses, and the sole control parameter set to generate the mesh has been the so-called ‘global element size’, which controls the mean size of the finite elements. To obtain a pattern of finite elements oriented along the crack bisector line (see Figs. 6.1.3b and d), the geometry of the plate has been divided into six areas such that each crack tip is shared by four areas, as shown in Fig. 6.1.3a. By doing so, four elements (each one belonging to a different area) share the node located at the crack tip, and the relevant condition of applicability of the PSM is satisfied.

For the cracked geometries under analysis, $K_1 = K_I$, $K_2 = K_{II}$ and $\lambda_1 = \lambda_2 = 0.5$, while σ_{peak} and τ_{peak} are the maximum linear elastic normal (opening) and shear (sliding) nodal stresses referred to the bisector line and are evaluated at the crack tip according to Fig. 6.1.3a, c. The exact values of the mode I and mode II SIFs, K_I and K_{II} , have been evaluated by means of dedicated finite element analyses performed on the same geometries, but adopting very refined meshes (the smallest element size being on the order of 10^{-5} mm) in the close neighbourhood of the crack tip.

Figure 6.1.4 plots the results of the numerical analyses in terms of the non-dimensional SIFs K_{FE}^* and K_{FE}^{**} defined in Eqs. (6.1.5) and (6.1.6), respectively, for inclined cracks with $\phi = 10^\circ, 30^\circ, 45^\circ$ and 60° . The parameters K_{FE}^* and K_{FE}^{**} are seen to converge to the values 1.38 [43] and 3.38 [44], respectively, within a scatter band of the numerical results of $\pm 3\%$, according to the values previously calibrated for pure modes of loading. Convergence is guaranteed for a ratio a/d greater than a value between 3 and 6 for mode I loading and between 12 and 21 for mode II loading. It can be observed that the minimum mesh density ratio a/d values to assure applicability of the PSM under mixed mode (I+II) loading are only slightly greater than those obtained in [43] in the case of pure mode I ($a/d \cong 3$), and reported in [44] for pure mode II ($a/d \cong 14$). Moreover, it should be noted that mode II loading is more demanding to analyse with the PSM than mode I loading, i.e., it requires more refined finite element mesh patterns [44].





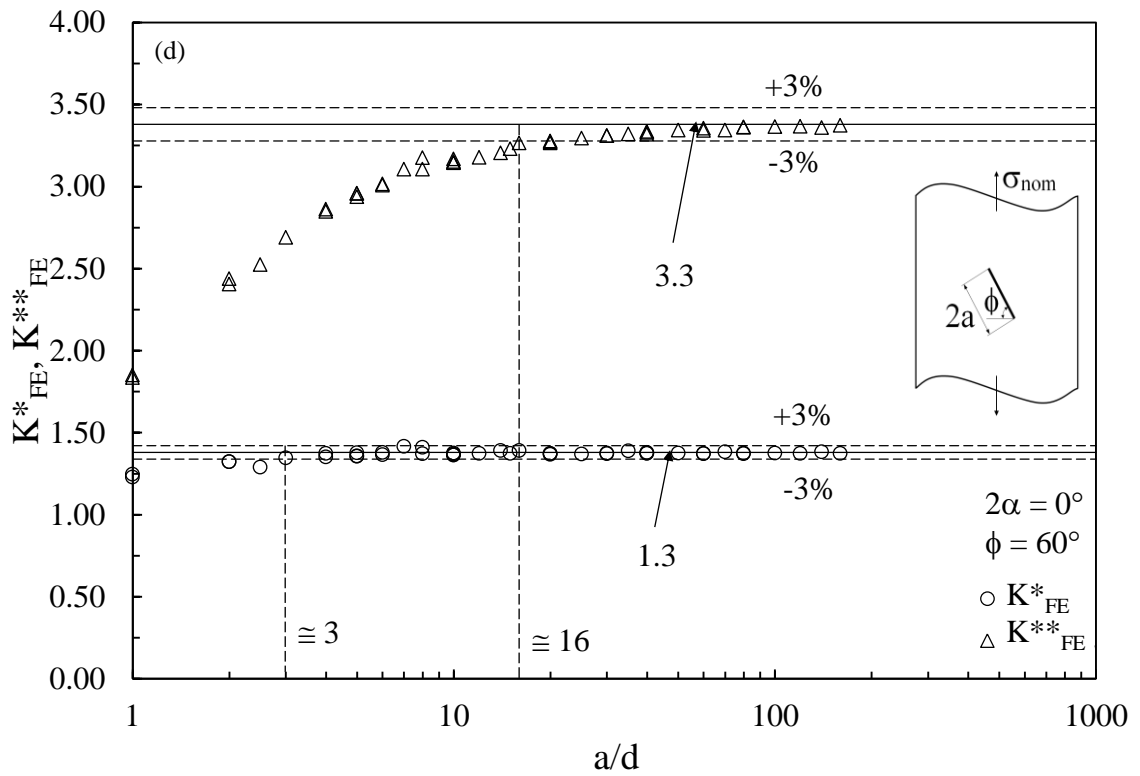


Figure 6.1.4: Calibration of the PSM for a crack ($2\alpha = 0^\circ$) under mixed mode (I+II) loading: (a) $\phi = 10^\circ$; (b) $\phi = 30^\circ$; (c) $\phi = 45^\circ$ and (d) $\phi = 60^\circ$. Non-dimensional SIFs related to mode I and mode II.

6.1.4. The peak stress approach to estimate the SED parameter for mixed mode (I+II) loading

6.1.4.1 Standard approach

In the present section, a link between the SED parameter [23] and the peak stresses [43,44] in the case of cracks subjected to mixed mode (I+II) loading is investigated. By substituting the peak stress-based relationships (Eqs. (6.1.5) and (6.1.6)) in the closed-form expression of the SED (Eq. (6.1.3)), the latter can be estimated by means of the elastic peak stresses evaluated at the crack tip with coarse meshes σ_{peak} and τ_{peak} :

$$\bar{W}_{\text{PSM}} = \frac{e_1}{E} \left[\mathbf{K}_{\text{FE}}^* \cdot \sigma_{\text{peak}} \cdot \left(\frac{d}{R_0} \right)^{0.5} \right]^2 + \frac{e_2}{E} \left[\mathbf{K}_{\text{FE}}^{**} \cdot \tau_{\text{peak}} \cdot \left(\frac{d}{R_0} \right)^{0.5} \right]^2 \quad (6.1.7)$$

where e_1 and e_2 are equal to 0.133 and 0.340, respectively, in the case of a notch opening angle $2\alpha = 0^\circ$ (crack case) and Poisson's ratio $\nu = 0.3$ [23].

To validate the peak stress approach according to Eq. (6.1.7), FE analyses have been carried out on the same cracked plates and the same pattern of elements taken into consideration in the previous Section with reference to Figure 6.1.3. In all cases, the 'exact' numerical values of the SED parameter have been calculated with the direct approach and adopting very refined meshes (approximately 500 FE inside the control volume), \bar{W}_{FEM} (Eq. (6.1.4)). The radius of the control volume R_0 has been kept constant and equal to 0.1 mm, which is relevant to aluminium alloys [29]. The mode mixity ratio (MM) has been evaluated according to the following definition:

$$MM = \frac{K_{II}}{K_I + K_{II}} \quad (6.1.8)$$

For an inclined crack in an infinitely wide plate, MM can be calculated as a function of the crack inclination angle (ϕ in Figure 6.1.3a) by substituting the theoretical expressions of K_I and K_{II} , according to [49], into Eq. (6.1.8):

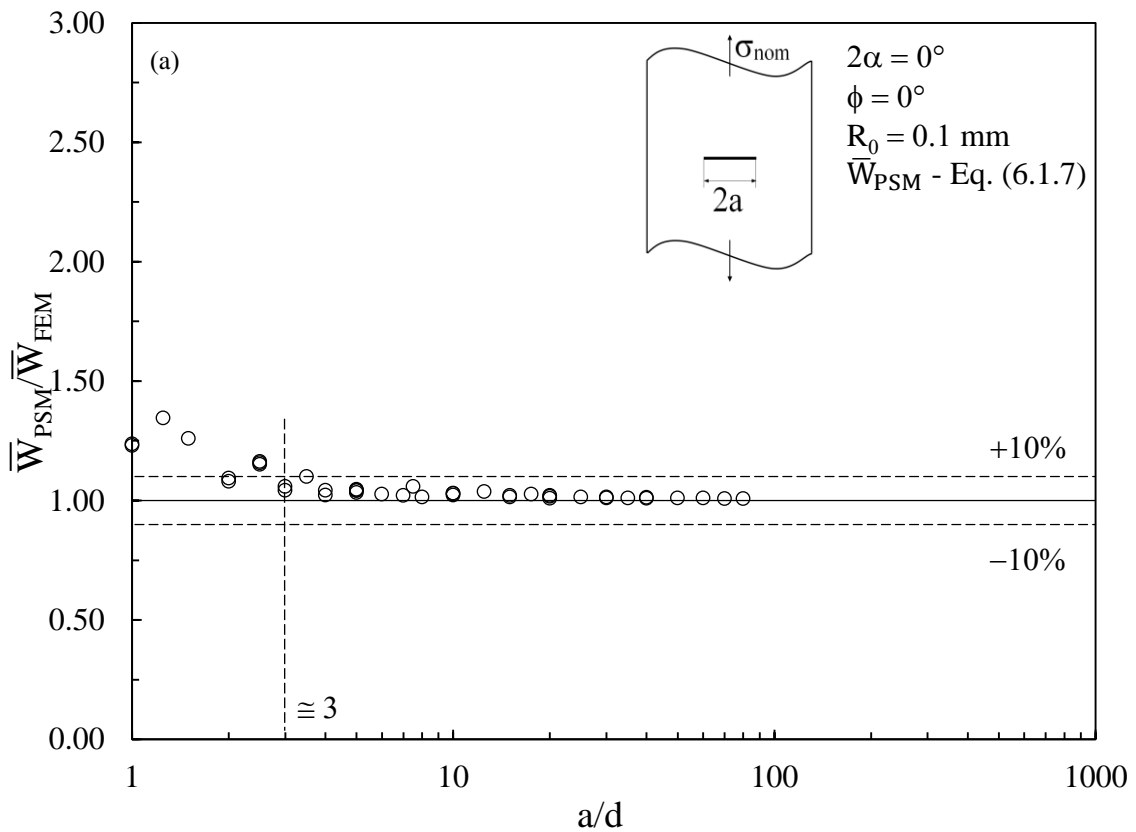
$$MM = \frac{\sin(\phi) \cdot \cos(\phi)}{\sin(\phi) \cdot \cos(\phi) + \cos^2(\phi)}. \text{ Eq. (6.1.8) provides, as a master case, } MM = 0 \text{ for}$$

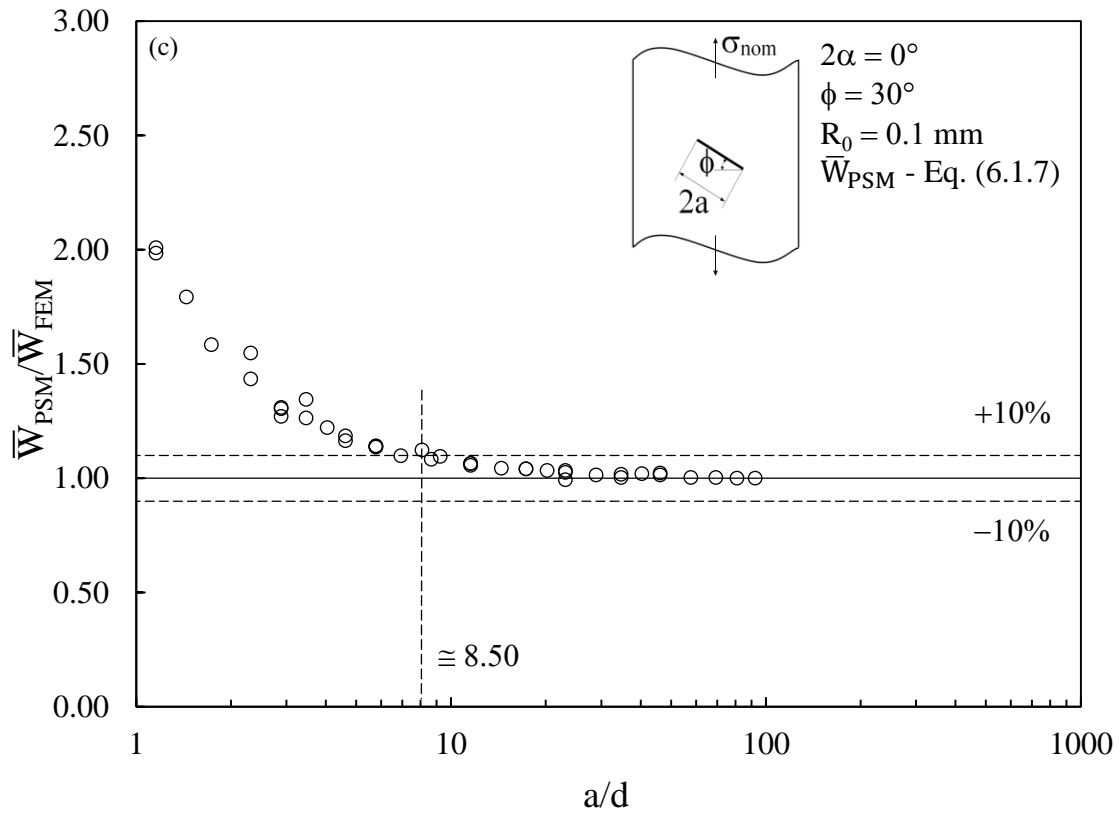
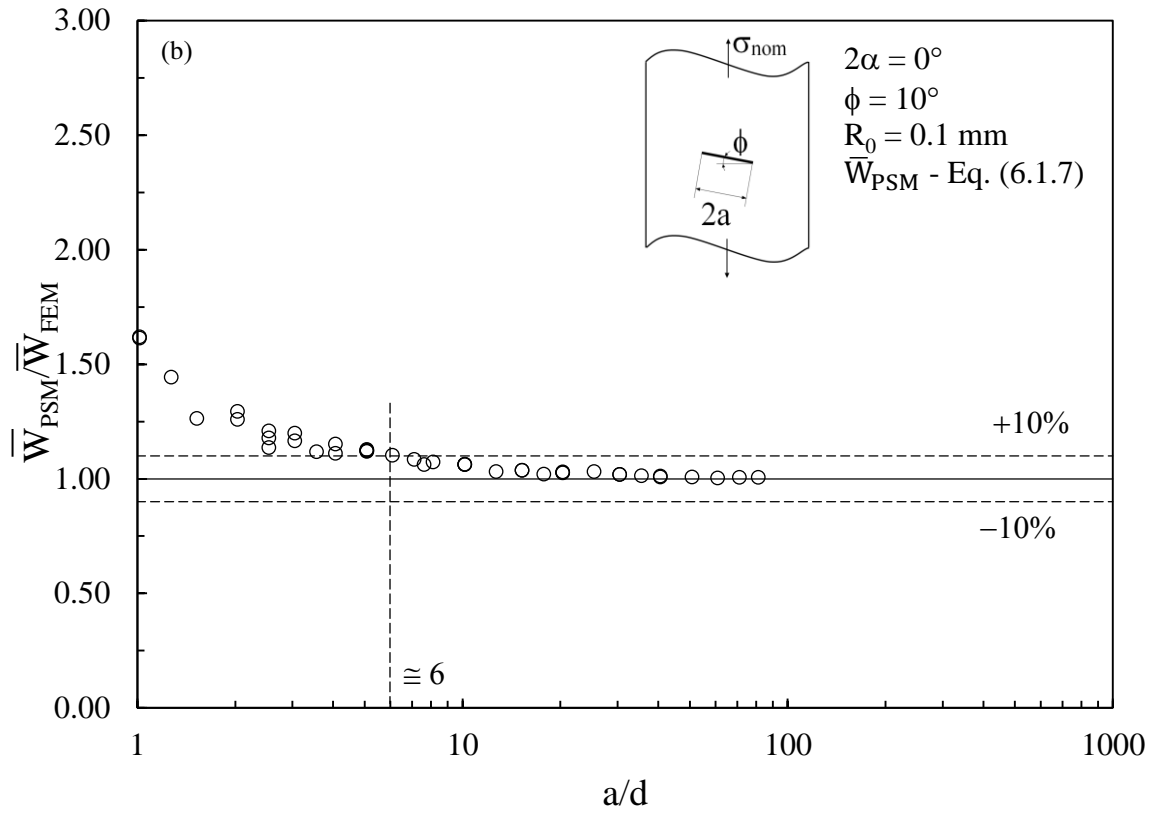
pure mode I with $\phi = 0^\circ$, $MM = 0.5$ for mixed mode with $\phi = 45^\circ$ and $MM = 1$ for pure mode II loading.

Before validating the peak stress approach, the SED parameter has also been evaluated according to Eq. (6.1.3), \bar{W}_{AN} , with the exact SIFs evaluated from dedicated very refined FE analyses, where the element size close to the crack tip has been reduced to 10^{-5} mm. The maximum difference between \bar{W}_{AN} (Eq. (6.1.3)) and \bar{W}_{FEM} (Eq. (6.1.4)) resulted in approximately 5% for the minimum crack length $2a = 10$ mm and crack inclination angle $\phi = 60^\circ$. This means that the influence of higher order terms, such as the T-stress, can be neglected in the present analyses, at least from an engineering point of view, and Eqs (6.1.3) and (6.1.7) are fully applicable.

The ratio between the SED calculated with the peak stress (\bar{W}_{PSM} , Eq. (6.1.7)) and the direct (\bar{W}_{FEM} , Eq. (6.1.4)) approaches is reported in Fig. 6.1.5 for each crack

inclination angle ϕ . It can be observed that the ratio $\bar{W}_{\text{PSM}}/\bar{W}_{\text{FEM}}$ converges to unity within a scatter band of $\pm 10\%$ for all different mode mixities taken into consideration. More precisely, convergence occurs for a mesh density ratio a/d greater than 3 for $\text{MM} = 0$ ($\phi = 0^\circ$), 6 for $\text{MM} = 0.15$ ($\phi = 10^\circ$), 8.50 for $\text{MM} = 0.37$ ($\phi = 30^\circ$), 11 for $\text{MM} = 0.50$ ($\phi = 45^\circ$) and 16 for $\text{MM} = 0.63$ ($\phi = 60^\circ$). As was expected, the minimum a/d ratio to assure the validity of the proposed method increases as the mode mixity ratio (MM) defined by Eq. (6.1.8) increases. In fact, Figure 6.1.4 shows that mode II loading is more demanding than mode I in terms of mesh density to estimate the NSIFs using the PSM [44].





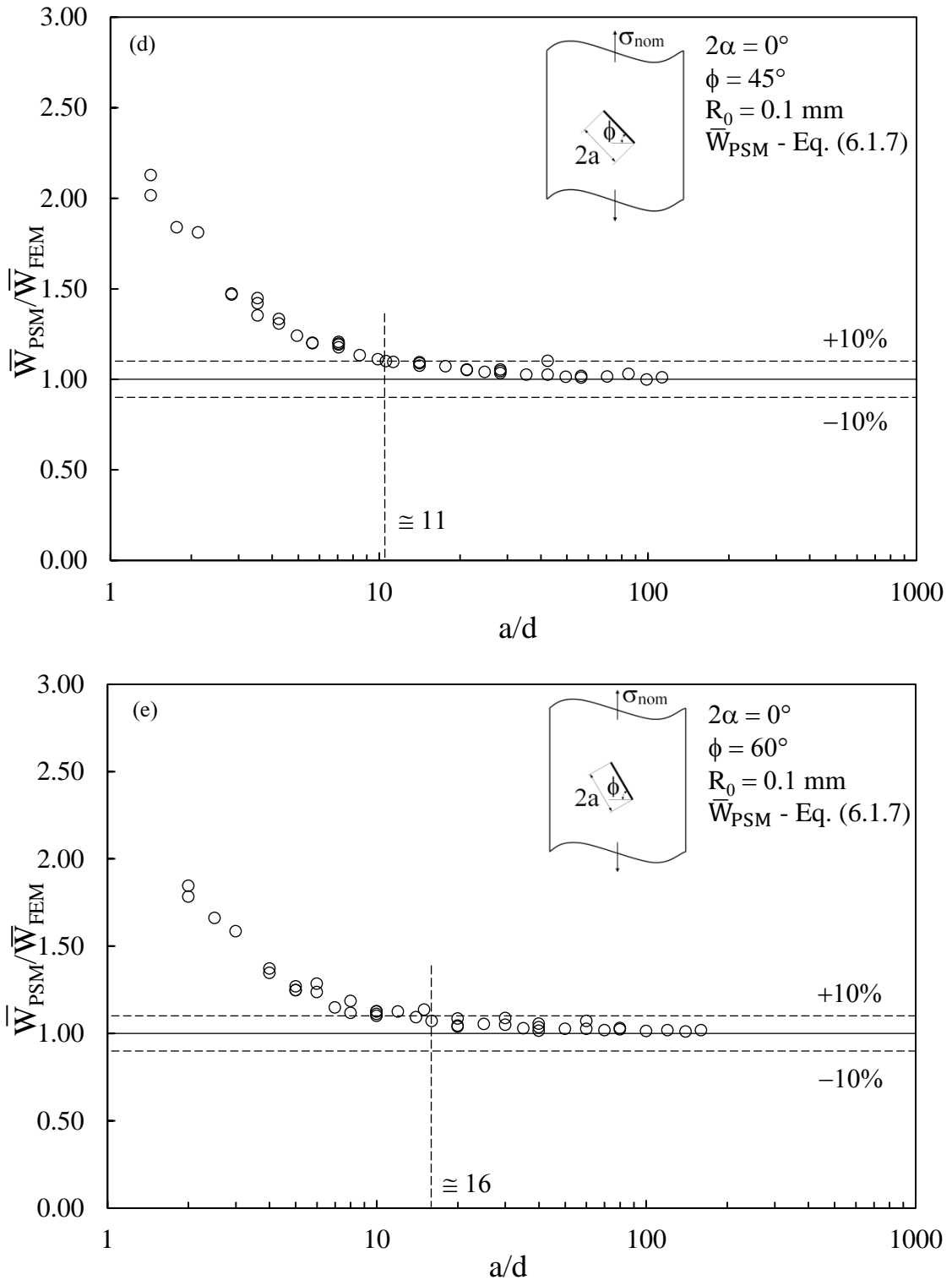


Figure 6.1.5: Ratio between approximated and exact SED parameter versus the mesh density ratio. \bar{W}_{PSM} according to the peak stress approach, Eq. (6.1.7); \bar{W}_{FEM} according to the direct approach, Eq. (6.1.4). Crack ($2\alpha = 0^\circ$) under mixed mode (I+II) loading: (a) $\phi = 0^\circ$ (MM = 0), (b) $\phi = 10^\circ$ (MM = 0.15), (c) $\phi = 30^\circ$ (MM = 0.37), (d) $\phi = 45^\circ$ (MM = 0.50) and (e) $\phi = 60^\circ$ (MM = 0.63).

It might be interesting to compare the mesh density requirements to apply the peak stress approach and the direct approach with coarse mesh option. By limiting the analysis to pure mode I loading ($\phi=0^\circ$, $MM=0$), the ratio between the SEDs evaluated with the direct approaches ($\bar{W}_{FEM,coarse}/\bar{W}_{FEM}$, each quantity being evaluated according to Eq. (6.1.4)) has been reported in Fig. 6.1.6 as a function of a/d . Figure 6.1.6 should be compared with Figure 6.1.5a. It can be observed that the ratio $\bar{W}_{FEM,coarse}/\bar{W}_{FEM}$ converges to unity within a scatter band of $\pm 10\%$ if a/d is greater than 5. However, considering only low crack size to plate width ratios ($2a/w < 0.25$), such that the plate free edge is very far from the control volume, it should be observed that the minimum mesh density ratio a/d reduces to 3, in agreement with the applicability analysis of the peak stress approach reported in Figure 6.1.5a. Even if a comparison for mixed mode cases has not been performed, Figures 6.1.2b and 3b nonetheless compare the most coarse FE meshes which can be used with the direct method and the peak stress method, respectively, for a crack inclination angle $\phi=30^\circ$. Outside the circles having radii R_0 and $10 \cdot R_0$, the direct approach allows a more coarse mesh to be defined. However, it should be noted that quadratic finite elements are used in the direct approach (Figure 6.1.2b) [37], while linear finite elements are used in the peak stress approach (Figure 6.1.3b). Therefore, eight FE nodes for each element contribute to increase the size of the stiffness matrix in the former case, while only four nodes for each element contribute in the latter case.

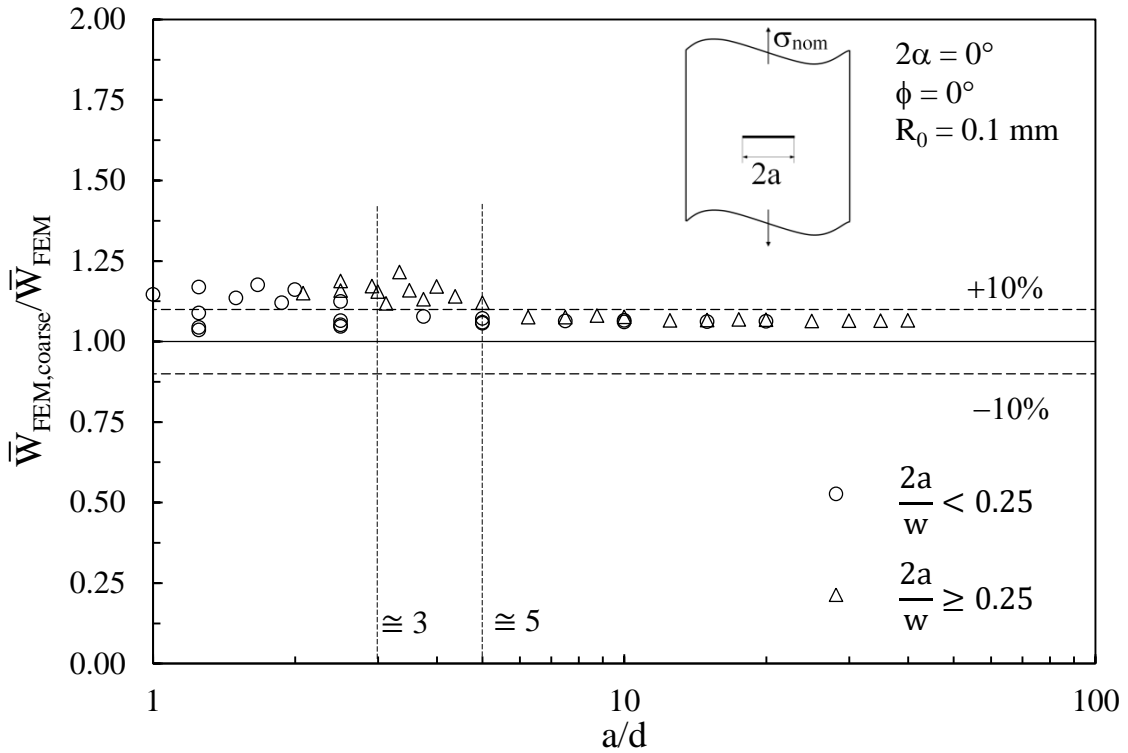


Figure 6.1.6: Minimum mesh density ratio a/d required to estimate the SED parameter according to the direct approach with coarse mesh option ($\bar{W}_{FEM,coarse}$, Eq. (6.1.4)) for a crack ($2\alpha = 0^\circ$) under pure mode I loading ($\phi = 0^\circ$, $MM = 0$). d is the average element size outside the control volume according to Fig. 6.1.2.

6.1.4.2 Minimum mesh density ratio a/d

The results of the numerical analyses reported in Fig. 6.1.4 suggest that proper convergence curves of the non-dimensional SIFs K_{FE}^* and K_{FE}^{**} against the mesh density ratio a/d may be fitted through numerical results. K_{FE}^* and K_{FE}^{**} are seen to be independent of the mode mixity ratio MM according to Figs. 6.1.7a and b, which report also the fitting functions f_I and f_{II} calculated by means of MATLAB[®]:

$$K_{FE}^* \left(\frac{a}{d} \right) = K_{FE}^* \cdot f_I \left(\frac{a}{d} \right) \cong 1.38 \cdot \frac{1}{1 + \frac{0.15}{\left(\frac{a}{d} \right)}} \quad (6.1.9)$$

$$K_{FE}^{**} \left(\frac{a}{d} \right) = K_{FE}^{**} \cdot f_{II} \left(\frac{a}{d} \right) \cong 3.38 \cdot \frac{1}{1 + \frac{0.75}{\left(\frac{a}{d} \right)}} \quad (6.1.10)$$

If the ratio a/d increases, then functions f_I and f_{II} tend to unity and parameters K_{FE}^* and K_{FE}^{**} converge to the values 1.38 [43] and 3.38 [44], respectively, that were calibrated previously.

Figure 6.1.7b shows that some K_{FE}^{**} values, related to a crack inclination angle ϕ equal to 10° , significantly deviate from Eq. (6.1.10). This is due to a distortion of the FE mesh close to the crack tip, resulting in a pattern of finite elements different from that shown in Figs. 6.1.3b, d. The FE distortion mostly influences the mode II non-dimensional SIF (K_{FE}^{**}), which is more sensitive to the shape of the finite elements as compared to the mode I SIF (K_{FE}^*).

Taking advantage of Eqs. (6.1.9) and (6.1.10), the mode I and mode II SIFs can be estimated as follows:

$$K_I \cong K_{FE}^* \left(\frac{a}{d} \right) \cdot \sigma_{peak} \cdot d^{0.5} \quad (6.1.11)$$

$$K_{II} \cong K_{FE}^{**} \left(\frac{a}{d} \right) \cdot \tau_{peak} \cdot d^{0.5} \quad (6.1.12)$$

By substituting Eqs. (6.1.11) and (6.1.12) into Eq. (6.1.3) and taking into account definition (6.1.8), the ratio between the SED according to the peak stress method (\bar{W}_{PSM}) and that evaluated analytically (\bar{W}_{AN}) can be written as a function of the mesh density parameter a/d and of the mode mixity ratio MM:

$$\frac{\bar{W}_{PSM}}{\bar{W}_{AN}} \cong \frac{1 + \frac{0.340}{0.133} \cdot \left(\frac{MM}{1-MM} \right)^2 \cdot \left(\frac{f_I \left(\frac{a}{d} \right)}{f_{II} \left(\frac{a}{d} \right)} \right)^2}{\left(f_I \left(\frac{a}{d} \right) \right)^2 \cdot \left(1 + \frac{0.340}{0.133} \cdot \left(\frac{MM}{1-MM} \right)^2 \right)} \quad (6.1.13)$$

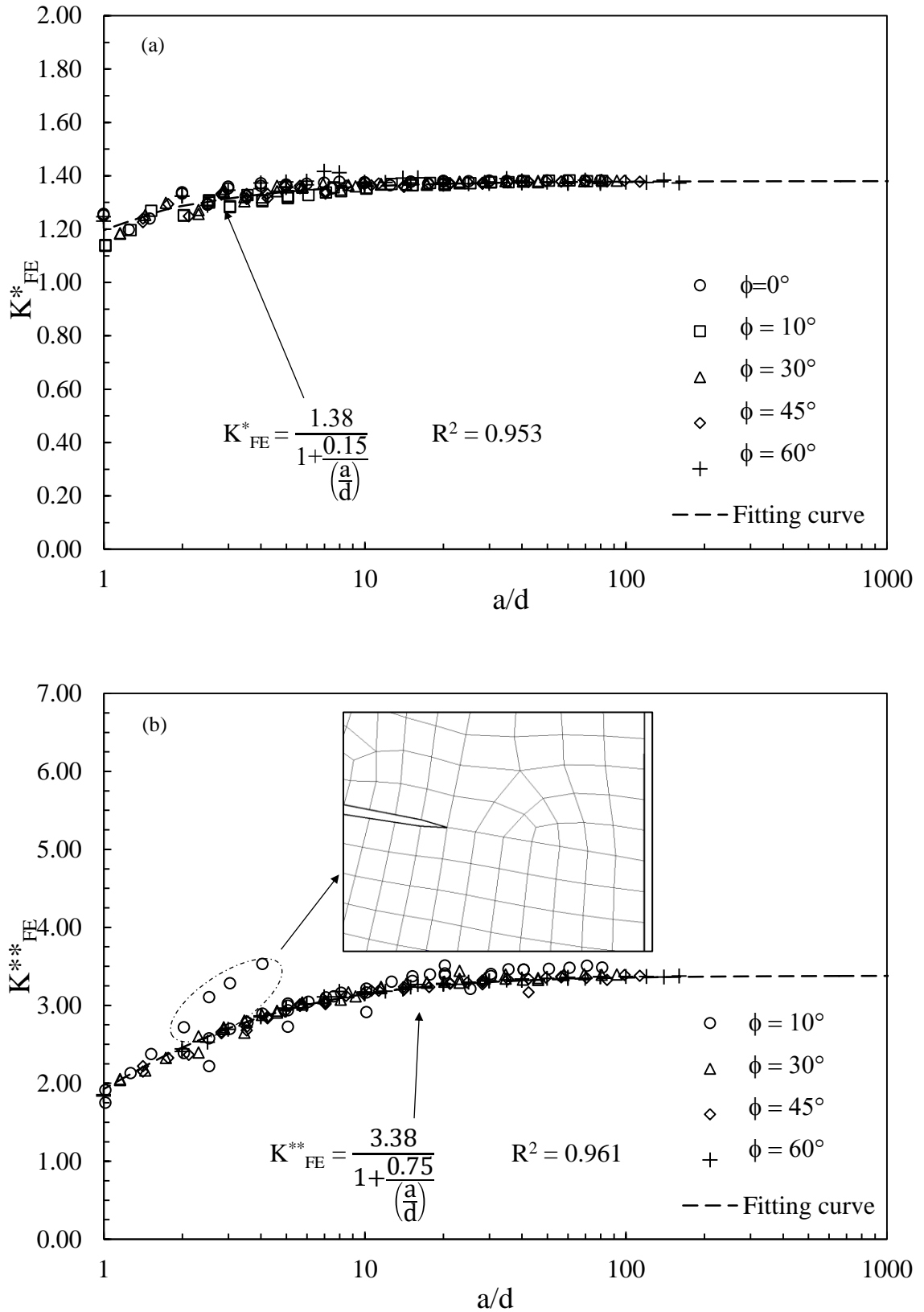


Figure 6.1.7: Non-dimensional SIFs and best fitting curves related to a crack ($2\alpha = 0^\circ$) under mixed mode (I+II) loading, as functions of the mesh density ratio a/d : (a) mode I and (b) mode II.

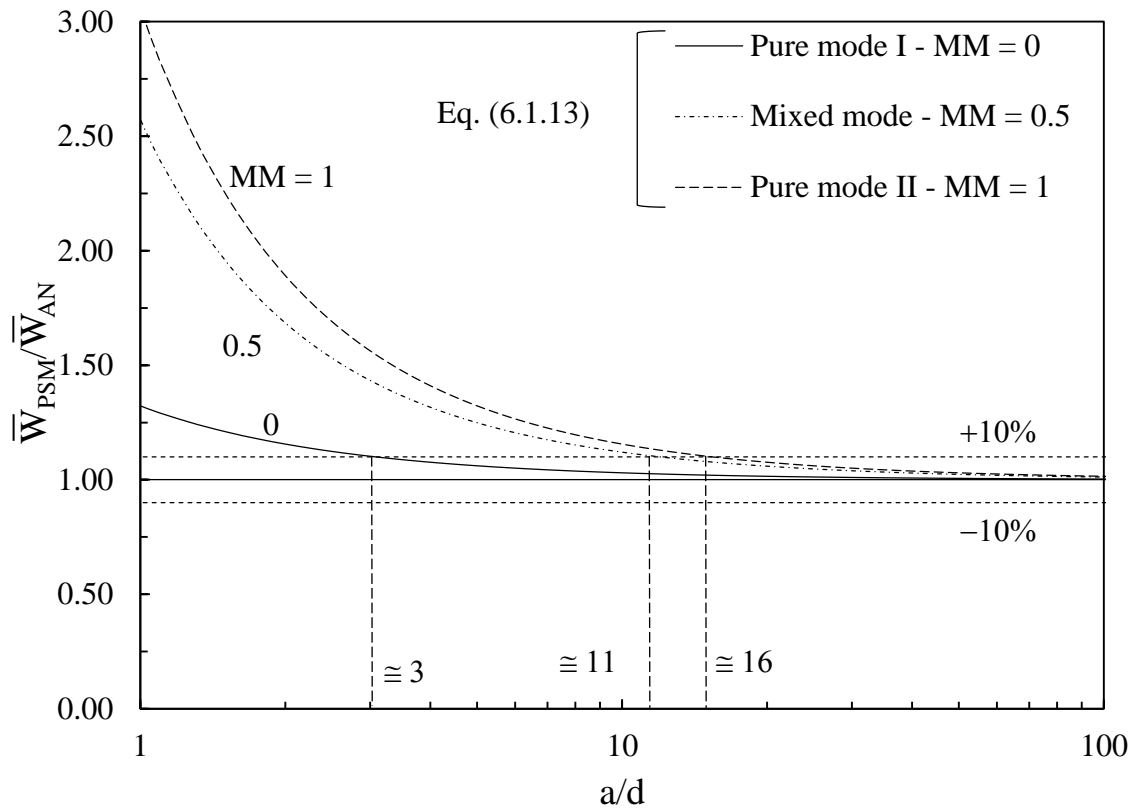


Figure 6.1.8: Minimum mesh density ratio a/d for the applicability of the peak stress approach under different mode mixities MM, according to Eq. (6.1.13).

It is worth recalling that, in the analyses performed here, it has been verified that $\bar{W}_{AN} \cong \bar{W}_{FEM}$. The above equation allows for estimating the minimum mesh density ratio a/d and for assuring the applicability of the PSM (Eq. (6.1.7)) once the mode mixity ratio MM of a given problem is known and the accepted level of approximation is fixed.

Figure 6.1.8 plots the ratio $\bar{W}_{PSM}/\bar{W}_{AN}$ as a function of a/d for different mode mixities, according to Eq. (6.1.13). It can be observed that the ratio $\bar{W}_{PSM}/\bar{W}_{AN}$ converges to unity within a scatter band of $\pm 10\%$ for a minimum ratio a/d that depends on the mode mixity ratio: it equals 3 for the case MM = 0 (pure mode I), 11 for MM = 0.50 (mixed mode I+II), and 16 for MM = 1 (pure mode II), according to the behaviour observed in Fig. 6.1.5.

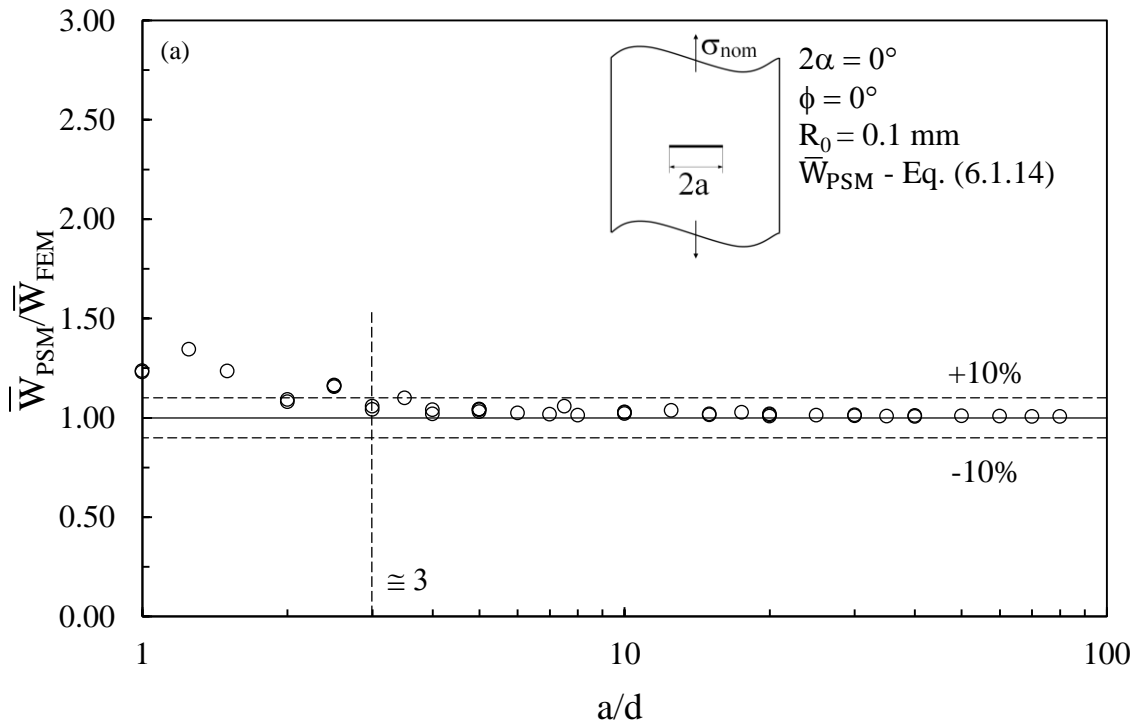
A further analysis of the peak stress approach is performed in the following two Sections.

6.1.4.3 The peak stress approach using the elastic maximum principal stress

Taking advantage of Eq. (6.1.7), the SED parameter in cases of prevailing mode I stresses might be estimated using only the maximum elastic principal stress evaluated at the crack tip, $\sigma_{I,peak}$:

$$\bar{W}_{PSM} = \frac{e_1}{E} \left[K_{FE}^* \cdot \sigma_{I,peak} \cdot \left(\frac{d}{R_0} \right)^{0.5} \right]^2 \quad (6.1.14)$$

Eq. (6.1.14) shows that only one stress value needs to be evaluated by means of an FE analysis. The ratio between the SED based on the maximum elastic principal stress (\bar{W}_{PSM} , Eq. (6.1.14)) and the SED calculated using the direct approach (\bar{W}_{FEM} , Eq. (6.1.4)) have been reported in Fig. 6.1.9, with reference to a crack inclination angle ϕ equal to 0° and 10° . It can be observed that the ratio $\bar{W}_{PSM}/\bar{W}_{FEM}$ converges to unity within a scatter band of $\pm 10\%$ for a ratio a/d greater than 3 for the case $MM = 0$ ($\phi = 0^\circ$) and 3.5 for $MM = 0.15$ ($\phi = 10^\circ$). On the basis of the FE results obtained here, it has been verified that Eq. (6.1.14) can be applied for MM lower than or equal to 0.15, i.e., $\phi \leq 10^\circ$.



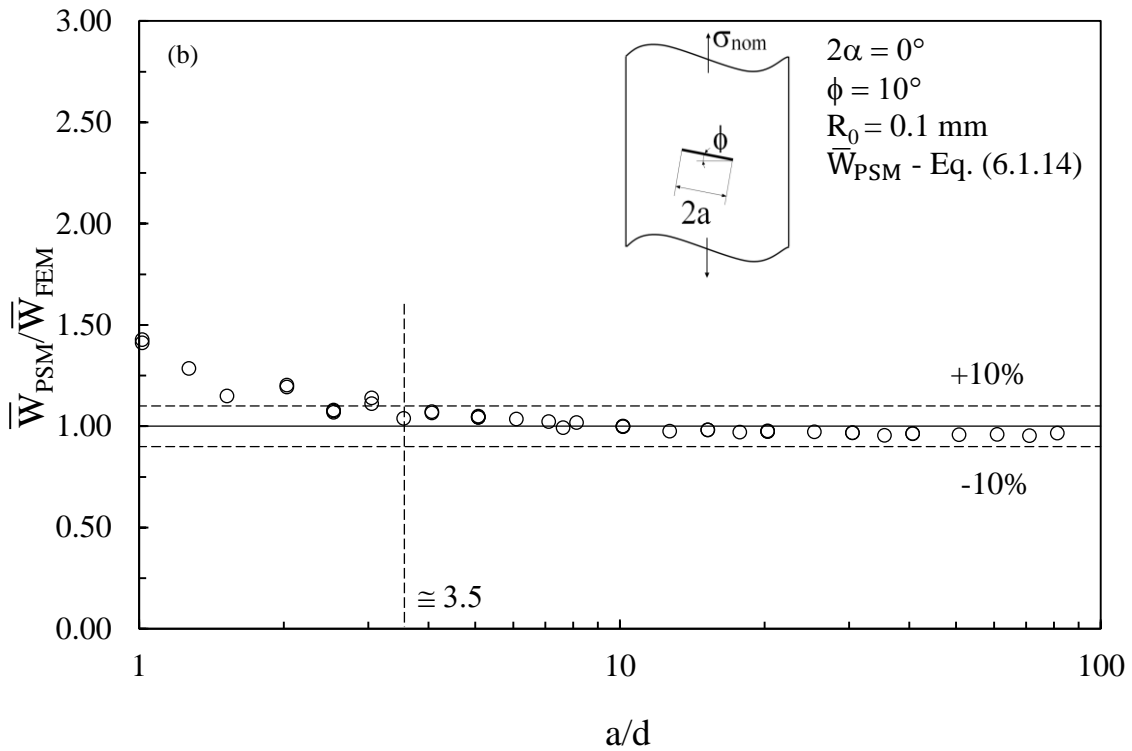


Figure 6.1.9: Ratio between approximated and exact SED parameter versus the mesh density ratio. \bar{W}_{PSM} from the maximum elastic principal stress, Eq. (6.1.14); \bar{W}_{FEM} according to the direct approach, Eq. (6.1.4). Crack ($2\alpha = 0^\circ$) under mixed mode (I+II) loading: (a) $\phi = 0^\circ$ (MM = 0), (b) $\phi = 10^\circ$ (MM = 0.15).

6.1.4.4 The peak stress approach coarsening the mesh further

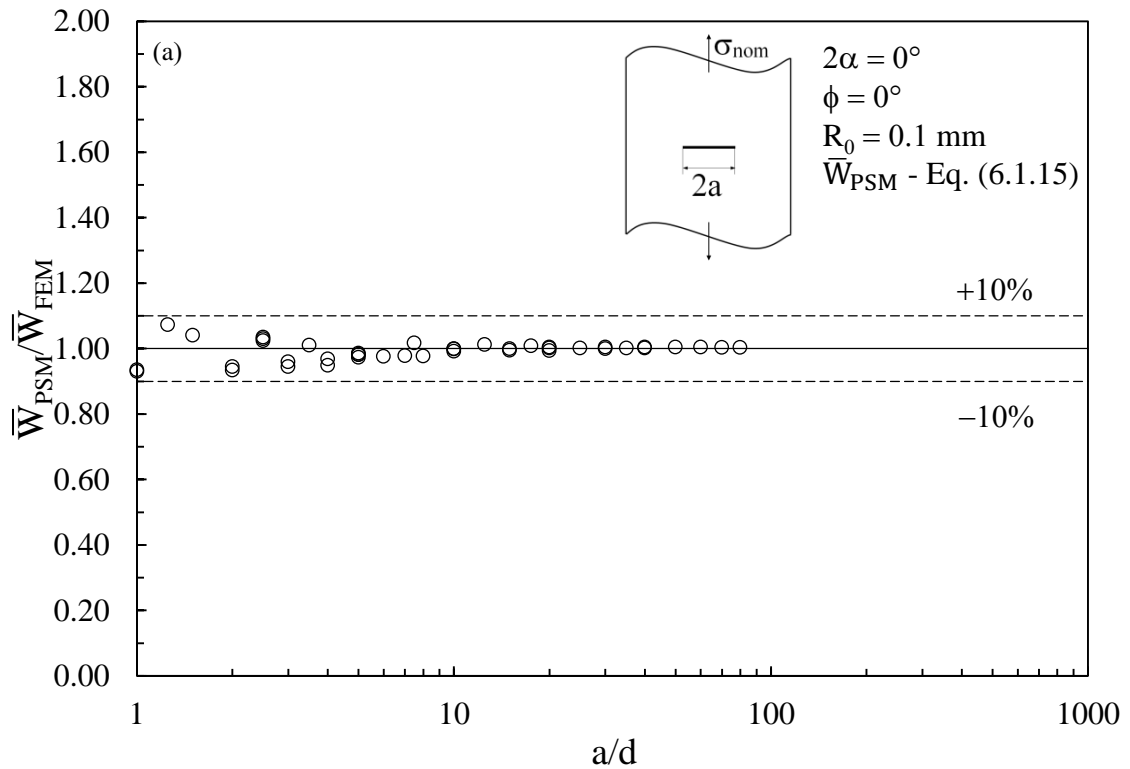
Given the fitting functions Eqs. (6.1.9) and (6.1.10), the averaged SED might be estimated by means of the peak stresses calculated using an arbitrary finite element size d , thus removing the minimum mesh density requirements (given by the minimum a/d ratio shown in Figure 6.1.5). By updating Eq. (6.1.7) using Eqs. (6.1.9) and (6.1.10), the following equation is obtained:

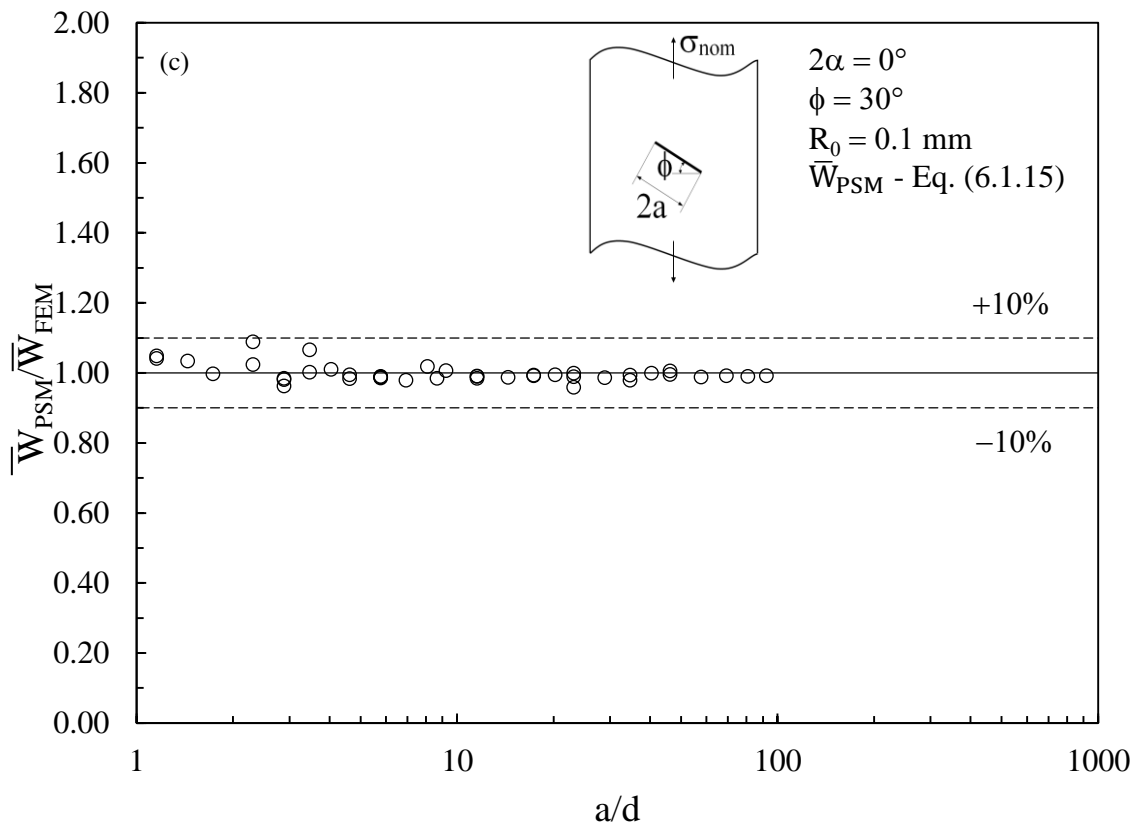
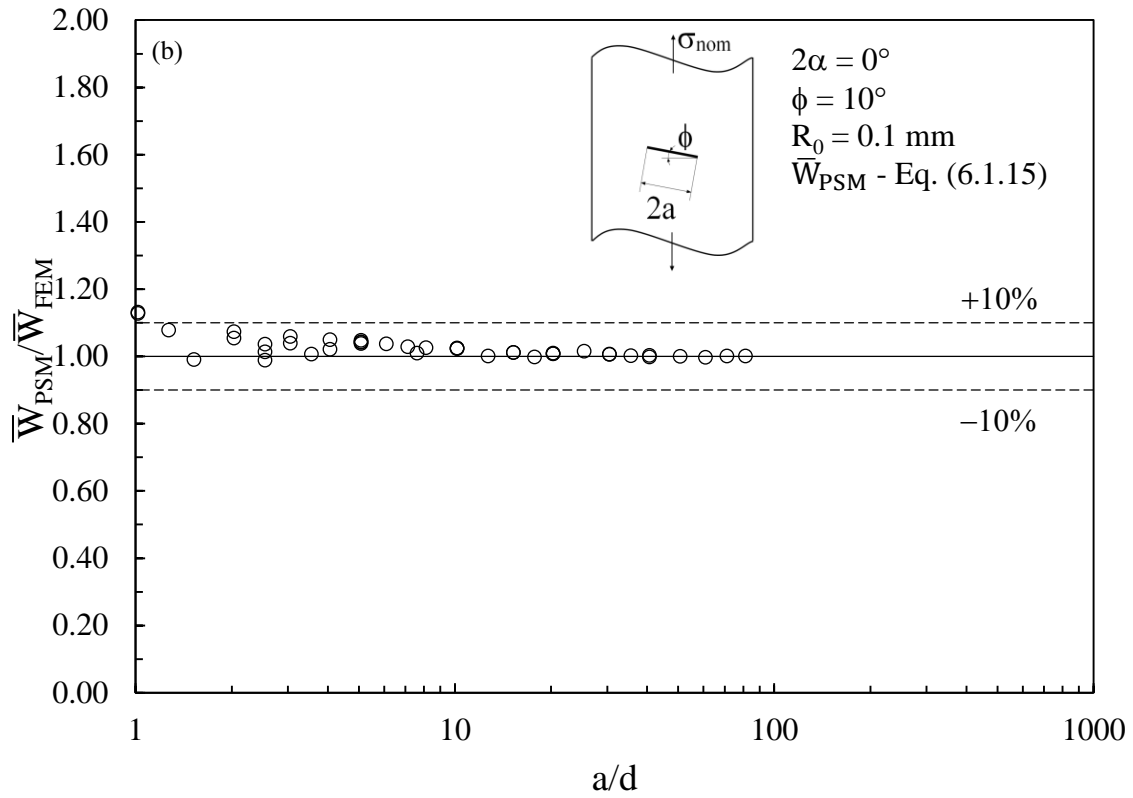
$$\bar{W}_{PSM} = \frac{e_1}{E} \left[\mathbf{K}_{FE}^* \cdot \sigma_{peak} \cdot f_I \left(\frac{a}{d} \right) \cdot \left(\frac{d}{R_0} \right)^{0.5} \right]^2 + \frac{e_2}{E} \left[\mathbf{K}_{FE}^{**} \cdot \tau_{peak} \cdot f_{II} \left(\frac{a}{d} \right) \cdot \left(\frac{d}{R_0} \right)^{0.5} \right]^2 \quad (6.1.15)$$

The ratio between the SED based on Eq. (6.1.15) and that calculated using the direct approach (\bar{W}_{FEM} , Eq. (6.1.4)) has been reported in Fig. 6.1.10 for different

crack inclination angles ϕ . Figure 6.1.10 (from (a) to (e)) should be compared with the corresponding Figure 6.1.5 (from (a) to (e)) to observe that, making use of Eq. (6.1.15), the ratio $\bar{W}_{\text{PSM}}/\bar{W}_{\text{FEM}}$ converges to unity within a scatter band of $\pm 10\%$ for all mesh density ratios a/d , down to the minimum feasible a/d equal to 1.

Although Eq. (6.1.15) results from a fitting exercise according to Fig. 6.1.7, it nevertheless extends the validity of the PSM to more coarse meshes than considered previously and therefore may be advantageous from a practical point of view.





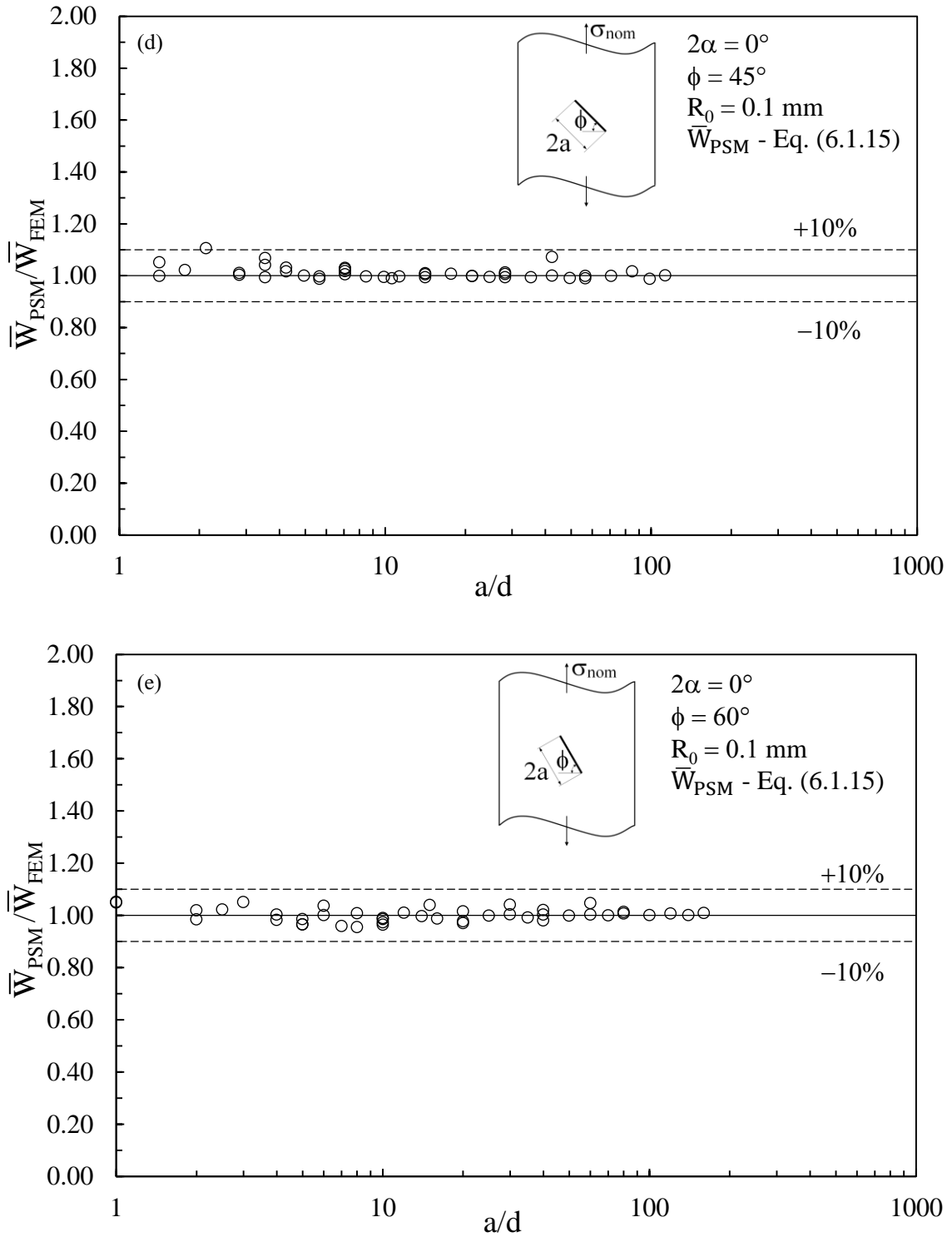


Figure 6.1.10: Ratio between approximated and exact SED parameter versus the mesh density ratio. \bar{W}_{PSM} according to the peak stress approach, Eq. (6.1.15); \bar{W}_{FEM} according to the direct approach, Eq. (6.1.4). Crack ($2\alpha = 0^\circ$) under mixed mode (I+II) loading: (a) $\phi = 0^\circ$ (MM = 0), (b) $\phi = 10^\circ$ (MM = 0.15), (c) $\phi = 30^\circ$ (MM = 0.37), (d) $\phi = 45^\circ$ (MM = 0.50) and (e) $\phi = 60^\circ$ (MM = 0.63).

6.1.5. An example of a practical application

The high cycle fatigue failure can be considered a brittle failure mode and usually occurs in the linear elastic regime. Keeping this in mind, the mean value of the strain energy density (SED) in a circular sector of radius R_0 located at the fatigue crack initiation sites has been used to summarize fatigue strength data from steel and aluminium welded joints [29]. Local strain energy density averaged in a finite size volume surrounding weld toes and roots is a scalar quantity that can be given as a function of mode I+II NSIFs in plane problems and mode I+II+III NSIFs in three dimensional problems. As to the structural volume size R_0 , it is thought of as a material property resulting from the welding process [29]. It was calibrated by combining two experimental data, namely the high-cycle fatigue strength $\Delta\sigma_A$ (typically at 2 million cycles) of the butt ground welded joints (in order to quantify the influence of the welding process, in the absence of any stress concentration effect) and the high-cycle NSIF-based fatigue strength of welded joints, ΔK_{IA} , having a V-notch angle at the weld toe large enough to ensure that mode II stresses are non-singular. By equaling the SED parameter evaluated in the two experimental situations, a convenient expression was derived [23,29]:

$$R_0 = \left(\frac{\sqrt{2e_1} \Delta K_{IA}}{\Delta\sigma_A} \right)^{\frac{1}{1-\lambda_1}} \quad (6.1.16)$$

where both λ_1 and e_1 depend on the V-notch angle. For aluminium welded joints a radius $R_0 = 0.12$ mm was obtained [29].

An example of application is presented here, that is relevant to the fatigue strength assessment of butt-welded joints made of aluminium alloys in terms of the averaged local strain energy density $\Delta\bar{W}$.

For the sake of brevity, only one experimental series due to Sonsino et al. has been considered [50,51], referring to 25-mm-thick, partial-penetration butt-welded joints with root failures. Welded joints were tested in the stress-relieved conditions by applying pulsating ($R = 0$, with R being the load ratio defined as the ratio between the minimum and the maximum applied loads) or completely

reversed ($R = -1$) axial fatigue loadings. More details can be found in a recent contribution [52].

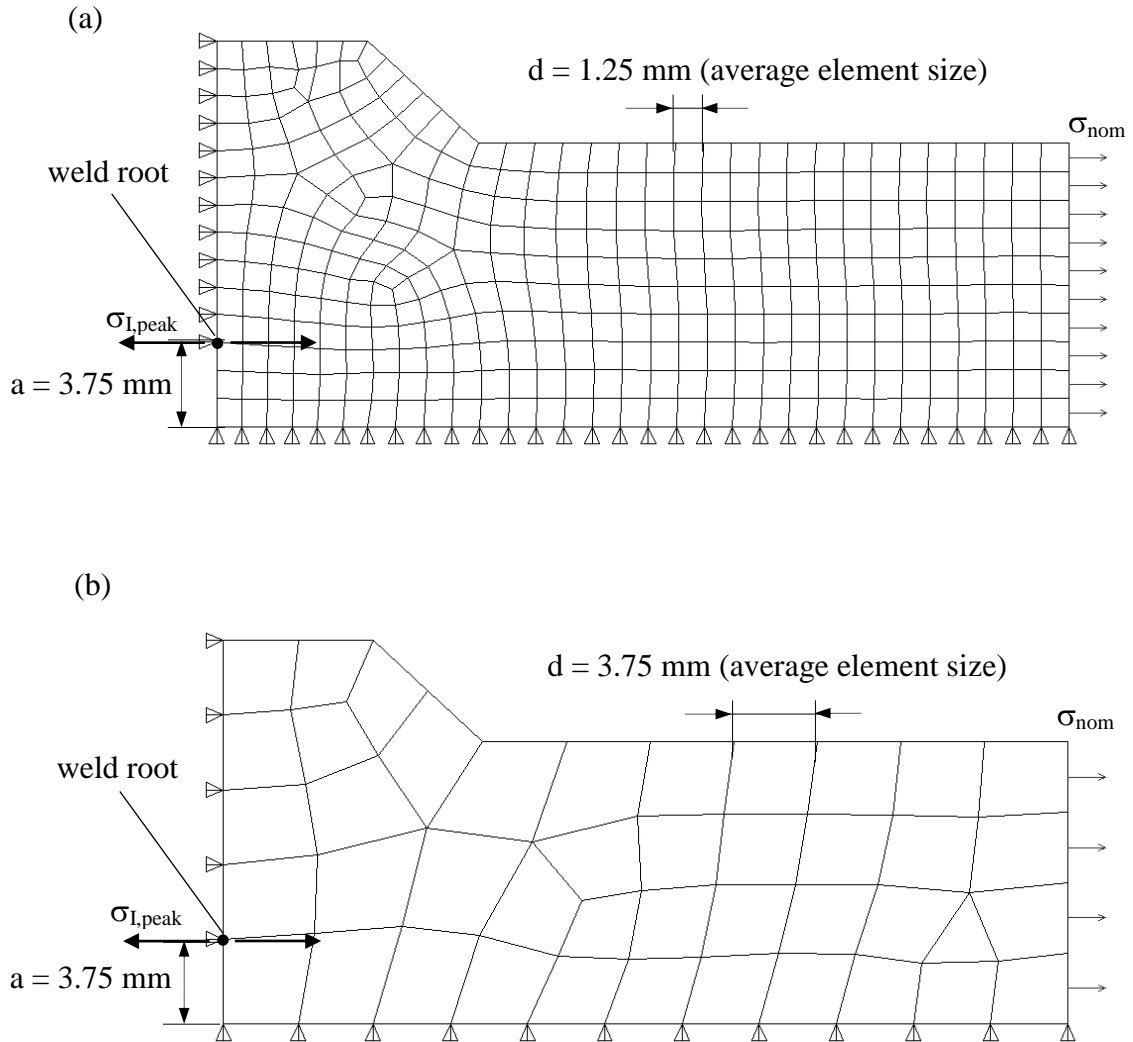


Figure 6.1.11: FE mesh adopted to evaluate the peak stress σ_{peak} at the weld root of 25-mm-thick partial-penetration butt welded joints made of aluminum alloys. SED evaluated according to the peak stress approach (a) Eq. (6.1.14) with $a/d = 3$ and (b) Eq. (6.1.15) with $a/d = 1$.

Due to the loading conditions, only mode I stresses are present at the weld root (pure mode I according to Fig. 6.1.11). Therefore, the mode mixity ratio MM (Eq. 6.1.8) is equal to 0, and Eq. (6.1.14) can be employed. Through Eq. (6.1.13), it is possible to estimate the minimum mesh density ratio a/d for the applicability of the peak stress approach. In the case $MM = 0$ and a chosen level of approximation

$\bar{W}_{\text{PSM}}/\bar{W}_{\text{AN}} \cong 1.10$, it results in $(a/d)_{\text{min}} = 3$, with a being the semi-crack length ($2a$ is the lack of penetration). Because $2a = 7.5$ mm, the maximum element size is $d_{\text{max}} = 3.75/3 = 1.25$ mm.

A free mesh pattern of quadrilateral, four-node PLANE 42 elements having a ‘global element size’ $d = 1.25$ mm was generated. By doing so, a 2D FE mesh of the type shown in Fig. 6.1.11a was obtained. After having evaluated the range of the elastic principal stress $\Delta\sigma_{\text{I,peak}}$ at the node located at the weld root, Eq. (6.1.14) has been applied to estimate the range of the averaged strain energy density $\Delta\bar{W}_{\text{PSM}}$ by using $e_1 = 0.125$, $E = 70000$ MPa and $R_0 = 0.12$ mm relevant to aluminium alloys [29,52]. Because the welded specimens have been tested in the stress-relieved conditions, the nominal load ratio R has been taken into account by means of a proper multiplicative factor defined in [53]. Thanks to the FE analysis according to the PSM sketched in Fig. 6.1.11a, the original fatigue test results given in terms of the nominal stress range have been re-converted into the range of the averaged strain energy density evaluated at the weld root. If Eq. (6.1.7) had been used instead of Eq. (6.1.14), the results would have been the same, with $\sigma_{\text{peak}} \cong \sigma_{\text{I,peak}}$ and $\tau_{\text{peak}} \cong 0$ at the weld root of the joints under examination. The experimental results in terms of $\Delta\bar{W}_{\text{PSM}}$ are reported in Fig. 6.1.12 using filled markers.

Taking advantage of Eq. (6.1.15), the SED parameter may also be estimated using a coarser FE mesh as compared to that reported in Fig. 6.1.11a. By adopting the minimum feasible mesh density a/d equal to 1, a free mesh pattern of quadrilateral four-node PLANE 42 elements having a ‘global element size’ $d = 3.75$ mm was generated, resulting in the 2D FE mesh shown in Fig. 6.1.11b. When applying Eq. (6.1.15), it should be kept in mind again that $\sigma_{\text{peak}} \cong \sigma_{\text{I,peak}}$ and $\tau_{\text{peak}} \cong 0$ for the joints under analysis. The results have been reported in Fig. 6.1.12 with open markers.

All results are compared with the SED-based design scatter band, which was calibrated previously using several experimental results taken from the literature (see Ref. [29]). A good agreement between experimental results and the SED-based design scatter band is seen in Fig. 6.1.12; however, the validation exercise of the SED approach in fatigue problems is not primarily the focus of the present

investigation. The fundamental conclusion that can be drawn is that the same level of correlation between experimental results and the SED-based design scatter band shown in Fig. 6.1.12 was also reported in [54], where the SED parameter had been evaluated using the direct approach according to Eq. (6.1.4) combined with very refined meshes. The relevant results have been reported in Fig. 6.1.12.

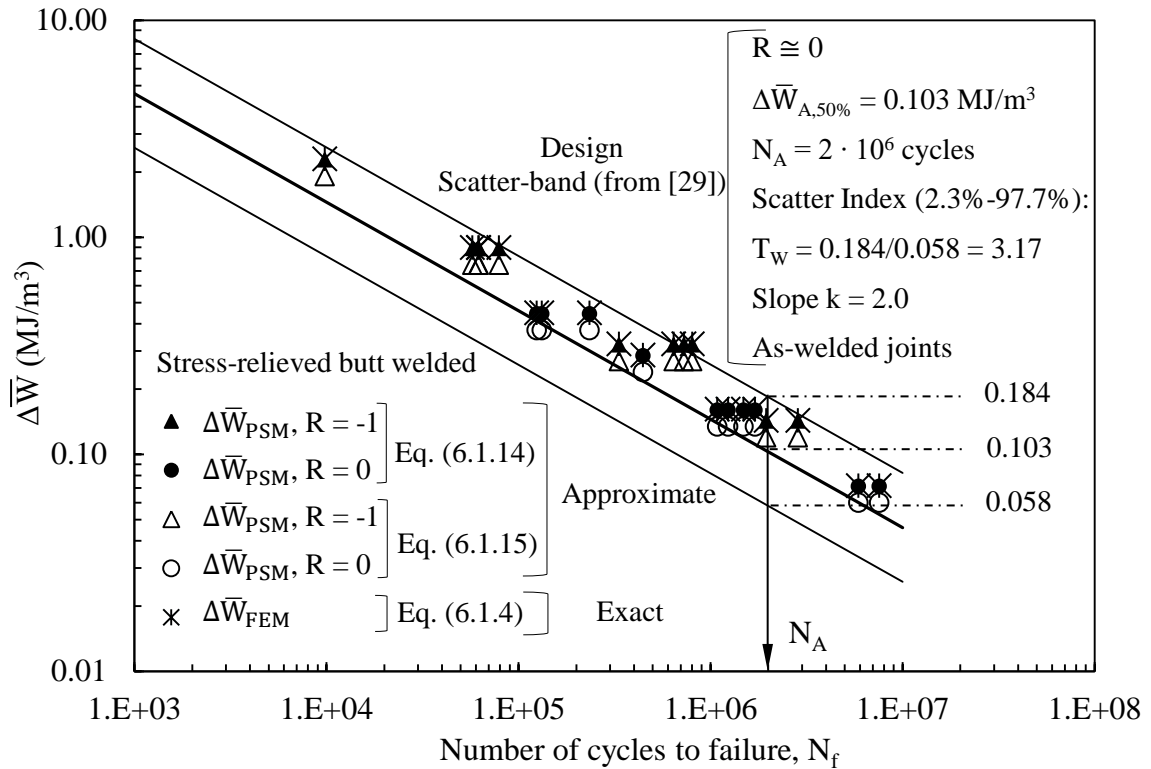


Figure 6.1.12: Fatigue strength of aluminum butt welded joints in terms of the averaged local strain energy density (SED parameter). Design scatter-band according to reference [29]. Comparison of approximate $\Delta\bar{W}_{PSM}$ values (Eq. (6.1.14) adopting $a/d = 3$ or Eq. (6.1.15) adopting $a/d = 1$) with exact $\Delta\bar{W}_{FEM}$ according to Eq. (6.1.4).

From an engineering point of view, the PSM according to Eqs. (6.1.7), (6.1.14) or (6.1.15) is a useful, FE-oriented tool to readily calculate the SED parameter in practical design problems by virtue of (i) the coarse pattern of finite elements that can be adopted, as shown in Figures 6.1.3b and d and 6.1.11; (ii) the use of just the singular nodal stresses picked up at the stress singularity point where an FE node always exists, so that interpolation of nodal stresses or analysis of stress-

distance data is unnecessary; and (iii) the simplified geometrical model to deal with because the structural volume is removed.

6.1.6. Discussion

The peak stress method (PSM) to estimate the strain energy density averaged in a structural volume (i.e., the SED parameter) has been formulated and applied in the case of two-dimensional cracks subjected to mixed mode (I+II) loading. In its original formulation, the PSM is a simplified, FE-oriented numerical method to estimate the SIFs using much coarser meshes than those required to post-process the local linear elastic stress fields evaluated close to the crack tip. The following conclusions can be drawn:

- Because the normal (opening) and shear (sliding) linear elastic peak stresses evaluated at the crack tip by FEM using coarse meshes are proportional to the mode I and mode II SIFs, respectively, a link can immediately be established with the SED parameter by means of Eqs. (6.1.3), (6.1.5) and (6.1.6). As a result, the SED parameter can be estimated by means of the elastic peak stresses evaluated at the crack tip (Eqs. (6.1.7) and (6.1.14)).
- To apply the PSM with coarse meshes, it has been found that the mesh density must be increased as the mode mixity ratio (MM) increases; as a guideline, the minimum ratio between the semi-crack length a and the mean element size d adopted in FE analyses is equal to 3 for $MM = 0$ (pure mode I loading) and 16 for $MM = 0.63$ (mixed mode (I+II) loading).
- Once the mode mixity ratio MM of a given problem can be estimated, the minimum mesh density a/d which ensures the applicability of the PSM can be estimated by means of Eq. (6.1.13) for a chosen level of approximation.
- By using proper correction functions fitted over the numerical results, applicability of the PSM to estimate the SED parameter can be extended to more coarse meshes according to Eq. (6.1.15), where the mesh density a/d can be reduced to unity. Eq. (6.1.15) may be advantageous from a practical point of view; as an application example, fatigue strength assessments of

butt-welded joints made of aluminium alloys have been performed by estimating the SED parameter using Eq. (6.1.14) as well as Eq. (6.1.15).

- The usefulness of the PSM to estimate the SED parameter is that (i) only the elastic peak stresses numerically evaluated at the crack tip are needed; because an FE node always exists at the stress singularity point, independently of the pattern of finite elements adopted, an FE analyst can easily pick up the design stresses in the post-processor environment of a commercial software program; (ii) the (small) control volume inside which the strain energy is to be averaged does not have to be included in the numerical model; and (iii) the employed meshes are coarse, such that, in the most wild application of the PSM performed here (Eq. (6.1.15)), the maximum finite element size adopted has been set equal to the crack size.

6.2 Link between the Peak Stress Method (PSM) and the averaged Strain Energy Density (SED): short cracks under mixed mode (I+II) loading with inclusion of T-stress contribution (*)

Nomenclature

2a	crack length
a_0	El Haddad-Smith-Topper length parameter of the material
d	mean size of a finite element
ΔK_{th}	threshold value of the SIF range for long cracks under mode I loading conditions
e_1, e_2	parameters for averaged SED evaluation
E	elastic modulus
f_I, f_{II}	fitting functions for K_{FE}^* and K_{FE}^{**} convergence curves
K_I, K_{II}	mode I and II SIFs
K_{FE}^*, K_{FE}^{**}	non-dimensional K_I and K_{II} relevant to the peak stress method
MM	mode mixity ratio
Nodal-T	T-stress estimated by FEM using selected nodal stresses
R_0	radius of the control volume for the averaged SED evaluation
r, θ	polar coordinates
T	slit-parallel tensile or compressive stress, T-stress
\bar{W}_{AN}	analytical, closed-form expression of the averaged SED including both SIFs and T-stress contributions
$\bar{W}_{AN,I+II}$	analytical, closed-form expression of the averaged SED, taking into account only SIFs contributions
\bar{W}_{FEM}	averaged SED calculated by FEM using very refined meshes (direct approach)
$\bar{W}_{FEM,coarse}$	averaged SED calculated by FEM using coarse meshes (direct approach with coarse mesh option)

\overline{W}_{NS}	averaged SED calculated by FEM according to the nodal stress approach: $\overline{W}_{NS} = \overline{W}_{PSM,I+II} + \overline{W}_{nodal-T}$
$\overline{W}_{PSM,I+II}$	averaged SED calculated according to the existing PSM (only SIFs contributions are taken into account)
$\overline{W}_{nodal-T}$	T-stress contribution to the averaged SED estimated using selected FE nodal stresses

Symbols

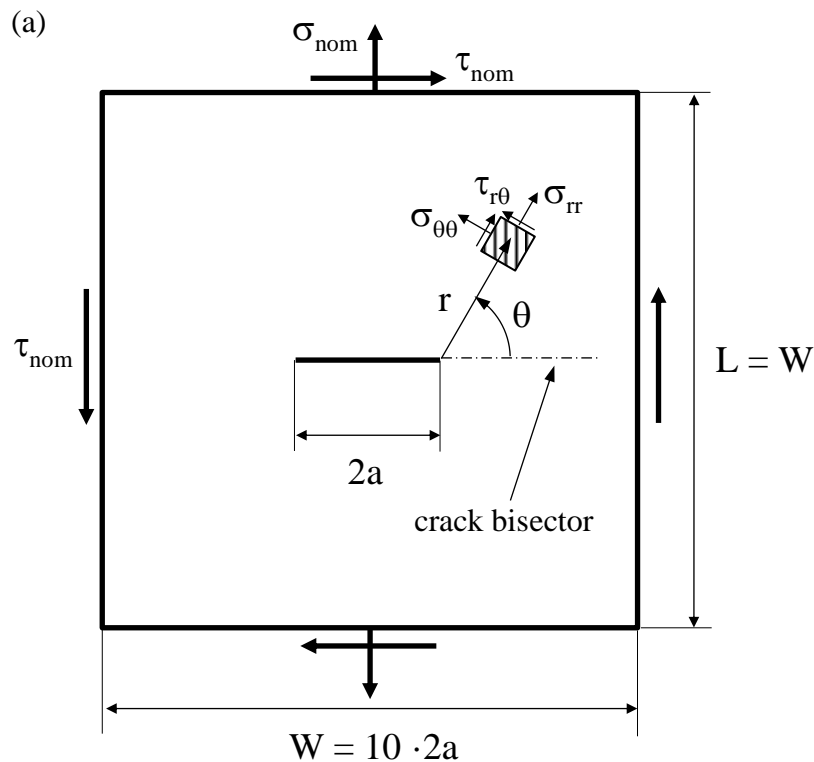
2α	opening angle
$\Delta\sigma_0$	plain material fatigue limit in terms of stress range
ν	Poisson's ratio
σ_{nom}	nominal tensile stress
σ_{peak}	singular, linear elastic opening peak stress evaluated at the crack tip by FEM using the PSM
$\sigma_{rr}, \sigma_{\theta\theta}, \tau_{r\theta}$	normal and shear stress components in the polar frame of reference
τ_{nom}	nominal shear stress
τ_{peak}	singular, linear elastic sliding peak stress evaluated at the crack tip by FEM using the PSM

(*) See also:

Campagnolo, A.; Meneghetti, G.; Berto, F. Rapid evaluation by FEM of the averaged strain energy density of mixed-mode (I+II) crack tip fields including the T-stress contribution. *Fatigue and Fracture of Engineering Materials and Structures* (under review).

6.2.1 Introduction

As formerly highlighted in the literature first by Brahtz [55] in 1933, stresses in the close neighborhood of sharp corners are characterized by a singular behavior. In the context of a broader analysis concerning plates weakened by sharp notches [31], the particular case of a zero notch opening angle, i.e. a crack, was deeply investigated by Williams [56] complementing some previous studies carried out by Griffith [57], Westergaard [58] and Irwin [59]. With regard to the crack case, Williams showed that the stress field can be formulated as a series expansion, whose coefficients are unknown and depend on the geometry and on the mode of loading. According to Williams [56], the stress field expressed in a polar coordinate system (r, θ) centred at the crack tip (Fig. 6.2.1a), as a function of the mode I and mode II stress intensity factors (SIFs), K_I and K_{II} , and of T-stress, T , is as follows:



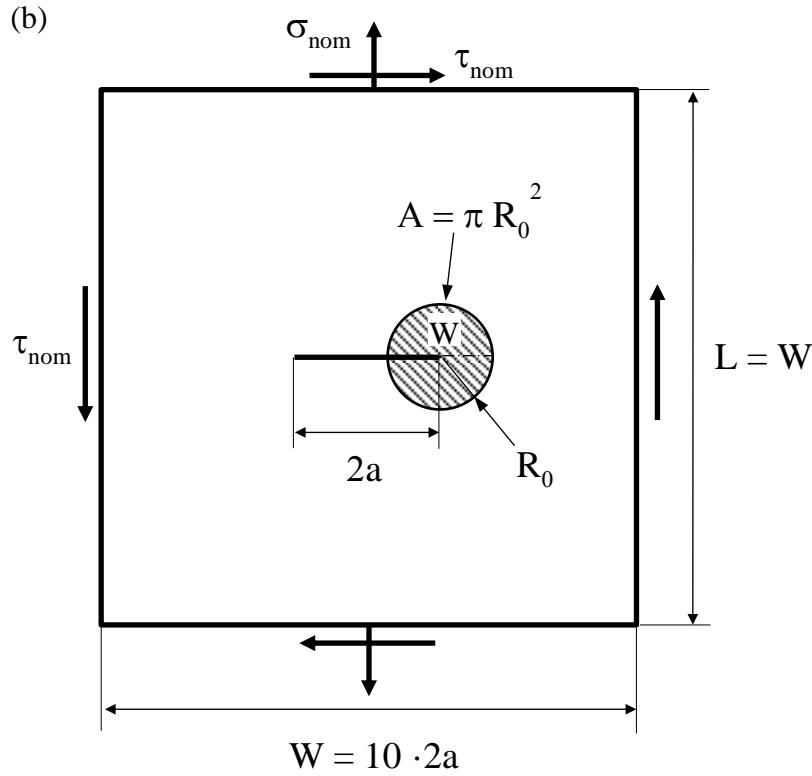


Figure 6.2.1: (a) Polar coordinate system centred at the crack tip. (b) Strain energy density averaged over a control volume (area) of radius R_0 surrounding the crack tip, $\bar{W} = \frac{W}{A}$.

$$\begin{aligned}
 \begin{Bmatrix} \sigma_{rr} \\ \sigma_{\theta\theta} \\ \tau_{r\theta} \end{Bmatrix} &= \frac{K_I}{\sqrt{2\pi r}} \begin{Bmatrix} -\frac{1}{4} \cos\left(\frac{3}{2}\theta\right) + \frac{5}{4} \cos\left(\frac{\theta}{2}\right) \\ \cos^3\left(\frac{\theta}{2}\right) \\ \frac{1}{4} \sin\left(\frac{\theta}{2}\right) + \frac{1}{4} \sin\left(\frac{3}{2}\theta\right) \end{Bmatrix} + \frac{K_{II}}{\sqrt{2\pi r}} \begin{Bmatrix} \frac{3}{4} \sin\left(\frac{3}{2}\theta\right) - \frac{5}{4} \sin\left(\frac{\theta}{2}\right) \\ -3 \sin\left(\frac{\theta}{2}\right) \cos^2\left(\frac{\theta}{2}\right) \\ \frac{1}{4} \cos\left(\frac{\theta}{2}\right) + \frac{3}{4} \cos\left(\frac{3}{2}\theta\right) \end{Bmatrix} \\
 &+ T \begin{Bmatrix} \cos^2(\theta) \\ \sin^2(\theta) \\ -\frac{1}{2} \sin(2\theta) \end{Bmatrix} + O(r^{1/2})
 \end{aligned}
 \tag{6.2.1}$$

Gross and Mendelson [30] proposed a method to evaluate the mode I and mode II SIFs by adopting a boundary collocation technique. This procedure has been

employed also by Carpenter [60] to derive the coefficients related to singular and non-singular terms. According to Gross and Mendelson the mode I and mode II SIFs can be defined by means of Eqs. (6.2.2) and (6.2.3), reported below:

$$K_I = \sqrt{2\pi} \cdot \lim_{r \rightarrow 0} \left[(\sigma_{\theta\theta})_{\theta=0} \cdot r^{0.5} \right] \quad (6.2.2)$$

$$K_{II} = \sqrt{2\pi} \cdot \lim_{r \rightarrow 0} \left[(\tau_{r\theta})_{\theta=0} \cdot r^{0.5} \right] \quad (6.2.3)$$

In the case of an infinite cracked plate under mixed mode I+II loading (Fig. 6.2.1a), the following engineering formulas can be used:

$$K_I = \sigma_{\text{nom}} \sqrt{\pi \cdot a} \quad (6.2.4)$$

$$K_{II} = \tau_{\text{nom}} \sqrt{\pi \cdot a} \quad (6.2.5)$$

The constant term T which is a slit-parallel tensile or compressive stress, named “T-stress” by Larsson and Carlsson [61], can be defined according to the following equation:

$$T = \lim_{r \rightarrow 0} \left[(\sigma_{rr})_{\theta=0} - (\sigma_{\theta\theta})_{\theta=0} \right] \quad (6.2.6)$$

where the condition $\theta = 0$ identifies the crack bisector line. In particular, in the case of an infinite cracked plate under uniaxial tension loading, Radaj [62] reported the following simplified expression:

$$T = -\sigma_{\text{nom}} \quad (6.2.7)$$

Because $T = 0$ under pure mode II loading (according to definition (6.2.6) and Eq. (6.2.1)), $T = -\sigma_{\text{nom}}$ in all mixed mode (I+II) problems analysed here.

In the context of fracture mechanics it is largely assumed that the stress field in the close neighborhood of the crack tip can be properly characterized by means of the coefficients of the leading order terms, i.e. the SIFs. However, detailed analyses reported in the literature have highlighted the fundamental role of the T-stress in defining the stress state close to the crack tip [61,63–68]. Larsson and

Carlson [61] and later Rice [63] argued on the effect of T-stress on the plastic zone ahead of the crack tip in materials characterized by elastic–plastic behaviour. The influence of T-stress on failure mechanisms of brittle materials was investigated by Ayatollahi et al. [64,67,68] and Fett and Munz [66], who employed a modified maximum tangential stress approach (MTS [69]), taking into account mode I and mode II SIFs, T-stress and a material-dependent length parameter. Some recent studies have been devoted to the investigation of the T-stress effect in lap welded joints characterized by different thicknesses [62,70].

Several methods for T-stress determination have been reported in the recent literature. Chen et al. [71] proposed a procedure based on the complex potentials and expressed the T-stress dependence on the load conditions by means of the Dirac delta function properties. Different approaches based on weight functions have been presented [72,73]. Moreover, T-stresses for small notch-emanating cracks, such as a circular hole centered in a large plate and a U-notch in a finite thickness plate, were derived by Wang et al. [74].

Furthermore, the effects of higher order non-singular terms are still an open issue. Ramesh et al. [75,76] proposed an over-deterministic least squares approach coupled with the photoelasticity method with the purpose of deriving the mixed mode I+II multiparametric stress field. More recently a procedure for rapid evaluation of the unknown coefficients on the basis of the displacement fields directly obtained from finite element (FE) results has been developed by Ayatollahi and Nejati [77]. Xiao et al. [16,78] presented an approach with the aim to directly determine the SIFs and the higher order terms by using a hybrid crack element, which can be efficiently used also dealing with in-plane mixed mode crack problems.

The combined effects of SIFs and T-stress on structural strength problems of cracked components under mixed mode I+II loadings can be easily evaluated by means of the strain energy density (SED) averaged over a control volume, thought of as dependent only on material properties and modelled as a circular sector of radius R_0 , as shown in Fig. 6.2.1b, according to Lazzarin and Zambardi [23]. The averaged SED criterion has been widely adopted in the recent literature for static [32,33,79,80] and fatigue [29,34,81] strength assessments. The control radius R_0

for fatigue strength assessment of notched components has been defined by combining two material properties [29,82]: the plain material fatigue limit (or the high-cycle fatigue strength of smooth specimens) and the threshold value of the SIF range for long cracks under mode I loading conditions, ΔK_{th} . By imposing the equality of the averaged SED, evaluated in the two considered cases (smooth and cracked component, respectively), the following expression has been derived [29,82]:

$$R_0 = 2e_1 \cdot \left(\frac{\Delta K_{th}}{\Delta \sigma_0} \right)^2 = \frac{(1+\nu)(5-8\nu)}{4\pi} \cdot \left(\frac{\Delta K_{th}}{\Delta \sigma_0} \right)^2 \quad (6.2.8)$$

For welded construction steels a radius $R_0 = 0.28$ mm was obtained [29] and has been adopted in the present investigation as a reference value. Using a Poisson's coefficient $\nu = 0.3$, Eq. (6.2.8) can be re-written as follows [29,82]:

$$R_0 = 0.85 \cdot \frac{1}{\pi} \cdot \left(\frac{\Delta K_{th}}{\Delta \sigma_0} \right)^2 \Rightarrow 0.85 \cdot a_0 \quad (6.2.9)$$

Therefore, R_0 in Fig. 6.2.1b is on the order of the El Haddad-Smith-Topper length parameter [83].

Dealing with mixed mode crack problems under plane strain conditions, the averaged SED can be expressed in closed-form as a function of the stress intensity factors (SIFs), K_I and K_{II} , and of the T-stress, T , according to the following analytical expression [36,70]:

$$\overline{W}_{AN} = \frac{e_1}{E} \frac{K_I^2}{R_0} + \frac{e_2}{E} \frac{K_{II}^2}{R_0} + \frac{1-\nu^2}{2E} T^2 + \frac{8\sqrt{2}}{15 \cdot (\pi)^{3/2}} \frac{(1+\nu) \cdot (2-5\nu)}{E} \frac{K_I \cdot T}{\sqrt{R_0}} \quad (6.2.10a)$$

In the above equation, e_1 and e_2 are two known parameters dependent on the opening angle of a general pointed V-notch and of the Poisson's ratio ν [23] (see Table 6.2.1), while E is the Young's modulus of the considered material. As an example, Lazzarin et al. [36,70] adopted Eq. (6.2.10a) to evaluate successfully the SED values relevant to thin welded lap-joints having thicknesses ranging from 1

to 5 mm. When the T-stress contribution is negligible, only K_I and K_{II} contributes to the averaged SED and Eq. (6.2.10a) simplifies to:

$$\overline{W}_{AN,I+II} = \frac{e_1}{E} \frac{K_I^2}{R_0} + \frac{e_2}{E} \frac{K_{II}^2}{R_0} \quad (6.2.10b)$$

Table 6.2.1: Parameters for averaged SED evaluation in the crack case ($2\alpha = 0$) as a function of the Poisson's ratio ν .

2α (deg)	λ_2	$\nu = 0.3$		$\nu = 0.33$	
		e_1	e_2	e_1	e_2
0	0.500	0.133	0.340	0.125	0.337

Making use of Eqs (6.2.4), (6.2.5) and (6.2.7) into Eqs (6.2.10a) and (6.2.10b), the following ratio can be calculated:

$$\frac{\overline{W}_{AN}}{\overline{W}_{AN,I+II}} = 1 + \frac{\frac{1-\nu^2}{2} \cdot \frac{1}{a/R_0} - \frac{8\sqrt{2}}{15 \cdot \pi} (1+\nu)(2-5\nu) \cdot \frac{1}{\sqrt{a/R_0}}}{\pi \cdot \left[e_1 + e_2 \cdot \left(\frac{MM}{1-MM} \right)^2 \right]} \quad (6.2.11)$$

where MM is the mode mixity ratio, defined as:

$$MM = \frac{K_{II}}{K_I + K_{II}} \quad (6.2.12a)$$

In Eq. (6.2.11), the mode mixity has been expressed for the particular case of the centrally cracked plate shown in Figure 6.2.1, for which expressions (6.2.4) and (6.2.5) can be substituted in definition (6.2.12a):

$$MM = \frac{1}{1 + \frac{\sigma_{nom}}{\tau_{nom}}} \quad (6.2.12b)$$

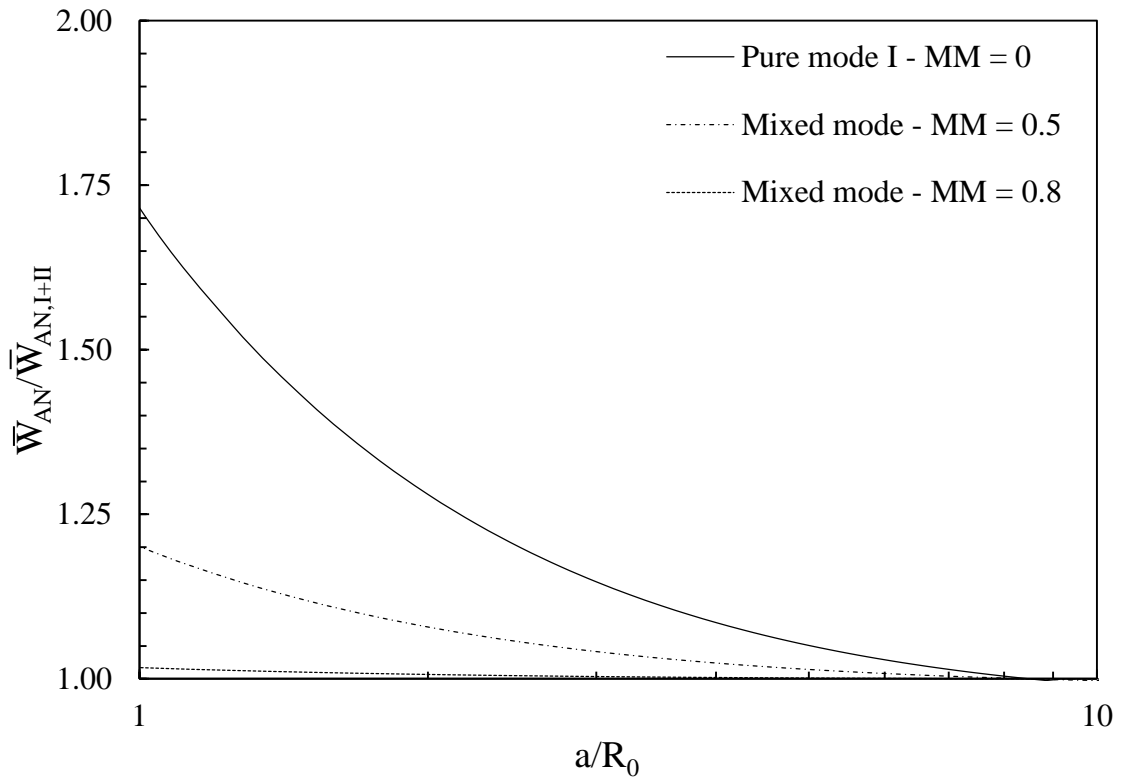


Figure 6.2.2: Ratio between exact and approximated averaged SED values according to Eq. (6.2.11) with $\nu = 0.3$, $e_1 = 0.133$ and $e_2 = 0.340$.

Figure 6.2.2 plots Eq. (6.2.11) for three MM values 0 (pure mode I, $\tau_{nom} = 0$), 0.5 and 0.8. The figure highlights that for a crack size equal to radius of the material dependent control volume ($a/R_0 = 1$) and pure mode I loading (MM = 0) the error in the averaged SED estimation is about 70% if the T-stress contribution is neglected, i.e. Eq. (6.2.10b) is used in place of Eq. (6.2.10a). However, for the same crack size to control radius ratio, the error is decreased to 20% if MM = 0.5 and further reduced to only 1.7% if MM = 0.8.

In a previous paper [84], long cracks in the range $25 \leq a/R_0 \leq 800$ and mode mixities $0 \leq MM \leq 0.63$ had been considered. Therefore, in light of Fig. 6.2.2, Eq. (6.2.10b) had been used. In the present investigation, small cracks spanning in the range $1.8 \leq a/R_0 \leq 9$ and the full range of mode mixities between 0 and 1 will be considered. Therefore, due to the reduced crack size to control radius ratios considered here, an approach consistent with Eq. (6.2.10a) which include the T-stress must be followed.

The use of Eq. (6.2.10) combined with (6.2.2), (6.2.3) and (6.2.6) in engineering problems presents a major drawback, since very refined meshes are required to evaluate the SIFs and the T-stress on the basis of definitions (6.2.2), (6.2.3) and (6.2.6), respectively, applied to a number of stress-distance FE data. This is due to the fact that the whole local stress field must be determined accurately. The practical application is even more time-consuming in the case of 3D FE models. However, the averaged SED can be evaluated directly from the FE results, \overline{W}_{FEM} , by summing the strain-energies $W_{FEM,i}$ calculated for each i -th finite element belonging to the control volume and by dividing by the volume (A in Fig. 6.2.1b):

$$\overline{W}_{FEM} = \frac{\sum_A W_{FEM,i}}{A} \quad (6.2.13)$$

Equation (6.2.13) represents the so-called direct approach to calculate the averaged SED. According to a recent contribution of Lazzarin et al. [37] very coarse FE meshes can be used within the control volume A . The required geometric model to apply the direct approach with coarse mesh option is reported in Figure 6.2.3a, while Figure 6.2.3b shows the coarse FE mesh (second order plane elements, PLANE 183 of the Ansys[®] element library) that can be adopted to analyse an in-plane mixed mode crack problem [37]. Figure 6.2.3b shows that eight finite elements have been generated inside the control volume, while two concentric rings, each of one made up of eight elements, have been located outside the reference volume in the annulus $R_0 < r < 10 \cdot R_0$; finally a free FE mesh characterized by a mean element size d has been adopted outside. The mesh reported in Figure 6.2.3b is as coarse as possible in order to obtain a deviation between $\overline{W}_{FEM,coarse}$ and \overline{W}_{FEM} lower than 10%, where $\overline{W}_{FEM,coarse}$ and \overline{W}_{FEM} are the averaged SED derived on the basis of Eq. (6.2.13) by adopting coarse meshes and very refined meshes (about 500 finite elements within the reference volume), respectively. Due to the highly increased mesh refinement, \overline{W}_{FEM} is interpreted as the exact value.

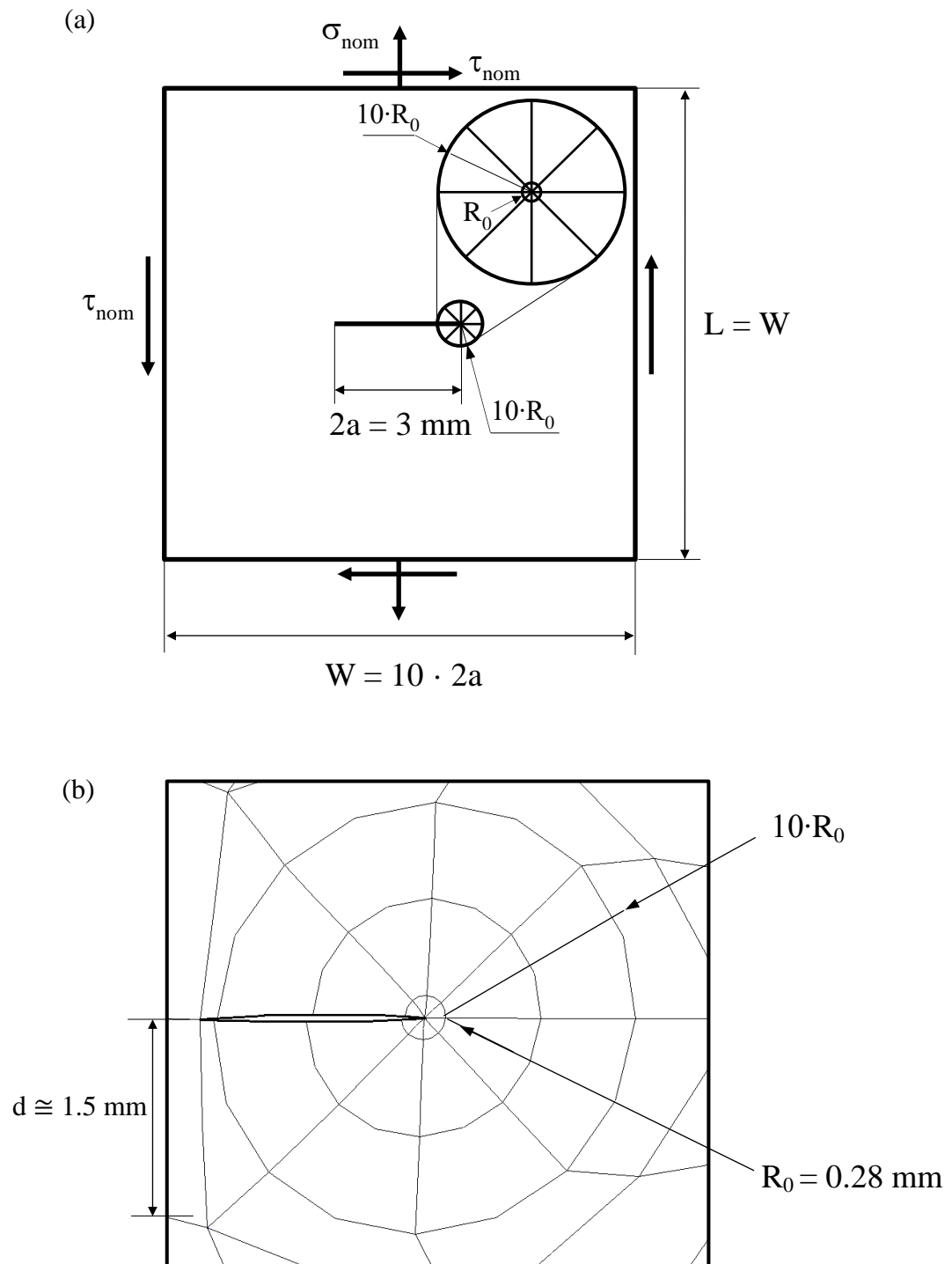


Figure 6.2.3: Averaged SED evaluated according to the direct approach (Eq. (6.2.13)) with coarse mesh option, $\bar{W}_{\text{FEM,coarse}}$ [37]; (a) geometry and loading conditions. (b) Coarse FE mesh (second order plane elements, PLANE 183 of Ansys Element Library) producing a reduced error of 3% in the case $2a = 3 \text{ mm}$ and $MM = 0.50$. Control radius $R_0 = 0.28 \text{ mm}$.

Recently the peak stress method (PSM) has been proposed to rapidly calculate the averaged SED by means of the singular, linear elastic peak stresses evaluated from FE analyses at the tip of cracks under in-plane mixed mode loading [84]. The PSM allows to avoid the control volume modelling while keeping the coarse mesh option. Essentially, the PSM estimates the SIFs using coarse FE meshes rapidly. Having in hands the SIFs, the averaged SED can also be estimated, provided that the T-stress contribution is negligible. Such intrinsic limitation of the PSM rules out the case of short cracks.

The purpose of the present work is exactly to extend the PSM to estimate the averaged SED also in the case of cracks that are small as compared to the control radius R_0 , or, alternatively stated, in cases where the stress fields within the control volume (A in Fig. 6.2.1b) are no longer governed solely by the SIFs, but also by higher order terms and primarily the T-stress. The proposed FE-based approach is referred to as nodal stress approach: it combines the singular crack tip stresses to account for the SIFs contribution (according to the previous PSM [84]) with the nodal stresses at a selected location of the crack free edges to include the T-stress contribution.

The peak stress method to calculate K_I and K_{II} with coarse meshes is shortly recalled in the following Section. After that, the contents of the present paragraph are as follows:

- to present the nodal stress approach, i.e. a numerical approach based on appropriate nodal stresses calculated with coarse FE analyses to rapidly estimate the averaged SED of mixed-mode (I+II) crack tip fields including the T-stress contribution;
- to validate the nodal stress approach by analysing infinite plates weakened by short cracks, while varying (i) the crack lengths, (ii) the mode mixity and (iii) the finite element size adopted in the numerical analyses.

6.2.2. The Peak Stress Method to rapidly evaluate K_I and K_{II}

The Peak Stress Method (PSM) is an approximate numerical technique to evaluate the SIFs as well as the NSIFs. The approach is based on the numerical procedure proposed in the pioneering works by Nisitani and Teranishi [41,42] oriented to

rapidly evaluate the mode I SIF K_I of a crack emanating from an ellipsoidal cavity. This technique takes advantage of the singular, linear elastic opening peak stress σ_{peak} calculated at the crack tip from a FE analysis in which a finite element mesh with a constant element size is adopted. According to Nisitani and Teranishi [41,42] the ratio K_I/σ_{peak} is a function only of the FE size, in such a way that σ_{peak} can be employed to rapidly evaluate the stress intensity factor K_I , on condition that the mesh pattern was formerly calibrated on crack problems characterized by known SIF values. A theoretical justification to such technique has been provided subsequently and it has been shown that the above method can be extended also to sharp V-notches where only mode I singular stresses are present [43] (i.e., $K_2 = 0$ or mode II stresses are negligible), allowing to evaluate the mode I notch stress intensity factor (NSIF) approximately. Later on, the peak stress approach has been extended also to cracked components under mode II loading conditions [44].

The PSM allows to rapidly estimate the mode I and mode II SIFs K_I and K_{II} (Eqs. (6.2.2) and (6.2.3)) from the crack tip singular, linear elastic opening and sliding peak stresses σ_{peak} and τ_{peak} , respectively, referred to the bisector line according to Fig. 6.2.4a evaluated by FEM with coarse meshes. More precisely, the following expressions are valid [43,44]:

$$K_{\text{FE}}^* = \frac{K_I}{\sigma_{\text{peak}} \cdot d^{0.5}} \cong 1.38 \quad (6.2.14)$$

$$K_{\text{FE}}^{**} = \frac{K_{II}}{\tau_{\text{peak}} \cdot d^{0.5}} \cong 3.38 \quad (6.2.15)$$

where d is the so-called ‘global element size’ parameter to input in Ansys FE code, i.e. the average FE size adopted by the free mesh generation algorithm available in the software. As an example, Fig. 6.2.4b shows a free mesh where $d = 0.15$ mm was input in Ansys software. More precisely, the mesh pattern shown in Fig. 6.2.4b is as coarse as possible to estimate the averaged SED with a 10% error. However, a proper guideline to choose the coarsest mesh for a selected maximum acceptable error will be the subject of a next section. Here it is important to underline that no additional input parameters other than d or

additional special settings are required to the FE analyst to generate a FE mesh according to the PSM. It should be noted that Eqs. (6.2.14) and (6.2.15) have been calibrated by using K_I and K_{II} evaluated from definitions (6.2.2) and (6.2.3) applied to FE results of numerical analyses characterized by very refined meshes [43,44], where the element size close to the crack tip was reduced to 10^{-5} mm. Eqs. (6.2.14) and (6.2.15) are valid when the following conditions are met:

- use of 4-node quadrilateral finite elements characterized by linear shape functions, available in ANSYS[®] (PLANE 42 of the Ansys[®] element library or equivalently PLANE 182 with K-option 1 set to 3);
- the FE mesh pattern close to the crack tip must be that reported in Fig. 6.2.4b, where four elements share the node at the crack tip. It is worth recognizing that the mesh pattern of Fig. 6.2.4 is automatically generated by the free mesh generation algorithm available in Ansys, so that only the global element size parameter d must be input by the FE analyst. The standard FE mesh patterns adopted in the case of sharp V-notches can be found in recent contributions [43,44];
- the mesh density ratio a/d must exceed 3 in order to have $K_{FE}^* = 1.38 \pm 3\%$, where a is the semi-crack length. In the case of mode II loading conditions, more refined FE meshes are required, in fact the ratio a/d must exceed 14 to have $K_{FE}^{**} = 3.38 \pm 3\%$.

The FE size required to estimate K_I and K_{II} from σ_{peak} and τ_{peak} , respectively, is some orders of magnitude larger than that needed to directly calculate the local stress fields. Moreover, differently from the application of Eqs. (6.2.2) and (6.2.3), which require a number of stress-distance numerical results, an additional advantage of the PSM is that only a single stress value allows to evaluate K_I and K_{II} , respectively. The PSM according to Eqs. (6.2.14) and (6.2.15) made possible to assess weld root failures welded joints characterized by two-dimensional [44,52] as well as three-dimensional geometries [47,48]. It should be noted that Eqs. (6.2.14) and (6.2.15) should be recalibrated in the case of FE meshes

consisting of higher-order elements or characterized by significantly different mesh patterns as compared to the reference one reported in Fig. 6.2.4b.

To illustrate the PSM, K_I and K_{II} have been estimated using Eqs. (6.2.14) and (6.2.15) for a number of crack sizes, that will be considered also later on for the averaged SED evaluations, where the work is focussed on. An infinite plate weakened by a central crack and subjected to in-plane mixed mode loading was considered according to Fig. 6.2.4a. Several crack lengths $2a$ (from 1 to 5 mm) have been considered, while width W and length L of the plate were set both equal to 10 times the crack length.

The mean FE size d to evaluate σ_{peak} and τ_{peak} in Eqs. (6.2.14) and (6.2.15) was varied from 0.0125 to 1.25 mm. All different geometrical and loading parameters taken into account here are listed in Table 6.2.2, that highlights the range of (small) crack size to control radius ratios analysed, i.e. $1.8 \leq a/R_0 \leq 8.9$. According to the PSM, FE analyses have been carried out by using Ansys[®] software and by adopting free mesh patterns consisting of 4-node quadrilateral elements (PLANE 182 with K-option 1 set to 3).

The exact mode I and mode II stress intensity factors, K_I and K_{II} , to input in Eqs. (6.2.14) and (6.2.15) were evaluated from Eqs. (6.2.4) and (6.2.5), respectively.

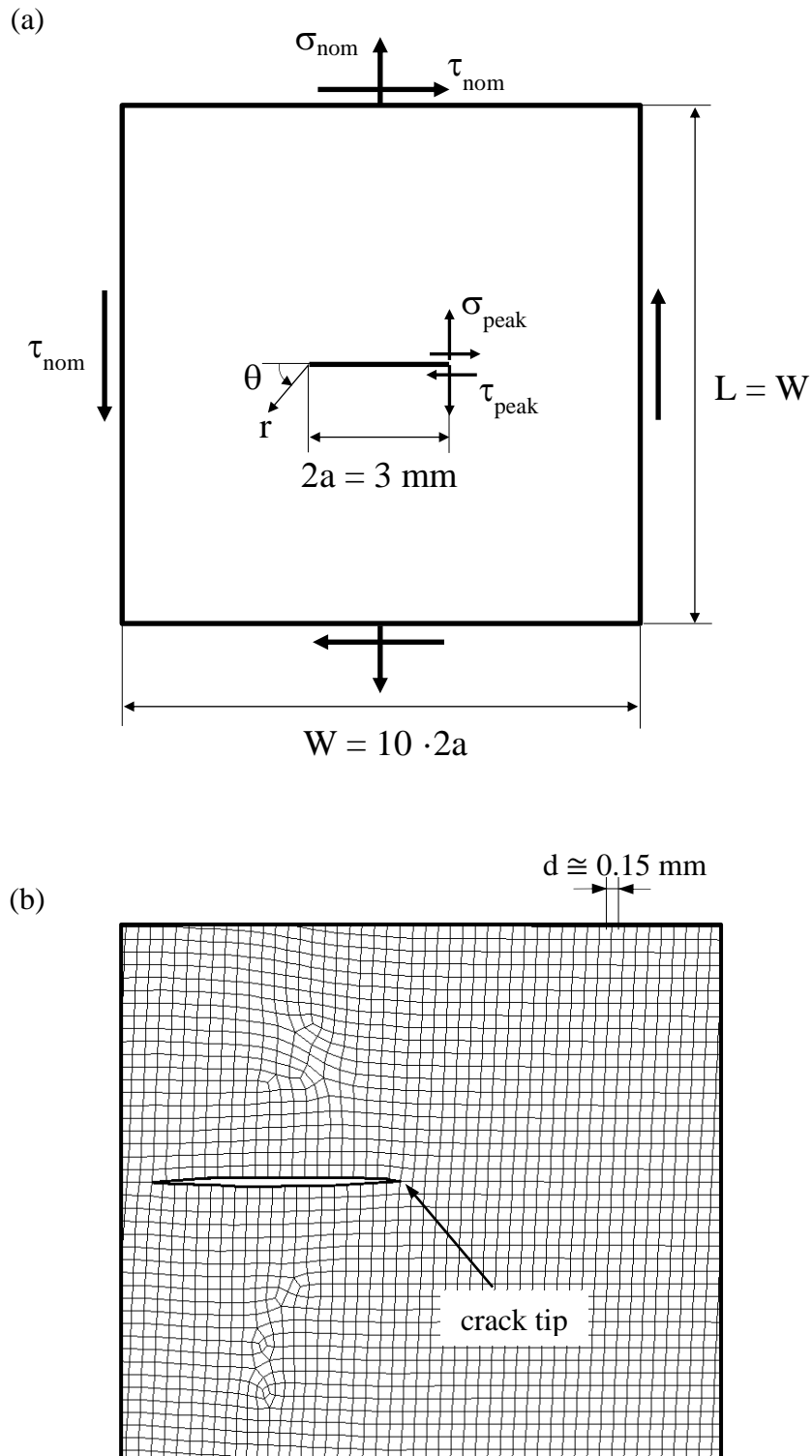
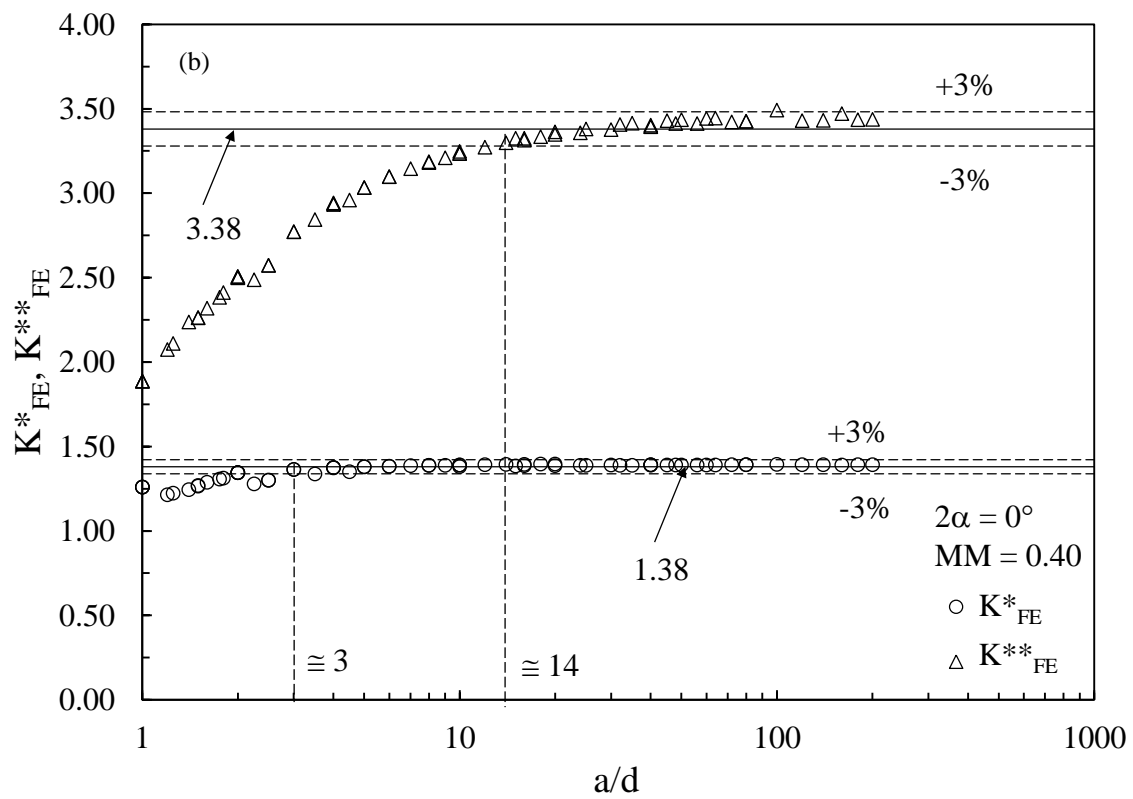
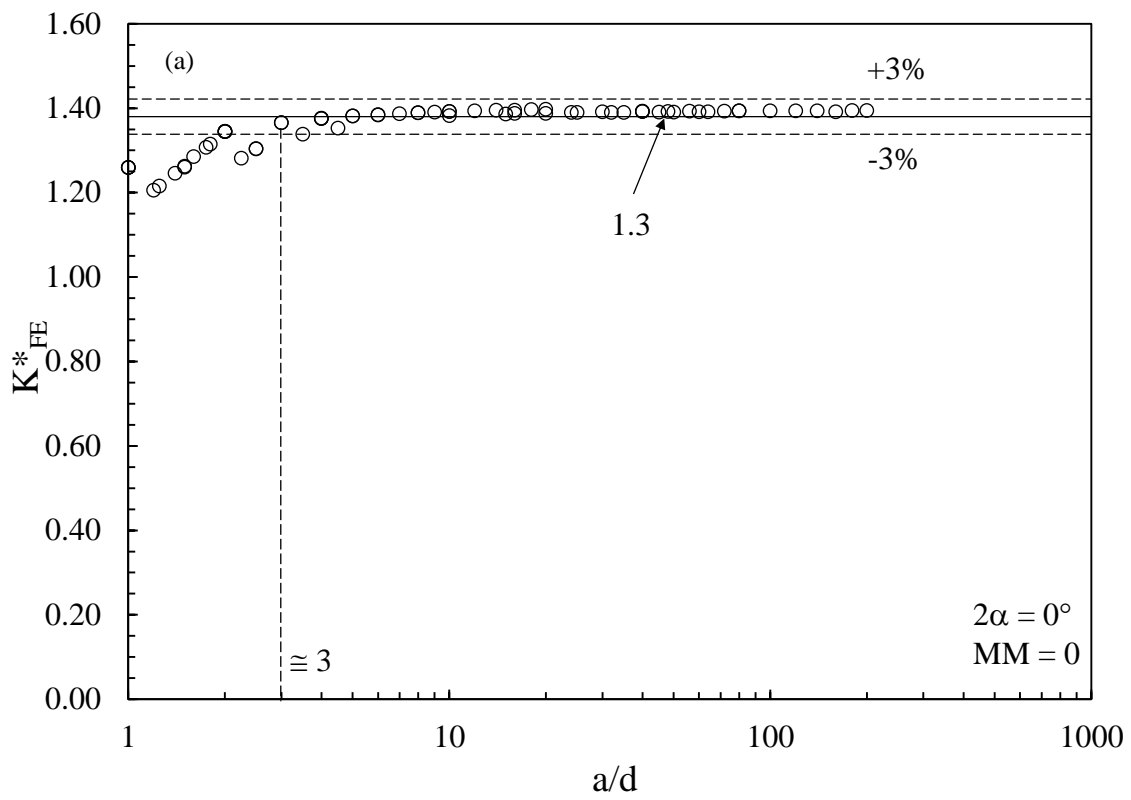


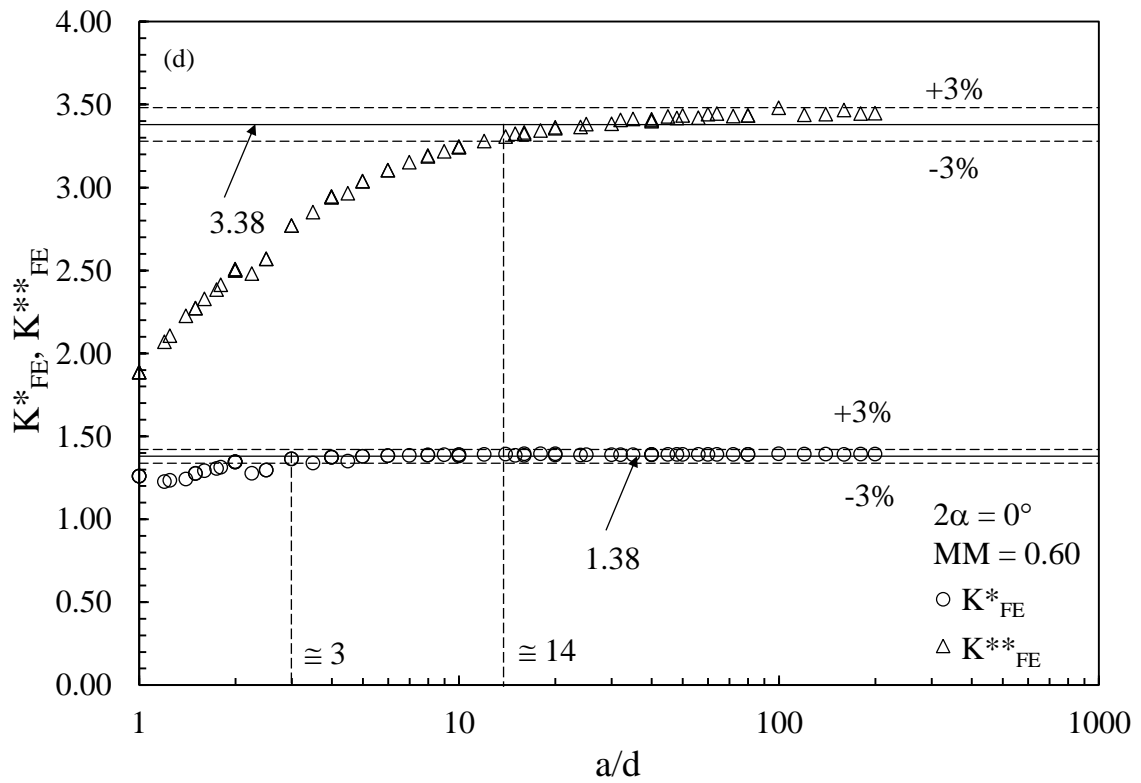
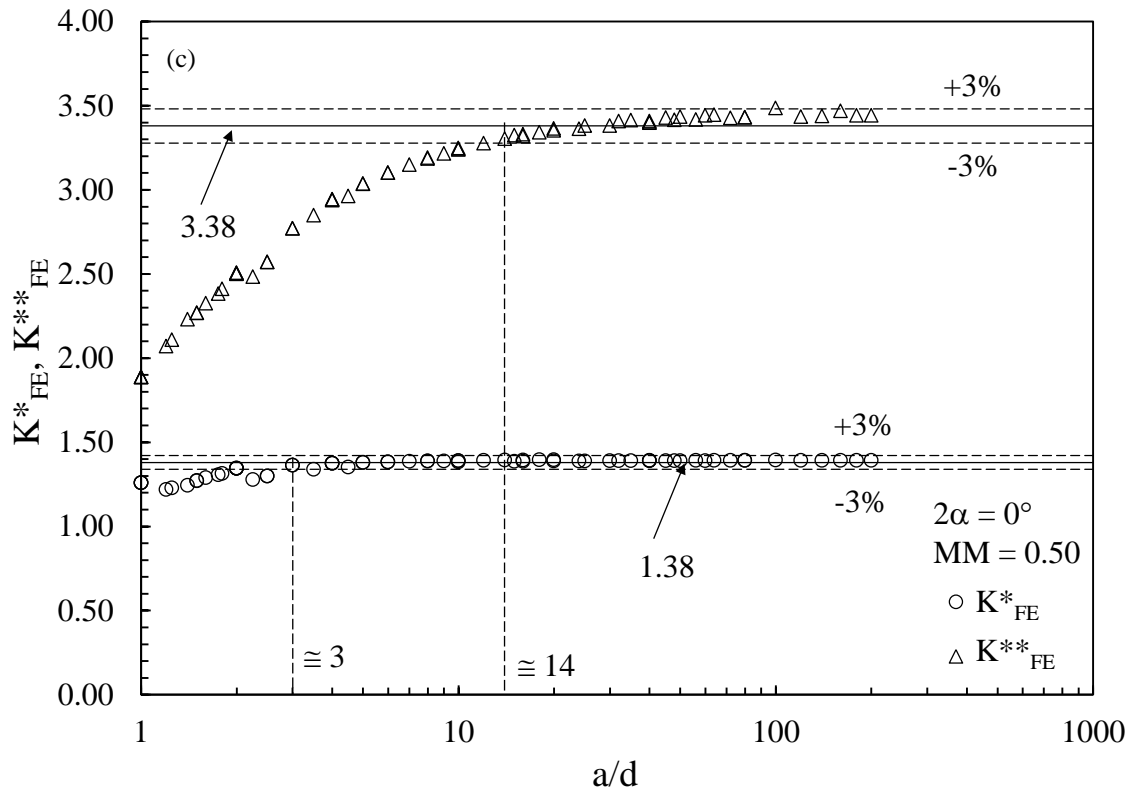
Figure 6.2.4: Averaged SED evaluated according to the nodal stress approach (Eq. (6.2.20)); (a) geometry and loading conditions. (b) Coarsest FE mesh (first order plane elements, PLANE 182 of Ansys element library with K-option 1 set to 3) to obtain a reduced error of 10% in the case $2a = 3 \text{ mm}$ and $MM = 0.50$.

Results are reported in Fig. 6.2.5, in terms of non-dimensional stress intensity factors K_{FE}^* and K_{FE}^{**} according to Eqs. (6.2.14) and (6.2.15), respectively. For the sake of brevity, only the results for selected mode mixity ratios $MM = 0, 0.4, 0.5, 0.6$ and 1 are shown. It can be observed that K_{FE}^* and K_{FE}^{**} converge to the values 1.38 and 3.38 , respectively, inside a scatter-band of $\pm 3\%$, in accordance with the results previously obtained for longer cracks under mixed mode I+II loading [84]. As expected from previous contributions [43,44], convergence is assured when the ratio a/d is greater than 3 for pure mode I and 14 for pure mode II loading. According to previous results [44,84], mode II loading is more demanding in terms of mesh density ratio a/d than mode I loading .

Table 6.2.2: Geometrical and loading parameters taken into consideration in the present investigation. All combinations have been analysed, provided that the ratio a/d was greater than the minimum feasible one, i.e. $a/d = 1$.

Parameter	Values
2a [mm]	1, 1.5, 2...4.5, 5
d [mm]	0.0125, 0.03125, 0.05, 0.125, 0.25, 0.5, 1, 1.25
MM	0, 0.2, 0.4, 0.5, 0.6, 0.8, 1
R₀ [mm]	0.28





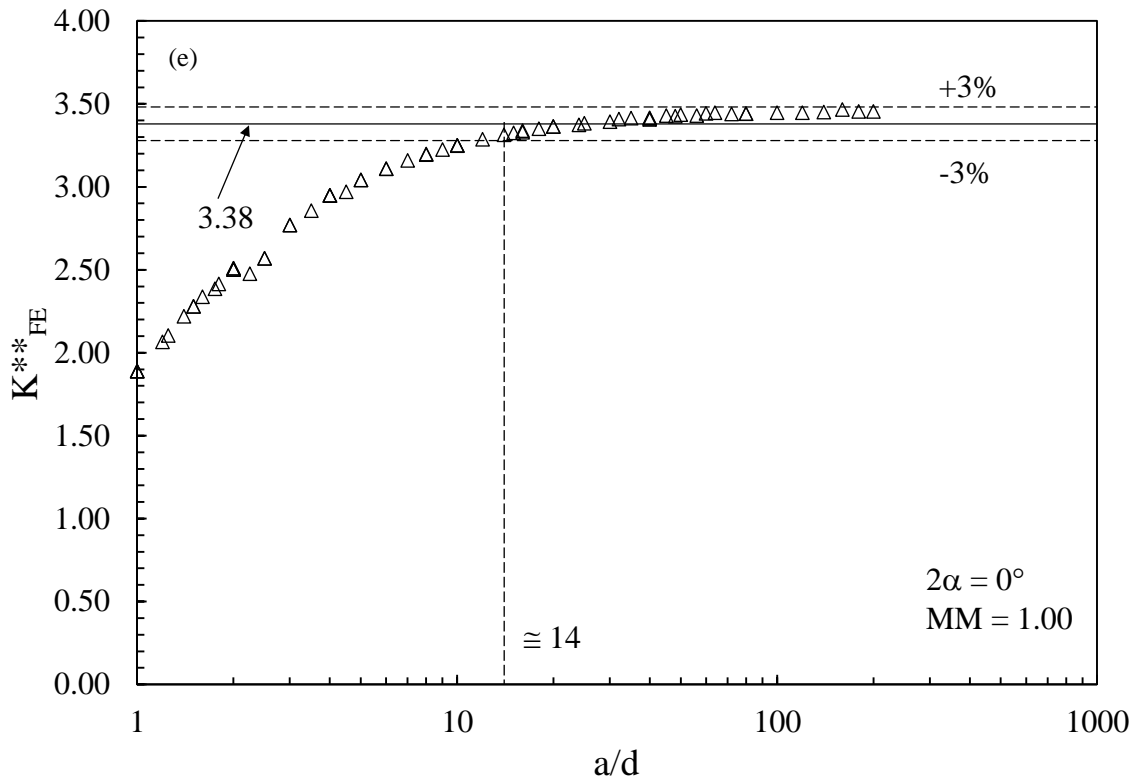


Figure 6.2.5: Convergence of the PSM applied to cracks ($2\alpha = 0^\circ$) under mixed mode I+II loading: (a) $MM = 0$; (b) $MM = 0.40$; (c) $MM = 0.50$; (d) $MM = 0.60$ and (e) $MM = 1.00$. Non-dimensional SIFs according to Eqs (6.2.14) and (6.2.15).

Given the limitations of applicability of Eqs. (6.2.14) and (6.2.15) illustrated previously, substitution into Eq. (6.2.10b) immediately delivers:

$$\bar{W}_{\text{PSM,I+II}} = \frac{e_1}{E} \left[K_{\text{FE}}^* \cdot \sigma_{\text{peak}} \cdot \left(\frac{d}{R_0} \right)^{0.5} \right]^2 + \frac{e_2}{E} \left[K_{\text{FE}}^{**} \cdot \tau_{\text{peak}} \cdot \left(\frac{d}{R_0} \right)^{0.5} \right]^2 \quad (6.2.16)$$

which can be used to estimate the averaged SED for long cracks according to the PSM. Equation (6.2.16) has been proposed and validated in a previous paper [84].

6.2.3. A FE-based technique to evaluate rapidly the T-stress

The analytical expressions of the radial stresses σ_{rr} along the crack free edges [36], obtained substituting the polar coordinate $\theta = +\pi$ and $-\pi$ in Eq. (6.2.1), are given in Eqs. (6.2.17a) and (6.2.17b), respectively:

$$(\sigma_{rr})_{\theta=\pi} = -\frac{2K_{II}}{\sqrt{2\pi r}} + T + O(r^{1/2}) \quad (6.2.17a)$$

$$(\sigma_{rr})_{\theta=-\pi} = +\frac{2K_{II}}{\sqrt{2\pi r}} + T + O(r^{1/2}) \quad (6.2.17b)$$

Therefore, the T-stress contribution can be derived according to Eq. (6.2.18), as previously highlighted by Ayatollahi et al. [64] and also by Radaj [62]:

$$T = \frac{(\sigma_{rr})_{\theta=\pi} + (\sigma_{rr})_{\theta=-\pi}}{2} \quad (6.2.18)$$

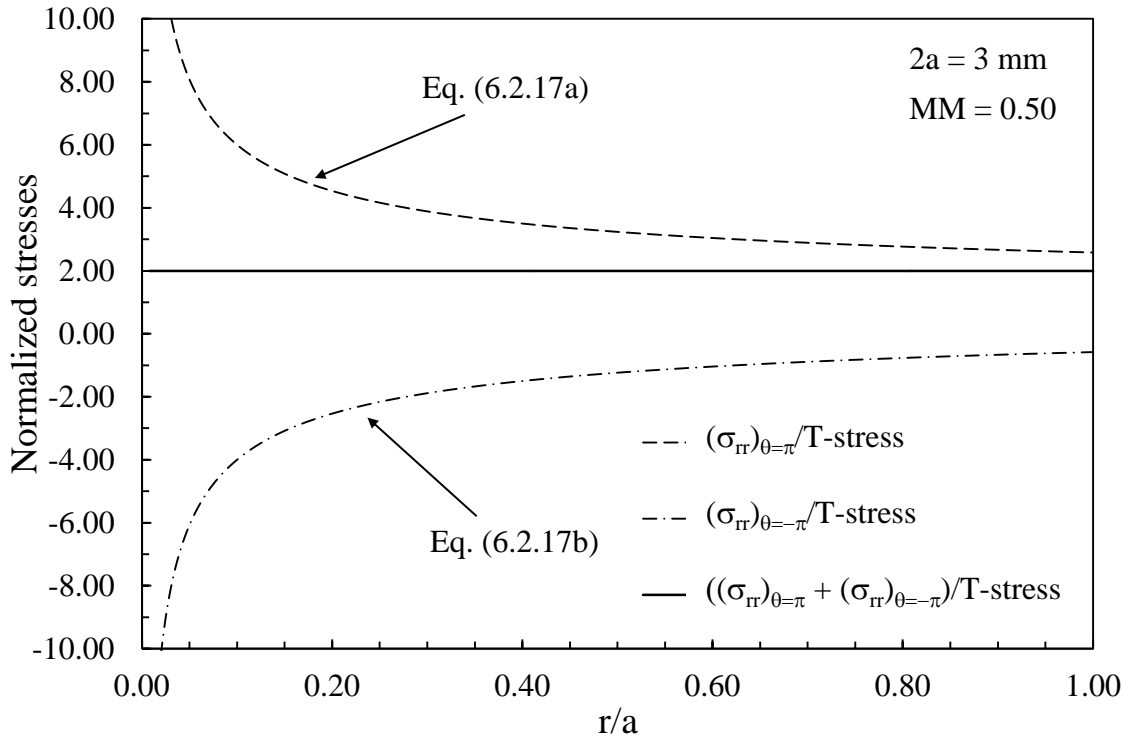
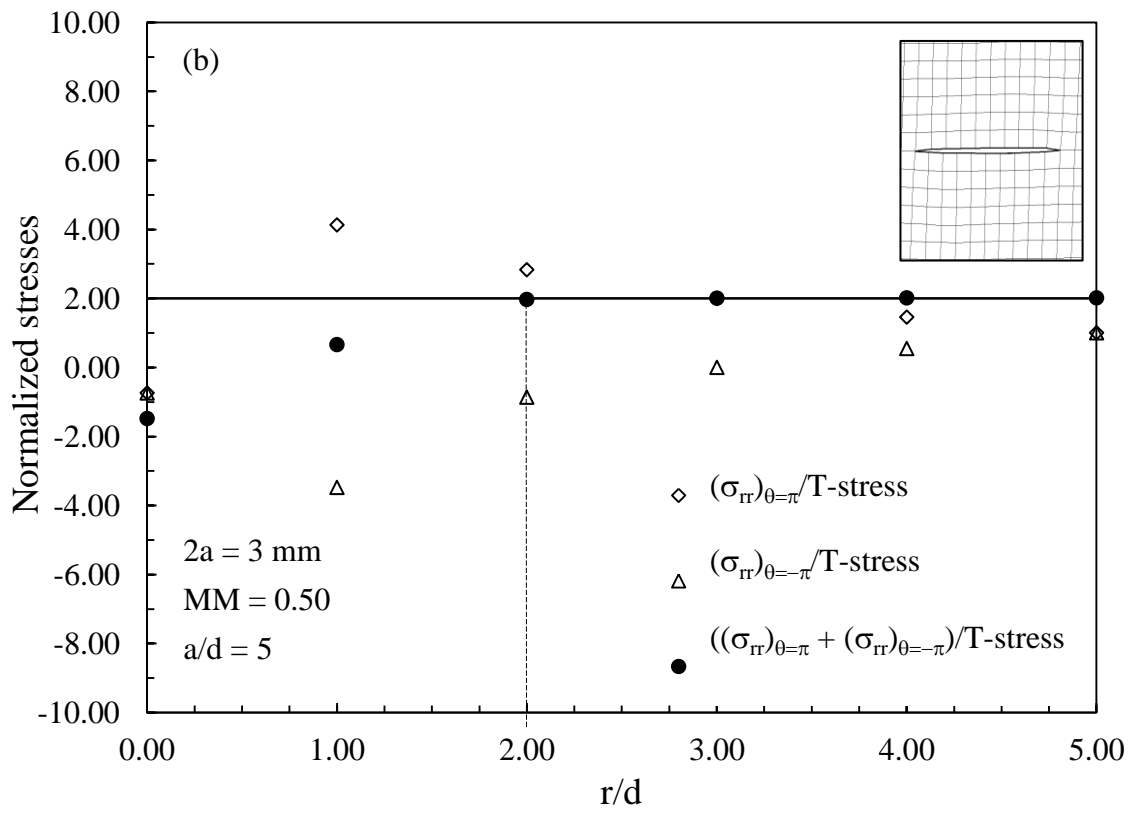
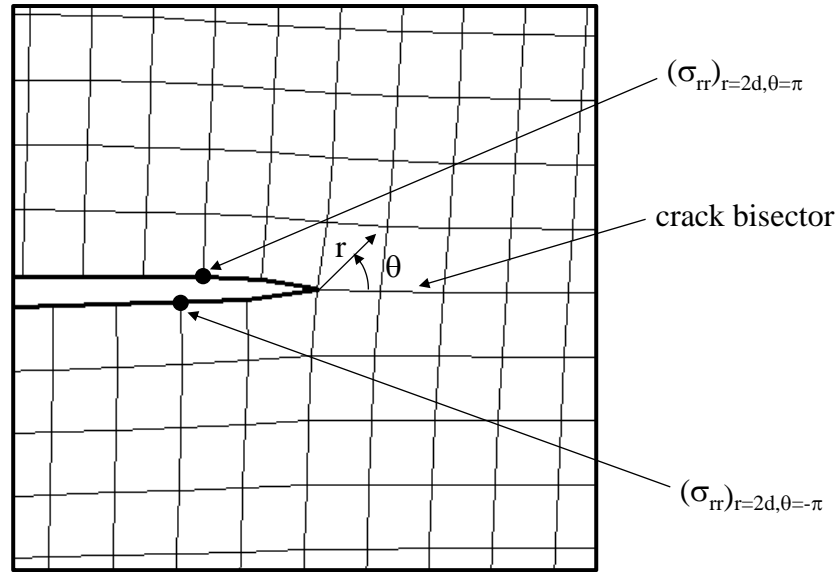


Figure 6.2.6: Distributions of the radial stresses σ_{rr} (Eq. 6.2.17) and of the T-stress (Eq. 6.2.18) along the crack free edges [36].

(a)



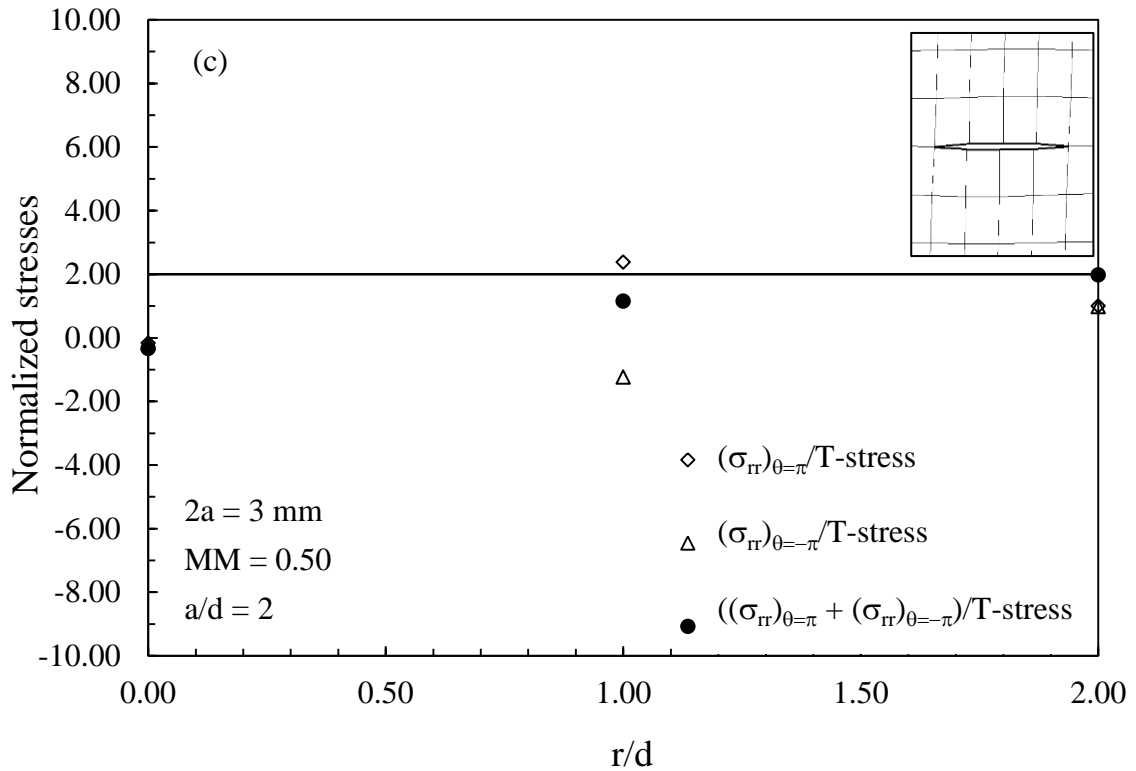
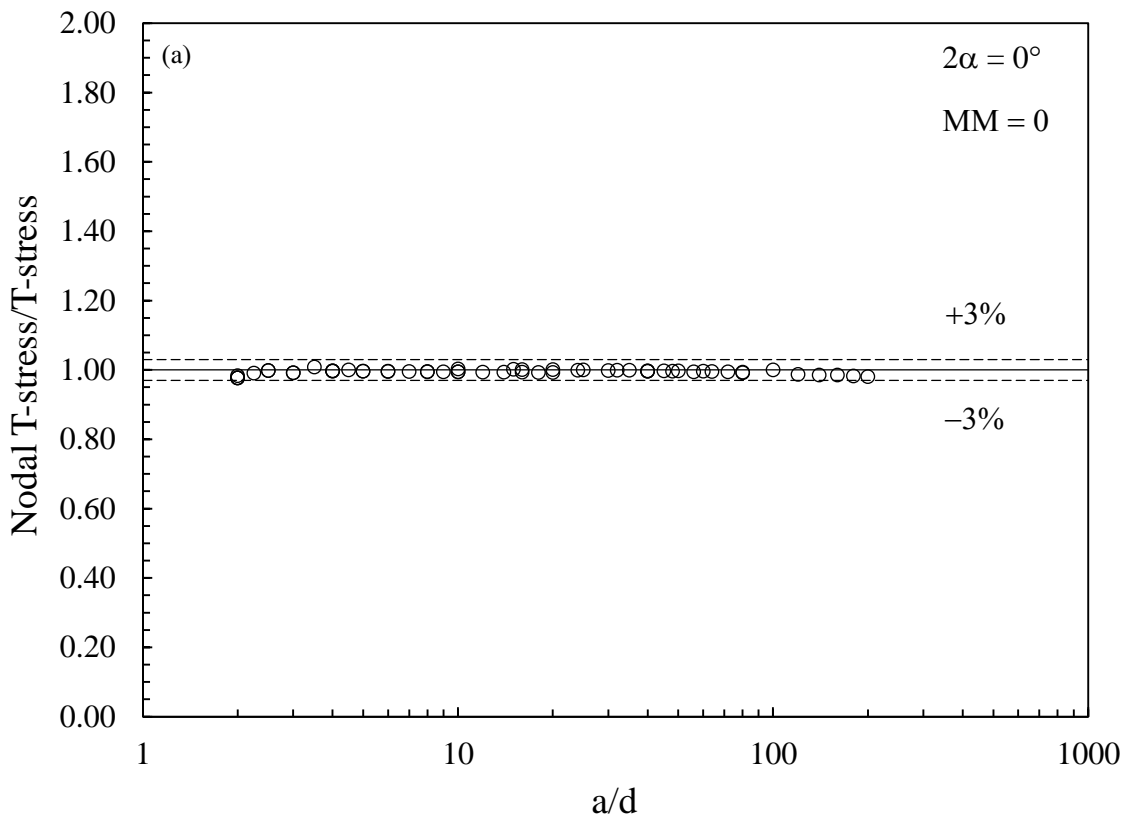


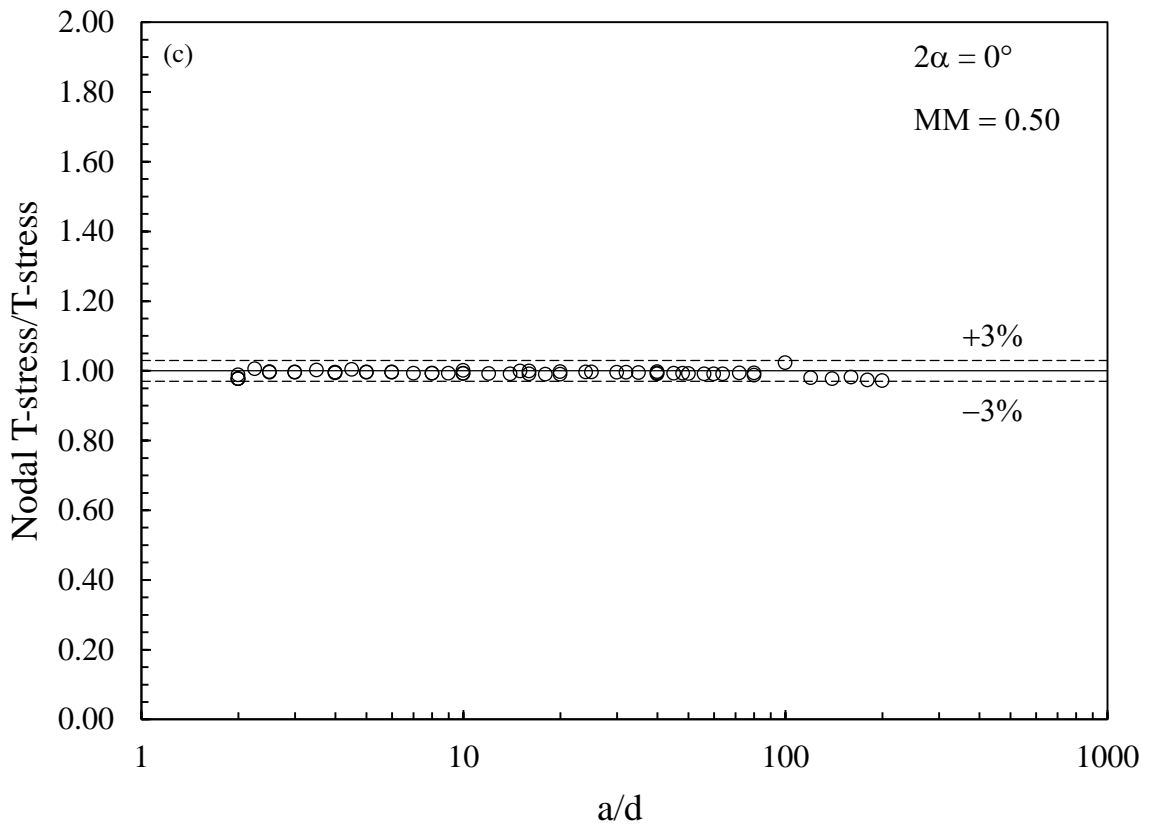
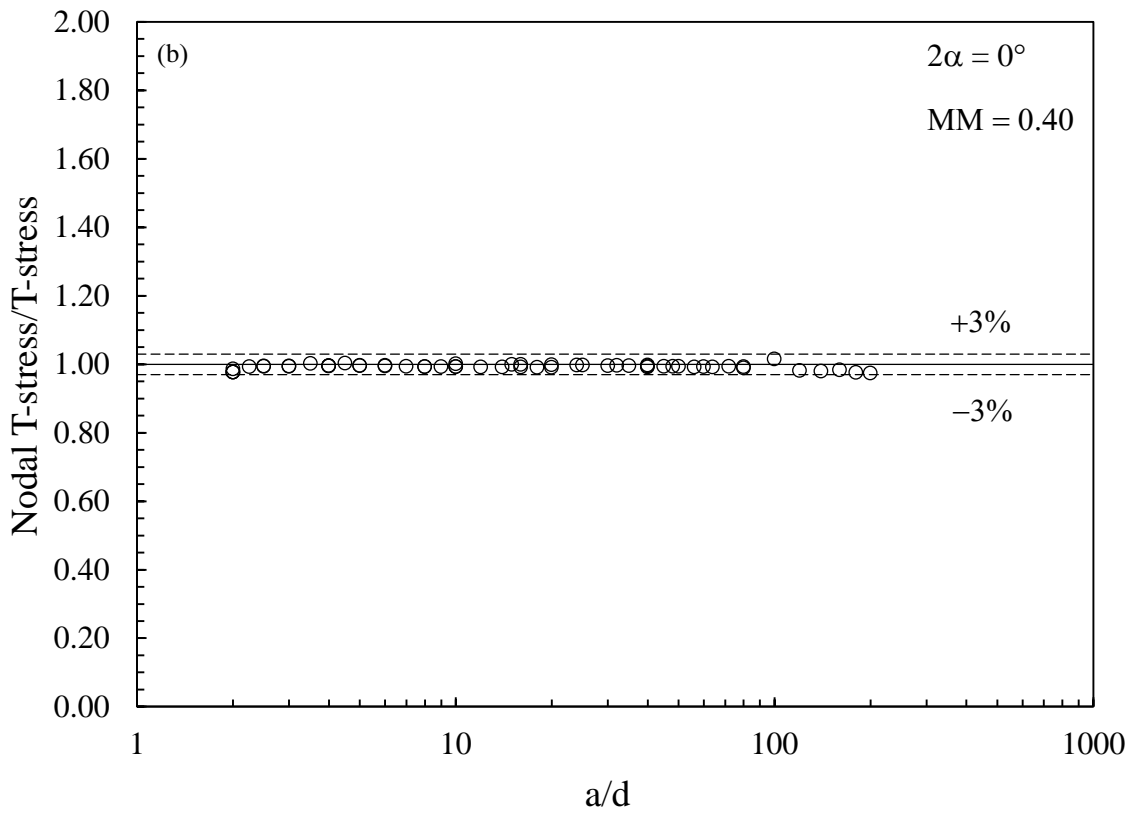
Figure 6.2.7: T-stress evaluated according to the nodal stress approach (Eq. (6.2.19)); (a) FE coarse mesh. FE radial stresses σ_{rr} along the crack free edges by adopting a mesh density ratio (b) $a/d = 5$ and (c) $a/d = 2$. $2a = 3$ mm and $MM = 0.50$.

Eqs. (6.2.17) and (6.2.18) are plotted in Fig. 6.2.6 and suggest to evaluate the T-stress numerically using the nodal stresses illustrated in Fig. 6.2.7a. The obtained results are shown in Figs 6.2.7b and 6.2.7c for two different mesh density ratios $a/d = 5$ and $a/d = 2$, respectively, applied to the same crack problem of previous Fig. 6.2.4a. Figs. 6.2.7b and 6.2.7c show that due to numerical errors caused by the crack tip singularity, Eq. (6.2.18) based on FE results is satisfied with a reduced error lower than 3% only at a distance from the crack tip $r \geq 2d$. Moreover it is interesting to note from Fig. 6.2.7c that the minimum feasible mesh density ratio $a/d = 2$ to be able to generate a node located at $r = 2d$ is sufficient to evaluate accurately the T-stress exactly at that FE node. On the basis of the obtained results, a FE-based technique to rapidly evaluate the T-stress can be defined according to the following expression:

$$\text{Nodal T-stress} = \frac{(\sigma_{rr})_{\theta=\pi, r=2d} + (\sigma_{\theta\theta})_{\theta=-\pi, r=2d}}{2} \quad (6.2.19)$$

To verify the applicability of Eq. (6.2.19) to the small cracks subjected to mixed mode I+II loading analysed in the present investigation the ratio between the T-stress according to Eq. (6.2.19) and the exact T-stress, $T = -\sigma_{\text{nom}}$ according to Eq. (6.2.7), is shown in Fig. 6.2.8 for a selection of mode mixity ratios. Fig. 6.2.8 shows that in all cases the minimum feasible mesh density ratio $a/d = 2$ assures the applicability of Eq. (6.2.19), because all numerical results fall within a restricted scatter-band of $\pm 3\%$.





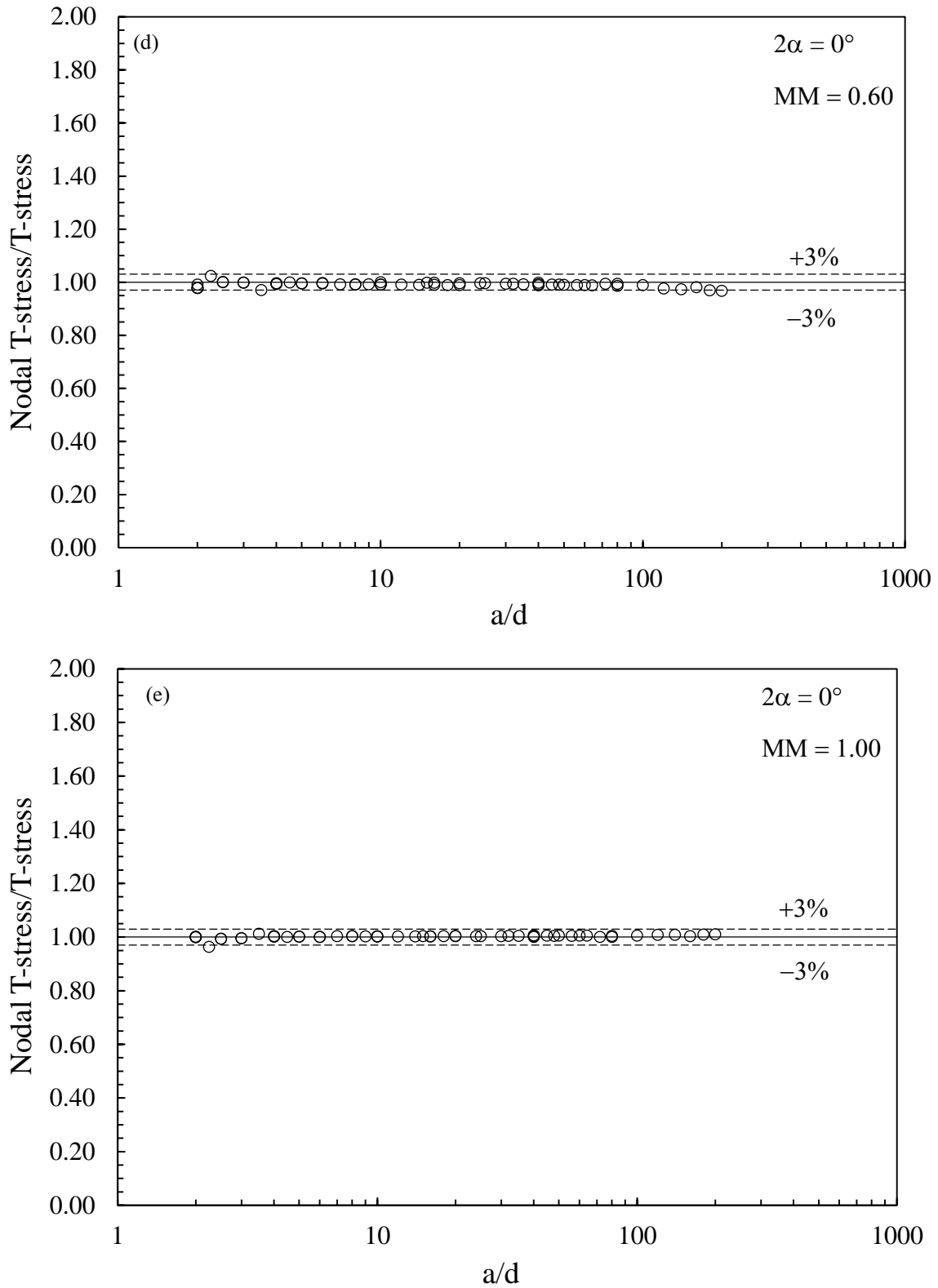


Figure 6.2.8: Ratio between approximated and exact T-stress versus the mesh density ratio. Nodal T – stress according to the nodal stress approach, Eq. (6.2.19); T – stress according to the analytical expression (Eq. (6.2.7)). Short cracks ($2\alpha = 0^\circ$) under mixed mode I+II loading: (a) $MM = 0$; (b) $MM = 0.40$; (c) $MM = 0.50$; (d) $MM = 0.60$ and (e) $MM = 1.00$.

6.2.4. The nodal stress approach to rapidly estimate the averaged SED with inclusion of the T-stress

6.2.4.1 Standard approach

In this Section, the PSM to estimate the averaged SED for long cracks (Eq. (6.2.16) [84]), is extended to the case of short cracks under mixed mode I+II loading, where the T-stress cannot be neglected. The technique is referred to as the nodal stress approach, that can immediately be formalized by substituting Eqs. (6.2.14), (6.2.15) and (6.2.19) into the analytical SED formulation Eq. (6.2.10a):

$$\begin{aligned} \overline{W}_{NS} &= \{ \overline{W}_{PSM, I+II} \} + \{ \overline{W}_{nodal-T} \} \\ \overline{W}_{NS} &= \frac{e_1}{E} \left[\mathbf{K}_{FE}^* \cdot \sigma_{peak} \cdot \left(\frac{d}{R_0} \right)^{0.5} \right]^2 + \frac{e_2}{E} \left[\mathbf{K}_{FE}^{**} \cdot \tau_{peak} \cdot \left(\frac{d}{R_0} \right)^{0.5} \right]^2 + \\ &\frac{1-v^2}{2E} \left(\frac{(\sigma_{rr})_{\theta=\pi, r=2d} + (\sigma_{rr})_{\theta=-\pi, r=2d}}{2} \right)^2 \\ &+ \frac{8\sqrt{2}}{15 \cdot (\pi)^{3/2}} \frac{(1+v) \cdot (2-5v)}{E} \left[\mathbf{K}_{FE}^* \cdot \sigma_{peak} \cdot \left(\frac{d}{R_0} \right)^{0.5} \right] \cdot \left[\frac{(\sigma_{rr})_{\theta=\pi, r=2d} + (\sigma_{rr})_{\theta=-\pi, r=2d}}{2} \right] \end{aligned} \quad (6.2.20)$$

Equation (6.2.20) shows that only few selected nodal stresses calculated from coarse FE mesh patterns can be used to estimate the averaged SED. Figure 6.2.9 shows a sketch of the four nodal stresses involved in Eq. (6.2.20): the crack tip, linear elastic opening (σ_{peak}) and sliding (τ_{peak}) peak stresses referred to the crack bisector line evaluated by FEM using coarse FE mesh patterns with an average FE size equal to d ; and the linear elastic radial stresses evaluated at the FE nodes located along the crack free edges at $r = 2d$.

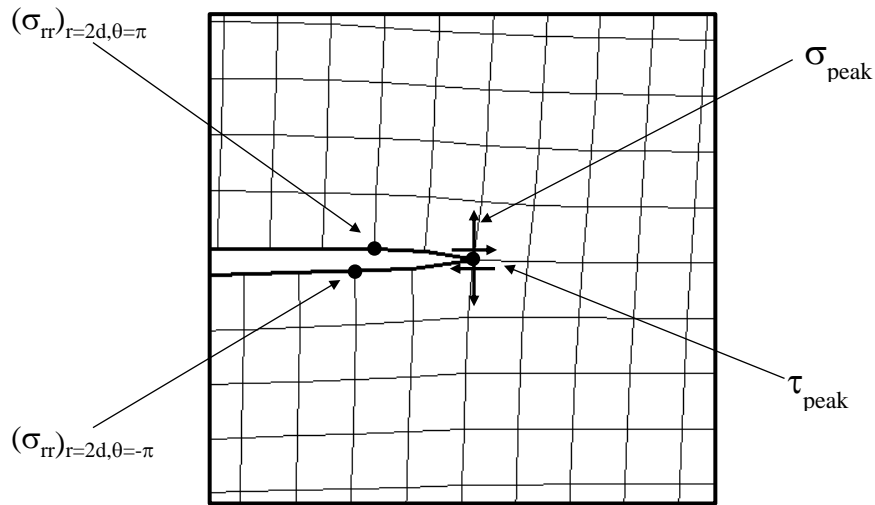


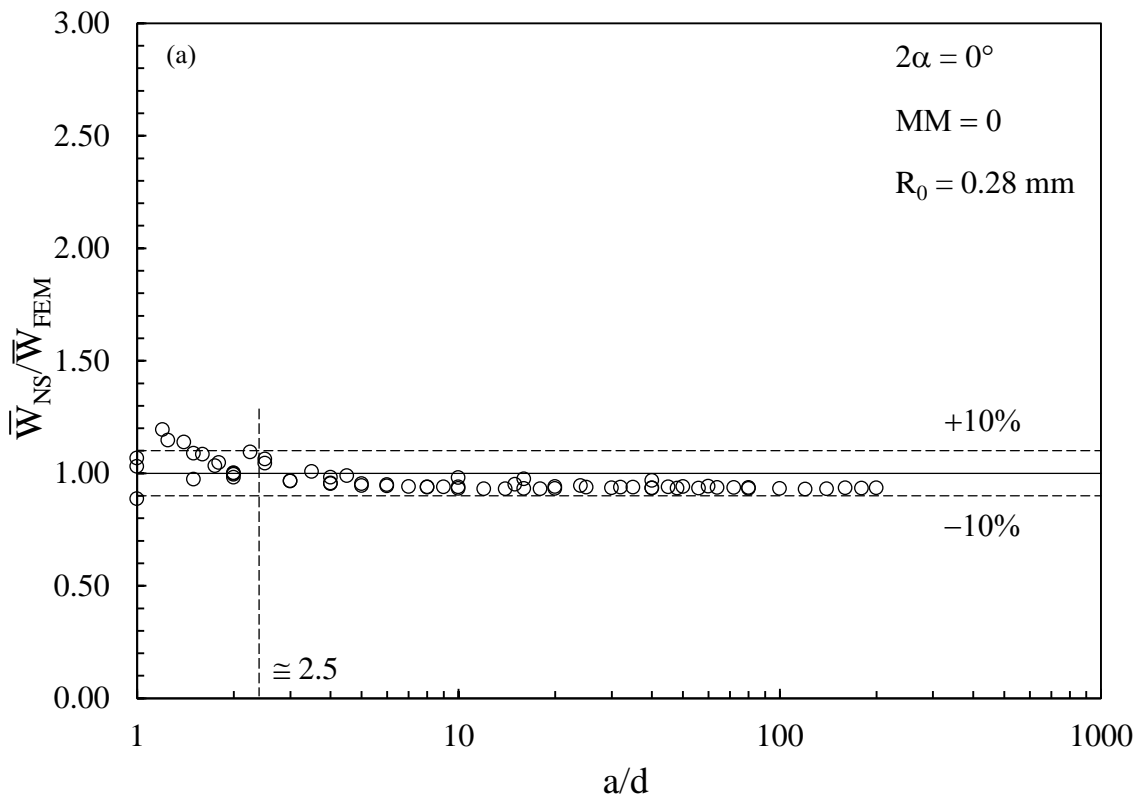
Figure 6.2.9: Selected FE nodal stresses to rapidly evaluate the averaged SED according to the nodal stress approach (Eq. (6.2.20)).

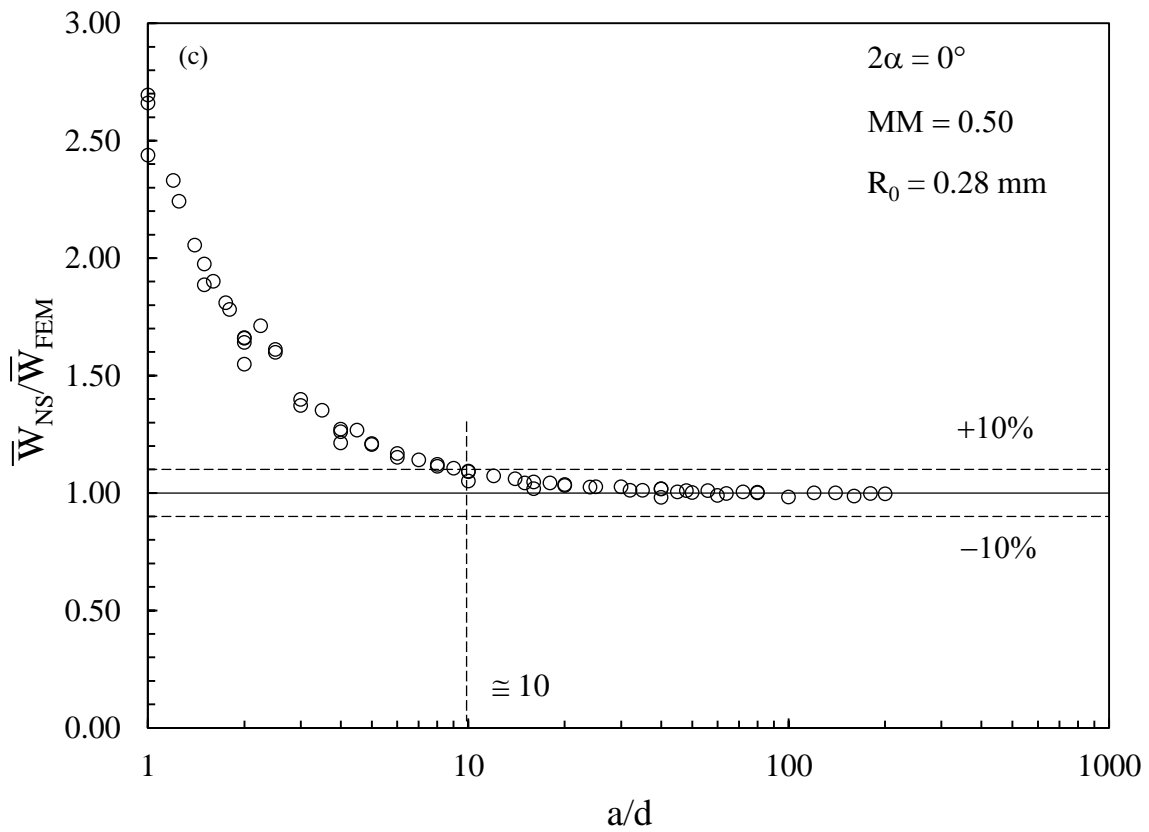
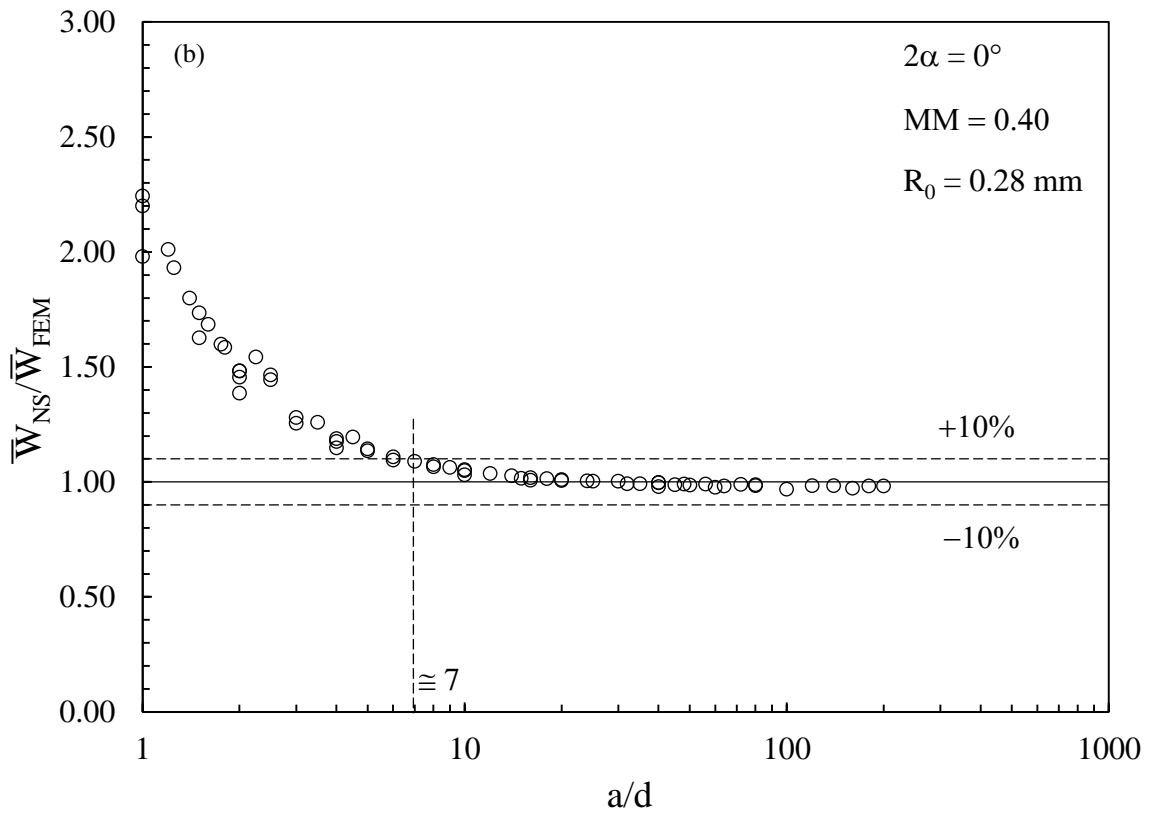
To validate the nodal stress approach based on Eq. (6.2.20), numerical analyses were performed by considering again the crack problem shown in Fig. 6.2.4a and by adopting the standard FE mesh patterns according to previous Figs. 6.2.4b and 6.2.9. All considered geometrical and loading parameters are reported in Table 6.2.2. Exact values of the averaged SED, \bar{W}_{FEM} (Eq. (6.2.13)), have been evaluated by adopting the direct approach with very refined meshes (patterns with about 500 FE within the reference volume).

Before comparing \bar{W}_{NS} (Eq. (6.2.20)) with \bar{W}_{FEM} (Eq. (6.2.13)), the averaged SED was calculated from Eq. (6.2.10a), \bar{W}_{AN} , by means of the exact SIFs K_{I} and K_{II} and the exact T-stress, analytically calculated according to Eqs. (6.2.4), (6.2.5) and (6.2.7), respectively. The analytical SED, \bar{W}_{AN} (Eq. (6.2.10a)), deviated from the exact value, \bar{W}_{FEM} (Eq. (6.2.13)), by less than 5% in the case of the minimum considered crack length $2a = 1$ mm for all analysed MMs. Therefore, the contribution of stress terms having order higher than the T-stress is negligible from an engineering point of view and Eq. (6.2.10a) as well as its numerical implementation Eq. (6.2.20) are applicable to the analysed crack problems. Furthermore, Eq. (6.2.11) and Fig. 6.2.2 demonstrated that the maximum T-stress contribution to the averaged SED is approximately 30% in the case of the

minimum considered crack length $2a = 1$ mm under pure mode I loading (MM = 0).

Figure 6.2.10 reports the ratio between approximate (\bar{W}_{NS} , nodal stress approach Eq. (6.2.20)) and exact (\bar{W}_{FEM} , direct approach Eq. (6.2.13)) averaged SED values for selected mode mixity ratios MM. The ratio $\bar{W}_{NS}/\bar{W}_{FEM}$ is seen to converge to unity inside a $\pm 10\%$ scatter-band for all considered MMs. In particular, Fig. 6.2.10 shows that convergence occurs for mesh density ratios a/d greater than 2.5 for MM = 0, 10 for MM = 0.50 and 14 for MM = 1. The obtained results show that the minimum mesh density ratio a/d to apply the nodal stress approach increases with increasing the mode mixity ratio MM.





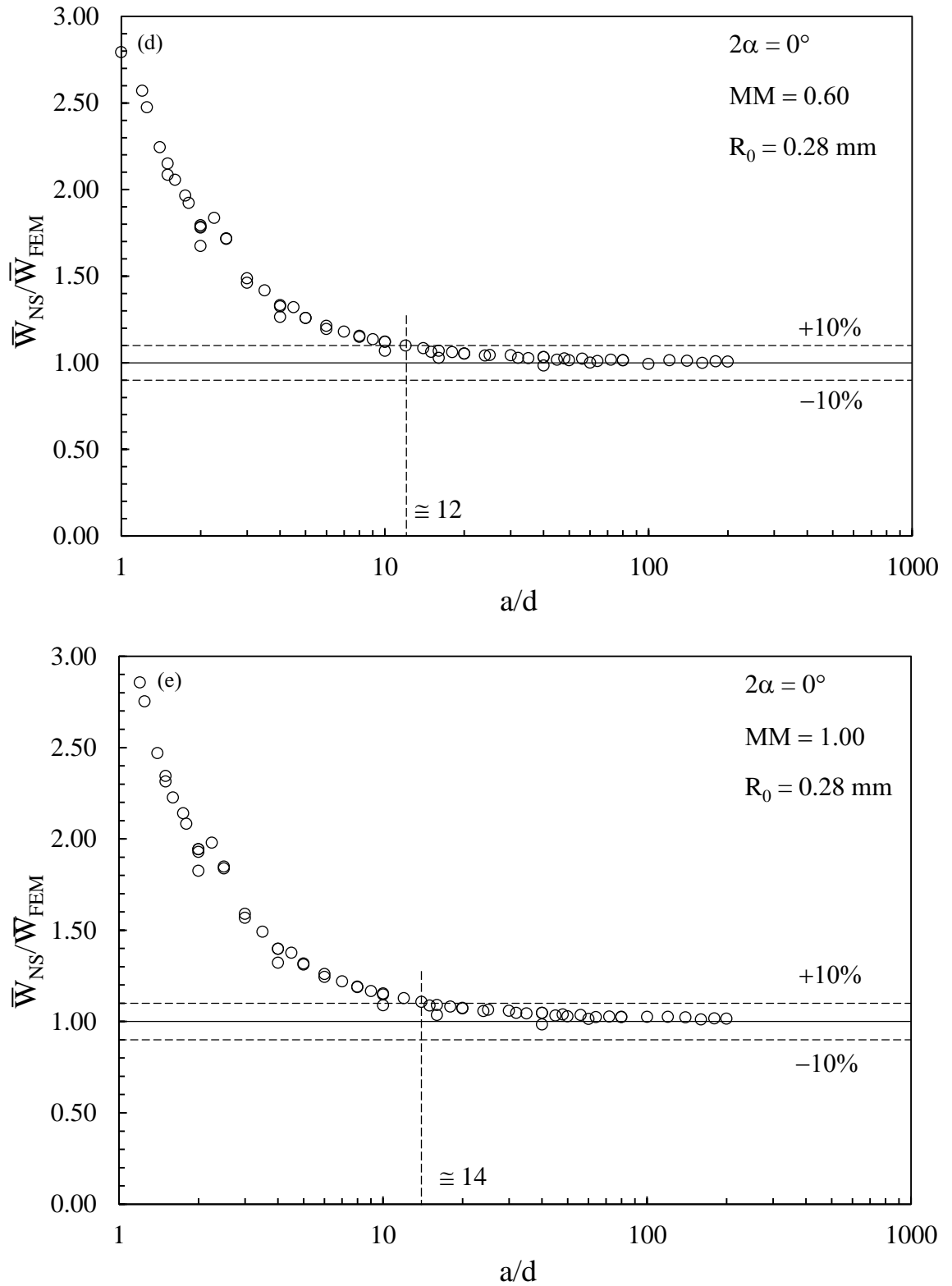


Figure 6.2.10: Ratio between approximated (\bar{W}_{NS}) and exact (\bar{W}_{FEM}) averaged SED versus the mesh density ratio. \bar{W}_{NS} according to the nodal stress approach, Eq. (6.2.20); \bar{W}_{FEM} according to the direct approach, Eq. (6.2.13). Short cracks under mixed mode I+II loading: (a) $MM = 0$; (b) $MM = 0.40$; (c) $MM = 0.50$; (d) $MM = 0.60$ and (e) $MM = 1.00$.

The minimum mesh density ratios a/d , reported in Fig. 6.2.10, are about the same previously found [84] dealing with long cracks under mixed mode I+II loading and they are also in agreement with that highlighted in previous Fig. 6.2.5, as far as pure modes of loading are concerned. The reason is that the minimum mesh density ratio a/d for each MM is driven by K_I ($a/d \geq 3$) and K_{II} ($a/d \geq 14$) contributions to the averaged SED, being the requirement of the $\overline{W}_{\text{nodal-T}}$ contribution in Eq. (6.2.20) ($a/d \geq 2$) less demanding than that of the $\overline{W}_{\text{PSM,I+II}}$ term.

6.2.4.2 Minimum mesh density ratio a/d

Figure 6.2.10 shows that the minimum mesh density ratio a/d depends on the mode mixity. Therefore, a criterion to choose the mesh density would be desirable. In the previous contribution [84] related to long cracks under mixed mode I+II loading, such criterion was expressed as follows:

$$\frac{\overline{W}_{\text{PSM,I+II}}}{\overline{W}_{\text{AN,I+II}}} \cong \frac{1 + \frac{e_2}{e_1} \cdot \left(\frac{\text{MM}}{1 - \text{MM}}\right)^2 \cdot \left(\frac{f_I\left(\frac{a}{d}\right)}{f_{II}\left(\frac{a}{d}\right)}\right)^2}{\left(f_I\left(\frac{a}{d}\right)\right)^2 \cdot \left(1 + \frac{e_2}{e_1} \cdot \left(\frac{\text{MM}}{1 - \text{MM}}\right)^2\right)} \quad (6.2.21)$$

where $\overline{W}_{\text{PSM,I+II}}$ is the approximate averaged SED, and $\overline{W}_{\text{AN,I+II}}$ is the exact expression.

f_I and f_{II} appearing in Eq. (6.2.21) are two functions fitting the numerical results collected when validating the PSM expressions (6.2.14) e (6.2.15) [84] :

$$f_I\left(\frac{a}{d}\right) = \frac{1}{1 + \frac{0.15}{\left(\frac{a}{d}\right)}} \quad (6.2.22)$$

$$f_{II}\left(\frac{a}{d}\right) = \frac{1}{1 + \frac{0.75}{\left(\frac{a}{d}\right)}} \quad (6.2.23)$$

Figure 6.2.11 shows the present results (reported in previous Fig. 6.2.5) and the fitting functions f_I and f_{II} [84] and highlights their applicability also in the present short crack problem.

Equation (6.2.21) was introduced to evaluate the minimum mesh density ratio a/d that can be adopted to apply Eq. (6.2.16), as soon as the ratio MM of the considered crack problem is known and the accepted degree of approximation in

terms of $\frac{\bar{W}_{PSM,I+II}}{\bar{W}_{AN,I+II}}$ is defined. Equation (6.2.21) is plotted in Fig. 6.2.12. In

particular, the ratio $\bar{W}_{PSM,I+II}/\bar{W}_{AN,I+II}$ is seen to converge to a unit value inside a scatter-band of $\pm 10\%$ when the adopted mesh density ratio a/d is greater than a minimum value that depends on the mode mixity ratio: approximate values reported in Fig. 6.2.12 are 3 for $MM = 0$ (pure mode I loading), 11 for $MM = 0.50$ (mixed mode I+II), and 16 for $MM = 1$ (pure mode II).

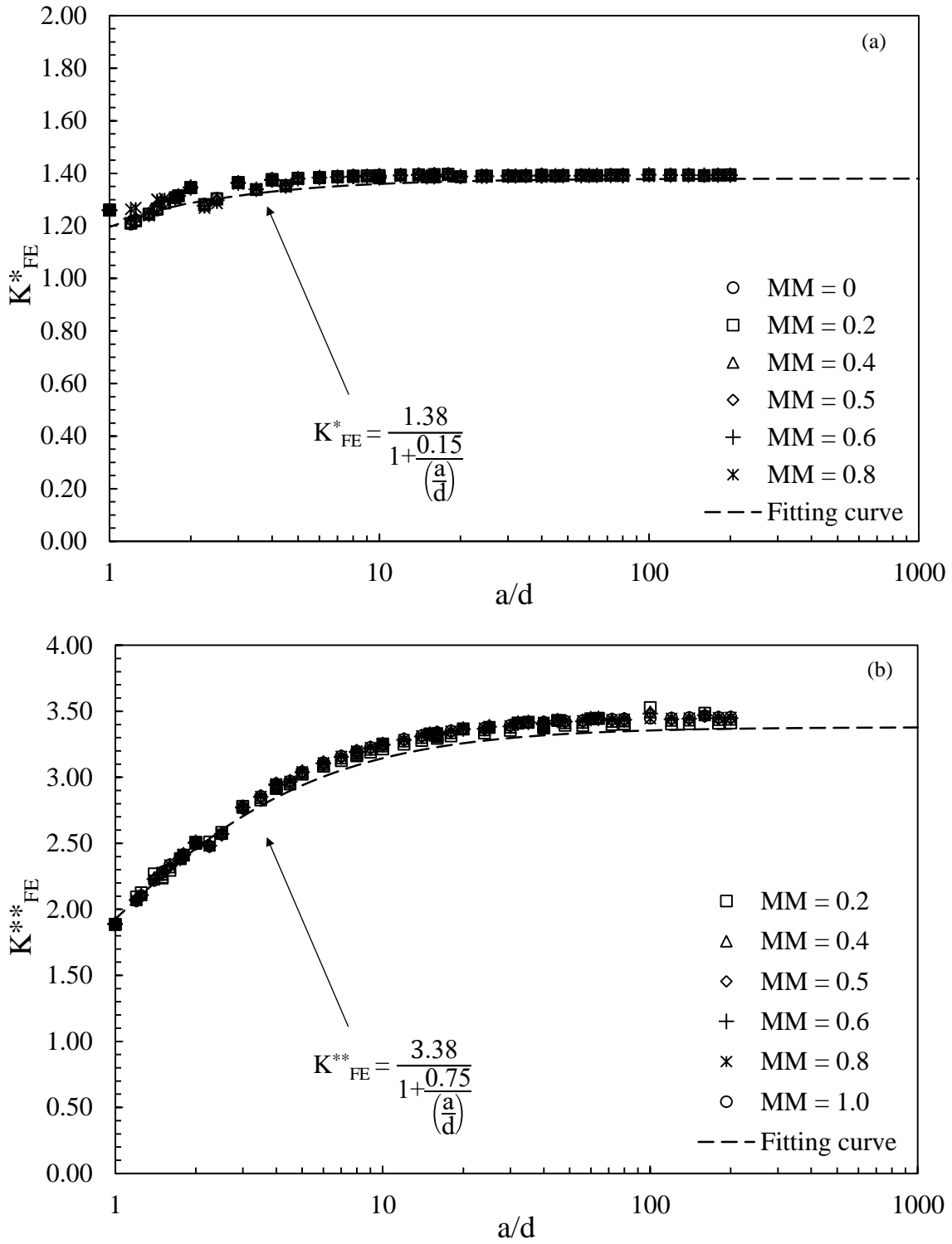


Figure 6.2.11: Comparison between non-dimensional SIFs calculated in previous Fig. 6.2.5 and best fitting functions, Eqs. (6.2.22) and (6.2.23) derived in ref. [84]: (a) mode I and (b) mode II.

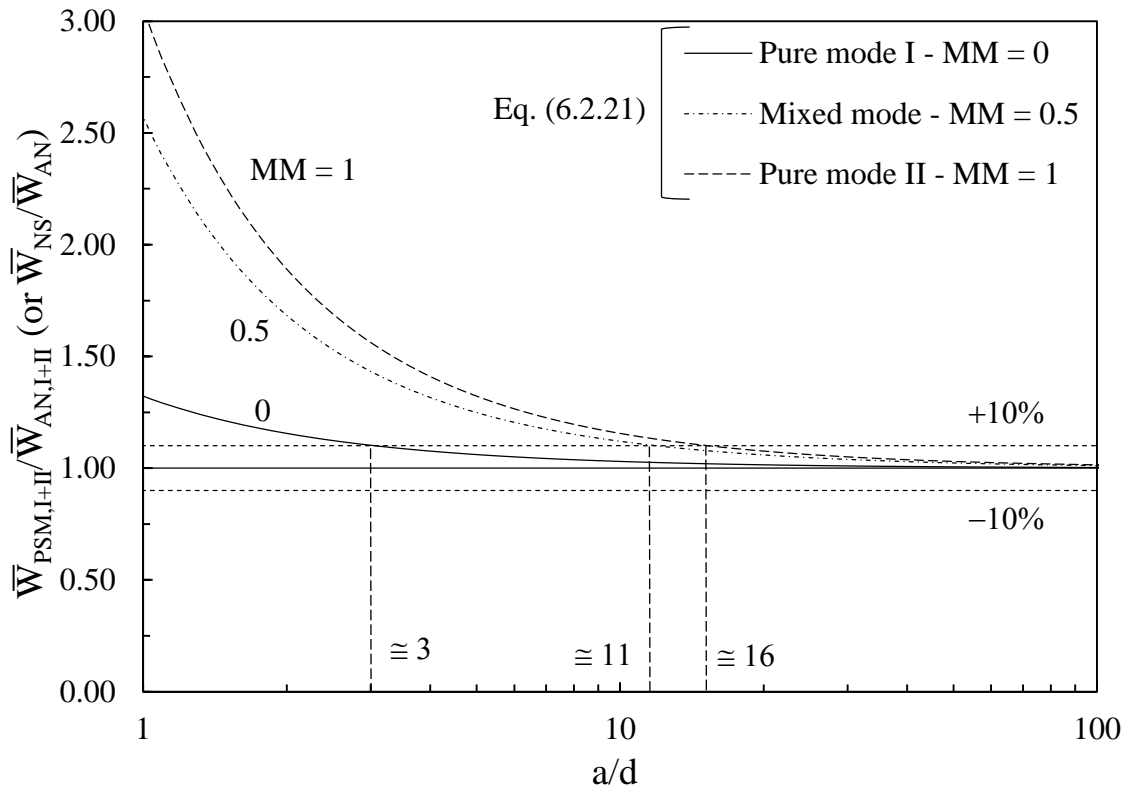


Figure 6.2.12: Estimation of the minimum mesh density ratio a/d for the applicability of the nodal stress approach under different mode mixities MM, according to Eq. (6.2.21).

Such results are in fairly good agreement with Fig. 6.2.10. That is not surprising because it should be remembered that the T-stress contribution in Eq. (6.2.20), $\bar{W}_{nodal-T}$, is less demanding in terms of mesh density ($a/d \geq 2$) than the SIFs contribution, $\bar{W}_{PSM,I+II}$ ($a/d \geq 3$). Therefore, it is proposed that Eq. (6.2.21) and Fig. 6.2.12 are applied also to the present short crack problems, i.e. to estimate the minimum mesh density ratio that can be adopted to apply the nodal stress approach (Eq. (6.2.20)), although they were originally derived only for long cracks, where the PSM (Eq. (6.2.16)) can be applied. Moreover, by making the crack shorter and shorter, the T-stress contribution $\bar{W}_{nodal-T}$ to the averaged SED becomes increasingly significant as compared to the SIFs contribution $\bar{W}_{PSM,I+II}$, in such a way that decreasing the crack size Eq. (6.2.21) delivers mesh density ratios a/d more and more on the safe side.

6.2.4.3 The nodal stress approach coarsening the mesh further

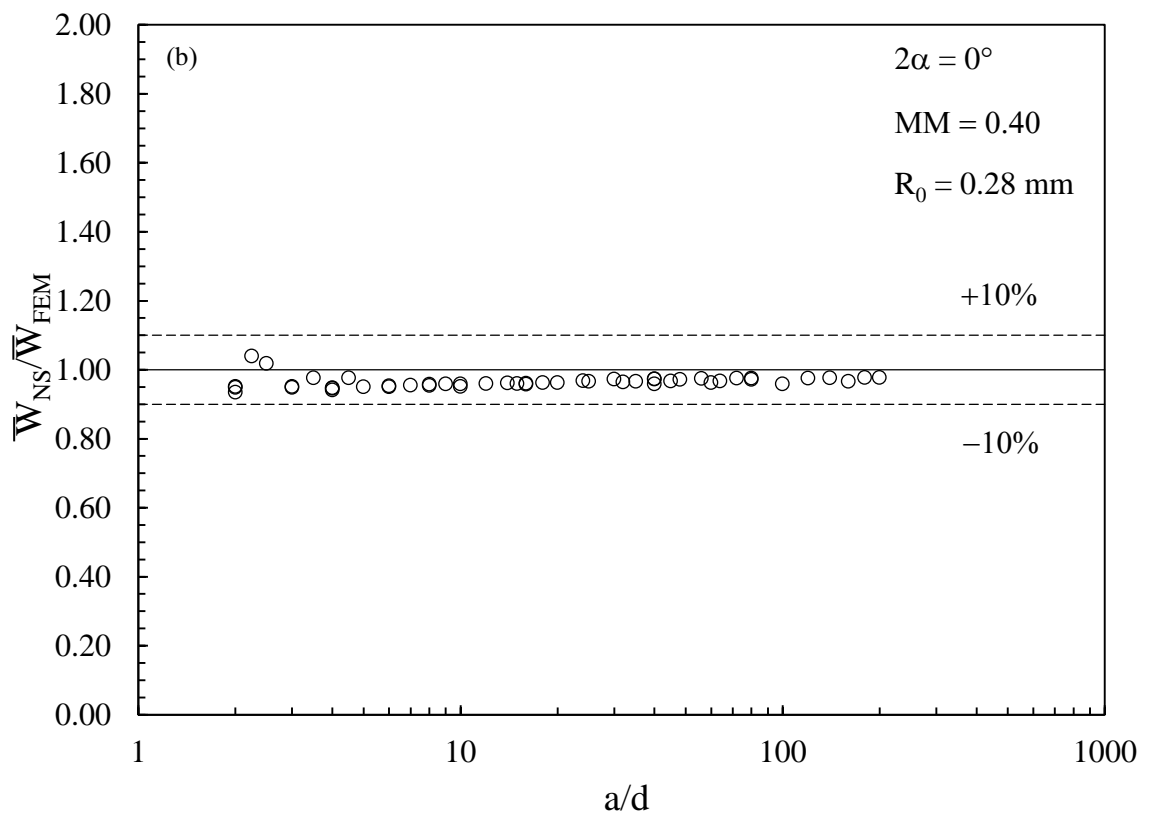
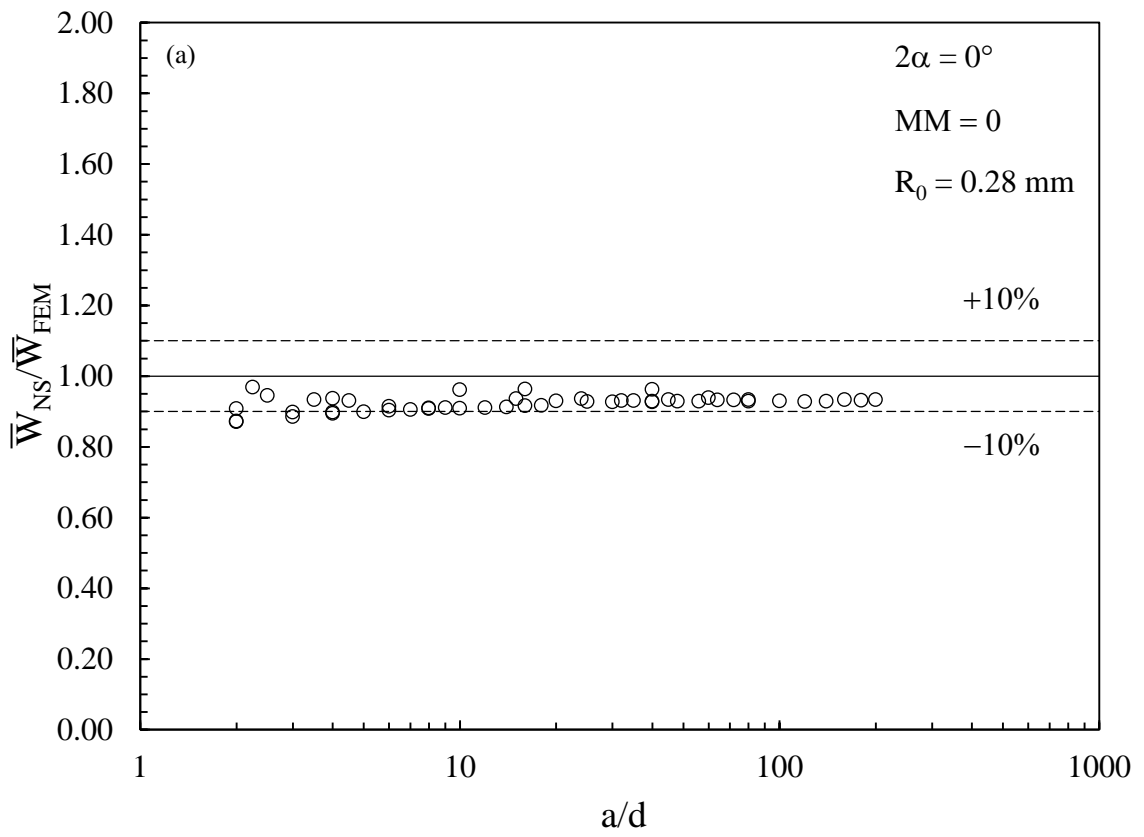
Making use of the fitting function f_I and f_{II} , the validity of the non-dimensional SIFs expressions (6.2.14) and (6.2.15) can be extended to much coarser FE meshes according to Fig. 6.2.11. By substituting f_I and f_{II} , Eqs. (6.2.22) and (6.2.23), into Eq. (6.2.20), the following expression can be written:

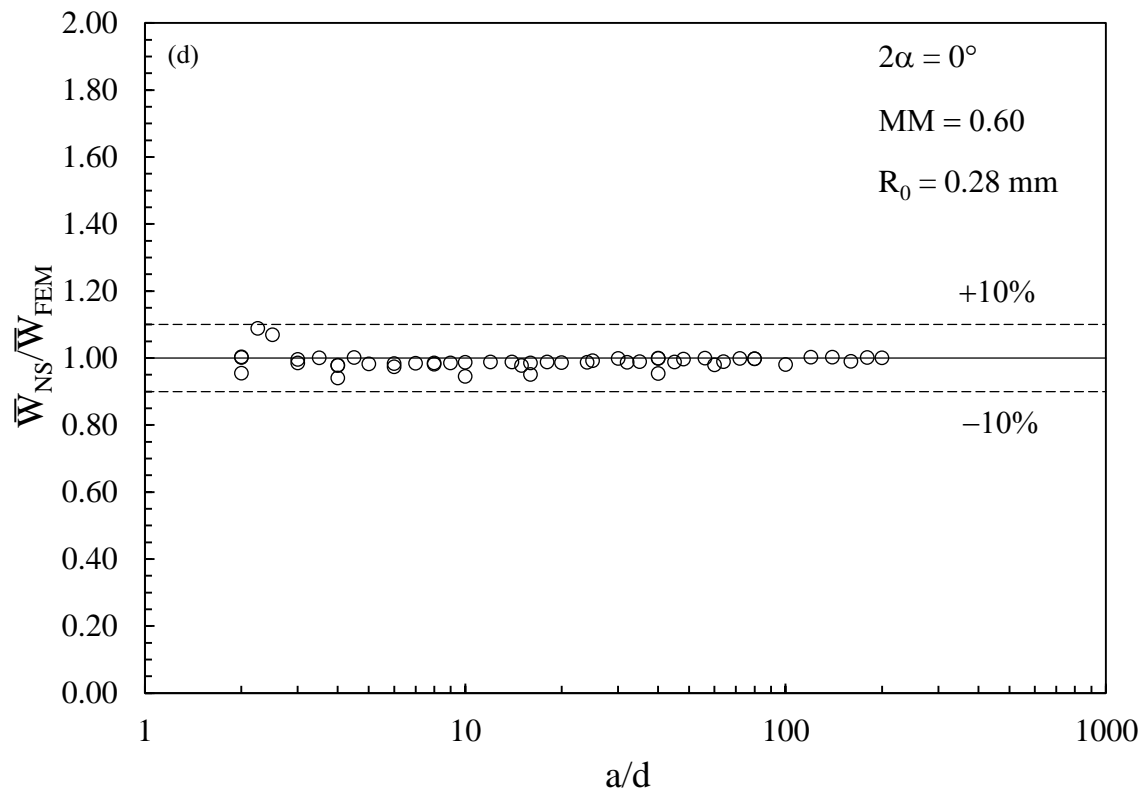
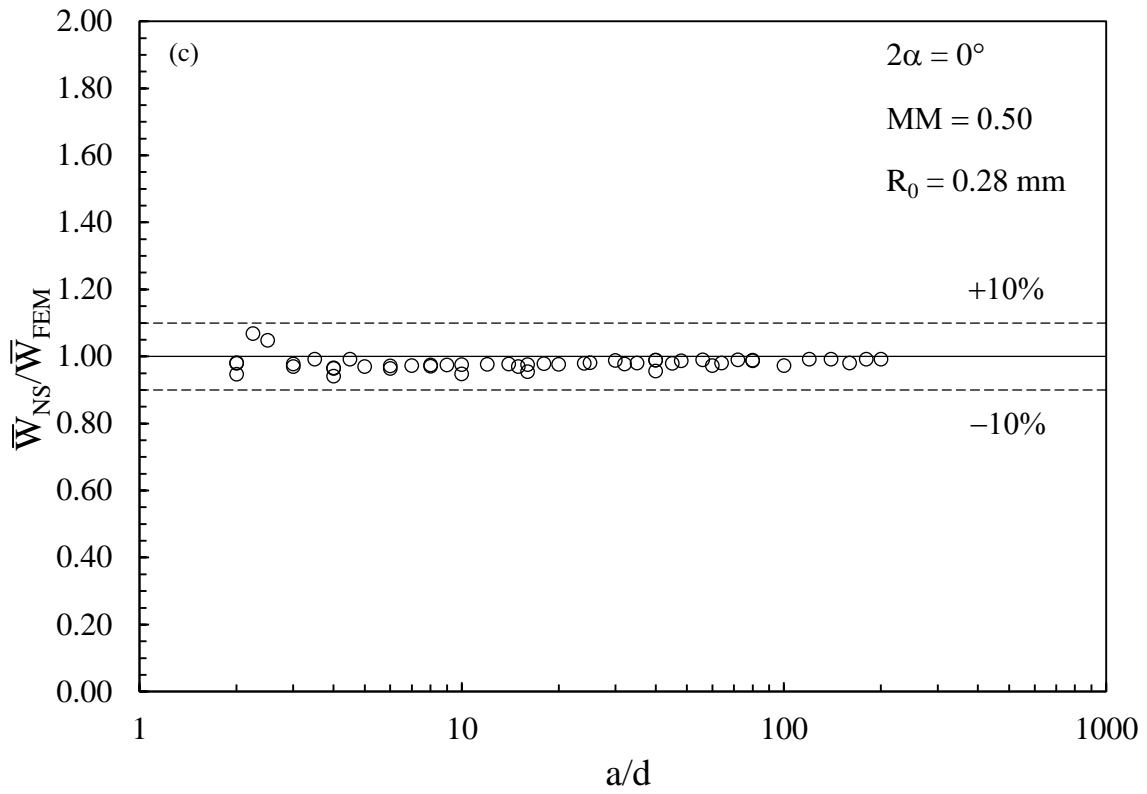
$$\begin{aligned} \bar{W}_{NS} = & \frac{e_1}{E} \left[\mathbf{K}_{FE}^* \cdot \sigma_{peak} \cdot f_I \left(\frac{a}{d} \right) \cdot \left(\frac{d}{R_0} \right)^{0.5} \right]^2 + \frac{e_2}{E} \left[\mathbf{K}_{FE}^{**} \cdot \tau_{peak} \cdot f_{II} \left(\frac{a}{d} \right) \cdot \left(\frac{d}{R_0} \right)^{0.5} \right]^2 + \\ & \frac{1-\nu^2}{2E} \left(\frac{(\sigma_{rr})_{\theta=\pi, r=2d} + (\sigma_{rr})_{\theta=-\pi, r=2d}}{2} \right)^2 + \\ & \frac{8\sqrt{2}}{15 \cdot (\pi)^{3/2}} \frac{(1+\nu) \cdot (2-5\nu)}{E} \left[\mathbf{K}_{FE}^* \cdot \sigma_{peak} \cdot f_I \left(\frac{a}{d} \right) \cdot \left(\frac{d}{R_0} \right)^{0.5} \right] \cdot \left[\frac{(\sigma_{rr})_{\theta=\pi, r=2d} + (\sigma_{rr})_{\theta=-\pi, r=2d}}{2} \right] \end{aligned}$$

(6.2.24)

Where the minimum mesh density ratios required to estimate the SIFs contribution $\bar{W}_{PSM, I+II}$ in Eq. (6.2.20) and illustrated in previous Fig. 6.2.12 are now removed, the sole requirement $a/d \geq 2$, relevant to the estimation of $\bar{W}_{nodal-T}$ in Eq. (6.2.20), being now valid.

The ratio between the approximate averaged SED according to Eq. (6.2.24) and the exact value according to the direct approach (\bar{W}_{FEM} , Eq. (6.2.13)) is reported in Fig. 6.2.13 for selected mode mixity ratios along with an error band of $\pm 10\%$. Fig. 6.2.13 should be compared with the previous Fig. 6.2.10 to appreciate the relaxation of the mesh density requirements introduced by Eq. (6.2.24) as compared to previous Eq. (6.2.20). Fig. 6.2.13 shows that a mesh density ratio $a/d = 2$ can be adopted for engineering estimations of the averaged SED, in agreement with previous results [84] relevant to long cracks under mixed mode I+II loading.





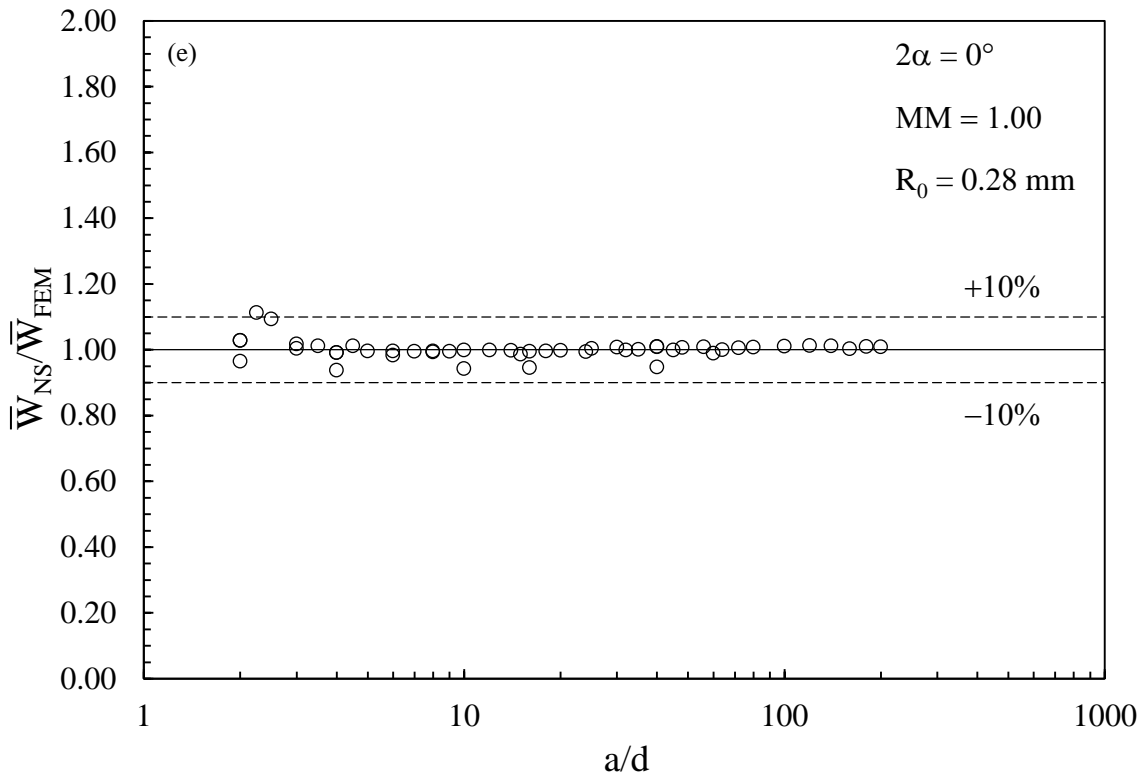


Figure 6.2.13: Ratio between approximate (\bar{W}_{NS}) and exact (\bar{W}_{FEM}) averaged SED versus the mesh density ratio. \bar{W}_{NS} according to the nodal stress approach, Eq. (6.2.24); \bar{W}_{FEM} according to the direct approach, Eq. (6.2.13). Short cracks under mixed mode I+II loading: (a) $MM = 0$; (b) $MM = 0.40$; (c) $MM = 0.50$; (d) $MM = 0.60$ and (e) $MM = 1.00$.

6.2.5. Discussion

The nodal stress approach has been proposed to estimate the averaged strain energy density (SED) of mixed-mode (I+II) crack tip fields including the T-stress contribution. The method takes four FE nodal stresses calculated with coarse FE meshes: two of them are the singular, linear elastic crack tip opening and sliding peak stresses, respectively, which take into account the stress intensity factor contribution; the remaining two ones are the nodal stresses evaluated along the crack free edges at a selected distance from the crack tip and take into account the T-stress contribution. The conclusions can be summarised as follows:

- Taking advantage of the closed-form expression of the averaged SED (Eq. 6.2.10a), the nodal stress approach can be expressed by means of Eq.

(6.2.20); depending on the mode mixity (MM) ratio, the minimum mesh density ratio to apply Eq. (6.2.20) with a given level of approximation can be determined by means of Eq. (6.2.21) or Figure 6.2.12.

- More refined FE mesh patterns are required, the higher the mode mixity ratio MM is. In particular, the minimum ratio a/d between the semi-crack length a and the average FE size d is found to be equal to 2.5 in the case of pure mode I (MM = 0), 10 in the case of mixed mode I+II with MM = 0.50 and 14 for pure mode II loading (MM = 1).
- The use of proper fitting functions allows to extend the validity of the proposed nodal stress approach to coarser FE meshes according to Eq. (6.2.24), where a minimum mesh density ratio, $a/d = 2$, can be adopted. Because of the increased admissible mesh coarseness, Eq. (6.2.24) might be advantageous from an engineering point of view.
- Even though it has been recognised that the averaged SED can be evaluated directly by means of FE analyses using coarse meshes inside the control volume and including automatically the T-stress contribution, nonetheless some additional advantages of the nodal stress approach to estimate the averaged SED can be singled out: (i) only the linear elastic nodal stresses calculated at selected FE nodes are necessary; (ii) geometrical modelling the control volume in FE models is no longer necessary, while the coarse mesh option is maintained in the nodal stress approach.

6.3 Link between the PSM and the averaged SED - example of practical application: fatigue strength assessment of butt welded joints under mode I loading ^(*)

Nomenclature

2a	length of the lack of penetration
c_w	parameter which accounts the influence of the nominal load ratio
d	mean size of a finite element
e_1, e_2	parameters for the determination of the strain energy density (SED)
E	elastic modulus
f_{w1}, f_{w2}	weight parameters of the peak stresses
h	bead height
k	inverse slope of the design scatter band
K_1, K_2	mode I and II notch stress intensity factors (NSIFs)
K_{FE}^*	normalised K_1 in the application of the peak stress method
K_{FE}^{**}	normalised K_2 in the application of the peak stress method
N_A	reference number of cycles
N_f	number of cycles to failure
R	load ratio (ratio between the minimum and the maximum applied load in a fatigue test)
R_0	radius of the structural volume where local stresses are averaged
r, θ	polar coordinates
T_σ	scatter index of the design scatter band
t	thickness of the welded plate
\bar{W}	strain energy density averaged over the control volume
w_{toe}	bead width

Symbols

2α	notch opening angle
Δ	range of the considered quantity

λ_1, λ_2	mode I, mode II eigenvalues in Williams' equation
ν	Poisson's ratio
$\sigma_{11,peak}$	linear elastic maximum principal stress evaluated at a V-notch tip (the weld toe or the weld root) by the finite element method using the mesh according to the PSM
$\sigma_{A,50\%}$	fatigue strength at the reference number of cycles for a probability of survival equal to 50%
σ_b	nominal stress relevant to secondary bending loading
$\sigma_{eq,peak}$	linear elastic equivalent peak stress evaluated at a V-notch tip (the weld toe or the weld root)
σ_{nom}	nominal stress relevant to axial loading
$\sigma_{\theta\theta}, \tau_{r\theta}$	normal and shear stress components in the polar frame of reference
ρ	radius at the weld root or toe

Abbreviations

EBM	Electron beam welding
MAG	Metal active gas welding
MAW	Metal arc welding
SAW	Submerged arc welding
TIG	Tungsten inert gas welding

(*) *See also:*

Meneghetti, G.; Campagnolo, A.; Berto, F. Fatigue strength assessment of partial and full penetration steel and aluminium butt welded joints according to the peak stress method. *Fatigue and Fracture of Engineering Materials and Structures*; 38: 1419-1431 (2015).

6.3.1. Introduction

In the notch stress intensity factor approach to the fatigue assessment of welded joints, the toe and the root side are modelled as sharp V-notches, $\rho = 0$ (worst case condition), and local stress distributions in plane configurations are given on the basis of the relevant mode I and mode II notch stress intensity factors (NSIFs). These factors quantify the magnitude of the asymptotic stress distribution obeying Williams' solution [31]. Figure 6.3.1 illustrates the geometrical assumptions of the NSIF approach to the fatigue analysis of welded joints.

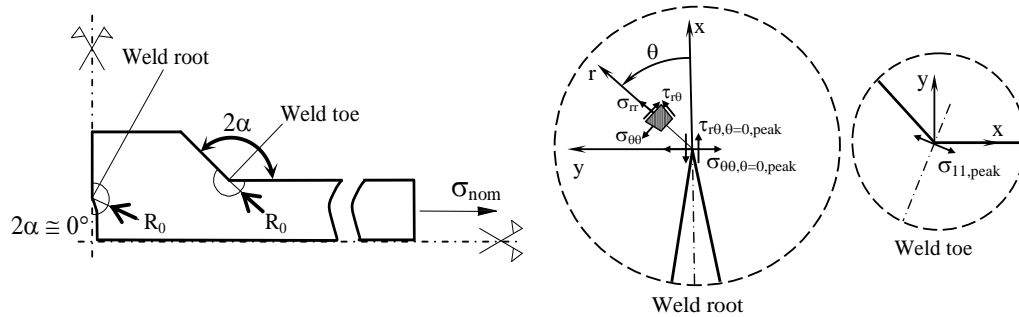


Figure 6.3.1: Definition of peak stresses evaluated by means of a linear elastic finite element analysis at the weld toe and the weld root of a partial-penetration butt joint. The V-notch opening angle 2α is typically 0° at the weld root. For the partially-penetrated butt joint shown in the figure, the sliding peak stress $\tau_{r,\theta=0,\text{peak}}$ at the weld root is negligible, being the root subjected to nearly pure mode I loading.

NSIFs are adequate to describe crack initiation at sharp corner notches, as stress intensity factors (SIFs) do at crack-like notches. However, it was observed experimentally that NSIFs can also be used to correlate the total fatigue life due to cracks traversing the plate thickness of small size laboratory welded details. This is explained by the fact that a large amount of the fatigue life is spent to initiate a short crack in a zone governed by the V-notch singularity.

The degree of singularity of the stress field ahead of sharp V-notches depends on the notch opening angle [31] and the magnitude of asymptotic stress distribution in plane problems is quantified by means of the mode I and mode II NSIFs. By

using a polar coordinate system (r, θ) having its origin located at the sharp notch tip, Fig. 6.3.1, the NSIFs are defined according to Gross and Mendelson [30]:

$$K_1 = \sqrt{2\pi} \cdot \lim_{r \rightarrow 0} \left[\sigma_{\theta\theta, \theta=0} \cdot r^{1-\lambda_1} \right] \quad (6.3.1)$$

$$K_2 = \sqrt{2\pi} \cdot \lim_{r \rightarrow 0} \left[\tau_{r\theta, \theta=0} \cdot r^{1-\lambda_2} \right] \quad (6.3.2)$$

where λ_1 and λ_2 are Williams' eigenvalues [31], which depend on the notch opening angle 2α (see Figure 6.3.1), while the normal $\sigma_{\theta\theta}$ and shear $\tau_{r\theta}$ stress components are evaluated in the polar coordinate system (r, θ) centred at the V-notch tip along the notch bisector line $\theta=0$. When the V-notch angle 2α is greater than 102.6 degrees, the mode II stress distribution is no longer singular and therefore it is usually neglected in fatigue strength assessments [27]. As far as a constant weld toe angle can be assumed and this angle is large enough to make the mode II contribution non-singular, the mode I NSIF can directly be used to correlate the fatigue strength of fillet welded joints having different geometries and absolute dimensions [27].

Practical application of the NSIF approach may be restricted because variations of the V-notch opening angle destroy the direct comparability of the NSIFs, due to the exponents appearing in definitions (6.3.1) and (6.3.2). Comparability can be re-established by using the strain energy density (SED) averaged over a control volume surrounding the weld root or the weld toe as fatigue relevant parameter. In some previous papers by Lazzarin et al. [23,29,85], the SED parameter was given in closed form on the basis of the relevant NSIFs, and the radius R_0 of the averaging zone was carefully identified with reference to conventional arc welding processes and uniaxial loading. In particular R_0 for welded joints made of structural steel and aluminium alloy was found to be 0.28 mm and 0.12 mm, respectively [29,85]. The two different values for R_0 suggest that welded joints made of construction steels are less notch sensitive under cyclic loading than those made of aluminium alloys.

Under plane strain conditions, the strain energy density averaged over the control volume shown in Fig. 6.3.1 can be given as follows [23]:

$$\Delta \bar{W} = \frac{e_1}{E} \left[\frac{\Delta K_1}{R_0^{1-\lambda_1}} \right]^2 + \frac{e_2}{E} \left[\frac{\Delta K_2}{R_0^{1-\lambda_2}} \right]^2 \quad (6.3.3)$$

Table 6.3.1: Values of parameter f_{w1} according to Eq. (6.3.10).

2α (deg)	λ_1 ^(a)	e_1 ^(b)	$R_0 = 0.28$ mm		e_1 ^(c)	$R_0 = 0.12$ mm	
			$f_{w1,d=0.5mm}$ ^(b)	$f_{w1,d=1mm}$ ^(b)		$f_{w1,d=0.5mm}$ ^(c)	$f_{w1,d=1mm}$ ^(c)
0	0.500	0.133	0.997	1.410	0.125	1.491	2.109
90	0.544	0.145	1.015	1.392	0.138	1.472	2.019
110	0.586	0.136	0.959	1.278	0.130	1.345	1.792
120	0.616	0.129	0.918	1.198	0.124	1.259	1.644
125	0.633	0.126	0.898	1.159	0.120	1.211	1.562
130	0.652	0.122	0.873	1.111	0.117	1.160	1.476
135	0.674	0.118	0.849	1.064	0.113	1.106	1.387
140	0.697	0.113	0.818	1.010	0.109	1.050	1.295
145	0.723	0.109	0.793	0.961	0.104	0.991	1.200
150	0.752	0.104	0.762	0.905	0.100	0.930	1.105
155	0.784	0.098	0.726	0.844	0.095	0.868	1.009
160	0.819	0.093	0.693	0.786	0.090	0.805	0.913

^(a): values from previous contributions [23,29]

^(b): values calculated with $\nu = 0.3$, $K_{FE}^* = 1.38$

^(c): values calculated with $\nu = 0.33$, $K_{FE}^* = 1.38$

Table 6.3.2: Values of parameter f_{w2} according to Eq. (6.3.11).

2α (deg)	λ_2 ^(a)	e_2 ^(b)	$R_0 = 0.28$ mm		e_2 ^(c)	$R_0 = 0.12$ mm	
			$f_{w2,d=0.5mm}$ ^(b)	$f_{w2,d=1mm}$ ^(b)		$f_{w2,d=0.5mm}$ ^(c)	$f_{w2,d=1mm}$ ^(c)
0	0.500	0.340	3.904	5.522	0.337	5.996	8.480

^(a): value from previous contributions [23,29]

^(b): values calculated with $\nu = 0.3$, $K_{FE}^{**} = 3.38$

^(c): values calculated with $\nu = 0.33$, $K_{FE}^{**} = 3.38$

where R_0 represents the control radius (see Figure 6.3.1), ΔK_1 and ΔK_2 are the ranges of the relevant NSIFs, E is the Young's modulus while e_1 and e_2 are known

parameters depending on the notch opening angle 2α and the Poisson's ratio ν , see Tables 6.3.1, 6.3.2 [23,29].

In the case of stress-relieved welded joints, it is possible to take into account the influence of the nominal load ratio, R (defined as the ratio between the minimum and the maximum applied load), by using the following expression:

$$\Delta\bar{W} = c_w \left(\frac{e_1}{E} \left[\frac{\Delta K_1}{R_0^{1-\lambda_1}} \right]^2 + \frac{e_2}{E} \left[\frac{\Delta K_2}{R_0^{1-\lambda_2}} \right]^2 \right) \quad (6.3.4)$$

where parameter c_w is defined as follows [53]:

$$c_w(R) = \begin{cases} \frac{1+R^2}{(1-R)^2} & \text{if } -1 \leq R \leq 0 \\ \frac{1-R^2}{(1-R)^2} & \text{if } 0 \leq R \leq 1 \end{cases} \quad (6.3.5)$$

The coefficient c_w is equal to 1 for $R = 0$ and to 0.5 for $R = -1$ when considering the stress-relieved condition. One should note that the corresponding equivalent local stress varies according to the ratio $\sqrt{0.5} = 0.71$. Such coefficient is in good agreement with the IIW Recommendations [86], which suggest a ratio of the fatigue classes $1.2/1.6 = 0.75$ for the cases $R = 0$ and $R = -1$. Conversely, in the case of welded joints under as-welded conditions, c_w is always set equal to 1, independently on the load ratio R . In fact, in the presence of high tensile residual stresses, the fatigue strength of welded joints depends only slightly on the load ratio, particularly in the case of full size structures.

A disadvantage in practical application of the NSIF-based approach is that very refined meshes are needed to calculate the NSIFs by means of definitions (6.3.1) and (6.3.2). The modelling procedure becomes particularly time-consuming for components that cannot be analysed by means of two-dimensional models. However, it has been shown that $\Delta\bar{W}$ can be estimated directly from FE analyses using coarse meshes inside the structural volume having radius R_0 [37]. Modelling the circular sector-shaped structural volume can be avoided and coarse FE meshes

can be used thanks to the Peak Stress Method, which is summarised in the following.

Nisitani and Teranishi [41,42] presented a new technique to estimate K_I for a crack emanating from an ellipsoidal cavity. Such a procedure is based on the usefulness of the linear elastic stress $\sigma_{\theta\theta,\theta=0,\text{peak}}$ calculated at the crack tip by means of FE analyses characterized by a mesh pattern having a constant element size (see Figure 6.3.1). In particular Nisitani and Teranishi [41,42] were able to show that the ratio $K_I/\sigma_{\theta\theta,\theta=0,\text{peak}}$ depends only on the element size, if the adopted element type is the same. Therefore the $\sigma_{\theta\theta,\theta=0,\text{peak}}$ value can be used to rapidly estimate K_I , provided that the adopted mesh pattern has been previously calibrated on geometries for which the exact value of K_I is known. It has been shown that such a criterion can be extended also to sharp V-notches subject to mode I loading [43] giving rise to the so-called Peak Stress Method (PSM), which can be regarded as an approximate FE-based method to estimate the NSIF. Later on, the PSM has been extended to cracks subject to mode I as well as mode II stresses [44]. The element size required to evaluate K_1 and K_2 from $\sigma_{\theta\theta,\theta=0,\text{peak}}$ and $\tau_{r\theta,\theta=0,\text{peak}}$, respectively, is several orders of magnitude greater than that required to evaluate accurately the local stress field. The second advantage using $\sigma_{\theta\theta,\theta=0,\text{peak}}$ and $\tau_{r\theta,\theta=0,\text{peak}}$ is that only a single stress value is sufficient to estimate K_1 and K_2 , respectively, instead of a number of stress-distance FE data, as usually required in order to apply definitions (6.3.1) and (6.3.2). Originally, the PSM was formulated for cases where only mode I singular stresses exist (i.e. $K_2 = 0$ or mode II stresses are negligible) and it has been based on a link between the exact value of mode I NSIF K_I , see Eq. (6.3.1), and the linear elastic opening peak stress $\sigma_{\theta\theta,\theta=0,\text{peak}}$ calculated at the V-notch tip [43].

$$K_{\text{FE}}^* = \frac{K_I}{\sigma_{\theta\theta,\theta=0,\text{peak}} \cdot d^{1-\lambda_1}} \cong 1.38 \quad (6.3.6)$$

The PSM according to Eq. (6.3.6) has been applied extensively to correlate the fatigue strength of fillet- and full penetration welded joints subjected to mode I loading [45,46,87].

Later on, the PSM was extended to mode II crack problems with reference to weld root failures with significant opening as well as sliding stresses applied at the crack tip. A link between the exact value of mode II NSIF K_2 , see Eq. (6.3.2) with $2\alpha = 0^\circ$ and $\lambda_2 = 0.5$ (i.e. the crack case), and the linear elastic sliding peak stress $\tau_{r\theta, \theta=0, \text{peak}}$ calculated at the crack tip was established according to Eq. (6.3.7) [44].

$$K_{\text{FE}}^{**} = \frac{K_2}{\tau_{r\theta, \theta=0, \text{peak}} \cdot d^{1-\lambda_2}} \cong 3.38 \quad (6.3.7)$$

In Eqs. (6.3.6) and (6.3.7) d is the mean finite element size adopted when using the free mesh generation algorithm available in Ansys® numerical code, while “exact NSIF values” for K_1 and K_2 must be meant as the values obtained by applying definitions (6.3.1) and (6.3.2) to the stress-distance numerical results calculated from very refined FE mesh patterns (the size of the smallest element close to the V-notch tip is often in the order of 10^{-5} mm). Eqs. (6.3.6) and (6.3.7) are useful in practical applications because given the adopted average element size d , then also $K_1/\sigma_{\theta\theta, \theta=0, \text{peak}}$ and $K_2/\tau_{r\theta, \theta=0, \text{peak}}$ ratios are constants.

Values of 1.38 and 3.38 given by Eqs. (6.3.6) and (6.3.7), respectively, were derived under the following conditions [43,44]:

- use of 4-node linear quadrilateral elements, as implemented in ANSYS® numerical code (PLANE 42 of Ansys element library or alternatively PLANE 182 with K-option 1 set to 3);
- pattern of finite elements around the V-notch tip as shown in Fig. 6.3.2 (see also [43,44]): in particular, two elements share the node located at the weld toe (where $2\alpha \cong 135^\circ$), while four elements share the node located at the weld root (where $2\alpha = 0^\circ$);
- concerning Eq. (6.3.6), V-notches characterised by an opening angle 2α ranging from 0° to 135° ;
- concerning mode I loading, the ratio a/d must be greater than 3 in order to obtain $K_{\text{FE}}^* = 1.38 \pm 3\%$: when assessing the root side, a is the minimum value between the semi-crack length (crack is due to the lack

of penetration) and the ligament length, while a represents the plate thickness t when the toe side is taken into consideration; when also mode II (sliding) stresses are of interest at the root side, meshes must be more refined such that the ratio a/d must be greater than 14 in order to obtain $K_{FE}^{**} = 3.38 \pm 3\%$.

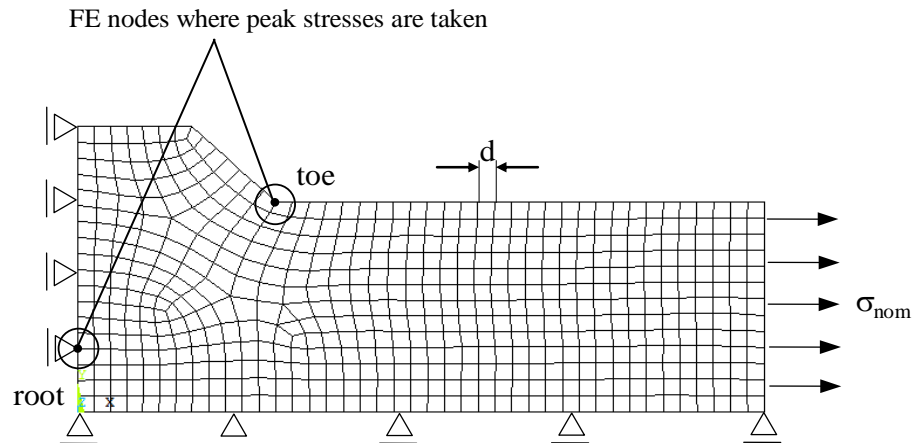


Figure 6.3.2: Typical 2D free mesh [43–46,87] to assess the fatigue strength according to the peak stress method (PSM) referred to a partial-penetration butt welded joint. The mean finite element size d is the sole parameter adopted to drive the free mesh generation algorithm in Ansys® code.

It should be noted that the FE patterns according to the PSM, like that reported in Fig. 6.3.2, are readily and easily obtained by running the free mesh algorithm available in Ansys® numerical code, where d must be input as the so-called ‘global element size’ parameter required by the software. There are not additional parameters to input in order to generate the mesh. Moreover, it is not necessary to create the structural volume in the FE model.

Recently the PSM has been combined also with 3D FE models and eight-node brick elements to assess the fatigue strength of steel welded joints having complex geometry and characterised by toe as well as root cracking [47,48]. Finite element analyses performed using higher order elements or significantly different FE patterns would lead to different results, so that the coefficients of Eqs. (6.3.6) and (6.3.7) should be recalculated. The notch stress intensity factor approach [88] as

well as the local strain energy density concept and its relation to the peak stress method [89] have been recently reviewed thoroughly.

By substituting Eqs. (6.3.6) and (6.3.7) into Eq. (6.3.4), the SED expression can be rewritten as a function of the linear elastic peak stresses $\sigma_{\theta\theta,\theta=0,\text{peak}}$ and $\tau_{r\theta,\theta=0,\text{peak}}$. Then an equivalent peak stress under plain strain conditions can be derived according to the following relationship:

$$\begin{aligned}\Delta\bar{W} &= c_w \left(\frac{e_1}{E} \left[\mathbf{K}_{FE}^* \cdot \Delta\sigma_{\theta\theta,\theta=0,\text{peak}} \cdot \left(\frac{d}{R_0} \right)^{1-\lambda_1} \right]^2 + \frac{e_2}{E} \left[\mathbf{K}_{FE}^{**} \cdot \Delta\tau_{r\theta,\theta=0,\text{peak}} \cdot \left(\frac{d}{R_0} \right)^{1-\lambda_2} \right]^2 \right) \\ &= \frac{1-\nu^2}{2E} \Delta\sigma_{\text{eq,peak}}^2\end{aligned}$$

(6.3.8)

Finally it is obtained:

$$\Delta\sigma_{\text{eq,peak}} = \sqrt{c_w \cdot \left(f_{w1}^2 \cdot \Delta\sigma_{\theta\theta,\theta=0,\text{peak}}^2 + f_{w2}^2 \cdot \Delta\tau_{r\theta,\theta=0,\text{peak}}^2 \right)} \quad (6.3.9)$$

The parameters f_{w1} and f_{w2} weight the peak stresses both around the V-notch (θ direction in Fig. 6.3.1) and along the radial direction (r direction in Fig. 6.3.1). The coefficient f_{w1} turns out to be [87]:

$$f_{w1} = \mathbf{K}_{FE}^* \cdot \sqrt{\frac{2e_1}{1-\nu^2}} \cdot \left(\frac{d}{R_0} \right)^{1-\lambda_1} \quad (6.3.10)$$

while f_{w2} is defined as [44]:

$$f_{w2} = \mathbf{K}_{FE}^{**} \cdot \sqrt{\frac{2e_2}{1-\nu^2}} \cdot \left(\frac{d}{R_0} \right)^{1-\lambda_2} \quad (6.3.11)$$

Values of f_{w1} and f_{w2} according to Eqs. (6.3.10) and (6.3.11) are reported in Tables 6.3.1 and 6.3.2, respectively, with reference to two values of the mean FE size d , namely $d = 1$ mm and 0.50 mm, and two sizes of the control volume for

SED evaluation, $R_0 = 0.28$ mm (structural steels) and 0.12 mm (aluminium alloys) [29,85].

When stress components tied to mode II loading are null (for example: pure opening stresses applied to the weld root) or non-singular (for example: at the weld toe as far as $2\alpha > 102^\circ$), Eq. (6.3.9) can be simplified as:

$$\Delta\sigma_{eq,peak} = \sqrt{c_w} \cdot f_{w1} \cdot \Delta\sigma_{11,peak} \quad (6.3.12)$$

where $\sigma_{11,peak}$ is the maximum principal stress evaluated at the V-notch tip (see Figure 6.3.1).

It should be noted that in the case of as-welded joints Eq. (6.3.12) simplifies to [44,48,87]:

$$\Delta\sigma_{eq,peak} = f_{w1} \cdot \Delta\sigma_{11,peak} \quad (6.3.13)$$

In the context of the PSM, aim of the present work is to apply for the first time the PSM to transverse butt welded joints in aluminium alloys as well as structural steel.

6.3.2. Joint geometries and FE stress analyses according to the Peak Stress Method

6.3.2.1. Butt-welded joints made of aluminium alloy

Three different series of experimental fatigue data concerning butt welded joints made of AlMg4.5Mn aluminium alloy have been taken from the literature. Original data are due to Sonsino et al. [50,51]. Table 6.3.3 summarizes the material, welding process and testing conditions taken into consideration. All main local geometrical parameters (i.e. bead width w_{toe} , toe opening angle 2α and bead height h as well as the length of the lack of penetration zone $2a$, if applicable) are taken from the original references and reported in Table 6.3.4 along with fatigue test details. The bead width w_{toe} and the bead height h have been obtained from the published geometrical parameters, if they were missing in the original papers.

The data refer to partial penetration butt welded joints (Model 1 in Table 6.3.7) and full penetration butt welded joints (Model 2 in Table 6.3.7). All joints consisted of 5- or 25-mm-thick gas metal arc-welded (GMAW) plates. Pulsating ($R = 0$) or completely reversed ($R = -1$) axial fatigue loadings were applied in the experimental tests. In the original papers, the number of cycles to obtain complete failure of the joints was reported and it has been considered as fatigue life in the present investigation.

Table 6.3.3: Material, welding process and testing conditions of aluminium joints.

Ref.	Material	Yield strength [MPa]	Ultimate strength [MPa]	Welding process	Testing condition
Sonsino et al. [50,51]	AlMg4.5Mn	175÷195	303	GMAW	Stress-relieved

Table 6.3.4: Fatigue test details of aluminium joints [50,51]
(joint geometries are reported in Table 6.3.7).

Joint geometry	Load ratio R	Failure location	t [mm]	h [mm]	2α [°]	w_{toe} [mm]	2a [mm]	$\sigma_{11peak,root}/\sigma_{nom}$	$\sigma_{11peak,toe}/\sigma_{nom}$	σ_b/σ_{nom}
1	-1	Weld root	5	1.5	129	6.25	2.5	2.690 ^(a)	2.424 ^(a)	-
1	0	Weld root	5	1.5	129	6.25	2.5	2.690 ^(a)	2.424 ^(a)	-
1	-1	Weld root	25	4.5	137	23.04	7.5	2.529 ^(b)	2.174 ^(b)	-
1	0	Weld root	25	4.5	137	23.04	7.5	2.529 ^(b)	2.174 ^(b)	-
2	-1	Weld toe	5	1.5	148	10.39	-	-	1.586 ^(c)	0.29
2	0	Weld toe	5	1.5	148	10.39	-	-	1.586 ^(c)	0.29

^(a): values calculated adopting a FE global size $d = 0.25$ mm.

^(b): values calculated adopting a FE global size $d = 1.00$ mm.

^(c): values calculated adopting a FE global size $d = 0.50$ mm.

Table 6.3.7 lists the joint geometries and summarises the details of the stress analyses according to the PSM. Two-dimensional, plane strain FE models were defined in order to convert the original experimental data from the nominal stress approach to the equivalent peak stress parameter. For sake of simplicity, the actual geometry of the weld bead has been approximated in the FE models with a trapezoidal shape (see Table 6.3.7), defined as a function of the bead height h , width w_{toe} and inclination angle 2α derived from the original papers. Furthermore, being the notch tip radius ρ at the weld toe lower than 2 mm in all cases under investigation, the assumption of the worst case condition, $\rho = 0$, might be considered acceptable in the FE analyses [54]. For this reason the weld toe and the weld root were modelled as sharp notches (V-shaped or crack-like) in all considered cases. Only one quarter of each welded joint was modelled (see Table 6.3.7), taking advantage of the double symmetry. A free mesh pattern of quadrilateral four-node PLANE 42 elements having a ‘global element size’ equal to d was generated. By doing so, a 2D FE mesh of the type shown in Fig. 6.3.2 was obtained. The mesh size d was chosen in the range from 0.25 mm to 1 mm in order to comply with the conditions of applicability of Eq. (6.3.6). More precisely, the mesh requirement $a/d > 3$ applies as follows: for partial penetration joints $2a$ is the lack of penetration (provided it is lower than or equal to the ligament length), while for the fully penetrated joint geometry a is the main plate thickness.

Since all welded joints were stress-relieved, the influence of the nominal load ratio R was taken into account by applying the PSM through Eq. (6.3.12), which includes the correction parameter c_w defined in Eq. (6.3.5). Moreover, at the weld root of partial-penetration joints mode II stresses are negligible and at the weld toe mode II stresses are non-singular (all geometries considered here are characterised by $2\alpha > 102^\circ$). Therefore Eq. (6.3.12) with f_{w1} relevant to $R_0 = 0.12$ mm (Table 6.3.1), was used to calculate the equivalent peak stress at the points of crack initiation. It is interesting to note that in partial-penetration welded joints, fatigue crack initiation always occurred at the weld root whilst in full-penetration welded joints the critical point was the weld toe. Table 6.3.4 shows that crack initiation location for partial-penetration joints (Model 1 in Table 6.3.7) is correctly estimated by means of the PSM, being the maximum principal stress $\sigma_{11,peak}$

always higher at the weld root than at the weld toe. Therefore the equivalent peak stress will be even higher at the weld root, by virtue of f_w values to use in Eq. (6.3.12).

The presence of a secondary bending effect in the full-penetration butt welded joints, due to an angular distortion about equal to 1° , has been taken into account to evaluate the equivalent peak stress (see the ratio σ_b/σ_{nom} in Tab. 6.3.4). The stress increase caused by secondary bending was computed according to Brandt et al. [90], who re-analysed the data reported by Sonsino et al. [50,51]. The correction factor, $(\sigma_b + \sigma_{nom})/\sigma_{nom}$, was found to be 1.29 for joints with plate thicknesses of 5 mm [90]. It is worth noting that the ratios between the peak stress and the applied nominal stress reported in Table 6.3.4 were obtained under pure axial loading. Since the stress concentration effects are different under axial and bending loadings, an additional FE analysis was performed for joint Model 2 (Table 6.3.7) in order to account for the secondary bending contribution to the peak stress. Finally, Eq. (6.3.14) has been applied to compute the peak stress at the points of crack initiation.

$$\Delta\sigma_{11,peak} = \left(\frac{\sigma_{11,peak}}{\sigma_{nom}} \right)_{axial} \cdot \Delta\sigma_{nom} + \left(\frac{\sigma_{11,peak}}{\sigma_b} \right)_{bend} \cdot \Delta\sigma_b \quad (6.3.14)$$

In the previous expression, $\Delta\sigma_{nom}$ and $\Delta\sigma_b$ are the nominal stress ranges taken from the original references and relevant to axial and secondary bending loadings, respectively, while the ratios $(\sigma_{11,peak}/\sigma_{nom})_{axial}$ and $(\sigma_{11,peak}/\sigma_b)_{bend}$ have been evaluated by means of 2D FE analyses using the mesh according to the PSM.

6.3.2.2. Butt-welded joints made of structural steels

A number of experimental fatigue data related to butt welded joints made of structural steels have been taken from the literature. Original data are due to Petershagen et al. [91], Hentschel et al. [92] and Yakubovskii and Valteris [93]. The materials taken into consideration, the welding processes and testing conditions are reported in Table 6.3.5. All relevant local geometrical parameters (i.e. bead width w_{toe} , toe opening angle 2α and bead height h) were obtained from

the original references and are reported in Table 6.3.6 along with fatigue test details. Similarly to Table 6.3.4, the bead width w_{toe} and the bead height h have been obtained from the published geometrical parameters, if they were missing in the original papers.

The data refer to full penetration two-sided butt welded joints (Model 2 in Table 6.3.7) and one-sided butt welded joints (Model 3 in Table 6.3.7), while the plate thickness ranged between 10 and 20 mm. Axial fatigue loadings were applied in the experimental tests considering different nominal load ratios, namely $R = 0, 0.2$ and -1 . In the original papers, the number of cycles to obtain a complete failure of the welded joints was reported and it has been considered as fatigue life in the present investigation. The fatigue crack initiation always occurred at the weld toe in all joints under investigation, because of the fully penetrated welding execution.

Table 6.3.5: Steel materials, welding processes and testing conditions.

Ref.	Material	Welding process	Testing condition
Petershagen et al. [91]	St 52-3	SAW	As-welded
Hentschel et al. [92] (C)	St 38	MAG	As-welded
Hentschel et al. [92] (F)	St 38	MAW	As-welded
Hentschel et al. [92] (W)	St 38	SAW, TIG	As-welded
Yakubovskii and Valteris [93] (A)	St 3	MAW	As-welded
Yakubovskii and Valteris [93] (B)	15 HSND	EBW	As-welded
Yakubovskii and Valteris [93] (C)	15G2AFD	MAW	As-welded

Joint geometries and details of the stress analyses according to the PSM are reported in Table 6.3.7. The original experimental data expressed in terms of nominal stress have been converted to equivalent peak stress by means of two-dimensional FE models, under plane strain conditions. Again the actual geometry of the weld bead has been approximated in the FE models with a trapezoidal shape (see Table 6.3.7), defined by the bead height h , width w_{toe} and inclination angle 2α derived from the original contributions. The assumption of the worst case condition, notch tip radius $\rho = 0$, has been adopted in the FE analyses by modelling the weld toe as a sharp V-notch. This assumption is acceptable [54]

being ρ at the weld toe lower than 2 mm in all the examined cases. In the case of full penetration two-sided welded joints (Model 2 in Table 6.3.7) only one quarter of each joint has been modelled (see Table 6.3.7), taking advantage of the double symmetry, while in the case of one-sided butt joints (Model 3 in Table 6.3.7) one half has been modelled (see Table 6.3.7).

Table 6.3.6: Fatigue test details of welded joints in steel
(joint geometries are reported in Table 6.3.7).

Ref.	Joint geometry	Load ratio R	t [mm]	h [mm]	2α [°]	w_{toe} [mm]	$\sigma_{11\text{peak,toe}}/\sigma_{\text{nom}}$	$\sigma_b/\sigma_{\text{nom}}$
Petershagen et al. [91] (2)	2	-1	20	1.226	138	17.04	1.519 ^(a)	0.72÷0.76
Petershagen et al. [91] (2)	2	0	20	1.226	138	17.04	1.519 ^(a)	0.48÷0.80
Petershagen et al. [91] (3)	2	-1	20	1.226	138	17.50	1.520 ^(a)	0.71
Petershagen et al. [91] (3)	2	0	20	1.226	138	17.50	1.520 ^(a)	0.71÷0.72
Petershagen et al. [91] (5)	2	-1	20	1.226	150	20.52	1.455 ^(a)	0.57
Petershagen et al. [91] (5)	2	0	20	1.226	150	20.52	1.455 ^(a)	0.60
Petershagen et al. [91] (10)	2	0	20	1.226	133	17.00	1.537 ^(a)	0.68÷0.74
Hentschel et al. [92] (C)	3	0.2	20	3	140	16.48	1.292 ^(b)	-
Hentschel et al. [92] (F)	2	0.2	10	3	148	20.92	1.565 ^(a)	-
Hentschel et al. [92] (W)	2	0.2	20	3	160	34.03	1.376 ^(b)	-
Yakubovskii and Valteris [93] (A)	2	0	16	4	146	26.17	1.475 ^(b)	-
Yakubovskii and Valteris [93] (B)	2	0	16	3	155	27.06	1.596 ^(a)	-
Yakubovskii and Valteris [93] (C)	2	0	16	4	146	26.17	1.475 ^(b)	-

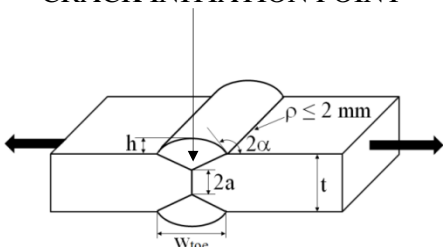
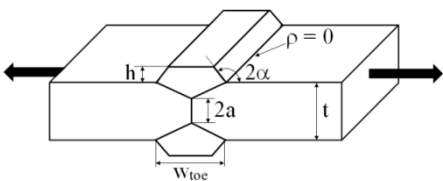
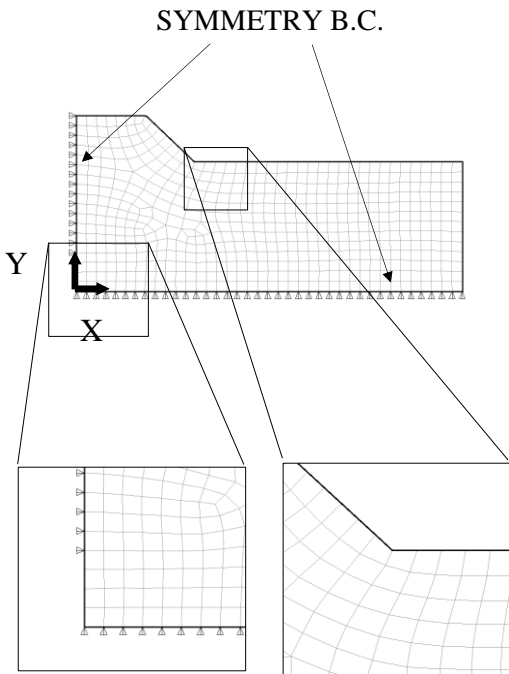
^(a): values calculated adopting a FE global size $d = 1.00$ mm.

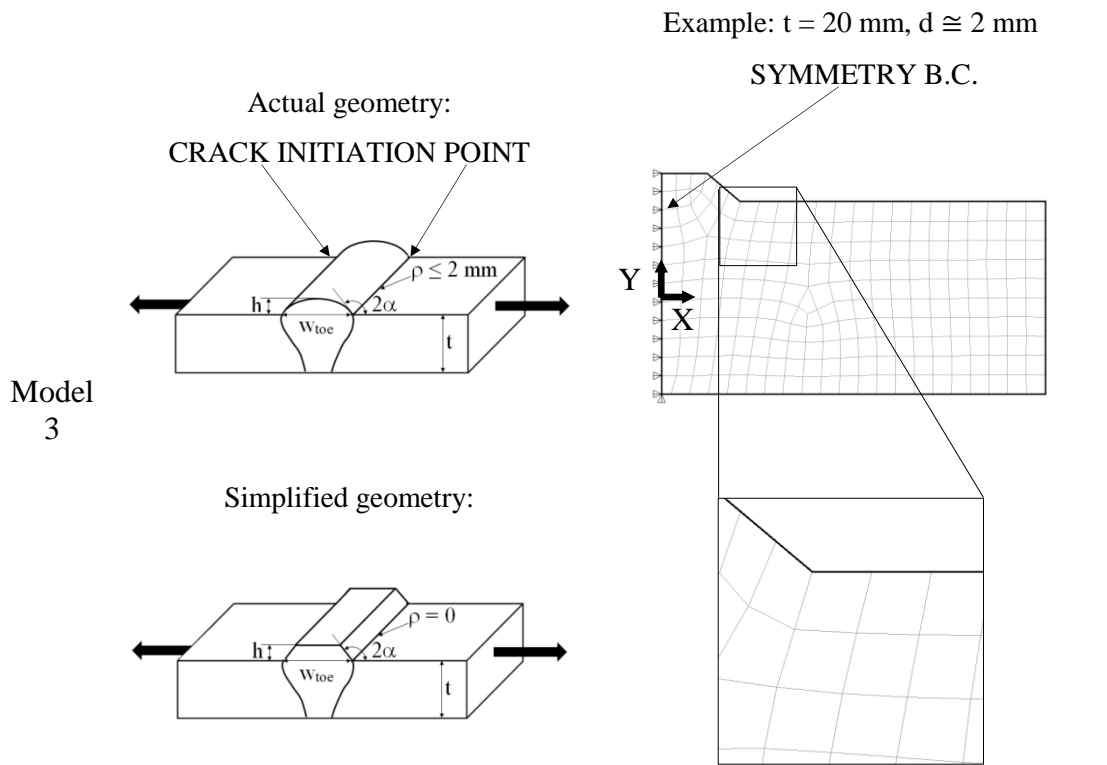
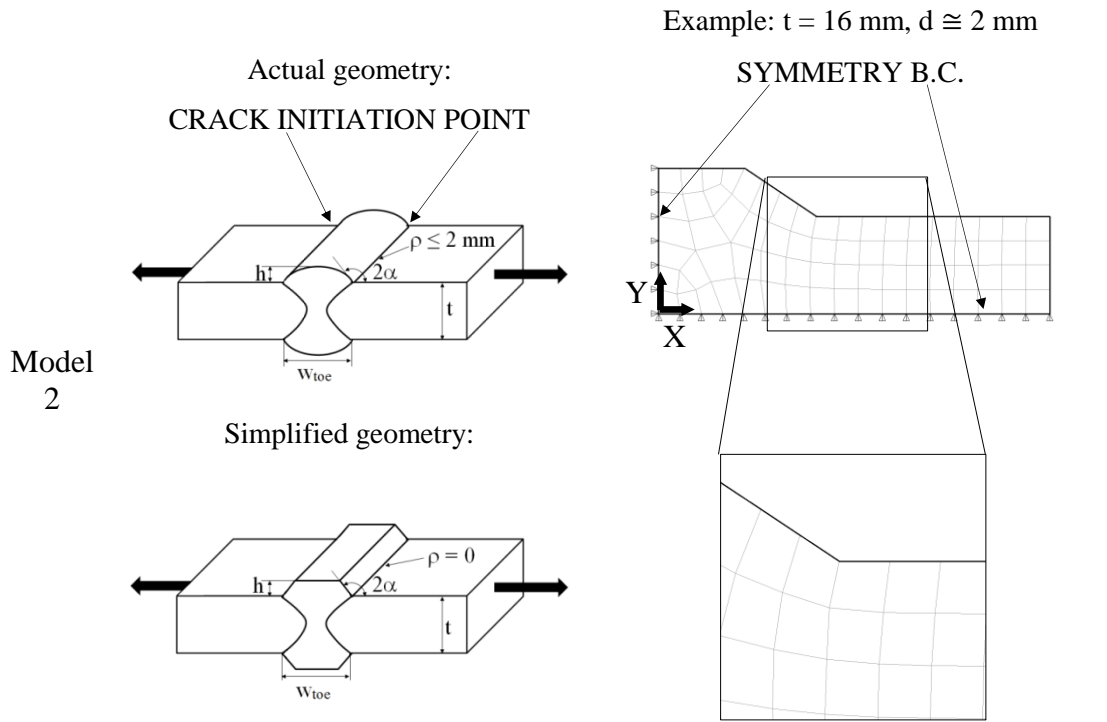
^(b): values calculated adopting a FE global size $d = 2.00$ mm.

The FE analyses were performed adopting a free mesh pattern (see Fig. 6.3.2) of quadrilateral four-node PLANE 42 elements having a ‘global element size’ equal to d . The mesh size d was selected in the range between 1 mm and 2 mm to satisfy the conditions of applicability of the PSM, i.e. t/d greater than 3 when assessing the toe side with negligible mode II stresses and pattern of elements as shown in Figure 6.3.2. Similarly to the FE analysis procedure applied to Model 2 of Table

6.3.4, the ratios between the peak stress and the applied nominal stress reported in Table 6.3.6 were calculated under pure axial loading; therefore, the contribution of secondary bending stress σ_b to the peak stress $\sigma_{11,peak,toe}$ was taken into account by means of a dedicated FE analysis and subsequently by applying Eq. (6.3.14). Since all welded joints were in the as-welded conditions, the influence of the nominal load ratio R was not taken into account; moreover, mode II stresses are non-singular being the toe opening angle 2α greater than 102° in all joints reported in Table 6.3.6. Therefore, the PSM has been applied according to Eq. (6.3.13), where f_{w1} is related to $R_0 = 0.28$ mm (Table 6.3.1).

Table 6.3.7: Joint geometries and FE analyses for fatigue strength assessment according to the PSM.

Model	Joint Geometry – Loading Conditions	FE analyses according to PSM
Model 1	<p data-bbox="525 1021 735 1055">Actual geometry:</p>  <p data-bbox="502 1648 756 1682">Simplified geometry:</p> 	<p data-bbox="924 1032 1342 1111">Example: $t = 25$ mm, $2a = 7.5$ mm, $d \cong 1$ mm</p> 



In the following, specific comments concerning the analysis procedure of each test series are reported.

Data from Petershagen et al. [91]:

All welded joints tested by Petershagen et al. [91] show a significant secondary bending effect due to an angular distortion between 2° and 4° (see the ratio σ_b/σ_{nom} in Tab. 6.3.6). The increase of the stresses caused by secondary bending was quantified in the original paper by means of a correction factor, that is $(\sigma_b + \sigma_{nom})/\sigma_{nom}$, which varied between 1.48 and 1.80 according to the original work [91].

Data from Hentschel et al. [92]:

The series C tested by Hentschel et al. [92] is related to full penetration one-sided butt joints (Model 3 in Table 6.3.7), while series F and W consist of two-sided welded joints (Model 2 in Table 6.3.7).

Data from Yakubovskii and Valteris [93]:

The test series B reported by Yakubovskii and Valteris [93] was manufactured by means of electron beam welding (EBW). The original paper does not report all local geometrical parameters for series B; therefore, the values of the bead height h and the bead width w were assumed equal to those reported by Yakubovskii and Valteris [93] for a test series made of metal-arc welding (MAW) SM50B steel, which has not been considered here. The same assumption was made by Lazzarin et al. in a previous contribution [54]. Concerning test series A and C reported in Table 6.3.6, the original paper [93] reports all geometrical parameters of the weld bead.

6.3.3. Assessment of weld toe and weld root fatigue failures

After analysing the welded joint geometries using the peak stress method, the original fatigue test results expressed in terms of range of nominal stress could be re-converted in terms of range of the linear elastic equivalent peak stress evaluated at the point of crack initiation of each joint using Eq. (6.3.12) for stress-relieved welded joints and Eq. (6.3.13) for as-welded ones.

Experimental results related to butt welded joints made of aluminium alloy are compared in Fig. 6.3.3 with the design scatter band, which has been calibrated previously [43] by fitting about 90 experimental data taken from the literature and relevant only to weld toe failures ($2\alpha \cong 135^\circ$). Such data were generated by testing laboratory specimens in the as-welded conditions with a nominal load ratio close to zero. The specimens were T- or cruciform load-carrying as well as non-load-carrying fillet-welded joints with main plate thickness ranging from 3 to 24 mm and were manufactured by aluminium alloy sheets belonging to the 5000 and 6000 series with a yield stress varying between 250 and 304 MPa [43]. All fatigue failures started from the weld toe ($2\alpha \cong 135^\circ$). While the design scatter band reported in ref. [43] was expressed in terms of range of the linear elastic peak stress evaluated by the finite element method at the weld toe with an average element size $d = 1$ mm, the one reported in Fig. 6.3.3 has been converted to equivalent peak stress using Eq. (6.3.13) and with f_{w1} value reported in Table 6.3.1 ($R_0 = 0.12$ mm, $d = 1$ mm, $f_{w1} = 1.387$). By so doing, either weld toe and weld root failures can be assessed in Fig. 6.3.3, which shows a very good agreement between theoretical estimations and experimental data.

Fig. 6.3.4 compares the experimental data obtained from butt welded joints made of structural steels with the design scatter band, which has been calibrated previously [87] by using about 180 experimental results taken from the literature relevant only to weld toe failures ($2\alpha \cong 135^\circ$). Such data were obtained by testing laboratory specimens in the as-welded conditions with a nominal load ratio R close to zero. The main plate thickness varied between 6 and 100 mm and the joints were made of structural steels characterized by a yield stress ranging from 250 to 690 MPa. T- as well as cruciform fillet-welded joints subject to axial or bending fatigue loading were included in the analysis. A good agreement between

estimations according to the PSM and experimental data has been obtained, as it can be observed from Fig. 6.3.4.

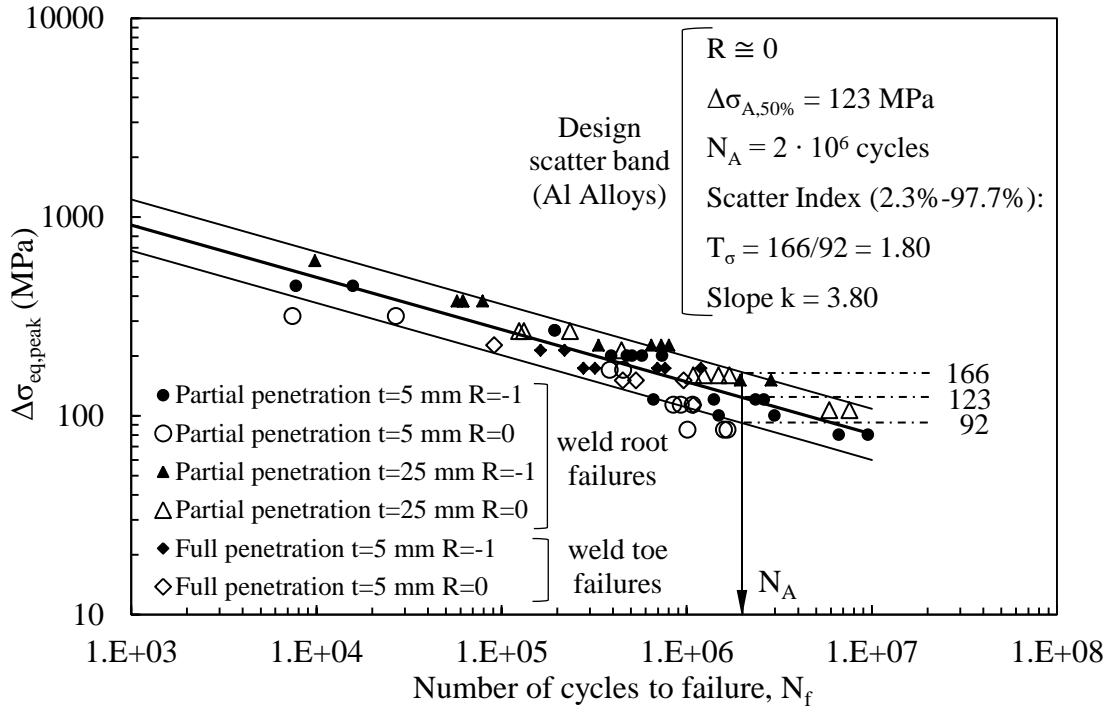


Figure 6.3.3: Fatigue assessment of butt welded joints made of aluminium alloy according to the PSM. Comparison between the design scatter band from refs. [43,45] and experimental results [50,51] analysed here.

The number of cycles reported in Figs. 6.3.3 and 6.3.4 refers to complete failure of the specimens. It should be noted that the NSIF-based approach is expected to correlate the fatigue life related to initiation and short crack propagation inside the small volume where local stresses are governed by the NSIF leading terms. However, as far as small scale laboratory specimens are considered, the total fatigue life is correlated fairly well by the NSIF-based approach [23,27,29,85]. Conversely, in order to analyse the total fatigue life of full size structures, where very long crack propagation paths may exist, the crack propagation life should be analysed separately from the crack initiation life by means of Linear Elastic Fracture Mechanics (LEFM) approach.

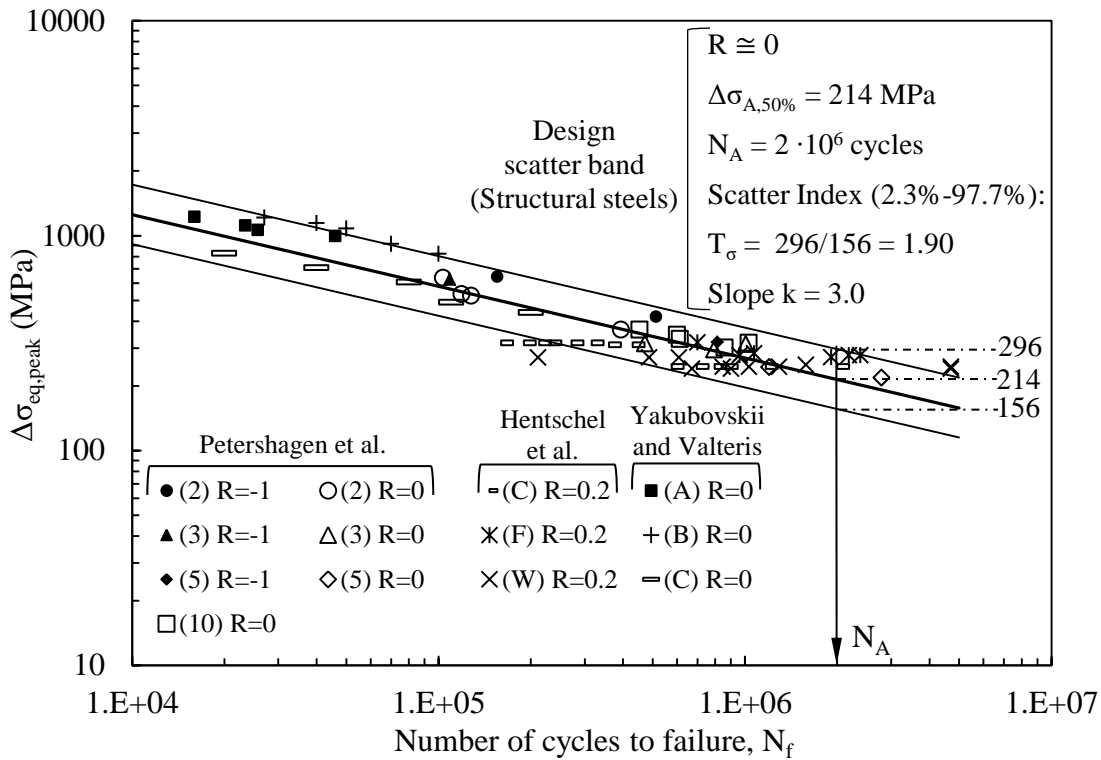


Figure 6.3.4: Fatigue assessment of butt welded joints made of structural steels according to the PSM. Comparison between the design scatter band reported in refs. [44,48,87] and experimental results [91–93] analysed here.

6.3.4. Discussion

The peak stress method (PSM) has been applied to estimate the fatigue strength of butt welded joints made of aluminium alloys and structural steels with toe and root failures.

From a practical point of view, the PSM is an engineering FE-oriented application of the NSIF approach, which basically assumes that the weld toe profile is a sharp V-notch having a tip radius equal to zero, while the root side is a pre-crack in the structure. It takes advantage of the elastic peak stresses evaluated from FE analyses carried out by using a given mesh pattern, where the element type is kept constant and the element size can be chosen arbitrarily within the applicability range of the method.

A properly defined equivalent peak stress based on the strain energy density enables one to estimate the failure location (either the weld toe or the weld root)

and secondly to correlate the fatigue strength of butt welded joints of different thickness and local weld bead geometry. The design scatter bands in terms of equivalent peak stress, which had been calibrated originally by means of experimental results generated from fillet welded joints with toe failures only, have been successfully adopted here to assess the fatigue strength of aluminium and steel butt welded joints, respectively, with toe and root failures.

The comparison between the theoretical estimations and the experimental fatigue test results was satisfactory both for aluminium and for steel welded joints. Because of the simplicity of a point-like method combined with the robustness of the NSIF approach, it is believed that the PSM may be useful in the design practice of industrial application.

6.4 Link between the Peak Stress Method (PSM) and the averaged Strain Energy Density (SED): cracked bars under mixed mode (I+III) loading ^(*)

Nomenclature

a	crack length
a_0	El Haddad-Smith-Topper length parameter of the material
d	mean size of a finite element
$\Delta K_{I,th}$	threshold value of the SIF range for long cracks under mode I loading conditions
$\Delta K_{III,th}$	threshold value of the SIF range for long cracks under mode III loading conditions
e_1, e_2, e_3	parameters for averaged SED evaluation
E	elastic modulus
K_I, K_{II}, K_{III}	mode I, mode II and mode III SIFs
$K_{FE}^*, K_{FE}^{**}, K_{FE}^{***}$	non-dimensional K_I, K_{II} and K_{III} relevant to the peak stress method (constant parameters)
MM	mode mixity ratio
R_0	radius of the control volume for the averaged SED evaluation
$R_{0,I}$	radius of the control volume for the averaged SED evaluation under mode I loading
$R_{0,III}$	radius of the control volume for the averaged SED evaluation under mode III loading
r, θ	polar coordinates
T	slit-parallel tensile or compressive stress, T-stress
\overline{W}_{AN}	analytical, closed-form expression of the averaged SED, taking into account only SIFs contributions
\overline{W}_{FEM}	averaged SED calculated by FEM using very refined meshes (direct approach)

$\overline{W}_{FEM,coarse}$	averaged SED calculated by FEM using coarse meshes (direct approach with coarse mesh option)
$\overline{W}_{PSM,I+II}$	averaged SED calculated according to the PSM (only mode I and II SIFs contributions are taken into account)
$\overline{W}_{PSM,I+III}$	averaged SED calculated according to the PSM (only mode I and III SIFs contributions are taken into account)
x,y,z	Cartesian coordinates

Symbols

2α	opening angle
$\Delta\sigma_0$	plain material axial fatigue limit in terms of stress range
$\Delta\tau_0$	plain material torsion fatigue limit in terms of stress range
ν	Poisson's ratio
σ_{nom}	nominal direct stress
$\sigma_{xx}, \sigma_{yy}, \tau_{xy}$	normal and shear stress components in the Cartesian frame of reference
$\sigma_{yy,peak}$	singular, linear elastic, opening peak stress evaluated at the crack tip by FEM using the PSM
$\tau_{xy,peak}$	singular, linear elastic, sliding peak stress evaluated at the crack tip by FEM using the PSM
τ_{xz}, τ_{yz}	anti-plane shear stress components in the Cartesian frame of reference
$\tau_{yz,peak}$	singular, linear elastic, anti-plane peak stress evaluated at the crack tip by FEM using the PSM

Abbreviations

PSM	Peak stress method
SED	Strain energy density
SIFs	Stress intensity factors

(*) See also:

Meneghetti, G.; Campagnolo, A; Berto, F. Averaged strain energy density estimated rapidly from the singular peak stresses by FEM: cracked bars under mixed-mode (I+III) loading. Engineering Fracture Mechanics (Under review).

6.4.1 Introduction

The strain energy density (SED) averaged over a control volume, thought of as a material property and modelled as a circular sector of radius R_0 according to Lazzarin and Zambardi [23] (see Fig. 6.4.1a), proved to efficiently account for notch effects both in static [32,79,94,95] and fatigue [29,34,81,96–98] structural strength problems. The idea is reminiscent of the stress averaging to perform inside a material dependent structural volume, according to the approach proposed by Neuber [99–101]. The control radius R_0 for fatigue strength assessment of notched components has been defined by equaling the averaged SED in two situations, i.e. the fatigue limit of un-notched and cracked specimens, respectively [29,81,82]. Therefore R_0 combines two material properties: the plain material fatigue limit (or the high-cycle fatigue strength of smooth specimens) and the threshold value of the SIF range for long cracks. The following expressions have been derived [29,81,82]:

$$R_{0,I} = 2e_1 \cdot \left(\frac{\Delta K_{I,th}}{\Delta \sigma_0} \right)^2 = \frac{(1+\nu)(5-8\nu)}{4\pi} \cdot \left(\frac{\Delta K_{I,th}}{\Delta \sigma_0} \right)^2 \quad (6.4.1)$$

$$R_{0,III} = \frac{e_3}{1+\nu} \cdot \left(\frac{\Delta K_{III,th}}{\Delta \tau_0} \right)^2 \quad (6.4.2)$$

It should be noted that, in principle, the control radius R_0 could assume different values under mode I and mode III, so that the energy contributions related to the two different loading conditions should be averaged in control volumes of different size. The idea of a control volume size dependent on the loading mode has been proposed for the first time in [81] dealing with the multiaxial fatigue strength assessment of notched specimens made of 39NiCrMo3 steel, then it has been successfully applied also for the fatigue strength assessment of notched

components made of AISI 416 [96], cast iron EN-GJS400 [97] and titanium grade 5 alloy Ti-6Al-4V [34] subjected to combined tension and torsional loading. In particular, for welded construction steels a single radius $R_0 = 0.28$ mm was assumed [29] and is adopted here as a reference value. It is important to underline that using a Poisson's coefficient $\nu = 0.30$, Eq. (6.4.1) (being valid under plain strain hypothesis) can be re-written as follows [29,82]:

$$R_{0,I} = 0.85 \cdot \frac{1}{\pi} \cdot \left(\frac{\Delta K_{I,th}}{\Delta \sigma_0} \right)^2 \rightarrow 0.85 \cdot a_0 \quad (6.4.3)$$

Therefore, R_0 in Fig. 6.4.1a results on the order of the El Haddad-Smith-Topper length parameter [83].

Dealing with a general mixed mode crack problem, the averaged SED was expressed in closed-form as a function of the stress intensity factors (SIFs), K_I , K_{II} and K_{III} , according to the following analytical expression [102]:

$$\overline{W}_{AN} = \frac{e_1}{E} \frac{K_I^2}{R_0} + \frac{e_2}{E} \frac{K_{II}^2}{R_0} + \frac{e_3}{E} \frac{K_{III}^2}{R_0} \quad (6.4.4)$$

In the above equation, e_1 , e_2 and e_3 are known parameters dependent on the opening angle of a general sharp V-notch (2α) and of the Poisson's ratio ν [23,102] (see Table 6.4.1), while E is the Young's modulus of the considered material. Equation (6.4.4) is valid when the influence of the higher-order, non-singular terms can be neglected inside the control volume. The mode I and mode II SIFs can be defined according to Gross and Mendelson [30] by means of Eqs. (6.4.5) and (6.4.6), respectively.

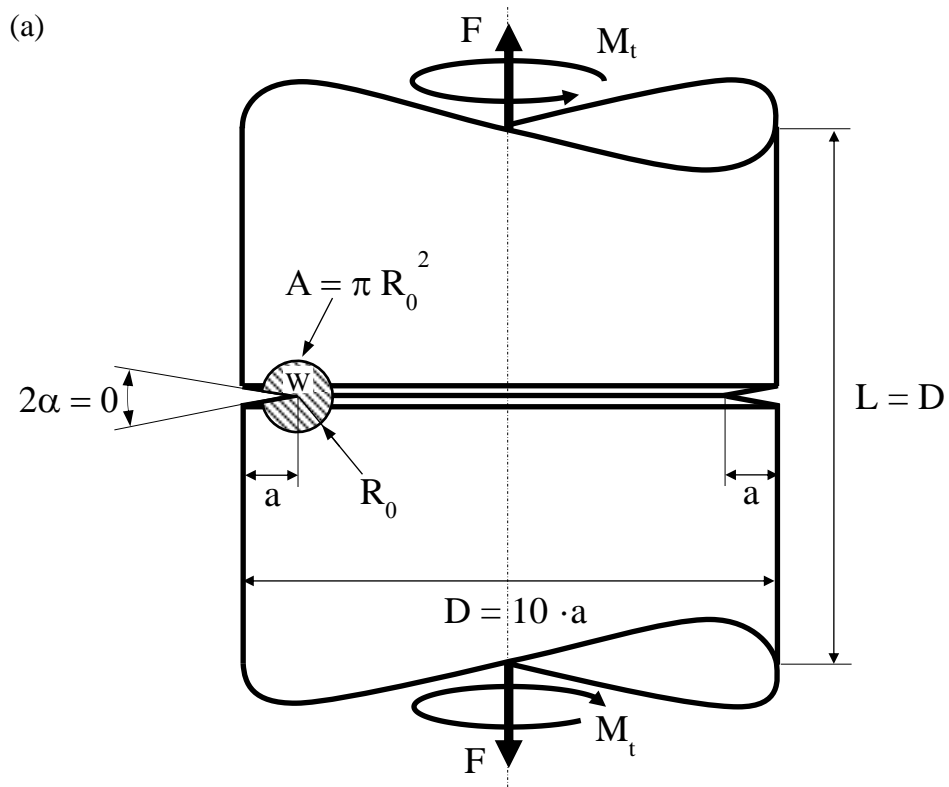
$$K_I = \sqrt{2\pi} \cdot \lim_{r \rightarrow 0} \left[(\sigma_{yy})_{\theta=0} \cdot r^{0.5} \right] \quad (6.4.5)$$

$$K_{II} = \sqrt{2\pi} \cdot \lim_{r \rightarrow 0} \left[(\tau_{xy})_{\theta=0} \cdot r^{0.5} \right] \quad (6.4.6)$$

Similarly, by extending previous definitions, the mode III SIF can be defined by means of Eq. (6.4.7).

$$K_{III} = \sqrt{2\pi} \cdot \lim_{r \rightarrow 0} [(\tau_{yz})_{\theta=0} \cdot r^{0.5}] \quad (6.4.7)$$

The above equations, (6.4.5), (6.4.6) and (6.4.7), are referred to the Cartesian stress components expressed as functions of the polar coordinates (r, θ) , with origin at the crack tip (see Fig. 6.4.1b); however, it should be noted that along the crack bisector line the polar reference system (r, θ) coincides with the Cartesian one (x, y) , so that $\sigma_{\theta\theta} = \sigma_{yy}$, $\tau_{r\theta} = \tau_{xy}$ and $\tau_{\theta z} = \tau_{yz}$.



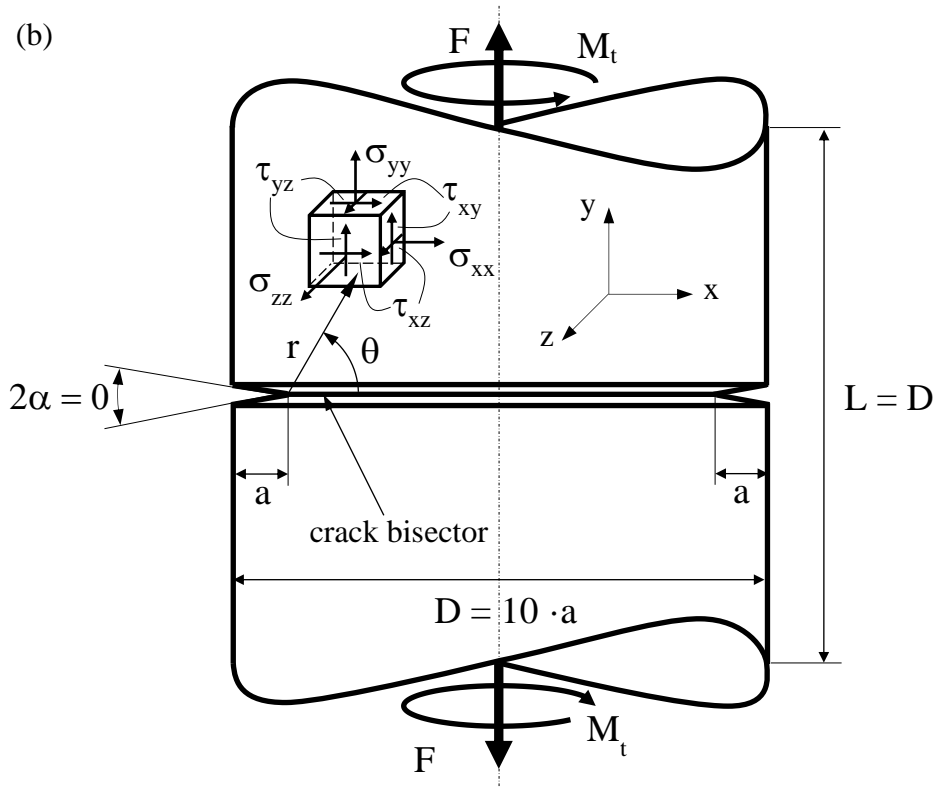


Figure 6.4.1: Out-of-plane mixed mode I+III crack problem: (a) Strain energy density averaged over a control volume (area) of radius R_0 surrounding the crack tip, $\bar{W} = \frac{W}{A}$. (b) Cartesian stress components and polar coordinates with origin at the crack tip. F and M_t are the axial and torsion loadings, respectively.

Table 6.4.1: Parameters for averaged SED evaluation in the crack case ($2\alpha = 0^\circ$) for a Poisson's ratio $\nu = 0.30$.

2α (deg)	$\lambda_1, \lambda_2, \lambda_3$	$\nu = 0.30$		
		$e_1^{(a)}$	$e_2^{(a)}$	$e_3^{(b)}$
0	0.500	0.133	0.340	0.414

^(a) values under plane strain conditions [23]

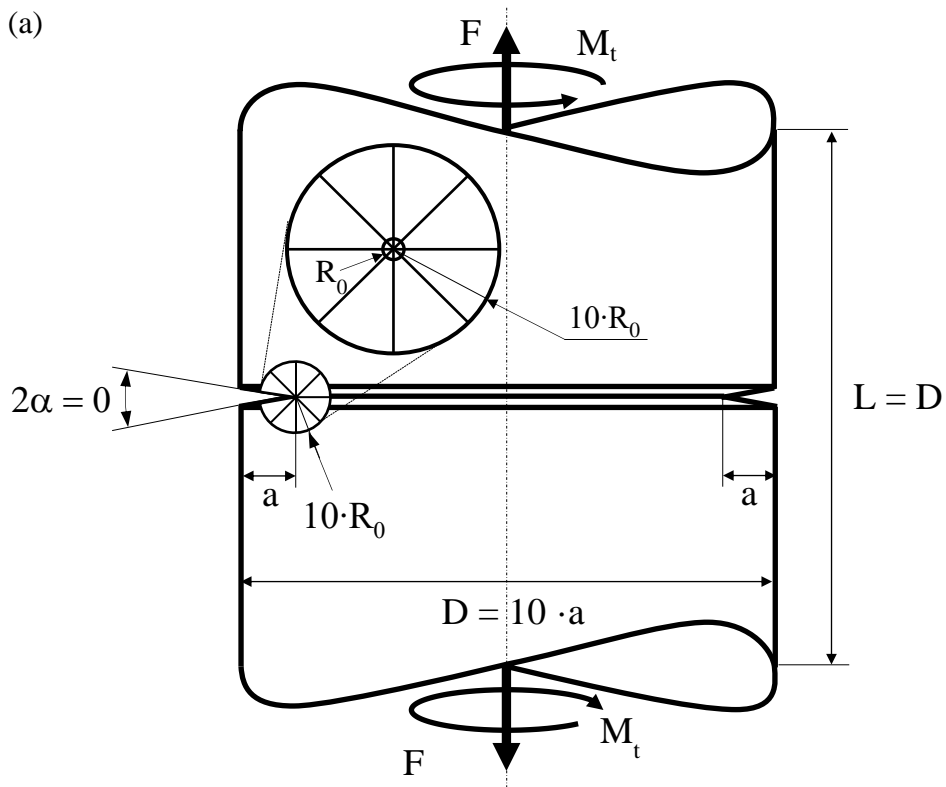
^(b) values under axis-symmetric conditions [102]

The use of Eq. (6.4.4) in engineering applications presents a major drawback, because the entire local stress field must be determined accurately to evaluate the SIFs according to definitions (6.4.5), (6.4.6) and (6.4.7); therefore, very refined

meshes are required. Mesh preparation and solving the model is even more time-consuming in the case of 3D FE models.

Despite this, the averaged SED can also be evaluated directly from the FE results, \bar{W}_{FEM} , by summation of the strain-energies $W_{FEM,i}$ calculated for each i -th finite element belonging to the control area and by dividing by the area (A in Fig. 6.4.1a):

$$\bar{W}_{FEM} = \frac{\sum_A W_{FEM,i}}{A} \quad (6.4.8)$$



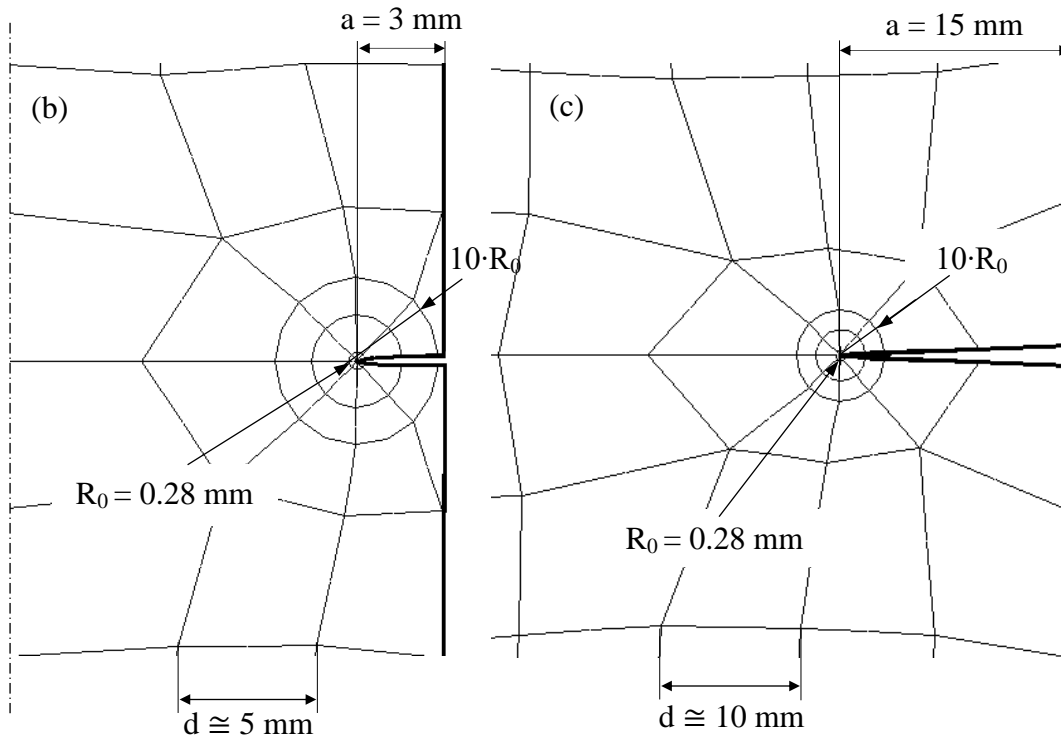


Figure 6.4.2: Out-of-plane mixed mode I+III crack problem: averaged SED evaluated according to the direct approach (Eq. (6.4.8)) with coarse mesh option, $\bar{W}_{\text{FEM,coarse}}$ [37]; (a) geometry and loading conditions; (b) and (c) coarsest FE mesh (second order harmonic plane elements, PLANE 83 of the Ansys® element library) producing a reduced error of 5% in the cases $a = 3$ mm and $a = 15$ mm with $\text{MM} = 0.50$. Control radius $R_0 = 0.28$ mm.

Equation (6.4.8) represents the so-called direct approach to calculate the averaged SED. According to a recent contribution of Lazzarin et al. [37], very coarse FE meshes within the control volume A can be used. The required geometric model to apply the direct approach with coarse mesh option [37] is reported in Figure 6.4.2a with reference to an axisymmetric mixed mode (I+III) problem, while Figures 6.4.2b and 6.4.2c show two examples of the coarsest FE meshes that can be adopted.

The adopted finite element is the second order harmonic plane element, PLANE 83 of the Ansys® element library. Figures 6.4.2b,c show that eight finite elements have been generated inside the control volume, while two concentric rings, each one made up of eight elements, have been located outside the reference volume and, precisely, in the annulus $R_0 < r < 10 \cdot R_0$; finally a free FE mesh characterized

by a mean element size d has been adopted in the external region $r > 10 \cdot R_0$. The FE meshes reported in Figures 6.4.2b and 6.4.2c are as coarse as possible in order to obtain a deviation between $\bar{W}_{\text{FEM,coarse}}$ and \bar{W}_{FEM} lower than 5% in the case of a mode mixity ratio MM equal to 0.5. The mode mixity MM is defined according to Eq. (6.4.9):

$$\text{MM} = \frac{K_{\text{III}}}{K_{\text{I}} + K_{\text{III}}} \quad (6.4.9)$$

while $\bar{W}_{\text{FEM,coarse}}$ and \bar{W}_{FEM} are the averaged SED calculated using Eq. (6.4.8) and by adopting the coarse mesh and a very refined mesh (about 500 finite elements inside the control volume), respectively. Due to the very refined FE mesh employed, \bar{W}_{FEM} is considered the exact value.

Recently, the peak stress method (PSM) has been proposed to rapidly calculate the averaged SED using the singular, linear elastic peak stresses evaluated at the tip of cracks with FE analyses and coarse meshes. The PSM allows to avoid modeling the control volume, while keeping the coarse mesh option. Strictly speaking, the PSM rapidly estimates the SIFs using coarse FE meshes, but thanks to Eq. (6.4.4) the averaged SED can also be estimated, provided that the contribution of higher-order, non-singular terms (which are not included in Eq. (6.4.4)) is negligible. The PSM takes its origins by a numerical technique proposed by Nisitani and Teranishi [41,42] to rapidly estimate by FEM the SIF of a crack emanating from an ellipsoidal cavity. A theoretical justification to the PSM has been provided later on and the method has been extended also to sharp and open V-notches in order to rapidly evaluate the mode I Notch Stress Intensity Factor (NSIF) [43]. Subsequently, the PSM has been formalised to include also cracked components under mode II loading conditions [44] and open V-notches subjected to pure mode III (anti-plane) stresses [103]. The local strain energy density concept and its relation to the peak stress method have been recently reviewed thoroughly by Radaj [89].

In more detail, the PSM enables to rapidly estimate the SIFs K_{I} , K_{II} and K_{III} (Eqs. (6.4.5)-(6.4.7)) from the crack tip singular, linear elastic, opening, sliding and

tearing FE peak stresses $\sigma_{yy,peak}$, $\tau_{xy,peak}$ and $\tau_{yz,peak}$, respectively, which are referred to the bisector line according to Fig. 6.4.3, concerning the in-plane stress components, and Fig. 6.4.4a, as to the out-of-plane stress component. More precisely, the following expressions are valid [43,44,103]:

$$K_{FE}^* = \frac{K_I}{\sigma_{yy,peak} \cdot d^{0.5}} \cong 1.38 \quad (6.4.10)$$

$$K_{FE}^{**} = \frac{K_{II}}{\tau_{xy,peak} \cdot d^{0.5}} \cong 3.38 \quad (6.4.11)$$

$$K_{FE}^{***} = \frac{K_{III}}{\tau_{yz,peak} \cdot d^{0.5}} \cong 1.93 \quad (6.4.12)$$

where d is the so-called ‘global element size’ parameter to input in Ansys[®] FE code, i.e. the average FE size adopted by the free mesh generation algorithm available in the FE code. Eqs. (6.4.10)-(6.4.12) were derived using particular 2D or 3D finite element types and sizes, so that a range of applicability exists, which has been presented in detail in previous contributions [43,44,103], to which the reader is referred. Here it is worth recalling that for mode I loading (Eq. (6.4.10)) the mesh density ratio a/d that can be adopted in numerical analyses must be $a/d \geq 3$, a being the minimum between the crack and the ligament lengths; for mode II loading (Eq. (6.4.11)) more refined meshes are required, the mesh density ratio a/d having to satisfy $a/d \geq 14$; in case of mode III loading (Eq. (6.4.12)) the condition $a/d \geq 3$ must again be satisfied, as it will be presented in the next section.

As an example, Fig. 6.4.4b shows a free mesh where the average FE size d to input in Ansys[®] software, is in constant proportion with the crack length a , $a/d = 3$. The mesh pattern shown in Fig. 6.4.4b is as coarse as possible to estimate the averaged SED with a 10% error using next Eq. (6.4.13). It is important to underline that no additional input parameters other than d and no additional special settings are required to generate an FE mesh according to the PSM. When Eqs. (6.4.10)-(6.4.12) were calibrated [43,44,103], the ‘exact’ K_I , K_{II} and K_{III} SIFs

were evaluated using definitions (6.4.5)-(6.4.7), respectively, applied to FE results of numerical analyses characterized by very refined meshes, where the element size close to the crack tip was reduced to about 10^{-5} mm. Therefore, the FE size required to estimate K_I , K_{II} and K_{III} from $\sigma_{yy,peak}$, $\tau_{xy,peak}$ and $\tau_{yz,peak}$, respectively, is likely to be some orders of magnitude larger than that needed to directly calculate the local stress fields in order to apply definitions (6.4.5)-(6.4.7). Moreover, while Eqs. (6.4.5)-(6.4.7) require to process a number of stress-distance numerical results, the PSM requires a single stress value to evaluate the SIFs.

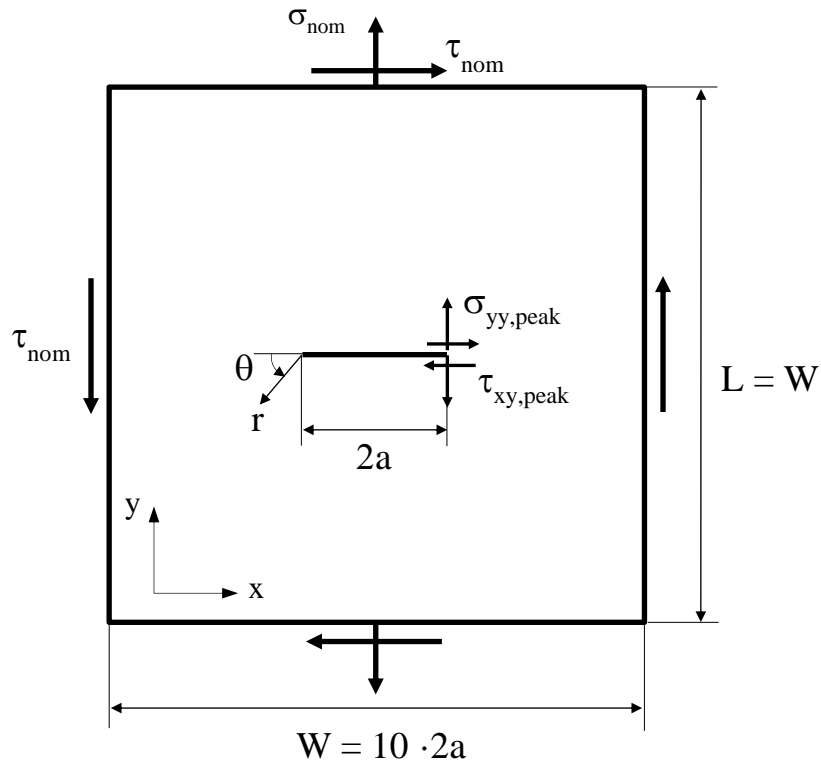


Figure 6.4.3: In-plane mixed mode I+II loading: averaged SED evaluated according to the peak stress approach (Eq. (6.4.14)) [84,104]. Geometry and loading conditions.

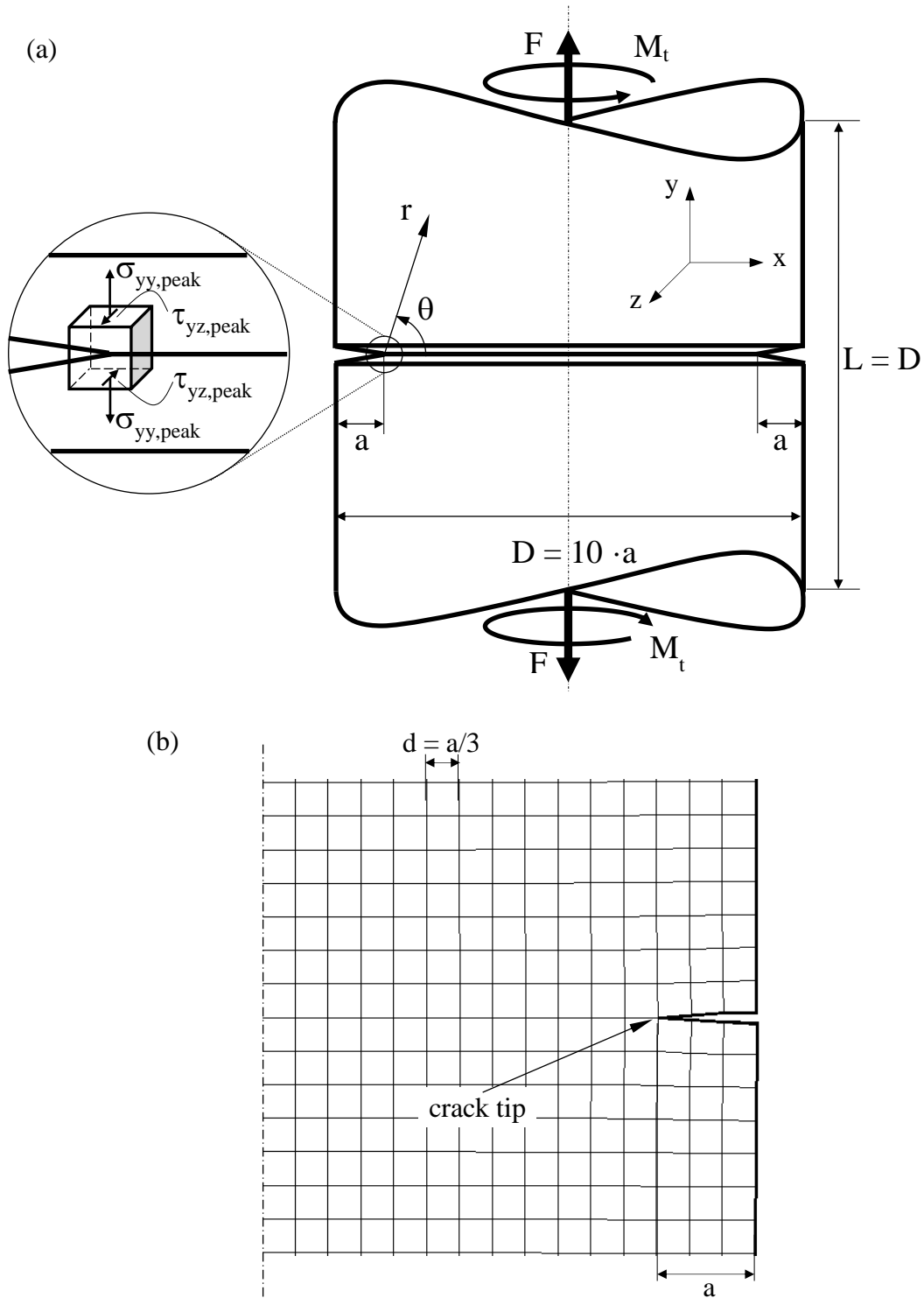


Figure 6.4.4: Mixed mode I+III crack problem: averaged SED evaluated according to the peak stress approach (Eq. (6.4.13)); (a) geometry and loading conditions. (b) Coarsest FE mesh (first order harmonic plane elements, PLANE 25 of Ansys® element library) to obtain a reduced error of 10%, for any mode mixity ratio MM and crack length a .

The novelties of the present investigation can be summarised as follows:

- to present the peak stress approach to rapidly estimate the averaged SED of out-of-plane mixed mode I+III crack tip fields and discuss the range of applicability of the method;
- to validate the peak stress approach by analysing circumferentially cracked bars, while varying (i) the crack length, (ii) the mode mixity and (iii) the average finite element size adopted in the numerical analyses.

6.4.2 The peak stress approach to estimate the averaged SED under mixed mode I+III loading

To illustrate the PSM applied to cracks under out-of-plane mixed mode loading, K_I and K_{III} have been estimated using Eqs. (6.4.10) and (6.4.12) for a number of crack sizes, that will be considered also later on for the averaged SED calculations. A bar weakened by a circumferential outer crack and subjected to out-of-plane mixed mode I+III loading was considered according to Fig. 6.4.1. Several crack lengths a (from 3 to 50 mm) have been considered, while diameter D and length L of the bar were set both equal to 10 times the crack length. The mode mixity ratio MM , defined according to Eq. (6.4.9), has been varied from pure mode I ($MM = 0$) to pure mode III ($MM = 1$) loading conditions.

The average FE size d to evaluate the peak stresses $\sigma_{yy,peak}$ and $\tau_{yz,peak}$ (see Fig. 6.4.4a) in Eqs. (6.4.10) and (6.4.12) was varied from 0.05 to 10 mm. All different geometrical and loading parameters taken into account in the present investigation are listed in Table 6.4.2. According to the PSM, FE analyses have been carried out by means of Ansys[®] software and by adopting free mesh patterns consisting of two-dimensional, harmonic, 4-node linear quadrilateral elements (PLANE 25 of Ansys[®] element library). The adopted finite element enables to analyse axis-symmetric components subjected to external loads that can be expressed according to a Fourier series expansion. Therefore, it can be employed for modelling three-dimensional axis-symmetric components under axial, bending or torsional loadings, keeping the advantage of treating two-dimensional FE analyses. After setting the chosen d value as the ‘global element size’ in Ansys[®]

meshing environment, the free mesh generation algorithm was run and mesh patterns like that reported in Fig. 6.4.4b were obtained. Finally the nodal peak stresses $\sigma_{yy,peak}$ and $\tau_{yz,peak}$ at the crack tip were taken. The exact mode I and mode III stress intensity factors, K_I and K_{III} , to input in Eqs. (6.4.10) and (6.4.12), were evaluated by means of definitions (6.4.5) and (6.4.7) applied to the results of dedicated FE analyses with very refined FE meshes (the smallest adopted element size being on the order of 10^{-5} mm) in the close neighbourhood of the crack tip.

Table 6.4.2: Geometrical and loading parameters taken into consideration in the present investigation. All combinations have been analysed, provided that the ratio a/d was greater than or equal to the minimum feasible one, i.e. $a/d = 1$.

Parameter	Values
a [mm]	3, 4, 6, 8, 10, 15...45, 50
d [mm]	0.05, 0.1, 0.2, 0.5, 1, 2, 3, 4, 5, 10
MM	0, 0.2, 0.4, 0.5, 0.6, 0.8, 1
R₀ [mm]	0.28

The obtained results are reported in Fig. 6.4.5, in terms of non-dimensional stress intensity factors K_{FE}^* and K_{FE}^{***} according to Eqs. (6.4.10) and (6.4.12), respectively. It should be noted that the results shown in Fig. 6.4.5 are valid for all considered mode mixity ratios MM, since mode I and mode III stress fields are always mutually independent. It can be observed that K_{FE}^* and K_{FE}^{***} converge to the values 1.38 and 1.93, respectively, inside a scatter-band of $\pm 3\%$, in accordance with the results previously obtained for pure mode I [22] and pure mode III [43,103]. Convergence is assured when the ratio a/d is greater than 3 for both mode I and mode III contributions. While the minimum mesh density ratio $a/d = 3$ (required to have $K_{FE}^* \cong 1.38$) is in agreement with that obtained in previous contributions [43,84,104,105], it had been found $a/d > 12$ in order to have $K_{FE}^{***} \cong 1.93$ in ref. [103]. Such difference in the case of mode III loading is justified because in the present contribution a is the crack depth, while in [103], dealing with the weld root side of tube-to-flange welded joints, a was the tube thickness.

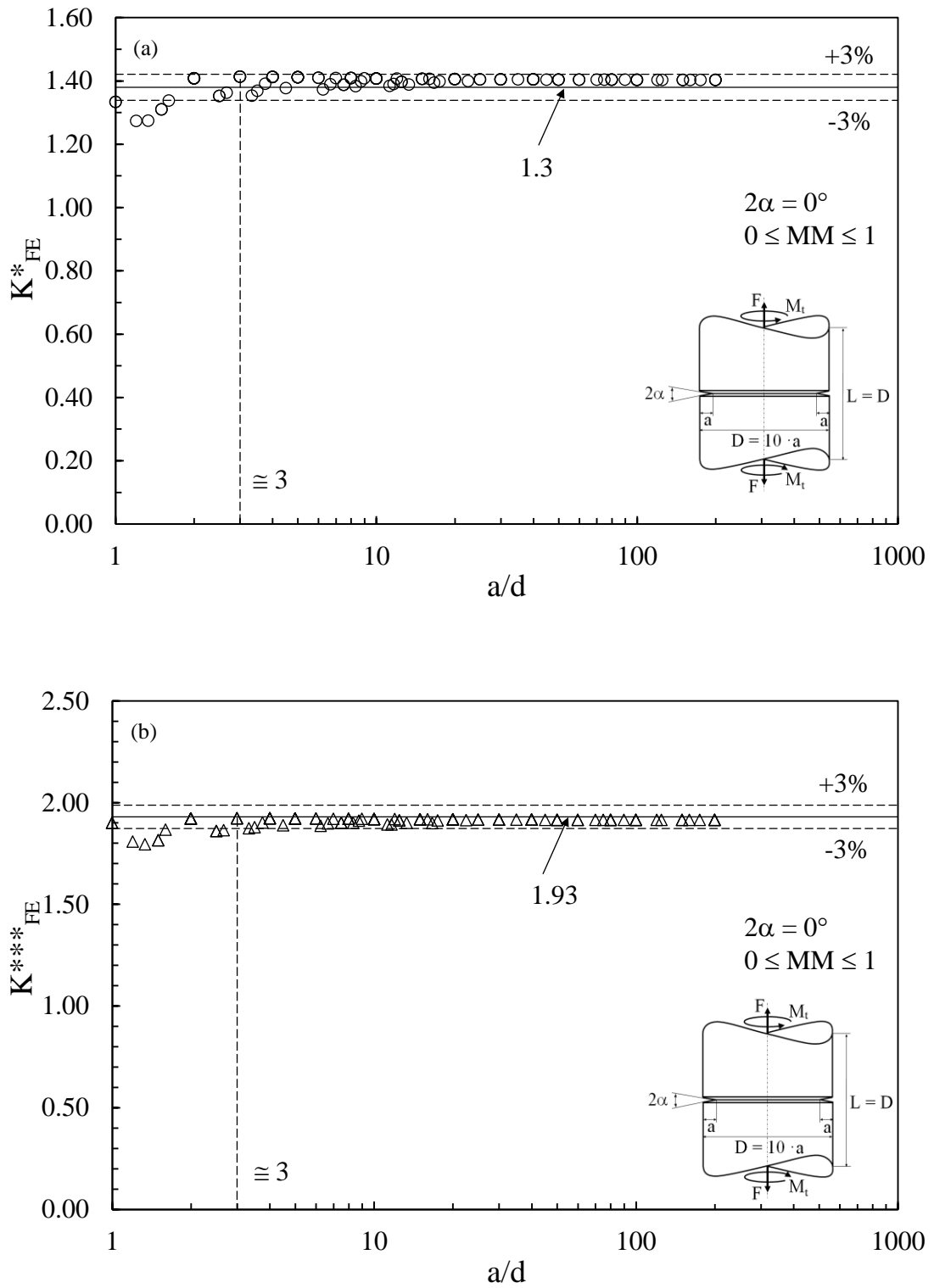


Figure 6.4.5: Convergence of the PSM applied to cracks ($2\alpha = 0^\circ$) under out-of-plane mixed mode I+III loading ($0 \leq MM \leq 1$): (a) mode I and (b) mode III non-dimensional SIFs according to Eqs. (6.4.10) and (6.4.12).

Provided that the minimum mesh density requirements to apply Eqs. (6.4.10) and (6.4.12) are satisfied, substitution into Eq. (6.4.4) particularized for mixed mode I+III loading ($K_{II} = 0$), immediately delivers the following expression:

$$\bar{W}_{\text{PSM,I+III}} = \frac{e_1}{E} \left[K_{\text{FE}}^* \cdot \sigma_{yy,\text{peak}} \cdot \left(\frac{d}{R_0} \right)^{0.5} \right]^2 + \frac{e_3}{E} \left[K_{\text{FE}}^{***} \cdot \tau_{yz,\text{peak}} \cdot \left(\frac{d}{R_0} \right)^{0.5} \right]^2 \quad (6.4.13)$$

which can be employed to rapidly estimate the averaged SED according to the PSM.

A similar expression had been derived under in-plane mixed mode I+II loading (see Fig. 6.4.3 [84,104]).

$$\bar{W}_{\text{PSM,I+II}} = \frac{e_1}{E} \left[K_{\text{FE}}^* \cdot \sigma_{yy,\text{peak}} \cdot \left(\frac{d}{R_0} \right)^{0.5} \right]^2 + \frac{e_2}{E} \left[K_{\text{FE}}^{**} \cdot \tau_{xy,\text{peak}} \cdot \left(\frac{d}{R_0} \right)^{0.5} \right]^2 \quad (6.4.14)$$

Afterwards, Eq. (6.4.14) has been corrected to include the case of small cracks, i.e. cracks that are small if compared to the control radius R_0 , or, alternatively stated, cracks where the stress fields within the control volume (A in Fig. 6.4.1a) are no longer governed solely by the leading order terms, but also by higher order terms and primarily the T-stress [105]. Similarly, Eq. (6.4.4) contains only the leading order terms. Therefore its range of applicability must be checked.

6.4.3. Range of applicability of the SED expression (6.4.4)

The range of applicability of Eq. (6.4.4), which Eq. (6.4.13) is based on, is analysed in the present section. In view of this, the same geometry described in the previous Section has been considered (see Fig. 6.4.1), but a new set of crack depths has been considered with respect to that reported in Table 6.4.2, a having been varied between 1 and 50 mm. The control radius R_0 was varied between 0.01 and 50 mm, provided that the ratio a/R_0 was always greater than or equal to 1. The averaged SED was first evaluated from Eq. (6.4.4), \bar{W}_{AN} , particularized for mixed mode I+III loading ($K_{II} = 0$) and using the exact SIFs K_I and K_{III} evaluated from very refined FE analyses according to Eqs. (6.4.5) and (6.4.7), respectively. Secondly, the exact averaged SED values were calculated using the direct

approach, \bar{W}_{FEM} , according to Eq. (6.4.8) (with about 500 finite elements inside the control volume).

Figure 6.4.6 plots the ratio between analytical (\bar{W}_{AN} , Eq. (6.4.4)) and exact (\bar{W}_{FEM} , direct approach Eq. (6.4.8)) averaged SED values for pure mode I (MM = 0) and pure mode III (MM = 1) loading. The figure highlights that for a crack size equal to radius of the material dependent control volume ($a/R_0 = 1$) the error in the averaged SED estimation is about -15% for pure mode I loading (MM = 0), while it increases to about +30% for pure mode III loading (MM = 1). These deviations are due to the contribution of higher-order, non-singular terms, which is disregarded in the analytical expression, Eq. (6.4.4). These effects can be better understood by analysing separately the local stress fields tied to mode I and mode III loading conditions.

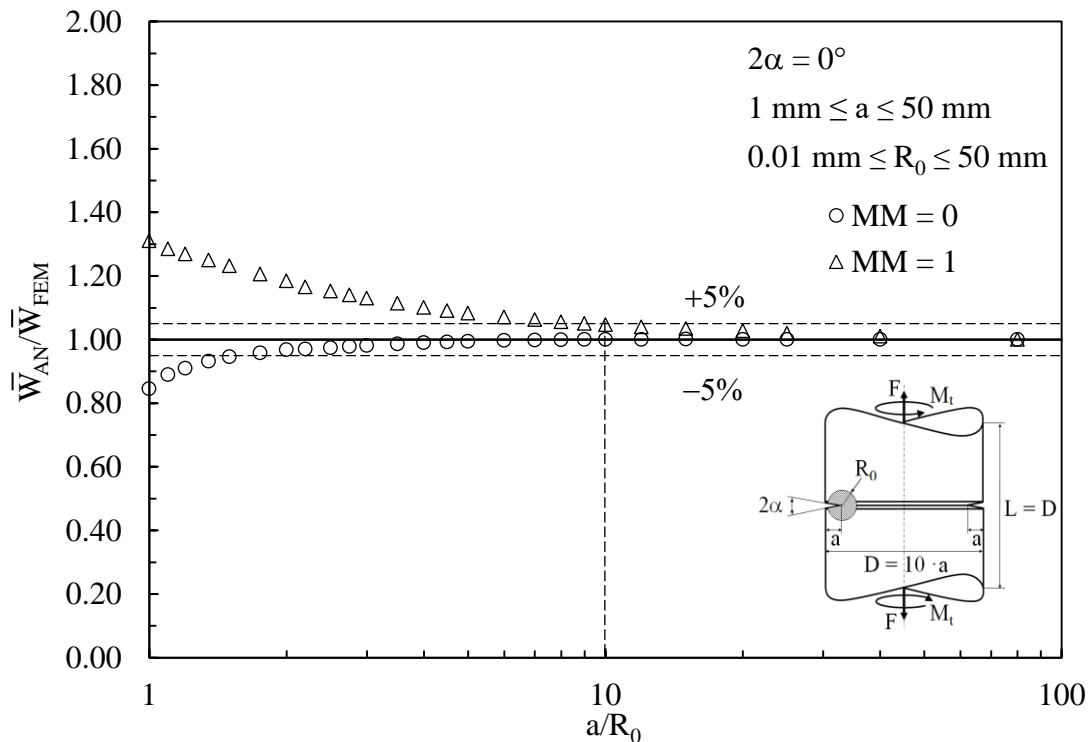


Figure 6.4.6: Out-of-plane mixed mode I+III crack problem: ratio between analytical and exact averaged SED values according to Eqs. (6.4.4) (\bar{W}_{AN}) and (6.4.8) (\bar{W}_{FEM}), respectively.

According to Williams [56], the mode I local stress fields expressed in terms of Cartesian stress components as functions of the polar coordinates (r, θ) , with origin at the crack tip (Fig. 6.4.1b), can be written in the following convenient form:

$$\begin{Bmatrix} \sigma_{xx} \\ \sigma_{yy} \\ \tau_{xy} \end{Bmatrix} = \frac{K_I}{\sqrt{2\pi r}} \begin{Bmatrix} \cos\left(\frac{\theta}{2}\right) - \frac{1}{2} \sin(\theta) \sin\left(\frac{3}{2}\theta\right) \\ \cos\left(\frac{\theta}{2}\right) + \frac{1}{2} \sin(\theta) \sin\left(\frac{3}{2}\theta\right) \\ \frac{1}{2} \sin(\theta) \cos\left(\frac{3}{2}\theta\right) \end{Bmatrix} + T \begin{Bmatrix} 1 \\ 0 \\ 0 \end{Bmatrix} + O(r^{1/2}) \quad (6.4.15)$$

The constant term T is a slit-parallel tensile or compressive stress, named ‘‘T-stress’’ by Larsson and Carlsson [61], and can be defined according to the following equation:

$$T = \lim_{r \rightarrow 0} \left[(\sigma_{xx})_{\theta=0} - (\sigma_{yy})_{\theta=0} \right] \quad (6.4.16)$$

where $\theta = 0$ identifies the crack bisector line.

In a recent contribution [105] dealing with centrally cracked infinite plates subjected to mixed I+II loading, it has been highlighted that the T-stress contribution must be included in the SED calculation when the crack size to control radius ratio a/R_0 is reduced. In particular, it was observed that for a crack size equal to the control radius ($a/R_0 = 1$) and pure mode I loading the error in the averaged SED estimation was about 70% if the T-stress contribution was neglected. However, it should be noted that in the present case the deviation between SED values is significantly lower (about 15% for $a/R_0 = 1$). This is consistent with the much lower T-stress contribution to the averaged SED of the present case as compared to the previous one [105]. Indeed, for the centrally cracked infinite plates analysed in [105] the T-stress to nominal stress ratio (T/σ_{nom}) is equal to -1 according to Radaj [62], while for the cylindrical bar weakened by a circumferential outer crack, with $a/D = 0.10$ according to Fig. 6.4.1, Sherry et al. [106] reported the following approximate expression, based on numerical analyses:

$$\frac{T}{\sigma_{\text{nom}}} \cong -0.5 \quad (6.4.17)$$

The T-stress contribution being neglected, Eq. (6.4.4) underestimates the averaged SED as shown in Fig. 6.4.6. However, if only K_I and T-stress contributions were taken into account to evaluate the averaged SED, an error would still exist. In fact, it should be noted that the stress components σ_{xx} must be zero at the bar's free edge due to equilibrium conditions. Conversely, if only K_I and T-stress contributions were considered in Eq. (6.4.15), σ_{xx} evaluated at $\theta = \pi$ would result constant and equal to T. Therefore, further higher order terms, $O(r^{1/2})$ in Eq. (6.4.15), are needed to account for the free-edge boundary conditions. One might note that fortunately the stress component σ_{xx} evaluated at $\theta = \pi$ is not singular at the crack tip (being $\sigma_{xx} = T \rightarrow \cong -0.5 \cdot \sigma_{\text{nom}}$ as r approaches zero) and it is zero at the bar's free edge. Therefore, neglecting either the T- and the $O(r^{1/2})$ stress contributions in Eq. (6.4.4) is of relatively little consequence in the averaged SED evaluation. This is not the case for mode III loading, as presented in the following. With reference to cracks under mode III loading conditions, the asymptotic, singular stress distributions have been determined by Qian and Hasebe [107], following Williams' procedure [56]. The local stress field in terms of Cartesian stress components as functions of the polar coordinates (r, θ) , with origin at the crack tip (Fig. 6.4.1b), is the following:

$$\begin{Bmatrix} \tau_{xz} \\ \tau_{yz} \end{Bmatrix} = \frac{K_{\text{III}}}{\sqrt{2\pi r}} \begin{Bmatrix} \sin\left(\frac{\theta}{2}\right) \\ \cos\left(\frac{\theta}{2}\right) \end{Bmatrix} + O(r^{1/2}) \quad (6.4.18)$$

It should be noted that, in this case, the constant term T is zero [107], so that the discrepancy between analytical and exact averaged SED values under mode III loading shown in Fig. 6.4.6 should be ascribed to the contribution of higher-order, non-singular $O(r^{1/2})$ terms in Eq. (6.4.18). The leading order term of the stress component τ_{xz} is singular if evaluated at $\theta = \pi$ (the crack free surface (see Fig. 6.4.1b)), the analytical expression being equal to $\frac{K_{\text{III}}}{\sqrt{2\pi r}}$ according to Eq. (6.4.18).

This means that the contribution $\frac{K_{III}}{\sqrt{2\pi r}}$ evaluated along the crack free surface is increasingly significant, the closer the crack tip approaches the bar's free edge; but the stress component τ_{xz} must be zero at the bar's free edge, due to equilibrium conditions. Therefore, such fictitious contribution brought by τ_{xz} in Eq. (6.4.4) leads to an over-estimation of the averaged SED, as illustrated in Fig. 6.4.6. Again, if higher-order, non-singular terms, $O(r^{1/2})$ in Eq. (6.4.18) were taken into account, the effect of the bar's free edge on the τ_{xz} distribution would be correctly accounted for and consequently the averaged SED would be correctly calculated.

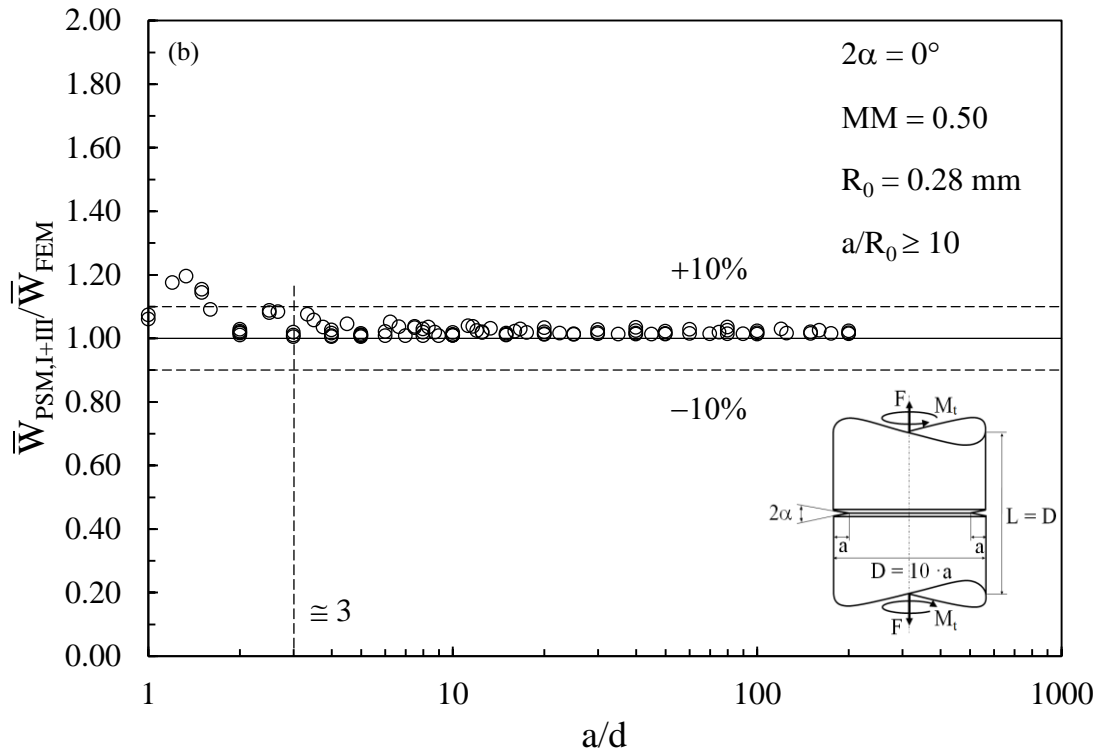
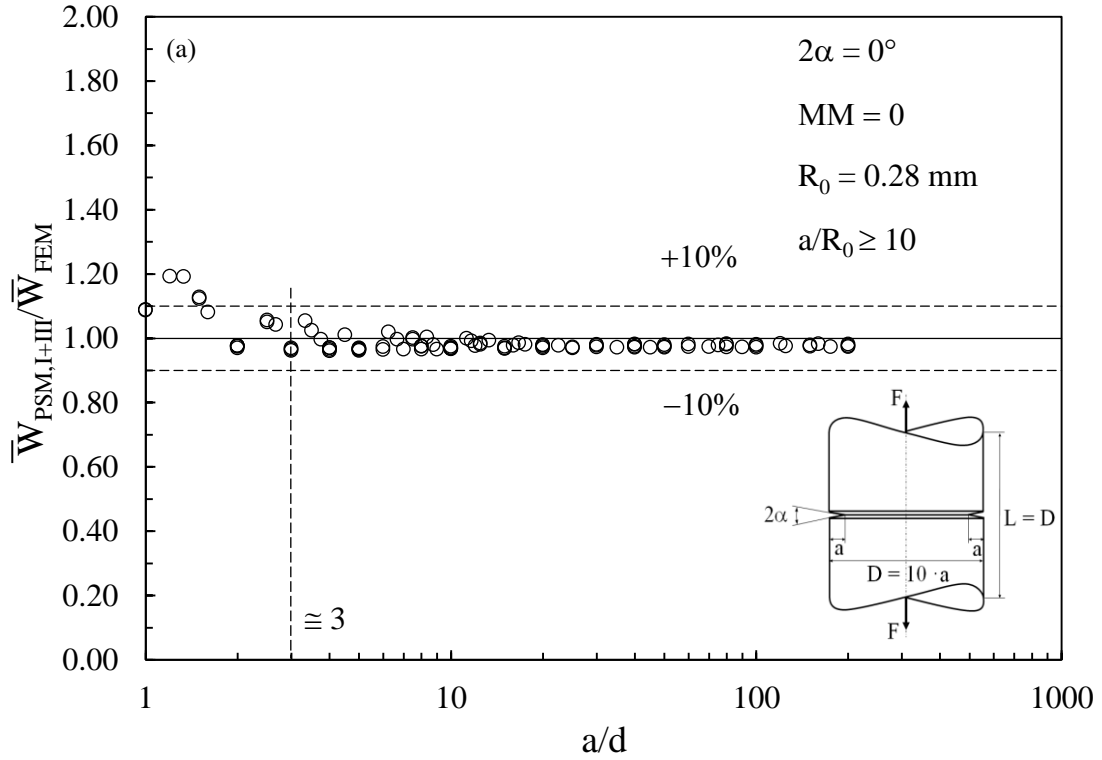
It should be reminded that recently the T-stress contribution to the averaged SED has been successfully included both in the analytical [36,70] and in the approximate [105] formulations; on the other hand averaged SED expressions which account for the contribution of further higher-order, non-singular terms, $O(r^{1/2})$ in Eqs. (6.4.15) and (6.4.18), are not currently available in the literature.

That said, it can be observed from Fig. 6.4.6 that the analytical SED, \bar{W}_{AN} (Eq. (6.4.4)), deviates from the exact value, \bar{W}_{FEM} (Eq. (6.4.8)), by less than 5% for a ratio $a/R_0 \geq 10$. Under this condition, the contribution of higher-order, non-singular terms are believed to be negligible from an engineering point of view, so that Eq. (6.4.4) as well as its numerical implementation Eq. (6.4.13), are applicable. Therefore, cracks characterised by $a/R_0 > 10$ will be analysed in the following, in order to comply with the range of applicability of Eq. (6.4.4), according to results shown in Fig. 6.4.6.

6.4.4. Validation of the peak stress method to estimate the averaged SED under mixed mode (I+III) loading

To validate the peak stress approach based on Eq. (6.4.13), numerical analyses have been performed by considering again the out-of-plane mixed mode I+III crack problem shown in Fig. 6.4.1. All considered geometrical and loading parameters are reported in Table 6.4.2. Exact values of the averaged SED, \bar{W}_{FEM} (Eq. (6.4.8)), have been evaluated by adopting the direct approach with very

refined meshes. Peak stresses were already available from the analyses described in previous Section 6.4.2 and presented in Fig. 6.4.5.



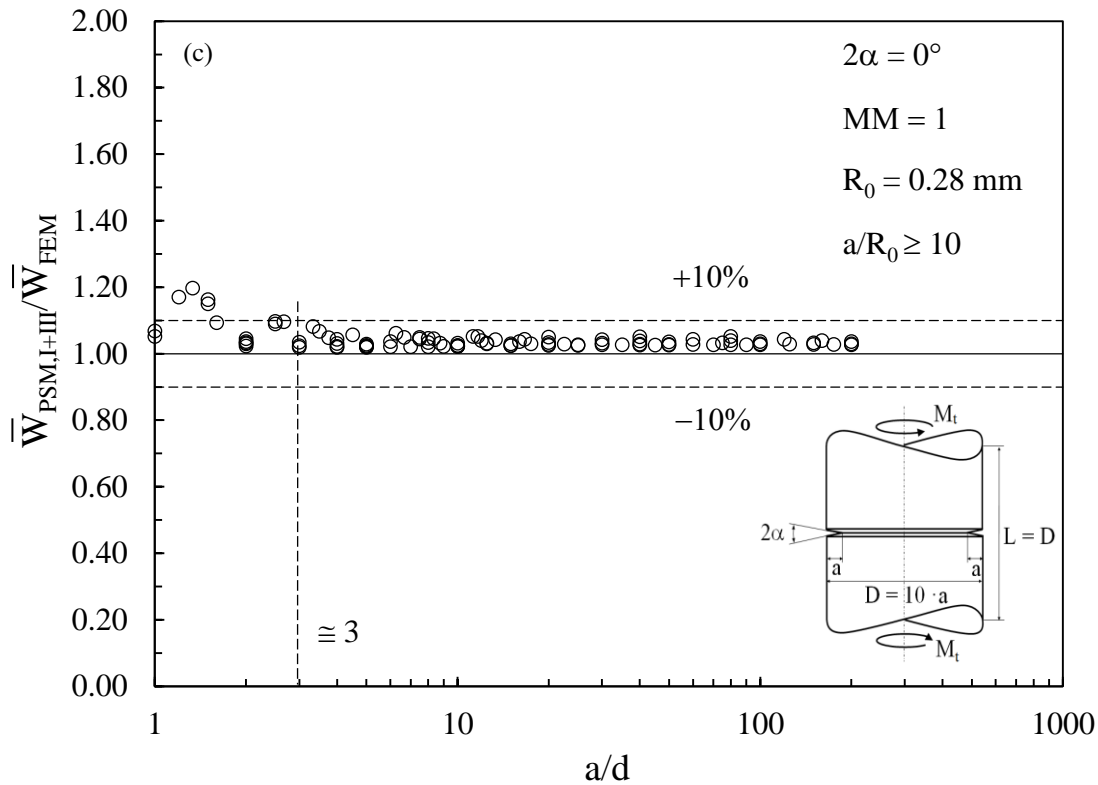


Figure 6.4.7: Out-of-plane mixed mode I+III crack problem: ratio between approximate ($\bar{W}_{PSM,I+III}$) and exact (\bar{W}_{FEM}) averaged SED versus the mesh density ratio (a/d). $\bar{W}_{PSM,I+III}$ according to the peak stress approach, Eq. (6.4.13); \bar{W}_{FEM} according to the direct approach, Eq. (6.4.8). (a) $MM = 0$; (b) $MM = 0.50$ and (c) $MM = 1.00$.

Figure 6.4.7 reports the ratio between approximate ($\bar{W}_{PSM,I+III}$, peak stress approach Eq. (6.4.13)) and exact (\bar{W}_{FEM} , direct approach Eq. (6.4.8)) averaged SED values for selected mode mixity ratios MM . The ratio $\bar{W}_{PSM,I+III}/\bar{W}_{FEM}$ is seen to converge to unity inside a $\pm 10\%$ scatter-band for all considered MM s. In particular, Fig. 6.4.7 shows that convergence occurs for a mesh density ratio a/d greater than 3 for all mode mixity ratios MM taken into account. The obtained results show that the minimum crack size to FE size ratio a/d to apply the peak stress approach (Eq. (6.4.13)) remains constant regardless of the mode mixity ratio MM . This differs from what was obtained in previous contributions [84,104,105] dealing with cracks subjected to in-plane mixed mode I+II loading, for which the minimum mesh density ratio a/d to apply the peak stress approach (Eq. (6.4.14)) increased with increasing the mode mixity ratio MM , since mode II

loading is more demanding in terms of mesh density ratio a/d than mode I loading. The minimum ratio a/d reported in Fig. 6.4.7 is in agreement with that obtained in previous Fig. 6.4.5.

6.4.5. The peak stress approach coarsening the mesh further

Figure 6.4.7 shows the ratio between the approximate averaged SED according to the PSM ($\bar{W}_{\text{PSM,I+III}}$, Eq. (6.4.13)) and the exact value according to the direct approach (\bar{W}_{FEM} , Eq. (6.4.8)) along with an error band of $\pm 10\%$ and suggests that the validity of peak stress approach (Eq. (6.4.13)) could be extended to coarser FE meshes (i.e. $a/d < 3$), by accepting a somewhat higher level of approximation. In particular, the maximum adoptable finite element size d could equal the crack size a , if the acceptable error was increased to approximately 20%. Letting a/d be equal to or greater than 1 removes any mesh density requirement, since $a/d = 1$ is the minimum feasible crack size to FE size ratio when generating the FE mesh, and might be useful in practical design situations.

The above extension is made possible thanks to the flat convergence of the non-dimensional SIFs expressions (6.4.10) and (6.4.12), as shown in Fig. 6.4.5. In previous contributions [84,105] dealing with cracks subjected to in-plane mixed mode I+II loading, it had also been possible to extend the validity of the mode I and mode II non-dimensional SIFs expressions to coarser FE meshes than those required for convergence of the PSM. However, in refs. [84,105] proper fitting functions had to be used due to the steeper convergence trends of K_{FE}^* and K_{FE}^{**} as compared to the trends shown in Fig. 6.4.5.

6.4.6 Discussion

The peak stress method (PSM) to estimate the strain energy density (SED) averaged in a structural control volume has been extended here to the case of out-of-plane mixed-mode (I+III) crack tip fields of cylindrical bars with external circumferential cracks. Essentially, the PSM is a simplified, FE-oriented numerical technique to estimate rapidly the Stress Intensity Factors (SIFs) on the basis of the linear elastic, crack tip peak stresses calculated with coarse FE

meshes. By knowing the approximate SIFs values, the averaged SED can also be estimated. The following conclusions can be drawn:

- Taking advantage of the closed-form expression of the averaged SED (Eq. (6.4.4)), the peak stress approach has been formalised according to Eq. (6.4.13). Crack size to control radius ratios equal to or greater than 10 have been analysed in order to comply with the condition of applicability of Eq. (6.4.4) to the analysed geometries.
- The minimum mesh density ratio a/d to apply the peak stress approach (Eq. (6.4.13)) with a level of approximation equal to 10% is equal to 3, independent of the mode mixity.
- The advantages of the peak stress approach to estimate the averaged SED can be singled out as follows: (i) the sole linear elastic peak stresses calculated at the crack tip from FE analyses are needed; because an FE node always exists at the stress singularity point, an FE analyst can easily pick up the design stresses in the post-processor environment of a commercial FE code; (ii) geometrical modelling the material dependent structural volume, inside which the SED is to be averaged, is no longer necessary; (iii) the adopted FE meshes are coarse, such that the maximum adoptable FE size could equal the crack size if the acceptable level of approximation was approximately 20%.

6.5 Link between the PSM and the averaged SED - example of practical application: fatigue strength assessment of tube-to-flange steel welded joints under mode III loading ^(*)

Nomenclature

c_w	parameter which accounts the influence of the nominal load ratio
d	mean size of a finite element
e_3	parameter for the determination of the strain energy density (SED)
E	elastic modulus
f_{w3}	weight parameter of the peak stress
k	inverse slope of the design scatter band
K_3	mode III notch stress intensity factor (NSIF)
K_{FE}^{***}	normalised K_3 in the application of the peak stress method
N_A	reference number of cycles
N_{bt}	number of cycles to break-through
N_f	number of cycles to failure
R	load ratio (ratio between the minimum and the maximum applied load in a fatigue test)
R_0	radius of the structural volume where local stresses are averaged
r, θ	polar coordinates
T_σ	scatter index of the design scatter band
t	thickness of the welded tube
\overline{W}	strain energy density averaged over the control volume

Symbols

2α	notch opening angle
Δ	range of the considered quantity
λ_3	mode III eigenvalue in Qian-Hasebe equation
ν	Poisson's ratio

$\sigma_{A,50\%}$	fatigue strength at the reference number of cycles for a probability of survival equal to 50%
$\sigma_{eq,peak}$	linear elastic equivalent peak stress evaluated at a V-notch tip (the weld toe or the weld root)
τ_{nom}	nominal stress relevant to torsion loading
$\tau_{\theta z, \theta=0, peak}$	linear elastic maximum principal stress evaluated at a V-notch tip (the weld toe or the weld root) by the finite element method using the mesh according to the PSM
$\tau_{\theta z}, \tau_{rz}$	normal and shear stress components in the polar frame of reference

(*) *See also:*

Meneghetti, G.; De Marchi, A.; Campagnolo, A. Fatigue strength assessment of tube-to-flange welded joints under torsion loading according to the peak stress method. *Theoretical and Applied Fracture Mechanics* (under review);

6.5.1. Introduction: theoretical background

In the fatigue design of welded joints according to the local approach based on the notch stress intensity factors (NSIFs), the weld toe and the weld root profiles are assumed as sharp V-notches, having a notch tip radius $\rho = 0$ and notch opening angle greater than zero (typically 135°) and equal to zero, respectively, as depicted in Fig. 6.5.1 [27,88,89,108].

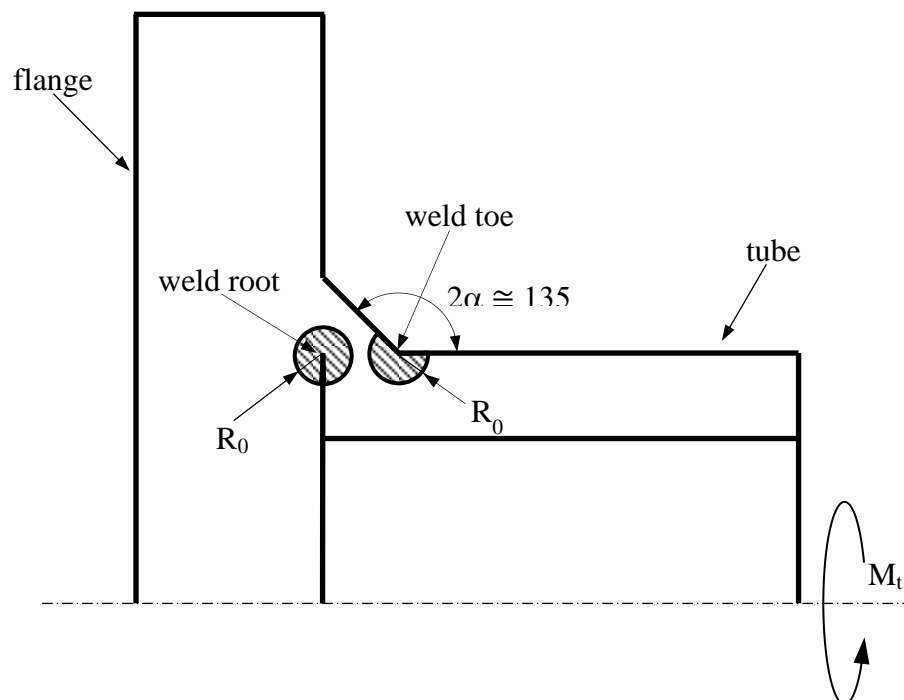


Figure 6.5.1: Assumptions of the NSIF-based approach in the fatigue design of welded joints. Geometrical model of a tube-to-flange fillet-welded joint. The sharp V-notch opening angle 2α is typically 0° at the weld root and 135° at the weld toe.

The assumption of notch tip radius equal to zero either at the weld toe and at the weld root is consistent with the reduced radii made by conventional arc-welding technologies and with the hypothesis of un-machined welds; moreover, the assumption represents also a worst case condition. Under these assumptions, the local, linear elastic stress fields in the vicinity of the notch tip can be expressed as functions of the relevant NSIFs, which quantify the magnitude of the asymptotic singular stress distributions. NSIFs are used to correlate the medium and the high

cycle fatigue strength of sharp V-notches [25,26,109], because they play the same role that stress intensity factors (SIFs) do at crack-like notches [110–112]. Since NSIFs are local stress parameters, they are by nature prone to estimate fatigue life including initiation and short crack propagation inside the (small) material volume where stresses are governed by the NSIFs. In other words, fatigue life up to a technical crack initiation is estimated by the NSIF approach. Nevertheless, there is sufficient experimental evidence that NSIFs do correlate the total fatigue life of small size laboratory specimens, and in particular of welded joints. This is due to the large amount of the total fatigue life which is spent for nucleation and short crack propagation in a region close to the notch tip governed by stress singularity. Let us consider the NSIF approach to a typical welded joint geometry under torsion loading, as depicted in Figure 6.5.2. While the figure illustrates the stresses only at the toe side, anti-plane shear stresses tied to mode III act also at the root. The asymptotic, singular stress distributions ahead of sharp V-notches under mode III loading have been determined by Qian and Hasebe [107], similarly to Williams [31], who instead derived the mode I and mode II local stress fields along with their degree of singularity dealing with plane problems. The local stress distributions for mode III loading referred to a polar reference system (r, θ) centred at the V-notch tip are the following (see Fig. 6.5.2):

$$\begin{Bmatrix} \tau_{\theta z} \\ \tau_{rz} \end{Bmatrix}_{\rho=0} = \frac{K_3}{\sqrt{2\pi}} \cdot r^{-(1-\lambda_3)} \cdot \begin{Bmatrix} \cos(\lambda_3 \theta) \\ \sin(\lambda_3 \theta) \end{Bmatrix} \quad (6.5.1)$$

The mode III NSIF, K_3 , quantifies the magnitude of the local stress fields and it can be defined by extending the definitions of mode I and II NSIFs previously proposed by Gross and Mendelson [30]:

$$K_3 = \sqrt{2\pi} \cdot \lim_{r \rightarrow 0} [\tau_{\theta z, \theta=0} \cdot r^{1-\lambda_3}] \quad (6.5.2)$$

where λ_3 is the stress singularity exponent [107], which depends on the notch opening angle 2α ($\gamma = \pi - \alpha$) according to Eq. (6.5.3)

$$\lambda_3 = \frac{\pi}{2\gamma} \tag{6.5.3}$$

while the out-of-plane shear stress component $\tau_{\theta z}$ is calculated along the notch bisector line, defined by the angular coordinate $\theta=0$.

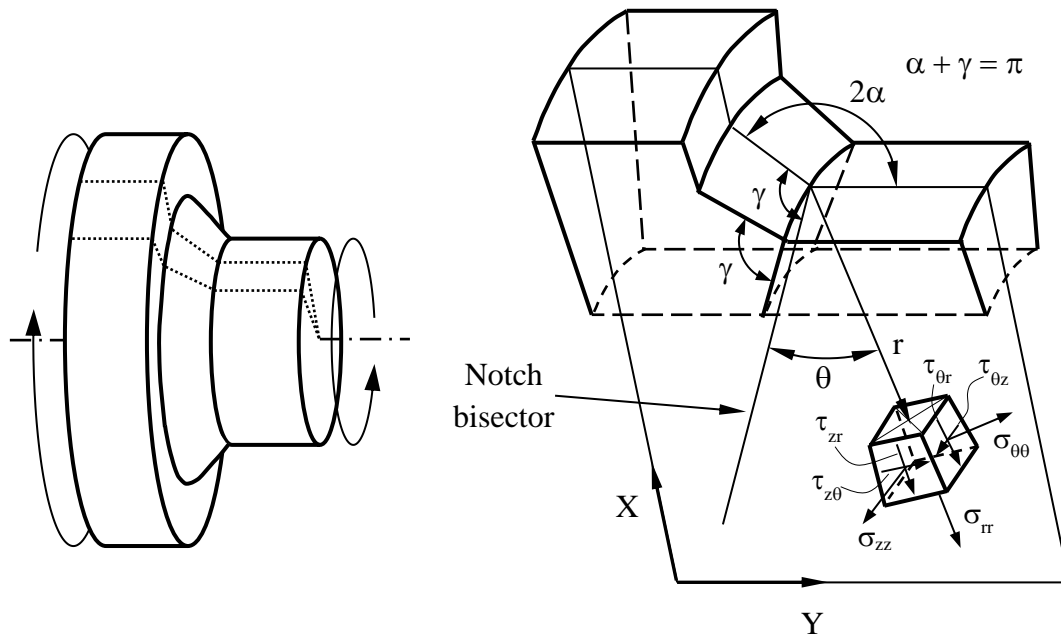


Figure 6.5.2: Polar reference system centred at the weld toe of a typical tube-to-flange welded joint geometry subjected to torsional loading.

When mode III NSIFs are adopted to assess the fatigue strength, their direct comparability is not possible if notches having different opening angles 2α are taken into consideration, since the exponent appearing in Eq. (6.5.2) changes the NSIF units. To restore comparability, Lazzarin and co-workers [23,29,85] suggested the use of the strain energy density (SED) averaged over a structural volume surrounding the V-notch tip . The idea is reminiscent of the stress averaging to perform inside a material dependent structural volume, according to the approach proposed by Neuber [100]. Lazzarin et al. [23,29,85] assumed a circular shape of the structural volume having radius R_0 as shown in Fig. 6.5.1 and provided the closed-form expression of the averaged SED parameter as a

function of the relevant NSIFs. Under pure torsion loading, the strain energy density averaged over the control volume can be expressed as follows [102]:

$$\Delta \bar{W} = \frac{e_3}{E} \left[\frac{\Delta K_3}{R_0^{1-\lambda_3}} \right]^2 \quad (6.5.4)$$

In the previous expression, E is the modulus of elasticity, e_3 is a known parameter which depends on the notch opening angle 2α and the Poisson's ratio ν , and ΔK_3 is the range of the mode III NSIF (maximum value minus minimum value). Table 6.5.1 reports the values of λ_3 and e_3 for a range of the notch opening angles 2α and with reference to a Poisson's ratio $\nu = 0.3$ [102].

Table 6.5.1: Values of parameter f_{w3} according to Eq. (6.5.10).

2α (deg)	λ_3 ^(a)	e_3 ^(a)	$f_{w3,d=0.5mm}$ ^(b)	$f_{w3,d=1mm}$ ^(b)
0	0.500	0.414	2.460	3.478
90	0.667	0.310	1.934	2.436
120	0.750	0.276	1.737	2.066
135	0.800	0.259	1.634	1.877

^(a): values from a previous contribution [102]

^(b): values calculated with $R_0 = 0.28$ mm, $\nu = 0.3$, $K_{FE}^{***} = 1.93$

Dealing with welded joints, the control radius R_0 was calibrated on experimental results by equalling the high cycle averaged SED (typically at 2 million cycles) of butt-welded laboratory specimens with weld caps ground flush and of fillet-welded specimens manufactured with conventional arc-welding processes, tested in the as-welded conditions and subjected to uniaxial fatigue loading with nominal load ratio close to zero. For welded construction steels a radius $R_0 = 0.28$ mm was obtained [29,85].

Equation (6.5.4) is valid in the case of a nominal load ratio equal to zero ($R = 0$); in the case of nominal load ratios different from zero, the expression of the averaged SED must be corrected as follows:

$$\Delta \bar{W} = c_w \frac{e_3}{E} \left[\frac{\Delta K_3}{R_0^{1-\lambda_3}} \right]^2 \quad (6.5.5)$$

where the coefficient c_w depends on the nominal load ratio R according to the following expression [53]:

$$c_w(R) = \begin{cases} \frac{1+R^2}{(1-R)^2} & \text{if } -1 \leq R \leq 0 \\ \frac{1-R^2}{(1-R)^2} & \text{if } 0 \leq R < 1 \end{cases} \quad (6.5.6)$$

As an example, the parameter c_w equals 0.5 for $R = -1$. In fatigue design of stress-relieved welded joints, Eq. (6.5.5) should be used, because the influence of mean stresses must be taken into account, according to Design Standards [86,113]. However, when as-welded joints are concerned, Eq. (6.5.4) should be used, the influence of the load ratio being negligible in this case.

Evaluating the NSIF to input in Eqs. (6.5.4) and (6.5.5) presents a major drawback, because very refined FE meshes are needed in order to evaluate the NSIF using definition (6.5.2). In the case of three-dimensional components, the FE analyses and the post-processing of the numerical results become even more time-consuming. Alternatively, the averaged SED can be directly estimated using FE analyses, where Lazzarin and co-workers showed that coarse meshes can be used inside the control volume having radius R_0 [37]. Keeping or even enhancing the coarse mesh option in FE analyses, the Peak Stress Method (PSM) allows to rapidly evaluate the mode III NSIF to input in Eq. (6.5.4) or (6.5.5) avoiding to model the control volume. Moreover, the PSM requires only the singular, linear elastic peak stress evaluated at the V-notch tip, instead of a number of stress-distance FE results, as application of definition (6.5.2) would require.

Therefore the plan of the present investigation is as follows:

- to introduce the Peak Stress Method for pure mode III loading and present an existing fatigue design curve valid for torsional fatigue of arc-welded steel joints with toe and root failure;

- to present new experimental fatigue test results relevant to tube-to-flange fillet-welded steel joints under torsional loading with weld root failures;
- to assess the fatigue strength using the peak stress method.

6.5.2. Peak Stress Method for mode III loading

The PSM was inspired by a numerical procedure proposed by Nisitani and Teranishi [41,42] to rapidly evaluate by FEM the SIF of a crack emanating from an ellipsoidal cavity. Following the track adopted to formalise the Peak Stress Method (PSM) in the case of mode I [43] and mode II [44] loading conditions, in a previous contribution [103] a link has been established between the exact value of mode III NSIF K_3 , see Eq. (6.5.2), and the singular, linear elastic, anti-plane shear stress evaluated by FEM in the plane of the V-notch bisector at the notch tip, $\tau_{\theta z, \theta=0, \text{peak}}$, according to the following expression:

$$K_{\text{FE}}^{***} = \frac{K_3}{\tau_{\theta z, \theta=0, \text{peak}} \cdot d^{1-\lambda_3}} \cong 1.93 \quad (6.5.7)$$

where d is the so-called ‘global element size’ parameter to input in Ansys® FE code, i.e. the average FE size adopted by the free mesh generation algorithm available in the software. It should be noted that the ‘exact’ K_3 value in Eq. (6.5.7) must be meant as the value obtained from definition (6.5.2) applied to the stress-distance numerical results calculated from very refined FE mesh patterns (the size of the smallest element close to the V-notch tip is often in the order of 10^{-5} mm). Equation (6.5.7) was calibrated in Ref. [103] by considering the weld toe as well as the weld root side of a number of joint geometries taken from the technical literature [114–121], consisting of tube-to-flange specimens, which were arc-welded with full-penetration or fillet-welds.

The average value of 1.93 provided by Eq. (6.5.7) has been obtained under the following conditions [103]:

- use of two-dimensional, harmonic, four-node linear quadrilateral elements, as implemented in ANSYS® numerical code (PLANE 25 of Ansys® element library) or three-dimensional, eight-node brick elements

(SOLID 45 of Ansys® element library or equivalently SOLID 185 with K-option 2 set to 3);

- the FE mesh pattern close to the weld toe must be that reported in Fig. 6.5.3 (see also [103]), where two elements share the node at the weld toe ($2\alpha \cong 135^\circ$), while four elements share the node at the weld root ($2\alpha = 0^\circ$), as shown in next Fig. 6.5.10. It is worth recognizing that the mesh patterns according to the PSM, like that reported in Fig. 6.5.3 and in next Fig. 6.5.10, are automatically generated by the free mesh generation algorithm available in Ansys®, so that only the ‘global element size’ parameter d must be input by the FE analyst. There are not additional parameters or special settings to input in order to generate the mesh.
- V-notches characterised by an opening angle 2α equal to 0° (typical for the weld root side) or 135° (typical for the weld toe side); as an example, Figure 6.5.3 shows the 135° -V-notch at the toe side of a full penetration welded joint;
- the mesh density ratio a/d must be equal to or greater than 3 at the weld toe (where $2\alpha \cong 135^\circ$) and 12 at the root side (where $2\alpha = 0^\circ$) in order to obtain $K_{FE}^{***} = 1.93 \pm 3\%$: when assessing the root side, a is the minimum value between the crack length (crack is due to the lack of penetration) and the ligament length [48], while a represents the tube thickness t when the toe side is considered. As an example, for the full-penetration joint shown in Fig. 6.5.3, the mesh density ratio $t/d = 10/2.5 \rightarrow 4$ satisfies the condition of applicability at the toe side. For the fillet-welded joint shown in next Fig. 6.5.10, the minimum between the crack length (t) and the ligament length (z) is z , therefore the mesh density ratio $z/d = 9/0.7 \rightarrow 12$ is appropriate to apply Eq. (6.5.7) either at the root and at the toe side.

Equation (6.5.7) is useful for a design engineer to rapidly estimate the NSIF K_3 using the FE nodal peak stress $\tau_{\theta z, \theta=0, peak}$. It should be noted that Eq. (6.5.7) should be recalibrated in the case of FE meshes consisting of higher-order elements or characterized by significantly different mesh patterns as compared to the reference ones reported in Figs. 6.5.3 and 6.5.10.

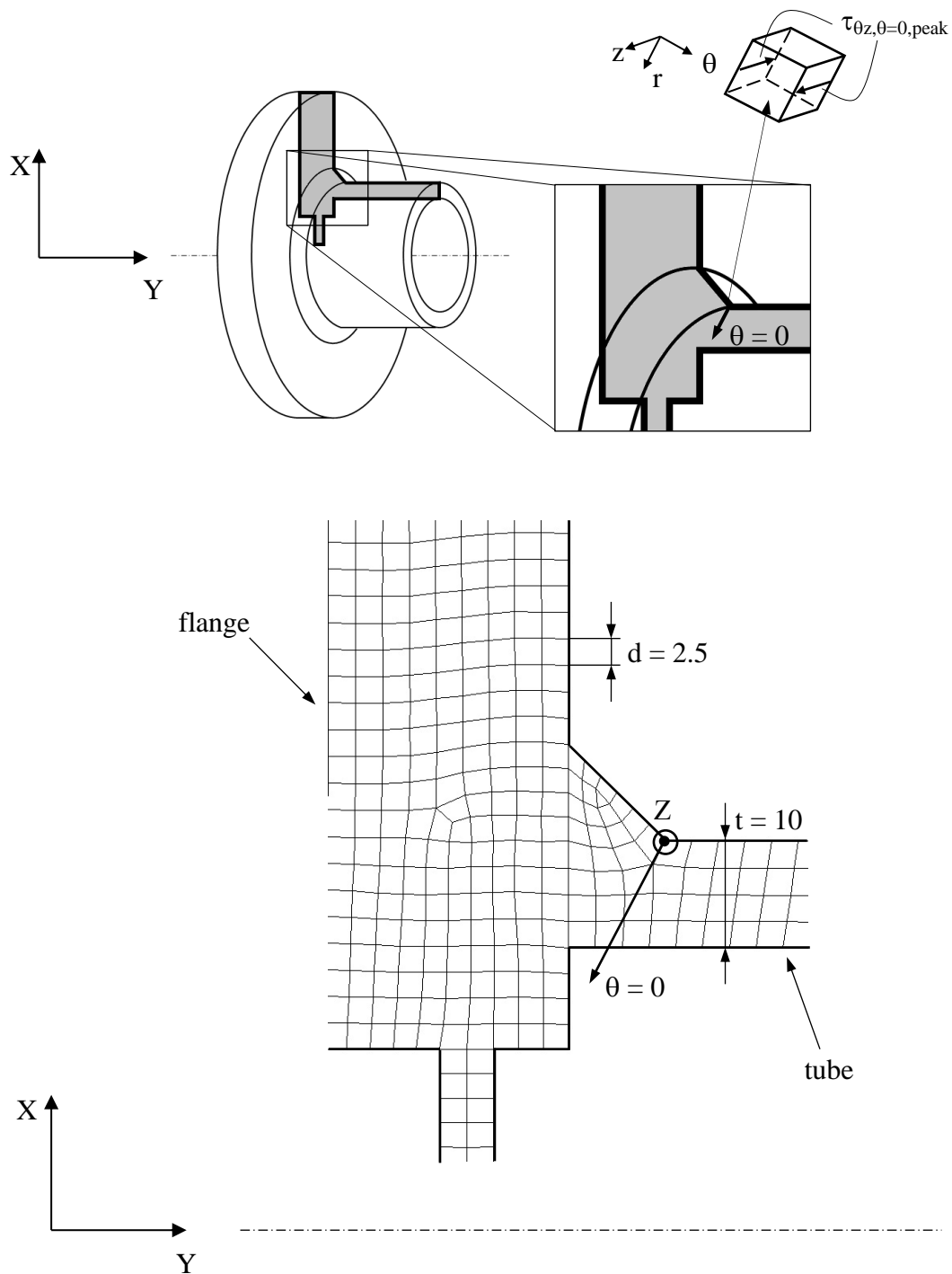


Figure 6.5.3: Typical 2D FE mesh adopted in [103] to apply the PSM according to Eq. (9); the example reported in the figure shows a full penetration tube-to-flange welded joint [114]. The four-node, quadrilateral, harmonic PLANE 25 elements available in Ansys Element Library were adopted to generate the free mesh shown in the figure. The Y-axis coincides with the axis of the tube.

6.5.3. Defining a SED-based design stress using the PSM

Taking advantage of the PSM (Eq. (6.5.7)), the averaged SED, Eq. (6.5.5), can be rewritten as a function of the linear elastic anti-plane peak stress $\tau_{\theta z, \theta=0, \text{peak}}$. Then, by using the equality $W = (1 - \nu^2) \cdot \sigma_{\text{eq, peak}}^2 / 2E$ valid under plane strain conditions, an equivalent peak stress, $\sigma_{\text{eq, peak}}$, can be defined as follows [103]:

$$\Delta \bar{W} = c_w \frac{e_3}{E} \left[K_{\text{FE}}^{***} \cdot \Delta \tau_{\theta z, \theta=0, \text{peak}} \cdot \left(\frac{d}{R_0} \right)^{1-\lambda_3} \right]^2 \rightarrow \frac{1-\nu^2}{2E} \Delta \sigma_{\text{eq, peak}}^2 \quad (6.5.8)$$

After all, the following expression is obtained:

$$\Delta \sigma_{\text{eq, peak}} = \sqrt{c_w} \cdot f_{w3} \cdot \Delta \tau_{\theta z, \theta=0, \text{peak}} \quad (6.5.9)$$

The correction coefficient f_{w3} weights the linear elastic anti-plane peak stress both around the notch tip (θ coordinate in Fig. 6.5.2) and along the radial direction (r coordinate in Fig. 6.5.2). The parameter f_{w3} is given by:

$$f_{w3} = K_{\text{FE}}^{***} \cdot \sqrt{\frac{2e_3}{1-\nu^2}} \cdot \left(\frac{d}{R_0} \right)^{1-\lambda_3} \quad (6.5.10)$$

Values of f_{w3} according to Eq. (6.5.10) are listed in Table 6.5.1, considering two values of the average finite element size d , namely $d = 0.50$ mm and 1 mm, different notch opening angles 2α and the value $R_0 = 0.28$ mm [29,85]. In the case of as-welded joints tested at any load ratio, Eq. (6.5.9) simplifies to [53]:

$$\Delta \sigma_{\text{eq, peak}} = f_{w3} \cdot \Delta \tau_{\theta z, \theta=0, \text{peak}} \quad (6.5.11)$$

being the correction factor c_w equal to 1. It should be noted that while both the parameter f_{w3} and the peak stress depend on the employed FE size d , the equivalent peak stress, defined by Eqs. (6.5.9) and (6.5.11), does not.

It has been demonstrated that the equivalent peak stress, according to Eqs. (6.5.9) or (6.5.11), can be used to correlate the fatigue strength of tube-to-flange structural steel welded joints subjected to torsional loading. Figure 6.5.4 reports a

previous synthesis [103] of about 50 experimental data taken from the literature [114–118,120] relevant to full penetration or fillet-welded tube-to-flange structural steel specimens with un-machined welds, tested in the stress-relieved condition under a nominal load ratio equal to -1. Weld toe as well as weld root failures were reported in the original papers.

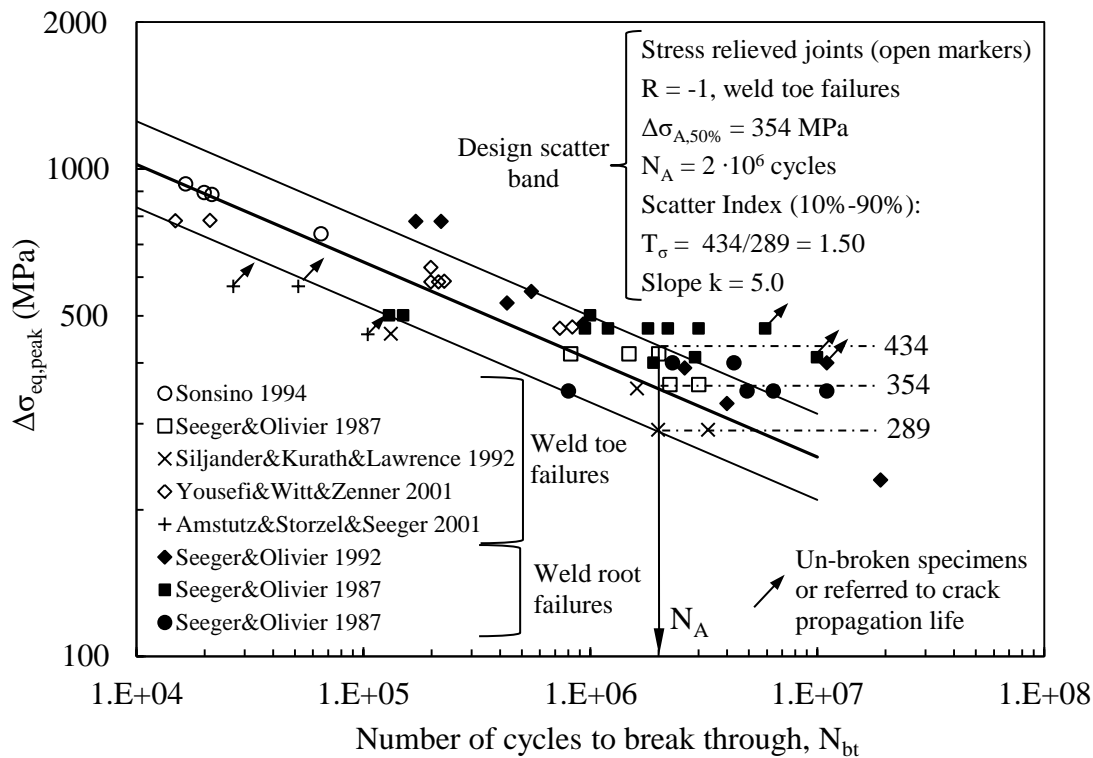


Figure 6.5.4: Correlation of experimental data relevant to weld toe and weld root failures according to the peak stress method (from [103]). Experimental data generated from full penetration or fillet-welded tube-to-flange structural steel specimens tested in the stress-relieved condition under a nominal load ratio equal to -1 [114–118,120].

The tube thickness ranged from 7.7 to 10 mm while the employed structural steels had a yield stress varying between 240 and 552 MPa. The reader is referred to Ref. [103] for additional details about materials, joint geometries and testing conditions. The scatter band reported in Fig. 6.5.4 has been calibrated on the experimental results [114–117,120] relevant only from weld toe failures ($2\alpha \cong 135^\circ$). It is noteworthy that a variety of experimental fatigue test results generated from joint geometries involving either toe and root cracking is included in the

same scatter band with good accuracy. It should also be noted that the scatter index of the 10% and 90% survival probability curves plotted in Figure 6.5.4 equals $T_\sigma = 1.50$, which is typical of single test series [122]. In the present investigation new experimental results have been generated by testing tube-to-flange structural steel welded joints under torsional fatigue loading and results have been analysed according to the PSM.

6.5.4. Torsional fatigue tests on tube-to-flange steel welded joints

Torsional fatigue tests have been performed on tube-to-flange fillet-welded specimens in structural steel. Table 6.5.2 provides details of the material, welding process and testing conditions. All main geometrical parameters of the joints are reported in Fig. 6.5.5a, while a specimen after manufacturing is shown in Fig. 6.5.5b. Table 6.5.2 shows that most specimens were stress-relieved prior to testing by means of a post-welding heat treatment (600 °C for 2 to 4 hours followed by a slow cooling down to 300÷350 °C), while few ones were tested in the as-welded conditions.

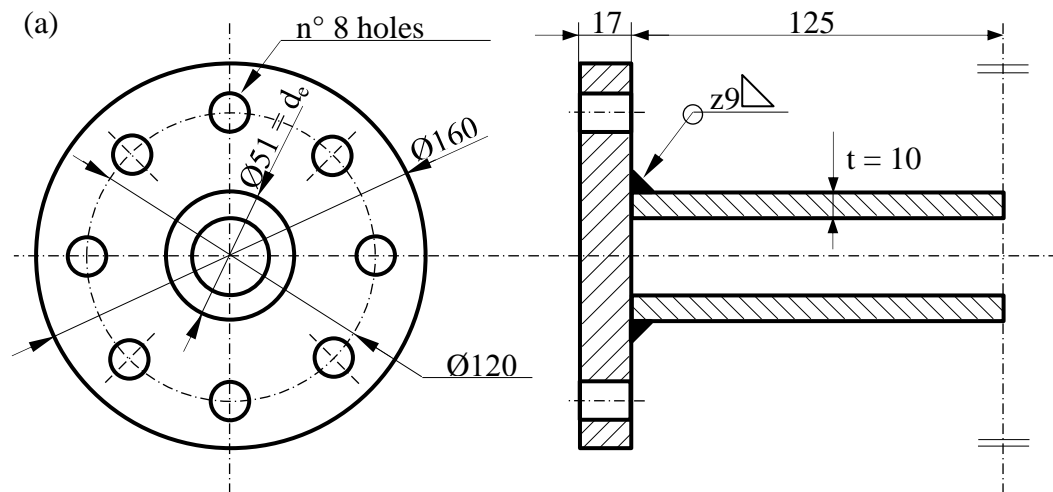




Figure 6.5.5: (a) Geometry and nominal dimensions of tube-to-flange structural steel welded joints used in the experimental tests under torsion loading. The specimens were arc-welded with fillet-welds. (b) An example of tube-to-flange specimen.

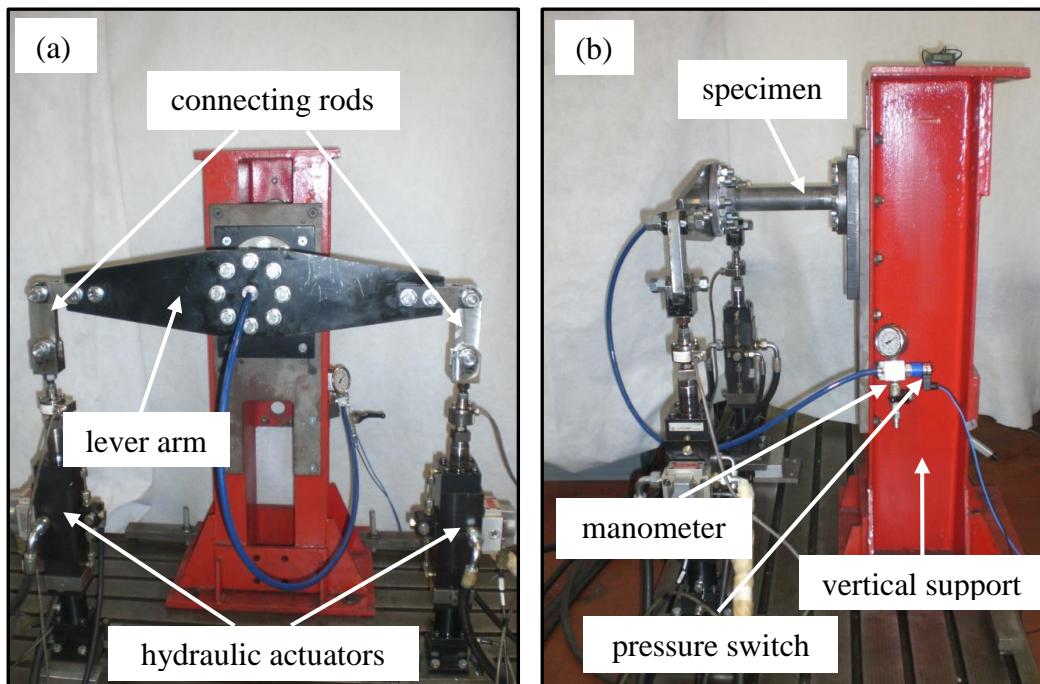




Figure 6.5.6: (a) Test rig for pure torsion fatigue loading. (b) Pneumatic system used to monitor the number of cycles to break through. (c) A detail of the connecting rod between the servo-hydraulic actuator and the lever arm.

Table 6.5.2: Material, welding process and testing conditions.

Material	Yield strength [MPa]	Ultimate strength [MPa]	Welding process	Testing condition
S355JR	355	510	MIG	Stress-relieved ^(a) As-welded ^(b)

^(a): 16 specimens

^(b): 4 specimens

Figure 6.5.6 illustrates the test rig. One specimen's flange is bolted to a vertical support, as shown in Figs. 6.5.6a,b, the other one being bolted to a lever arm, that is loaded at its extremities by means of two servo-hydraulic actuators, respectively, equipped with 10 kN load cells (see Fig. 6.5.6a). The flange has a threaded central hole, where a tube delivering pressurized air at 0.8 MPa is connected.

Since the backing plate of each actuator is fixed to the ground and in order to allow for the arc-shaped trajectory of the lever arm extremities caused by the torsional rotation, a connecting rod was employed between each servo-hydraulic cylinder and the lever arm, as reported in Fig. 6.5.6c.

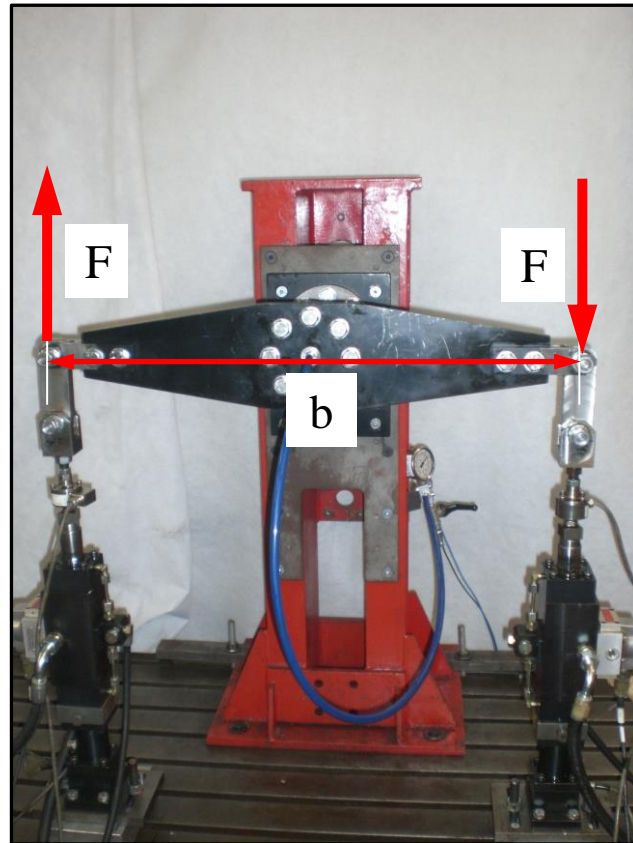


Figure 6.5.7: Force system applied to the tube-to-flange joints (see Eq. (6.5.12)).

Pure torsion was applied by running the hydraulic cylinders with equal in magnitude and opposite forces (see Fig. 6.5.7). By doing so, the resulting torsion moment is as follows:

$$M_t(t) = F(t) \cdot b \quad (6.5.12)$$

where b is the moment arm of force couple shown in Fig. 6.5.7, while F is the load exerted by each actuator. Given the torque, the torsion shear stress in the tube can be expressed as:

$$\tau_{\text{nom}}(t) = \frac{M_t(t)}{W_t} \quad (6.5.13)$$

being the section modulus W_t defined as:

$$W_t = \frac{\pi}{16} \cdot \frac{d_e^4 - (d_e - 2t)^4}{d_e} \quad (6.5.14)$$

where d_e is the tube outer diameter and t is the tube thickness, as reported in Fig. 6.5.5a. Before starting the experimental campaign, the applied shear stress and the absence of undesired bending loadings in the tested specimens have been successfully verified by using a strain rosette fixed on the tube of a specimen, consisting of three strain gauges oriented at -45° , 0° and 45° , respectively.

Tests were carried out at constant amplitude under pulsating ($R = 0$) or completely reversed ($R = -1$) torsion fatigue loadings. All fatigue tests were run under closed-loop load control by using a MTS Flex Test GT60 digital controller in standard laboratory environment.

In order to determine the number of cycles to break-through, the specimen's flange at the lever arm side was connected to a pneumatic circuit operating at about 0.8 MPa, see Figs. 6.5.6a,b. A sudden pressure drop in the tube occurred when root cracks became through the thickness. The number of cycles to break-through (N_{bt}) was determined from the known load test frequency and from the time elapsed from the beginning of the test, which was provided by an hour meter equipped with a digital input to trigger the stoppage of time counting as soon as a pressure drop of 0.4 MPa was detected by the pressure switch (see Fig. 6.5.6b). The number of cycles to break-through was assumed as failure criterion according to [114–116,121]. Eventually tests were interrupted at the complete stiffness loss or at $2 \cdot 10^6$ cycles (runouts), if no failure was detected.

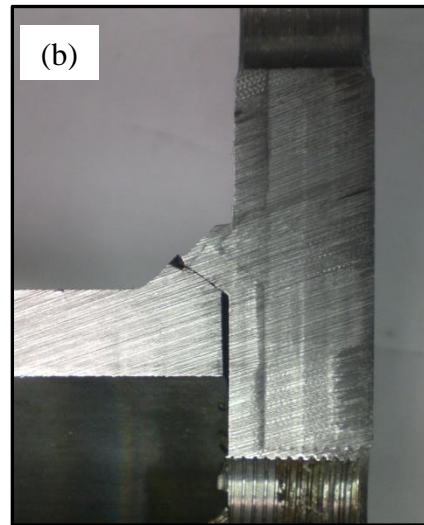
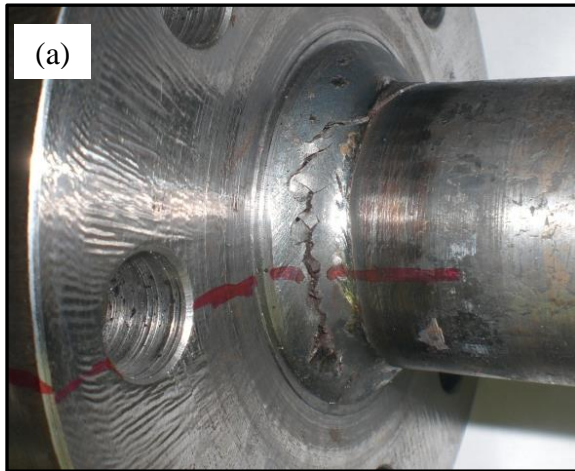
After each fatigue test, the real geometry of the tube-to-flange welded joints has been carefully checked. In particular the actual weld leg length has been measured and it ranged between 8.50 and 9.50 mm.

Table 6.5.3 reports the crack initiation location for all different series of tested specimens. In the as-welded joints, fatigue crack initiation always occurred at the

weld root, as shown in the examples reported in Figs. 6.5.8a-c. As to the stress-relieved joints, the critical point remained the weld root in most cases (see Fig. 6.5.8d); however, some specimens failed in the tube, as shown in Figs. 6.5.8e,f. In one case fatigue crack initiation occurred at the weld toe.

Table 6.5.3: Fatigue test details.

Load ratio R	Tube thickness [mm]	Failure criterion	N of fatigue test results	Failure location	Range of cycles
-1	10	Through crack	14 stress-relieved	10 weld root 1 weld toe 3 tube	$6 \cdot 10^3 \div 2 \cdot 10^6$
			3 as-welded	weld root	
0	10	Through crack	2 stress-relieved 1 as-welded	weld root	$6 \cdot 10^5 \div 2 \cdot 10^6$



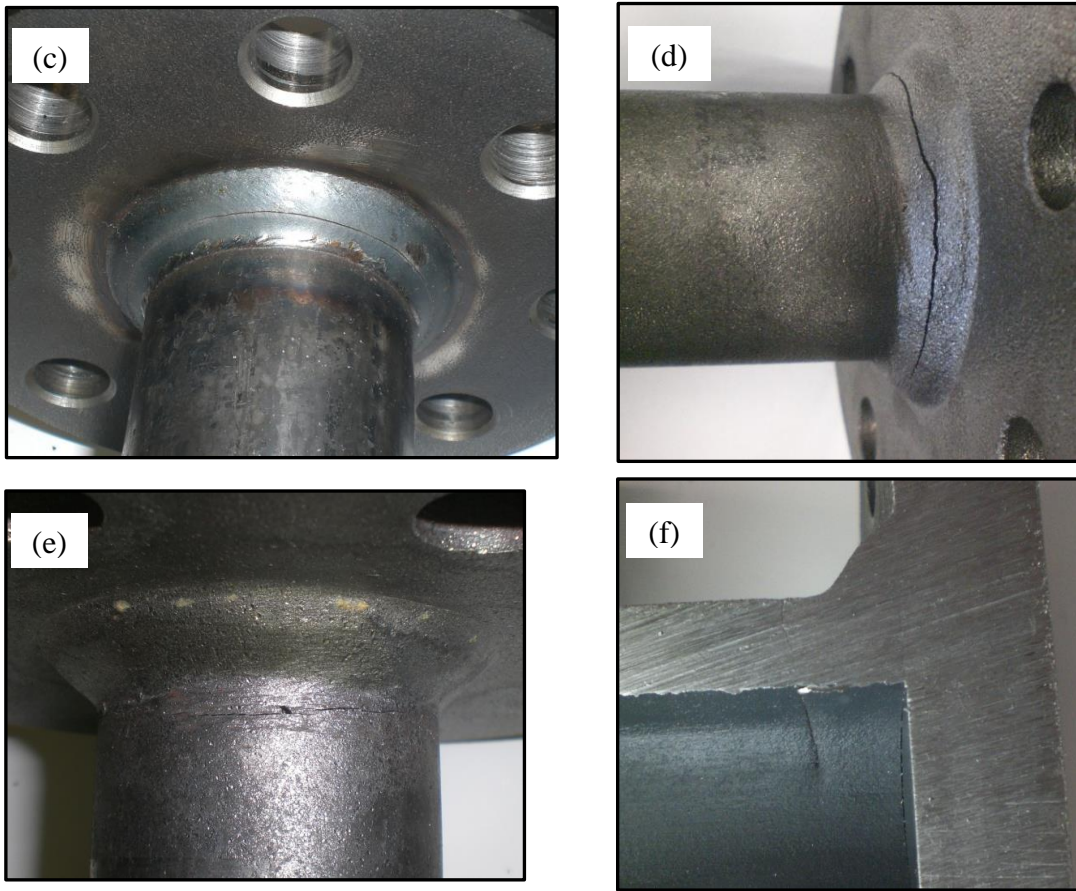


Figure 6.5.8: Examples of failures under pure torsion fatigue loading; weld root failures of as-welded joints: (a) and (b) obtained with $R = 0$, $\Delta\tau_{\text{nom}} = 190$ MPa ($N_{\text{bt}} = 697815$, $N_f = 1135497$), (c) obtained with $R = -1$, $\Delta\tau_{\text{nom}} = 300$ MPa ($N_{\text{bt}} = 45246$, $N_f = 46858$); (d) weld root failure of a stress relieved joint ($R = -1$, $\Delta\tau_{\text{nom}} = 300$ MPa, $N_{\text{bt}} = 125226$, $N_f = 133448$); (e) and (f) failure in the tube of a stress relieved joint ($R = -1$, $\Delta\tau_{\text{nom}} = 350$ MPa, $N_{\text{bt}} = 32519$, $N_f = 32616$).

6.5.5. Fatigue test results in terms of nominal stress

Figure 6.5.9 reports the number of cycles as a function of the applied nominal shear stress range (defined as maximum value minus minimum value) in the tube evaluated using Eq. (6.5.14), for all performed fatigue tests. For each tested specimen the figure reports the number of cycles to break-through (N_{bt}), determined on the basis of the air pressure drop, and the number of cycles to failure (N_f), based on the complete stiffness loss. It should be noted that the ratio between the number of cycles to break-through and the total fatigue life, N_{bt}/N_f , of each tested specimen is between 60 and 99%, with the great majority of experimental data characterized by a ratio greater than 90%.

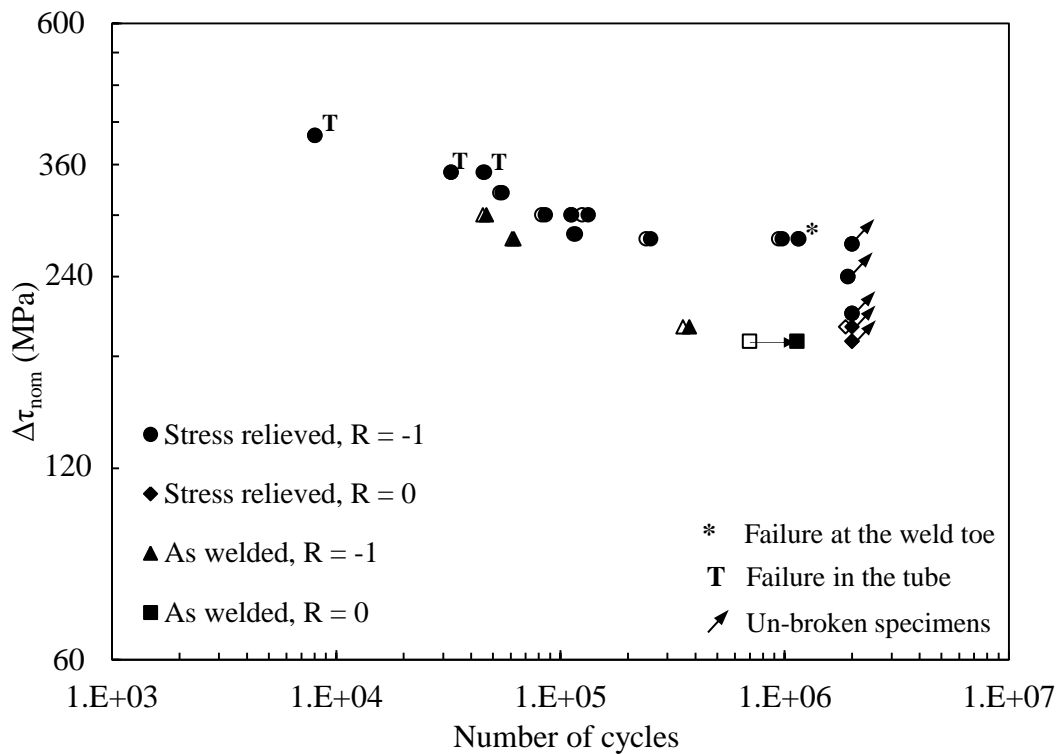


Figure 6.5.9: Experimental results of pure torsion fatigue tests; the nominal shear stress range evaluated in the tube (Eq. (6.5.13)). Open markers refer to the fatigue life N_{bt} to break through (air pressure drop inside the tube), while filled markers refer to the total fatigue life N_f (complete stiffness loss).

On the basis of Fig. 6.5.9, a reduced influence of the post-welding heat treatment on the fatigue strength was observed. According to the available data, the experimental results for as-welded and stress-relieved joints seem to fall in the same scatter. As far as stress-relieved joints are concerned, the specimen tested at $\Delta\tau_{nom} = 200$ MPa under $R = 0$ exhibited a fatigue life of $N_{bt} = 1.87 \cdot 10^6$ cycles, which seems to indicate a certain reduction in the fatigue strength if compared to stress-relieved specimens tested at $R = -1$.

6.5.6. Analysis of experimental data using the equivalent peak stress

To calculate the equivalent peak stress, Eq. (6.5.9) was adopted for stress-relieved joints ($c_w = 1$ for $R = 0$, and $c_w = 0.5$ for $R = -1$), while Eq. (6.5.11) was adopted for as-welded joints. Figure 6.5.5 reports the joint geometry, while Fig. 6.5.10

shows the two-dimensional, axis-symmetric FE model employed to calculate the singular, linear elastic, shear peak stress $\tau_{\theta z, \theta=0, \text{peak}}$ either at the weld root and at the weld toe. The mesh density ratio a/d was chosen to comply with the most demanding condition of applicability of the PSM presented in a previous section, i.e. the ratio between the ligament length z and average FE size d must be equal to or greater than 12: therefore the mesh density ratio $z/d = 9/0.7 \rightarrow \cong 12.8$ shown in Fig. 6.5.10 is adequate to apply the PSM either at the root and at the toe side. On the basis of the joint's geometry reported in Fig. 6.5.8, the weld toe reinforcement angle was assumed 45° , which corresponds to a V-notch opening angle $2\alpha = 135^\circ$. Furthermore, all welded joints being tested in the un-machined conditions, the worst case $\rho = 0$ has been taken into consideration in the numerical analyses, so that the weld toe and the weld root have been modelled as a sharp open V-notch and a crack, respectively. The average value of the measured weld leg lengths, namely $z = 9$ mm (see Fig. 6.5.5a), has been adopted in the FE model.

A free mesh pattern of quadrilateral four-node harmonic elements PLANE 25 of the Ansys® element library having a 'global element size' equal to d was automatically generated by the software. The adopted PLANE 25 finite element allows to analyse axis-symmetric components subjected to non axis-symmetric external loads, but expressible as a Fourier series expansion. Therefore, it can be employed for modelling three-dimensional axis-symmetric components under bending or torsion loads, keeping the advantage of treating two-dimensional FE analyses, as shown in Fig. 6.5.10.

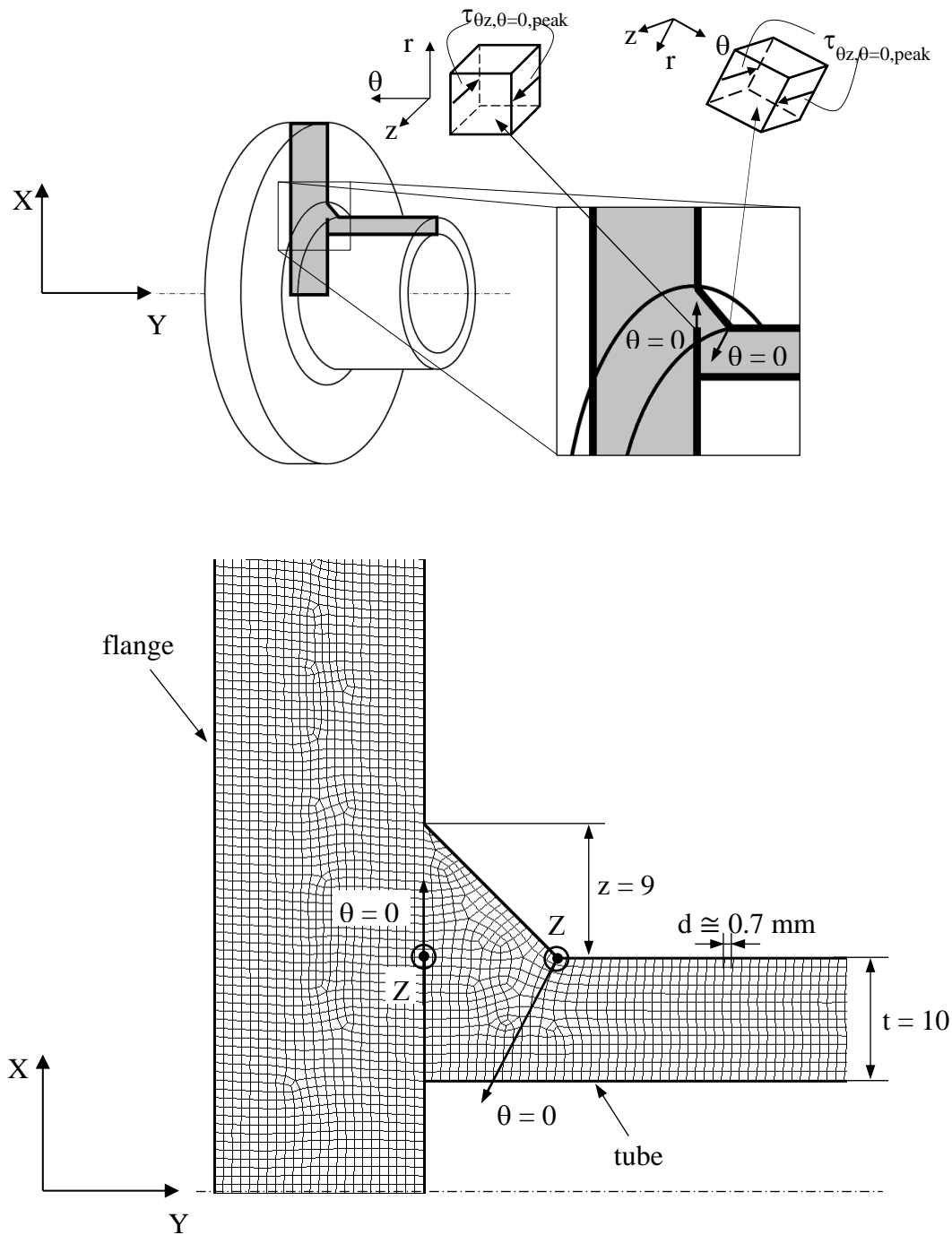


Figure 6.5.10: 2D FE mesh adopted to calculate the equivalent peak stress (Eq. (6.5.9)) at the toe and root sides of tube to flange fillet-welded joints. The four-node, quadrilateral, harmonic PLANE 25 elements of the Ansys® element library were adopted to generate the free mesh shown in the figure. The Y-axis coincides with the axis of the tube.

After having analysed the welded joint geometry according to the PSM, the experimental fatigue data expressed in terms of range of nominal shear stress could be converted in terms of range of the linear elastic equivalent peak stress calculated at the crack initiation site. It should be noted that the ratio between the equivalent peak stress (Eq. (6.5.11)) and the nominal shear stress (Eq. (6.5.13)), $\sigma_{\text{eq,peak}}/\tau_{\text{nom}}$, results 2.96 at the weld toe and 2.55 at weld root. Therefore, according to the PSM, the weld toe is somehow more critical than the weld root, being the equivalent peak stress 16% higher. Nevertheless, cracks initiated more frequently in the root than at the toe. According to a previous investigation [44], it has been verified that reduced differences of the equivalent peak stress (on the order of $\pm 20\%$) can hardly anticipate the cracking location. Conversely, much more successfully predictions of the crack initiation location have been performed when more pronounced differences are calculated [44,48]. Additional difficulties in estimating the crack initiation location, when multiple sites are in competition in the same joints, arise in presence of highly non-uniform residual stress fields, which the equivalent peak stress does not account for [48].

The experimental fatigue results are reported in Fig. 6.5.11 and compared with the design scatter band, calibrated in a previous contribution [103] and presented previously in Fig. 6.5.4. Figure 6.5.11 highlights a good agreement between theoretical estimations and the experimental results, where it should be recalled that the design fatigue curves shown in the figure have been calibrated on experimental data relevant to weld toe failures only. Few tests have also been conducted on as-welded specimens under completely reversed torsion. The relevant results are also reported in Fig. 6.5.11 and seem to indicate a slight increase of the fatigue strength. A similar behaviour has been noted by Young and Lawrence [119], who measured high compressive residual stresses close to the weld both in the longitudinal and in the circumferential directions.

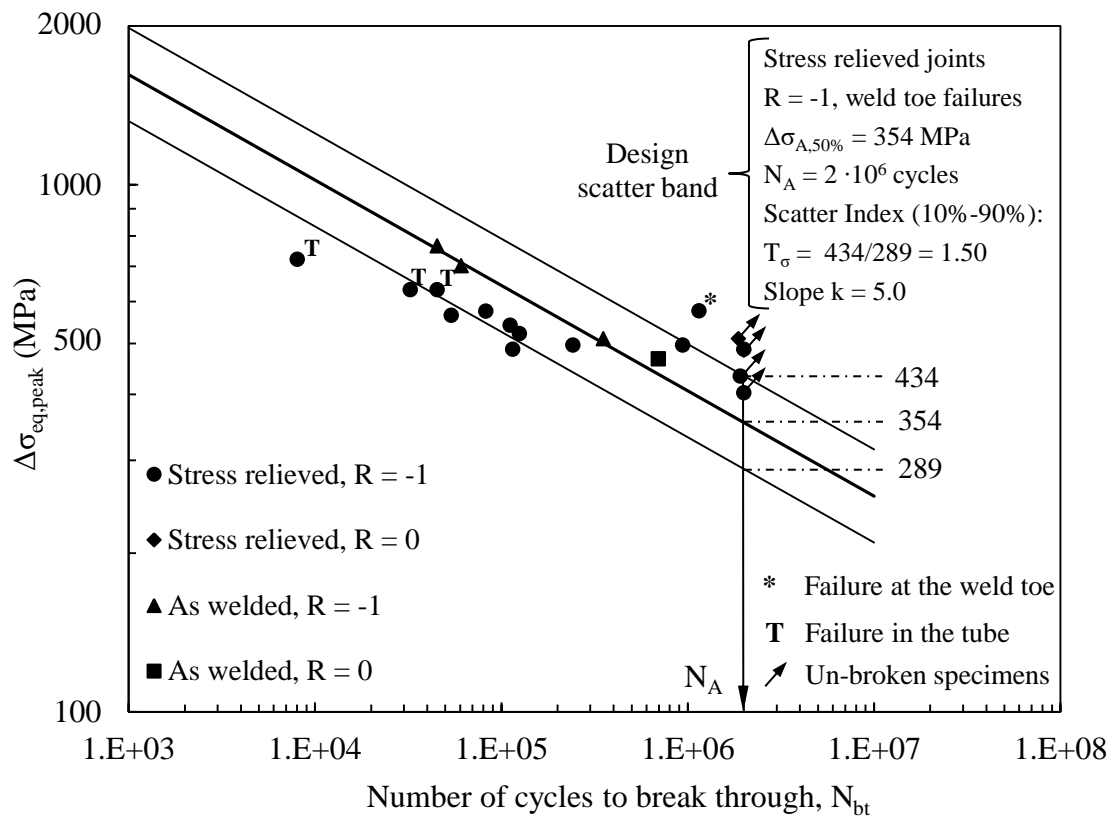


Figure 6.5.11: Fatigue assessment of root failures in tube-to-flange structural steel welded joints under torsional loading according to the PSM. The design scatter band was calibrated in Ref. [103] considering only weld toe failures.

6.5.7. Discussion

The peak stress method (PSM) has been applied to assess weld root failures in tube-to-flange structural steel welded joints tested under torsional loading. The method is based on the notch stress intensity factors, which assumes a sharp V-notch existing at the weld toe and a pre-crack at the weld root. The design stress (the so-called equivalent peak stress) is the singular, linear elastic, anti-plane shear stress evaluated at toe and at the root tip by using automatically generated FE meshes, multiplied by a known coefficient dependent primarily on the V-notch opening angle. Physically, the equivalent peak stress expresses a strain energy density averaged inside a structural volume surrounding the V-notch tip. When multiple crack initiation sites are in competition in the same joint, comparison among the equivalent peak stresses allows to single out the most critical one, out

of a range of sensitivity which can be estimated as 20%. The effect of non-uniform residual stresses distributed among the competing failure locations complicates the scenario, reducing the significance of the comparison among the equivalent peak stresses, which, in turn, take into account only the notch effect.

Most of the tested joints were tested in the stress-relieved conditions under completely reversed torsion. A design scatter band previously calibrated on experimental fatigue test results including only weld toe failures, has been satisfactorily applied here to correlate weld root failures.

References

- [1] Henshell RD, Shaw KG. Crack tip finite elements are unnecessary. *Int J Numer Methods Eng* 1975;9:495–507.
 - [2] Barsoum RS. Further application of quadratic isoparametric finite elements to linear fracture mechanics of plate bending and general shells. *Int J Fract* 1975;11:167–9.
 - [3] Akin JE. The generation of elements with singularities. *Int J Numer Methods Eng* 1976;10:1249–59.
 - [4] Portela A, Aliabadi MH, Rooke DP. Efficient boundary element analysis of sharp notched plates. *Int J Numer Methods Eng* 1991;32:445–70.
 - [5] Babuška I, Miller A. The post-processing approach in the finite element method—Part 2: The calculation of stress intensity factors. *Int J Numer Methods Eng* 1984;20:1111–29.
 - [6] Szabò BA, Yosibash Z. Numerical analysis of singularities in two dimensions. Part 2: computation of generalized flux/stress intensity factors. *Int J Numer Methods Eng* 1996;39:409–34.
 - [7] Tracey DM. Finite elements for determination of crack tip elastic stress intensity factors. *Eng Fract Mech* 1971;3:255–65.
 - [8] Pu SL, Hussain MA, Lorensen WE. The collapsed cubic isoparametric element as a singular element for crack problems. *Int J Numer Methods Eng* 1978;12:1727–42.
 - [9] Heyliger PR, Kriz RD. Stress intensity factors by enriched mixed finite elements. *Int J Numer Methods Eng* 1989;28:1461–73.
 - [10] Benzley SE. Representation of singularities with isoparametric finite elements. *Int J Numer Methods Eng* 1974;8:537–45.
 - [11] Moes N, Dolbow J, Belytschko T. A finite element method for crack growth without remeshing. *Int J Numer Methods Eng* 1999;46:131–50.
 - [12] Abdelaziz Y, Hamouine A. A survey of the extended finite element. *Comput Struct* 2008;86:1141–51. d
 - [13] Givoli D, Rivkin L. The DtN finite element method for elastic domains with cracks and re-entrant corners. *Comput Struct* 1993;49:633–42.
 - [14] Tong P, Pian THH, Lasry SJ. A hybrid-element approach to crack problems in plane elasticity. *Int J Numer Methods Eng* 1973;7:297–308.
 - [15] Karihaloo BL, Xiao QZ. Hybrid stress elements for accurate solution of elasticity problems with traction-free segments n.d.:109–25.
 - [16] Xiao QZZ, Karihaloo BLL, Liu XYY. Direct determination of SIF and higher order terms of mixed mode cracks by a hybrid crack element. *Int J Fract* 2004;125:207–25.
 - [17] Lin KY, Tong P. Singular finite elements for the fracture analysis of V-notched plate. *Int J Numer Methods Eng* 1980;15:1343–54.
-

- [18] Seweryn A. Modeling of singular stress fields using finite element method. *Int J Solids Struct* 2002;39:4787–804.
- [19] Seweryn A. Brittle fracture criterion for structures with sharp notches. *Eng Fract Mech* 1994;47:673–81.
- [20] Nui LS, Chehimi C, Pluvinage G. Stress field near a large blunted tip V-notch and application of the concept of the critical notch stress intensity factor (NSIF) to the fracture toughness of very brittle materials. *Eng Fract Mech* 1994;49:325–35.
- [21] Fett T. Failure of brittle materials near stress singularities. *Eng Fract Mech* 1996;53:511–8.
- [22] Dunn ML, Suwito W, Cunningham S, May CW. Fracture initiation at sharp notches under mode I, mode II, and mild mixed mode loading. *Int J Fract* 1997;84:367–81.
- [23] Lazzarin P, Zambardi R. A finite-volume-energy based approach to predict the static and fatigue behavior of components with sharp V-shaped notches. *Int J Fract* 2001;112:275–98.
- [24] Kihara S, Yoshii A. A strength evaluation method of a sharply notched structure by a new parameter, “the equivalent stress intensity factor”. *JSME Int J* 1991;34:70–5.
- [25] Boukharouba T, Tamine T, Niu L, Chehimi C, Pluvinage G. The use of notch stress intensity factor as a fatigue crack initiation parameter. *Eng Fract Mech* 1995;52:503–12.
- [26] Verreman Y, Nie B. Early development of fatigue cracking at manual fillet welds. *Fatigue Fract Eng Mater Struct* 1996;19:669–81.
- [27] Lazzarin P, Tovo R. A notch intensity factor approach to the stress analysis of welds. *Fatigue Fract Eng Mater Struct* 1998;21:1089–103.
- [28] Atzori B, Meneghetti G. Fatigue strength of fillet welded structural steels: finite elements, strain gauges and reality. *Int J Fatigue* 2001;23:713–21.
- [29] Livieri P, Lazzarin P. Fatigue strength of steel and aluminium welded joints based on generalised stress intensity factors and local strain energy values. *Int J Fract* 2005;133:247–76.
- [30] Gross B, Mendelson A. Plane elastostatic analysis of V-notched plates. *Int J Fract Mech* 1972;8:267–76.
- [31] Williams ML. Stress singularities resulting from various boundary conditions in angular corners of plates in tension. *J Appl Mech* 1952;19:526–8.
- [32] Berto F, Lazzarin P. Recent developments in brittle and quasi-brittle failure assessment of engineering materials by means of local approaches. *Mater Sci Eng R Reports* 2014;75:1–48.
- [33] Lazzarin P, Campagnolo A, Berto F. A comparison among some recent energy- and stress-based criteria for the fracture assessment of sharp V-notched components under Mode I loading. *Theor Appl Fract Mech*

- 2014;71:21–30.
- [34] Berto F, Campagnolo A, Lazzarin P. Fatigue strength of severely notched specimens made of Ti-6Al-4V under multiaxial loading. *Fatigue Fract Eng Mater Struct* 2015;38:503–17.
- [35] Gallo P, Berto F, Lazzarin P. High temperature fatigue tests of notched specimens made of titanium Grade 2. *Theor Appl Fract Mech* 2015;76:27–34.
- [36] Berto F, Lazzarin P. Multiparametric full-field representations of the in-plane stress fields ahead of cracked components under mixed mode loading. *Int J Fatigue* 2013;46:16–26.
- [37] Lazzarin P, Berto F, Zappalorto M. Rapid calculations of notch stress intensity factors based on averaged strain energy density from coarse meshes: Theoretical bases and applications. *Int J Fatigue* 2010;32:1559–67.
- [38] Pook LP. A 50 year retrospective review of three-dimensional effects at cracks and sharp notches. *Fatigue Fract Eng Mater Struct* 2013;36:699–723.
- [39] Pook LP, Campagnolo A, Berto F, Lazzarin P. Coupled fracture mode of a cracked plate under anti-plane loading. *Eng Fract Mech* 2015;134:391–403.
- [40] Campagnolo A, Berto F, Lazzarin P. The effects of different boundary conditions on three-dimensional cracked discs under anti-plane loading. *Eur J Mech - A/Solids* 2015;50:76–86.
- [41] Nisitani H, Teranishi T. KI value of a circumferential crack emanating from an ellipsoidal cavity obtained by the crack tip stress method in FEM. In: Guagliano M, Aliabadi MH, editors. *Proc. 2nd Int. Conf. Fract. damage Mech.*, 2001, p. 141–6.
- [42] Nisitani H, Teranishi T. KI of a circumferential crack emanating from an ellipsoidal cavity obtained by the crack tip stress method in FEM. *Eng Fract Mech* 2004;71:579–85.
- [43] Meneghetti G, Lazzarin P. Significance of the elastic peak stress evaluated by FE analyses at the point of singularity of sharp V-notched components. *Fatigue Fract Eng Mater Struct* 2007;30:95–106.
- [44] Meneghetti G. The use of peak stresses for fatigue strength assessments of welded lap joints and cover plates with toe and root failures. *Eng Fract Mech* 2012;89:40–51.
- [45] Meneghetti G. The peak stress method applied to fatigue assessments of steel and aluminium fillet-welded joints subjected to mode I loading. *Fatigue Fract Eng Mater Struct* 2008;31:346–69.
- [46] Meneghetti G, Atzori B, Manara G. The Peak Stress Method applied to fatigue assessments of steel tubular welded joints subject to mode-I loading. *Eng Fract Mech* 2010;77:2100–14.
- [47] Meneghetti G, Guzzella C. The peak stress method to estimate the mode I notch stress intensity factor in welded joints using three-dimensional finite
-

- element models. *Eng Fract Mech* 2014;115:154–71.
- [48] Meneghetti G, Guzzella C, Atzori B. The peak stress method combined with 3D finite element models for fatigue assessment of toe and root cracking in steel welded joints subjected to axial or bending loading. *Fatigue Fract Eng Mater Struct* 2014;37:722–39.
- [49] Anderson TL. *Fracture Mechanics, Fundamentals and Applications*. 2nd ed. Boca Raton: CRC Press LLC; 1994.
- [50] Brandt U, Lehrke HP, Sonsino CM, Radaj D. Anwendung des Kergrundkonzeptes für die schwingfeste Bemessung von Schweissverbindungen aus Aluminiumknetlegierungen. Darmstadt: 1999.
- [51] Sonsino CM, Radaj D, Brandt U, Lehrke HP. Fatigue assessment of welded joints in AlMg 4.5Mn aluminum alloy (AA 5083) by local approaches. *Int J Fatigue* 1999;21:985–99.
- [52] Meneghetti G, Campagnolo A, Berto F. Fatigue strength assessment of partial and full-penetration steel and aluminium butt-welded joints according to the peak stress method. *Fatigue Fract Eng Mater Struct* 2015;38:1419–31.
- [53] Lazzarin P, Sonsino CM, Zambardi R. A notch stress intensity approach to assess the multiaxial fatigue strength of welded tube-to-flange joints subjected to combined loadings. *Fatigue Fract Eng Mater Struct* 2004;27:127–40.
- [54] Lazzarin P, Berto F, Radaj D. Uniform fatigue strength of butt and fillet welded joints in terms of the local strain energy density. *Proceeding 9th Int. Fatigue Congr., Atlanta, USA: 2006*.
- [55] Brahtz J. Stress Distribution in a Reentrant Corner. *Trans Am Soc Mech Eng* 1933;55:31–7.
- [56] Williams ML. On the stress distribution at the base of a stationary crack. *J Appl Mech* 1957;24:109–14.
- [57] Griffith AA. The phenomena of rupture and flow in solids. *Philos Trans R Soc London A* 1921;221:163–98.
- [58] Westergaard MH. Bearing pressures and cracks. *J Appl Mech* 1939;6:A49–53.
- [59] Irwin GR. Analysis of stresses and strains near the end of a crack traversing a plate. *J Appl Mech* 1957;24:361–4.
- [60] Carpenter WC. The eigenvector solution for a general corner or finite opening crack with further studies on the collocation procedure. *Int J Fract* 1985;27:63–73.
- [61] Larsson SG, Carlsson AJ. Influence of non-singular stress terms and specimen geometry on small-scale yielding at crack tips in elastic-plastic materials. *J Mech Phys Solids* 1973;21:263–77.
- [62] Radaj D. T-stress corrected notch stress intensity factors with application to welded lap joints. *Fatigue Fract Eng Mater Struct* 2010;33:378–89.
-

-
- [63] Rice JR. Limitations to the small scale yielding approximation for crack tip plasticity. *J Mech Phys Solids* 1974;22:17–26.
- [64] Ayatollahi MR, Pavier MJ, Smith DJ. Determination of T -stress from finite element analysis for mode I and mixed mode I/II loading. *Int J Fract* 1998;91:283–98.
- [65] Chen YZ. Closed form solutions of T-stress in plane elasticity crack problems. *Int J Solids Struct* 2000;37:1629–37.
- [66] Fett T, Munz D. T-stress and crack path stability of DCDC specimens. *Int J Fract* 2003;124:L165–70.
- [67] Smith DJ, Ayatollahi MR, Pavier MJ. The role of T-stress in brittle fracture for linear elastic materials under mixed-mode loading. *Fatigue Fract Eng Mater Struct* 2001;24:137–50.
- [68] Ayatollahi MR, Saboori B. T-stress effects in mixed mode I/II/III brittle fracture. *Eng Fract Mech* 2015;144:32–45.
- [69] Erdogan F, Sih GC. On the Crack Extension in Plates Under Plane Loading and Transverse Shear. *J Basic Eng* 1963;85:519.
- [70] Lazzarin P, Berto F, Radaj D. Fatigue-relevant stress field parameters of welded lap joints: pointed slit tip compared with keyhole notch. *Fatigue Fract Eng Mater Struct* 2009;32:713–35.
- [71] Chen YZ, Lin XY, Wang ZX. A rigorous derivation for T-stress in line crack problem. *Eng Fract Mech* 2010;77:753–7.
- [72] Fett T, Rizzi G. Weight Functions for Stress Intensity Factors and T-Stress for Oblique Cracks in A Half-Space. *Int J Fract* 2005;132:L9–16.
- [73] Fett T, Rizzi G, Bahr H-A. Green's functions for the T-stress of small kink and fork cracks. *Eng Fract Mech* 2006;73:1426–35.
- [74] Wang X, Lewis T, Bell R. Estimations of the T-stress for small cracks at notches. *Eng Fract Mech* 2006;73:366–75.
- [75] Ramesh K, Gupta S, Srivastava AK. Equivalence of multi-parameter stress field equations in fracture mechanics. *Int J Fract* 1996;79.
- [76] Ramesh K, Gupta S, Kelkar AA. Evaluation of stress field parameters in fracture mechanics by photoelasticity -revisited. *Eng Fract Mech* 1997;56:25–45.
- [77] Ayatollahi MR, Nejati M. An over-deterministic method for calculation of coefficients of crack tip asymptotic field from finite element analysis. *Fatigue Fract Eng Mater Struct* 2011;34:159–76.
- [78] Xiao QZ, Karihaloo BL. An overview of a hybrid crack element and determination of its complete displacement field. *Eng Fract Mech* 2007;74:1107–17.
- [79] Berto F, Lazzarin P. A review of the volume-based strain energy density approach applied to V-notches and welded structures. *Theor Appl Fract Mech* 2009;52:183–94.
-

- [80] Torabi AR, Campagnolo A, Berto F. Experimental and theoretical investigation of brittle fracture in key-hole notches under mixed mode I/II loading. *Acta Mech* 2015;226:2313–22.
- [81] Berto F, Lazzarin P, Yates JR. Multiaxial fatigue of V-notched steel specimens: A non-conventional application of the local energy method. *Fatigue Fract Eng Mater Struct* 2011;34:921–43.
- [82] Lazzarin P, Berto F. From Neuber's Elementary Volume to Kitagawa and Atzori's Diagrams: An Interpretation Based on Local Energy. *Int J Fract* 2005;135:L33–8.
- [83] El Haddad MH, Topper TH, Smith KN. Prediction of non propagating cracks. *Eng Fract Mech* 1979;11:573–84.
- [84] Meneghetti G, Campagnolo A, Berto F, Atzori B. Averaged strain energy density evaluated rapidly from the singular peak stresses by FEM: cracked components under mixed-mode (I+II) loading. *Theor Appl Fract Mech* 2015;79:113–24.
- [85] Lazzarin P, Lassen T, Livieri P. A notch stress intensity approach applied to fatigue life predictions of welded joints with different local toe geometry. *Fatigue Fract Eng Mater Struct* 2003;26:49–58.
- [86] Hobbacher A. Recommendations for Fatigue design of welded joints and components. 2008.
- [87] Meneghetti G, Lazzarin P. The Peak Stress Method for Fatigue Strength Assessment of welded joints with weld toe or weld root failures. *Weld World* 2011;55:22–9.
- [88] Radaj D. State-of-the-art review on extended stress intensity factor concepts. *Fatigue Fract Eng Mater Struct* 2014;37:1–28.
- [89] Radaj D. State-of-the-art review on the local strain energy density concept and its relation to the J -integral and peak stress method. *Fatigue Fract Eng Mater Struct* 2015;38:2–28.
- [90] Brandt U, Lawrence F V., Sonsino CM. Fatigue crack initiation and growth in AlMg4.5Mn butt weldments. *Fatigue Fract Eng Mater Struct* 2001;24:117–26.
- [91] Petershagen H. Fatigue tests with hyperbaric dry butt welded specimens. 1992.
- [92] Hentschel K, Berger P, Rossler K, Schmidt M. Weld geometry as a factor controlling the fatigue strength of butt welded joints. *Weld Int* 1990;4:494.
- [93] Yakubovskii V V., Valteris IJI. Geometrical parameters of butt and fillet welds and their influence on the welded joints fatigue life. 1989.
- [94] Torabi ARR, Campagnolo A, Berto F. Tensile fracture analysis of V-notches with end holes by means of the local energy. *Phys Mesomech* 2015;18:194–202.
- [95] Campagnolo A, Berto F, Leguillon D. Mode II loading in sharp V-notched components: a comparison among some recent criteria. *Theor Appl Fract*

Mech 2016:Submitted.

- [96] Berto F, Lazzarin P. Fatigue strength of structural components under multi-axial loading in terms of local energy density averaged on a control volume. *Int J Fatigue* 2011;33:1055–65.
- [97] Berto F, Lazzarin P, Tovo R. Multiaxial fatigue strength of severely notched cast iron specimens. *Int J Fatigue* 2014;67:15–27.
- [98] Berto F, Campagnolo A, Chebat F, Cincera M, Santini M. Fatigue strength of steel rollers with failure occurring at the weld root based on the local strain energy values: modelling and fatigue assessment. *Int J Fatigue* 2016;82:643–57.
- [99] Neuber H. *Kerbspannungslehre*, 2nd Edition. Berlin: Springer-Verlag; 1958.
- [100] Neuber H. *Theory of Notch Stresses*. Berlin: Springer-Verlag; 1958.
- [101] Neuber H. Über die Berücksichtigung der Spannungskonzentration bei Festigkeitsberechnungen. *Konstruktion* 1968;20:245–51.
- [102] Lazzarin P, Livieri P, Berto F, Zappalorto M. Local strain energy density and fatigue strength of welded joints under uniaxial and multiaxial loading. *Eng Fract Mech* 2008;75:1875–89.
- [103] Meneghetti G. The peak stress method for fatigue strength assessment of tube-to-flange welded joints under torsion loading. *Weld World* 2013;57:265–75.
- [104] Meneghetti G, Atzori B, Campagnolo A, Berto F. A link between the peak stresses and the averaged strain energy density for cracks under mixed-mode (I+II) loading. *Fract Struct Integr* 2015.
- [105] Campagnolo A, Meneghetti G, Berto F. Rapid evaluation by FEM of the averaged strain energy density of mixed-mode (I+II) crack tip fields including the T-stress contribution. *Fatigue Fract Eng Mater Struct* 2016;Submitted .
- [106] Sherry AH, France CC, Goldthorpe MR. Compendium of T-stress solutions for two and three dimensional cracked geometries. *Fatigue Fract Eng Mater Struct* 1995;18:141–55.
- [107] Qian J, Hasebe N. Property of eigenvalues and eigenfunctions for an interface V-notch in antiplane elasticity. *Eng Fract Mech* 1997;56:729–34.
- [108] Radaj D, Sonsino CM, Fricke W. *Fatigue Assessment of Welded Joints by Local Approaches*. 2nd ed. Cambridge: Woodhead Publishing; 2006.
- [109] Radaj D, Vormwald M. *Advanced Methods of Fatigue Assessment*. Berlin, Heidelberg: Springer Berlin Heidelberg; 2013.
- [110] Smith RA, Miller KJ. Prediction of fatigue regimes in notched components. *Int J Mech Sci* 1978;20:201–6.
- [111] Taylor D. Geometrical effects in fatigue: a unifying theoretical model. *Int J Fatigue* 1999;21:413–20.

- [112] Atzori B, Lazzarin P, Meneghetti G. Fracture mechanics and notch sensitivity. *Fatigue Fract Eng Mater Struct* 2003;26:257–67.
- [113] Eurocode 3: design of steel structures – part 1–9: fatigue. European Committee for Standardization: n.d. doi:en.1993.1.1.2005.
- [114] Sonsino CM. Fatigue strength of welded components under complex elasto-plastic, multiaxial deformations. 1997.
- [115] Yousefi F, Witt M, Zenner H. Fatigue strength of welded joints under multiaxial loading: experiments and calculations. *Fatigue Fract Eng Mater Struct* 2001;24:339–55.
- [116] Amstutz H, Storzel K, Seeger T. Fatigue crack growth of a welded tube-flange connection under bending and torsional loading. *Fatigue Fract Eng Mater Struct* 2001;24:357–68.
- [117] Seeger T, Olivier R. Tolerable and allowable shear stresses at fatigue loaded welded joints. *Stahlbau* (in Ger 1987;8:231–8.
- [118] Seeger T, Olivier R. Slope and knee-point of the S-N curve of shear loaded fillet welds. *Stahlbau* (in Ger 1992;61:137–42.
- [119] Yung JY, Lawrence F V. Predicting the fatigue life of welds under combined bending and torsion. In: Brown M, Miller K, editors. *Biaxial multiaxial fatigue EGF 3.*, London: Mechanical Engineering Publications; 1989, p. 53–69.
- [120] Siljander A, Kurath P, Lawrence F. Non proportional fatigue of welded structures. In: Mitchell M, Landgraf R, editors. *Adv. fatigue lifetime Predict. Tech. ASTMSTP 1122*, Philadelphia, USA: American Society for Testing and Materials; 1992, p. 319–38.
- [121] Razmjoo GR. Fatigue of load carrying fillet welded joints under multiaxial loading. *Fatigue core research from TWI*. Abington: Abington Publishing; 1996.
- [122] Haibach E. *Service Fatigue-Strength – Methods and data for structural analysis*. Berlin: Springer Verlag; 2002.

Conclusions

In this PhD thesis, some of the most important and widely employed local approaches have been adopted in fracture and fatigue problems of notched and cracked structural components, with particular attention to eventual three-dimensional effects. The considered local approaches have also been compared with other fundamental criteria proposed in the literature and the link between different methods have been investigated.

Dealing with brittle fracture under mixed mode static loading, it has been highlighted that the strain energy density (SED) approach allowed to assess the static critical loads with excellent accuracy also in the case of complex loading conditions.

With regard to multiaxial fatigue, the SED approach allowed to assess the fatigue strength of severely notched titanium grade 5 alloy, Ti-6Al-4V, under combined tension and torsion loading, both in-phase and out-of-phase. In particular, a single narrow scatter band including all experimental data regardless of the nominal load ratio and the phase angle has been proposed for the multiaxial fatigue design of titanium notched components. Then, the SED criterion has been applied for the multiaxial fatigue strength assessment of steel welded rollers produced by Rulmeca S.p.a. It has been shown that the scatter band proposed in the literature for structural welded steels can be satisfactorily applied also to the fatigue strength assessment of the considered rollers. Finally, some observations about the phase angle effect on sharp V-notched components under multiaxial fatigue, which have been drawn on the basis of a new proposed analytical frame, have been qualitatively compared also with experimental results.

Dealing with 3D effects in notched and cracked components, it has been highlighted that the SED parameter is able to quantify the 3D effects in comparison with the sensitivity of the specific material so providing precious information for the fracture assessment. Then, dealing with notched components under cyclic plasticity conditions, it has been demonstrated that 3D effects related to the presence of a finite thickness in a notched component cannot be neglected *a*

priori either in linear-elastic problems or in the presence of a yielded region ahead of the notch tip. Moreover, it has been shown that the plastic strain hysteretic energy, considered in the literature to be a parameter linked to the fatigue damage, can be directly determined by means of the averaged SED, obtained from a static FE analysis, via a multiplicative factor.

Then, dealing with the comparison between the SED approach and that based on the Finite Fracture Mechanics, it has been shown that for all considered criteria the same proportionality relation exists between the critical value of the notch stress intensity factor (NSIF) and two mechanical properties of the material: the fracture toughness and the ultimate tensile strength. Moreover, a new expression for estimating the control radius under pure Mode II loading has been proposed and discussed in comparison with that valid for pure Mode I. The experimental comparison has shown that the agreement between the theoretical estimates and the experimental values of the critical value of the NSIF is very good in all cases.

Finally, a link between the SED approach and the Peak Stress Method (PSM) has been investigated. Cracks under in-plane mixed mode I+II and out-of-plane mixed mode I+III loading have been considered. A method to rapidly evaluate the averaged SED based on the peak stresses at the crack tip has been proposed. On the basis of the derived link, some practical applications related to the fatigue strength assessment of aluminium and steel butt welded joints and of tube-to-flange steel welded joints have been successfully carried out.

In conclusion, the effectiveness and potentialities of the considered local approaches, and in particular of the SED approach, in the fracture and fatigue assessment of structural components characterized by different geometries and subjected to complex loading conditions have been proved both theoretically and experimentally.

Bibliography

For a better reading, numbered references have been included at the end of each Chapter. Below, the complete list of references is reported in alphabetical order.

- Abdelaziz, Y., Hamouine, A., 2008. A survey of the extended finite element. *Comput. Struct.* 86, 1141–1151.
- Akin, J.E., 1976. The generation of elements with singularities. *Int. J. Numer. Methods Eng.* 10, 1249–1259.
- Aliha, M.R.M., Ayatollahi, M.R., 2014. Rock fracture toughness study using cracked chevron notched Brazilian disc specimen under pure modes I and II loading – A statistical approach. *Theor. Appl. Fract. Mech.* 69, 17–25.
- Aliha, M.R.M., Ayatollahi, M.R., 2012. Analysis of fracture initiation angle in some cracked ceramics using the generalized maximum tangential stress criterion. *Int. J. Solids Struct.* 49, 1877–1883.
- Aliha, M.R.M., Hosseinpour, G.R., Ayatollahi, M.R., 2012. Application of Cracked Triangular Specimen Subjected to Three-Point Bending for Investigating Fracture Behavior of Rock Materials. *Rock Mech. Rock Eng.* 46, 1023–1034.
- Allard, B., Rouby, D., Fantozzi, G., Dumas, D., Lacroix, P., 1991. Fracture behaviour of carbon materials. *Carbon N. Y.* 29, 457–468.
- Amstutz, H., Storzel, K., Seeger, T., 2001. Fatigue crack growth of a welded tube-flange connection under bending and torsional loading. *Fatigue Fract. Eng. Mater. Struct.* 24, 357–368.
- Anderson, T.L., 1994. *Fracture Mechanics, Fundamentals and Applications*, 2nd ed. CRC Press LLC, Boca Raton.
- Ardito, R., Corigliano, A., Frangi, A., Rizzini, F., 2014. Advanced models for the calculation of capillary attraction in axisymmetric configurations. *Eur. J. Mech. - A/Solids* 47, 298–308.
- Armstrong, P., Frederick, C.O., 1966. A mathematical representation of the multiaxial Bauschinger effect. Rep. RD/B/N 731, Cent. Electr. Gener. Board.
- ASTM E399-90 (1997). *Standard Test Method for Plane-Strain Fracture Toughness of Metallic Materials*, 1997.
- Atzori, B., 1985. Fracture mechanics or notch effect for fatigue design, in: XIII National Congress of the Italian Society for Strain Analysis (Edited by AIAS). Bergamo Italy (in Italian).
- Atzori, B., Berto, F., Lazzarin, P., Quaresimin, M., 2006. Multi-axial fatigue behaviour of a severely notched carbon steel. *Int. J. Fatigue* 28, 485–493.

- Atzori, B., Dattoma, V., 1983. A comparison of the fatigue behaviour of welded joints in steels and in aluminium alloys. IIW Doc XXXIII-1089-1983.
- Atzori, B., Lazzarin, P., Meneghetti, G., 2003. Fracture mechanics and notch sensitivity. *Fatigue Fract. Eng. Mater. Struct.* 26, 257–267.
- Atzori, B., Lazzarin, P., Tovo, R., 1999. From a local stress approach to fracture mechanics: a comprehensive evaluation of the fatigue strength of welded joints. *Fatigue Fract. Eng. Mater. Struct.* 22, 369–381.
- Atzori, B., Lazzarin, P., Tovo, R., 1999. Stress field parameters to predict the fatigue strength of notched components. *J. Strain Anal. Eng. Des.* 34, 437–453.
- Atzori, B., Lazzarin, P., Tovo, R., 1997. Stress distributions for V-shaped notches under tensile and bending loads. *Fatigue Fract. Eng. Mater. Struct.* 20, 1083–1092.
- Atzori, B., Meneghetti, G., 2001. Fatigue strength of fillet welded structural steels: finite elements, strain gauges and reality. *Int. J. Fatigue* 23, 713–721.
- Awaji, H., Sato, S., 1978. Combined Mode Fracture Toughness Measurement by the Disk Test. *J. Eng. Mater. Technol.* 100, 175–182.
- Ayatollahi, M., Saboori, B., 2014. Maximum tangential strain energy density criterion for general mixed mode I/II/III brittle fracture. *Int. J. Damage Mech.* 24, 263–278.
- Ayatollahi, M.R., Aliha, M.R.M., 2009. Analysis of a new specimen for mixed mode fracture tests on brittle materials. *Eng. Fract. Mech.* 76, 1563–1573.
- Ayatollahi, M.R., Aliha, M.R.M., 2008. Mixed mode fracture analysis of polycrystalline graphite – A modified MTS criterion. *Carbon N. Y.* 46, 1302–1308.
- Ayatollahi, M.R., Dehghany, M., Mirsayar, M.M., 2013. A comprehensive photoelastic study for mode I sharp V-notches. *Eur. J. Mech. - A/Solids* 37, 216–230.
- Ayatollahi, M.R., Mirsayar, M.M., Dehghany, M., 2011. Experimental determination of stress field parameters in bi-material notches using photoelasticity. *Mater. Des.* 32, 4901–4908.
- Ayatollahi, M.R., Nejati, M., 2011. An over-deterministic method for calculation of coefficients of crack tip asymptotic field from finite element analysis. *Fatigue Fract. Eng. Mater. Struct.* 34, 159–176.
- Ayatollahi, M.R., Pavier, M.J., Smith, D.J., 1998. Determination of T -stress from finite element analysis for mode I and mixed mode I/II loading. *Int. J. Fract.* 91, 283–298.
- Ayatollahi, M.R., Saboori, B., 2015. A new fixture for fracture tests under mixed mode I/III loading. *Eur. J. Mech. - A/Solids* 51, 67–76.
- Ayatollahi, M.R., Saboori, B., 2015. T-stress effects in mixed mode I/II/III brittle fracture. *Eng. Fract. Mech.* 144, 32–45.

- Ayatollahi, M.R., Torabi, A.R., 2011. Experimental verification of RV-MTS model for fracture in soda-lime glass weakened by a V-notch. *J. Mech. Sci. Technol.* 25, 2529–2534.
- Ayatollahi, M.R., Torabi, A.R., 2010a. Brittle fracture in rounded-tip V-shaped notches. *Mater. Des.* 31, 60–67.
- Ayatollahi, M.R., Torabi, A.R., 2010b. Determination of mode II fracture toughness for U-shaped notches using Brazilian disc specimen. *Int. J. Solids Struct.* 47, 454–465.
- Ayatollahi, M.R., Torabi, A.R., 2010c. Investigation of mixed mode brittle fracture in rounded-tip V-notched components. *Eng. Fract. Mech.* 77, 3087–3104.
- Ayatollahi, M.R., Torabi, A.R., 2009. A criterion for brittle fracture in U-notched components under mixed mode loading. *Eng. Fract. Mech.* 76, 1883–1896.
- Ayatollahi, M.R., Torabi, A.R.R., Azizi, P., 2010. Experimental and Theoretical Assessment of Brittle Fracture in Engineering Components Containing a Sharp V-Notch. *Exp. Mech.* 51, 919–932.
- Ayatollahi, M.R.R., Berto, F., Lazzarin, P., 2011. Mixed mode brittle fracture of sharp and blunt V-notches in polycrystalline graphite. *Carbon N. Y.* 49, 2465–2474.
- Ayatollahi, M.R.R., Torabi, A.R.R., 2011. Failure assessment of notched polycrystalline graphite under tensile-shear loading. *Mater. Sci. Eng. A* 528, 5685–5695.
- Ayatollahi, M.R.R., Torabi, A.R.R., 2010. Tensile fracture in notched polycrystalline graphite specimens. *Carbon N. Y.* 48, 2255–2265.
- Babuška, I., Miller, A., 1984. The post-processing approach in the finite element method—Part 2: The calculation of stress intensity factors. *Int. J. Numer. Methods Eng.* 20, 1111–1129.
- Barati, E., Aghazadeh Mohandesi, J., Alizadeh, Y., 2010a. The effect of notch depth on J-integral and critical fracture load in plates made of functionally graded aluminum–silicon carbide composite with U-notches under bending. *Mater. Des.* 31, 4686–4692.
- Barati, E., Alizadeh, Y., 2011. A numerical method for evaluation of J-integral in plates made of functionally graded materials with sharp and blunt V-notches. *Fatigue Fract. Eng. Mater. Struct.* 34, 1041–1052.
- Barati, E., Alizadeh, Y., Aghazadeh, J., Berto, F., 2010b. Some new practical equations for rapid calculation of J-integral in plates weakened by U-notches under bending. *Mater. Des.* 31, 2964–2971.
- Barsoum, R.S., 1975. Further application of quadratic isoparametric finite elements to linear fracture mechanics of plate bending and general shells. *Int. J. Fract.* 11, 167–169.
- Bazaj, D.K., Cox, E.E., 1969. Stress-concentration factors and notch-sensitivity of graphite. *Carbon N. Y.* 7, 689–697.

- Bažant, Z.P., Estenssoro, L.F., 1979. Surface singularity and crack propagation. *Int. J. Solids Struct.* 15, 405–426.
- Becker, T.H., Mostafavi, M., Tait, R.B., Marrow, T.J., 2012. An approach to calculate the J-integral by digital image correlation displacement field measurement. *Fatigue Fract. Eng. Mater. Struct.* 35, 971–984.
- Beghini, M., Bertini, L., Di Lello, R., Fontanari, V., 2007. A general weight function for inclined cracks at sharp V-notches. *Eng. Fract. Mech.* 74, 602–611.
- Beltrami, E., 1885. Sulle condizioni di resistenza dei corpi elastici. *Il Nuovo Cimento* 18 (in Italian).
- Benedetti, M., Bertini, L., Fontanari, V., 2004. Behaviour of fatigue cracks emanating from circular notches in Ti-6Al-4V under bending. *Fatigue Fract. Eng. Mater. Struct.* 27, 111–125.
- Benedetti, M., Fontanari, V., 2004. The effect of bi-modal and lamellar microstructures of Ti-6Al-4V on the behaviour of fatigue cracks emanating from edge-notches. *Fatigue Fract. Eng. Mater. Struct.* 27, 1073–1089.
- Bentachfine, S., 1999. Notch effect in low cycle fatigue. *Int. J. Fatigue* 21, 421–430.
- Bentham, J.P., 1980. The quarter-infinite crack in a half space; Alternative and additional solutions. *Int. J. Solids Struct.* 16, 119–130.
- Benzley, S.E., 1974. Representation of singularities with isoparametric finite elements. *Int. J. Numer. Methods Eng.* 8, 537–545.
- Berto, F., 2015. Some recent results on the fatigue strength of notched specimens made of 40CrMoV13.9 steel at room and high temperature. *Phys. Mesomech.* 18, 105–126.
- Berto, F., Ayatollahi, M.R.R., 2011. Fracture assessment of Brazilian disc specimens weakened by blunt V-notches under mixed mode loading by means of local energy. *Mater. Des.* 32, 2858–2869.
- Berto, F., Campagnolo, A., Chebat, F., Cincera, M., Santini, M., 2016. Fatigue strength of steel rollers with failure occurring at the weld root based on the local strain energy values: modelling and fatigue assessment. *Int. J. Fatigue* 82, 643–657.
- Berto, F., Campagnolo, A., Elices, M., Lazzarin, P., 2013a. A synthesis of Polymethylmethacrylate data from U-notched specimens and V-notches with end holes by means of local energy. *Mater. Des.* 49, 826–833.
- Berto, F., Campagnolo, A., Gallo, P., 2015a. Brittle Failure of Graphite Weakened by V-Notches: A Review of Some Recent Results Under Different Loading Modes. *Strength Mater.* 47, 488–506.
- Berto, F., Campagnolo, A., Lazzarin, P., 2015b. Fatigue strength of severely notched specimens made of Ti-6Al-4V under multiaxial loading. *Fatigue Fract. Eng. Mater. Struct.* 38, 503–517.
- Berto, F., Cendon, D.A.A., Lazzarin, P., Elices, M., 2013b. Fracture behaviour of

- notched round bars made of PMMA subjected to torsion at -60°C . *Eng. Fract. Mech.* 102, 271–287.
- Berto, F., Elices, M., Lazzarin, P., Zappalorto, M., 2012a. Fracture behaviour of notched round bars made of PMMA subjected to torsion at room temperature. *Eng. Fract. Mech.* 90, 143–160.
- Berto, F., Gallo, P., Lazzarin, P., 2014. High temperature fatigue tests of un-notched and notched specimens made of 40CrMoV13.9 steel. *Mater. Des.* 63, 609–619.
- Berto, F., Kotousov, A., Lazzarin, P., Pegorin, F., 2013. On a coupled mode at sharp notches subjected to anti-plane loading. *Eur. J. Mech. - A/Solids* 38, 70–78.
- Berto, F., Lazzarin, P., 2014. Recent developments in brittle and quasi-brittle failure assessment of engineering materials by means of local approaches. *Mater. Sci. Eng. R Reports* 75, 1–48.
- Berto, F., Lazzarin, P., 2013. Multiparametric full-field representations of the in-plane stress fields ahead of cracked components under mixed mode loading. *Int. J. Fatigue* 46, 16–26.
- Berto, F., Lazzarin, P., 2011. Fatigue strength of structural components under multi-axial loading in terms of local energy density averaged on a control volume. *Int. J. Fatigue* 33, 1055–1065.
- Berto, F., Lazzarin, P., 2009. A review of the volume-based strain energy density approach applied to V-notches and welded structures. *Theor. Appl. Fract. Mech.* 52, 183–194.
- Berto, F., Lazzarin, P., 2007. Relationships between J-integral and the strain energy evaluated in a finite volume surrounding the tip of sharp and blunt V-notches. *Int. J. Solids Struct.* 44, 4621–4645.
- Berto, F., Lazzarin, P., Ayatollahi, M.R., 2012b. Brittle fracture of sharp and blunt V-notches in isostatic graphite under torsion loading. *Carbon* N. Y. 50, 1942–1952.
- Berto, F., Lazzarin, P., Ayatollahi, M.R.R., 2013c. Brittle fracture of sharp and blunt V-notches in isostatic graphite under pure compression loading. *Carbon* N. Y. 63, 101–116.
- Berto, F., Lazzarin, P., Gallo, P., 2013d. High-temperature fatigue strength of a copper-cobalt-beryllium alloy. *J. Strain Anal. Eng. Des.* 49, 244–256
- Berto, F., Lazzarin, P., Gómez, F.J., Elices, M., 2007a. Fracture assessment of U-notches under mixed mode loading: two procedures based on the “equivalent local mode I” concept. *Int. J. Fract.* 148, 415–433.
- Berto, F., Lazzarin, P., Kotousov, A., 2011a. On higher order terms and out-of-plane singular mode. *Mech. Mater.* 43, 332–341.
- Berto, F., Lazzarin, P., Kotousov, A., Harding, S., 2011b. Out-of-plane singular stress fields in V-notched plates and welded lap joints induced by in-plane shear load conditions. *Fatigue Fract. Eng. Mater. Struct.* 34, 291–304.

- Berto, F., Lazzarin, P., Kotousov, A., Pook, L.P., 2012c. Induced out-of-plane mode at the tip of blunt lateral notches and holes under in-plane shear loading. *Fatigue Fract. Eng. Mater. Struct.* 35, 538–555.
- Berto, F., Lazzarin, P., Marangon, C., 2014a. Fatigue strength of notched specimens made of 40CrMoV13.9 under multiaxial loading. *Mater. Des.* 54, 57–66.
- Berto, F., Lazzarin, P., Marangon, C., 2012d. Brittle fracture of U-notched graphite plates under mixed mode loading. *Mater. Des.* 41, 421–432.
- Berto, F., Lazzarin, P., Marangon, C., 2012. The effect of the boundary conditions on in-plane and out-of-plane stress field in three dimensional plates weakened by free-clamped V-notches. *Phys. Mesomech.* 15, 26–36.
- Berto, F., Lazzarin, P., Matvienko, Y.G., 2007b. J-integral evaluation for U- and V-blunt notches under Mode I loading and materials obeying a power hardening law. *Int. J. Fract.* 146, 33–51.
- Berto, F., Lazzarin, P., Radaj, D., 2009. Fictitious notch rounding concept applied to sharp V-notches: Evaluation of the microstructural support factor for different failure hypotheses. *Eng. Fract. Mech.* 76, 1151–1175.
- Berto, F., Lazzarin, P., Radaj, D., 2008. Fictitious notch rounding concept applied to sharp V-notches: Evaluation of the microstructural support factor for different failure hypotheses. Part I: Basic stress equations. *Eng. Fract. Mech.* 75, 3060–3072.
- Berto, F., Lazzarin, P., Tovo, R., 2014b. Multiaxial fatigue strength of severely notched cast iron specimens. *Int. J. Fatigue* 67, 15–27.
- Berto, F., Lazzarin, P., Yates, J.R., 2011c. Multiaxial fatigue of V-notched steel specimens: A non-conventional application of the local energy method. *Fatigue Fract. Eng. Mater. Struct.* 34, 921–943.
- Berto, F., Marangon, C., 2013. Three-dimensional effects in finite thickness plates weakened by rounded notches and holes under in-plane shear. *Fatigue Fract. Eng. Mater. Struct.* 36, 1139–1152.
- Bhattacharjee, D., Knott, J.F., 1995. Effect of mixed mode I and II loading on the fracture surface of polymethyl methacrylate (PMMA). *Int. J. Fract.* 72, 359–381.
- Boukharouba, T., Tamine, T., Niu, L., Chehimi, C., Pluvinage, G., 1995. The use of notch stress intensity factor as a fatigue crack initiation parameter. *Eng. Fract. Mech.* 52, 503–512.
- Bower, A.F., 1987. Some aspects of plastic flow, residual stress and fatigue cracks due to rolling and sliding contact. University of Cambridge.
- Bower, A.F., Johnson, K.L., 1989. The influence of strain hardening on cumulative plastic deformation in rolling and sliding line contact. *J. Mech. Phys. Solids* 37, 471–493.
- Brahtz, J., 1933. Stress Distribution in a Reentrant Corner. *Trans. Am. Soc. Mech. Eng.* 55, 31–37.

- Brandt, U., Lawrence, F. V., Sonsino, C.M., 2001. Fatigue crack initiation and growth in AlMg4.5Mn butt weldments. *Fatigue Fract. Eng. Mater. Struct.* 24, 117–126.
- Brandt, U., Lehrke, H.P., Sonsino, C.M., Radaj, D., 1999. Anwendung des Kergrundkonzeptes für die schwingfeste Bemessung von Schweissverbindungen aus Aluminiumknetlegierungen. Darmstadt.
- Brown, M., Miller, K., 1973. A theory for fatigue under multiaxial stress–strain conditions. *Proc. Inst. Mech. Eng.* 187, 745–756.
- Burchell, T.D., 1996. A microstructurally based fracture model for polygranular graphites. *Carbon N. Y.* 34, 297–316.
- Campagnolo, A., Berto, F., Lazzarin, P., 2015. The effects of different boundary conditions on three-dimensional cracked discs under anti-plane loading. *Eur. J. Mech. - A/Solids* 50, 76–86.
- Campagnolo, A., Berto, F., Leguillon, D., 2016. Mode II loading in sharp V-notched components: a comparison among some recent criteria. *Theor. Appl. Fract. Mech.* (Submitted).
- Campagnolo, A., Berto, F., Marangon, C., 2015. Cyclic plasticity in three-dimensional notched components under in-phase multiaxial loading at $R=-1$. *Theor. Appl. Fract. Mech.* doi:10.1016/j.tafmec.2015.10.004
- Campagnolo, A., Meneghetti, G., Berto, F., 2016. Rapid evaluation by FEM of the averaged strain energy density of mixed-mode (I+II) crack tip fields including the T-stress contribution. *Fatigue Fract. Eng. Mater. Struct.* (Submitted).
- Capetta, S., Tovo, R., Taylor, D., Livieri, P., 2011. Numerical evaluation of fatigue strength on mechanical notched components under multiaxial loadings. *Int. J. Fatigue* 33, 661–671.
- Cardano, G., 1545. *Artis magnaë sive de regulis algebraicis, liber unus.*, Translated. ed. Nuremberg.
- Carpenter, W.C., 1985. The eigenvector solution for a general corner or finite opening crack with further studies on the collocation procedure. *Int. J. Fract.* 27, 63–73.
- Carpinteri, A., 1987. Stress-singularity and generalized fracture toughness at the vertex of re-entrant corners. *Eng. Fract. Mech.*
- Carpinteri, A., Cornetti, P., Pugno, N., Sapora, A., Taylor, D., 2008. A finite fracture mechanics approach to structures with sharp V-notches. *Eng. Fract. Mech.* 75, 1736–1752.
- Carpinteri, A., Spagnoli, A., 2004. A fractal analysis of size effect on fatigue crack growth. *Int. J. Fatigue* 26, 125–133
- Carpinteri, A., Spagnoli, A., 2001. Multiaxial high-cycle fatigue criterion for hard metals. *Int. J. Fatigue* 23, 135–145
- Carpinteri, A., Spagnoli, A., Vantadori, S., 2014. Reformulation in the frequency domain of a critical plane-based multiaxial fatigue criterion. *Int. J. Fatigue*

67, 55–61.

- Carpinteri, A., Spagnoli, A., Vantadori, S., 2011. Multiaxial fatigue assessment using a simplified critical plane-based criterion. *Int. J. Fatigue* 33, 969–976.
- Carpinteri, A., Spagnoli, A., Vantadori, S., Bagni, C., 2013. Structural integrity assessment of metallic components under multiaxial fatigue: the C-S criterion and its evolution. *Fatigue Fract. Eng. Mater. Struct.* 36, 870–883.
- Chaboche, J.L., 2008. A review of some plasticity and viscoplasticity constitutive theories. *Int. J. Plast.* 24, 1642–1693.
- Chaboche, J.L., 1991. On some modifications of kinematic hardening to improve the description of ratchetting effects. *Int. J. Plast.* 7, 661–678.
- Chaboche, J.L., 1987. Cyclic plasticity modelling and ratchetting effects, in: *Proceedings of the Second International Conference on Constitutive Laws for Engineering Materials: Theory and Applications*. Elsevier Ltd, Tucson, Arizona, pp. 47–58.
- Chaboche, J.L., 1986. Time-independent constitutive theories for cyclic plasticity. *Int. J. Plast.* 2, 149–188.
- Chaboche, J.L., Dang Van, K., Cordier, G., 1979. Modelization of the strain memory effect on the cyclic hardening of the 316 stainless steel. *Structural Mechanical in Reactor Technology*, in: *Structural Mechanical in Reactor Technology*, Transaction of the 5th International Conference on Structural Mechanics in Reactor Technology. Berlin.
- Chang, J., Xu, J., Mutoh, Y., 2006. A general mixed-mode brittle fracture criterion for cracked materials. *Eng. Fract. Mech.* 73, 1249–1263.
- Chen, D.H., Ozaki, S., 2008. Investigation of failure criteria for a sharp notch. *Int. J. Fract.* 152, 63–74.
- Chen, Y.Z., 2000. Closed form solutions of T-stress in plane elasticity crack problems. *Int. J. Solids Struct.* 37, 1629–1637.
- Chen, Y.Z., Lin, X.Y., Wang, Z.X., 2010. A rigorous derivation for T-stress in line crack problem. *Eng. Fract. Mech.* 77, 753–757.
- Cho, S., Nakamura, Y., Mohanty, B., Kaneko, K., 2006. Study on control of crack-propagation in blasting, in: *Fragblast 8*. Santiago (Chile), pp. 124–128.
- Choi, S., Sankar, B. V., 2007. Fracture toughness of transverse cracks in graphite/epoxy laminates at cryogenic conditions. *Compos. Part B Eng.* 38, 193–200.
- Christopher, C.J., James, M.N., Patterson, E.A., Tee, K.F., 2008. A quantitative evaluation of fatigue crack shielding forces using photoelasticity. *Eng. Fract. Mech.* 75, 4190–4199.
- Christopher, C.J., James, M.N., Patterson, E.A., Tee, K.F., 2007. Towards a new model of crack tip stress fields. *Int. J. Fract.* 148, 361–371.
- Chu, C.-C., 1995. Fatigue Damage Calculation Using the Critical Plane Approach. *J. Eng. Mater. Technol.* 117, 41.

- Chu, C.-C., 1995. Incremental Multiaxial Neuber Correction for Fatigue Analysis. SAE Tech. Pap.
- Cooke, M.L., Pollard, D.D., 1996. Fracture propagation paths under mixed mode loading within rectangular blocks of polymethyl methacrylate. *J. Geophys. Res.* 101, 3387.
- Corigliano, A., Ghisi, A., Langfelder, G., Longoni, A., Zaraga, F., Merassi, A., 2011. A microsystem for the fracture characterization of polysilicon at the micro-scale. *Eur. J. Mech. - A/Solids* 30, 127–136.
- Cornetti, P., Pugno, N., Carpinteri, A., Taylor, D., 2006. Finite fracture mechanics: A coupled stress and energy failure criterion. *Eng. Fract. Mech.* 73, 2021–2033.
- Cristofori, A., Benasciutti, D., Tovo, R., 2011. A stress invariant based spectral method to estimate fatigue life under multiaxial random loading. *Int. J. Fatigue* 33, 887–899.
- Crupi, G., Crupi, V., Guglielmino, E., Taylor, D., 2005. Fatigue assessment of welded joints using critical distance and other methods. *Eng. Fail. Anal.* 12, 129–142.
- Davis, B.R., Wawrzynek, P.A., Ingraffea, A.R., 2014. 3-D simulation of arbitrary crack growth using an energy-based formulation – Part I: Planar growth. *Eng. Fract. Mech.* 115, 204–220.
- Dhondt, G., 1998. On corner point singularities along a quarter circular crack subject to shear loading. *Int. J. Fract.* 89, L13–L18.
- Doring, R., Hoffmeyer, J., Seeger, T., Vormwald, M., 2006. Short fatigue crack growth under nonproportional multiaxial elastic–plastic strains. *Int. J. Fatigue* 28, 972–982.
- Drucker, D.C., 1960. Plasticity in structural mechanics, in: Hoff, G. and (Ed.), *Proceeding of the First Symposium on Naval Structural Mechanics*. Pergamon, Macmillan, New York, pp. 331–350.
- Dunn, M.L., Suwito, W., Cunningham, S., 1997a. Fracture initiation at sharp notches: Correlation using critical stress intensities. *Int. J. Solids Struct.* 34, 3873–3883.
- Dunn, M.L., Suwito, W., Cunningham, S., 1997b. Stress intensities at notch singularities. *Eng. Fract. Mech.* 57, 417–430.
- Dunn, M.L., Suwito, W., Cunningham, S., May, C.W., 1997c. Fracture initiation at sharp notches under mode I, mode II, and mild mixed mode loading. *Int. J. Fract.* 84, 367–381.
- El Haddad, M.H., Topper, T.H., Smith, K.N., 1979. Prediction of non propagating cracks. *Eng. Fract. Mech.* 11, 573–584.
- Elices, M., Guinea, G.V., Gómez, J., Planas, J., Elices, M., G, J., 2002. The cohesive zone model: advantages, limitations and challenges. *Eng. Fract. Mech.* 69, 137–163.
- Ellyin, F., 1997. Fatigue damage, crack growth and life prediction.

- Ellyin, F., 1989. Cyclic strain energy density as a criterion for multiaxial fatigue failure, Biaxial an. ed. EGF Publication, London.
- Ellyin, F., 1974. A criterion for fatigue under multiaxial states of stress. *Mech. Res. Commun.* 1, 219–224.
- Ellyin, F., Kujawski, D., 1989. Generalization of notch analysis and its extension to cyclic loading. *Eng. Fract. Mech.* 32, 819–826.
- Ellyin, F., Kujawski, D., 1984. Plastic Strain Energy in Fatigue Failure. *J. Press. Vessel Technol.* 106, 342.
- Erdogan, F., Sih, G.C., 1963. On the Crack Extension in Plates Under Plane Loading and Transverse Shear. *J. Basic Eng.* 85, 519.
- Etter, T., Kuebler, J., Frey, T., Schulz, P., Löffler, J.F., Uggowitzer, P.J., 2004. Strength and fracture toughness of interpenetrating graphite/aluminium composites produced by the indirect squeeze casting process. *Mater. Sci. Eng. A* 386, 61–67.
- Eurocode 3: design of steel structures – part 1–9: fatigue, n.d. . European Committee for Standardization.
- Ewing, J.A., Humfrey, J.C.W., 1903. The Fracture of Metals under Repeated Alternations of Stress. *Philos. Trans. R. Soc. A Math. Phys. Eng. Sci.* 200, 241–250.
- Ewing, P.D., Swedlow, J.L., Williams, J.G., n.d. Further results on the angled crack problem. *Int. J. Fract.* 12, 85–93.
- Fatemi, A., Kurath, P., 1988. Multiaxial Fatigue Life Predictions Under the Influence of Mean-Stresses. *J. Eng. Mater. Technol.* 110, 380.
- Fatemi, A., Shamsaei, N., 2011. Multiaxial fatigue: An overview and some approximation models for life estimation. *Int. J. Fatigue* 33, 948–958.
- Fatemi, A., Socie, D.F., 1988. A critical plane approach to multiaxial fatigue damage including out-of-phase loading. *Fatigue Fract. Eng. Mater. Struct.* 11, 149–165.
- Feltner, C.E., Morrow, J.D., 1961. Microplastic Strain Hysteresis Energy as a Criterion for Fatigue Fracture. *J. Basic Eng.* 83, 15.
- Ferro, P., 2014. The local strain energy density approach applied to pre-stressed components subjected to cyclic load. *Fatigue Fract. Eng. Mater. Struct.* 37, 1268–1280.
- Fett, T., 1996. Failure of brittle materials near stress singularities. *Eng. Fract. Mech.* 53, 511–518.
- Fett, T., Munz, D., 2003. T-stress and crack path stability of DCDC specimens. *Int. J. Fract.* 124, L165–L170.
- Fett, T., Rizzi, G., 2005. Weight Functions for Stress Intensity Factors and T-Stress for Oblique Cracks in A Half-Space. *Int. J. Fract.* 132, L9–L16.
- Fett, T., Rizzi, G., Bahr, H.-A., 2006. Green’s functions for the T-stress of small kink and fork cracks. *Eng. Fract. Mech.* 73, 1426–1435.

- Filippi, S., Lazzarin, P., Tovo, R., 2002. Developments of some explicit formulas useful to describe elastic stress fields ahead of notches in plates. *Int. J. Solids Struct.* 39, 4543–4565.
- Firat, M., 2012. Cyclic plasticity modeling and finite element analyzes of a circumferentially notched round bar under combined axial and torsion loadings. *Mater. Des.* 34, 842–852.
- Firat, M., 2011. A notch strain calculation of a notched specimen under axial-torsion loadings. *Mater. Des.* 32, 3876–3882.
- Forsyth, P., 1961. A two stage process of fatigue crack growth, in: *Crack Propagation Symposium - Cranfield: The College of Aeronautics*. pp. 76–94.
- Gallo, P., Berto, F., Lazzarin, P., 2015. High temperature fatigue tests of notched specimens made of titanium Grade 2. *Theor. Appl. Fract. Mech.* 76, 27–34.
- Gao, Z., Qiu, B., Wang, X., Jiang, Y., 2010. An investigation of fatigue of a notched member. *Int. J. Fatigue* 32, 1960–1969.
- García, I.G., Leguillon, D., 2012. Mixed-mode crack initiation at a v-notch in presence of an adhesive joint. *Int. J. Solids Struct.* 49, 2138–2149.
- Givoli, D., Rivkin, L., 1993. The DtN finite element method for elastic domains with cracks and re-entrant corners. *Comput. Struct.* 49, 633–642.
- Gladskyi, M., Fatemi, A., 2014. Load sequence effects on fatigue crack growth in notched tubular specimens subjected to axial and torsion loadings. *Theor. Appl. Fract. Mech.* 69, 63–70.
- Gladskyi, M., Fatemi, A., 2013. Notched fatigue behavior including load sequence effects under axial and torsional loadings. *Int. J. Fatigue* 55, 43–53.
- Glinka, G., 1985. Energy density approach to calculation of inelastic strain-stress near notches and cracks. *Eng. Fract. Mech.* 22, 485–508.
- Glinka, G., Wang, G., Plumtree, A., 2007. Mean stress effects in multiaxial fatigue. *Fatigue Fract. Eng. Mater. Struct.* 18, 755–764.
- Glushkov, E., Glushkova, N., Lapina, O., 1999. 3-D elastic stress singularity at polyhedral corner points. *Int. J. Solids Struct.* 36, 1105–1128.
- Golden, P.J., Nicholas, T., 2005. The effect of angle on dovetail fretting experiments in Ti-6Al-4V. *Fatigue Fract. Eng. Mater. Struct.* 28, 1169–1175.
- Gómez, F.J., Elices, M., 2003a. A fracture criterion for sharp V-notched samples. *Int. J. Fract.* 123, 163–175.
- Gómez, F.J., Elices, M., 2003b. Fracture of components with V-shaped notches. *Eng. Fract. Mech.* 70, 1913–1927.
- Gómez, F.J., Elices, M., Berto, F., Lazzarin, P., 2007. Local strain energy to assess the static failure of U-notches in plates under mixed mode loading. *Int. J. Fract.* 145, 29–45.
- Gomez, F.J., Elices, M., Valiente, A., 2000. Cracking in PMMA containing U-shaped notches. *Fatigue Fract. Eng. Mater. Struct.* 23, 795–803.

- Gómez, F.J.J., Elices, M., 2004. A fracture criterion for blunted V-notched samples. *Int. J. Fract.* 127, 239–264.
- Gough, H.J., Pollard, H. V, 1936. Properties of some materials for cast crankshafts, with special reference to combined stresses. *Arch. Proc. Inst. Automob. Eng.* 1906-1947 (vols 1-41) 31, 821–893.
- Grabner, K., Grimmer, K.J., Kessler, F., 1993. Research into normal-forces between belt and idlers at critical locations on the belt conveyor track. *Bulk solids Handl.* 13, 727–734.
- Gradin, A., 1982. A Fracture Criterion for Edge-Bonded Bimaterial Bodies. *J. Compos. Mater.* 16, 448–456.
- Greenstreet, W.L., 1968. Mechanical Properties of Artificial Graphites – A Survey Report. Oak Ridge, TN.
- Griffith, A.A., 1921. The phenomena of rupture and flow in solids. *Philos. Trans. R. Soc. London A* 221, 163–198.
- Gross, B., Mendelson, A., 1972. Plane elastostatic analysis of V-notched plates. *Int. J. Fract. Mech.* 8, 267–276.
- Haibach, E., 2002. *Service Fatigue-Strength – Methods and data for structural analysis.* Springer Verlag, Berlin.
- Harding, S., Kotousov, A., Lazzarin, P., Berto, F., 2010. Transverse singular effects in V-shaped notches stressed in mode II. *Int. J. Fract.* 164, 1–14.
- Hardrath, F., Ohman, L., 1953. A study of elastic and plastic stress concentration factors due to notches and fillets in flat plates. NASA TC 1117.
- Haritos, G., Nicholas, T., Lanning, D.B., 1999. Notch size effects in HCF behavior of Ti–6Al–4V. *Int. J. Fatigue* 21, 643–652.
- Hasebe, N., Kutanda, Y., 1978. Calculation of stress intensity factor from stress concentration factor. *Eng. Fract. Mech.* 10, 215–221.
- He, Z., Kotousov, A., Berto, F., 2015. Effect of vertex singularities on stress intensities near plate free surfaces. *Fatigue Fract. Eng. Mater. Struct.* doi:10.1111/ffe.12294
- Hellen, T.K., 2001. How to undertake fracture mechanics analysis with finite elements. NAFEMS, Hamilton, Scotland.
- Henshell, R.D., Shaw, K.G., 1975. Crack tip finite elements are unnecessary. *Int. J. Numer. Methods Eng.* 9, 495–507.
- Henschel, K., Berger, P., Rossler, K., Schmidt, M., 1990. Weld geometry as a factor controlling the fatigue strength of butt welded joints. *Weld. Int.* 4, 494.
- Hertel, O., Vormwald, M., 2011. Short-crack-growth-based fatigue assessment of notched components under multiaxial variable amplitude loading. *Eng. Fract. Mech.* 78, 1614–1627.
- Heyliger, P.R., Kriz, R.D., 1989. Stress intensity factors by enriched mixed finite elements. *Int. J. Numer. Methods Eng.* 28, 1461–1473.

- Hobbacher, A., 2008. Recommendations for Fatigue design of welded joints and components.
- Hoffmann, M., Seeger, T., 1985. A Generalized Method for Estimating Multiaxial Elastic-Plastic Notch Stresses and Strains, Part 1: Theory. *J. Eng. Mater. Technol.* 107, 250.
- Hoshide, T., Kakiuchi, E., Hirota, T., 1997. Microstructural effect on low cycle fatigue behaviour in Ti-alloys under biaxial loading. *Fatigue Fract. Eng. Mater. Struct.* 20, 941–950.
- Ince, A., Glinka, G., 2013. A numerical method for elasto-plastic notch-root stress-strain analysis. *J. Strain Anal. Eng. Des.* 48, 229–244.
- Irwin, G.R., 1962. Crack-Extension Force for a Part-Through Crack in a Plate. *J. Appl. Mech.* 29, 651.
- Irwin, G.R., 1957. Analysis of stresses and strains near the end of a crack traversing a plate. *J. Appl. Mech.* 24, 361–364.
- James, M.N., Christopher, C.J., Lu, Y., Patterson, E.A., 2013. Local crack plasticity and its influences on the global elastic stress field. *Int. J. Fatigue* 46, 4–15.
- Jasper, T.M., 1923. The value of the energy relation in the testing of ferrous metals at varying ranges of stress and at intermediate and high temperatures. *Philos. Mag. Ser. 6* 46, 609–627.
- Jiang, Y., 2000. A fatigue criterion for general multiaxial loading. *Fatigue Fract. Eng. Mater. Struct.* 23, 19–32.
- Jiang, Y., 1994. Cyclic plasticity with an emphasis on ratchetting. University of Illinois at Urbana Champagne.
- Jiang, Y., Feng, M., 2004. Modeling of Fatigue Crack Propagation. *J. Eng. Mater. Technol.* 126, 77.
- Jiang, Y., Kurath, P., 1997. Nonproportional cyclic deformation: critical experiments and analytical modeling. *Int. J. Plast.* 13, 743–763.
- Jiang, Y., Kurath, P., 1996. Characteristics of the Armstrong-Frederick type plasticity models. *Int. J. Plast.* 12, 387–415.
- Jiang, Y., Sehitoglu, H., 1996a. Modeling of Cyclic Ratchetting Plasticity, Part I: Development of Constitutive Relations. *J. Appl. Mech.* 63, 720.
- Jiang, Y., Sehitoglu, H., 1996b. Modeling of Cyclic Ratchetting Plasticity, Part II: Comparison of Model Simulations With Experiments. *J. Appl. Mech.* 63, 726.
- Jiang, Y., Xu, B., 2001. Deformation analysis of notched components and assessment of approximate methods. *Fatigue Fract. Eng. Mater. Struct.* 24, 729–740.
- Jurf, R.A., Pipes, R.B., 1982. Interlaminar fracture of composite materials. *J. Compos. Mater.* 16, 386–394.
- Kallmeyer, A.R., Krgo, A., Kurath, P., 2002. Evaluation of Multiaxial Fatigue

- Life Prediction Methodologies for Ti-6Al-4V. *J. Eng. Mater. Technol.* 124, 229.
- Kamat, S., Srinivas, M., Rama Rao, P., 1998. Mixed mode I/III fracture toughness of Armco iron. *Acta Mater.* 46, 4985–4992.
- Karihaloo, B.L., Xiao, Q.Z., n.d. Hybrid stress elements for accurate solution of elasticity problems with traction-free segments 109–125.
- Kawakami, H., 1985. Notch sensitivity of graphite materials for VHTR. *J. At. Energy Soc. Japan / At. Energy Soc. Japan* 27, 357–364.
- Kihara, S., Yoshii, A., 1991. A strength evaluation method of a sharply notched structure by a new parameter, “the equivalent stress intensity factor”. *JSME Int. J.* 34, 70–75.
- Kim, J.H., Lee, Y.S., Kim, D.H., Park, N.S., Suh, J., Kim, J.O., Il Moon, S., 2004. Evaluation of thermal shock strengths for graphite materials using a laser irradiation method. *Mater. Sci. Eng. A* 387-389, 385–389.
- Knesl, Z., 1991. A criterion of V-notch stability. *Int. J. Fract.* 48, R79–R83.
- Knibbs, R.H., 1967. Fracture in polycrystalline graphite. *J. Nucl. Mater.* 24, 174–187.
- Kotousov, A., Berto, F., Lazzarin, P., Pegorin, F., 2012. Three dimensional finite element mixed fracture mode under anti-plane loading of a crack. *Theor. Appl. Fract. Mech.* 62, 26–33.
- Kotousov, A., Lazzarin, P., Berto, F., Harding, S., 2010. Effect of the thickness on elastic deformation and quasi-brittle fracture of plate components. *Eng. Fract. Mech.* 77, 1665–1681.
- Kotousov, A., Lazzarin, P., Berto, F., Pook, L.P., 2013. Three-dimensional stress states at crack tip induced by shear and anti-plane loading. *Eng. Fract. Mech.* 108, 65–74.
- Lagoda, T., Macha, E., Bedkowski, W., 1999. A critical plane approach based on energy concepts: application to biaxial random tension-compression high-cycle fatigue regime. *Int. J. Fatigue* 21, 431–443.
- Lan, W., Deng, X., Sutton, M.A., Cheng, C.-S., 2006. Study of slant fracture in ductile materials. *Int. J. Fract.* 141, 469–496.
- Lanning, D., Haritos, G.K., Nicholas, T., 1999. Influence of stress state on high cycle fatigue of notched Ti-6Al-4V specimens. *Int. J. Fatigue* 21, 87–95.
- Lanning, D., Haritos, G.K., Nicholas, T., Maxwell, D.C., 2001. Low-cycle fatigue/high-cycle fatigue interactions in notched Ti-6Al-4V. *Fatigue Fract. Eng. Mater. Struct.* 24, 565–577.
- Larsson, S.G., Carlsson, A.J., 1973. Influence of non-singular stress terms and specimen geometry on small-scale yielding at crack tips in elastic-plastic materials. *J. Mech. Phys. Solids* 21, 263–277.
- Lassen, T., 1990. The effect of the welding process on the fatigue crack growth. *Weld. Res. Suppl.* 69, 75S–81S.

- Latella, B.A., Liu, T., 2006. The initiation and propagation of thermal shock cracks in graphite. *Carbon* N. Y. 44, 3043–3048.
- Lazzarin, P., Berto, F., 2008. Control volumes and strain energy density under small and large scale yielding due to tension and torsion loading. *Fatigue Fract. Eng. Mater. Struct.* 31, 95–107.
- Lazzarin, P., Berto, F., 2005. From Neuber's Elementary Volume to Kitagawa and Atzori's Diagrams: An Interpretation Based on Local Energy. *Int. J. Fract.* 135, L33–L38.
- Lazzarin, P., Berto, F., 2005. Some expressions for the strain energy in a finite volume surrounding the root of blunt V-notches. *Int. J. Fract.* 135, 161–185.
- Lazzarin, P., Berto, F., Atzori, B., 2013a. A synthesis of data from steel spot welded joints of reduced thickness by means of local SED. *Theor. Appl. Fract. Mech.* 63-64, 32–39.
- Lazzarin, P., Berto, F., Ayatollahi, M.R., 2013b. Brittle failure of inclined key-hole notches in isostatic graphite under in-plane mixed mode loading. *Fatigue Fract. Eng. Mater. Struct.* 36, 942–955.
- Lazzarin, P., Berto, F., Elices, M., Gómez, J., 2009a. Brittle failures from U- and V-notches in mode I and mixed, I + II, mode: a synthesis based on the strain energy density averaged on finite-size volumes. *Fatigue Fract. Eng. Mater. Struct.* 32, 671–684.
- Lazzarin, P., Berto, F., Gomez, F., Zappalorto, M., 2008. Some advantages derived from the use of the strain energy density over a control volume in fatigue strength assessments of welded joints. *Int. J. Fatigue* 30, 1345–1357.
- Lazzarin, P., Berto, F., Radaj, D., 2009b. Fatigue-relevant stress field parameters of welded lap joints: pointed slit tip compared with keyhole notch. *Fatigue Fract. Eng. Mater. Struct.* 32, 713–735.
- Lazzarin, P., Berto, F., Radaj, D., 2006. Uniform fatigue strength of butt and fillet welded joints in terms of the local strain energy density, in: *Proceeding of the 9th International Fatigue Congress*. Atlanta, USA.
- Lazzarin, P., Berto, F., Zappalorto, M., 2010. Rapid calculations of notch stress intensity factors based on averaged strain energy density from coarse meshes: Theoretical bases and applications. *Int. J. Fatigue* 32, 1559–1567.
- Lazzarin, P., Campagnolo, A., Berto, F., 2014. A comparison among some recent energy- and stress-based criteria for the fracture assessment of sharp V-notched components under Mode I loading. *Theor. Appl. Fract. Mech.* 71, 21–30.
- Lazzarin, P., Filippi, S., 2006. A generalized stress intensity factor to be applied to rounded V-shaped notches. *Int. J. Solids Struct.* 43, 2461–2478.
- Lazzarin, P., Lassen, T., Livieri, P., 2003. A notch stress intensity approach applied to fatigue life predictions of welded joints with different local toe geometry. *Fatigue Fract. Eng. Mater. Struct.* 26, 49–58.
- Lazzarin, P., Livieri, P., Berto, F., Zappalorto, M., 2008. Local strain energy

- density and fatigue strength of welded joints under uniaxial and multiaxial loading. *Eng. Fract. Mech.* 75, 1875–1889.
- Lazzarin, P., Sonsino, C.M., Zambardi, R., 2004. A notch stress intensity approach to assess the multiaxial fatigue strength of welded tube-to-flange joints subjected to combined loadings. *Fatigue Fract. Eng. Mater. Struct.* 27, 127–140.
- Lazzarin, P., Tovo, R., 1998. A notch intensity factor approach to the stress analysis of welds. *Fatigue Fract. Eng. Mater. Struct.* 21, 1089–1103.
- Lazzarin, P., Tovo, R., 1996. A unified approach to the evaluation of linear elastic stress fields in the neighborhood of cracks and notches. *Int. J. Fract.* 78, 3–19.
- Lazzarin, P., Tovo, R., Filippi, S., 1998. Elastic stress distributions in finite size plates with edge notches. *Int. J. Fract.* 91, 269–282.
- Lazzarin, P., Tovo, R., Meneghetti, G., 1997. Fatigue crack initiation and propagation phases near notches in metals with low notch sensitivity. *Int. J. Fatigue* 19, 647–657.
- Lazzarin, P., Zambardi, R., 2002. The Equivalent Strain Energy Density approach re-formulated and applied to sharp V-shaped notches under localized and generalized plasticity. *Fatigue Fract. Eng. Mater. Struct.* 25, 917–928.
- Lazzarin, P., Zambardi, R., 2001. A finite-volume-energy based approach to predict the static and fatigue behavior of components with sharp V-shaped notches. *Int. J. Fract.* 112, 275–298.
- Lazzarin, P., Zappalorto, M., 2012. A three-dimensional stress field solution for pointed and sharply radiused V-notches in plates of finite thickness. *Fatigue Fract. Eng. Mater. Struct.* 35, 1105–1119.
- Le Biavant, K., Pommier, S., Prioul, C., 2002. Local texture and fatigue crack initiation in a Ti-6Al-4V titanium alloy. *Fatigue Fract. Eng. Mater. Struct.* 25, 527–545.
- Leguillon, D., 2002. Strength or toughness? A criterion for crack onset at a notch. *Eur. J. Mech. - A/Solids* 21, 61–72.
- Leguillon, D., 2001. A criterion for crack nucleation at a notch in homogeneous materials. *Comptes Rendus l'Académie des Sci. - Ser. IIB - Mech.*
- Leguillon, D., Murer, S., 2012. Fatigue crack nucleation at a stress concentration point, in: 4th International Conference on Crack Paths (CP2012), Gaeta, Italy, September 19-21.
- Leguillon, D., Yosibash, Z., 2003. Crack onset at a v-notch. Influence of the notch tip radius. *Int. J. Fract.* 122, 1–21.
- Leicester, R.H., 1973. Effect of size on the strength of structures.
- Lemaitre, J., Chaboche, J.-L., 1994. *Mechanics of solid materials*. New ed. Cambridge University Press.
- Li, M., Tsujimura, M., Sakai, M., 1999. Crack-face grain interlocking/bridging of

- a polycrystalline graphite: The role in mixed mode fracture. *Carbon* N. Y. 37, 1633–1639.
- Li, Z., Guo, W., n.d. Three-dimensional elastic stress fields ahead of blunt V-notches in finite thickness plates. *Int. J. Fract.* 107, 53–71.
- Li, Z., Guo, W., Kuang, Z., 2000. Three-dimensional elastic stress fields near notches in finite thickness plates. *Int. J. Solids Struct.* 37, 7617–7632.
- Lin, B., Mear, M.E., Ravi-Chandar, K., 2010. Criterion for initiation of cracks under mixed-mode I + III loading. *Int. J. Fract.* 165, 175–188.
- Lin, K.Y., Tong, P., 1980. Singular finite elements for the fracture analysis of V-notched plate. *Int. J. Numer. Methods Eng.* 15, 1343–1354.
- Liu, K., 1993. A Method Based on Virtual Strain-Energy Parameters for Multiaxial Fatigue Life Prediction, in: *Advances in Multiaxial Fatigue*, ASTM STP 1191. ASTM International, 100 Barr Harbor Drive, PO Box C700, West Conshohocken, PA 19428-2959, pp. 67–84.
- Livieri, P., 2008. Use of J-integral to predict static failures in sharp V-notches and rounded U-notches. *Eng. Fract. Mech.* 75, 1779–1793.
- Livieri, P., 2003. A new path independent integral applied to notched components under mode I loadings. *Int. J. Fract.* 123, 107–125.
- Livieri, P., Lazzarin, P., 2005. Fatigue strength of steel and aluminium welded joints based on generalised stress intensity factors and local strain energy values. *Int. J. Fract.* 133, 247–276.
- Lomakin, E. V., Zobnin, A.I., Berezin, A. V., 1975. Finding the fracture toughness characteristics of graphite materials in plane strain. *Strength Mater.* 7, 484–487.
- Losty, H.H.W., Orchard, J.S., 1962. The Strength of Graphite, in: *In Fifth Conference on Carbon*. Pennsylvania State University, Macmillan.
- Macha, E., Sonsino, C.M., 1999. Energy criteria of multiaxial fatigue failure. *Fatigue Fract. Eng. Mater. Struct.* 22, 1053–1070.
- Mandelbrot, B.M., 1983. *The fractal geometry of nature*. W H Freeman and Company, New York, USA.
- Manoharan, M., Hirth, J.P., Rosenfield, A.R., 1991. Combined mode I-mode III fracture toughness of a spherodized 1090 steel. *Acta Metall. Mater.* 39, 1203–1210.
- Marangon, C., Campagnolo, A., Berto, F., 2015. Three-dimensional effects at the tip of rounded notches subjected to mode-I loading under cyclic plasticity. *J. Strain Anal. Eng. Des.* 50, 299–313.
- Marangon, C., Lazzarin, P., Berto, F., Campagnolo, A., 2014. Some analytical remarks on the influence of phase angle on stress fields ahead of sharp V-notches under tension and torsion loads. *Theor. Appl. Fract. Mech.* 74, 64–72.
- Marmi, A.K., Habraken, A.M., Duchene, L., 2009. Multiaxial fatigue damage

- modelling at macro scale of Ti–6Al–4V alloy. *Int. J. Fatigue* 31, 2031–2040.
- Marsavina, L., Constantinescu, D.M., Linul, E., Apostol, D.A., Voiconi, T., Sadowski, T., 2014. Refinements on fracture toughness of PUR foams. *Eng. Fract. Mech.* 129, 54–66.
- Marsavina, L., Sadowski, T., Kneć, M., 2013. Crack propagation paths in four point bend Aluminium–PMMA specimens. *Eng. Fract. Mech.* 108, 139–151.
- Matvienko, Y.U.G., Morozov, E.M., 2004. Calculation of the energy J -integral for bodies with notches and. *Int. J. Fract.* 125, 249–261.
- McClintock, F.A., Irwin, G.R., n.d. Plasticity aspects of fracture mechanics, in: *Fracture Toughness Testing and Its Applications*. ASTM STP 381. American Society for Testing and Materials, Philadelphia, USA, pp. 84–113.
- Melin, S., 1994. Accurate Data for Stress Intensity Factors at Infinitesimal Kinks. *J. Appl. Mech.* 61, 467.
- Meneghetti, G., 2013. The peak stress method for fatigue strength assessment of tube-to-flange welded joints under torsion loading. *Weld. World* 57, 265–275.
- Meneghetti, G., 2012. The use of peak stresses for fatigue strength assessments of welded lap joints and cover plates with toe and root failures. *Eng. Fract. Mech.* 89, 40–51.
- Meneghetti, G., 2008. The peak stress method applied to fatigue assessments of steel and aluminium fillet-welded joints subjected to mode I loading. *Fatigue Fract. Eng. Mater. Struct.* 31, 346–369.
- Meneghetti, G., Atzori, B., Campagnolo, A., Berto, F., 2015a. A link between the peak stresses and the averaged strain energy density for cracks under mixed-mode (I+II) loading. *Fract. Struct. Integr.* doi:10.3221/IGF-ESIS.34.11
- Meneghetti, G., Atzori, B., Manara, G., 2010. The Peak Stress Method applied to fatigue assessments of steel tubular welded joints subject to mode-I loading. *Eng. Fract. Mech.* 77, 2100–2114.
- Meneghetti, G., Campagnolo, A., Berto, F., 2015b. Fatigue strength assessment of partial and full-penetration steel and aluminium butt-welded joints according to the peak stress method. *Fatigue Fract. Eng. Mater. Struct.* 38, 1419–1431.
- Meneghetti, G., Campagnolo, A., Berto, F., Atzori, B., 2015c. Averaged strain energy density evaluated rapidly from the singular peak stresses by FEM: cracked components under mixed-mode (I+II) loading. *Theor. Appl. Fract. Mech.* 79, 113–124.
- Meneghetti, G., Guzzella, C., 2014. The peak stress method to estimate the mode I notch stress intensity factor in welded joints using three-dimensional finite element models. *Eng. Fract. Mech.* 115, 154–171.
- Meneghetti, G., Guzzella, C., Atzori, B., 2014. The peak stress method combined with 3D finite element models for fatigue assessment of toe and root cracking in steel welded joints subjected to axial or bending loading. *Fatigue Fract. Eng. Mater. Struct.* 37, 722–739.

- Meneghetti, G., Lazzarin, P., 2011. The Peak Stress Method for Fatigue Strength Assessment of welded joints with weld toe or weld root failures. *Weld. World* 55, 22–29.
- Meneghetti, G., Lazzarin, P., 2007. Significance of the elastic peak stress evaluated by FE analyses at the point of singularity of sharp V-notched components. *Fatigue Fract. Eng. Mater. Struct.* 30, 95–106.
- Meneghetti, G., Ricotta, M., 2012. The use of the specific heat loss to analyse the low- and high-cycle fatigue behaviour of plain and notched specimens made of a stainless steel. *Eng. Fract. Mech.* 81, 2–16.
- Mirsayar, M.M., 2014. On fracture of kinked interface cracks – The role of T-stress. *Mater. Des.* 61, 117–123.
- Moes, N., Dolbow, J., Belytschko, T., 1999. A finite element method for crack growth without remeshing. *Int. J. Numer. Methods Eng.* 46, 131–150.
- Moftakhar, A., Buczynski, A., Glinka, G., 1995. Calculation of elasto-plastic strains and stresses in notches under multiaxial loading. *Int. J. Fract.* 70, 357–373.
- Molski, K., Glinka, G., 1981. A method of elastic-plastic stress and strain calculation at a notch root. *Mater. Sci. Eng.* 50, 93–100.
- Morrissey, R., McDowell, D.L., Nicholas, T., 1999. Frequency and stress ratio effects in high cycle fatigue of Ti-6Al-4V. *Int. J. Fatigue* 21, 679–685.
- Morrissey, R., Nicholas, T., 2005. Fatigue strength of Ti-6Al-4V at very long lives. *Int. J. Fatigue* 27, 1608–1612.
- Mostafavi, M., Marrow, T.J., 2011. In situ observation of crack nuclei in polygranular graphite under ring-on-ring equi-biaxial and flexural loading. *Eng. Fract. Mech.* 78, 1756–1770.
- Murer, S., Leguillon, D., 2010. Static and fatigue failure of quasi-brittle materials at a V-notch using a Dugdale model. *Eur. J. Mech. - A/Solids* 29, 109–118.
- Nakamura, H., Takanashi, M., Itoh, T., Wu, M., Shimizu, Y., 2011. Fatigue crack initiation and growth behavior of Ti-6Al-4V under non-proportional multiaxial loading. *Int. J. Fatigue* 33, 842–848.
- Nakamura, T., Parks, D.M., 1989. Antisymmetrical 3-D stress field near the crack front of a thin elastic plate. *Int. J. Solids Struct.* 25, 1411–1426.
- Nakamura, T., Parks, D.M., 1988. Three-Dimensional Stress Field Near the Crack Front of a Thin Elastic Plate. *J. Appl. Mech.* 55, 805.
- Neuber, H., 1985. *Kerbspannungslehre*, 3rd Edition. Springer-Verlag, Berlin.
- Neuber, H., 1968. Über die Berücksichtigung der Spannungskonzentration bei Festigkeitsberechnungen. *Konstruktion* 20, 245–251.
- Neuber, H., 1961. Theory of Stress Concentration for Shear-Strained Prismatical Bodies With Arbitrary Nonlinear Stress-Strain Law. *J. Appl. Mech.* 28, 544.
- Neuber, H., 1958a. *Kerbspannungslehre*, 2nd Edition. Springer-Verlag, Berlin.

- Neuber, H., 1958b. Theory of Notch Stresses. Springer-Verlag, Berlin.
- Neuber, H., 1936. Zur Theorie der technischen Formzahl. *Forsch Ing Wes* 7, 271–274.
- Nicholas, T., 2002. Step loading for very high cycle fatigue. *Fatigue Fract. Eng. Mater. Struct.* 25, 861–869.
- Nieslony, A., Sonsino, C.M., 2008. Comparison of some selected multiaxial fatigue assessment criteria.
- Nisitani, H., Teranishi, T., 2004. KI of a circumferential crack emanating from an ellipsoidal cavity obtained by the crack tip stress method in FEM. *Eng. Fract. Mech.* 71, 579–585.
- Nisitani, H., Teranishi, T., 2001. KI value of a circumferential crack emanating from an ellipsoidal cavity obtained by the crack tip stress method in FEM, in: Guagliano, M., Aliabadi, M.H. (Eds.), *Proceedings of the 2nd International Conference on Fracture and Damage Mechanics*. pp. 141–146.
- Novozhilov, V., 1969. On a necessary and sufficient criterion for brittle strength. *J. Appl. Math. Mech. (Translation PMM)* 33, 201–210.
- Nui, L.S., Chehimi, C., Pluvinage, G., 1994. Stress field near a large blunted tip V-notch and application of the concept of the critical notch stress intensity factor (NSIF) to the fracture toughness of very brittle materials. *Eng. Fract. Mech.* 49, 325–335.
- Ohkawa, C., Ohkawa, I., 2011. Notch effect on torsional fatigue of austenitic stainless steel: Comparison with low carbon steel. *Eng. Fract. Mech.* 78, 1577–1589.
- Ohno, N., Wang, J.D., 1991. Non linear kinematic hardening rule: proposition and application to ratchetting problems, in: *Structural Mechanical in Reactor Technology*, Transaction of the 11th International Conference on Structural Mechanics in Reactor Technology. Shibata.
- Omer, N., Yosibash, Z., 2005. On the Path Independency of the Point-wise J Integral in Three-dimensions. *Int. J. Fract.* 136, 1–36.
- Paris, P.G., Sih, G.C., 1965. Stress analysis of cracks, in: *Fracture Toughness Testing and Its Applications*. ASTM STP 381. American Society for Testing and Materials, Philadelphia, USA, pp. 30–81.
- Park, J., Nelson, D., 2000. Evaluation of an energy-based approach and a critical plane approach for predicting constant amplitude multiaxial fatigue life. *Int. J. Fatigue* 22, 23–39.
- Petersen, D., Kumar, A., Hirth, J., Hoagland, R., Feng, X., 1994. A Suggested Test Procedure to Measure Mixed Mode I–III Fracture Toughness of Brittle Materials. *J. Test. Eval.* 22, 327.
- Petershagen, H., 1992. Fatigue tests with hyperbaric dry butt welded specimens.
- Peterson, R.E., 1959. Notch sensitivity. *Metal fatigue*, McGraw Hill, New York (USA).

- Pippan, R., Zelger, C., Gach, E., Bichler, C., Weinhandl, H., 2011. On the mechanism of fatigue crack propagation in ductile metallic materials. *Fatigue Fract. Eng. Mater. Struct.* 34, 1–16.
- Planas, J., Elices, M., Guinea, G., Gómez, F., Cendón, D., Arbilla, I., 2003. Generalizations and specializations of cohesive crack models. *Eng. Fract. Mech.* 70, 1759–1776.
- Pluvinage, G., 1997. Rupture and fatigue initiated from notches. Application of the notch intensity factor. *Rev. Fr. Mec. (in French)* 53–61.
- Pook, 2000. Crack profiles and corner point singularities. *Fatigue Fract. Eng. Mater. Struct.* 23, 141–150.
- Pook, L., 2003. A finite element analysis of cracked square plates and bars under antiplane loading. *Fatigue Fract. Eng. Mater.* 533–541.
- Pook, L.P., 2015. The linear elastic analysis of cracked bodies and crack paths. *Theor. Appl. Fract. Mech.*
- Pook, L.P., 2013. A 50 year retrospective review of three-dimensional effects at cracks and sharp notches. *Fatigue Fract. Eng. Mater. Struct.* 36, 699–723.
- Pook, L.P., 2007. *Metal fatigue: what it is, why it matters.*, Solid Mechanics and Its Applications. Springer Netherlands, Dordrecht.
- Pook, L.P., 2002. *Crack paths.* WIT Press, Southampton, UK.
- Pook, L.P., 2001. A finite element analysis of cracked square plates and bars under antiplane loading, in: de Freitas, M. (Ed.), *Fatigue and Fracture of Engineering Materials and Structures.* Instituto Superior Técnico, Lisbon, Portugal, pp. 701–708.
- Pook, L.P., 2000. *Linear elastic fracture mechanics for engineers. Theory and applications.* WIT Press, Southampton, UK.
- Pook, L.P., 1994. Some implications of corner point singularities. *Eng. Fract. Mech.* 48, 367–378.
- Pook, L.P., 1985. The fatigue crack direction and threshold behaviour of mild steel under mixed mode I and III loading. *Int. J. Fatigue* 7, 21–30.
- Pook, L.P., Berto, F., Campagnolo, A., Lazzarin, P., 2014. Coupled fracture mode of a cracked disc under anti-plane loading. *Eng. Fract. Mech.* 128, 22–36.
- Pook, L.P., Campagnolo, A., Berto, F., Lazzarin, P., 2015. Coupled fracture mode of a cracked plate under anti-plane loading. *Eng. Fract. Mech.* 134, 391–403.
- Pook, L.P., Sharples, J.K., 1979. The mode III fatigue crack growth threshold for mild steel. *Int. J. Fract.* 15, R223–R226.
- Portela, A., Aliabadi, M.H., Rooke, D.P., 1991. Efficient boundary element analysis of sharp notched plates. *Int. J. Numer. Methods Eng.* 32, 445–470.
- Prager, W., 1955. The theory of plasticity: a survey of recent achievements. *Arch. Proc. Inst. Mech. Eng. 1847-1982 (vols 1-196)* 169, 41–57.
- Priel, E., Yosibash, Z., Leguillon, D., 2008. Failure initiation at a blunt V-notch

- tip under mixed mode loading. *Int. J. Fract.* 149, 143–173.
- Pu, S.L., Hussain, M.A., Lorensen, W.E., 1978. The collapsed cubic isoparametric element as a singular element for crack problems. *Int. J. Numer. Methods Eng.* 12, 1727–1742.
- Qian, J., Hasebe, N., 1997. Property of eigenvalues and eigenfunctions for an interface V-notch in antiplane elasticity. *Eng. Fract. Mech.* 56, 729–734.
- Qiu, B., Gao, Z., Wang, X., 2009. Fatigue Life Prediction of Notched Components Based on Multiaxial Local Stress-Strain Approach, in: Volume 6: Materials and Fabrication, Parts A and B. ASME, pp. 183–189.
- Radaj, D., 2015. State-of-the-art review on the local strain energy density concept and its relation to the J -integral and peak stress method. *Fatigue Fract. Eng. Mater. Struct.* 38, 2–28.
- Radaj, D., 2014. State-of-the-art review on extended stress intensity factor concepts. *Fatigue Fract. Eng. Mater. Struct.* 37, 1–28.
- Radaj, D., 2010. T-stress corrected notch stress intensity factors with application to welded lap joints. *Fatigue Fract. Eng. Mater. Struct.* 33, 378–389.
- Radaj, D., 1990. *Design and Analysis of Fatigue Resistant Welded Structures*. Abington Publishing, Cambridge.
- Radaj, D., Berto, F., Lazzarin, P., 2009a. Local fatigue strength parameters for welded joints based on strain energy density with inclusion of small-size notches. *Eng. Fract. Mech.* 76, 1109–1130.
- Radaj, D., Lazzarin, P., Berto, F., 2013. Generalised Neuber concept of fictitious notch rounding. *Int. J. Fatigue* 51, 105–115.
- Radaj, D., Lazzarin, P., Berto, F., 2009b. Fatigue assessment of welded joints under slit-parallel loading based on strain energy density or notch rounding. *Int. J. Fatigue* 31, 1490–1504.
- Radaj, D., Sonsino, C.M., Fricke, W., 2006. *Fatigue Assessment of Welded Joints by Local Approaches*, 2nd ed. Woodhead Publishing, Cambridge.
- Radaj, D., Vormwald, M., 2013. *Advanced Methods of Fatigue Assessment*. Springer Berlin Heidelberg, Berlin, Heidelberg.
- Ramesh, K., Gupta, S., Kelkar, A.A., 1997. Evaluation of stress field parameters in fracture mechanics by photoelasticity -revisited. *Eng. Fract. Mech.*
- Ramesh, K., Gupta, S., Srivastava, A.K., 1996. Equivalence of multi-parameter stress field equations in fracture mechanics. *Int. J. Fract.* 79.
- Razmjoo, G.R., 1996. *Fatigue of load carrying fillet welded joints under multiaxial loading*. Fatigue core research from TWI. Abington Publishing, Abington.
- Reis, L., Li, B., de Freitas, M., 2009. Crack initiation and growth path under multiaxial fatigue loading in structural steels. *Int. J. Fatigue* 31, 1660–1668.
- Rice, J.R., 1974. Limitations to the small scale yielding approximation for crack tip plasticity. *J. Mech. Phys. Solids* 22, 17–26.

- Richard, H.A., Benitz, K., 1983. A loading device for the creation of mixed mode in fracture mechanics. *Int. J. Fract.* 22, R55–R58.
- Richard, H.A., Fulland, M., Sander, M., 2005. Theoretical crack path prediction. *Fatigue Fract. Eng. Mater. Struct.* 28, 3–12.
- Ritchie, R.O., 1988. Mechanisms of fatigue crack propagation in metals, ceramics and composites: Role of crack tip shielding. *Mater. Sci. Eng. A* 103, 15–28.
- Rulmeca Bulk Catalogue, 2015.
URL
http://www.rulmeca.it/en/products_bulk/catalogue/1/trasporto_a_nastro/1/rollers
- Saghafi, H., Ayatollahi, M.R., Sistaninia, M., 2010. A modified MTS criterion (MMTS) for mixed-mode fracture toughness assessment of brittle materials. *Mater. Sci. Eng. A* 527, 5624–5630.
- Sakai, M., Urashima, K., Inagaki, M., 1983. Energy Principle of Elastic-Plastic Fracture and Its Application to the Fracture Mechanics of a Polycrystalline Graphite. *J. Am. Ceram. Soc.* 66, 868–874.
- Salavati, H., Alizadeh, Y., Berto, F., 2014. Effect of notch depth and radius on the critical fracture load of bainitic functionally graded steels under mixed mode I + II loading. *Phys. Mesomech.* 17, 178–189.
- Sapora, A., Cornetti, P., Carpinteri, A., 2014. V-notched elements under mode II loading conditions. *Struct. Eng. Mech.* 49, 499–508.
- Sapora, A., Cornetti, P., Carpinteri, A., 2013. A Finite Fracture Mechanics approach to V-notched elements subjected to mixed-mode loading. *Eng. Fract. Mech.* 97, 216–226.
- Sato, S., Awaji, H., Akuzawa, H., 1978. Fracture toughness of reactor graphite at high temperature. *Carbon N. Y.* 16, 95–102.
- Sato, S., Kawamata, K., Awaji, H., Osawa, M., Manaka, M., 1981. Thermal shock resistance and fracture toughness during the graphitization process. *Carbon N. Y.* 19, 111–118.
- Schleicher, F., 1926. Der Spannungszustand an der Fließgrenze (Plastizitätsbedingung). *Z. Angew. Math. Mech.* 6, 199–216.
- Seeger, T., Olivier, R., 1992. Slope and knee-point of the S-N curve of shear loaded fillet welds. *Stahlbau (in Ger.)* 61, 137–142.
- Seeger, T., Olivier, R., 1987. Tolerable and allowable shear stresses at fatigue loaded welded joints. *Stahlbau (in Ger.)* 8, 231–238.
- Serpieri, R., Sacco, E., Alfano, G., 2015. A thermodynamically consistent derivation of a frictional-damage cohesive-zone model with different mode I and mode II fracture energies. *Eur. J. Mech. - A/Solids* 49, 13–25.
- Sethuraman, R., Viswanadha Gupta, S., 2004. Evaluation of notch root elasto-plastic stress–strain state for general loadings using an elastic solution. *Int. J. Press. Vessel. Pip.* 81, 313–325.

- Seweryn, A., 2002. Modeling of singular stress fields using finite element method. *Int. J. Solids Struct.* 39, 4787–4804.
- Seweryn, A., 1994. Brittle fracture criterion for structures with sharp notches. *Eng. Fract. Mech.* 47, 673–681.
- Seweryn, A., Łukaszewicz, A., 2002. Verification of brittle fracture criteria for elements with V-shaped notches. *Eng. Fract. Mech.* 69, 1487–1510.
- Seweryn, A., Molski, K., 1996. Elastic stress singularities and corresponding generalized stress intensity factors for angular corners under various boundary conditions. *Eng. Fract. Mech.* 55, 529–556.
- Seweryn, A., Mróz, Z., 1995. A non-local stress failure condition for structural elements under multiaxial loading. *Eng. Fract. Mech.* 51, 955–973.
- Seweryn, A., Poskrobko, Sł., Mróz, Z., 1997. Brittle Fracture in Plane Elements with Sharp Notches under Mixed-Mode Loading. *J. Eng. Mech.* 123, 535–543.
- Shamsaei, N., Fatemi, A., 2010. Effect of microstructure and hardness on non-proportional cyclic hardening coefficient and predictions. *Mater. Sci. Eng. A* 527, 3015–3024.
- Shang, D., 2001. Local stress–strain field intensity approach to fatigue life prediction under random cyclic loading. *Int. J. Fatigue* 23, 903–910.
- Sheldon, I., 2008. Chaboche Nonlinear Kinematic Hardening Model. Memo Number STI0805A, ANSYS. URL http://ansys.net/tips_sheldon/STI0805_Chaboche.pdf
- Sheppard, S.D., 1991. Field Effects in Fatigue Crack Initiation: Long Life Fatigue Strength. *J. Mech. Des.* 113, 188.
- Sherry, A.H., France, C.C., Goldthorpe, M.R., 1995. Compendium of T-stress solutions for two and three dimensional cracked geometries. *Fatigue Fract. Eng. Mater. Struct.* 18, 141–155.
- Shetty, D.K., Rosenfield, A.R., Duckworth, W.H., 1987. Mixed-mode fracture in biaxial stress state: Application of the diametral-compression (Brazilian disk) test. *Eng. Fract. Mech.* 26, 825–840.
- Shi, L., Li, H., Zou, Z., Fok, A.S.L., Marsden, B.J., Hodgkins, A., Mummery, P.M., Marrow, J., 2008. Analysis of crack propagation in nuclear graphite using three-point bending of sandwiched specimens. *J. Nucl. Mater.* 372, 141–151.
- Sih, G.C., 1991. *Mechanics of Fracture Initiation and Propagation*. Springer Netherlands, Dordrecht.
- Sih, G.C., 1974. Strain-energy-density factor applied to mixed mode crack problems. *Int. J. Fract.* 10, 305–321.
- Sih, G.C., Tang, X.S., 2005. Scaling of volume energy density function reflecting damage by singularities at macro-, meso- and microscopic level. *Theor. Appl. Fract. Mech.* 43, 211–231.

- Siljander, A., Kurath, P., Lawrence, F., 1992. Non proportional fatigue of welded structures, in: Mitchell, M., Landgraf, R. (Eds.), *Advances in Fatigue Lifetime Predictive Techniques*, ASTMSTP 1122. American Society for Testing and Materials, Philadelphia, USA, pp. 319–338.
- Singh, M.N.K., Glinka, G., Dubey, R.N., 1996. Elastic-plastic stress-strain calculation in notched bodies subjected to non-proportional loading. *Int. J. Fract.* 76, 39–60.
- Singh, P.J., Achar, D.R.G., Guha, B., Nordberg, H., 2003a. Fatigue life prediction of gas tungsten arc welded AISI 304L cruciform joints with different LOP sizes. *Int. J. Fatigue* 25, 1–7.
- Singh, P.J., Guha, B., Achar, D.R., 2003b. Fatigue life improvement of AISI 304L cruciform welded joints by cryogenic treatment. *Eng. Fail. Anal.* 10, 1–12.
- Smith, D.J., Ayatollahi, M.R., Pavier, M.J., 2001. The role of T-stress in brittle fracture for linear elastic materials under mixed-mode loading. *Fatigue Fract. Eng. Mater. Struct.* 24, 137–150.
- Smith, R., Watson, P., Topper, T., 1970. A stress–strain function for the fatigue of metal. *J Mater* 5, 767–778.
- Smith, R.A., Miller, K.J., 1978. Prediction of fatigue regimes in notched components. *Int. J. Mech. Sci.* 20, 201–206.
- Socie, D., Marquis, G., 2000. *Multiaxial fatigue*. Society of Automotive Engineers, Warrendale (PA).
- Sonsino, C., 2009. Multiaxial fatigue assessment of welded joints – Recommendations for design codes. *Int. J. Fatigue* 31, 173–187.
- Sonsino, C., 1995. Multiaxial fatigue of welded joints under in-phase and out-of-phase local strains and stresses. *Int. J. Fatigue* 17, 55–70.
- Sonsino, C.M., 1997. Fatigue strength of welded components under complex elasto-plastic, multiaxial deformations.
- Sonsino, C.M., Kueppers, M., 2001. Multiaxial fatigue of welded joints under constant and variable amplitude loadings. *Fatigue Fract. Eng. Mater. Struct.* 24, 309–327.
- Sonsino, C.M., Radaj, D., Brandt, U., Lehrke, H.P., 1999. Fatigue assessment of welded joints in AlMg 4.5Mn aluminum alloy (AA 5083) by local approaches. *Int. J. Fatigue* 21, 985–999.
- Stowell, E.Z., 1950. Stress and strain concentration at a circular hole in an infinite plate. NACA TN 2073.
- Susmel, L., 2013. On the estimation of the material fatigue properties required to perform the multiaxial fatigue assessment. *Fatigue Fract. Eng. Mater. Struct.* 36, 565–585.
- Susmel, L., 2010. Estimating fatigue lifetime of steel weldments locally damaged by variable amplitude multiaxial stress fields. *Int. J. Fatigue* 32, 1057–1080.

- Susmel, L., 2009. The Modified Wöhler Curve Method calibrated by using standard fatigue curves and applied in conjunction with the Theory of Critical Distances to estimate fatigue lifetime of aluminium weldments. *Int. J. Fatigue* 31, 197–212.
- Susmel, L., 2009. *Multiaxial notch fatigue*. Woodhead publishing, Cambridge.
- Susmel, L., 2008. The theory of critical distances: a review of its applications in fatigue. *Eng. Fract. Mech.* 75, 1706–1724.
- Susmel, L., 2008. Modified Wöhler curve method, theory of critical distances and Eurocode 3: A novel engineering procedure to predict the lifetime of steel welded joints subjected to both uniaxial and multiaxial fatigue loading. *Int. J. Fatigue* 30, 888–907.
- Susmel, L., Taylor, D., 2012. A critical distance/plane method to estimate finite life of notched components under variable amplitude uniaxial/multiaxial fatigue loading. *Int. J. Fatigue* 38, 7–24.
- Susmel, L., Taylor, D., 2011. The Theory of Critical Distances to estimate lifetime of notched components subjected to variable amplitude uniaxial fatigue loading. *Int. J. Fatigue* 33, 900–911.
- Susmel, L., Taylor, D., 2008. The theory of critical distances to predict static strength of notched brittle components subjected to mixed-mode loading. *Eng. Fract. Mech.* 75, 534–550.
- Susmel, L., Taylor, D., 2003. Fatigue design in the presence of stress concentrations. *J. Strain Anal. Eng. Des.* 38, 443–452.
- Sutton, M.A., Deng, X., Reynolds, A., 2006. *Crack Growth and Stress Intensity Prediction Techniques*.
- Szabò, B.A., Yosibash, Z., 1996. Numerical analysis of singularities in two dimensions. Part 2: computation of generalized flux/stress intensity factors. *Int. J. Numer. Methods Eng.* 39, 409–434.
- Tada, H., Paris, P., Irwin, G., 1985. *The stress analysis of cracks, Handbook*. Paris Productions Incorporated, St Louis MO (USA).
- Takeuchi, E., Furuya, Y., Nagashima, N., Matsuoka, S., 2008. The effect of frequency on the giga-cycle fatigue properties of a Ti-6Al-4V alloy. *Fatigue Fract. Eng. Mater. Struct.* 31, 599–605.
- Tanaka, K., 2014. Crack initiation and propagation in torsional fatigue of circumferentially notched steel bars. *Int. J. Fatigue* 58, 114–125.
- Tanaka, K., 1983. Engineering formulae for fatigue strength reduction due to crack-like notches. *Int. J. Fract.* 22, R39–R46.
- Tanaka, K., Akiniwa, Y., Yu, H., 1999. The propagation of a circumferential fatigue crack in medium-carbon steel bars under combined torsional and axial loadings. In: *Mixed-Mode Crack Behaviour*, in: Miller, K., McDowell, D. (Eds.), *Mixed-Mode Crack Behaviour*, ASTM 1359. West Conshohocked, PA, pp. 295–311.
- Tang, X.S., Sih, G.C., 2005a. Weak and strong singularities reflecting multiscale

- damage: Micro-boundary conditions for free–free, fixed–fixed and free–fixed constraints. *Theor. Appl. Fract. Mech.* 43, 5–62.
- Tang, X.S., Sih, G.C., 2005b. Equilibrium mechanics model of multiscaling by segmentation: Asymptotic solution for macro-meso-micro damage in anti-plane shear deformation. *Theor. Appl. Fract. Mech.* 44, 1–15.
- Tang, X.S., Wei, T.T., 2015. Microscopic inhomogeneity coupled with macroscopic homogeneity: A localized zone of energy density for fatigue crack growth. *Int. J. Fatigue* 70, 270–277.
- Taylor, D., 1999. Geometrical effects in fatigue: a unifying theoretical model. *Int. J. Fatigue* 21, 413–420.
- Taylor, D., Barrett, N., Lucano, G., 2002. Some new methods for predicting fatigue in welded joints. *Int. J. Fatigue*.
- Timoshenko, S.P., Goodier, J.N., 1970. *Theory of elasticity*, 3rd ed. McGraw-Hill Book Company, New York, USA.
- Tong, J., Yates, J.R., Brown, M.W., 1996. Some aspects of fatigue thresholds under mode III and mixed mode III and I loadings. *Int. J. Fatigue* 18, 279–285.
- Tong, P., Pian, T.H.H., Lasry, S.J., 1973. A hybrid-element approach to crack problems in plane elasticity. *Int. J. Numer. Methods Eng.* 7, 297–308.
- Topper, T.H., Wetzel, R.M., Morrow, J., 1969. Neuber's rule applied to fatigue of notched specimens. *J. Mater.* 4, 200.
- Torabi, A., Amininejad, S., 2014. Brittle fracture in V-notches with end holes. *Int. J. Damage Mech.* doi:10.1177/1056789514538293
- Torabi, A., Berto, F., 2014. Strain energy density to assess mode II fracture in U-notched disk-type graphite plates. *Int. J. Damage Mech.* 23, 917–930.
- Torabi, A., Fakoor, M., Darbani, M., 2013. Pure shear fracture study in a brittle graphite material containing a U-notch. *Int. J. Damage Mech.* 23, 839–854.
- Torabi, A.R., 2013a. Fracture Assessment of U-Notched Graphite Plates Under Tension. *Int. J. Fract.* 181, 285–292.
- Torabi, A.R., 2013. On the use of the Equivalent Material Concept to predict tensile load-bearing capacity of ductile steel bolts containing V-shaped threads. *Eng. Fract. Mech.* 97, 136–147.
- Torabi, A.R., 2013b. Ultimate Bending Strength Evaluation of U-Notched Ductile Steel Samples Under Large-Scale Yielding Conditions. *Int. J. Fract.* 180, 261–268.
- Torabi, A.R., 2013c. Sudden Fracture from U-Notches in Fine-Grained Isostatic Graphite Under Mixed Mode I/II Loading. *Int. J. Fract.* 181, 309–316.
- Torabi, A.R., 2012. Estimation of tensile load-bearing capacity of ductile metallic materials weakened by a V-notch: The equivalent material concept. *Mater. Sci. Eng. A* 536, 249–255.
- Torabi, A.R., Ayatollahi, M.R., 2014. Compressive brittle fracture in V-notches

- with end holes. *Eur. J. Mech. - A/Solids* 45, 32–40.
- Torabi, A.R., Berto, F., 2014. Notch Fracture Toughness Evaluation for a Brittle Graphite Material. *Mater. Perform. Charact.* MPC20130041. doi:10.1520/MPC20130041
- Torabi, A.R., Berto, F., 2014. Mixed mode fracture assessment of U-notched graphite Brazilian disk specimens by means of the local energy. *Struct. Eng. Mech.* 50, 723–740.
- Torabi, A.R., Berto, F., 2013. Strain energy density to assess mode II fracture in U-notched disk-type graphite plates. *Int. J. Damage Mech.*
- Torabi, A.R., Berto, F., 2013. Fracture Assessment of Blunt V-Notched Graphite Specimens by Means of the Strain Energy Density. *Strength Mater.* 45, 635–647.
- Torabi, A.R., Campagnolo, A., Berto, F., 2016. Mode II Brittle Fracture Assessment of Key-Hole Notches by Means of the Local Energy. *J. Test. Eval.* 44. doi:10.1520/JTE20140295
- Torabi, A.R., Campagnolo, A., Berto, F., 2015. Experimental and theoretical investigation of brittle fracture in key-hole notches under mixed mode I/II loading. *Acta Mech.* 226, 2313–2322.
- Torabi, A.R., Campagnolo, A., Berto, F., 2014a. Local strain energy density to predict mode II brittle fracture in Brazilian disk specimens weakened by V-notches with end holes. *Mater. Des.* 69, 22–29.
- Torabi, A.R., Fakoor, M., Pirhadi, E., 2014b. Fracture analysis of U-notched disc-type graphite specimens under mixed mode loading. *Int. J. Solids Struct.* 51, 1287–1298.
- Torabi, A.R., Fakoor, M., Pirhadi, E., 2013. Tensile fracture in coarse-grained polycrystalline graphite weakened by a U-shaped notch. *Eng. Fract. Mech.* 111, 77–85.
- Torabi, A.R., Pirhadi, E., 2015. Stress-based criteria for brittle fracture in key-hole notches under mixed mode loading. *Eur. J. Mech. - A/Solids* 49, 1–12.
- Torabi, A.R.R., Campagnolo, A., Berto, F., 2015. Tensile fracture analysis of V-notches with end holes by means of the local energy. *Phys. Mesomech.* 18, 194–202.
- Tracey, D.M., 1971. Finite elements for determination of crack tip elastic stress intensity factors. *Eng. Fract. Mech.* 3, 255–265.
- Tran, V.-X., Leguillon, D., Krishnan, A., Xu, L.R., 2012. Interface crack initiation at V-notches along adhesive bonding in weakly bonded polymers subjected to mixed-mode loading. *Int. J. Fract.* 176, 65–79.
- Treifi, M., Oyadiji, S.O., 2013. Strain energy approach to compute stress intensity factors for isotropic homogeneous and bi-material V-notches. *Int. J. Solids Struct.* 50, 2196–2212.
- Verreman, Y., Nie, B., 1996. Early development of fatigue cracking at manual fillet welds. *Fatigue Fract. Eng. Mater. Struct.* 19, 669–681.

- Wang, J.-A.J., Liu, K.C., 2008. An innovative technique for evaluating fracture toughness of graphite materials. *J. Nucl. Mater.* 381, 177–184.
- Wang, X., Lewis, T., Bell, R., 2006. Estimations of the T-stress for small cracks at notches. *Eng. Fract. Mech.* 73, 366–375.
- Weixing, Y., 1992. On the notched strength of composite laminates. *Compos. Sci. Technol.* 45, 105–110.
- Westergaard, M.H., 1939. Bearing pressures and cracks. *J. Appl. Mech.* 6, A49–53.
- Wetzel, R.M., 1968. Smooth specimen simulation of the fatigue behavior of notches. *J. Mater. Am. Soc. Test. Mater.* 3, 646–657.
- Williams, J.G., Ewing, P.D., 1972. Fracture under complex stress - The angled crack problem. *Int. J. Fract. Mech.* 8.
- Williams, M.L., 1957. On the stress distribution at the base of a stationary crack. *J. Appl. Mech.* 24, 109–114.
- Williams, M.L., 1952. Stress singularities resulting from various boundary conditions in angular corners of plates in tension. *J Appl Mech* 19, 526–528.
- Wosu, S.N., Hui, D., Dutta, P.K., 2005. Dynamic mixed-mode I/II delamination fracture and energy release rate of unidirectional graphite/epoxy composites. *Eng. Fract. Mech.* 72, 1531–1558.
- Xeidakis, G.S., Samaras, I.S., Zacharopoulos, D.A., Papakaliatakis, G.E., 1996. Crack growth in a mixed-mode loading on marble beams under three point bending. *Int. J. Fract.* 79, 197–208.
- Xiao, Q.Z., Karihaloo, B.L., 2007. An overview of a hybrid crack element and determination of its complete displacement field. *Eng. Fract. Mech.* 74, 1107–1117.
- Xiao, Q.Z.Z., Karihaloo, B.L.L., Liu, X.Y.Y., 2004. Direct determination of SIF and higher order terms of mixed mode cracks by a hybrid crack element. *Int. J. Fract.* 125, 207–225.
- Yakubovskii, V. V., Valteris, I.J.I., 1989. Geometrical parameters of butt and fillet welds and their influence on the welded joints fatigue life, IIW Doc XIII-1326-1989.
- Yamauchi, Y., Nakano, M., Kishida, K., Okabe, T., 2001. Measurement of mixed-mode fracture toughness for brittle materials using edge-notched half-disk specimen. *Zair. Soc. Mater. Sci. Japan* 50, 229–234.
- Yamauchi, Y., Nakano, M., Kishida, K., Okabe, T., 2000. Measurement of Fracture Toughness for Brittle Materials under Mixed-Mode Impact Loading Using Center-Notched Disk Specimen. *J. Soc. Mater. Sci. Japan* 49, 1324–1329.
- Yang, J., Jin, X., Jin, N., 2014. A penny-shaped crack in an infinite linear transversely isotropic medium subjected to uniform anti-symmetric heat flux: Closed-form solution. *Eur. J. Mech. - A/Solids* 47, 254–270.

- Ye, D., Hertel, O., Vormwald, M., 2008. A unified expression of elastic–plastic notch stress–strain calculation in bodies subjected to multiaxial cyclic loading. *Int. J. Solids Struct.* 45, 6177–6189.
- Ye, D., Matsuoka, S., Suzuki, N., Maeda, Y., 2004. Further investigation of Neuber’s rule and the equivalent strain energy density (ESED) method. *Int. J. Fatigue* 26, 447–455.
- Yosibash, Z., Bussiba, A., Gilad, I., 2004. Failure criteria for brittle elastic materials. *Int. J. Fract.* 307–333.
- Yosibash, Z., Priel, E., Leguillon, D., 2006. A failure criterion for brittle elastic materials under mixed-mode loading. *Int. J. Fract.* 141, 291–312.
- Yosibash, Z., Shannon, S., 2014. Computing edge stress intensity functions (ESIFs) along circular 3-D edges. *Eng. Fract. Mech.* 117, 127–151.
- Yousefi, F., Witt, M., Zenner, H., 2001. Fatigue strength of welded joints under multiaxial loading: experiments and calculations. *Fatigue Fract. Eng. Mater. Struct.* 24, 339–355.
- Yu, H., Tanaka, K., Akiniwa, Y., 1998. Estimation of torsional fatigue strength of medium carbon steel bars with a circumferential crack by the cyclic resistance-curve method. *Fatigue Fract. Eng. Mater. Struct.* 21, 1067–1076.
- Yukio, U., Kazuo, I., Tetsuya, Y., Mitsuru, A., 1983. Characteristics of brittle fracture under general combined modes including those under bi-axial tensile loads. *Eng. Fract. Mech.* 18, 1131–1158.
- Yum, Y.-J.Y.-J., You, H., You, A.H., 2001. Pure Mode I, II and Mixed Mode Interlaminar Fracture of Graphite/Epoxy Composite Materials. *J. Reinf. Plast. Compos.* 20, 794–808.
- Yung, J.Y., Lawrence, F. V., 1989. Predicting the fatigue life of welds under combined bending and torsion, in: Brown, M., Miller, K. (Eds.), *Biaxial and Multiaxial Fatigue EGF 3*. Mechanical Engineering Publications, London, pp. 53–69.
- Zappalorto, M., Lazzarin, P., 2013. Three-dimensional elastic stress fields ahead of notches in thick plates under various loading conditions. *Eng. Fract. Mech.* 108, 75–88.
- Zappalorto, M., Lazzarin, P., 2010. A unified approach to the analysis of nonlinear stress and strain fields ahead of mode III-loaded notches and cracks. *Int. J. Solids Struct.* 47, 851–864.
- Zappalorto, M., Lazzarin, P., Yates, J.R., 2008. Elastic stress distributions for hyperbolic and parabolic notches in round sh
- Zheng, X., Zhao, K., Wang, H., Yan, J., 2003. Failure criterion with given survivability for ceramic notched elements under combined tension/torsion. *Mater. Sci. Eng. A* 357, 196–202.
- Zheng, X.L., Zhao, K., Yan, J.H., 2005. Fracture and strength of notched elements of brittle material under torsion. *Mater. Sci. Technol.* 21, 539–545.

Ringraziamenti

Le persone che devo ringraziare per essermi state vicine in questi tre anni sono davvero tante, in particolar modo quelle che hanno contribuito a rendere meravigliose molte giornate.

Prima di tutto devo ringraziare il Professor Paolo Lazzarin, per il costante incoraggiamento ed il prezioso supporto durante l'attività di ricerca, per l'enorme entusiasmo e passione per la materia che è riuscito a trasmettermi e per la fiducia che ha sempre dimostrato nei miei confronti. Lo ringrazio di cuore e dedico questo lavoro alla sua memoria. Sarà sempre per me un esempio dal punto di vista scientifico ed umano.

Un ringraziamento speciale va al Professor Filippo Berto. Lo ringrazio per il costante supporto con cui mi ha affiancato durante tutta l'attività di ricerca, per la passione ed il valore del sacrificio che mi ha trasmesso, per gli spunti di riflessione e gli utili consigli, per tutti i momenti di lavoro ma anche di amicizia che ci hanno legato e che mi hanno permesso di crescere come ricercatore. Lo ringrazio di cuore per le possibilità che mi ha dato e per quelle mi sta dando.

Ringrazio inoltre il Professor Giovanni Meneghetti, per la fiducia che ha dimostrato nei miei confronti, che non mancherò di ricambiare con impegno e dedizione.

Ringrazio i miei genitori per la loro costante presenza e per aver sempre ricambiato il mio affetto, anche nei momenti in cui non sono riuscito ad esprimerlo appieno. Li ringrazio in modo particolare perché con i loro sacrifici mi hanno permesso di intraprendere la strada della ricerca e della conoscenza.

Ringrazio di cuore mio fratello Luca per aver condiviso con me i numerosi momenti di gioia per i risultati ottenuti e per aver avuto anche la pazienza di sopportare i momenti di tensione.

Un grazie davvero unico va a Giulia, per aver sempre creduto in me, per essermi stata vicina e avermi capito, per aver sempre ricambiato il mio amore, costante e incondizionato. Lo stesso amore che ci sta conducendo verso una vita insieme ricca di gioia per essere l'uno con l'altra.

Ringrazio la famiglia di Giulia, Emiliano, Marta, Marco e Sara, che mi hanno accolto con affetto e mi hanno fatto sempre sentire parte integrante della loro famiglia.

Uno speciale ringraziamento va poi a tutti gli amici che mi hanno sostenuto e incoraggiato in questi anni: Mattia, Marco T., Stefano, Davide, Marco P., Matteo, Giovanni, Jordan, Devis, Anthony, Marco F., Andrea M.

Un grazie infine a tutti i giovani ricercatori, dottorandi, tecnici e borsisti che in questi anni ho avuto modo di conoscere e apprezzare: Alessandro, Christian, Giacomo, Pasquale, Michele, Martina, Marco, Luca, Thomas, Paolo, Lucio, Mauro, Andrea, Francesco, Elisa, Enrico, Mirco, Camilla, Sabrina.